Interplay between the microstructure and tribological performance in heat-treated high chromium cast iron alloys

Dissertation

zur Erlangung des Grades
des Doktors der Ingenieurswissenschaften
der Naturwissenschaftlich-Technischen Fakultät
der Universität des Saarlandes

UNIVERSITÄT
DES
SAARLANDES

Von

Ullal Pranav Nayak

Saarbrücken

2023

Printed with the support of the German Academic Exchange Service (DAAD)

Tag des Kolloquiums:	11. September 2023
Dekan:	Prof. Dr. Ludger Santen
Berichterstatter:	Prof. Dr.-Ing. Frank Mücklich
	Prof. Dr. mont. Christian Motz
	Prof. Dr.-Ing. Carsten Gachot
Akad. Mitglied:	Dr. Steven Quirin
Vorsitz	Prof. Dr. Guido Kickelbick

PREFACE

This dissertation is a result of the work conducted between 2018 and 2023 at the Chair of Functional Materials, Saarland University, Germany. It was carried out within the framework of the Joint European Doctoral Program in Advanced Materials Science and Engineering (DocMASE), and the German Academic Exchange Service (DAAD) Graduate School Scholarship Programme (GSSP) bearing the funding ID: 57395813.

The results published in peer-reviewed scientific journals are appended at the end of this dissertation.

U. Pranav Nayak

Saarbrücken, 2023

ACKNOWLEDGEMENTS

I would like to begin by acknowledging that a PhD is not a solitary journey but a collective effort. While my name may appear on the cover page, this dissertation is the result of the contributions and support of many individuals.

First and foremost, I express my sincere gratitude to Prof. Dr. Frank Mücklich, my first supervisor and the head of the Chair of Functional Materials (FuWe) at Saarland University, for his ever-positive approach and exceptional communication skills. I am grateful for his trust in me and for providing me with unrestricted access to everything I needed to conduct this research.

I am also immensely thankful to Prof. Dr. Christian Motz, my second supervisor, for his unwavering support in all matters related to my work. His valuable feedback, constructive criticism, and insightful suggestions greatly improved the quality of this work.

I extend my heartfelt thanks to the German Academic Exchange Service (DAAD) for their financial assistance during the initial 4.5 years of my research work.

I am grateful to Dr. Flavio Soldera, the managing director of the European School of Materials (EUSMAT), for giving me the opportunity to work within the framework of EUSMAT and the DocMase Program.

I owe a special debt of gratitude to my mentor, Dr. María Agustina Guitar (Ma'am). Her invaluable scientific discussions, encouragement, and motivation kept me focused and driven throughout this journey. Her constant guidance has been instrumental in shaping my research. I vividly remember the time when I called her 'Ma'am,' and her then three-year-old son mistook it for 'Mom' – a memory that still brings a smile to my face. I also want to acknowledge her endless support in reading and correcting my dissertation, which helped bring it to the final version where it stands now.

Additionally, I would like to reflect on the time in 2017 when Dr. Dominik Britz and Agustina conducted my interview, which eventually led to me landing a position at the institute. Their confidence in my potential has been an essential source of inspiration throughout my doctoral journey.

My sincere gratitude goes to Dr. Sebastian Suarez (Seba), who has been a constant companion during my research journey. Our daily ritual of convening over coffee at 8:15 am to engage in stimulating discussions under the sun (or rather, the ceiling) has been a tremendous source of motivation and inspiration. His insights and guidance have been invaluable in helping me navigate the challenges of my research, and I am grateful for his unwavering dedication to my success.

I would like to express my sincere appreciation to Dr. Christoph Pauly, Seba, and Mr. Bruno Alderete for their invaluable help in proofreading my dissertation and providing me with constructive feedback. Their critical eye and attention to detail have greatly improved the quality of this work, and I am grateful for their contributions.

I wish to extend my heartfelt appreciation to Dr. Martin Duarte for providing the samples to work with and for his invaluable assistance and support during my research stay in Uruguay.

I am immensely grateful to my fellow office mates in the 'Pi Raum' for their constant support, encouragement, and inspiration throughout my doctoral journey. Their presence and camaraderie have made the experience all the more fulfilling and enjoyable. I would also like to thank the members of the Iron-based Materials Group (formerly known as the Steel Group) for their fruitful discussions and scientific input. My heartfelt appreciation goes out to the members of the "Coffee Gang" for the engaging conversations and stimulating discussions that often-sparked new ideas and allowed me to broaden my horizons. The energizing cups of coffee shared during these meetings were also instrumental in keeping me refreshed and motivated.

My warmest thanks goes to all my former and current colleagues at FuWe for their steadfast support and cooperation. I acknowledge all the co-authors of the publications included in this thesis. Their contributions were crucial to the successful completion of this work.

I would like to express my heartfelt gratitude to Aniket, Poonam, Rakesh, Sandeep, Nidhi, Kasia, Gurudutt, Karthik, and members of various WhatsApp groups such as 'Lost Boys', 'Dulce de Leche', 'Panchadik in Germany', 'Until next time', etc., for their moral support, uplifting words, and motivational pep talks. I would also like to extend my sincere thanks to all the individuals who have supported me during my doctoral journey, whether directly or indirectly but could not be mentioned in this acknowledgment section.

The emergence of the COVID-19 pandemic in early 2020 posed a significant challenge to my research journey, requiring an abrupt shift to remote work and limited access to the laboratory. Despite these obstacles, I would like to express my gratitude to all those who supported me during these trying times, particularly my friends, colleagues, and supervisors who provided invaluable guidance and encouragement. I am also thankful for the resilience and resourcefulness I developed during this period.

I am also grateful to the online communities, including Reddit, 9Gag, and others, for their virtual support and a much-needed escape from academic rigor. The endless entertainment through memes, cat videos, and other light-hearted content helped me stay positive and focused, especially during times of stress and burnout.

Lastly, I am indebted to my beloved parents, U. Sadashiva Nayak and Pratibha S Nayak for their unwavering support and encouragement throughout my PhD journey. Their love, guidance, and sacrifices have been instrumental in helping me achieve this milestone in my academic career.

TABLE OF CONTENTS

ABSTRACT

In this dissertation, the microstructural evolution of a 26 wt.% Cr high chromium cast iron (HCCI) alloy was systematically investigated when subjected to varying heat treatment (HT) processes. Due to the vast number of possible parameter combinations, computational tools were utilized to optimize the HT parameters and monitor the resulting modifications before the actual experimental HT was performed. Furthermore, to understand how various microstructural constituents affected the tribological behaviour of the as-cast and heat-treated HCCI alloy, an extensive insight into the sequence of carbide precipitation and the transformation of the surrounding matrix was necessary, given the alloy's complex multi-scale, multi-phase microstructure.

A thorough investigation of the microstructure was conducted at various length scales, and a need for a specificity in the HT was established. Even though the microstructural constituents in heat-treated (HTed) samples were identical, their varying amounts and distribution had a significant impact on the final tribological behaviour, underlining the importance of matrix support in improving the tribological performance of the alloy. Finally, the results obtained from this research shed light on the feasibility of modifying the HT parameters to tailor the microstructure according to the application prerequisite.

ZUSAMMENFASSUNG

Hauptziel dieser Dissertation ist die systematische Untersuchung der mikrostrukturellen Entwicklung einer hochchromhaltigen Legierung (HCCI) mit 26 Gew.-% Cr, die verschiedene Wärmebehandlungsverfahren (HT) unterzogen wird. In Anbetracht der umfangreichen Parameterkombinationen werden vor der experimentellen HT computergestützte Werkzeuge zur Feinabstimmung der HT-Parameter und zur Überwachung der auftretenden Veränderungen eingesetzt. Um zu verstehen, wie das tribologische Verhalten der wärmebehandelten HCCI-Legierung durch die verschiedenen mikrostrukturellen Bestandteile beeinflusst wird, ist ein grundlegendes Verständnis der Karbidausscheidungssequenz und der Umwandlung der umgebenden Matrix im komplexen mehrskaligen und mehrphasigen Gefüge der Legierung von entscheidender Bedeutung.

Das Gefüge wurde über mehrere Längenskalen hinweg charakterisiert und es wurde festgestellt, dass eine Spezifität der HT erforderlich ist. Obwohl die mikrostrukturellen Bestandteile in den HT-behandelten Proben identisch waren, hatten ihre unterschiedlichen Mengen und Verteilungen einen signifikanten Einfluss auf das endgültige tribologische Verhalten, was die Bedeutung der Matrixunterstützung für die Verbesserung der tribologischen Leistung der Legierung unterstreicht. Die Ergebnisse dieser Forschung zeigen das Potenzial der HT-Parametermodifikation zur Anpassung der Mikrostruktur je nach Anwendungsvoraussetzung.

ABBREVIATIONS AND SYMBOLS

Abbreviation	Definition
1D	One-dimensional
2D	Two-dimensional
3D	Three-dimensional
AC	As-cast
APT	Atom probe tomography
AR	Abrasion-resistant
ASTM	American society for testing and materials
BSE	Backscattered electron
CALPHAD	Calculation of phase diagrams
CE	Carbon equivalent
CI	Confidence index
CLSM	Confocal laser scanning microscope
COF	Coefficient of friction
COV	Coefficient of variation
CVF	Carbide volume fraction
DSC	Differential scanning calorimetry
EBSD	Electron backscattered diffraction
EC	Eutectic carbide
EDS	Energy dispersive X-ray spectroscopy
EPMA	Electron probe micro analysis
FESEM	Field emission scanning electron microscopy

FFT	Fast Fourier Transform
FIB	Focused ion beam
FIJI	FIJI is just Image J
GB	Graphite bearing
GCI	Gray cast iron
GROD	Grain reference orientation deviation
HCCI	High chromium cast iron
HR	Heating rate
HRC	Rockwell hardness scale C
HRTEM	High resolution transmission electron microscopy
HT	Heat treatment
HV	Vickers hardness
IA	Image analysis
KAM	Kernel average misorientation
MAUD	Material analysis using diffraction
MCWCI	Multi-component white cast irons
MP	Misorientation profile
nnd	Near neighbour distance
OM	Optical microscopy
PFIB	Plasma focused ion beam
Q	Quenched
RA	Retained austenite
RT	Room temperature
SC	Secondary carbide

SCD	Sub-critical diffusion
SEM	Scanning electron microscopy
SIM	Strain induced martensite
STEM	Scanning transmission electron microscopy
TEM	Transmission electron microscopy
WCI	White cast iron
WEKA	Waikato environment for knowledge analysis
WR	Wear rate
WVL	Wear volume loss
XRD	X-ray diffraction

Symbol	**Definition**
°	Degrees
γ	Austenite
at.%	Atomic percent
α	Ferrite
C	Yield strength coefficient
α'	Martensite
t	Time
E	Elastic Modulus (GPa)
θ	Angle of diffraction (°)
E_1, E_2	Elastic modulus of material 1 and 2
σ	Standard deviation
l	Total sliding distance (mm)
H	Hardness (GPa)
ν	Poisson's ratio

μ	Mean coefficient of friction
ν_1, ν_2	Poisson's ratio of material 1 and 2
L	Liquid
M_s	Martensite start temperature (°C)
P	Applied load (N)
P_c	Critical load (N)
R	Radius (m)
S.D	Sliding direction
S_y	Yield strength (H/2.84)
T	Temperature
T_u	Undercooling range (°)
V	Wear volume (mm^3)
wt.%	Weight percent

I. INTRODUCTION

The term tribology has its etymology from the Greek word tribos (Τριβο) meaning "rubbing", and the suffix -logia (λογία) meaning "knowledge of" [1, 2]. It was first coined by Dr. J Peter Jost in 1966 in the well-known *Jost Report* commissioned by the British government to investigate the damage from wear and friction [3]. Even though the term "tribology" may be a relatively recent addition to scientific jargon, its importance has been recognized for thousands of years [4] and has piqued the curiosity of scientists since time immemorial [5, 6]. Archaeological findings have provided evidence that humans have been utilizing the principles of tribology since as early as 400,000 B.C. [7].

Tribology is a multidisciplinary field that revolves around three main areas of interest: friction, wear, and lubrication. Friction pertains to the resistance experienced by surfaces in relative motion, whereas wear refers to the loss of material due to such motion. Lubrication, on the other hand, involves the application of a fluid or solid substance to minimize the effects of friction and wear [8, 9]. The Oxford English dictionary now defines tribology as "the branch of science and technology concerned with interacting surfaces in relative motion and with associated matters (as friction, wear, lubrication, and the design of bearings)." [10].

Almost 25% of the world's annual energy production is spent in overcoming tribology-related issues. Additionally, the friction and wear-related failures in the mining and mineral sector alone constitute for about 6% of the global energy consumption [11, 12]. Other industries can also experience significant economic losses as a result of this. For instance, increased friction and wear in engines and other components in the transportation industry can lead to reduced fuel efficiency, resulting in higher fuel costs and increased emissions. In addition to these direct costs, tribology-related issues can also lead to indirect costs such as

decreased productivity, increased downtime, and degraded product quality [13]. To overcome these concerns, researchers and engineers are working to improve wear resistance by either developing new materials or modifying the microstructure of existing materials, to extend the lifespan of the application [14–17].

High chromium cast irons (HCCIs) belong to the category of abrasion-resistant (AR) white cast irons (WCIs) and are recognized as providing the best combination of abrasion resistance and toughness attainable among all the WCIs [18, 19]. Since their creation around the turn of the 20th century, continuous improvements have been made and they are already being used in applications that demand excellent wear resistance and moderate toughness in mining and mineral industries [20]. In recent decades, however, the utilization of metallurgical advancements coupled with improvements in manufacturing processes, such as thermal treatments and fabrication techniques, have broadened the range of applications of these alloys [21].

HCCIs contain between 11-30 wt.% chromium (Cr) and 2-4 wt.% carbon (C) and belong to the Fe-Cr-C ternary system [22, 23], as described in the ASTM A532 standard [24]. Additionally, they contain minor additions of molybdenum (Mo) (up to 3.5 wt.%), nickel (Ni), copper (Cu), and manganese (Mn) as secondary alloying constituents [25]. Their microstructures are characterized by the presence of hard M_7C_3 (M: Cr, Fe) eutectic carbides (EC) dispersed in a supportive and modifiable (austenite, ferrite, martensite) matrix [16, 26–28]. Moreover, the wide compositional range results in HCCI microstructures possessing up to 50% carbides by volume with a hardness between 1200-1600 HV [29, 30]. The HCCIs owe their success to this combination wherein the carbides contribute to the hardness and wear resistance, and the relatively softer matrix helps in improving the toughness [31]. Combining this with the overall associated cost of production makes it an attractive choice to be used in a myriad of industries [15, 32, 33]. They

are currently employed for components such as ore crushers, pulverizing and shot-blasting equipment, liner plates and vertical roller mill liners, etc [25, 27, 34–36].

In most commercial HCCI alloys, a typical as-cast (AC) microstructure would consist of an austenitic matrix with dispersed EC, and a thin layer of martensite at the interface [25, 28, 37–39]. It is a well-known fact that the property of any given material is mainly dictated by its microstructure and modifying it (either by alloying or heat treatment (HT)) will alter the final properties making the material versatile to be used for several different applications [40, 41]. HT processes such as destabilization or sub-critical treatments are commonly carried out to induce secondary carbide (SC) precipitation at elevated temperatures, and a partial matrix transformation to martensite upon cooling to room temperature (RT) [25, 31, 42–46].

Over the years, several works focused on the influence of alloying and HT on the final properties of these alloys with major attention directed towards finding an optimum carbide volume fraction (CVF) to obtain the maximum hardness and wear resistance [42, 44, 47–52]. In addition to the CVF, the type and nature of the SC is highly dependent on the Cr/C ratio and the HT parameters, not to mention the diverse matrix microstructures that can be produced [53–57].

Initially, the resistance to wear was thought to be mainly influenced by the hardness of the material but it is now understood that a lot of factors contribute to the overall wear resistance, such as the carbide's type, morphology, volume fraction, and its interaction with the host matrix. Therefore, the overall wear resistance can be thought of a synergistic contribution between both the carbide and the matrix that surrounds it [58, 59]. The matrix structure in HCCI alloys plays an important role in promoting resistance to micro-cracking, deformation, and spalling [60, 61].

Pearlitic and ferritic matrix structures are often considered to be undesirable as they tend to lower both wear and fracture resistance [38, 62–64]. Nevertheless, there is often conflicting information in the literature whether HT modifications made to the AC hypoeutectic HCCI alloy has improved the wear resistance or not. Some studies indicate that the presence of retained austenite (RA) helps in improving the wear resistance by virtue of its inherent ductility [54, 56, 62, 65] and others suggest possessing a harder martensitic matrix might be the better option owing to the mechanical support it could provide [38, 57, 58, 66]. Moreover, the wear behaviour of HCCI alloys is affected by more than just their microstructure. Other factors such as testing conditions, loading, movement of the contact surfaces, type and hardness of the abrasive material play a role, highlighting the complexity and variability involved in tribological testing [13, 67].

The accurate control of phase transformation and carbide precipitation during HT is crucial in tailoring the multi-phase, multi-scale microstructure of HCCI alloys, necessitating a comprehensive understanding of the mechanisms governing the transformation kinetics [68–71]. Moreover, given the difference in the size range of the phases, ranging from micron sized EC to the sub-micron sized SC, it is imperative to thoroughly characterize the microstructure and to accurately quantify the phases in any given state [72–76]. Owing to the extensive combinatorial possibilities, adjusting each parameter of the HT cycle, and performing experimental tests can be a laborious and resource-intensive endeavour. Thus, computational simulation represents a more efficient alternative in helping to select the optimal HT parameters for a given alloy composition with the targeted application in mind.

Accordingly, the main objective of this dissertation is to understand the microstructural evolution during the HT of a 26 wt.% Cr HCCI alloy and its implications on the alloy's tribological performance, with an aim to tailor the microstructure for a specific application. Microstructural characterization of the

AC and heat treated (HTed) samples will be carried out using a correlative microscopy approach comprising of optical microscopy, scanning electron microscopy and electron backscattered diffraction (OM-SEM-EBSD). Particular emphasis will be placed on controlling the size, fraction, morphology, and distribution of SC precipitation as well as its interaction with the transformed matrix during the HT process. By gaining insight into the relationship between the microstructure and tribological behaviour for the different HT conditions, the applications' longevity can be prolonged, thereby reducing the energy consumption and economic losses incurred during the run-time.

This thesis is organized into six chapters, with introduction being the first chapter. Chapter **2** offers a bibliographic review of the extensive research conducted on various HCCI alloys, with a focus on exploring the effects of alloying and varying HT parameters on microstructure and corresponding mechanical response based on relevant literature. Chapter **3** describes the various experimental techniques employed in this work to characterize the microstructure and the wear behaviour of the 26 wt.% Cr HCCI alloy in the AC and HTed state. Chapter **4** outlines how the results obtained relate to the primary objectives of the thesis and provides a thorough summary of the findings. Chapter **5** of this dissertation includes ten articles that provide a comprehensive presentation of the results, including detailed discussions of the observed effects and information about the methods employed. As such, it is recommended that the reader peruses these articles to gain a deeper understanding of the research presented in this dissertation. Chapter **6** summarizes the major conclusions drawn from this work and finally, Chapter **7** provides recommendations for future research, including potential avenues for further investigation.

2. STATE OF THE ART

2.1 Cast Irons

Cast irons, similar to steel, are categorized as ferrous alloys, but they differ in that they have higher carbon (C) levels, exceeding 2.1 wt.% and up to 4.5 wt.%. They also contain a considerable amount of silicon (Si) (1–3 wt.%), phosphorous (P), manganese (Mn) and sulphur (S) [40, 77]. A wide array of properties can be achieved in these materials by varying the solidification parameters or alloying with various metallic elements. From the iron – iron carbide (Fe-Fe_3C) phase diagram (presented in *Figure 1*), the alloys within this compositional range become liquid at temperatures between ~ 1150 °C to 1300 °C. This makes it possible to cast them with relative ease making them quite inexpensive compared to steel. Moreover, owing to the high brittleness exhibited by certain cast irons, casting is the most convenient fabrication technique [78].

During the solidification of the alloy, carbon can be forced to precipitate either as cementite or graphite depending on the silicon content. Silicon, in addition to improving the fluidity during casting, acts as a graphitizing agent resulting in the formation of graphitic flakes [21, 79]. The fracture surface of these alloys has a distinct grey appearance due to the graphite flakes and hence they are called grey cast irons (GCIs). The morphology and inherent brittleness of the graphite flakes impart poor toughness to the grey cast iron which is a major drawback. Nevertheless, GCIs have excellent damping capacity and owing to the self-lubricating characteristics of graphite, they have very good machinability and wear resistance [79]. Other elements such as nickel (Ni) and copper (Cu) favour the formation of graphite, although, not as effective as Si [80].

To differentiate grey and white cast irons, a possible initial strategy is to calculate the equivalent carbon content using the 'carbon equivalent' (CE) formula, which takes into account the Si and P levels as well [81]. The CE formula is presented in

Equation (1) and this value indicates whether the cast iron is hypoeutectic (< 4.3 wt.% C) or hypereutectic (> 4.3 wt.% C). Generally, the tendency to form white cast iron is more when the carbon equivalent value is low and cooling rate is high, whereas grey cast iron favours high carbon equivalent value and slow cooling rates [81, 82].

$$\mathrm{CE\ (wt.\%)} = \mathrm{C\ (wt.\%)} + \frac{\mathrm{Si\ (wt.\%)} + \mathrm{P\ (wt.\%)}}{3} \qquad (1)$$

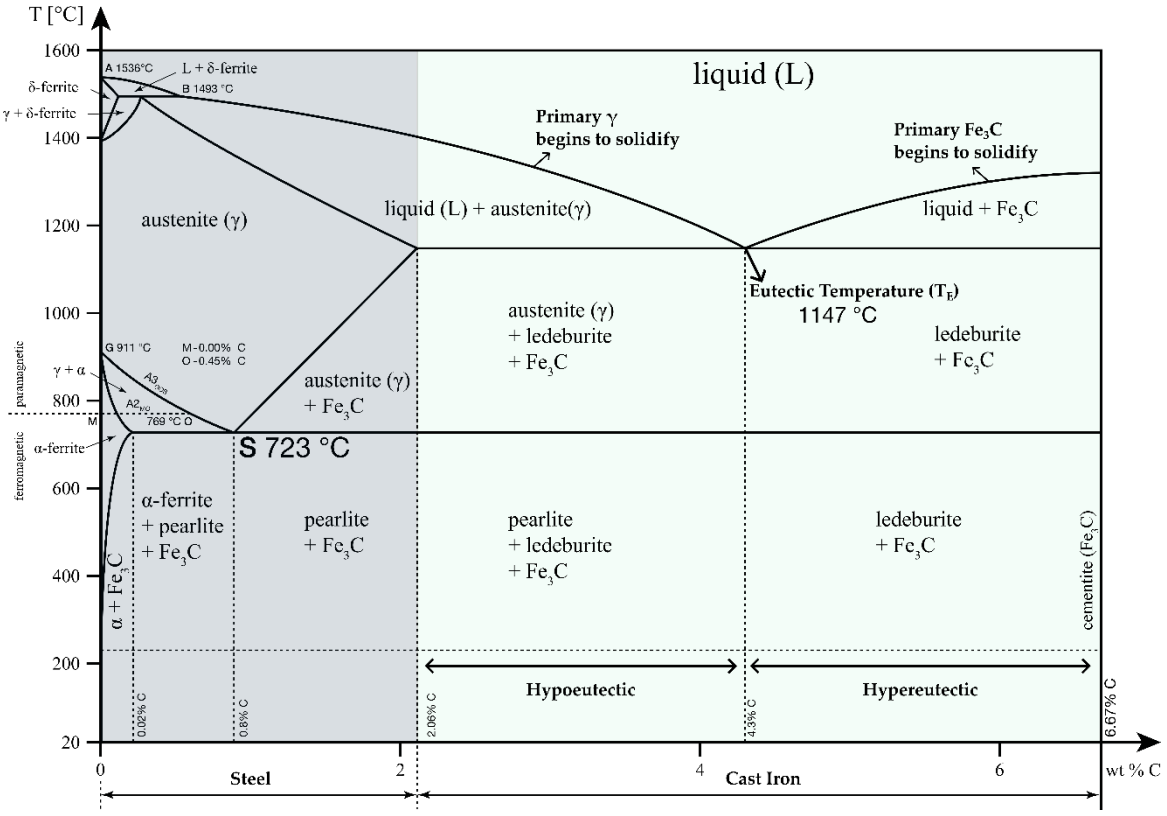

Figure 1: Iron - iron carbide (Fe-Fe3C) phase diagram. Adapted from [83].

White cast irons (WCIs) on the other hand contain chromium, which is an excellent carbide former and stabilizer resulting in carbon being precipitated in the form of hard interconnected cementite (Fe_3C) or other metallic carbides [18, 81]. Moreover, chromium increases the chill depth, suppressing the formation of graphite flakes/GCI [84], as depicted in *Figure 2*. The resulting fracture surface is distinctively white owing to the presence of these carbides (hence, white cast irons) [79]. Other transition elements such as vanadium (V), manganese (Mn),

molybdenum (Mo), titanium (Ti), etc., also favour the formation of WCIs though not as efficient as Cr. The carbides impart high hardness and excellent abrasion resistance consequently resulting in poor ductility and toughness. In order to address this issue and improve their resistance to corrosion, various grades of WCIs have been developed.

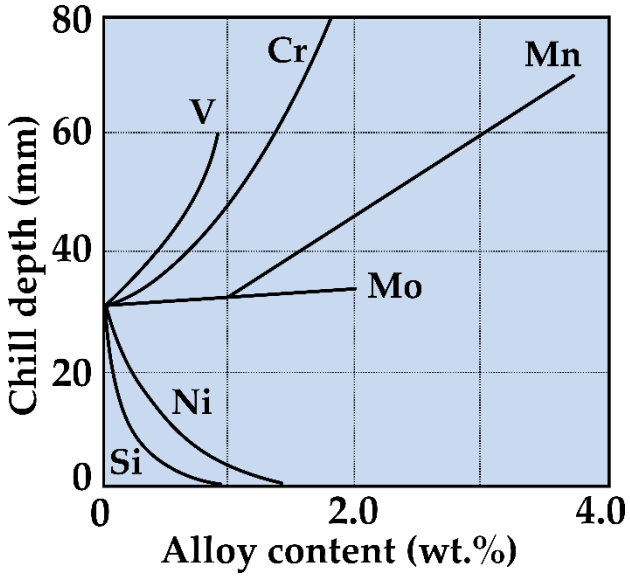

Figure 2: Influence of various alloying elements on the chill depth. In the unalloyed condition, the iron was cast against a chill and the chill depth obtained was ~ 35 mm. Adapted and redrawn from [18].

A range of abrasion-resistant white cast irons are now specified in ISO 21988 [85] and also in ASTM A532 [24]. They can be broadly classified into three categories based on the Cr level in the material:

1. Plain or unalloyed WCI and low alloy WCI (max Cr of 2 wt.%)
2. Ni-Cr WCI i.e., Ni Hard alloys (1.4 – 11 wt.% Cr)
3. High chromium cast iron (HCCI) (> 11% wt.% Cr)

The addition of Ni (3-5 wt.%) and Cr (1-4 wt.%) produces one type of medium alloy WCIs, whereas increasing the Ni (4-7 wt.%) and Cr (7-11 wt.%) content creates another class of alloys. The higher Cr content in the latter helps to transform the M_3C carbide type to M_7C_3 as the eutectic carbide, resulting in a slight increase in

fracture toughness by reducing the contiguity of the carbides [21, 86]. The matrix of these alloys is martensitic due to the presence of Ni, which is an austenite stabilizer, and they are designated as Ni-hard cast irons. In the past half-century, the abrasion wear-resistant materials have progressed from low-alloy cast iron through Ni-hard iron and finally to high chromium white cast irons [87].

2.2 High Chromium Cast Irons (HCCIs)

The first HCCI alloy was patented by Frederick M. Becket in 1917 after it was found to be less brittle, with excellent wear and corrosion resistance compared to unalloyed white irons [88]. Subsequently, several alloys containing 15-35 wt.% Cr and 1.5-3 wt.% C were developed by the Electro Metallurgical Company in the 1920s and used in high-temperature applications and to reduce the maintenance of crushing equipment [18, 89, 90]. Since the 1980s, HCCI alloys with compositions ranging from 2-4.3 wt.% C and 12-30 wt.% Cr were applied to roll materials for hot rolling [27, 87, 91]. In wear applications not demanding corrosion resistance, alloys with chromium contents up to 22% can be used but when they do require corrosion resistance (e.g., slurry pumping and processing), higher levels of chromium and molybdenum (up to 3.5 wt.%) are preferred [33, 92, 93]. The ASTM A532 provides a standard description and classification concerning abrasion resistance cast irons [24]. The high chromium cast irons containing 23-30 wt.% chromium is classified under ASTM A532 Class III Type A as shown in *Table 1*.

Although the chromium content in these alloys is quite high, the majority of this is tied up with carbon as carbides. Hence, the Cr content remaining in the matrix is quite low and other alloying elements are added to ensure sufficient hardenability, especially for thicker section sizes [38, 94–97]. Mo is usually added in amounts ranging from 0.5-3.5 wt.% to supress pearlite formation by preventing SC precipitation during cooling and increase hardenability [25, 94, 98]. Moreover, the efficacies of Ni and Cu in pearlite inhibition is improved if added in conjunction

with Mo [18, 25, 99]. The amount of Si is usually limited to 1-1.5 wt.% considering its propensity towards pearlite formation [53] and decreased hardenability [91, 96].

Table 1: ASTM standard chemical requirements (in wt.%) for abrasion-resistant cast irons. Taken from [24].

Class	Type	Designation	C	Cr	Mn	Ni	Mo
I	A	Ni-Cr-HiC	2.8–3.6	1.4–4.0	2.0 max	3.3–5.0	1.0 max
	B	Ni-Cr-LoC	2.4–3.0	1.4–4.0	2.0 max	3.3–5.0	1.0 max
	C	Ni-Cr-GB	2.5–3.7	1.0–2.5	2.0 max	4.0 max	1.0 max
	D	Ni-HiCr	2.5–3.6	7.0–11.0	2.0 max	4.5-7.0	1.5 max
II	A	12% Cr	2.0–3.3	11.0–14.0	2.0 max	2.5 max	3.0 max
	B	15% Cr-Mo	2.0–3.3	14.0–18.0	2.0 max	2.5max	3.0 max
	D	20% Cr-Mo	2.0–3.3	18.0–23.0	2.0 max	2.5max	3.0 max
III*	**A**	**25% Cr**	**2.0–3.3**	**23.0–30.0**	**2.0 max**	**2.5max**	**3.0 max**

* Additionally, Si up to 1.5%, Cu up to 1.2%, P and S up to 0.1% max.
HiC = High Carbon; LoC = Low Carbon; GB = Graphite Bearing.

Despite the presence of several alloying elements, the phase equilibrium of HCCI alloys can be simplified to the Fe-Cr-C ternary system. Over the years, this system has been extensively studied and reviewed by various researchers [22, 23, 100–102]. In fact, the Fe-Cr-C metastable liquidus surface (as presented in *Figure 3*), governs the solidification behaviour of 95% of today's commercial AR irons [18] and majority of the commercially employed HCCI alloys solidify within the primary austenitic field, as indicated by the dashed enclosure in *Figure 3* [95]. The blue dot indicates the HCCI composition (~ 26 wt.% Cr and 2.5 wt.% C) used in the current work.

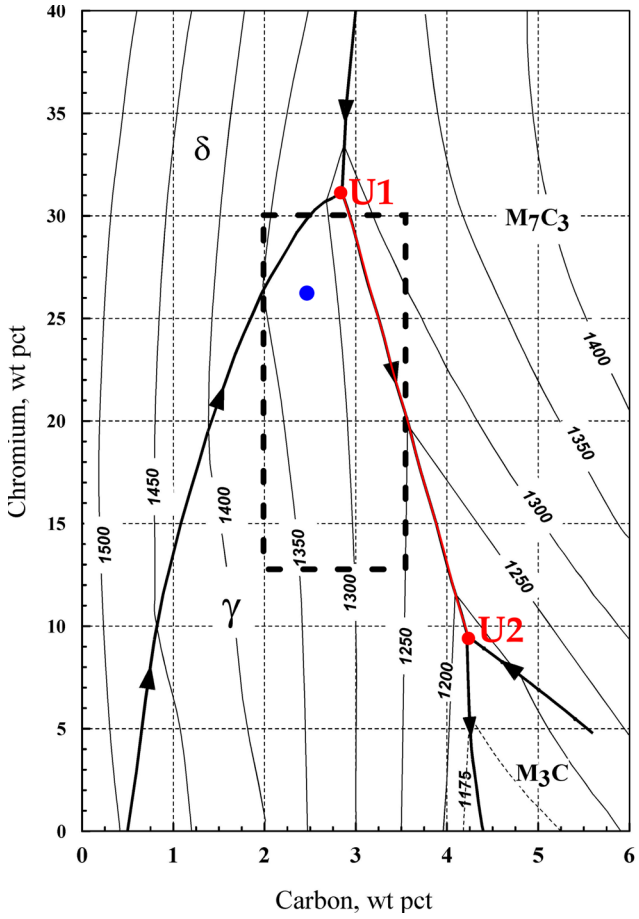

Figure 3: 2D representation of Fe-rich corner of the metastable liquidus surface of the Fe-Cr-C system [100] *(Adapted from* [18]*). The rectangular enclosure represents the majority of the commercially used HCCI alloys* [25]*, and the blue dot indicates the HCCI composition used in the current work/present dissertation.*

By adjusting the carbon content, the HCCI alloy can either solidify as hypoeutectic, eutectic, or hypereutectic composition [18, 103, 104], as observed from *Figure 1*. The solidification of these alloys proceeds initially by the formation of a ferrous phase in a dendritic structure until the temperature reaches the eutectic level, where the reaction, given by the U1-U2 line (marked in red) in *Figure 3* takes place [18, 100]. It is described as:

$$\text{Liquid (L)} \rightarrow \gamma \text{ (austenite)} + M_7C_3 \text{ (EC)} \qquad (2)$$

Where M_7C_3 is the EC that forms (M represents the metallic species, most commonly a mixture of Cr and Fe). Although equilibrium solidification (to room temperature) would result in a ferritic matrix (see *Figure 1*), the final microstructure

primarily contains an austenitic matrix (pro-eutectic + eutectic austenite) indicating a non-equilibrium nature of solidification.

HCCIs can therefore be considered as 'composite materials' composing of large EC dispersed in a softer ferrous matrix. The M_7C_3 carbides contribute to the hardness and wear resistance whereas the relatively softer matrix helps in improving the toughness of the HCCI alloy. The hardness of the M_7C_3 carbide is in the range of 1200 HV, which can go up to 1600 HV depending on the composition [29, 105]. This combination renders them as the most abrasion resistant of all ferrous alloys [18, 19, 34]. Their unmatched wear resistance makes them a preferred choice in the cement and mining industries for producing ball mill liners, grinding and pulverizing equipment, gears, piston rings, blades, etc [53, 70, 90, 106–108].

Hypereutectic HCCI alloys, on the other hand, solidify first in the primary M_7C_3 region until reaching the eutectic temperature where the remaining liquid undergoes a eutectic reaction [95, 109]. The increased C and Cr content results in a higher CVF, inevitably increasing the bulk hardness compared to the hypoeutectic HCCI alloys. The higher CVF may be tempting to employ these alloys for wear-related applications, but caution must be exercised as the primary M_7C_3 carbides are larger and coarser which can have a negative influence on the wear resistance [92, 109]. Hence, many studies have explored the influence of alloy addition aiming to refine the solidification structure and improve the final properties [47, 110–115]. Nevertheless, hypereutectic variants are extensively used as hard facing alloys in aggressive environments [116–118]. While there are several studies devoted to hypereutectic HCCI alloys [92, 109, 110, 113, 115, 119–125], the focus of this dissertation is on the hypoeutectic variant.

2.3 Influence of Alloying

In HCCI alloys, increasing the Cr content will modify the type and nature of the eutectic carbides (EC), from a continuous M_3C type to a discontinuous M_7C_3 type [23, 28]. Given the inherent brittleness associated with the carbide, continuous precipitates are not favoured for abrasion resistance and therefore, the discontinuous, and relatively tougher M_7C_3 carbides are advantageous [38]. Nevertheless, the HCCI alloys generally possess a relatively low toughness ($K_{IC} < 30$ MPa $m^{-0.5}$) [15].

One way to alleviate this is to refine and modify the EC structure through inoculation during solidification/casting [25, 112, 126]. Furthermore, when the carbide morphology is rounded, it can effectively minimize stress concentration at the sharp carbide needle tips, thereby reducing the likelihood of crack initiation [127–129]. The influence of several alloying elements such as Ti [47, 111, 130], Mo [49, 131, 132], W [50, 133–135], Nb [107, 136, 137], V [129, 138, 139], etc., on the solidification behaviour of the as-cast melt and the subsequent tribological behaviour have been assessed. The aim of these additions is usually to achieve some modification of the eutectic carbide structure, although they may improve the hardenability of the matrix.

For instance, Radulovic et al. [129] found that the Fe-C-Cr-V alloy with a V content of 3.28 wt.% exhibited superior abrasion resistance compared to a basic Fe-C-Cr alloy, with a 27% increase in performance. This improvement was mainly attributed to a higher volume fraction of carbide phase, a finer and more uniform structure, a smaller distance between M_7C_3 carbide particles, and changes in the morphology of eutectic colonies that helped enhance wear resistance.

Apart from the usual incorporation of transition elements, the addition of B and rare-earths on the solidification and sliding behaviour were also examined [48, 112, 140]. The presence of B is believed to reduce the carbon solubility in austenite, leading to a higher number of carbide nuclei and, consequently, a greater quantity

of fine carbides in the solidified structure. Furthermore, the rare-earth additives modify the eutectic growth front, such that the austenite phase precedes the carbide phase, leading to a refined carbide structure [112, 140].

The term "multi-component white cast irons" (MCWCIs) has been recently coined by researchers to describe the simultaneous addition of several transition elements (such as Ti, V, Nb, and Mo) in order to leverage the potential synergistic effects between each alloying element [141–144]. The inclusion of carbide-forming elements was found to significantly enhance the hardness of the alloy through various mechanisms. Vanadium, for instance, was observed to completely partition into the eutectic carbide phase, increasing both the volume fraction of this phase and the overall hardness of the alloy. Similarly, niobium and titanium formed hard NbC and TiC particles, respectively, which refined the structure of the iron and contributed to the overall increase in hardness [144].

While it is advantageous to add various alloying elements to induce EC modifications during solidification, the high cost of re-melting large casts makes it crucial to consider alternative approaches. One such approach is to exploit the solid-state transformation that takes place within the microstructure of HCCI alloys by subjecting them to a variety of heat treatment processes.

2.4 Influence of Heat Treatment

Over the years, several studies on the influence of various heat treatments on the microstructure and properties of HCCIs have been carried out [25, 33, 35, 43, 45, 55, 68, 106, 145–151]. Destabilization of the carbon supersaturated austenite is the most common HT for HCCI, and it is typically carried out at temperatures ranging from 900-1150 °C and holding times up to 8 hours [31, 43, 44, 52, 53, 55, 68]. This heat treatment will cause a partial matrix transformation, in addition to the precipitation of fine SC, whereas the EC remain relatively unchanged [25, 31]. A general schematic of the microstructural constituents present in as-cast and heat-treated hypoeutectic HCCI alloys is presented in *Figure 4*.

The destabilization process allows carbon and chromium to come out of the austenitic matrix by precipitating Cr-rich SC. The carbon depletion from the austenite results in an increase of the martensite start temperature (M_s), allowing the HCCI to be hardened by both carbide precipitation and martensite formation [55, 70, 106, 152–155] during quenching. Resulting microstructures typically consist of up to 50% carbides by volume (EC + SC) in a hardened martensitic matrix with a hardness of ~ 700 HV. Moreover, some austenite will be retained upon cooling, although, quenching it to cryogenic temperatures significantly reduces the percentage [42, 156, 157].

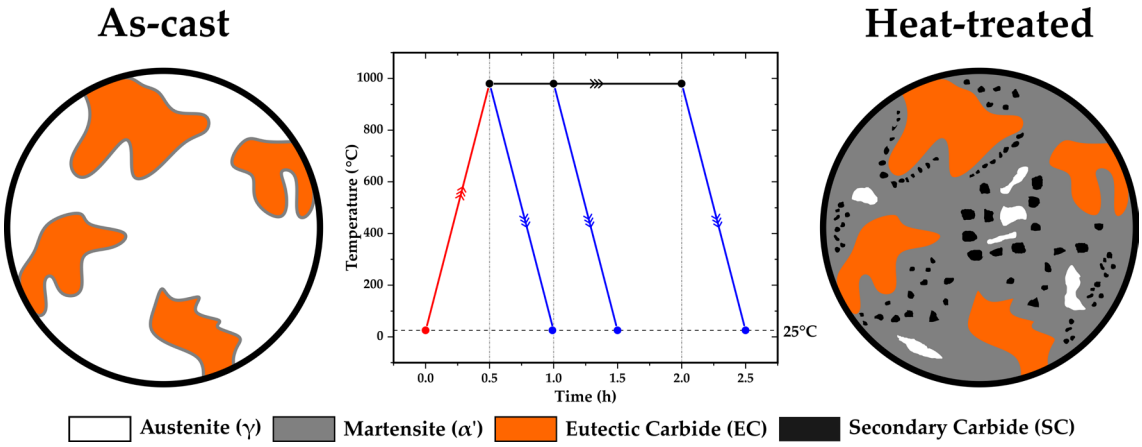

Figure 4: Schematic of the typical as-cast and heat-treated (destabilized) microstructure in hypoeutectic HCCI alloys.

The type of secondary carbides formed i.e., MC (2400-4000 HV [158]), M_7C_3 (1200-1600 HV [29, 105]), M_3C (800-1000 HV [159]) or $M_{23}C_6$ (1600-2520 HV [160])) depends on several factors, including the destabilization temperature, the alloy composition (especially Cr/C ratio), and the destabilization holding time [25, 92, 98, 126, 161]. Precipitation of M_7C_3 is expected for alloys with lower Cr content (15-20 wt.%) and Cr/C < 6.8 [25, 31], whereas for alloys with higher Cr content (> 25 wt.%) and Cr/C > 6.8, the precipitated carbides are of the $M_{23}C_6$ type [25, 44, 53, 55].

Performing destabilization at higher temperatures can reduce the driving force for carbide precipitation, which leads to a lower M_s temperature and greater retention of austenite in the martensitic matrix, resulting in a lower overall material hardness

[18, 25]. However, destabilization at lower temperatures can lead to a higher amount of carbide precipitation and a lower hardness martensite due to the low carbon content [25, 36, 53, 106]. Therefore, for each composition, there is an optimum destabilization temperature to achieve maximum hardness, as indicated by *Figure 5*.

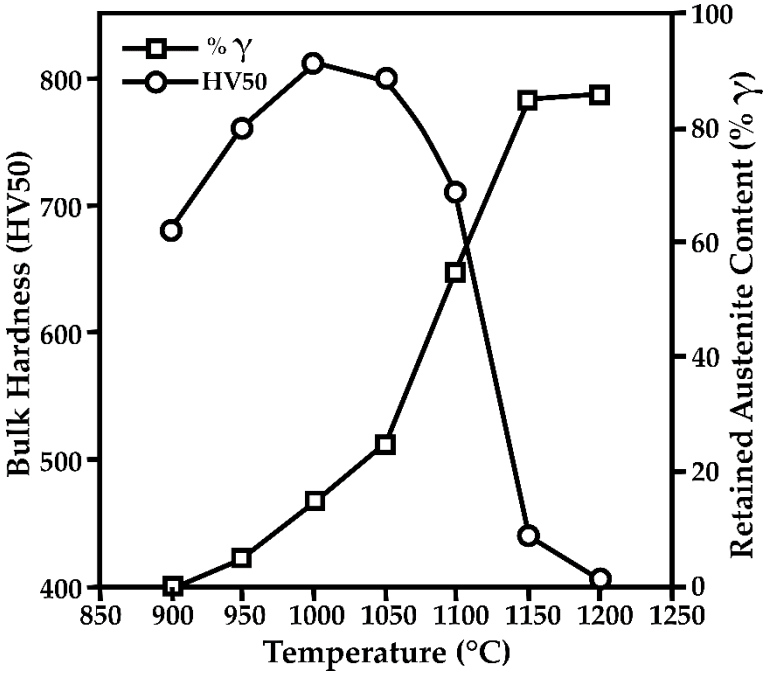

Figure 5: Influence of destabilization temperature on hardness and retained austenite content. Redrawn from [91].

Bedolla-Jacuinde et al. [68] analysed the influence of varying destabilization temperatures and times on the precipitation of secondary carbides. The 17 wt.% Cr HCCI was destabilized at temperatures between 900 °C and 1150 °C with times ranging from 5 min. to 8 h. It was seen that lower destabilization temperature and longer holding time resulted in a larger volume of secondary carbide precipitation as shown in *Figure 6* (a). Irrespective of the destabilization temperature and holding time, the volume fraction of the eutectic carbides (precipitated as M_7C_3) remained unchanged. At higher temperatures, the maximum volume fraction of secondary carbides was reached much faster but longer times resulted in an increase of the carbides' size. This, combined with the increased retained austenite

resulted in a lowering of the materials' hardness as shown in *Figure 6* (b)-(d). This was corroborated by other studies as well [35, 53, 55, 162].

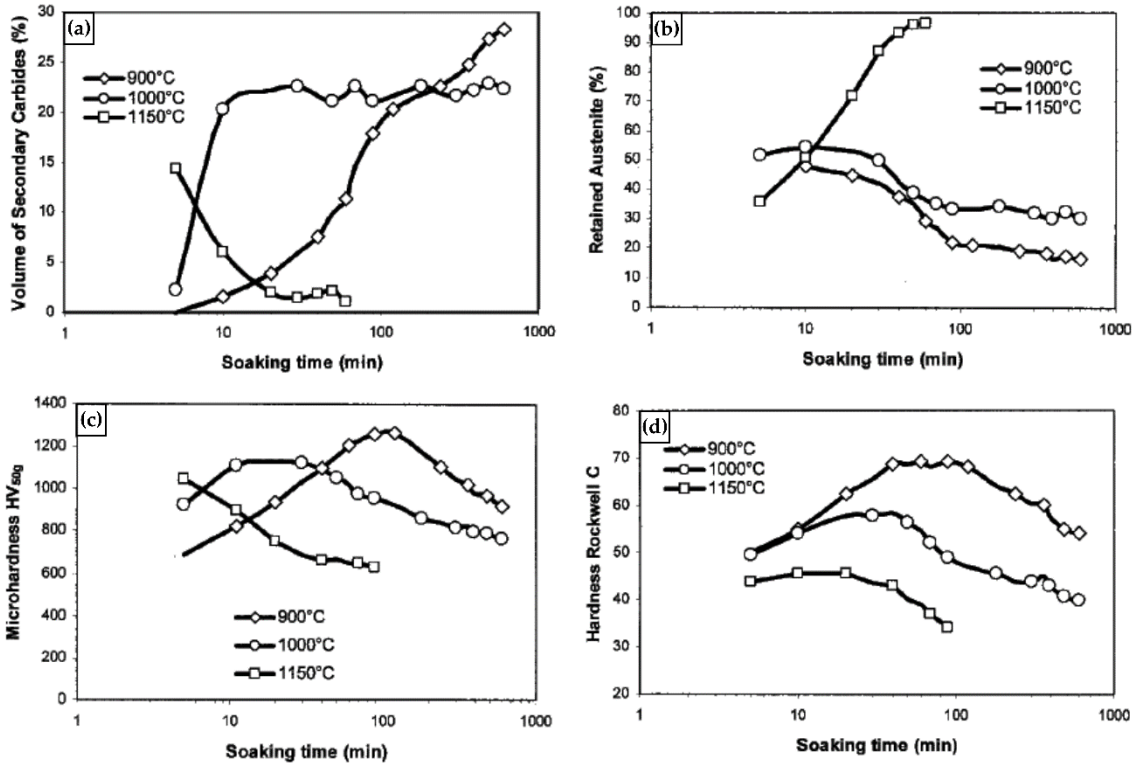

Figure 6: The influence of destabilization temperature and soaking time on (a) SC CVF, (b) RA, (c) Microhardness and (d) Bulk hardness of the 17 wt.% Cr HCCI alloy. Taken from [68].

In addition to destabilization, a sub-critical treatment (tempering) is employed to reduce the amount of retained austenite and increase the resistance to spalling, with temperatures ranging between 200-650 °C and times between 8-12 h [25, 33, 36, 163, 164]. Furthermore, the complexity of multi-step HT processes that incorporate both destabilization and tempering treatments is heightened by the fact that the final microstructure is impacted not only by the different HT parameters used but also by the sequence in which they are applied [33].

In a recent study, Guitar et al. [31] applied a multi-step HT process to a 16 wt.% Cr HCCI alloy that involved carrying out the sub-critical treatment immediately after destabilizing the austenite, followed by a second destabilization step and finally, air cooling. The heat-treated samples showed marked improvements in hardness and wear resistance compared to the as-cast, which was attributed to the

precipitation of SC and the matrix transformation to martensite. Interestingly, despite the similar nature of the microstructural constituents between the multi-step HT sample and the destabilized sample, the wear rate had reduced by ~ 70% in the former, highlighting the criticality between the carbide-matrix interplay.

As mills and crushers have become larger and more efficient in recent decades, it is imperative to have a sound understanding of the SC precipitation and their relationship with the parent matrix. Moreover, it is advantageous to explore alternative heat treatments to tailor the microstructure, aiming for a specific application. Considering the extensive parametrical combinations, adjusting each parameter of the HT cycle, and performing experimental tests can be a laborious and resource-intensive endeavour. Thus, computational simulation represents a more efficient alternative in helping to select the optimal HT parameters for a given alloy composition with the targeted application in mind.

Comprehension of the phase diagram and phase equilibria enables large number of isothermal sections and isopleths to be plotted, facilitating the detailed study of their variation with temperature or composition [21]. A wide range of calculation codes are now available, and they are progressively becoming more advanced in their ability to accurately describe phase interactions. Noteworthy examples include FactSage® [165], MatCalc [166], Pandat® [167], Thermocalc® [168], etc. While complete phase diagrams exist for some binary and a few ternary alloys, their construction becomes increasingly difficult with each additional element due to the growing number of parameters. Moreover, in the case of multicomponent systems, the calculations can quickly become cumbersome, even for powerful computers [169]. MatCalc (Materials Calculator) is a thermo-kinetic software package designed to simulate precipitation kinetics that occur during various metallurgical processes [166]. It uses the CALPHAD type database, which is currently the only theoretical approach for performing thermodynamic and kinetic calculations in multicomponent systems [170].

Studies combining simulation and experimentation have previously been carried out. Li et al. [171] utilized the Thermocalc software to compute the phase diagram of a 15 wt.% Cr HCCI alloy and compared the predicted precipitation sequence with differential scanning calorimetry (DSC) measurements, with the results in accordance with each other. Similarly, Albertin et al. [172] successfully employed computational thermodynamics (Thermocalc) to analyse different HCCI compositions with the aim of optimizing hardness and wear resistance after thermal treatments. In another study, Akyildiz et al. [173] used MatCalc to simulate pseudo-binary phase diagrams for two HCCI alloys with varying Mo contents. The predicted transformation temperatures were later compared to the DSC values to matching success. In this work, the necessary computational simulations will be performed using MatCalc.

2.5 Tribological Ambivalence

The hardness of a material was traditionally considered as the primary factor affecting its wear resistance, based on Archard's empirical findings [174]. However, further research has revealed that a variety of factors, including carbide type, morphology, and volume fraction, as well as its interaction with the host matrix, contribute to the overall wear resistance in multi-component systems [54, 59]. Despite the crucial contribution of the hard M_7C_3 carbides in improving the overall wear resistance of the HCCI alloy, the degree of mechanical support provided by the matrix structure plays a pivotal role [18, 175], as it promotes resistance to micro-cracking, deformation, and spalling [31, 60]. The studies carried out by Zum Gahr et. al. [54] and Doğan et. al. [176] revealed that while the hardness of the material increased with greater CVF, there was no commensurate increase in the material's resistance to wear. In fact, in the study carried out by Doğan et. al. [176], it was observed that the 26 wt.% Cr WCI with an austenitic matrix and a CVF of 28% showed a decrease in the volume wear rate by almost 50% compared to the 16 wt.% Cr WCI with a pearlitic/bainitic matrix having a CVF of 45%, as indicated

by the red squares in *Figure 7*. Furthermore, the stereological characteristics of the SC (size, type, volume fraction, etc.) may have an influence on the overall wear behaviour, as in the case of low-stress abrasion applications [139, 177, 178].

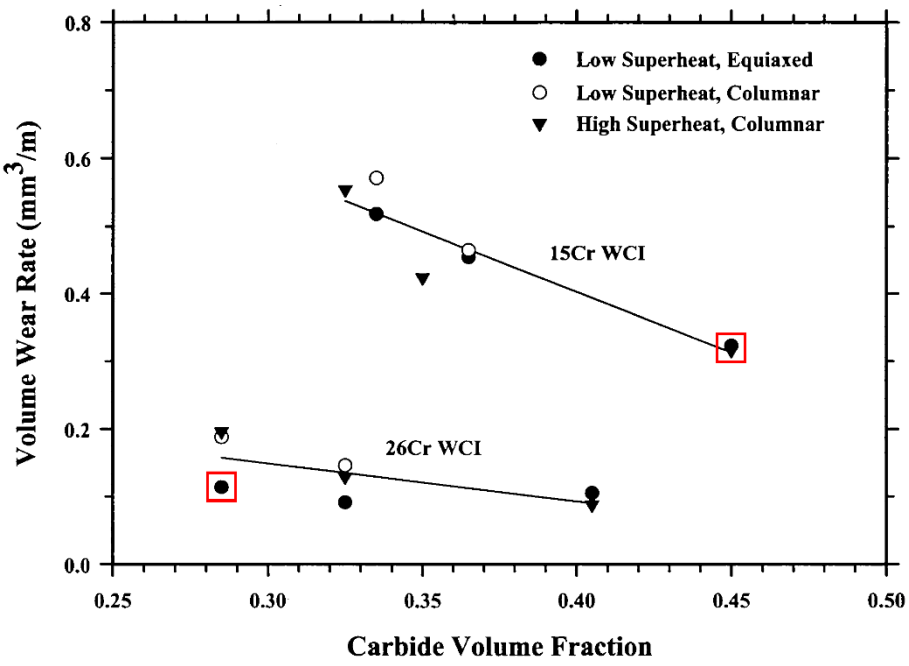

Figure 7: Influence of carbide volume fraction on the abrasion rates of HCCIs. Adapted from [176].

Pearlitic and ferritic matrix structures are often considered to be undesirable for their negative effects on wear and fracture resistance [38, 62–64]. Nevertheless, there is an ongoing debate about the best matrix structure for HCCI alloys with regards to wear performance. Some researchers argue that an as-cast austenitic matrix is superior [54, 56, 62, 65], whereas others argue that heat-treated martensitic matrix is more effective [38, 57, 58, 66]. Generally, it is observed that low-stress abrasion typically favours the martensitic microstructure, whereas high-stress abrasion, especially with very hard abrasives, tends to favour the austenitic matrix for better performance. This can be attributed to the strain hardening capability, strain-induced martensite, and higher ductility of the austenitic matrix [25].

Additionally, numerous studies indicate a tendency of increasing wear resistance with increasing CVF when an abrasive softer than the M_7C_3 carbide is used,

although there is no consensus among the community when the hardness of the abrasive (SiC/Al_2O_3) exceeds that of the carbide [54, 65]. Moreover, the wear behaviour of HCCI alloys is affected by more than just their microstructure. Other factors such as testing conditions, loading, movement of the contact surfaces, type and hardness of the abrasive material play a role, highlighting the complexity and variability involved in tribological testing [18].

In addition to the wear-induced microstructural modifications taking place at the sample surface, examining the microstructure underneath the wear track would be beneficial for further analysis [179, 180]. Moreover, in a ball on flat configuration (non-conformal contact), as the maximum stress is experienced at the centre of the wear track, making transverse cuts across the entirety of the track would help in gaining a better insight into the tribological behaviour of the HCCI alloy [179–182]. Microstructural characterization of the sub-surface was previously done to assess the deformation behaviour of Cu and Fe [181, 183, 184]. Furthermore, investigating the sub-surface microstructure proved to be highly valuable in comprehending the tribological behaviour of certain HCCI alloys as well [185–187].

Penagos et al. [185] studied the effect of structure refinement on the wear resistance of a hypoeutectic HCCI alloy that was cast in a single mould, resulting in a microstructure with a gradient of fine to coarse M_7C_3 carbides. Analysis of the sub-surface revealed that the microstructure with coarse M_7C_3 carbides exhibited sub-critical cracking and no fracture, resulting in a higher wear resistance than its finer counterpart. The larger carbides acted as a barrier to abrasive grit. Matsuo et al. [186] demonstrated that spray-formed HCCI alloys had improved wear resistance over conventionally cast HCCI alloys, as the former possessed a finer and more homogeneously distributed M_7C_3 carbide and a well-balanced matrix consisting of austenite and martensite, resulting in deeper cracks underneath the wear track in the latter. The two investigations evince a paradoxical relation, wherein one study advocates the superiority of a finer carbide distribution for enhanced wear resistance, while the other contends the contrary. This dichotomy highlights the

intricate interplay between microstructure and wear and underscores the influence of testing conditions.

The previous investigations demonstrate that adjusting the heat treatment parameters and modifying the chemical composition of HCCI alloys can have a significant impact on the type and nature of secondary carbides, opening up a wide range of potential applications. While it is widely acknowledged that the properties of high-chromium white irons, such as abrasion resistance, toughness, and impact resistance, are mainly determined by the carbide structure characteristics, including volume fraction, size, and hardness, the role of the matrix remains less definitively comprehended. Hence, major focus will be devoted in understanding the underlying mechanisms that govern the nature and characteristics of the secondary carbide precipitation and their interaction with the matrix during each step of the heat treatment process. The ultimate objective is to tailor the microstructure for a specific and targeted application.

3. EXPERIMENTAL METHODOLOGY

3.1 Material and Heat Treatment

The material used in this work was a HCCI alloy containing 26 wt.% Cr. It was manufactured in an arc furnace and casted at 1450 °C into a rectangular (Y) shaped mould hardened with phenolic resin. The AC samples were cut from the lower half of the test block measuring 175 × 90 × 25 mm to ensure that they were free from casting defects. Optical emission spectroscopy (GNR Metal Lab 75/80) was used to determine the bulk chemical composition which is represented in *Table 2*.

Table 2: Bulk chemical composition (in wt.%) of the HCCI alloy measured by optical emission spectroscopy.

Alloy	**C**	**Cr**	**Mn**	**Ni**	**Mo**	**Si**	**Cu**	**P**	**S**	**Fe**
26% HCCI	2.53	26.60	0.66	0.26	0.24	0.37	0.03	<0.01	0.04	Bal.

The AC samples were further cut into smaller pieces measuring 20 × 20 × 10 mm using an abrasive disc. The AC samples were also subjected to a variety of HT processes with varying parameters to induce changes within the microstructure. *Figure 8* represents a general schematic of the HT, whereas the specific treatments can be found in papers ***IV***, ***VII***, ***IX*** and ***X***. It is worth mentioning that the specific destabilization HT parameters were selected based on the thermodynamic and kinetic simulations performed using MatCalc, and in previous works, that used 980 °C as 'commercial HT' [106, 166]. Paper ***IV*** further elaborates on this aspect.

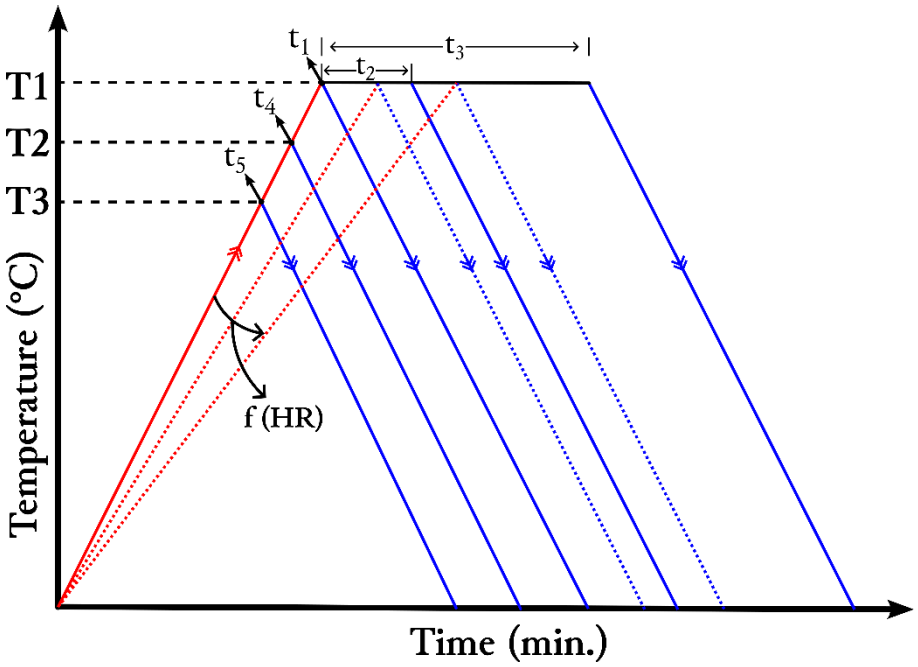

Figure 8: Schematic of the heat treatment (HT) employed in this work.

Both the AC and the HTed samples were hot mounted in a conductive resin and metallographically prepared following the protocol detailed in paper ***II*** [188], which basically involved grinding using silicon carbide (SiC) paper with a decreasing grit size (up to P1200), polishing using a diamond suspension (down to 1 μm) and a final polishing round with a 0.04 μm colloidal silica suspension (OPS) to obtain a scratch-free, mirror polished surface. It is beneficial to note that after each step, the samples were washed with water, rinsed with ethanol, and air-dried. Additionally, before proceeding with the next stage, the samples were slightly wetted with water to ensure that the sample is lubricated enough to endure the sudden initial jerk.

The polished samples were later etched with different etchants depending on the purpose. In all cases, the samples were immersed in the freshly prepared etchant for the appropriate time, rinsed with water and ethanol, and air-dried. Finally, the etched samples were ultrasonicated in isopropanol for 5 minutes before air-drying. Paper ***II*** comprehensively describes the procedure in obtaining the optimal etching parameters along with the etching methodology. *Table 3* summarizes the etching specifics employed.

Table 3: Summary of the etching specifics and the intended purpose.

Etchant	Composition	Etching Parameters		Objective
		Temperature	Time	
Vilella's Reagent	100mL Ethanol + 5mL HCl + 1g Picric Acid	Room temperature (RT)	7 - 10s	General microstructure observation
Modified Murakami's reagent	4g potassium ferricyanide + 8g Sodium hydroxide + 100mL water	RT	15s	Carbide quantification
Deep etchant	10% HCl in Methanol	RT	24h	3D carbide network observation

3.2 Microstructural Characterization and Carbide Quantification

Optical microscopy (OM) observations of the polished and etched samples were carried out using a LEXT OLS 4100 confocal laser scanning microscope (CLSM) (Olympus Corporation, Tokyo, Japan). The fine microstructural details of the samples were obtained using a FEI Helios™ Nanolab 600 field emission SEM (FE-SEM) in conjunction with a Thermo-Fisher Helios™ G4 PFIB (Plasma Focused-Ion Beam) CXe DualBeam™ FIB/SEM. The SEM was operated at an acceleration voltage of 5 – 15 kV and a beam current of 1.4 – 1.6 nA. Additionally, the individual matrix and EC compositions in the AC sample was measured by electron probe microanalysis (EMPA) (8900 R JEOL Superprobe) and the mean of 10 readings was considered.

The back-scattered electron (BSE) micrographs obtained from the SEM were used to determine the stereological characteristics (volume fraction, size, near neighbour distance (nnd) etc.) of the SC, using the open-source image analysis software, FIJI (Fiji Is Just ImageJ) [189]. The micrographs were captured at a magnification of 2500x (~ 50 × 50 μm^2) and at least 5 micrographs were considered

in each case. A threshold segmentation was applied to the BSE micrographs to obtain a binarized image comprising of the carbides and the matrix. This was followed by selectively eliminating the larger EC from the image and performing the particle analysis on the SC. Further details concerning the determination of the SC specifics is given in paper ***III*** [190].

The electron backscattered diffraction (EBSD) measurements were performed using the FEI Helios™ Nanolab 600 FE-SEM workstation equipped with an EDAX Hikari EBSD camera. An acceleration voltage of 20 kV, a beam current of 11 nA, 5 × 5 binning on a hexagonal grid and a step size of 30 - 100 nm were employed for all measurements. The EBSD data was analysed using the Orientation Imaging Microscopy (OIM™ v. 7) Data Analysis software by EDAX Corporation. The post processing of the obtained EBSD dataset commenced by applying the standard noise reduction algorithms (grain confidence index (CI) standardization and grain dilation), followed by removal of all points with a CI of less than 0.1.

Phase identification in the AC and HTed samples was performed by carrying out X-ray diffraction (XRD) measurements at room temperature using a PANalytical Empyrean diffractometer system equipped with a Bragg Brentano^{HD} module and an ultra-fast PIXcel^{3D} detector in 1D scanning mode. A symmetrical θ-2θ scan geometry and Cobalt (Co) (Kα = 0.1791 nm) radiation source were used. The acceleration voltage and current applied during the measurements were 40 kV and 40 mA, respectively. The scans were made over a 2θ range of 40° to 130° with a step size of 0.013° and a counting time of 250 s, constituting a total scanning time of approximately 2 hours. The peak identification was performed using the X'Pert High Score Plus software. Additionally, the volume fraction of the RA in the HTed samples was estimated by the Rietveld refinement approach [191], using the software Material Analysis Using Diffraction (MAUD) [192]. Further details are mentioned in section 2.3 of paper ***VII*** [193].

Owing to the sub-μm size of the SC, transmission electron microscopy (TEM) in conjunction with high-resolution TEM (HRTEM), and atom probe tomography (APT) measurements were used to identify the SC type. TEM was performed using a JEOL JEM-2010F (JEOL, Ltd.) equipped with a LaB_6 source operating at 200 kV. HRTEM measurements were carried out using a JEOL ARM 200 TEM/STEM equipped with a Cs corrector (CEOS GmbH), whereas a LEAP™ 3000X HR (CAMECA Instruments, Madison, WI, USA) was used for performing APT. The carbides were indexed on Fast Fourier Transform (FFT) images from HTREM micrographs, and the CrysTBox software was used to identify the SC type [194]. The APT measurements were carried out in voltage mode at a temperature between 60 - 70 K, pulse frequency 200 kHz, voltage pulse 20% of standing voltage and evaporation target of 1 event per 200 pulses. The TEM and APT samples were prepared with the FIB (FEI Helios™ Nanolab 600) as detailed in [195] and [196], respectively. In order to reduce the gallium (Ga) contamination, a final polishing with 5 kV (TEM samples) and 2 kV (APT samples) was performed. Further specifications concerning the HRTEM and APT measurements are given in the 'Materials and Methodology' section in paper ***IX***.

During the quantification of carbon-rich phases, it was observed that there were challenges associated with accurately measuring the carbon levels. This was due to the overlapping of molecular carbon preferential evaporation and pile-up effects, which could result in both overestimation and underestimation. A detailed analysis of these effects and their impact on carbon quantification was provided in the 'Supplementary material' in paper ***IX***.

3.3 Hardness

Hardness was measured across all scales ranging from bulk to micro to nano depending on the objective. The bulk hardness of the HCCI samples were measured using the Rockwell hardness method, with a diamond indenter and a load of 150 kgf (HRC). The matrix hardness on the other hand was determined by

the Vickers method using a Struers Dura Scan 50 microhardness tester with a load of 0.9807 N (HV 0.1). The load was chosen to ensure that the matrix hardness measurement would not be affected by the surrounding entities (EC and/or the interfacial α') and the indentation marks were clearly visible under the microscope. In both cases, the indentation was held for 15 s and the readings were averaged over 15-20 measurements.

Nanoindentation (NI) measurements were carried out using a Hysitron TI900 TriboIndenter® Nanomechanical Testing System with nanoDMA-upgrade with a Berkovich 142.3°, 3-sided pyramidal indenter. In this work, NI was performed both on the surface and sub-surface of the HCCI samples to determine the individual phase hardness (H) and reduced indentation modulus (E_r) in the former [197], and to observe the variation of the matrix hardness underneath the wear track in the latter [198]. The values of H (in GPa) and E_r (in GPa) were obtained after analysing the NI curves employing the Oliver-Pharr method [199, 200]. APPENDIX A provides a concise description of how the H and E_r values are determined from NI curves using the Oliver-Pharr method.

To determine the matrix and eutectic carbide H and E_r, the NI measurements were carried out in displacement mode with a tip depth of 200 nm. The indentation was held for 2 minutes, and the values were averaged over 10-12 readings. Further specifics concerning NI is detailed in paper ***I***, where a comparison between the EC hardness of two different as-cast HCCI compositions is made [197]. Furthermore, the obtained matrix H and E_r was used an input in Hertzian contact calculations to calculate the critical load (P_c), as elaborated in paper ***V*** [201].

NI measurements were also performed on the transverse section of the HCCI sample with a loading rate of 1 mN/s and a peak load of 3 mN. At least 100 indentations (10 by 10) were performed in a regularly spaced grid directly underneath the wear track, and also away from the wear track. To avoid any overlapping effect, a distance of 3 μm was maintained between two indents

regarding a maximum indent diameter below 1 μm. Further information concerning these measurements is elaborated in the 'Experimental Methodology' section in paper ***VIII*** [198].

3.4 Tribological Testing and Characterization

Dry-sliding linear reciprocating tests were conducted on the AC and HT samples using a ball-on-disc micro-tribometer (CSM instruments), while the whole setup was placed in an environmental chamber. 3 mm alumina (Al_2O_3) balls (99.00 – 99.99 % purity; Grade GD28) were used as the sliding counter-body. CLSM was used to measure the roughness of the samples and balls. It should be noted that before commencement of the wear testing, the balls were rinsed in an ultrasonic bath separately with acetone and isopropanol for 10 minutes each. *Figure 9* provides a schematic representation of the tribological testing carried out. The 'Materials and Methodology' section in paper ***V*** further elaborates on the testing specifics.

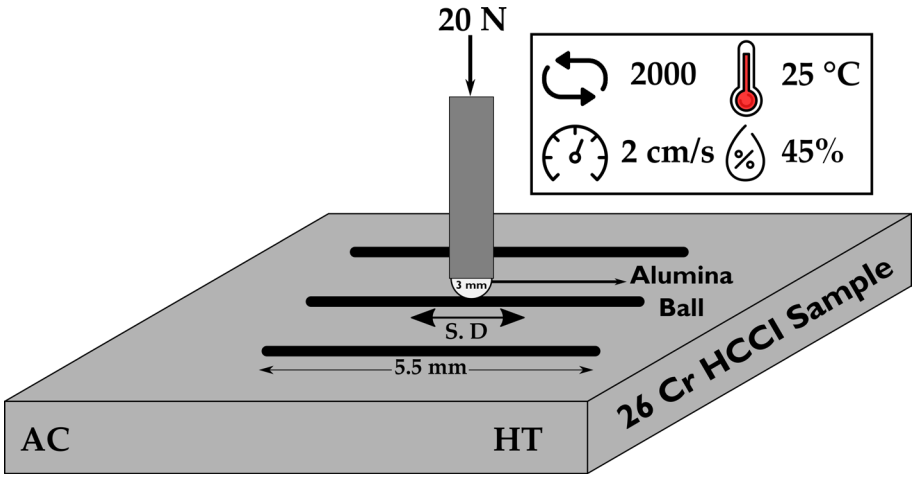

Figure 9: Schematic representation of the tribological tests including the testing parameters. The sliding direction (S.D) is also mentioned for reference.

The morphological aspects of the wear tracks as well as the acting wear mechanisms were ascertained using a combination of CLSM and FE-SEM. Energy-dispersive X-ray spectroscopy (EDS) was used to chemically map the worn and the unworn surface. Additionally, to observe the deformed microstructure underneath the wear track and to prevent further modifications from the mechanical sectioning

and polishing, the surface was electrolytically coated with Ni, as detailed in paper ***VI*** [202]. *Figure 10* provides a schematic representation of the HCCI sample with and without the Ni coating.

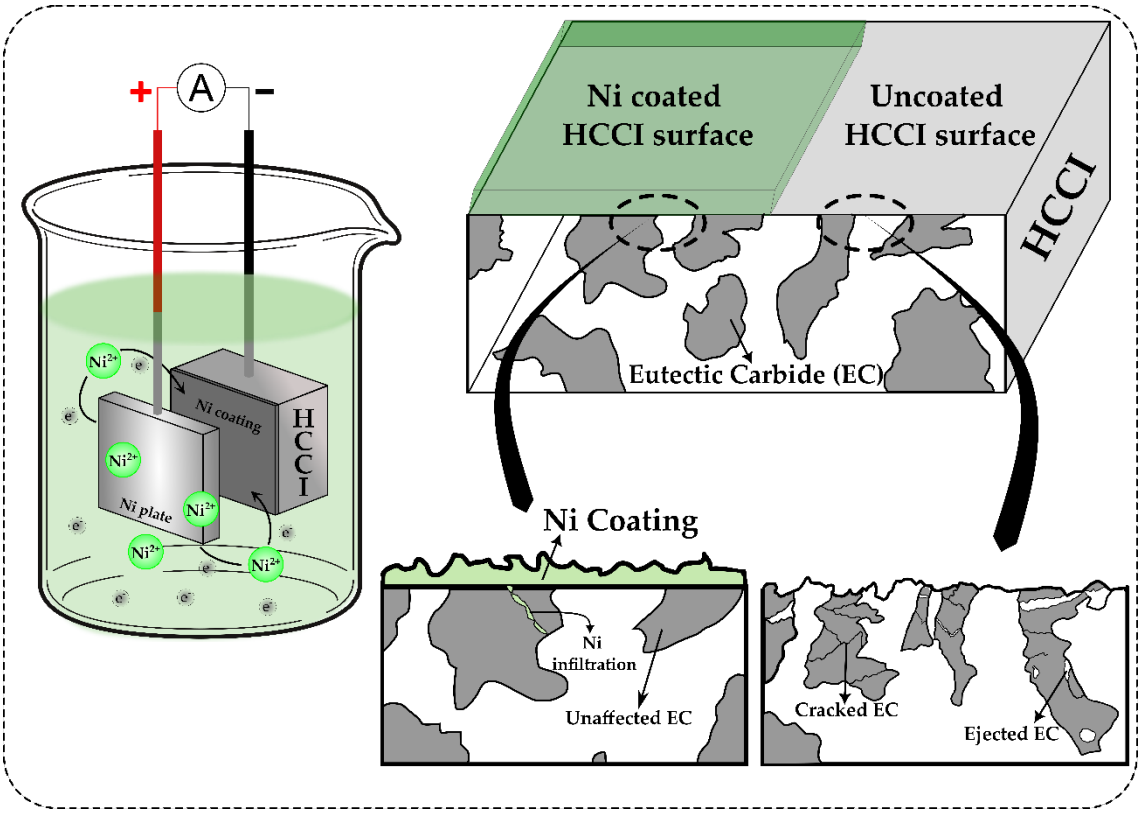

Figure 10: Schematic of the Ni electrodeposition process and its implications on the transverse section of the HCCI sample.

The local deformation and the strain distribution at the vicinity of the wear track at the surface and sub-surface was investigated by EBSD. Kernel average misorientation (KAM) measurements were carried out to extract orientation data within the deformed regions. Owing to the very small step size (30–50 nm), 2nd neighbour KAM with a 5° threshold was considered for the analysis. Additionally, grain reference orientation deviation (GROD) and misorientation profile (MP) analysis were performed around the deformed region to obtain the orientational variation. Further details are elaborated in papers ***V - VIII*** [193, 198, 201, 202]. APPENDIX B provides a detailed theoretical description of the EBSD parameters that were utilized in the analysis.

Wear quantification was described in terms of wear rate (WR), and it was determined by calculating the volume loss encountered in each track using the proprietary LEXT software in the CLSM. The entire wear track, including the ends were considered in the calculations, and Equation (3) was used to compute the WR ($mm^3\ N^{-1}\ mm^{-1}$), where V represents the wear volume (mm^3), l is the total sliding distance (5.5 × 2 × 2000 mm), and P is the applied load (N)

$$WR = \frac{V}{l \times P} \tag{3}$$

4. SUMMARY OF RESULTS

This chapter aims to establish a connection between the objectives of the dissertation and its outcomes while presenting a comprehensive summary of the findings. For a more in-depth analysis of the results, including a detailed discussion of the observed effects and information about the methods employed, it is suggested to refer to the appended articles in Chapter **5**.

The primary objective of this research was to systematically investigate the microstructural evolution of the HCCI alloy when subjected to varying HT processes. To comprehend how the tribological behaviour of the heat-treated HCCI alloy is affected by various microstructural features, it is necessary to have an extensive insight into the sequence of SC precipitation and the transformation of the surrounding matrix, given the alloy's complex multi-scale, multi-phase microstructure. This knowledge is essential for designing subsequent HT appropriately and further alloy development, which can lead to conscious utilization of modified alloys in specific applications, ultimately resulting in cost-effectiveness and energy efficiency. Additionally, rather than laboriously modifying the individual HT parameters experimentally, incorporating simulation tools would save both time and resources. Hence, it is crucial to validate the usage of such tools in HT design. Therefore, a thorough characterization in the as-cast state will serve as a terminus a quo for further microstructural modifications combining thermodynamic and kinetic calculations. Then, the HT can be performed experimentally to achieve the desired microstructure.

4.1 Microstructural Evolution and Simulations

4.1.1 As-cast samples

As a starting point, computational tools and experimental results were combined with the aim to validate the usage of MatCalc simulations for the prediction of phase fractions and elemental distribution in HCCI's in the AC condition, for the convincing implementation of these tools for further HT design (Paper ***I***). Two HCCI alloys (containing 16 wt.% and 26 wt.% Cr) were fabricated under similar conditions with the main variance being the Cr content. Their microstructure consisted of a network of M_7C_3 type EC dispersed in a matrix of austenite dendrites. In addition to the major phases, a thin layer of martensite was observed at the interface between the EC and the matrix. The impoverishment of alloying elements at the contact zone results in an increase in the martensitic start (M_s) temperature leading to its formation during subsequent cool down and is a commonly reported phenomenon during the casting of these alloys. OM and SEM micrographs indicated that the matrix was completely austenitic in the 26 wt.% Cr HCCI sample, whereas a partial transformation to pearlite had taken place in the 16 wt.% Cr HCCI sample.

Pseudo-binary phase diagrams were computed for both alloys using MatCalc, and it was observed that increasing the bulk Cr content resulted in an increase in the eutectic transition temperature (1285_{16Cr} → 1315_{26Cr}°C) and a decrease in the eutectic carbon content (3.88_{16Cr} wt.% → 3.24_{26Cr} wt.% C). The phase diagram also predicted the formation of an additional carbide, $M_{23}C_6$, in the 26 wt.% Cr HCCI sample around 1000 °C but was not experimentally observed in the AC sample, possibly due to faster cooling rate and very low Mo content.

The EC volume fraction in both alloys was determined in three ways, i.e., numerically, experimentally, and through simulation. The total bulk chemical composition was used as the input for the software in simulating the equilibrium fraction of each phase. To experimentally determine the EC volume fraction, the

alloys were etched with a specific etchant and later subjected to image analysis. It was observed that an addition of 10 wt.% Cr resulted in a CVF increase of about 50% (~ 20% CVF_{16Cr} → ~ 30% CVF_{26Cr}).

In both alloys, the % CVF predicted by MatCalc was lower than the values obtained experimentally which was explained by the non-equilibrium solidification during casting. Accordingly, an undercooling range, T_u = 150 °C was considered and by averaging the phase fraction values in that range, the predicted and experimental % CVF values corresponded well and differences between them fell within an error of less than 5%. The accuracy of the simulation software was further validated comparing the % CVF of several alloys (with different C and Cr contents) to the experimental values obtained by other authors by metallography.

In addition to the phase fractions, individual phase compositions were determined experimentally using electron probe microanalysis (EPMA) and later correlated with the simulated values calculated using MatCalc. The addition of chromium reduced the carbon solubility in austenite and as a result, the 26 wt.% Cr HCCI alloy had a lower matrix C content. The predictions made by MatCalc were in accordance with the values obtained by EPMA.

Since this work focused heavily on characterizing the microstructure of the alloy, the methodology for achieving a scratch-free, mirror-polished surface and accurately revealing the individual microstructural constituents that align with the research objectives was developed. Additionally, the procedure for reliable quantification of the microstructure was devised, with a specific emphasis placed on the stereological properties of the carbides. A schematic overview of both methodological papers is presented in *Figure 11* and described in detail in papers ***II*** and ***III***.

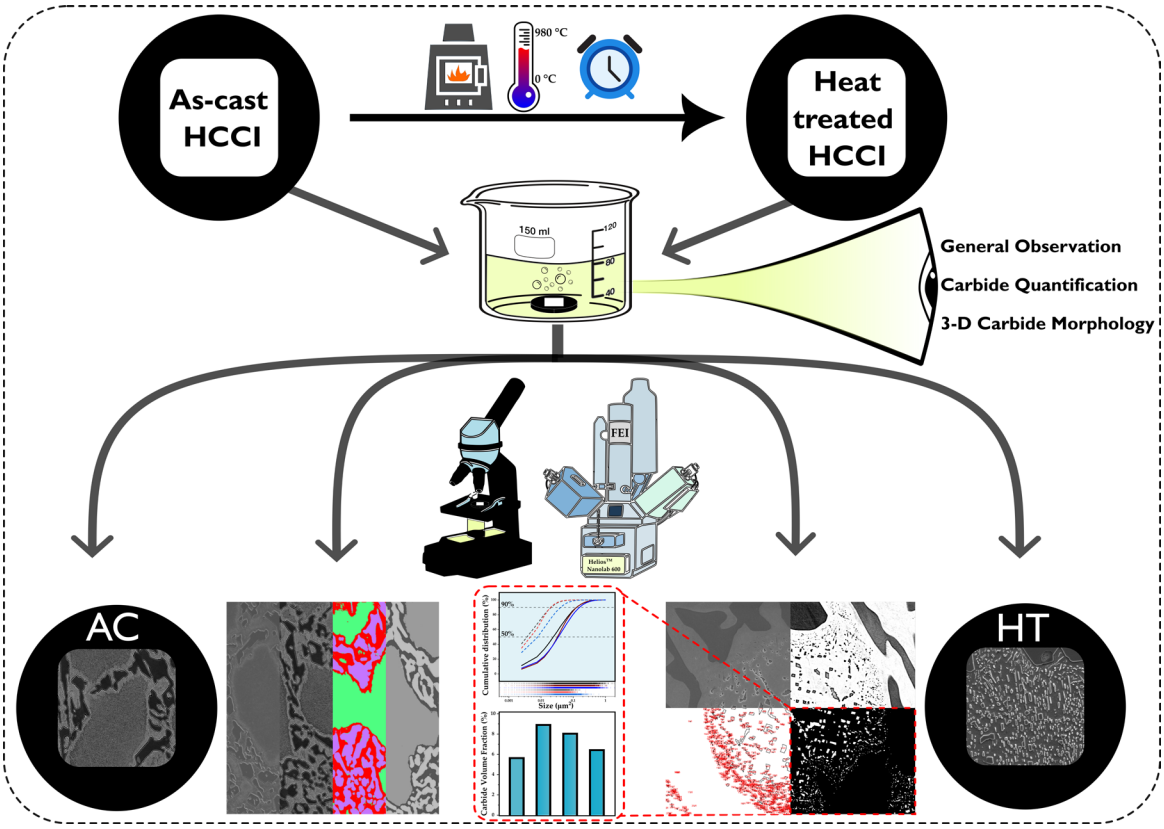

Figure 11: Schematic overview of papers II and III. Paper II deals with the metallographic preparation and etching of as-cast and heat-treated HCCI samples. Paper III focuses on their quantitative microstructural analyses.

The 26 wt.% Cr HCCI alloy's general microstructure was revealed by immersing the sample in Vilella's reagent for 7 seconds, which provided sufficient phase contrast for observation under CLSM and quantification with SEM. Additionally, a modified Murakami's etchant (RT for 15 s) with NaOH replacing KOH was found to be optimal for the carbide quantification (both EC and SC), as it attacked the chromium carbides and provided a quasi-binary SEM image in BSE mode. The resulting high contrast between the phases simplified the subsequent IA process.

Hence, the proper selection and effective utilization of specific etchants were crucial in achieving the desired objectives. Furthermore, it was imperative to use the appropriate microscopy techniques to obtain reliable and representative microstructural information about the alloy, which could facilitate a better comprehension of the material's performance.

4.1.2 Heat-treated samples

As a first approach in understanding the microstructural evolution of the 26 wt.% Cr HCCI, the same multi-step HT (SCD, Q and SCD + Q) that had previously been applied successfully to another HCCI alloy (16 wt.% Cr) was used to assess the influence of increased Cr content on the final microstructure (Paper ***IV***). The microstructural analysis of the heat-treated samples showed that the nature of the SC precipitates during the various stages of the HT changed from M_7C_3 to $M_{23}C_6$, with increasing Cr content. Moreover, the matrix microstructure of the 26 wt.% Cr HTed samples varied from ferrite to martensite based on the multi-step HT applied, and this affected the final matrix microhardness.

Due to the complexity and variability associated with a simple HT process, it was necessary to break down the multi-step HT into smaller segments and tackle them individually. Consequently, kinetic simulations using MatCalc were performed, with a focus on the destabilization segment (@ 980 °C) of the multi-step HT process, which were later compared to the experimentally obtained results. Specifically, the holding time during the destabilization was varied (Q - 0, 30, 60 and 90 minutes) to evaluate its effect on the SC size and fraction.

The MatCalc thermodynamic and kinetic simulations of the destabilization (Q) HT process suggested that SC precipitation began during the heating phase (~ 800 °C) with M_7C_3 carbides initially precipitating, later paving way for the $M_{23}C_6$ carbides when the temperature of 980 °C was reached. Microstructural characterization and carbide quantification of the isothermally held destabilized samples corroborated with the simulations.

The destabilized microstructure was characterized by the presence of a primarily martensitic matrix (α'), finely precipitated SC ($M_{23}C_6$ type), the original (as-cast) EC (M_7C_3 type) and RA. Furthermore, SEM observations of the sample destabilized for 0 minutes (Q_0) showed the dispersion of SC within the matrix supporting that SC precipitation had begun during the heating phase. Correlative microscopy

(CLSM – SEM – EBSD) was useful in assessing the destabilized microstructure where a reduction in the RA content was observed with increasing the destabilization holding time (Q - 0, 30 and 90 minutes) (Paper ***VII***). Furthermore, the precipitation was noted to exhibit a characteristic pattern of initiation from the peripheral regions of the matrix before proceeding inward, thereby highlighting the crucial role of time-dependant factors in governing the microstructural evolution in HTed samples.

Stereological characteristics of the SC in terms of CVF (%) and size (μm^2) indicated that the CVF values of Q_0 and Q_90 samples were statistically comparable, although the average size increased two-fold in the latter. In addition, the homogeneity of the SC distribution was measured using the coefficient of variation (COV), which was based on the log normal distribution data of the nnds. The Q_0 sample exhibited the lowest COV value of approximately 40%, indicating a relatively more homogeneous dispersion of SC precipitates, whereas the Q_30 and Q_90 samples showed values of 49% and 47%, respectively. However, it is important to note that the homogeneity calculations alone cannot be the sole deciding factor, as they do not account for the fact that in the Q_0 sample, most of the precipitates are located around the periphery of the matrix, resulting in considerably closer spacing compared to the Q_30 and Q_90 samples. Although the introduction of the COV factor added another layer of complexity to the analysis of the SC distribution, the information obtained from the homogeneity calculations should also be combined with the size and nnd analysis to explain the changes taking place during the HT.

The quantification of RA using MAUD indicated a temporal decrease, and consequently, a corresponding increase in the matrix hardness. The presence of a large number of small-sized carbides located at the periphery of the matrix rendered the central part of the matrix primarily austenitic and as a result, the hardness of the Q_0 sample marginally increased (~ 15%) compared to the as-cast. With increased holding time, the precipitation proceeded inwards into the matrix

tending to grow and coalesce resulting in more of the austenite being transformed to martensite upon cooling and eventually a substantial increase in matrix hardness (~ 125%).

The kinetic simulations performed previously (Paper ***IV***) indicated that SC precipitation had taken place during heating (~ 800 °C) and that M_7C_3 type SC were the first ones to precipitate. Subsequently, the samples were heated to three different temperatures (800 °C, 900 °C and 980 °C) using two different heating rates (1 and 10 °C/min) and held for 0 minutes, before quenching them in water to room temperature in order to arrest the microstructure (Paper ***IX***). The impact of HR was investigated because, during the heating of sizable industrial HCCI components, complete thermal equilibrium may not be attained throughout the sample, particularly when the HR is high. This is due to the fact that the sides and edges of the sample may heat up more quickly than the centre, resulting in a microstructure gradient and variations in properties.

SEM observations of the destabilized samples indicated that SC precipitation took place even at 800 °C, which meant precipitation had occurred already during heating, corroborating with the simulations. Although it was not possible to find a concurrence in the literature concerning the start of carbide precipitation, the results obtained in this study represent the first experimental evidence of SC precipitating during heating at temperatures ~ 800 °C. Furthermore, the distribution of precipitation within the matrix was influenced by the HR utilized. In particular, with a high HR, precipitation mainly took place at the periphery of the matrix, whereas with a slower HR, precipitation advanced towards the matrix's centre. This is because slower heating rates allowed a larger time for homogenization of the alloy elements leading to precipitation across a larger area of the matrix. It was also observed that the CVF and size in the slower heated samples were about 4 times and 5 times, respectively, compared to the faster heated samples. Moreover, they showed similar values amongst the samples

heated at the same rate indicating that the heating rate had a greater influence on the SC characteristics than an increase in the temperature.

Owing to the size and volume fraction of the freshly precipitated SC, detection with XRD was not a viable option. Therefore, TEM samples were extracted from the 800_10 (destabilized at 800 °C with a HR of 10 °C/min) sample at the peripheral region of the matrix, where the beginning of SC precipitation was observed. From the HRTEM analysis, the SC type was indexed as M_7C_3 using the CrysTBox software, although it is worth mentioning that the presence of $M_{23}C_6$ type SC was also detected. Moreover, APT analysis was performed on the same region to determine the chemical composition of the SC. The peak decomposition analysis resulted in a C content of 29 ± 1 at.% which is very close to the 30 at.%, expected for the M_7C_3 carbide, corroborating with the simulation predictions.

4.2 Tribological Performance

4.2.1 As-cast samples

Dry-sliding linear reciprocating tests were carried out on the as-cast 26 wt.% Cr HCCI alloy under varying loading conditions as a preliminary approach to study its microstructural behaviour (Paper ***V***). The applied loads were selected based on Hertzian contact theory, where critical load (P_c) was calculated based on the materials' properties (see APPENDIX C). P_c is the load at which the outset of plastic deformation takes place in the material, and it was calculated to be ~ 15 N. Consequently, a sub-critical (5 N) and an over-critical load (20 N) were also selected. The influence of increasing the load during the wear test was investigated in terms of the matrix microstructural behaviour and its ability to support the surrounding carbides.

At sub-critical loads, no evidence of plastic deformation of the austenitic matrix adjacent to the wear track was observed, whereas the wear tracks loaded with 15 N and 20 N showed plastic deformation, evidenced by the presence of slip traces as

indicated by SEM and EBSD measurements. Moreover, the number of activated slip systems increased with increasing load. Carbide micro-cracking was also observed throughout the wear track, which was attributed to the increased hardness of the alumina ball (~ HV 1500) compared to the EC (~ HV 1200) or the matrix material.

The active wear mechanisms during sliding were a combination of both adhesive and abrasive wear, although increasing the load led to a shift towards abrasion being the dominant mechanism. This was primarily attributable to the increased propensity for carbide cracking and fracturing, combined with the inability of the hardened austenitic matrix surface and sub-surface to adequately support the broken carbide fragments. EDS mapping revealed the preferential accumulation of oxides at areas where the carbides were cracked, spalled, and ejected. As the wear mechanism was abrasion-dominated, micro-cutting and ploughing contributed to surface deterioration resulting in the generation of numerous defects such as cracks and voids. This was a crucial factor to consider, as the rate of carbide removal essentially indicated the rate at which the oxides accumulated and eventually breakdown, altering the subsequent wear behaviour. The shift in the dominant wear mechanism was also reflected in the wear volume and the wear rate, which increased with increasing load.

The thermal effects emanating during the dry sliding tests were also considered by calculating the potential temperature rise at the contact interface (i.e., flash temperature) as it could engender structural changes and/or phase transformations. Nevertheless, the calculated peak flash temperature was calculated to be 17 K for the maximum load used, which was considered very minimal for any thermally induced changes. The detailed calculations of the flash temperature are presented in APPENDIX D.

Moreover, analysing the deformed microstructure underneath the wear track can be advantageous for further analysis since the maximum stress is encountered at

the centre of the wear track width. Using a focused ion beam (FIB) to cut such a large section is both time and resource intensive, whereas mechanically sectioning the sample would facilitate a complete observation of the sub-surface microstructure beneath the wear track. As the latter route might induce certain undesired microstructural modifications, it was essential that the wear track and the underlying microstructure be suitably protected. Consequently, the worn surfaces were protected by a Ni coating, which was deposited using electrodeposition (Paper ***VI***).

The protection of the sub-surface of the worn samples enabled successful visualization of the deformation of the austenitic matrix beneath the wear track through EBSD. The GROD and image quality (IQ) maps indicated a decrease in the misorientation and deformation, respectively, with increasing depth. SEM observations revealed that austenite underwent plastic deformation at or above the critical load, but no SIM transformation was detected in this study, despite its documented occurrence in other research works. EBSD measurements failed to detect SIM in the deformed zone, adjacent to or beneath the wear track. Two factors may have contributed to this outcome: (1) the low strain rate employed in this study and (2) the absence of shear band intersections, which act as potential nucleating sites for SIM formation.

The present study offered valuable insight into the behaviour of the diverse microstructural constituents during tribological testing under varying loads. Moreover, this methodology of determining the critical load using the materials' properties can be extended to other alloys in the HCCI family to establish the load limits and to better comprehend the interaction between the different components in the system. This understanding can be effectively employed to evaluate the microstructural and tribological characteristics of heat-treated HCCIs.

4.2.2 Heat-treated samples

Although the microstructural constituents of the isothermally held samples (@ 980°C) were identical, the differences in their amounts and distribution had a consequence on the final tribological behaviour of the alloy (Paper ***VII***). In the case of the samples possessing a higher amount of austenite (as-cast and Q_0), the wear mechanisms were a combination of mild adhesion and abrasion although, the influence of oxidation could not be completely dismissed. In the Q_0 sample, the relatively higher amount of austenite likely provided additional mechanical support by undergoing plastic deformation during the wear test, as evidenced by the presence of slip lines in the SEM micrographs. On the other hand, in the Q_30 and Q_90 samples, in addition to adhesion and abrasion, oxidation also played a big role in the wear behaviour due to the detachment of SC from the matrix. The predominately martensitic matrix lacked the ability to plastically deform, making it incapable of providing the requisite support for the surrounding carbides, resulting in micro-fracture and eventual ejection of the carbides.

Furthermore, the HTed samples showed a decrease in the WR of up to 50% compared to the AC and amongst them, the sample with the lowest increase in the surface matrix hardness (Q_0) showed the best wear resistance. This meant that an increase in hardness did not necessarily correspond to an increase in wear resistance, shedding light on the importance of an optimal distribution of the microstructural constituents after destabilization. Samples Q_30 or Q_90 could be chosen if having a high hardness was a prerequisite as both the samples show a hardness of about twice that of the Q_0 sample. Hence, for applications where a high hardness is a requirement, it is recommended to destabilize for a longer period to ensure the amount of RA is reduced, whereas for wear resistant applications, the presence of ~ 10% RA in addition to the precipitated SC (~5%) is advantageous.

To obtain a more profound comprehension of the enhanced wear resistance observed in the HTed samples compared to the AC sample, and particularly why the Q_0 sample displayed the lowest wear rate, a thorough analysis of the worn sub-surface's microstructure was necessary (Paper ***VIII***). EBSD and NI measurements indicated that the matrix area underneath the wear track in Q_0 sample had undergone significant plastic deformation resulting in a drastic increase in hardness, whereas no such phenomena was observed in the Q_90. This was attributable to the relatively high amount of retained austenite in the former and a predominately martensitic matrix in the latter. Furthermore, the presence of martensite and the dispersed SC precipitates in all the destabilized samples led to an improvement in the load-bearing capacity, which subsequently resulted in a decrease in the susceptibility of EC micro-fracture compared to the as-cast sample.

The final article (Paper ***X***) of this research work took into account the insights gathered from all prior studies and focused on examining the implications of microstructural evolution on the tribological performance of the heat-treated 26 wt.% Cr HCCI alloy. While the higher matrix hardness in the slower heated samples was linked to the increased SC CVF and size, this did not result in an increased wear resistance. In fact, in all cases, the faster heated samples showed higher wear resistance compared to its slower heated counterparts, despite the hardness being ~ 50% lower.

All samples displayed a combination of abrasive and oxidative wear, with the lowest wear resistance at 800 °C and the highest at 980 °C, regardless of HR. EBSD measurements revealed the presence of ferrite islands throughout the matrix in the 800 °C samples whose presence was detrimental to the wear resistance. However, the martensitic matrix and the dispersed SC in the 980 °C samples also assisted in bearing the load, thereby ensuring a low wear rate.

In conclusion, the results obtained from this study, which are consistent with our previous work (Paper ***VII***), emphasized the vital role of the matrix support in

enhancing the tribological performance of the HCCI alloy. As far as tribological applications are concerned, it is advisable to destabilize at a higher temperature using a faster heating rate. Overall, the results obtained from this research offer insights into the potential to modify the HT parameters to tailor the microstructure to meet specific application requirements. *Figure 12* represents a schematic overview of the work carried out in this dissertation.

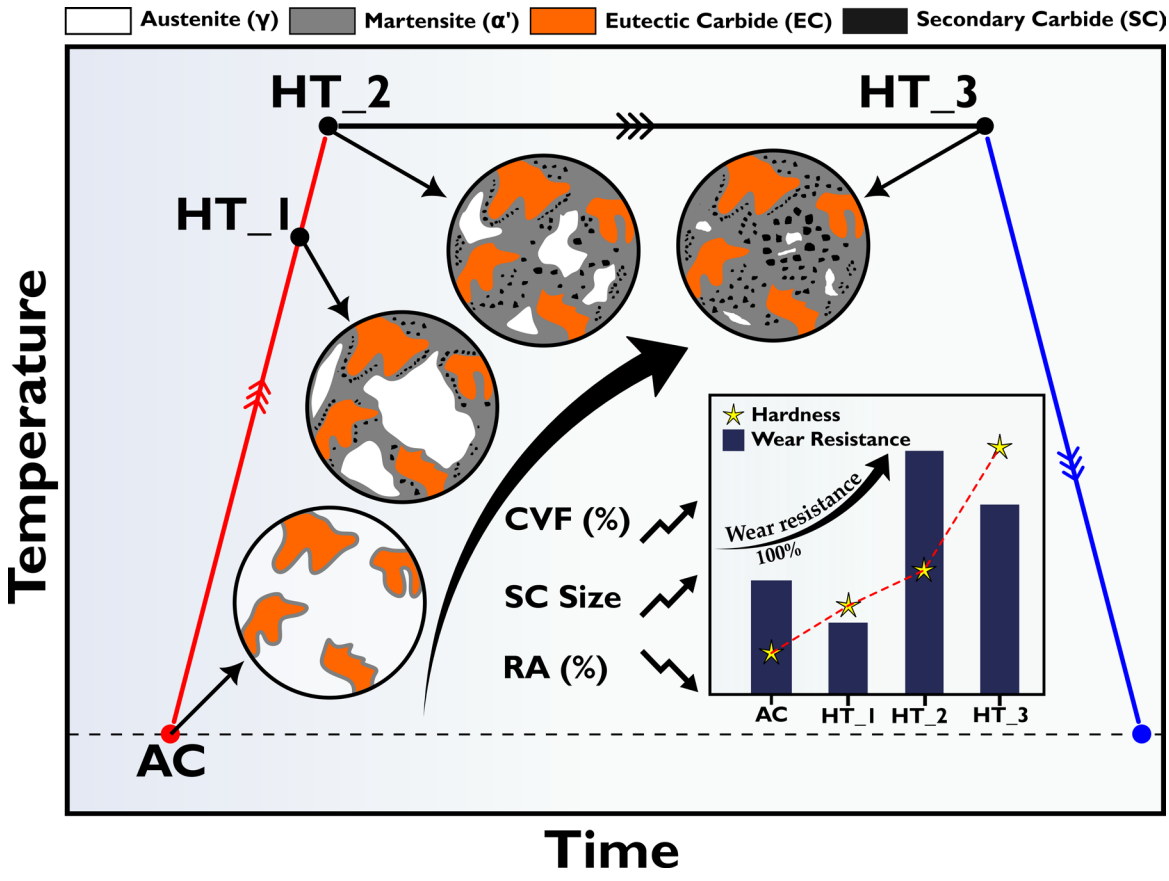

Figure 12: Schematic overview of the work carried out in this dissertation.

5. INCLUDED PAPERS

Outline

I	The aim of paper ***I*** was to examine the effect of adding Cr on the microstructural characteristics of the AC HCCI alloy, and to validate the use of the thermodynamic simulation tool MatCalc in determining the EC phase fraction and elemental composition. The results showed that a 10 wt.% addition of Cr resulted in a 50% increase in the EC phase fraction and a higher Cr/Fe ratio within the EC. The predictions made by MatCalc using pseudo-equilibrium diagrams were consistent with the experimental values, demonstrating the reliability of this tool in heat treatment design.
II	Paper ***II*** described a step-by-step procedure of metallographically preparing the HCCI samples to obtain a scratch-free, mirror polished surface. The efficacies of various etchants for characterizing the microstructure of the HCCI alloy in both as-cast and heat-treated conditions was also evaluated. It was seen that specific etchants are needed depending upon the final objective and that the choice of microscope significantly impacted the results. The methodology outlined in this paper served as the standard for all metallographic preparation in the accompanying articles.
III	The focus of paper ***III*** was to establish a sequential methodology to carry out image segmentation and perform quantitative microstructural analysis of carbides, which are critical to the current work. The information obtained from paper ***III*** served as a guideline for quantitative stereological analysis of carbides in subsequent articles.

IV

The objectives of paper ***IV*** were two-fold:

(i) The 26 wt.% Cr HCCI alloy was subjected to the same multi-step HT that was successfully applied previously to another HCCI alloy (16 wt.% Cr), to evaluate the influence of increased Cr content on the final microstructure. A thorough microstructural characterization was performed and the need for a specificity in HT was established.

(ii) Kinetic simulations were performed using MatCalc focusing on the destabilization segment of the multi-step HT process and was later compared to the experimentally obtained results, which showed good correspondence. The simulations indicated that SC precipitation began during the heating phase (~ 800 °C) with M_7C_3 carbides initially precipitating, later paving way for the $M_{23}C_6$ carbides when the temperature of 980 °C was reached.

V

Paper ***V*** investigated the microstructural evolution of the AC HCCI alloy when subjected to tribological testing. Rather than selecting a random load, Hertzian contact theory was used to determine the critical load based on the materials' properties and accordingly, the loads were defined. The influence of increasing the load during the wear test was investigated in terms of the matrix microstructural behaviour and its ability to support the surrounding carbides. The calculated values were in good correspondence with the microstructural observations and a clear shift in the dominant wear mechanism was identified.

VI

The main objective of the paper ***VI*** was to develop a simple, yet effective approach to coat the worn surface of HCCI samples in order to investigate the deformed microstructure underneath the wear track. Ni electroplating using Ni strike as the electrolyte was successfully able to protect the wear track, and the sub-surface characteristics of the wear track could be clearly visualized using SEM and EBSD. The results and findings were effectively applied in the examination of the sub-surface microstructure of HCCI alloys in their as-cast and heat-treated states, and other ferrous alloys such as 316L stainless steel and a low-carbon steel with 5 wt.% Ni.

VII

Paper ***VII*** investigated the influence of destabilization holding time on the microstructural evolution and subsequent tribological behaviour of the HCCI alloy. Results showed that the destabilized samples showed a decrease in the WR of up to 50% compared to the AC and amongst them, the sample with the lowest increase in the surface matrix hardness showed the best wear resistance. This meant that an increase in hardness did not necessarily correspond to an increase in wear resistance.

VIII

The primary objective of Paper ***VIII*** was to gain a better understanding of the tribological behaviour of the destabilized samples by investigating the area underneath the wear track. The knowledge from paper ***VI*** was utilized in protecting the transverse section from mechanical sectioning. The destabilized sample with the lowest increase in the matrix surface hardness showed the highest sub-surface hardness. This was attributed to the presence of small-sized, homogeneously distributed SC around the periphery combined with the martensite, and the relatively higher amount of retained austenite, which underwent plastic deformation.

IX

The focus of paper ***IX*** was to study how carbide precipitation and microstructure evolved with changes in heating rate and destabilization temperature. Previous kinetic simulations showed that SC precipitation occurred at around 800 °C during heating, with M_7C_3 being the initial precipitates. Although HRTEM analysis indexed both types of SC, APT measurements on the peripheral SC of samples destabilized at 800°C confirmed the presence of M_7C_3-type SC, which corroborate with predictions made by MatCalc. Finally, this work reports for first time, in a systematic manner, the precipitation of SC during heating of the HCCI alloy.

X

The implications of the microstructural evolution on the tribological performance of the HCCI alloy is investigated in paper ***X*** by utilizing the knowledge gained from all previous papers. It was observed that the HR had a greater influence on the SC characteristics than increasing the temperature. While slower heating can result in higher hardness and larger SC volume and size, they do not necessarily result in an increase in wear resistance. This highlights the criticality of the matrix support in improving the tribological performance of the HCCI alloy. As far as tribological applications are concerned, it is recommended to destabilize at a higher temperature with a faster heating rate.

I. *A Comparative Study on the Influence of Chromium on the Phase Fraction and Elemental Distribution in As-cast High Chromium Cast Irons: Simulation vs. Experimentation*

U. Pranav Nayak, María Agustina Guitar, Frank Mücklich

Department of Materials Science and Engineering, Saarland University, 66123 Saarbrücken, Germany

Published in "***Metals***" (2020) *(Impact Factor (IF) (2023): 2.695)*

Accessible online at: *https://doi.org/10.3390/met10010030*

Own Contribution: Conceptualization and methodology; sample preparation; simulation and experimental validation; data analysis; scientific discussion; paper writing – original draft preparation

metals

MDPI

Article

A Comparative Study on the Influence of Chromium on the Phase Fraction and Elemental Distribution in As-Cast High Chromium Cast Irons: Simulation vs. Experimentation

U. Pranav Nayak [1,*], María Agustina Guitar [1] and Frank Mücklich [1,2]

[1] Department of Materials Science, Saarland University. Campus D3.3, D-66123 Saarbrücken, Germany; a.guitar@mx.uni-saarland.de (M.A.G.); muecke@matsci.uni-sb.de (F.M.)

[2] Materials Engineering Center Saarland (MECS), Campus D3.3, D-66123 Saarbrücken, Germany

* Correspondence: pranav.nayak@uni-saarland.de; Tel.: +49-681-302-70517

Received: 21 November 2019; Accepted: 19 December 2019; Published: 23 December 2019

Abstract: The excellent abrasion resistance of high chromium cast irons (HCCIs) stems from the dispersion of the hard iron-chromium eutectic carbides. The surrounding matrix on the other hand, provides sufficient mechanical support, improving the resistance to cracking deformation and spalling. Prior knowledge of the microstructural characteristics is imperative to appropriately design subsequent heat treatments, and in this regard, employing computational tools is the current trend. In this work, computational and experimental results were correlated with the aim of validating the usage of MatCalc simulations to predict the eutectic carbide phase fraction and the elemental distribution in two HCCI alloys, in the as-cast condition. Microstructural observations were carried out using optical microscopy and SEM. The chemical composition and fraction of each phase was measured by electron probe microanalysis and image analysis, respectively. In all cases, the values predicted by the pseudo-equilibrium diagrams, computed with MatCalc, were in accordance with the experimentally determined values. Consequently, the results suggest that time and resource intensive experimental procedures can be replaced by simulation techniques to determine the phase fraction and especially, the individual phase compositions in the as-cast state.

Keywords: high chromium cast irons; eutectic carbide; carbide volume fraction; chemical composition; image analysis; simulation; MatCalc; hardness

1. Introduction

High chromium cast irons (HCCIs) are alloys containing 15–30 wt. % Cr and 2.5–4 wt. % C, and belong to the Fe–C–Cr ternary system, as described in the ASTM A532 [1,2]. Other international standards such as ISO 21988:2006(E) classifies HCCIs under five different grades with Cr contents ranging from 11 to 40 wt. % [3]. They primarily contain hard eutectic carbides (EC) of the M_7C_3 type dispersed in a supportive, modifiable matrix. Although equilibrium solidification would result in a ferritic matrix, the final microstructure primarily contains an austenitic matrix indicating a non-equilibrium nature of solidification. The M_7C_3 carbides contribute to the hardness and wear resistance whereas the relatively softer matrix helps in improving the toughness of the HCCI alloy. This combination makes it an attractive choice for usage in applications demanding excellent abrasion and moderate impact resistance, such as ore crushers, pulverizing equipment, ball mill liners etc., in coal and mineral industries [4,5].

Although the matrix of an HCCI alloy can be modified by employing proper heat treatment, the EC are relatively immune to it [4,6]. Once the EC are formed during solidification, the only way to

modify them is by re-melting the cast and chemically modifying the melt by alloying and/or varying the process parameters. Over the years, the influence of several alloying elements such as Ti [7,8], Mo [9,10], W [11,12] etc., on the solidification behavior of the as-cast melt have been assessed. In all cases, the addition of alloying elements modified the eutectic carbide structure which resulted in a change in the final microstructural and mechanical behavior. Initially, the wear resistance was thought to be mainly influenced by the hardness of the material but it is now understood that a lot of factors contribute to this, such as type, volume fraction, size, and morphology of eutectic carbides, and its interaction with the host matrix [13–15]. Not only the carbide characteristics but also the chemical composition of the matrix after solidification determines, to a large extent, the efficacy of the subsequent heat treatment on the microstructural modifications [5,16,17]. For these reasons, it is imperative to evaluate the carbide characteristics and the chemical composition of each phase in the as-cast state.

In order to understand the processes that govern the materials' properties, it is essential to comprehend the phase diagram and phase equilibria for the given alloy composition. Complete phase diagrams for several binary and a few ternary systems are available but their construction becomes cumbersome with every additional element [18]. In this regard, employing computational techniques would be useful to extract valuable thermodynamic properties of the phases rather than experimentation. MatCalc (Materials Calculator), is a thermo-kinetic software package developed for the simulation of precipitation kinetics that occur during various metallurgical processes [19]. It employs the CALPHAD type database, which, currently is the only theoretical approach to carry out thermodynamic and kinetic calculations in multicomponent systems [20].

Studies combining simulation and experimentation have been previously conducted. Li et al. [21] computed the phase diagram of an HCCI alloy containing 15% Cr using Thermo-Calc software and compared the predicted precipitation sequence with differential scanning calorimetry (DSC) measurements. The results were in agreement with each other. Albertin et al. [22] successfully employed computational thermodynamics (Thermo-Calc) in analyzing several different HCCI compositions with the intention of optimizing the hardness and wear resistance after thermal treatments. Akyildiz et al. [23] used MatCalc to simulate pseudo-binary phase diagrams for two HCCI alloys with varying Mo contents. The predicted transformation temperatures were later compared to the DSC values to matching success. Moreover, the increase in the amount of $M_{23}C_6$ carbides with increasing Mo as predicted by the software was also seen in the alloy microstructure.

Having an idea of the microstructural characteristics (carbide volume fraction, phase chemical composition etc.) beforehand would be strongly beneficial in the development of the alloy and an appropriate design of the subsequent heat treatment (HT) to maximize its potential. Therefore, a thorough characterization in the as-cast state will serve as a terminus a quo for further microstructural modifications combining thermodynamic and kinetic calculations, and experimentally performing the thermal treatments.

The main objective of the current work is to validate the usage of thermodynamic simulation as an approach to determine the eutectic carbide phase fraction and the corresponding matrix, and carbide chemical compositions of HCCIs in the as-cast condition. Accordingly, two HCCI compositions (16% Cr and 26% Cr) were manufactured under similar conditions and their corresponding microstructural characterization was carried out in the as-cast state. The bulk compositions of the two materials were used as the input in the simulation software, MatCalc 6, to estimate the phase fraction and the chemical composition of the matrix and carbides, post solidification. Moreover, predictions from Matcalc were experimentally validated by image analysis (I-A) and electron probe microanalysis (EPMA). Additionally, the influence of the Cr content in the hardness of each phase and of the 'composite' itself, was evaluated using nanoindentation, Rockwell and Vickers microhardness tests.

2. Materials and Methodology

High chromium cast iron samples with varying Cr contents (approximately 16% and 26%) were manufactured in an arc furnace and casted at ~1450 °C into rectangular (Y) shaped sand molds

hardened with phenolic resin. Test samples were cut from the lower half of the test block measuring 175 × 90 × 25 mm^3 to ensure they were free from casting defects. Optical emission spectroscopy (GNR Metal Lab 75/80; G.N.R. S.r.l., Agrate Conturbia, Novara, Italy) was used to determine the bulk chemical composition of the castings. Table 1 represents the chemical composition (wt. %) along with the Cr/C ratio of both alloys. The cast samples were cut into pieces measuring 20 × 20 × 10 mm^3 using an abrasive disc and later embedded for microstructural characterization. Standard metallographic procedure was followed as described in [24].

Table 1. Bulk chemical composition (in wt. %) of the samples measured by optical emission spectroscopy. HCCI: high chromium cast irons.

Alloy	C	Cr	Mn	Ni	Mo	Si	Cu	P	S	Fe	Cr/C
16% HCCI (Sample A)	2.43	15.84	0.76	0.18	0.41	0.47	0.04	0.02	0.02	Bal.	6.5
26% HCCI (Sample B)	2.53	26.60	0.66	0.26	0.24	0.37	0.03	<0.01	0.04	Bal.	10.5

In addition to the bulk composition, the individual matrix and carbide compositions was measured by EPMA (8900 R JEOL Superprobe; JEOL, Tokyo, Japan) and the mean of 10 readings was considered. Phase identification was performed using a PANalytical Empyrean X-ray diffractometer (PANalytical B.V., Almelo, The Netherlands) coupled with a Co source, an acceleration voltage of 40 kV and a 40 mA tube current.

The polished samples were etched with three different etchants depending on the objective. Villella's reagent (1 g picric acid + 5 mL HCl + 95 mL C_2H_5OH) for general microstructure revelation [25], a modified Murakami's reagent (4 g $K_3[Fe(CN)_6]$ + 8 g KOH + 100 mL distilled water) for eutectic carbide volume fraction (% CVF) determination [26] and a solution of 10% HCl in methanol (CH_3OH) for deep etching to reveal the three dimensional (3D) structure of the eutectic carbides [27]. The specifics of the etchings is mentioned in Table 2. In all cases, the samples were immersed in the etchant for the appropriate time, rinsed with water and ethanol, and air dried.

Table 2. Etching parameters for each etchant.

Etchant	Solution Temperature	Etching Time
Vilella's	Room temperature (20 °C)	7–15 s
Modified Murakami's	60 °C	5 min
10% HCl in methanol	Room temperature (20 °C)	24 h

Microscopy observations were carried out using a LEXT OLS 4100 Olympus confocal laser scanning microscope (CLSM) (Olympus Corporation, Tokyo, Japan). It uses a laser with 405 nm wavelength and, a lateral and vertical resolution of 120 and 10 nm, respectively. The microstructures of the samples along with the 3D structure of the carbides were analysed using a FEI Helios Nanolab field emission scanning electron microscope (FE-SEM) working with an acceleration voltage of 5–15 kV and a beam current of 1.4 nA. A high sensitivity backscattered electron detector (vCD) was also used in order to obtain a better contrast between the phases. Furthermore, a Leica CTR6000 microscope (Leica Camera AG, Wetzlar, Germany) coupled with a Jenoptik CCD camera (Jenoptik AG, Jena, Germany) was used for image acquisition of the samples for % CVF determination. The % CVF was calculated after a post processing of the images using the image analysis (I-A) software, ImageJ (version 1.52p) (LOCI, UW-Madison, WI, USA) [28]. The analyzed area was the same for all the images and an average of 10–12 micrographs were considered for each sample.

Equilibrium phase diagrams for both alloys along with thermodynamic, and equilibrium phase fraction calculations were computed using MatCalc 6 software (version 6.01) (MatCalc Engineering

GmbH, Vienna, Austria) with the thermodynamic database "ME_Fe 1.2". The results were then correlated with the experimentally and numerically determined values obtained from I-A and empirical equations described in [29,30], respectively. Moreover, the chemical composition of each phase was estimated at a certain temperature range and compared with the EPMA results.

The bulk hardness of the samples was measured using the Rockwell hardness method, with a diamond indenter and a load of 150 kgf (HRC) whereas the matrix hardness was determined using the Vickers method. A Struers Dura Scan 50 microhardness tester (Struers Inc., Cleveland, OH, USA) with a load of 0.9807N (HV0.1) was used for this purpose. In both testing methods, the dwell time was 15 s and an average of 15–20 readings was considered. Nano-indentation (Hysitron TI 900 TriboIndenter; Bruker Corporation, Billerica, MA, USA) was used to calculate the hardness of the eutectic carbides (in GPa). A Berkovich tip, with a tip depth of 200 nm was used in displacement mode. A loading/unloading rate of 50 was maintained and the scan size was approximately 30 microns. Each indentation time was 2 min and the values were averaged over 10–12 readings.

3. Results and Discussion

3.1. Phase and Microstructural Analysis

Figure 1 represents the microstructure of the Sample A (16% HCCI) and Sample B (26% HCCI) as observed under CLSM and SEM. Their microstructure consisted of a network of eutectic carbides (EC) dispersed in a matrix of austenite dendrites. The EC was identified to be M_7C_3 which is consistent with previous studies [1,4,31,32].

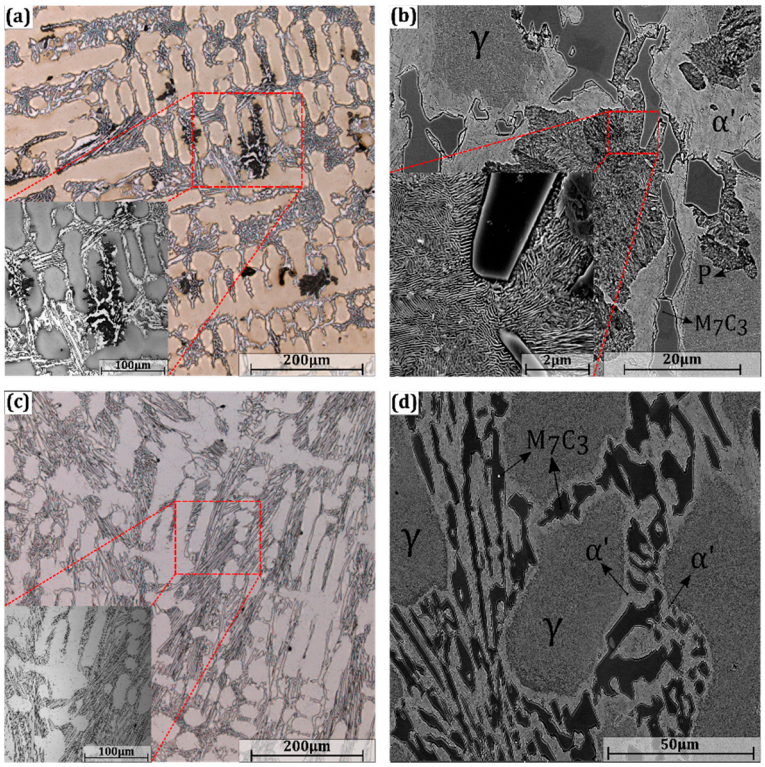

Figure 1. Representative OM (200×) and SEM micrographs of samples A (**a**,**b**) and B (**c**,**d**), respectively, after Vilella's etching. Inset in (**a**,**c**) represents a magnified image (500×) acquired using laser light. The different phases, austenite (γ), martensite (α'), pearlite (P), and eutectic carbides (M_7C_3) are indicated in images (**b**,**d**). The pearlite phase can be observed in the inset in (**b**).

From the OM and SEM micrographs, it was observed that the matrix of Sample B is completely austenitic whereas some partial transformation to pearlite has occurred in Sample A. Generally,

austenitic matrix structures are favored by high Ni and Mo contents, a high Cr/C ratio, and faster cooling rates during casting [33–35]. According to the graph presented by Maratray et al. [33], where the Cr/C ratio and the bulk Mo composition are related to the decomposition of the austenite upon cooling, for a cast alloy with a Mo content of 0.4 wt. %, the Cr/C ratio needs to be around 6.5 (which is the same as Sample A) to avoid austenite decomposition. Therefore, the partial austenite to pearlite transformation in Sample A can be primarily attributed to the low Cr/C ratio (6.5) since both samples, A and B contain negligible amounts of Ni and Mo, were casted under similar conditions, and Sample B presents a Cr/C ratio of 10.5.

In addition to the major phases, austenite and M_7C_3 EC, a thin layer of martensite was observed at the periphery of the carbides, which is clearly visible in the SEM micrographs (Figure 1b,d). The presence of these phases is further confirmed by XRD in Figure 2. The martensite formation is associated with the local C and Cr depletion which takes place during the solidification of the EC in contact with the pro-eutectic austenite, as also observed in other studies [14,24,29]. The impoverishment of alloying elements at the contact zone results in an increase in the martensitic start (M_s) temperature leading to its formation during subsequent cool down.

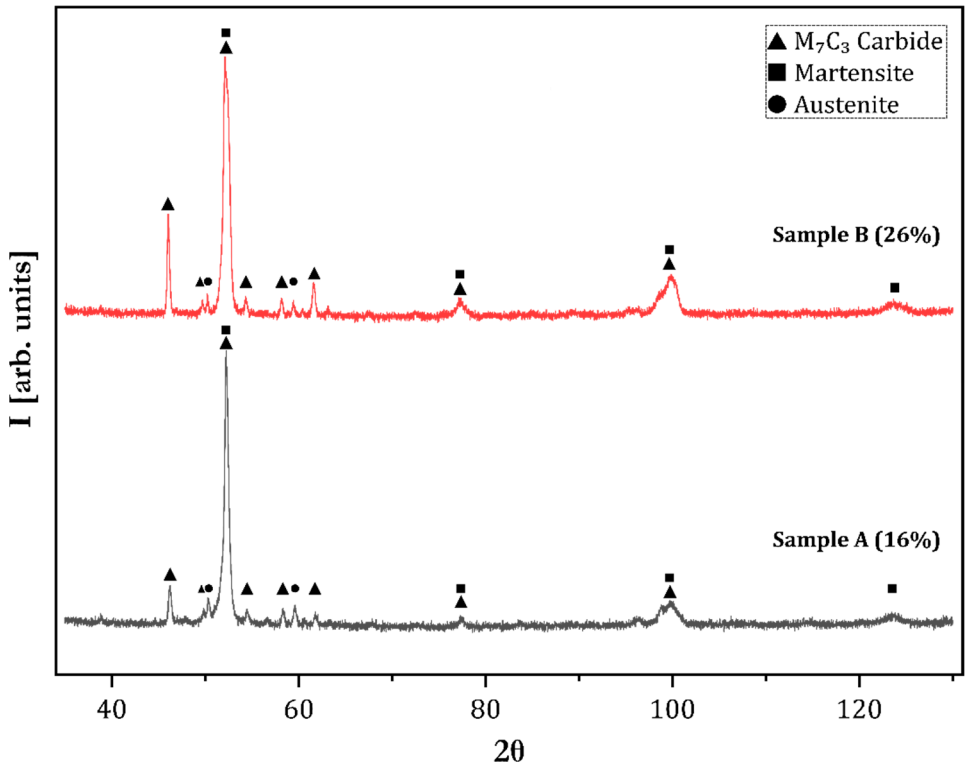

Figure 2. X-ray diffractograms of samples A and B. Austenite, martensite, and the M_7C_3 carbide are indexed for reference.

SEM micrographs depicting the three dimensional structure of the EC are shown in Figure 3. The carbides are located heterogeneously throughout the material possessing a rhombohedral/hexagonal cross section. Their growth mechanism during solidification has been explained elsewhere [31,36,37]. Both rod and plate-like EC are seen as this is a hypoeutectic alloy [15,38]. Moreover, the 'rosette' pattern can be observed in Figure 3a with hollow, fine rods at the center and larger blades as we move away. The difference in their sizes is associated with the decrease in undercooling as the solidification progresses, and the segregation of alloying elements in the melt [39].

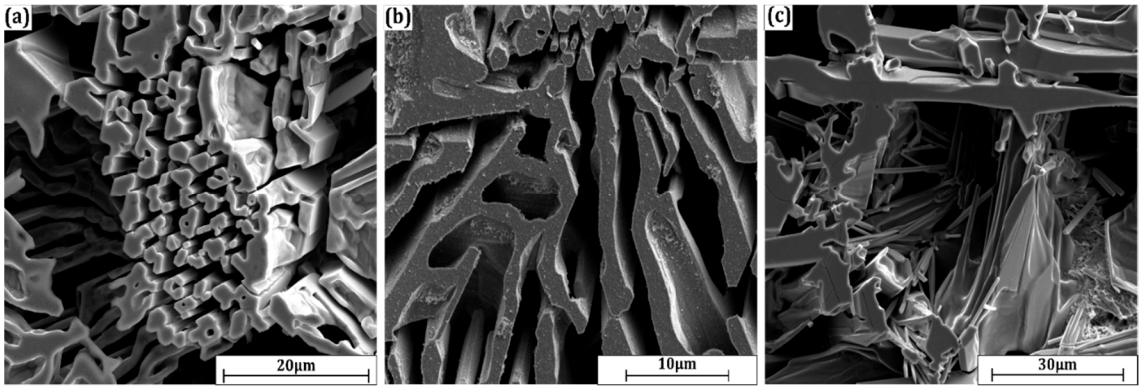

Figure 3. Representative SEM micrographs of Sample B after deep etching. The three-dimensional structure of the eutectic carbide is visible. (**a**) 'rosette' pattern, with the thin hexagonal rods at the center; (**b**) blade morphology; and (**c**) heterogenity in nucleation.

3.2. Pseudo-Binary Phase Diagram

The pseudo-binary phase diagrams for both alloys at carbon contents ranging from 2 wt. % to 5 wt. % were computed using MatCalc as shown in Figure 4. The generation of a pseudo-binary phase diagram will help in understanding the solidification sequence of the alloy and the corresponding equilibrium phase stabilities. This information is essential for alloy development and subsequent heat treatment design. From Figure 4, it can be seen that increasing the bulk chromium content results in an increase in the eutectic transition temperature (1285 → 1315 °C) and a decrease in the eutectic carbon content (3.88 wt. % → 3.24 wt. % C). Despite the similar carbon contents in the alloys, Sample B shows a smaller solidification range (30 °C) compared to its counterpart, Sample A (70 °C). It is due to the addition of chromium which increases the fraction of EC formed and improves its stability [21,23]. As a result, the formation temperature of the EC in Sample B is higher (1302 °C) in comparison with Sample A (1281 °C), indicating that it is stable for a larger range of temperatures compared to the latter. The phase diagram also predicts the formation of an additional carbide, $M_{23}C_6$, in Sample B around 1000 °C which suggests that increasing the Cr/C ratios stabilize the $M_{23}C_6$ carbide. Nevertheless, $M_{23}C_6$ was not experimentally observed, possibly due to faster cooling rate and very low Mo content [10,40].

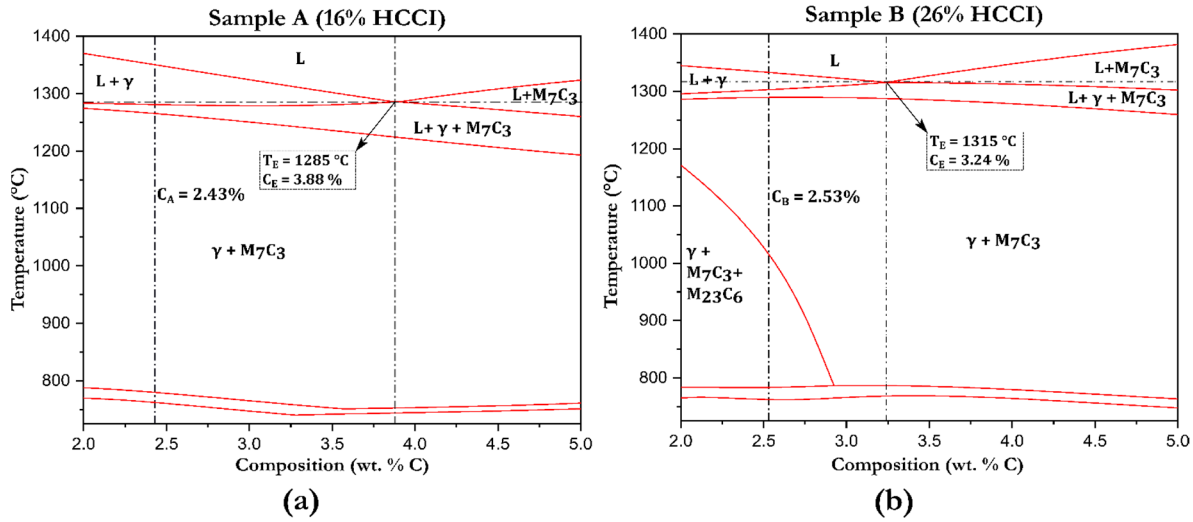

Figure 4. Pseudo-binary phase diagrams for samples, A and B computed using MatCalc 6. The eutectic transition temperature (T_E) and the corresponding eutectic carbon content (C_E) is indicated in the graphs along with the overall carbon content of (**a**) Sample A (C_A) and (**b**) Sample B (C_B).

Furthermore, to illustrate the influence of C and more specifically, Mo on the stability of the $M_{23}C_6$ carbide for various temperatures, phase boundaries were traced using MatCalc which is represented in Figure 5. It is observed, that at least 1% Mo is necessary for the low temperature stabilization of the $M_{23}C_6$ carbide at lower chromium contents for a constant carbon content, corroborating with other studies [10,41]. Moreover, at a given temperature, increasing the carbon content will necessitate an increase in the chromium content to ensure the stability of $M_{23}C_6$. This is because Cr is primarily a M_7C_3 carbide former for HCCI's up to 30% Cr after which, $M_{23}C_6$ becomes the stable carbide upon solidification [32,34].

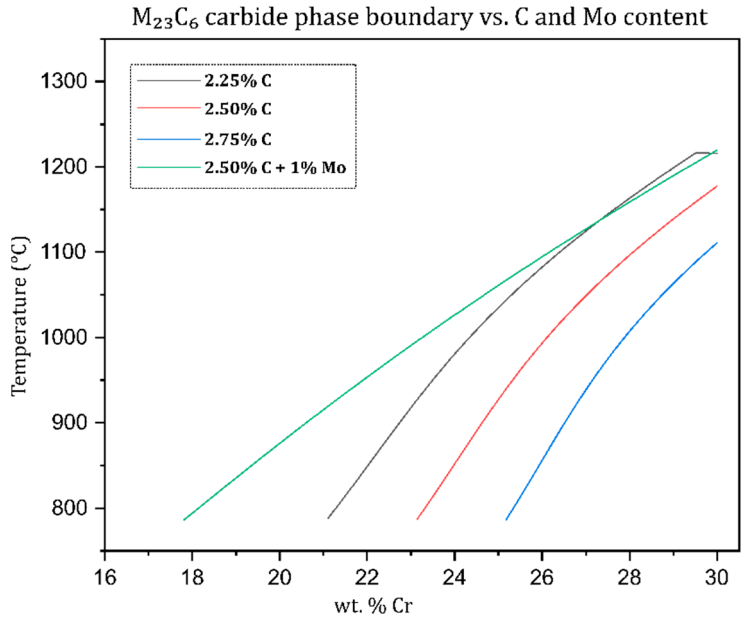

Figure 5. The influence of C and Mo on the phase boundary of the $M_{23}C_6$ carbide predicted by MatCalc 6.

3.3. Carbide Volume Fraction

It is well known that the nature and volume fraction of the EC is strongly influenced by the amount of chromium present in the alloy, as it is a strong carbide former [42]. The volume fraction of the EC corresponding to both samples, A and B was theoretically determined using empirical formulae suggested by Maratray et al. [29] (Equation (1)) and Doğan et al. [30] (Equation (2)), which was solely based on the bulk composition of C and Cr (in wt. %). Additionally, the total bulk chemical composition (Table 1) was used as the input for the software in simulating the equilibrium fraction of each phase. Figure 6 represents the equilibrium phase fractions determined for both alloys using MatCalc. The theoretical (Equations (1) and (2)) and simulated (MatCalc) values were then compared to the experimental results obtained from the I-A of microscopy images.

$$\% \text{ CVF} = 12.33\ (\%C) + 0.55\ (\%Cr) - 15.2 \quad (1)$$

$$\% \text{ CVF} = 14.05\ (\%C) + 0.43\ (\%Cr) - 22 \quad (2)$$

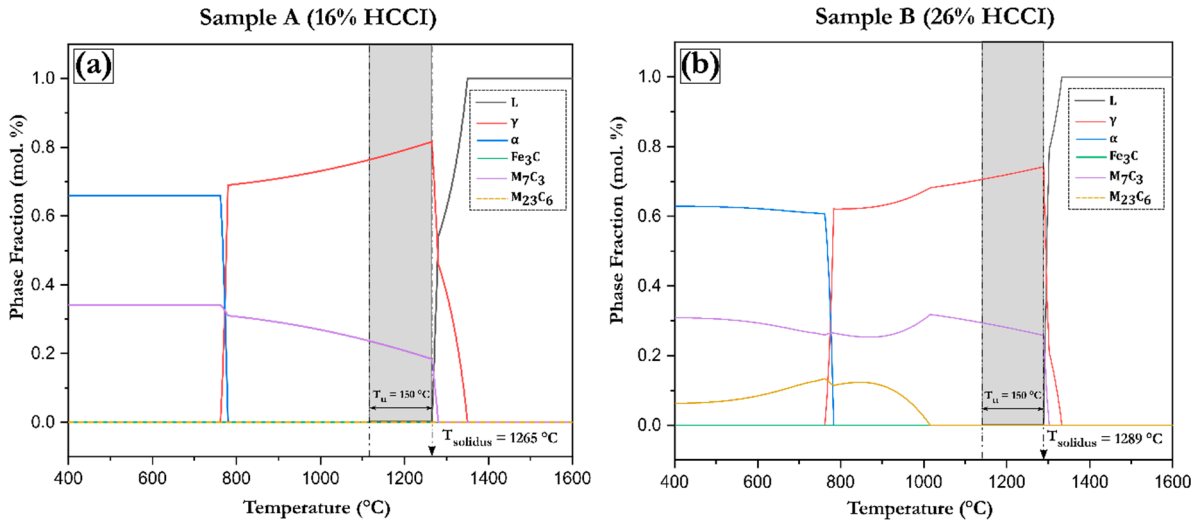

Figure 6. Equilibrium phase fractions for (**a**) Sample A (16% HCCI) and (**b**) Sample B (26% HCCI) as predicted by MatCalc. The solidus temperature, $T_{solidus}$ for both alloys including the range of undercooling considered, T_u = 150 °C is indicated in the schematic.

Table 3 compares the % CVF obtained using the different approaches. It is evident that the % CVF of Sample B is higher than Sample A owing to the increased chromium for a quasi-constant carbon content. The % CVF increased by approximately 50% for an additional 10 wt. % of chromium. The differences in the results shown by the two formulae could be due to the number of samples considered for the study and the accuracy of determining the % CVF for each alloy [29,30]. Equation (1) was deduced by Maratray et al. after studying over 40 different alloys with varying C (1.95 to 4.31 wt. %) and Cr (10.8 to 25.82 wt. %) contents. Equation (2) is a result of the work carried out by Doğan et al. on hypoeutectic, eutectic and hypereutectic cast iron compositions with Cr contents of 15 and 26 wt. %. The hypoeutectic compositions considered in [30] is analogous to the alloys used in this study. Although the experimental values are close to the numerically predicted values, care must be taken as the formulae only consider the influence of C and Cr [1].

Table 3. Comparison between the % carbide volume fractions (CVFs) of both alloys obtained using different approaches.

Sample	Emperical Formulae (%)		MatCalc (at $T_{solidus}$) (%)	MatCalc (at $T_{solidus}$ −150 °C) (%)	Experimental (I-A) (%)
	Maratray [29]	Doğan [30]			
A (16% HCCI)	23.4 ± 2.1	19.0	18.4	21.2 ± 1.5	19.4 ± 0.4
B (26% HCCI)	30.6 ± 2.1	25.0	25.8	27.7 ± 1.1	30.4 ± 0.6

The equilibrium EC phase fraction predicted by MatCalc was initially considered at the temperature where the liquid ceases to exist i.e., the solidus temperature, $T_{solidus}$. Due to the larger solidification range of Sample A, its $T_{solidus}$ is lower (1265 °C) than Sample B (1289 °C). In both cases, the % CVF predicted by MatCalc is lower than the values obtained experimentally which can be explained by the non-equilibrium solidification during casting, leading to the existence of an undercooling regime [31,39]. Considering a degree of undercooling, T_u = 150 °C, and averaging the phase fraction values in that range ($T_{solidus}$−150 °C) for both alloys yields a value of 21.2% ± 1.5% CVF for Sample A and 27.7% ± 1.1% CVF for Sample B. Comparing this % CVF with the value determined at $T_{solidus}$, an increase is observed in both cases (Sample A and Sample B). The increase in the % CVF with decreasing temperature can be attributed to the increased driving force for nucleation due to the undercooling effect. Consequently, it is observed that the predicted and experimental % CVF values correspond well and differences between them, fall within an error of less than 5%.

To further validate the results given by the simulation software, a few alloys with varying C and Cr contents were considered from the expansive study conducted by Maratray et al. [29] and Doğan et al. [30]. Table 4 lists the considered alloys and the % CVF obtained using metallography, Equations (1) and (2), and the prediction by MatCalc. The procedure employed to obtain the % CVF from MatCalc is similar to the one previously mentioned, i.e., determining the $T_{solidus}$ for each composition and considering an undercooling range, T_u = 150 °C. It is seen that for relatively low Cr/C ratios (3.7–4.3), the formula suggested by Doğan and experimental values match, whereas Maratray's formula can be used for higher Cr/C ratios. It is also worth mentioning that increasing the Cr content alone did not lead to a significant increase in % CVF as evident in alloys M1 and M3. Comparing the alloys M1, D1 and M2, it is observed that addition of C (2.08 → 3.54 → 4.10) for a relatively constant Cr led to a massive increase in the % CVF (18.7 → 33.0 → 42.0). This further consolidates the effect of C on the volume fraction of the carbides compared with Cr. Despite the drastic variation in C and Cr content in all samples, the % CVF predicted by MatCalc is always comparable to the experimentally determined values which supports the usage of simulation to predict the volume fraction of the eutectic carbide in the as-cast state.

Table 4. The % CVF of certain alloys experimentally determined by [29,30], the numerical estimations and the corresponding % CVF computed using MatCalc (in grey).

Study	Alloy	Chemical Composition (wt. %)							Cr/C	% CVF (Experiment)	% CVF Equation (1)	% CVF Equation (2)	% CVF (MatCalc)
		C	Cr	Mn	Mo	Si	Ni	Fe					
Maratray et al. [29]	M1	2.08	15.85	0.70	-	1.00	-	Bal.	7.6	18.7	19.2 ± 2.1	14.0	16.8 ± 1.5
	M2	4.10	15.10	0.70	-	1.00	-	Bal.	3.7	42.0	43.7 ± 2.1	42.1	40.9 ± 1.2
	M3	2.08	20.55	0.70	-	1.00	-	Bal.	9.9	20.5	21.7 ± 2.1	16.1	19.7 ± 1.3
	M4	2.95	25.82	0.70	0.02	1.00	-	Bal.	8.8	32.3	35.4 ± 2.1	30.6	32.3 ± 1.0
Doğan et al. [30]	D1	3.54	15.2	0.61	0.31	0.51	0.18	Bal.	4.3	33.0 ± 2.0	36.8 ± 2.1	34.3	34.0 ± 1.4
	D2	2.76	26.2	0.93	0.38	0.42	0.38	Bal.	9.5	29.0 ± 1.0	33.2 ± 2.1	28.0	30.4 ± 1.1

3.4. Chemical Composition

In order for effectively designing heat treatment cycles, it is essential to have an understanding of the individual matrix and carbide compositions [30]. The composition between the matrix and carbide will vary depending upon the alloying elements present, the cooling rate during casting and the bulk Cr/C ratio [1,5]. For these reasons, and in order to correlate experimental with simulated values, the matrix and carbide chemical composition were determined by EPMA and MatCalc (Table 5). The matrix and carbide elemental compositions determined with MatCalc, were calculated considering the weight fraction of the element present in the respective phase at the given temperature and taking the average value over the undercooling range ($T_{solidus} - T_u$).

Table 5. Matrix and carbide elemental compositions (in wt. %) for the two alloys as determined by electron probe microanalysis (EPMA) and MatCalc. The distribution of Cr and Fe within the M_7C_3 carbide is also compared.

Sample	Matrix			Carbide			$(Cr_xFe_y)C_3$	
	Element (wt. %)	EPMA	MatCalc	Element (wt. %)	EPMA	MatCalc	EPMA	MatCalc
A (16% HCCI)	C	0.86 ± 0.34	1.12 ± 0.12	C	7.54 ± 0.49	8.71 ± 0.00	$(Cr_{3.9}Fe_{3.1})C_3$	$(Cr_{3.9}Fe_{3.1})C_3$
	Cr	12.10 ± 0.21	8.79 ± 0.71	Cr	48.81 ± 3.63	49.5 ± 0.45		
	Mn	0.60 ± 0.02	0.77 ± 0.00	Mn	-	-		
	Ni	0.13 ± 0.03	0.21 ± 0.00	Ni	0	0		
	Mo	0.21 ± 0.04	0.27 ± 0.03	Mo	-	-		
	Fe	85.6 ± 0.3	88.84 ±0.85	Fe	41.99 ± 3.65	39.99 ± 0.52		
B (26% HCCI)	C	0.43 ± 0.13	0.69 ± 0.09	C	7.85 ± 0.53	8.83±0.00	$(Cr_5Fe_2)C_3$	$(Cr_5Fe_2)C_3$
	Cr	18.21 ± 1.24	15.37 ± 0.78	Cr	63.07 ± 1.87	65.13 ± 0.77		
	Mn	0.67 ± 0.03	0.72 ± 0.00	Mn	-	-		
	Ni	0.20 ± 0.04	0.33 ± 0.00	Ni	0	0		
	Mo	0.14 ± 0.03	0.2 ± 0.01	Mo	-	-		
	Fe	80.0 ± 1.3	82.68 ± 0.87	Fe	28.36 ± 2.11	25.19 ± 0.79		

From Table 5, it is evident that the Cr content (wt. %) of both the matrix and EC increased as the bulk Cr content increased although the C content (wt. %) in the EC remained at a stoichiometric level. The addition of chromium reduces the carbon solubility in austenite [17] and as a result, the 26% HCCI alloy has a lower matrix C content. This can be further elucidated by considering the partition ratio of the elements. The segregation or partition ratio, as coined by Laird [43], is the element's affinity to partition into the carbide or the matrix and can be defined as the ratio of the weight percent of the element in the carbide to the matrix. Higher ratios, as in the case of chromium and carbon suggest strong partitioning towards the carbides whereas elements such as Si, Ni, and Cu are found only at the matrix regions. The Cr partition ratio from EPMA measurements for Sample A and Sample B was 4 and 3.5, respectively. Furthermore, the partition ratio of C in Sample B (18.25) is higher compared to Sample A (8.77) indicating an increased affinity to the eutectic carbides (as evidenced by the lower C content of the 26% HCCI matrix).

The distribution of Cr and Fe within the EC was determined by converting the respective weight percentages into atomic percentage and normalizing with the carbon atomic percentage (30 at. %). Despite both materials having M_7C_3 as the EC, the Fe/Cr ratio is lower in the case of 26% HCCI indicating that less Cr atoms were substituted by Fe. It is also worthy to mention that although trace amounts of Mn and Mo were detected by EPMA and also predicted by MatCalc in the EC for both samples, it is not shown in Table 5. The Cr content (in at. %) of the EC increased from approximately 40% in Sample A to 50% in Sample B, which is the highest for these type of alloys [29]. In both cases, the elemental compositions of the matrix and EC, and the chromium–iron distribution in the EC predicted by MatCalc are in accordance with the values measured by EPMA.

A similar alloy (C, 2.72%; Cr, 26.6%; Mn, 0.2%; Si, 0.78%; Ni, 0.17%) was studied by Carpenter et al. [44] wherein the Cr content of the EC was determined to be 49.7 at. % ± 1.6 at. % by chemical microanalysis. Comparing this alloy with Sample B, it is observed that the Cr content of the EC is identical in both cases even though there is a slight increase in the bulk C content. This further upholds the notion that 50 at. % Cr ($Cr_5Fe_2C_3$) is the highest for M_7C_3 type of EC in HCCIs [33]. Moreover, the experimental value obtained by Carpenter et al. was corroborated by MatCalc, which predicted a Cr content of 49.7 at. % ± 0.7 at. % Cr in the EC.

3.5. Hardness

Table 6 details the values of hardness on three different scales. Sample B shows higher bulk hardness (HRC) owing to the higher volume fraction of the M_7C_3 carbides formed. Despite the differences in the chemical composition of the matrix, its microhardness (HV0.1) for both alloys remained similar. This coincidental value of the matrix hardness can be attributed to the presence of a high carbon matrix in Sample A and a high alloying in Sample B due to the Cr content [30]. It also sheds light on the efficacy of the carbon contribution to the hardness of the matrix compared to chromium. Furthermore, the hardness of the M_7C_3 carbide increases from Sample A to Sample B which could be attributed to the increasing Cr content of the carbide [45].

Table 6. Results of the bulk, matrix and carbide hardness for both alloys.

Sample	Rockwell (HRC) (Bulk)	Vickers (HV0.1) (Matrix)	Nanoindentation (GPa) (EC)
A (16% HCCI)	46.3 ± 0.8	356 ± 11	13.1 ± 1.7
B (26% HCCI)	49.3 ± 0.5	360 ± 21	19.0 ± 1.2

4. Conclusions

Computational tools and experimental results were combined in this work with the aim to validate the usage of MatCalc simulations for the prediction of phase fractions and elemental distribution in HCCI's in the as-cast condition, for the convincing implementation of these tools for further heat

treatment design. For that, two as-cast alloys (containing 16% and 26% Cr) were fabricated under similar conditions with the main variance being the Cr content. The EC phase fraction and the individual matrix, and carbide compositions were determined experimentally and compared with the values predicted by the MatCalc simulation. The principal conclusions that can be drawn from the above work are as follows:

- OM and SEM micrographs indicate a dispersion of M_7C_3 eutectic carbides in an austenitic matrix with a thin layer of martensite formed at the carbides' periphery for both alloys. Although the matrix is purely austenite in Sample B, some partial transformation to pearlite has occurred in Sample A, owing to the low Cr/C ratio.
- The pseudo-binary phase diagrams constructed using MatCalc indicate the formation of $M_{23}C_6$ carbide at temperatures below 1050 °C in Sample B. However, the presence of $M_{23}C_6$ carbide was not detected due to the non-equilibrium cooling and the low Mo content of the alloy.
- An addition of 10 wt. % Cr lead to an increase of about 50% of the EC as evidenced by image analysis. The % CVF was lower when determined from MatCalc at $T_{solidus}$. Nevertheless, by considering an undercooling range of 150 °C as a consequence of the non-equilibrium solidification, the predicted % CVF corresponded well with experimentally determined values. Therefore, the MatCalc simulated data is reliable for the determination of % CVF. The accuracy of the simulation software was further validated comparing the % CVF of several alloys (with different C and Cr contents) to the experimental values obtained by other authors from metallographic techniques.
- The predictions made by MatCalc are in accordance with the values obtained by EPMA. MatCalc also predicted an increase Cr/Fe ratio in the EC with increasing Cr content, which was corroborated by EPMA measurements. Additionally, the Cr/Fe ratio predicted by MatCalc for Sample B showed a good correspondence with experimental results found in the literature.
- Finally, the increase in the bulk hardness of Sample B was related to the increased M_7C_3 fraction, whereas the individual EC hardness was higher in Sample B than Sample A due to the increased Cr occupation in the EC. Despite the lower bulk and carbide hardness, the matrix hardness of Sample A was on par with B, probably due to the high C content in the matrix which prevented a decrement.

To sum up, this work demonstrated the capability of MatCalc to accurately predict the EC phase fraction and elemental distribution within the phases, which bolsters its implementation in the design of heat treatments. The time and resource intensive experimental procedures can be replaced by simulation techniques to determine the phase fraction and especially, the individual phase compositions in the as-cast state. Furthermore, the elemental distribution within the matrix and EC is reflected in its corresponding hardness. The knowledge provided by this tool about the elemental distribution within the phases beforehand will assist in designing a heat treatment cycle for an HCCI alloy to be used in a specific application and pave way for 'microstructural tailoring'. Accordingly, the microstructural modifications occurring in these alloys during heat treatments, including the carbide precipitation kinetics, will be investigated as a part of future work.

Author Contributions: Conceptualization and methodology, U.P.N. and M.A.G.; Simulation, experimental validation, formal analysis, data curation and writing–original draft preparation, U.P.N.; writing–review and editing, and supervision, M.A.G. and F.M.; project administration and funding acquisition, F.M. All authors have read and agreed to the published version of the manuscript.

Funding: The authors wish to acknowledge the EFRE Funds (C/4-EFRE-13/2009/Br) of the European Commission for supporting activities within the AME-Lab project.

Acknowledgments: The authors would like to thank Martin Duarte from Tubacero S.A. for providing the materials and Sandvik Materials Technology for the EPMA measurements. Additionally, UP Nayak is grateful to DAAD for the financial support.

Conflicts of Interest: The authors declare no conflict of interest.

References

1. Tabrett, C.P.; Sare, I.R.; Ghomashchi, M.R. Microstructure-property relationships in high chromium white iron alloys. *Int. Mater. Rev.* **1996**, *41*, 59–82. [CrossRef]
2. ASTM Standard A 532/A 532M-93a. *Standard Specification for Abrasion Resistance Cast Irons*; ASTM International: West Conshohocken, PA, USA, 2003. Available online: www.astm.org (accessed on 23 December 2019).
3. International Organization for Standardization. *Abrasion-Resistant Cast Irons-Classification (ISO 21988:2006)*; International Organization for Standardization: Geneva, Switzerland, 2006. Available online: www.iso.org (accessed on 23 December 2019).
4. Karantzalis, E.; Lekatou, A.; Mavros, H. Microstructure and properties of high chromium cast irons: Effect of heat treatments and alloying additions. *Int. J. Cast Met. Res.* **2009**, *22*, 448–456. [CrossRef]
5. Wiengmoon, A.; Pearce, J.T.H.; Chairuangsri, T. Relationship between microstructure, hardness and corrosion resistance in 20 wt. %Cr, 27 wt. %Cr and 36 wt. %Cr high chromium cast irons. *Mater. Chem. Phys.* **2011**, *125*, 739–748. [CrossRef]
6. Laird, G.; Powell, G.L.F. Solidification and solid-state transformation mechanisms in Si alloyed high-chromium white cast irons. *Metall. Trans. A* **1993**, *24*, 981–988. [CrossRef]
7. Bedolla-Jacuinde, A.; Correa, R.; Quezada, J.G.; Maldonado, C. Effect of titanium on the as-cast microstructure of a 16%chromium white iron. *Mater. Sci. Eng. A* **2005**, *398*, 297–308. [CrossRef]
8. Kopyciński, D.; Guzik, E.; Siekaniec, D.; Szczęsny, A. The effect of addition of titanium on the structure and properties of high chromium cast iron. *Arch. Foundry Eng.* **2015**, *15*, 35–38. [CrossRef]
9. Scandian, C.; Boher, C.; de Mello, J.D.B.; Rézaï-Aria, F. Effect of molybdenum and chromium contents in sliding wear of high-chromium white cast iron: The relationship between microstructure and wear. *Wear* **2009**, *267*, 401–408. [CrossRef]
10. Imurai, S.; Thanachayanont, C.; Pearce, J.T.H.; Tsuda, K.; Chairuangsri, T. Effects of Mo on microstructure of as-cast 28 wt. % Cr-2.6 wt. % C-(0-10) wt. % Mo irons. *Mater. Charact.* **2014**, *90*, 99–112. [CrossRef]
11. Lv, Y.; Sun, Y.; Zhao, J.; Yu, G.; Shen, J.; Hu, S. Effect of tungsten on microstructure and properties of high chromium cast iron. *Mater. Des.* **2012**, *39*, 303–308. [CrossRef]
12. Cortés-Carrillo, E.; Bedolla-Jacuinde, A.; Mejía, I.; Zepeda, C.M.; Zuno-Silva, J.; Guerra-Lopez, F.V. Effects of tungsten on the microstructure and on the abrasive wear behavior of a high-chromium white iron. *Wear* **2017**, *376–377*, 77–85. [CrossRef]
13. Doğan, Ö.N.; Hawk, J.A. Effect of carbide orientation on abrasion of high Cr white cast iron. *Wear* **1995**, *189*, 136–142. [CrossRef]
14. Gahr, K.H.Z.; Doane, D.V. Optimizing fracture toughness and abrasion resistance in white cast irons. *Metall. Trans. A* **1980**, *11*, 613–620. [CrossRef]
15. Asensio, J.; Pero-Sanz, J.A.; Verdeja, J.I. Microstructure selection criteria for cast irons with more than 10 wt. % chromium for wear applications. *Mater. Charact.* **2002**, *49*, 83–93. [CrossRef]
16. Maratray, F.; Poulalion, A. Austenite Retention in High-Chromium White Irons. *Trans. Am. Foundrym. Soc.* **1982**, *90*, 795–804.
17. Poolthong, N.; Nomura, H.; Takita, M. Effect of heat treatment on microstructure and properties of semi-solid chromium cast iron. *Mater. Trans.* **2004**, *45*, 880–887. [CrossRef]
18. *ASM Handbook Volume 3: Alloy Phase Diagrams*; ASM International: Materials Park, OH, USA, 2016; ISBN 978-1-62708-070-5. Available online: www.asminternational.org (accessed on 23 December 2019).
19. Kozeschnik, E.; Buchmayr, B. Matcalc—A simulation tool for multicomponent thermodynamics, diffusion and phase transformations. In Proceedings of the Mathematical Modelling of Weld Phenomena, Leibnitz, Austria, 1–3 October 2001; pp. 349–361.
20. Kroupa, A. Modelling of phase diagrams and thermodynamic properties using Calphad method—Development of thermodynamic databases. *Comput. Mater. Sci.* **2013**, *66*, 3–13. [CrossRef]
21. Li, D.; Liu, L.; Zhang, Y.; Ye, C.; Ren, X.; Yang, Y.; Yang, Q. Phase diagram calculation of high chromium cast irons and influence of its chemical composition. *Mater. Des.* **2009**, *30*, 340–345. [CrossRef]
22. Albertin, E.; Beneduce, F.; Matsumoto, M.; Teixeira, I. Optimizing heat treatment and wear resistance of high chromium cast irons using computational thermodynamics. *Wear* **2011**, *271*, 1813–1818. [CrossRef]
23. Akyildiz, Ö.; Candemir, D.; Yildirim, H. Simulation of Phase Equilibria in High Chromium White Cast Irons. *Uludağ Univ. J. Fac. Eng.* **2018**, *23*, 179–190. [CrossRef]

24. Guitar, M.A.; Scheid, A.; Suárez, S.; Britz, D.; Guigou, M.D.; Mücklich, F. Secondary carbides in high chromium cast irons: An alternative approach to their morphological and spatial distribution characterization. *Mater. Charact.* **2018**, *144*, 621–630. [CrossRef]
25. Guitar, M.A.; Suárez, S.; Prat, O.; Duarte Guigou, M.; Gari, V.; Pereira, G.; Mücklich, F. High Chromium Cast Irons: Destabilized-Subcritical Secondary Carbide Precipitation and Its Effect on Hardness and Wear Properties. *J. Mater. Eng. Perform.* **2018**, *27*, 3877–3885. [CrossRef]
26. Collins, W.K.; Watson, J.C. Metallographic etching for carbide volume fraction of high-chromium white cast irons. *Mater. Charact.* **1990**, *24*, 379–386. [CrossRef]
27. Wiengmoon, A.; Chairuangsri, T.; Poolthong, N.; Pearce, J.T.H. Electron microscopy and hardness study of a semi-solid processed 27 wt%Cr cast iron. *Mater. Sci. Eng. A* **2008**, *480*, 333–341. [CrossRef]
28. Schindelin, J.; Ignacio Arganda-Carreras, E.F.; Kaynig, V.; Longair, M.; Pietzsch, T.; Preibisch, S.; Rueden, C.; Saalfeld, S.; Schmid, B.; Tinevez, J.-Y.; et al. Fiji: An open-source platform for biological-image analysis. *Nat. Methods* **2012**, *9*, 676–682. [CrossRef]
29. Maratray, F.; Usseglio-Nanot, R. *Factors Affecting the Structure of Chromium and Chromium—Molybdenum White Irons*; Climax Molybdenum S. A: Paris, France, 1970.
30. Doğan, Ö.N.; Hawk, J.A.; Laird, G. Solidification structure and abrasion resistance of high chromium white irons. *Metall. Mater. Trans. A Phys. Metall. Mater. Sci.* **1997**, *28*, 1315–1328. [CrossRef]
31. Bedolla-Jacuinde, A.; Hernández, B.; Béjar-Gómez, L. SEM study on the M7C3 carbide nucleation during eutectic solidification of high chromium white irons. *Zeitschrift Met.* **2005**, *96*, 1380–1385.
32. Zumelzu, E.; Goyos, I.; Cabezas, C.; Opitz, O.; Parada, A. Wear and corrosion behaviour of high-chromium (14–30% Cr) cast iron alloys. *J. Mater. Process. Technol.* **2002**, *128*, 250–255. [CrossRef]
33. Maratray, F. Choice of appropriate compositions for chromium-molybdenum white irons. *AFS Trans.* **1971**, *79*, 121–124.
34. Abdel-Aziz, K.; El-Shennawy, M.; Omar, A.A. Microstructural Characteristics and Mechanical Properties of Heat Treated High-Cr White Cast Iron Alloys. *Int. J. Apll. Eng. Res.* **2017**, *12*, 4675–4686.
35. Doğan, Ö.N.; Laird, G.; Hawk, J.A. Abrasion resistance of the columnar zone in high Cr white cast irons. *Wear* **1995**, *181*, 342–349. [CrossRef]
36. Matsubara, Y.; Ogi, K.; Matsuda, K. Eutectic Solidification of High-Chromium Cast Iron—Eutectic Structures and Their Quantitative Analysis. *Trans. Am. Foundrym. Soc.* **1982**, *89*, 183–196.
37. Ohide, T.; Ohira, G. Solidification of High Chromium Alloyed Cast Iron. *Foundryman* **1983**, *76*, 7–14.
38. Doğan, Ö.N. Columnar to equiaxed transition in high Cr white iron castings. *Scr. Mater.* **1996**, *35*, 163–168. [CrossRef]
39. Filipovic, M.; Romhanji, E.; Kamberovic, Z. Chemical composition and morphology of M7C3 eutectic carbide in high chromium white cast iron alloyed with vanadium. *ISIJ Int.* **2012**, *52*, 2200–2204. [CrossRef]
40. Medvedeva, N.I.; Van Aken, D.C.; Medvedeva, J.E. Stability of binary and ternary M23C6 carbides from first principles. *Comput. Mater. Sci.* **2015**, *96*, 159–164. [CrossRef]
41. Choi, J.W.; Chang, S.K. Effects of Molybdenum and Copper Additions on Microstructure of High Chromium Cast Iron Rolls. *ISIJ Int.* **1992**, *32*, 1170–1176. [CrossRef]
42. Powell, G.L.F.; Laird, G. Structure, nucleation, growth and morphology of secondary carbides in high chromium and Cr-Ni white cast irons. *J. Mater. Sci.* **1992**, *27*, 29–35. [CrossRef]
43. Laird, G. Microstructures of Ni-Hard I, Ni-Hard IV and High-Cr White Cast Irons. *AFS Trans.* **1991**, *99*, 339–357.
44. Carpenter, S.D.; Carpenter, D.; Pearce, J.T.H. XRD and electron microscope study of an as-cast 26.6% chromium white iron microstructure. *Mater. Chem. Phys.* **2004**, *85*, 32–40. [CrossRef]
45. Kagawa, A.; Okamoto, T.; Saito, K.; Ohta, M. Hot hardness of (Fe, Cr)3C and (Fe, Cr)7C3 carbides. *J. Mater. Sci.* **1984**, *19*, 2546–2554. [CrossRef]

II. Evaluation of Etching Process Parameter Optimization in the Objective Specific Microstructural Characterization of As-Cast and Heat Treated HCCI Alloy

U. Pranav Nayak, María Agustina Guitar, Frank Mücklich

Department of Materials Science and Engineering, Saarland University, 66123 Saarbrücken, Germany

Published in "***Practical Metallography***" (2020) *(IF (2023): 0.225)*

Reproduced with permission from 'Walter de Gruyter GmbH'

Accessible online at: *https://doi.org/10.3139/147.110682*

Own Contribution: Conceptualization and methodology; sample preparation; experimentation; microstructural characterization and analysis; scientific discussion; paper writing – original draft preparation

U. P. Nayak, M. A. Guitar, F. Mücklich

Evaluation of Etching Process Parameter Optimization in the Objective Specific Microstructural Characterization of As-Cast and Heat Treated HCCI Alloy

Beurteilung der Parameteroptimierung des Ätzvorgangs zur ‚zweck-spezifischen' Charakterisierung der Mikrostruktur einer HCCI-Legierung im Gusszustand und nach Wärmebehandlung

Received: May 29, 2020
Accepted: August 06, 2020

Eingegangen: 29. Mai 2020
Angenommen: 06. August 2020
Übersetzung: V. Müller

Abstract

The optimization of the etching process parameters in high chromium cast irons (HCCI) for general microstructural observation, eutectic and secondary carbide quantification and 3D analysis of the carbide network is indispensable for further microstructure-properties correlation. The main aim of the current work is to evaluate the efficacy of certain etchants to aid in 'objective specific'

Kurzfassung

Die Parameteroptimierung bei der Ätzung hochchromhaltiger Gusseisenlegierungen (HCCI, high chromium cast irons) mit dem Ziel allgemeiner mikrostruktureller Beobachtungen, der Quantifizierung von eutektischen und sekundären Carbiden sowie der 3D-Analyse des Carbidnetzwerks sind für die Feststellung weiterer Mikrostruktur-Eigenschaftsbeziehungen unabdingbar. Hauptgegenstand der vorliegenden

Authors:

U. Pranav Nayak, María Agustina Guitar Department of Materials Science, Saarland University. Campus D3.3, D-66123, Saarbrücken, Germany; e-mail: pranav.nayak@uni-saarland.de
Frank Mücklich Materials Engineering Center Saarland (MECS), Campus D3.3, D-66123 Saarbrücken, Germany; e-mail: muecke@matsci.uni-sb.de

microstructural characterization of a 26 % Cr HCCI alloy in the as-cast (AC) and heat treated (HT) state. Samples were etched with various solutions, including Vilella's reagent, Nital, Murakami's reagent and its modification, and two other etchants.

It was seen that specific etchants are needed depending upon the final objective and the results are reliant on their selection and optimal usage. Etching the AC and HT samples with Vilella's reagent for 7 s was sufficient to develop a contrast between the phases which was observed both in confocal laser scanning microscope (CLSM) and scanning electron microscope (SEM). Murakami's reagent and a modification of the same, were used in successfully quantifying the eutectic and secondary carbide volume fraction (CVF) in the AC and HT samples, respectively. Consequently, the knowledge gained in this study will be used as a basis for further microstructural analyses of these alloys and be applied to other alloys in the family.

1. Introduction

High chromium cast iron (HCCI) alloys are a class of materials that belong to the Fe-C-Cr ternary system containing 15–30 wt. % Cr and 2.5–4 wt. % C as described in the ASTM A532 [1,2]. These alloys are primarily used in applications where excellent wear and moderate impact resistance is an advantageous prerequisite, such as in coal and mineral industries [3]. Upon casting, the alloy microstructure consists of an austenitic matrix and a network of M7C3 type eutectic carbides (EC) that surround it.

Arbeit ist die Beurteilung bestimmter Ätzmittel im Hinblick auf ihre Effizienz zur Unterstützung der 'zweck-spezifischen' mikrostrukturellen Charakterisierung einer HCCI-Legierung mit 26 % Cr im Gusszustand (AC, as-cast) und im Zustand nach Wärmebehandlung (HT, heat treated). Die Proben wurden mit Hilfe verschiedener Lösungen geätzt, darunter Nital, das Ätzmittel nach Vilella, das Ätzmittel nach Murakami und eine Modifizierung davon sowie zwei weitere Ätzmittel.

Es wurde festgestellt, dass bestimmte Ätzmittel in Abhängigkeit des letztendlichen Untersuchungsziels zu wählen sind und die Ergebnisse von deren Auswahl und optimalem Einsatz abhängen. Die AC- und HT-Proben wurden 7 s mit dem Ätzmittel nach Vilella geätzt. Diese Dauer war ausreichend, um einen Kontrast zwischen den Phasen zu erzeugen, der sowohl bei der konfokalen Lasermikroskopie (CLSM, confocal laser scanning microscopy) als auch bei der Rasterelektronenmikroskopie (REM) zu erkennen war. Das Ätzmittel nach Murakami und eine Modifizierung davon wurden erfolgreich zur Quantifizierung des Volumenanteils der eutektischen und sekundären Carbide (CVF, secondary carbide volume fraction) in den Proben im Gusszustand bzw. nach Wärmebehandlung eingesetzt. Somit dienen die aus dieser Untersuchung gewonnenen Erkenntnisse als Basis für weitere Mikrostrukturanalysen dieser Legierungen und können auf weitere Legierungen dieser Werkstofffamilie angewandt werden.

1. Einleitung

Hochchromhaltige Gusseisenlegierungen (HCCIs) stellen eine Werkstoffklasse dar, die gemäß ASTM A532 [1,2] zum ternären System Fe-C-Cr gehört und 15–30 Gew.-% Cr und 2,5–4 Gew.-% C enthält. Diese Legierungen werden hauptsächlich dort eingesetzt, wo hervorragende Verschleißfestigkeit und mittlere Schlagzähigkeit eine vorteilhafte Grundvoraussetzung sind, so z. B. in der Kohle- und Mineralindustrie [3]. Beim Gießen besteht die Mikrostruktur der Legierung aus einer austenitischen Matrix und einem die Matrix umgebenden Netzwerk aus eutektischen Carbiden (EC) des Typs M7C3.

It is a well-known fact that the properties of any given material is mainly dictated by its microstructure and modifying it (either by alloying or heat treatment) will alter the final properties making the material versatile to be used for several different applications [4]. Over the years, the influence of various heat treatments on the properties of HCCI alloys have been assessed [5–7]. The heat treatment of HCCI alloys will cause a matrix transformation, in addition to the precipitation of fine secondary carbides (SC) whereas the EC remain relatively unchanged [1, 3].

The stereological characteristics of the EC and SC, such as type, volume fraction, size and its interaction with the host matrix will largely determine the alloys' microstructural and mechanical response [8]. For these reasons, it is imperative to thoroughly characterize the microstructure and to accurately quantify the phases in any given state. Moreover, given the difference in the size range of the phases, ranging from micron sized EC to the sub-micron sized SC, it is necessary to use appropriate microscopical tools while analysing the microstructure.

Although there exists a wide array of qualitative and quantitative techniques to characterize a given microstructure, a major requirement is an optimally etched sample. The necessity to create a contrast on the metallic surface stems from the fact that under a microscope, a finely polished surface looks like a white cloud. Etchants are solutions that help in creating a contrast between the phases in the microstructure by inducing site-specific chemical reactions which greatly aid in visual observations. They also provide valuable information regarding the grain size, distribution of the phases, segregation, foreign particles etc., through which the alloys' behaviour may be determined [9]. Several factors such as so-

Es ist allgemein bekannt, dass die Eigenschaften eines jeden Werkstoffs hauptsächlich durch seine Mikrostruktur bestimmt werden und dass ein Verändern der Mikrostruktur (durch Legieren oder Wärmebehandlung) letztendlich zu einer Veränderung der Eigenschaften führt, was den Werkstoff vielseitig und für zahlreiche Anwendungen einsetzbar macht [4]. In den letzten Jahren wurde der Einfluss verschiedener Wärmebehandlungen auf die Eigenschaften von HCCI-Legierungen untersucht [5–7]. Die Wärmebehandlung von HCCIs führt neben der Ausscheidung feiner sekundärer Carbide (SC) zur Umwandlung der Matrix, während die EC relativ unverändert bleiben [1, 3].

Die stereologischen Eigenschaften der EC und SC wie z. B. Carbidtyp, Volumenanteil, Größe und Interaktion mit der Grundmatrix bestimmen im Wesentlichen das mikrostrukturelle und mechanische Verhalten der Legierung [8]. Aus diesem Grund sind eine eingehende Charakterisierung der Mikrostruktur und eine exakte Quantifizierung der Phasen für jeden Zustand zwingend erforderlich. Darüber hinaus erfordern die unterschiedlichen Größenordnungen der Phasen mit den EC im Mikrometerbereich und den SC im Sub-Mikrometerbereich den Einsatz geeigneter mikroskopischer Instrumente zur Analyse der Mikrostruktur.

Obwohl es eine Vielzahl an qualitativen und quantitativen Methoden zur Charakterisierung einer vorliegenden Mikrostruktur gibt, liegt die Hauptanforderung in einer optimal geätzten Probe. Die Notwendigkeit, einen Kontrast auf der metallischen Oberfläche zu erzeugen, rührt daher, dass eine feinpolierte Oberfläche im Mikroskop wie eine weiße Wolke aussieht. Ätzmittel sind Lösungen, die durch ortsspezifische chemische Reaktionen einen Kontrast zwischen den verschiedenen Phasen der Mikrostruktur hervorrufen und damit visuelle Beobachtungen ermöglichen. Daraus ergeben sich wertvolle Informationen in Bezug auf Korngröße, Phasenverteilung, Ausscheidungen, Fremdpartikel, etc., durch die das Verhalten der Legierung bestimmt werden kann [9]. Verschiedene Faktoren

lution composition, etching time and temperature, etching methodology etc., must be considered in the course of developing an optimal etching procedure [10].

A multitude of studies dealing with optimization of the etchant for various HCCI related alloys have previously been conducted [11–15]. Collins et. al. [11] employed several etchants in optimizing the etchant for automatic carbide volume fraction (CVF) determination in a given HCCI alloy whereas Powell et. al [12] focused on developing a deep etching technique in another HCCI alloy. Guitar et. al. studied the influence of several etchants in the quantification of secondary carbides in a 16 % Cr HCCI alloy and also combined it with a variety of characterization techniques [14, 15]. However, the etching process-parameter optimization for the 'objective specific' characterization in a specific HCCI alloy has not been carried out so far. This paper aims to provide information on using 'objective' specific etchants to assist in comprehensively characterizing the microstructure of a 26 % Cr HCCI alloy in the as-cast (AC) and heat treated (HT) state.

2. Materials and Methodology

The HCCI alloy used in this study was manufactured in an arc furnace and casted at 1450 °C into rectangular (Y) shaped sand molds hardened with phenolic resin. Optical emission spectroscopy (GNR Metal Lab 75/80; G.N.R. S.r.l., Agrate Conturbia, Novara, Italy) was used to determine the bulk chemical composition of the casting. Tab. 1 gives an account of the chemical composition (wt. %) of the 26 % HCCI alloy.

An abrasive disc was used to cut the cast samples into pieces measuring 20 mm ×

wie die Zusammensetzung der Lösung, Ätzzeit und -temperatur, Ätzmethode, etc., müssen bei der Entwicklung eines optimalen Ätzverfahrens berücksichtigt werden [10].

Eine Vielzahl an Untersuchungen zur Optimierung von Ätzmitteln für verschiedene mit HCCI verwandte Legierungen wurden bereits durchgeführt [11–15]. Collins et. al. [11] verfolgen auf Grundlage verschiedener Ätzmittel die Optimierung eines Ätzmittels für die automatisierte Bestimmung des Carbidvolumenanteils (CVF, carbide volume fraction) in einer bestimmten HCCI-Legierung, während Powell et. al [12] sich auf die Entwicklung eines Verfahrens zur Tiefenätzung einer anderen HCCI-Legierung konzentrieren. Guitar et. al. führten Untersuchungen zum Einfluss verschiedener Ätzmittel auf die Quantifizierung sekundärer Carbide in einer HCCI-Legierung mit 16 % Cr in Kombination mit verschiedenen Charakterisierungsmethoden durch [14, 15]. Jedoch wurde bisher keine Parameteroptimierung des Ätzprozesses zur 'zweck-spezifischen' Charakterisierung einer bestimmten HCCI-Legierung durchgeführt. Zielsetzung der vorliegenden Arbeit ist die Bereitstellung von Informationen zum Gebrauch verschiedener 'zweck-spezifischer' Ätzmittel, die zur umfassenden Charakterisierung der Mikrostruktur einer HCCI-Legierung mit 26 % Cr im Gusszustand (AC) und im Zustand nach Wärmebehandlung (HT) eingesetzt werden.

2. Werkstoffe und Methoden

Die für die vorliegende Untersuchung verwendete HCCI-Legierung wurde in einem Lichtbogenofen hergestellt. Bei 1450 °C erfolgte der Abguss in rechteckig (Y) geformte und mit Phenolharz gebundene Sandformen. Die Bestimmung der chemischen Zusammensetzung des Abgusses erfolgte durch optische Emissionsspektrometrie (GNR Metal Lab 75/80; G.N.R. S.r.l., Agrate Conturbia, Novara, Italien). Tab. 1 zeigt die Zusammensetzung (in Gew.-%) der HCCI-Legierung mit 26 % Cr.

Mit einer Trennscheibe wurde die Gussprobe in Stücke mit den Abmessungen 20 mm ×

Alloy / Legierung	C	Cr	Mn	Ni	Mo	Si	Cu	P	S	Fe
26 % HCCI	2.53	26.60	0.66	0.26	0.24	0.37	0.03	< 0.01	0.04	Bal.

Tab. 1: Bulk chemical composition (in wt. %) of the HCCI alloy measured by optical emission spectroscopy.

***Tab. 1:** Bestimmung der chemischen Zusammensetzung (in Gew.-%) der HCCI-Legierung durch optische Emissionsspektrometrie.*

20 mm × 10 mm. Two samples were subjected to a destabilization treatment at 980 °C for 30 (Q30) and 90 (Q90) minutes followed by air cooling and later embedded for metallographic preparation. The schematic of the heat treatment cycle is represented in Fig. 1.

The embedded samples were subjected to grinding and polishing according to the specifics mentioned in Tab. 2 to obtain a scratch-free, mirror surface. A Struers TegraPol-21 grinder/polisher (Struers Inc., Cleveland, OH, USA) was used for this purpose. It is beneficial to note that after each grinding and polishing step, the samples were washed with water, rinsed with ethanol,

20 mm × 10 mm getrennt. Zwei Proben wurden einer destabilisierenden Wärmebehandlung bei 980 °C über eine Dauer von 30 (Q30) bzw. 90 (Q90) Minuten unterzogen. Nach der anschließenden Abkühlung an Luft erfolgte im Zuge der metallographischen Präparation die Einbettung der Proben. Bild 1 zeigt eine schematische Darstellung der Wärmebehandlung.

Die eingebetteten Proben wurden gemäß der Schritte in Tab. 2 geschliffen und poliert, bis eine kratzerfreie und hochreflektierende Oberfläche erreicht wurde. Hierzu wurde die Schleif- und Poliermaschine TegraPol-21 von Struers (Struers Inc., Cleveland, OH, USA) verwendet. Anzumerken ist, dass die Proben nach jedem Schleif- und Polierschritt mit Wasser und anschließend Ethanol abgespült und an der Luft

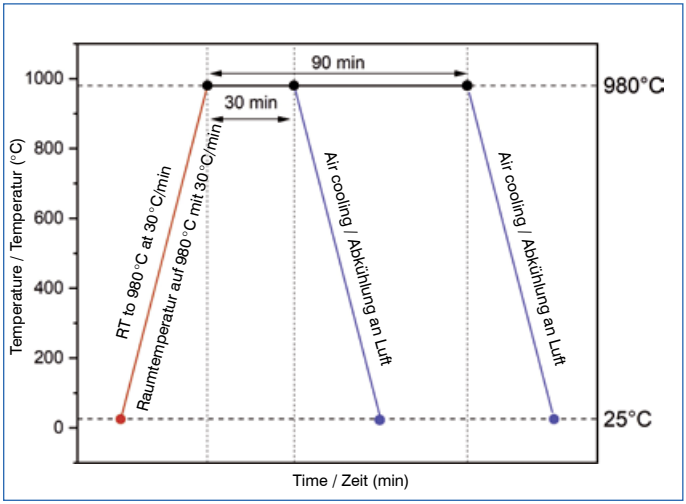

Fig. 1: Schematic of the heat treatment cycle employed.

***Bild 1:** Schematische Darstellung der angewandten Wärmebehandlung.*

Grinding/Polishing Pads Schleif-/Poliertücher	Grain Size / Körnung	Time (minutes) / Zeit (Minuten)
SiC grit paper / SiC-Schleifpapier	P80 – P180 – P320	2–3
	P600	5
	P1200	8
MD Dac	6µ diamond suspension / Diamantsuspension	10
MD Mol	3µ diamond suspension / Diamantsuspension	6
MD Nap	1µ diamond suspension / Diamantsuspension	5
MD Chem	0.04µ oxide polishing suspension (OPS) / Oxid-Polier-Suspension (OPS)	2 (OPS) + 5 (water / Wasser)

Tab. 2: *Grinding and polishing specifics employed for metallographic preparation of the samples.*

Tab. 2: *Schleif- und Polierschritte für die metallographische Probenpräparation.*

and air-dried. Additionally, before proceeding with the next stage, the samples were wetted slightly with water to ensure that the sample is lubricated enough to endure the sudden initial jerk.

The polished samples were later etched with various solutions depending upon the intended purpose as detailed in Tab. 3. In all cases, the samples were immersed in the freshly prepared etchant for the appropriate time, rinsed with water and ethanol, and air-dried. Finally, the etched samples were ultrasonicated in iso-propanol for 5 minutes before air-drying.

Microscopy observations of the polished and etched samples were carried out using a LEXT OLS 4100 Olympus confocal laser scanning microscope (CLSM) (Olympus Corporation, Tokyo, Japan). It uses a laser with 405 nm wavelength and, a lateral and vertical resolution of 120 and 10 nm, respectively [15]. Additionally, a FEI Helios Nanolab (Thermo Fisher Scientific, Waltham, MA, USA) field emission scanning electron microscope (FE-SEM), operating at an acceleration voltage of 5–15 kV and a beam current of 1.4 nA was used to observe the fine microstructural details of the AC and HT

getrocknet wurden. Zudem wurden die Proben vor dem jeweils nächsten Schritt leicht mit Wasser benetzt, sodass eine ausreichende Schmierung bestand, um dem plötzlichen Ruck zu Beginn des nächsten Schrittes standzuhalten.

Entsprechend dem in Tab. 3 aufgeführten Zweck der Untersuchung wurden die polierten Proben später mit verschiedenen Lösungen geätzt. In allen Fällen wurden die Proben für die angegebene Ätzzeit in das frisch hergestellte Ätzmittel getaucht, mit Wasser und anschließend Ethanol abgespült und an der Luft getrocknet. Abschließend wurden die geätzten Proben 5 Minuten lang in Isopropanol ultraschallgereinigt und an der Luft getrocknet.

Mikroskopische Beobachtungen der polierten und geätzten Proben wurden mit Hilfe des konfokalen Lasermikroskops (CLSM) LEXT OLS 4100 Olympus (Olympus Corporation, Tokyo, Japan) durchgeführt. Der Laser dieses Mikroskops hat eine Wellenlänge von 405 nm, eine laterale Auflösung von 120 nm und eine vertikale Auflösung von 10 nm [15]. Zusätzlich wurde das Feldemissions-Rasterelektronenmikroskop FEI Helios Nanolab (Thermo Fisher Scientific, Waltham, MA, USA) (FE-REM) mit einer Beschleunigungsspannung von 5–15 kV und einem Strahlstrom von 1,4 nA zur Beobachtung der feinen mikrostrukturellen Details

Sl. No / Lös. Nr.	Etchant / Ätzmittel	Composition / Zusammensetzung	Etching Parameters / Ätzparameter		Purpose/ Objective Absicht/Ziel
			Temperature / Temperatur	Time / Zeit	
1	Vilella's Reagent / Ätzmittel nach Vilella	100 mL Ethanol + 5 mL HCl + 1 g Picric Acid / 100 mL Ethanol + 5 mL HCl + 1 g Pikrinsäure	Room Temperature (RT) / Raum-temperatur (RT)	2–60 s	General Microstructure Observation / Allgemeine mikrostrukturelle Beobachtungen
2	Nital*	98 mL ethanol + 2 mL nitric acid + 0.5 mL HCl / 98 mL Ethanol + 2 mL Salpetersäure + 0.5 mL HCl	RT	20 s	General Microstructure Observation / Allgemeine mikrostrukturelle Beobachtungen
3	Murakami's reagent / Ätzmittel nach Murakami	4 g potassium ferricyanide + 8 g potassium hydroxide + 100 mL water / 4 g Kaliumhexacyanidoferrat(III) + 8 g Kaliumhydroxid + 100 mL Wasser	60 °C	5 min.	Carbide Quantification / Quantifizierung von Carbiden
4	Modified Murakami's reagent (MM) / Modifiziertes Ätzmittel nach Murakami (MM)	4 g potassium ferricyanide + 8 g Sodium hydroxide + 100 mL water / 4 g Kaliumhexacyanidoferrat(III) + 8 g Natriumhydroxid + 100 mL Wasser	RT	15 s	Carbide Quantification / Quantifizierung von Carbiden
5	Deep etchant 1 / Tiefenätzung 1	50 mL $FeCl_3$ + 20 mL HCl + 930 mL ethanol / 50 mL $FeCl_3$ + 20 mL HCl + 930 mL Ethanol	RT	3 h	3D carbide network observation / Beobachtung des 3D-Carbidnetzwerks
6	Deep etchant 2 / Tiefenätzung 2	10 % HCl in Methanol / 10 % HCl in Methanol	RT	24 h	3D carbide network observation / Beobachtung des 3D-Carbidnetzwerks

Tab. 3: *Description of the various etchants employed on the polished samples and their corresponding parameters, depending on the final objective.*

Tab. 3: *Beschreibung der für die polierten Proben verwendeten Ätzmittel und der entsprechenden Parameter in Abhängigkeit des Untersuchungsziels.*

samples along with the 3D structure of the carbides. A high sensitivity backscattered electron (BSE) detector was also used in order to obtain a better contrast between the phases.

Finally, the carbide volume fraction (CVF) of the eutectic and secondary carbides was determined after a post-processing of the CLSM/SEM micrographs using the image analysis (IA) software, ImageJ (version 1.52p) (LOCI, UW-Madison, WI, USA) [16]. The analysed area was maintained the same for all the images and an average of 10 micrographs were considered in each case.

3. Results and Discussions

3.1 As-cast Sample

General Microstructural Observations

The AC microstructure consists of an austenitic matrix surround by a network of EC, with no SC present. Fig. 2 represents the micrographs obtained using the CLSM after etching the AC sample with Vilella's reagent for up to 30 s. The etching was carried out at the same spot to better visualize the evolution of the contrast between the phases. Moreover, the phases present in the microstructures are color-arrow coded throughout the paper according to the following terminology:

- Red arrow pointing downwards: Austenite phase
- Black arrow pointing upwards: Martensite phase
- Blue arrow pointing left: M7C3 Phase (EC)
- White arrow pointing right: M23C6 Phase (SC)

From Fig. 2 (a), a noticeable contrast exists between the EC and the matrix even in the unetched state owing to the topographical difference between the two phases and the slight chemical etching imparted by the OPS [10]. It is also observed that etching for

der AC- und HT-Proben sowie der 3D-Struktur der Carbide eingesetzt. Ein hochempfindlicher Detektor für Rückstreuelektronen (RE) wurde ebenfalls verwendet, um einen besseren Kontrast zwischen den Phasen abzubilden.

Im Anschluss an die digitale Nachbearbeitung der CLSM- und REM-Aufnahmen mit Hilfe der Bildanalysesoftware ImageJ (Version 1.52p) (LOCI, UW-Madison, WI, USA) [16] erfolgte letztendlich die Bestimmung des Volumenanteils (CVF) der eutektischen und sekundären Carbide. Bei allen Aufnahmen wurde der gleiche Bereich analysiert. Im Durchschnitt wurden jeweils 10 Aufnahmen für die Untersuchung herangezogen.

3. Ergebnisse und Diskussion

3.1 Probe im Gusszustand

Allgemeine mikrostrukturelle Beobachtungen

Die Mikrostruktur der Probe im Gusszustand (AC) besteht aus einer austenitischen Matrix, die von einem Netzwerk aus eutektischen Carbiden umgeben ist. Sekundäre Carbide sind nicht vorhanden. Bild 2 zeigt die CLSM-Aufnahmen nach Ätzung der AC-Proben mit dem Ätzmittel nach Vilella mit einer Ätzzeit von bis zu 30 s. Die Ätzung erfolgte an der gleichen Stelle, um die Kontrastentwicklung zwischen den Phasen besser zu visualisieren. Zudem wurden die in der Mikrostruktur vorhandenen Phasen mit farbigen Pfeilen gekennzeichnet. Für die vorliegende Arbeit gelten dabei folgende Kennzeichnungen:

- Roter Pfeil nach unten: Austenitphase
- Schwarzer Pfeil nach oben: Martensitphase
- Blauer Pfeil nach links: M7C3-Phase (EC)
- Weißer Pfeil nach rechts: M23C6-Phase (SC)

Bild 2 (a) lässt einen merklichen Kontrast zwischen den EC und der Matrix sogar im ungeätzten Zustand erkennen, was an den topographischen Unterschieden der beiden Phasen und an der durch OPS hervorgerufenen leichten chemischen Ätzung liegt [10]. Außerdem wird

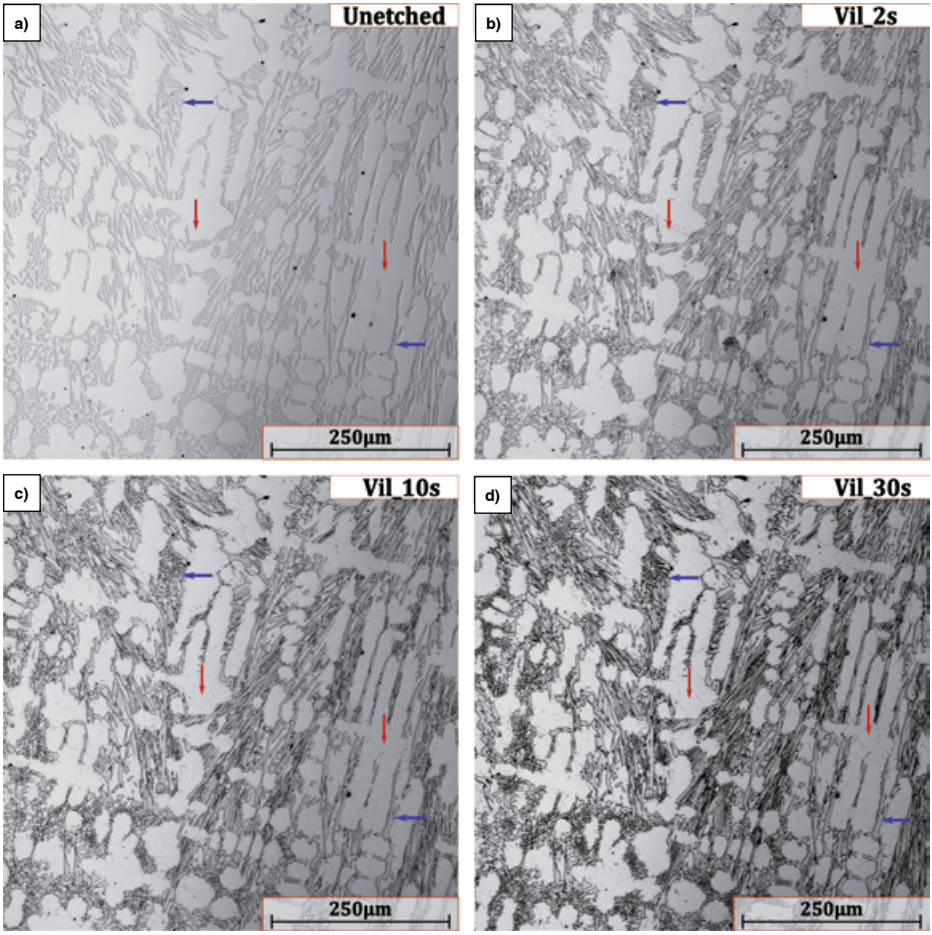

Figs. 2a to d: *Representative CLSM micrographs of the AC sample etched at the same spot with Vilella's reagent for various times. The phases are accordingly color/arrow-labelled for reference.*

Bilder 2a bis d: *Repräsentative CLSM-Aufnahmen der AC-Probe, die an der gleichen Stelle mit dem Ätzmittel nach Vilella und unterschiedlichen Ätzzeiten geätzt wurde. Die Phasen ergeben sich aus der entsprechenden Kennzeichnung mit farbigen Pfeilen.*

30 s results in over-etching in some areas and consequently, it is recommended to maintain an etching time between 5–10 s to ensure a good combination of contrast and phase revelation.

Furthermore, for better visualization of the microstructure and quantification of the

deutlich, dass die 30-sekündige Ätzung in bestimmten Bereichen zu einer Überätzung führt. Daher wird eine Ätzzeitvon 5–10 s empfohlen, um sowohl einen guten Kontrast als auch eine gute Sichtbarmachung der Phasen zu erreichen.

Darüber hinaus ist zur besseren Visualisierung der Mikrostruktur und Quantifizierung der

phases, it is necessary to observe the surface under SEM. Using the above knowledge, the AC sample was etched with Vilella's reagent for 7 s and the obtained SEM micrograph is represented in Fig. 3 (a). A closer examination also reveals the existence of martensite at the matrix-carbide interface, the presence of which is well documented [1, 6, 17]. Given the presence of an austenitic matrix and a high amount of Cr in this alloy, etching the AC sample with traditional Nital did not work and hence, the etchant was modified (Nital*) by adding 0.5 mL HCl [18]. Fig. 3 (b) depicts the SEM micrograph of the as-cast sample etched with Nital* for 20s.

Comparing Figs. 3 (a) with (b), although the three different constituents (austenite, martensite and EC) can be seen after etching with Nital*, the contrast between them

Phasen eine Untersuchung der Oberfläche im REM erforderlich. Entsprechend der zuvor aufgeführten Erkenntnisse wurde die AC-Probe mit dem Ätzmittel nach Vilella 7 s lang geätzt und die resultierende REM-Aufnahme in Bild 3 (a) dargestellt. Bei genauerer Untersuchung lässt sich zudem das Vorliegen von Martensit an den Grenzflächen von Matrix und Carbiden erkennen, was in der Literatur gut dokumentiert ist [1, 6, 17]. Durch die austenitische Matrix und den hohen Cr-Gehalt in dieser Legierung war die traditionelle Nitalätzung nicht erfolgreich, so dass das Ätzmittel durch Zusatz von 0,5 mL HCl modifiziert wurde (Nital*) [18]. Bild 3 (b) zeigt eine REM-Aufnahme der Probe im Gusszustand nach 20-sekündiger Ätzung mit Nital*.

Beim Vergleich der Bilder 3 (a) und (b) lässt sich erkennen, dass die drei verschiedenen Phasen (Austenit, Martensit und EC) nach der Ätzung mit Nital* zwar gut erkennbar sind, der Kontrast im

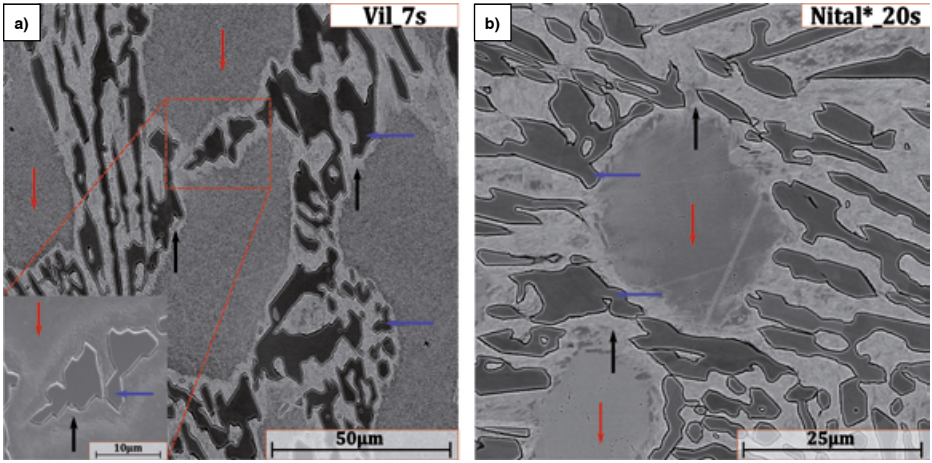

Figs. 3a and b: *Representative SEM micrographs of the AC sample etched with (a) Vilella's for 7 s and (b) Nital* for 20 s in backscattered electron (BSE) mode. The inset in (a) represents a magnified image of the region in secondary electron (SE) mode where the martensite at the interface is less contrasted. The various phases are labelled for reference.*

Bilder 3a und b: *Repräsentative REM-Aufnahmen der AC-Probe nach der Ätzung mit (a) dem Ätzmittel nach Vilella, Ätzzeit 7 s und (b) Nital*, Ätzzeit 20s, im Rückstreuelektronen(RE)-Kontrast. Das eingefügte Detail in (a) stellt den entsprechenden Bereich vergrößert im Sekundärelektronen(SE)-Kontrast dar, in dem Martensit an der Grenzfläche einen weniger starken Kontrast aufweist. Die verschiedenen Phasen sind entsprechend gekennzeichnet.*

Phase	Quantity (%) / Menge (%)
Austenite (Matrix) / Austenit (Matrix)	42.9 ± 2.2
Eutectic Carbide (EC) / Eutektische Carbide (EC)	28.9 ± 2.9
Martensite (interface) / Martensit (Grenzfläche)	28.2 ± 2.2

Tab. 4: *Phase quantification results as obtained by the trainable WEKA segmentation plugin in the AC HCCI sample.*

Tab. 4: *Ergebnisse der Quantifizierung der Phasen mit Hilfe der trainierbaren WEKA-Segmentierung bei der HCCI-Probe im Gusszustand.*

is inferior compared to Vilella's and hence, not recommended especially if the objective is to quantify the phases. The backscattered mode is well suited in quantifying the phases due to its increased contrast especially at the matrix-carbide interface as seen by comparing the enclosed region with the inset, in Fig. 3 (a).

Consequently, the phase quantification in the AC state was carried out by using the trainable WEKA segmentation plugin available in ImageJ [18,19]. The BSE micrograph (Fig. 4 (b)) was used as the input to train the model to generate a classified image (Fig. 4 (c)) and finally, the binarized image (Fig. 4 (d)). For the quantification, 6 micrographs were considered, and the results are presented in Tab. 4.

Eutectic CVF Determination

As the EC are relatively immune to the heat treatment [1, 3], their determination in the as-cast state would be sufficient for further analysis. Although Vilella's reagent is used for general microstructural observations which enables a good surface visualization, Murakami's reagent, which specifically attacks the chromium carbides is better suited for this objective [11]. Given the large size of the EC formed during the solidification, their

Vergleich mit der Ätzung nach Vilella allerdings schwächer ausfällt. Daher wird die Verwendung von Nital* nicht empfohlen, besonders wenn das Ziel der Untersuchung in der Quantifizierung der Phasen liegt. Der Rückstreuelektronenkontrast ist für die Quantifizierung der Phasen aufgrund des höheren Kontrasts gut geeignet, vor allem an den Übergängen zwischen Matrix und Carbiden, wie aus dem Vergleich des markierten Bereichs mit der eingefügten Detailansicht in Bild 3 (a) hervorgeht.

Somit erfolgte eine Quantifizierung der Phasen für die Probe im Gusszustand mit Hilfe der trainierbaren WEKA-Segmentierung, einem für ImageJ verfügbaren Plugin [18,19]. Die Aufnahme im RE-Kontrast (Bild 4 (b)) diente als Input zum Trainieren des Modells und zur Erzeugung eines klassifizierten (Bild 4 (c)) und schließlich eines binarisierten Bildes (Bild 4 (d)). Für die Quantifizierung wurden 6 Aufnahmen untersucht und die Ergebnisse in Tab. 4 dargestellt.

Bestimmung des Volumenanteils eutektischer Carbide

Da EC durch die Wärmebehandlung relativ unbeeinflusst bleiben [1, 3], wäre deren Bestimmung in der AC-Probe für weitere Analysen ausreichend. Obwohl das Ätzmittel nach Vilella zur allgemeinen Untersuchung der Mikrostruktur eingesetzt und eine gute Sichtbarmachung der Oberfläche erreicht wird, ist das Ätzmittel nach Murakami zu diesem Zweck besser geeignet, da speziell die Chromcarbide angegriffen werden [11]. Durch die be-

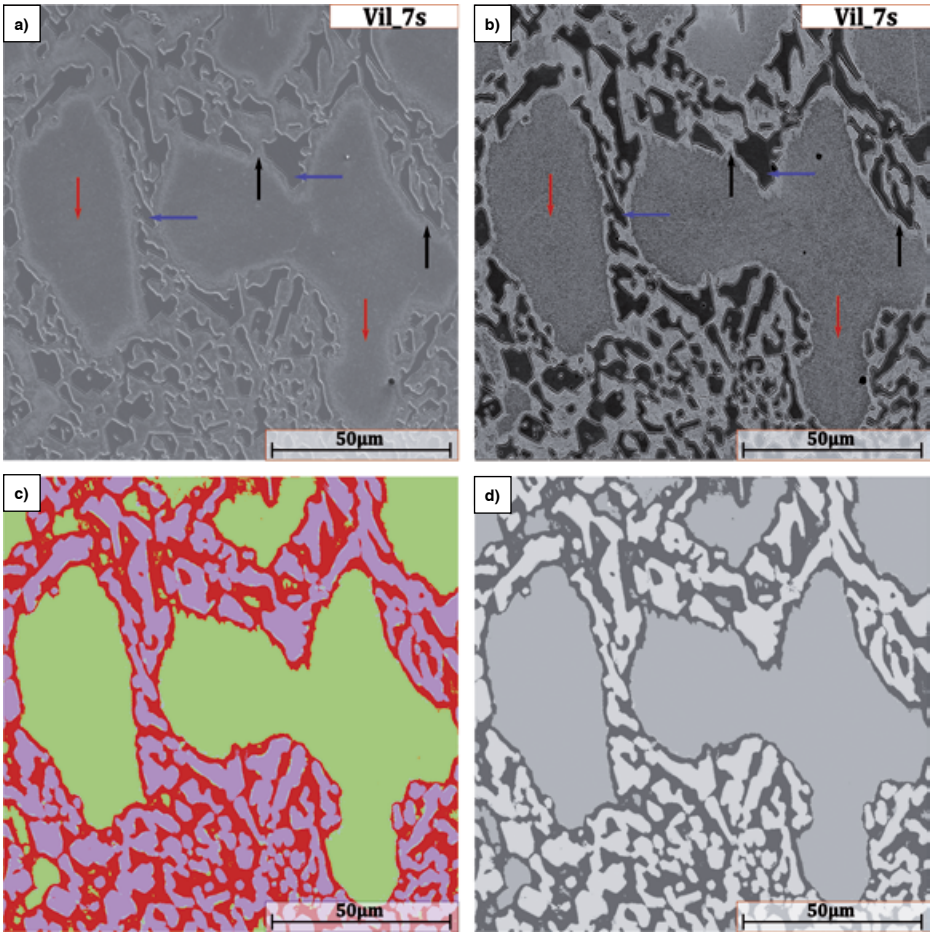

Figs. 4a to d: *(a) and (b) represent the SEM micrographs of the AC sample etched with Vilella's for 7 s in the SE and BSE mode, respectively. The phases are labelled according to the aforementioned terminology. (c) represents the classified image obtained using the trainable WEKA segmentation plugin in ImageJ where the different phases are colored differently, and the final binarized image is indicated in (d).*

Bilder 4a bis d: *(a) und (b) sind REM-Aufnahmen der AC-Probe nach der Ätzung mit dem Ätzmittel nach Vilella und einer Ätzzeit von 7 s im SE- bzw. RE-Kontrast. Die Phasen sind entsprechend des zuvor beschriebenen Schemas gekennzeichnet. (c) ist das durch die trainierbare WEKA-Segmentierung in ImageJ erzeugte klassifizierte Bild mit verschiedenfarbig dargestellten Phasen und (d) das finale binarisierte Bild.*

analysis and subsequent quantification can be achieved using CLSM as depicted in the Figs. 5 (a) and (c).

achtliche Größe der EC, die sich während der Erstarrung bilden, kann deren Analyse und anschließende Quantifizierung mit Hilfe von CLSM erfolgen, vgl. Bilder 5 (a) und (c).

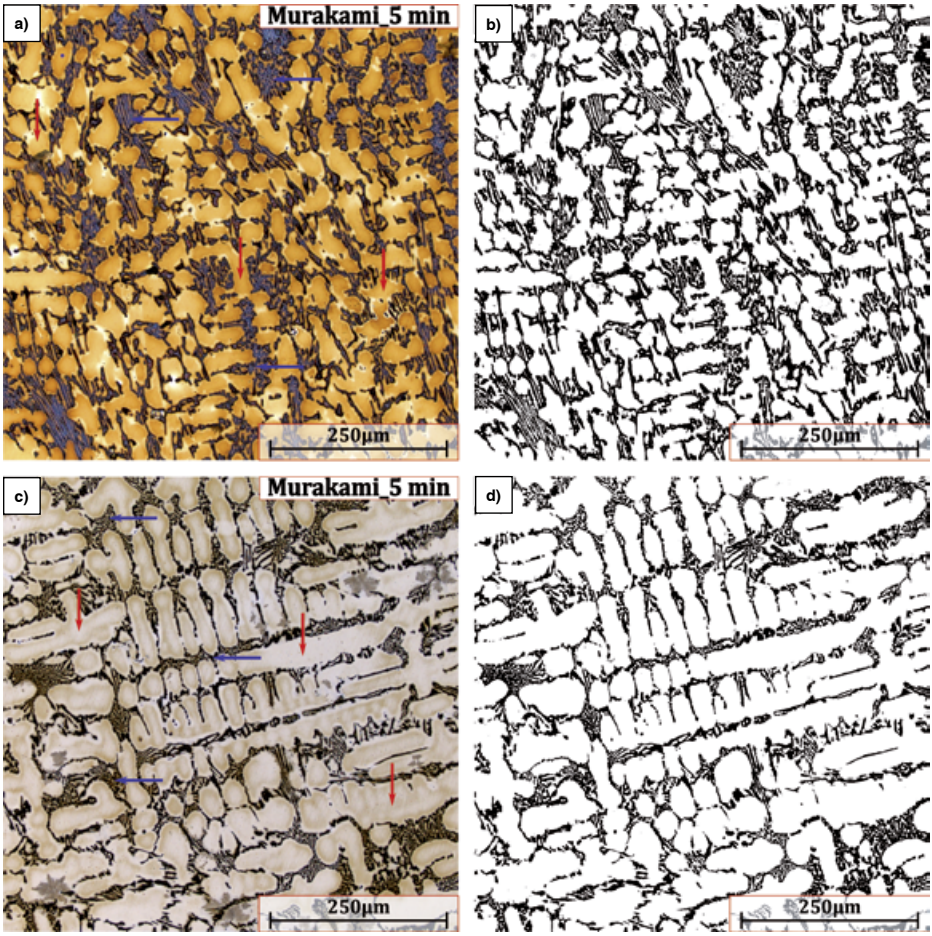

Figs. 5a to d: *The representative CLSM micrographs indicating the various phases in 26% Cr HCCI and 16% Cr HCCI AC samples after etching with Murakami's reagent are presented in (a) and (c), respectively. The corresponding binarized images obtained using ImageJ, are indicated in (b) and (d) respectively.*

Bilder 5a bis d: *Die repräsentativen CLSM-Aufnahmen mit den verschiedenen Phasen in den AC-Proben aus HCCI mit 26% Cr bzw. 16% Cr geätzt nach Murakami sind in (a) bzw. (c) zu sehen. Die jeweiligen mit ImageJ binarisierten Bilder sind in (b) bzw. (d) dargestellt.*

Furthermore, the EC fraction of another alloy from the same family, 16% Cr HCCI alloy (2.43% C, 15.84% Cr) was successfully determined by employing the same etching parameters, as presented in Tab. 5. Figs. 5 (b) and (d) represent the binarized image of

Darüber hinaus wurde der Anteil an EC in einer anderen Legierung derselben Familie, der HCCI-Legierung mit 16% Cr (2,43% C, 15,84% Cr), bereits erfolgreich unter Anwendung der gleichen Ätzparametern wie in Tab. 5 bestimmt. Bilder 5 (b) und (d) zeigen die bi-

Alloy / Legierung / Phase	26% HCCI			16% HCCI	
	WEKA	IA	MatCalc	IA	MatCalc
EC (%)	28.9 ± 2.9	30.6 ± 0.6	27.7 ± 1.1	19.4 ± 0.4	21.2 ± 1.5

Tab. 5: *Determination of eutectic CVF (%) using WEKA segmentation, IA and MatCalc in 26% and 16% HCCI alloy.*

Tab. 5: *Bestimmung des Volumenanteils der eutektischen Carbide (%) durch WEKA-Segmentierung, Bildanalyse (IA, image analysis) sowie MatCalc in der HCCI-Legierung mit 26% bzw. 16% Cr.*

the optical micrograph of the 26% and 16% HCCI alloy, respectively, through which the quantification was carried out. An average of 10 micrographs were considered for the quantification in both cases. Moreover, the EC fraction of both alloys estimated using the computational software, MatCalc 6 in [17] is also included in Tab. 5 for comparison with the two different experimental approaches.

It is observed from Tab. 5 that the EC fractions of the 26% HCCI alloy as determined by WEKA segmentation plugin using the SEM micrographs etched with Vilella's reagent (28.9 ± 2.9%) are in statistical agreement with the values obtained by simple IA using the CLSM micrographs etched with Murakami's reagent (30.6 ± 0.6%) and the computationally estimated value (27.7 ± 1.1%) by MatCalc. This validates the usage of different approaches in the quantification of the EC although care must be taken to appropriately use the microscopical tools to avoid erroneous results.

3.2 Heat Treated Samples

General Microstructural Observations

In the HT samples, the precipitation of SC (M23C6 type) has occurred in addition to the transformation of the austenitic matrix into martensite whereas, the EC remained unchanged [5].

narisierten lichtmikroskopischen Aufnahmen der HCCI-Legierung mit 26% bzw. 16% Cr, auf deren Grundlage die Quantifizierung erfolgte. Im Durchschnitt wurden für die Quantifizierung jeweils 10 Aufnahmen untersucht. Außerdem wurde der Anteil an EC in beiden Legierungen mit Hilfe der Software MatCalc 6 aus [17] bestimmt und in Tab. 5 zum Vergleich mit den beiden experimentellen Ansätzen aufgeführt.

Aus Tab. 5 geht hervor, dass die Anteile an EC in der HCCI-Legierung mit 26% Cr, die mit Hilfe der WEKA-Segmentierung ausgehend REM-Aufnahmen der nach Vilella geätzten Proben (28,9 ± 2,9%) bestimmt wurden, statistisch mit dem durch MatCalc errechneten Erwartungswert (27,7 ± 1,1%) und mit den Werten übereinstimmen, die durch einfache Bildanalyse der CLSM-Aufnahmen von Proben, die nach Murakami geätzt wurden (30,6 ± 0,6%) bestimmt wurden. Dies rechtfertigt die Verwendung unterschiedlicher Ansätze bei der Quantifizierung von EC, auch wenn auf den richtigen Einsatz der mikroskopischen Instrumente zur Vermeidung fehlerhafter Ergebnisse geachtet werden muss.

3.2 Wärmebehandelte Proben

Allgemeine mikrostrukturelle Beobachtungen

Bei den Proben im Zustand nach Wärmebehandlung wurde neben der Ausscheidung von SC (des Typs M23C6) die Umwandlung der austenitischen Matrix in Martensit beobachtet, während die EC unverändert blieben [5].

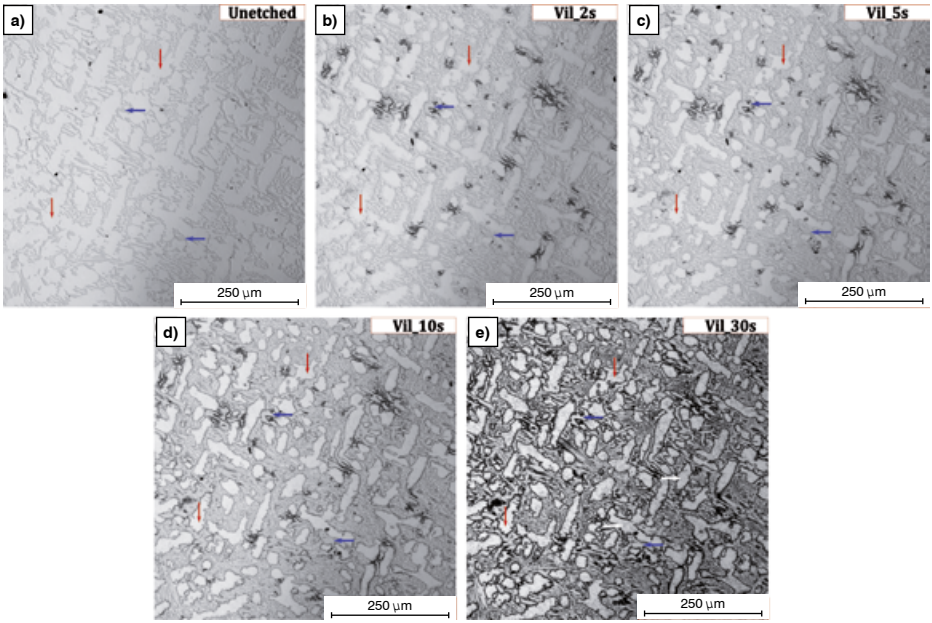

Fig. 6 a to e: *Representative CLSM micrographs of the Q30 HT samples etched at the same spot with Vilella's reagent for various times. The phases are accordingly color/arrow-labelled for reference.*

Bild 6 a bis e: *Repräsentative CLSM-Aufnahmen der HT-Proben (Q30) nach Ätzung der gleichen Stelle mit dem Ätzmittel nach Vilella und verschiedenen Ätzzeiten. Die Phasen sind entsprechend mit farbigen Pfeilen gekennzeichnet.*

Fig. 6 represents the phase contrast evolution with etching time for the Q30 sample obtained using CLSM. Similar to the AC sample, the Vilella's etching for 30 s results in non-uniform, over-etching. This could be attributed to the compositional gradients that arise in different areas of the microstructure resulting in different etching rates. The precipitated SC are sub-micron in size, unlike their eutectic counterparts, and their analysis would require the observation under an SEM, as the CLSM is not powerful enough to resolve them to assist in their quantification.

The influence of using OPS in the final step of polishing is represented in Fig. 7. Despite the Q30 (Fig. 7 (a)) and Q90 (Fig. 7 (b))

Bild 6 zeigt anhand von CLSM-Aufnahmen die Entwicklung des Phasenkontrasts mit zunehmender Ätzzeit für die Probe Q30. Wie bei der AC-Probe führt auch die 30-sekündige Ätzung mit dem Ätzmittel nach Vilella zu einer ungleichmäßigen Überätzung. Dies könnte an den Gradienten der Zusammensetzung liegen, die in verschiedenen Bereichen der Mikrostruktur auftreten und zu verschiedenen Ätzraten führen. Im Gegensatz zu den eutektischen Carbiden liegt die Größe der ausgeschiedenen SC im Sub-Mikrometerbereich, sodass deren Analyse den Einsatz eines REM erfordern würde, da durch CLSM keine genügend hohe Auflösung für deren Quantifizierung erreicht werden kann.

Inwieweit sich die Verwendung von OPS im letzten Polierschritt auswirkt, ist in Bild 7 dargestellt. Obwohl die Proben Q30 (Bild 7 (a)) und

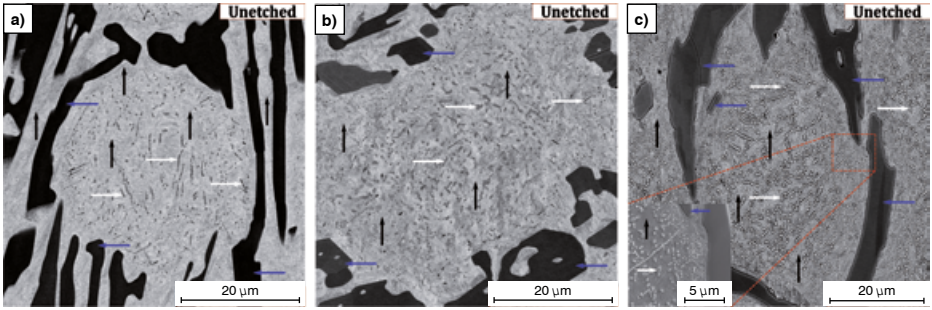

Figs. 7a to c: *Representative SEM BSE micrographs of (a) 1µ polished and unetched Q30 HT sample, (b) 1µ polished and unetched Q90 HT sample and (c) OPS polished and unetched Q90 HT sample. The inset in (c) represents a magnified image of the region around the EC in SE mode. The various phases present in the micrographs are appropriately labelled.*

Bilder 7 a bis c: *Repräsentative REM-Aufnahmen (RE-Kontrast) (a) der mit 1µ Diamantsuspension polierten und ungeätzten HT-Probe Q30, (b) der mit 1µ Diamantsuspension polierten und ungeätzten HT-Probe Q90 und (c) der mit OPS polierten und ungeätzten HT-Probe Q90. Die Detailansicht in (c) zeigt einen vergrößerten Bereich um die EC herum (SE-Kontrast). Die verschiedenen Phasen sind in den Aufnahmen entsprechend gekennzeichnet.*

being unetched, the microstructure of the OPS polished Q90 sample can be clearly observed in Fig. 7 (c). This is primarily due to the ability of the OPS to chemically etch the surface in addition to removing the scratches caused by the 1µ diamond suspension polishing [10]. Moreover, the 1µ polished samples show scratches and uneven contrast between the phases which might hinder proper visualization and subsequent quantification.

Analogous to the AC sample, etching with Nital* for 20 s was not successful in obtaining a better contrast between the phases compared to the Vilella's reagent as represented in Fig. 8. Accordingly, etching with Vilella's for 7 s is recommended for general microstructural observation of the HT samples.

Secondary CVF Determination

The precipitation of the SC during the heat treatment process would further improve the properties of the HCCI alloys and therefore,

Q90 (Bild 7 (b)) im ungeätzten Zustand vorliegen, ist die Mikrostruktur der mit OPS polierten Probe Q90 in Bild 7 (c) deutlich zu erkennen. Dies liegt vor allem daran, dass durch OPS sowohl die Oberfläche chemisch angeätzt als auch die Kratzer, die durch Polieren mit Diamantsuspension 1µ hervorgerufen werden, entfernt werden können [10]. Die mit 1µ Diamantsuspension polierten Proben weisen nicht nur Kratzer, sondern auch einen ungleichmäßigen Kontrast zwischen den Phasen auf, was eine korrekte Visualisierung und anschließende Quantifizierung erschweren könnte.

Wie bei der AC-Probe erzielt eine Ätzung mit Nital* über 20 s keinen verbesserten Kontrast zwischen den Phasen im Vergleich zum Ätzmittel nach Vilella, wie aus Bild 8 hervorgeht. Entsprechend werden zur allgemeinen mikrostrukturellen Untersuchung der HT-Proben die Verwendung des Ätzmittels nach Vilella und eine Ätzzeit von 7 s empfohlen.

Bestimmung des Volumenanteils Sekundärer Carbide

Die Ausscheidung von SC während der Wärmebehandlung würde die Eigenschaften von HCCI-Legierungen weiter verbessern. Daher

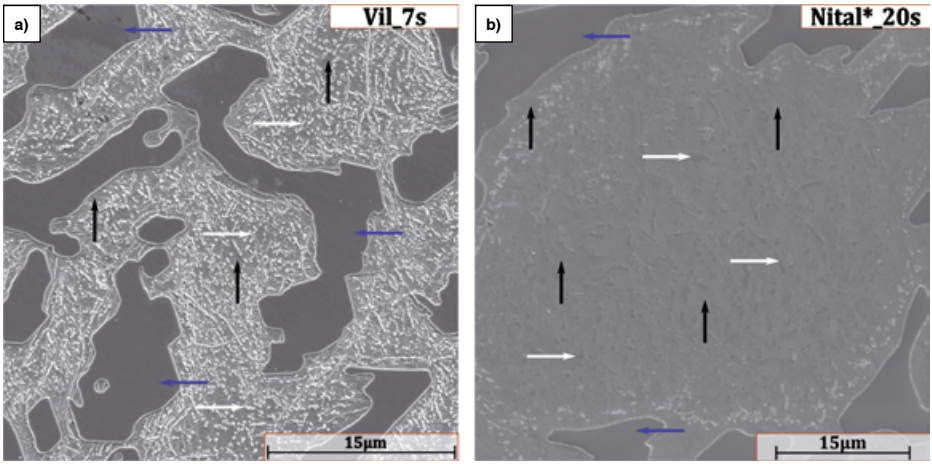

Figs. 8 a and b: *Representative SEM micrographs of Q90 HT sample etched with (a) Vilella's for 7 s and (b) Nital* for 20s. The phases are labelled in the micrographs for reference.*

Bilder 8 a und b: *Repräsentative REM-Aufnahmen der HT-Probe Q90 geätzt mit (a) dem Ätzmittel nach Vilella, Ätzzeit 7 s und (b) Nital*, Ätzzeit 20s. Die vorliegenden Phasen sind entsprechend gekennzeichnet.*

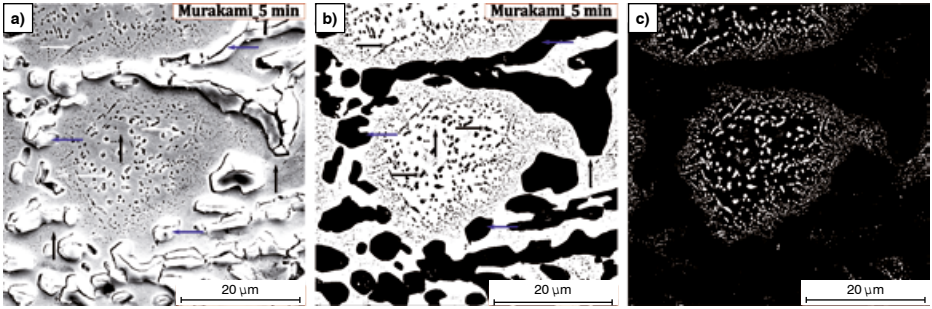

Figs. 9 a to c: *(a) and (b) represent the SEM micrographs of the Q90 HT sample etched with Murakami's reagent (5 min. at 60°C) in the SE and BSE mode, respectively. The binarized image depicting the SC, obtained using ImageJ is presented in (c).*

Bilder 9 a bis c: *(a) und (b) zeigen REM-Aufnahmen der HT-Probe Q90 geätzt mit dem Ätzmittel nach Murakami (5 min. bei 60°C) im SE- bzw. RE-Kontrast. (c) zeigt das mit ImageJ binarisierte Bild.*

it is important to determine the stereological characteristics of the SC precipitates to better understand the kinetics of precipitation during the HT [1, 6].

Fig. 9 (a) represents the SEM SE micrograph of the Q90 sample etched with Murakami's

ist es wichtig, die stereologischen Eigenschaften der SC-Ausscheidungen zu bestimmen, um die Kinetik von Ausscheidungsvorgängen während der Wärmebehandlung besser verstehen zu können [1, 6].

Bild 9 (a) zeigt REM-Aufnahmen (SE-Kontrast) der Probe Q90, die mit dem Ätzmittel nach Murakami

reagent. The breakage of the EC and the removal of the SC is clearly visible. Granted that IA could be carried out in the quantification of the SC owing to the contrast provided by the BSE image (Figs. 9 (b, c)), it is recommended to use a modified version of the etchant to ensure that: (1) the breakage of the EC does not interfere with the SC quantification and (2) the SC are not lost during the etching, leading to an inaccurate result. Furthermore, the IA was possible partially due to the topography caused by the removal of the carbides which resulted in a good contrast in the BSE mode.

A slightly modified version of Murakami's etchant was subsequently used (Tab. 3) at RT for 15s. Notwithstanding the lower etching time and temperature compared to the unmodified etchant, a sufficient matrix/carbide contrast was obtained and no carbide removal ensued, as seen in Fig. 10 (a). This could be attributed to the lower pkb value of NaOH (0.2) compared to KOH (0.5), which makes it a stronger and more reactive base [20]. It is also essential to note that etching

geätzt wurde. Das Zerbrechen der EC und der Abtrag von SC sind eindeutig erkennbar. Angenommen, dass eine Bildanalyse zur Quantifizierung von SC anhand des Kontrasts in den RE-Bildern durchgeführt werden könnte (Bild 9 (b, c)), wird empfohlen, eine modifizierte Variante dieses Ätzmittels zu verwenden, um zu gewährleisten, dass: (1) ein Zerbrechen der EC die Quantifizierung von SC nicht beeinflusst und (2) die SC während des Ätzvorgangs nicht „verloren gehen", was zu falschen Ergebnissen führen würde. Darüber hinaus wurde die Bildanalyse teilweise durch die Entstehung einer Topographie ermöglicht, die durch den Abtrag der Carbide entstand, was zu einem hohen Kontrast in den RE-Bildern führte.

Im Anschluss wurde eine leicht modifizierte Version des Ätzmittels nach Murakami bei RT für eine Dauer von 15 s verwendet (Tab. 3). Trotz der geringeren Ätzzeit und -temperatur im Vergleich zum nicht modifizierten Ätzmittel stellte sich ein ausreichender Kontrast zwischen Matrix und Carbiden ein und es kam nicht zum Abtrag der Carbide, wie aus Bild 10 (a) hervorgeht. Ein Grund hierfür könnte der im Vergleich zu KOH (0,5) niedrigere pkb-Wert von NaOH (0,2) sein, was bedeutet, dass

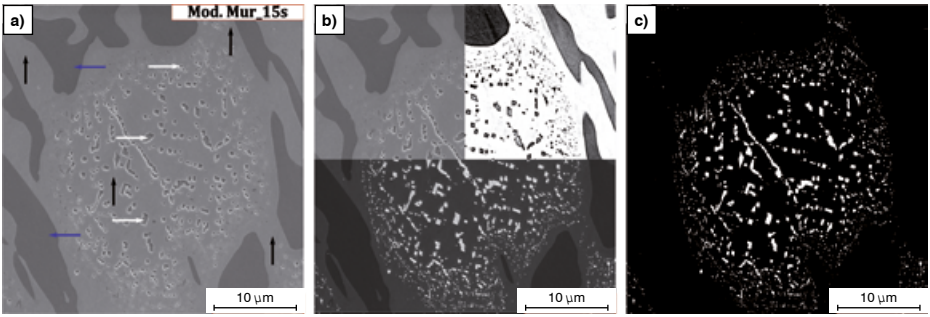

Figs. 10a to c: *(a) Representative SEM SE micrograph of the Q90 HT sample etched with a modified Murakami's etchant (15 s at RT); (b) represents a 100% overlay of the corresponding micrograph in the BSE mode (top right half) and a 50% overlay of the micrograph after IA using ImageJ (bottom half), and (c) binarized image of the micrograph showing the $M_{23}C_6$ SC after IA.*

Bilder 10a bis c: *(a) Repräsentative REM-Aufnahme (SE-Kontrast) der HT-Probe Q90 geätzt mit dem modifiziertem Ätzmittel nach Murakami (15 s bei RT); (b) 100%-Überlagerung der entsprechenden Aufnahme im RE-Kontrast (obere rechte Hälfte) und 50%-Überlagerung der Aufnahme nach IA mit ImageJ (untere Hälfte), und (c) binarisiertes Bild der Aufnahme mit $M_{23}C_6$ SC nach IA.*

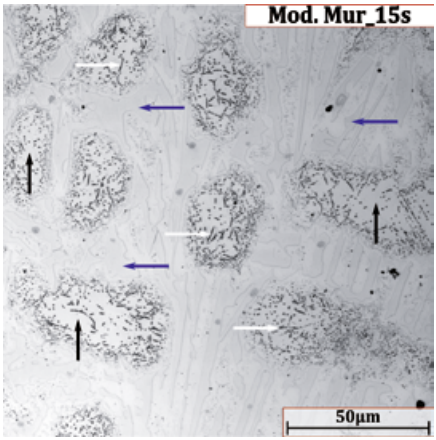

Fig. 11: Representative CLSM micrograph of the Q30 HT sample etched with modified Murakami's etchant (15 s at RT) where the various phases are indicated.

***Bild 11:** Repräsentative CLSM-Aufnahme der HT-Probe Q30 geätzt mit dem modifizierten Ätzmittel nach Murakami (15 s bei RT) und Kennzeichnung der verschiedenen Phasen.*

for longer times even with the modified Murakami's etchant would result in the breakage and removal of the EC/SC owing to the increase in chemical reactivity. Fig. 10 (b) shows an overlaid image which includes the SE, BSE and the binarized image whereas Fig. 10 (c) shows the overall binarized image through which the secondary CVF was determined.

NaOH die reaktivere Base ist [20]. Durch die höhere chemische Reaktionsfähigkeit ist außerdem zu beachten, dass Ätzungen mit längeren Ätzzeiten sogar mit dem modifizierten Ätzmittel nach Murakami zum Zerbrechen und Abtrag der EC/SC führen würde. Bild 10 (b) zeigt ein überlagertes Bild aus Aufnahmen im SE- und RE-Kontrast und dem binarisierten Bild, während Bild 10 (c) das vollständig binarisierte Bild zeigt, auf dessen Grundlage der Volumenanteil (CVF) an Sekundären Carbiden bestimmt wurde.

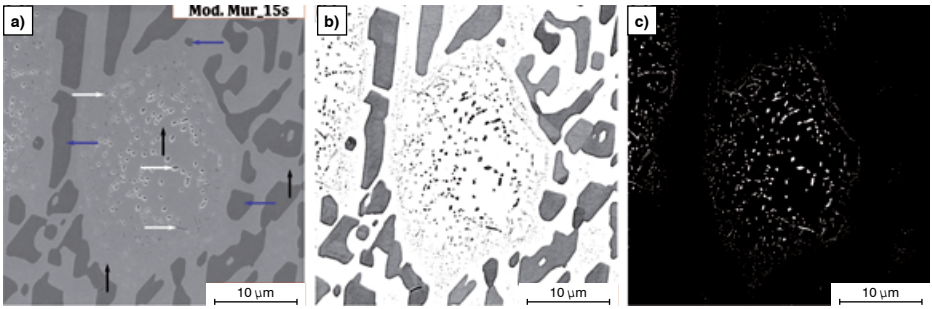

Figs. 12a to c: Representative SEM SE and BSE micrograph of the Q30 HT sample etched with modified Murakami's etchant (15 s at RT) are presented in (a) and (b), respectively. (c) The binarized image showing the $M_{23}C_6$ SC post IA using ImageJ.

***Bilder 12a bis c:** Repräsentative REM-Aufnahmen (SE- und RE-Kontrast) der HT-Probe Q30 geätzt mit dem modifizierten Ätzmittel nach Murakami (15 s bei RT) in (a) bzw. (b). (c) zeigt das binarisierte Bild mit SC des Typs $M_{23}C_6$ nach Bildanalyse mit ImageJ.*

The modified Murakami's etchant was successfully used to quantify the SC in the Q30 sample too. Although the SC precipitates are visible due to the modified Murakami's etchant as seen in Fig. 11, they are too small to be resolved using CLSM. Therefore, it is recommended to use SEM micrographs to quantify the SC as shown in Fig. 12.

Comparing Fig 12c with Fig 10c, the difference in the CVF can be easily observed and it has been elucidated in [5].

3.3 Deep Etching (for 3D analysis of carbides)

Upon solidification, the EC are heterogeneously nucleated throughout the material possessing a hexagonal/rhombohedral cross section [21]. Fig. 13 represents the influence of etching the Q30 sample with Vilella's reagent for up to 60s. The phases are clearly visible in the micrograph at an etching time of 7 s as seen in Fig. 13 (a). As the etching time is increased, non-uniform attack ensues as observed in Figs. 13 (b, c). Comparing Figs. 13 (b) and (c), it was observed that the etching mainly proceeds from the matrix-carbide interface towards the center of the matrix, attributable to the compositional gradient. Moreover, the Vilel-

Auch in der Probe Q30 wurde das modifizierte Ätzmittel nach Murakami erfolgreich zur Quantifizierung von SC eingesetzt. Auch wenn die SC-Ausscheidungen durch das modifizierte Ätzmittel sichtbar gemacht werden, vgl. Bild 11, sind sie für die Auflösung des CLSM zu klein. Daher wird die Verwendung von REM-Aufnahmen für die Quantifizierung von SC empfohlen, wie in Bild 12 zu sehen.

Beim Vergleich von Bild 12c und Bild 10c wird der Unterschied im Carbidvolumenanteil (CVF) deutlich sichtbar, wie in [5] näher beschrieben.

3.3 Tiefenätzung (zur 3D-Analyse von Carbiden)

Bei der Erstarrung bilden die EC im Werkstoff heterogen verteilte Keime mit einem hexagonal/rhomboedrischen Querschnitt aus [21]. Bild 13 zeigt den Einfluss des Ätzmittels nach Vilella auf die Probe Q30 bei einer Ätzzeit von bis zu 60s. In der Aufnahme sind die Phasen nach 7 s deutlich erkennbar, vgl. Bild 13 (a). Mit zunehmender Ätzzeit wird die Ätzung ungleichmäßig, vgl. Bilder 13 (b, c). Beim Vergleich der Bilder 13 (b) und (c) lässt sich erkennen, dass die Ätzung hauptsächlich von der Grenzfläche zwischen Matrix und Carbiden ausgehend in Richtung des Zentrums der Matrix abläuft, was dem Gradient der chemischen Zusammensetzung zuzuschreiben ist. Zudem verhält sich das

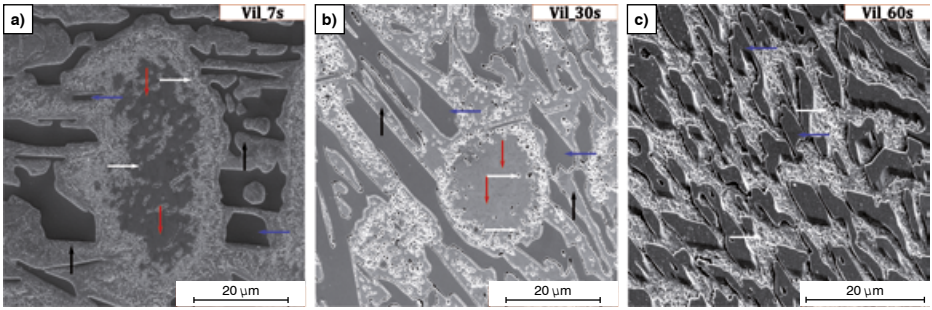

Figs. 13a to c: *Representative SEM SE micrographs of the Q30 HT sample etched with Vilella's reagent for various times. The corresponding phases are indicated for reference.*

Bilder 13a bis c: *Repräsentative REM-Aufnahme (SE-Kontrast) der HT-Probe Q30, geätzt mit dem Ätzmittel nach Vilella und verschiedenen Ätzzeiten. Die Phasen sind entsprechend gekennzeichnet.*

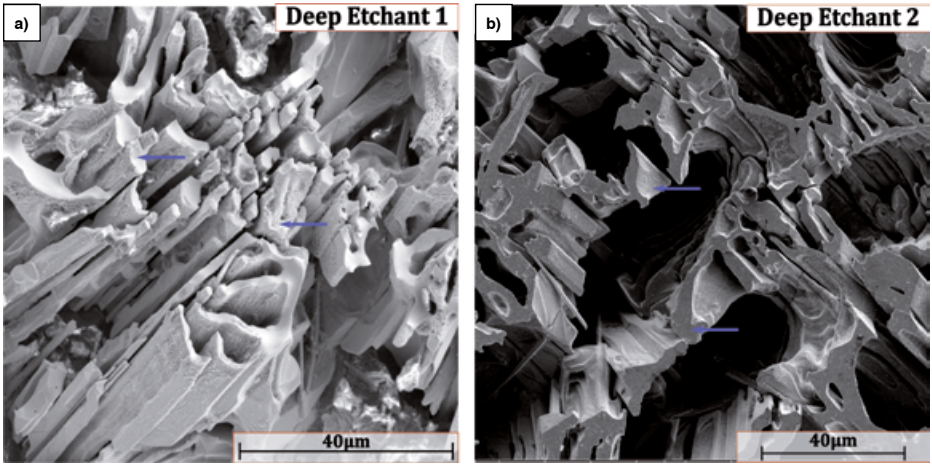

Figs. 14a and b: *Representative SEM SE micrographs of the AC sample etched with (a) Deep etchant 1 (50 mL FeCl3 + 20 mL HCl + 930 mL ethanol for 3 h at RT) and (b) Deep etchant 2 (10% HCl in Methanol for 24 h at RT).*

Bilder 14a und b: *Repräsentative REM-Aufnahmen (SE-Kontrast) der AC-Probe geätzt mit (a) Tiefenätzung 1 (50 mL FeCl3 + 20 mL HCl + 930 mL Ethanol über 3 h bei RT) und (b) Tiefenätzung 2 (10% HCl in Methanol über 24 h bei RT).*

la's reagent acts as a 'quasi' deep etchant when the sample was etched for 60 s but given its non-uniformity, it is recommended to use etchants specifically designed to uniformly remove the softer matrix material for a clearer analysis of the 3D carbide structure.

Ätzmittel nach Vilella bei 60-sekündiger Ätzzeit quasi wie eine Tiefenätzung. Aufgrund der Ungleichmäßigkeit des Ätzresultats wird jedoch die Verwendung von Ätzmitteln empfohlen, die für einen gleichmäßigen Abtrag der weicheren Matrix sorgen und damit eine eindeutigere Analyse der 3D-Carbidstruktur ermöglichen.

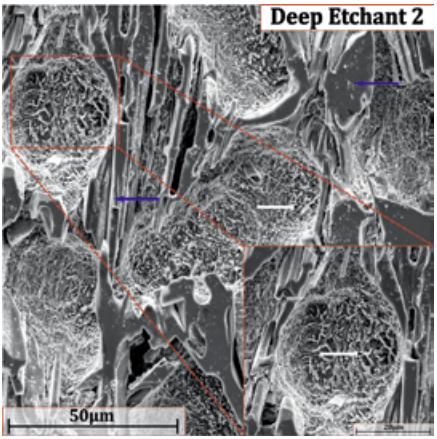

Fig. 15: *Representative SEM SE micrograph of the Q90 HT sample etched with deep etchant 2 (10% HCl in methanol for 24 h). The EC and SC are indicated for reference.*

Bild 15: *Repräsentative REM-Aufnahme im SE-Kontrast der HT-Probe Q90, geätzt mit Tiefenätzung 2 (10% HCl in Methanol über 24 h). Die EC und SC sind entsprechend gekennzeichnet.*

Tab. 6: *Recommended etching specifics for 'objective specific' microstructural characterization in AC and HT 26% Cr HCCI alloy.* ►

Tab. 6: *Empfohlene Ätzparameter für die ‚zweck-spezifische' Charakterisierung der Mikrostruktur bei AC- und HT-Proben der HCCI-Legierung mit 26% Cr.*

Fig. 14 represents the SEM micrographs of the AC sample depicting the three dimensional structure of the EC after etching with deep etchant 1 (Fig. 14 (a)) and deep etchant 2 (Fig. 14 (b)).

Etching with deep etchant 1 resulted in the presence of a residue which could possibly indicate an incomplete removal of the matrix attributable to lower HCl concentration and etching time compared to deep etchant 2.

The HT sample was etched using deep etchant 2 (10% HCl in Methanol for 24 h at RT) and as expected, in addition to the eutectic carbide network, the secondary carbides with varying morphology was seen nested in between the eutectic carbides, as depicted in Fig. 15. The varying morphology could suggest precipitation at different stages of the HT [3].

Finally, the recommended etching specifics and the corresponding observations for the AC and HT samples are presented in Tab. 6.

4. Conclusions

This work evaluated the efficacy of certain etchants in revealing various microstructural aspects of a specific HCCI alloy in the AC and HT condition. The optimal condition for each etchant is determined after visually observing the microstructures under the CLSM and SEM. A good contrast between the phases is crucial for the reliable quantification/analysis of the microstructure.

Bild 14 zeigt REM-Aufnahmen der AC-Probe mit der dreidimensionalen Struktur der EC nach Tiefenätzung 1 (Bild 14 (a)) bzw. Tiefenätzung 2 (Bild 14 (b)).

Nach Tiefenätzung 1 kam es zu Rückständen, die möglicherweise auf eine unvollständige Entfernung der Matrix hindeuten, was wiederum auf die geringere Konzentration von HCl und kürzere Ätzzeit im Vergleich zu Tiefenätzung 2 zurückzuführen ist.

Für die HT-Probe wurde Tiefenätzung 2 (10% HCl in Methanol über 24 h bei RT) verwendet und wie erwartet, war nicht nur das Netzwerk an eutektischen Carbiden zu erkennen, sondern auch sekundäre Carbide unterschiedlicher Morphologie, die eingebettet zwischen den EC auftreten (Bild 15). Die unterschiedlichen Morphologien könnten darauf hindeuten, dass Ausscheidungen während verschiedener Stufen der Wärmebehandlung stattgefunden haben [3].

Abschließend werden die empfohlenen Ätzparameter sowie die entsprechenden Beobachtungen bei der Untersuchung der AC- und HT-Proben in Tab. 6 vorgestellt.

4. Schlussfolgerungen

In der vorliegenden Arbeit wurde die Wirksamkeit bestimmter Ätzmittel zur Sichtbarmachung verschiedener mikrostruktureller Aspekte einer bestimmten HCCI-Legierung im Gusszustand und im Zustand nach Wärmebehandlung untersucht. Die optimalen Bedingungen für jedes der verwendeten Ätzmittel werden nach visueller Beobachtung der Mikrostrukturen mit Hilfe von CLSM und REM bestimmt. Ein ausreichend hoher Kontrast zwischen den Phasen ist dabei für eine zuverlässige Quantifizierung/Analyse der Mikrostruktur entscheidend.

Condition / Zustand	Objective/Purpose Ziel/Zweck	Recommended Etching Specifics / Empfohlene Ätzparameter			Observations / Beobachtungen
		Etchant / Ätzmittel	Temperature / Temperatur	Time / Zeit	
As-cast (AC) / Gusszustand (AC)	General Microstructure Revelation / Allgemeine Sichtbarmachung der Mikrostruktur	Vilella's Reagent / nach Vilella	RT	7 s	• The phases could be clearly seen in CLSM but SEM is needed to quantify them. / Die Phasen sind durch CLSM deutlich erkennbar, für deren Quantifizierung ist jedoch eine Untersuchung im REM erforderlich. • BSE mode provides a much better contrast to help in the quantification of the phases. / Aufnahmen im RE-Kontrast liefern einen deutlich besseren Kontrast, der bei der Quantifizierung der Phasen von Nutzen ist.
	Deep Etching / Tiefenätzung	10 % HCl in Methanol	RT	24 h	• The 3D network of the EC could be clearly observed in the SEM. / Das von den EC gebildete 3D-Netzwerk ist im REM deutlich erkennbar.
	Eutectic Carbide Quantification / Quantifizierung Eutektischer Carbide	Murakami's reagent / nach Murakami	60 °C	5 min	• The quantification was possible using only the CLSM primarily due the size of the EC and the resulting crisp contrast with the matrix. / Die Quantifizierung war nur mit Hilfe von CLSM möglich, hauptsächlich aufgrund der der Größe der EC und dem resultierenden scharfen Kontrast mit der Matrix.
Heat Treated (HT) / nach Wärmebehandlung (HT)	General Microstructure Revelation / Allgemeine Sichtbarmachung der Mikrostruktur	Vilella's Reagent / nach Vilella	RT	7 s	• Although the phases could be observed using the CLSM, the SC could not be clearly resolved. / Obwohl die verschiedenen Phasen im CLSM erkennbar waren, war dessen Auflösung für die SC zu gering. • The SC could be clearly observed in the SEM after etching. / Die SC waren nach entsprechender Ätzung im REM eindeutig erkennbar.
	Deep Etching / Tiefenätzung	10 % HCl in Methanol	RT	24 h	• In addition to the 3D EC network, the underlying SC was also evident. / Neben dem durch EC gebildeten 3D-Netzwerk waren auch die darin eingebetteten SC erkennbar.
	Secondary Carbide Quantification / Quantifizierung Eutektischer Carbide	Modified Murakami's reagent / nach Murakami	RT	15 s	• The efficacy of the etching was visible in CLSM but SEM was necessary to assist in the quantification given the small size of the precipitated SC. / Die Wirksamkeit der Ätzung lässt sich mit Hilfe von CLSM erkennen, jedoch ist aufgrund der geringen Größe der ausgeschiedenen SC die Untersuchung im REM für die Quantifizierung notwendig.

A prerequisite before etching is a damage-free, OPS mirror polished sample. Although a 1µ diamond polished sample would be sufficient for a quick observation under the CLSM, a deeper characterization and quantification of the phases would require the surface to be scratch-free to avoid erroneous results.

The general microstructure of the HCCI alloy can be clearly revealed by immersing the sample in a freshly prepared Vilella's reagent for 7 seconds. The etchant provided a sufficient contrast between the phases to be observable under the CLSM whereas the SEM was used to quantify the phases through the trainable WEKA segmentation plugin in ImageJ. Etching the sample with Nital* did not provide sufficient contrast and sharpness between the phases.

For EC quantification, Murakami's reagent was used (60 °C for 5 min) as the etchant owing to its affinity in attacking the chromium carbides. Given the size of the EC, they could be quantified using the CLSM micrographs. Additionally, the etchant was successfully applied to another alloy of the same family in determining the EC fraction. The addition of Cr led to a concomitant increase in the EC fraction amongst the two alloys. Furthermore, the EC fraction obtained from the WEKA segmentation of Vilella's etched SEM micrographs was in statistical agreement with the EC fraction obtained using the IA of the CLSM micrographs. The predictions made by MatCalc are also in accordance with the experimentally obtained values.

Upon observation in the SEM, the Murakami etched samples (60 °C for 5 min.) had developed cracks in the carbide network and parts of the carbides had been removed and hence, had to be modified by replacing KOH with NaOH. The resulting modified Murakami's etchant could ensure

Als Grundvoraussetzung für den Ätzvorgang gilt eine mit OPS hochglanzpolierte Probenoberfläche frei von Beschädigungen. Auch wenn eine mit 1µ Diamantsuspension polierte Probe für eine schnelle Begutachtung im CLSM ausreichend wäre, erfordert eine eingehendere Charakterisierung und Quantifizierung der Phasen zur Vermeidung von fehlerhaften Ergebnissen eine kratzerfreie Oberfläche.

Die allgemeine Mikrostruktur der HCCI-Legierung wird deutlich sichtbar durch 7-sekündiges Eintauchen in das frisch hergestellte Ätzmittel nach Vilella. Das Ätzmittel erzeugt einen ausreichend hohen Kontrast zwischen den Phasen, um diese mittels CLSM untersuchen zu können, während für die Quantifizierung der Phasen mit Hilfe der trainierbaren WEKA-Segmentierung in ImageJ eine Untersuchung im REM erforderlich ist. Die Ätzung der Probe mit Nital* erzeugte keinen ausreichend hohen Kontrast und keine ausreichende Schärfe zwischen den Phasen

Zur Quantifizierung der EC wurde das Ätzmittel nach Murakami verwendet (60 °C, Ätzzeit 5 min), da es eher dazu neigt, die Chromcarbide anzugreifen. Durch die Größe der EC war es möglich, diese anhand von CLSM-Aufnahmen zu quantifizieren. Zudem wurde das Ätzmittel erfolgreich zu Bestimmung des EC-Anteils einer weiteren Legierung derselben Familie angewandt. Bei beiden Legierungen führte der Zusatz von Cr zu einem Anstieg des EC-Anteils. Darüber hinaus stimmte der Anteil an EC, der durch WEKA-Segmentierung ausgehend von REM-Aufnahmen der nach Vilella geätzten Proben ermittelt wurde, statistisch mit dem durch IA ermittelten EC-Anteil auf Basis der CLSM-Aufnahmen überein. Die Vorhersagen durch MatCalc stimmen ebenfalls mit den experimentell ermittelten Werten überein.

Bei der Untersuchung im REM wiesen die Proben, die mit dem Ätzmittel nach Murakami geätzt wurden (60 °C, Ätzzeit 5 min.), Risse innerhalb des Carbidnetzwerks auf. Außerdem war ein Teil der Carbide abgetragen worden, was eine Modifizierung des Ätzmittels erforderte, indem KOH durch NaOH ersetzt wurde. Das so modifizierte

a sufficient contrast between the phases and prevent the carbides from cracking/removal. The quantification of the SC was successful by using the BSE micrographs as the input for IA.

It was also observed under the SEM that etching with Vilella's for longer times resulted in an uneven removal of the matrix and therefore, it is recommended to use deep etchant 2 (10 % HCl in methanol for 24 h) to analyze the eutectic and secondary carbides, in-depth. Deep etchant 1 (50 mL $FeCl_3$ + 20 mL HCl + 930 mL ethanol for 3 h at RT) left a considerable amount of residue behind and hence, not recommended.

Consequently, it was seen that specific etchants are needed depending upon the final objective and the results are dependent on their selection and optimal usage. In addition to the proper usage of the etching process parameters, it is imperative to use the right microscopical tools in obtaining reliable, representative microstructural information about the alloy. Finally, the knowledge gained in this study will be used as a basis for the further microstructural analyses of these alloys and be applied to other alloys in the family.

5. Acknowledgment

The authors would like to thank Martin Duarte from Tubacero S. A. for providing the materials. Additionally, UP Nayak is grateful for to DAAD for the financial support.

Ätzmittel nach Murakami erzeugte einen ausreichend hohen Kontrast zwischen den Phasen und verhinderte ein Zerbrechen/einen Abtrag der Carbide. Eine erfolgreiche Quantifizierung der SC erfolgte durch die Verwendung von Aufnahmen im RE-Kontrast als Input für die Bildanalyse.

Untersuchungen im REM zeigten ebenfalls, dass das Ätzmittel nach Vilella bei längeren Ätzzeiten zu einem ungleichmäßigen Abtrag der Matrix führt. Daher wird die Verwendung der Tiefenätzung 2 (10 % HCl in Methanol über 24 h) zur eingehenden Analyse der eutektischen und sekundären Carbide empfohlen. Tiefenätzung 1 (50 mL $FeCl_3$ + 20 mL HCl + 930 mL Ethanol über 3 h bei RT) führte zu deutlichen Rückständen und wird daher nicht empfohlen.

Demzufolge sind bestimmte Ätzmittel in Abhängigkeit vom Untersuchungsziel zu wählen, wobei die Ergebnisse von deren Wahl und optimalem Einsatz abhängen. Neben der richtigen Wahl der Ätzparameter ist der Einsatz geeigneter mikroskopischer Instrumente für den Erhalt zuverlässiger und repräsentativer Informationen über die Mikrostruktur der Legierung unbedingt erforderlich. Schließlich dienen die durch diese Untersuchung erlangten Erkenntnisse als Grundlage für weitere Mikrostrukturanalysen dieser Legierungen und werden auf weitere Legierungen derselben Familie angewandt.

5. Danksagung

Die Autoren danken Martin Duarte von Tubacero S. A. für die Zurverfügungstellung der Werkstoffe. UP Nayak dankt außerdem dem DAAD für die finanzielle Unterstützung.

References / Literatur

[1] Tabrett, C.P.; Sare, I.R.; Ghomashchi, M.R.: Int. Mater. Rev. (1996), 41, 59–82. DOI:10.1179/imr.1996.41.2.59

[2] ASTM International, A532 / A532M Standard Specification for Abrasion-Resistant Cast Irons, ASTM International, West Conshohocken, PA, (2003): 1–4.

[3] Guitar, M.A.; Suárez, S.; Prat, O.; Duarte Guigou, M.; Gari, V.; Pereira, G.; Mücklich, F. J.: Mater. Eng. Perform. (2018), 27, 3877–3885. DOI:10.1007/s11665-018-3347-1

[4] Reza Abbaschian; Abbaschian, L.; Reed-Hill, R.E.: Physical Metallurgy Principles; 4th edition.; Cengage Learning, (2008). ISBN 978-0495082545

[5] Guitar, M.A.; Nayak, U.P.; Britz, D.; Mücklich, F.: Int. J. Met. (2020).
[6] Karantzalis, A.E.; Lekatou, A.; Mavros, H.J. Mater. Eng. Perform. (2009), 18, 174–181. DOI:10.1007/s11665-008-9285-6
[7] Abdel-Aziz, K.; El-Shennawy, M.; Omar, A.A. Int. J. Appl. Eng. Res. (2017), 12, 4675–4686. ISSN 0973-4562
[8] Asensio, J.; Pero-Sanz, J.A.; Verdeja, J.I.: Mater. Charact. (2002), 49, 83–93. DOI:10.1016/S1044-5803(02)00260-7
[9] Baldwin, W. Metallography and Microstructures. ASM Handbook. Volume 9, ASM International, Materials Park, OH (2004).
[10] Vander Voort, G.F. Metallography: Principles and Practice; ASM International, Materials Park, OH (1999). ISBN 13: 9780871706720
[11] Collins, W.K.; Watson, J.C.: Mater. Charact. (1990), 24, 379–386. DOI:10.1016/1044-5803(90)90044-K
[12] Powell, G.L.F.; Lloyd, P.G.: Metallography (1981), 14, 271–274. DOI:10.1016/0026-0800(81)90032-X
[13] Mehranfar, S.; Banadkouki, S.S.G.; Kallantar, M.; Yazdi, M.M.: ISIJ Int. (2012), 52, 1649–1654. DOI:10.2355/isijinternational.52.1649
[14] Guitar, M.A.; Scheid, A.; Suárez, S.; Britz, D.; Guigou, M.D.; Mücklich, F.: Mater. Charact. (2018), 144, 621–630. DOI:10.1016/j.matchar.2018.08.020
[15] Guitar, M.A.; Scheid, A.; Britz, D.; Mücklich, F.: Prakt. Metallogr. 56 (2019) 4, 246–261. DOI:10.3139/147.110570
[16] Schindelin, J.; Arganda-Carreras, I.; Frise, E.; Kaynig, V.; Longair, M.; Pietzsch, T.; Preibisch, S.; Rueden, C.; Saalfeld, S.; Schmid, B.; et al.: Nat. Methods (2012), 9, 676–682. DOI:10.1038/nmeth.2019
[17] Nayak, U.P.; Guitar, M.A.; Mücklich, F. Metals (Basel). (2020), 10. DOI:10.3390/met10010030
[18] Arganda-Carreras, I.; Kaynig, V.; Rueden, C.; Eliceiri, K.W.; Schindelin, J.; Cardona, A.; Seung, H.S.: Bioinformatics (2017), 33, 2424–2426. DOI:10.1093/bioinformatics/btx180
[19] Müller, M.; Britz, D.; Mücklich, F.: Pract. Metallogr. 57 (2020), 337–358. DOI:10.3139/147.110640
[20] Lew, K. Acids and Bases; Chelsea House Publishers: Broomall, (2009). ISBN 13: 9780791097830.
[21] Bedolla-Jacuinde, A.; Hernández, B.; Béjar-Gómez, L.: Zeitschrift für Metallkunde (2005), 96, 1380–1385. DOI:10.3139/146.101188

Bibliography
DOI 10.3139/147.110682
Pract. Metallogr. 57 (2020) 10; page 688–713

ISSN 0032–678X

U. Pranav Nayak

Born in 1993, he completed his undergraduate studies at NITK Surathkal, India and MSc in Materials Science under the Erasmus Mundus FAME Program. Since 2018, he is a doctoral candidate at the Chair of Functional Materials with his research focusing on the microstructure tailoring in HCCI alloys through heat treatment modifications.

Agustina Guitar

Doctor of engineering / Materials science and engineering at Saarland University in 2014
Currently: Post-Doc at Chair of Functional Material at Saarland University (since 2016); Leader of Steel and Ferrous based Materials Group; Actual work is focused in the Microstructural design in high chromium cast irons for performance optimization

III. Image Processing using Open-Source Tools and their Implementation in the Analysis of Complex Microstructures

U. Pranav Nayak, Martin Müller, Dominik Britz, María Agustina Guitar, Frank Mücklich

Department of Materials Science and Engineering, Saarland University, 66123 Saarbrücken, Germany

Published in "***Practical Metallography***" (2021) *(IF (2023): 0.225)*

Reproduced with permission from 'Walter de Gruyter GmbH'

Accessible online at: *https://doi.org/10.1515/pm-2021-0039*

Own Contribution: Conceptualization and methodology; sample preparation; microstructural characterization and analysis; scientific discussion; paper writing – original draft preparation

U. P. Nayak, M. Müller, D. Britz, M.A. Guitar, F. Mücklich

Image Processing using Open Source Tools and their Implementation in the Analysis of Complex Microstructures

Bildverarbeitung mithilfe von Open-Source-Tools und deren Anwendung bei der Analyse komplexer Gefüge

Received: May 01, 2021
Accepted: May 02, 2021

Eingegangen: 01. Mai 2021
Angenommen: 02. Mai 2021
Übersetzung: E. Engert

Abstract

Considering the dependance of materials' properties on the microstructure, it is imperative to carry out a thorough microstructural characterization and analysis to bolster its development. This article is aimed to inform the users about the implementation of FIJI, an open source image processing software for image segmentation and quantitative microstructural analysis.

The rapid advancement of computer technology in the past years has made it possible to swiftly segment and analyze hun-

Kurzfassung

Vor dem Hintergrund der Abhängigkeit von Werkstoffeigenschaften vom Gefüge ist die Durchführung einer eingehenden mikrostrukturellen Charakterisierung und Analyse für die Weiterentwicklung von Werkstoffen unerlässlich. Die vorliegende Arbeit soll Benutzer über die Anwendung von FIJI, einer Open-Source-Bildverarbeitungssoftware für Bildsegmentierung und quantitative Gefügeanalyse informieren.

Die rasanten Fortschritte in der Computertechnik der letzten Jahre haben eine schnelle Segmentierung und Analyse hunderter Mikro-

Authors:

Ullal Pranav Nayak, Martin Müller, Dominik Britz, María Agustina Guitar, Frank Mücklich
Fachbereich Materialwissenschaft, Universität des Saarlandes. Campus D3 3, D-66123, Saarbrücken, Deutschland; e-mail: pranav.nayak@uni-saarland.de
Martin Müller, Dominik Britz, Frank Mücklich Material Engineering Center Saarland (MECS), Campus D3 3, D-66123 Saarbrücken, Deutschland

dreds of micrographs reducing hours' worth of analysis time to a mere matter of minutes. This has led to the availability of several commercial image processing software programs primarily aimed at relatively inexperienced users. Despite the advantages like 'one-click solutions' offered by commercial software, the high licensing cost limits its widespread use in the metallographic community.

Open-source platforms on the other hand, are free and easily available although rudimentary knowledge of the user-interface is a pre-requisite. In particular, the software FIJI has distinguished itself as a versatile tool, since it provides suitable extensions from image processing to segmentation to quantitative stereology and is continuously developed by a large user community. This article aims to introduce the FIJI program by familiarizing the user with its graphical user-interface and providing a sequential methodology to carry out image segmentation and quantitative microstructural analysis.

Keywords: *open source; image analysis; FIJI; segmentation; microstructure; phase quantification; stereological characteristics*

skopaufnahmen und eine Verkürzung der entsprechenden Analysedauer von Stunden auf wenige Minuten möglich gemacht. In der Folge konnten sich mehrere, auf relativ unerfahrene Anwender abzielende kommerzielle Bildverarbeitungsprogramme etablieren, die auf dem Markt erhältlich sind. Trotz ihrer Vorteile, beispielsweise „Ein-Klick-Lösungen", verhindern die hohen Lizenzkosten dieser kommerziellen Programme eine verbreitete Nutzung in der Metallographie-Community.

Open-Source-Plattformen hingegen sind kostenlos und leicht verfügbar. Allerdings sind hier rudimentäre Kenntnisse der Benutzeroberfläche Voraussetzung. Insbesondere die Software FIJI hat sich als ein vielfältiges Tool ausgezeichnet: Sie stellt, von der Bildverarbeitung über die Segmentierung bis hin zur quantitativen Stereologie, geeignete Erweiterungen bereit und unterliegt einer fortwährenden Weiterentwicklung durch einen großen Anwenderkreis. In dieser Arbeit soll das FIJI-Programm vorgestellt werden. Dabei wird der Anwender mit der entsprechenden grafischen Benutzeroberfläche vertraut gemacht und eine sequentielle Vorgehensweise zur Durchführung von Bildsegmentierung und quantitativer Gefügeanalyse vermittelt.

Schlagworte: *Open Source, Bildanalyse, FIJI, Segmentierung, Gefüge, Phasenquantifizierung, stereologische Merkmale*

1 Introduction

It is a well-known fact that the properties of any given material are mainly dictated by its microstructure. Inducing modifications in the microstructure will alter the final properties making the material versatile to be used for several different applications [1]. Alloys are used in a myriad of industries because their microstructure can be modified in numerous ways either by alloying, heat treatment and thermomechanical processing, or a combination thereof. The presence of the different types of phases/micro-constitu-

1 Einleitung

Allgemein bekannt ist, dass die Eigenschaften eines gegebenen Werkstoffs in erster Linie von seinem Gefüge bestimmt werden. Wird das Gefüge modifiziert, verändern sich die späteren Eigenschaften. Der Werkstoff gewinnt hierdurch an Vielseitigkeit, lässt sich für mehrere unterschiedliche Anwendungen einsetzen [1]. Da ein Gefüge auf vielfältige Weise entweder durch Legieren, Wärmebehandlung oder thermomechanische Verarbeitung bzw. deren Kombination verändert werden kann, kommen Legierungen in unzähligen Branchen zum Einsatz. Das

ents and their respective amounts in a given microstructure will dictate the final properties of the alloy. Fig. 1 represents the mutual dependence between the processing, microstructure, and properties in a material.

According to the correlations depicted in Fig. 1, the microstructure can be regarded as a *'multi-scale memory'*. Thus, the analysis of the microstructure is indispensable for quality control and an essential component for further material development. In practice, four characteristics should be described to fully characterize a microstructure [2]:

Vorhandensein verschiedener Phasentypen/Mikrobestandteile und ihrer jeweiligen Anteile bzw. Mengen in einem Gefüge bestimmen über die finalen Eigenschaften der Legierung. Bild 1 zeigt die in einem Werkstoff bestehenden wechselseitigen Abhängigkeiten zwischen Verarbeitung, Gefüge und Eigenschaften.

Vor dem Hintergrund der vorstehend genannten Zusammenhänge kann das Gefüge als ein *„Multiskalenspeicher"* angesehen werden. Die Analyse des Gefüges ist demnach einerseits unverzichtbar in der Qualitätskontrolle und stellt andererseits ein wesentliches Element für die Weiterentwicklung des Werkstoffs dar. In der Praxis sollten im Rahmen einer umfassenden Charakterisierung eines Gefüges vier Merkmale beschrieben werden [2]:

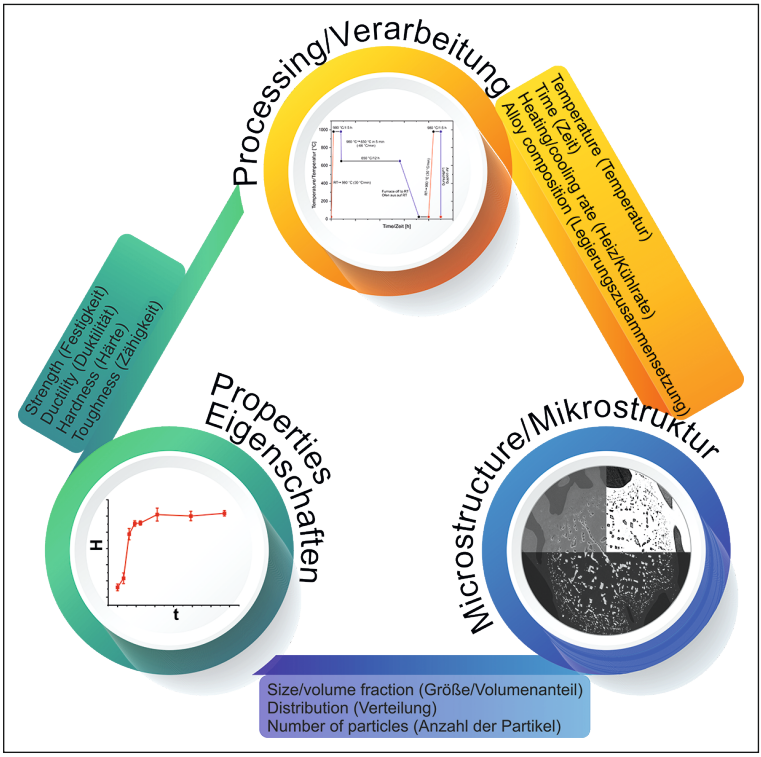

Fig. 1: *A mutual dependence between the processing, microstructure, and properties.*

Bild 1: *Wechselseitige Abhängigkeit von Verarbeitung, Mikrostruktur und Eigenschaften.*

- Amount of all the structural constituents.
- Size (of particles or their colonies).
- Shape (of individual particles).
- Spatial distribution or arrangement (form) of particles over the material volume.

The necessity for microstructural segmentation stems from the fact that the individual phases contribute differently (it is inherent) to the whole microstructure. This can be exemplified by considering a Dual-Phase (DP) steel whose microstructure is predominantly composed of ferrite and martensite [3]. The martensitic phase provides substantial strengthening while the ductile ferritic matrix gives good formability. Care must be taken that the material shows a proper balance of martensite/ferrite, since a large percentage of martensite may result in a brittle material and likewise, too much ferrite might reduce the materials' strength. A compromise must be reached so that the material can have the best of both. In this regard, knowing the percentage of each phase will help in further developing the alloy to improve the final properties [4].

Image processing approaches can be categorized into manual, semi-automated, or automated. The manual process involves the usage of a ruler and a calibrated photomicrograph [5]. Although manual segmentation has been carried out for a long time, it is tedious and cumbersome, especially considering the increasing complexities in the alloys' microstructure. Nevertheless, advancements in computer technology in the past few decades has made it possible to rapidly segment and analyze hundreds of micrographs reducing hours' worth of analyses time to a mere matter of minutes. Semi-automated and automated processes employ image analysis packages wherein the user must provide certain inputs to carry out the analysis. These packages have built-

- Die Menge aller Gefügebestandteile.
- Die Größe (von Partikeln oder ihrer Kolonien).
- Die Form (einzelner Partikel).
- Die räumliche Verteilung bzw. Anordnung (Form) von Partikeln im Werkstoffvolumen.

Die Notwendigkeit einer Gefügesegmentierung ergibt sich daraus, dass sich die einzelnen Phasen unterschiedlich (phaseninhärent) auf das Gefüge auswirken. Das kann am Beispiel eines Dualphasenstahls (DP) veranschaulicht werden, dessen Gefüge sich vorwiegend aus Ferrit und Martensit zusammensetzt [3]. Die martensitische Phase wirkt stark festigkeitssteigernd, während die duktile ferritische Matrix dem Material eine gute Verformbarkeit verleiht. Dabei muss auf ein ausgewogenes Gleichgewicht aus Martensit und Ferrit des Werkstoffs geachtet werden, da er bei einem großen Prozentanteil an Martensit versprödet. In ähnlicher Weise kann zu viel Ferrit zu einem Rückgang der Festigkeit des Werkstoffs führen. Es gilt, einen Kompromiss zu finden, der gewährleistet, dass der Werkstoff das Beste aus beiden Bestandteilen vereint. Vor diesem Hintergrund ist es in der Weiterentwicklung der Legierung zwecks Verbesserung der finalen Eigenschaften hilfreich, den Prozentanteil der einzelnen Phasen zu kennen [4].

Bildverarbeitungsverfahren können in die Kategorien manuell, halbautomatisch oder automatisch eingeteilt werden. Die manuelle Vorgehensweise erfordert ein Lineal und eine kalibrierte Mikroskopaufnahme [5]. Auch wenn die manuelle Segmentierung über einen langen Zeitraum hinweg durchgeführt wurde: Sie ist langwierig und mühsam, insbesondere in Anbetracht der zunehmenden Komplexität von Legierungsgefügen. Jedoch haben es Fortschritte der letzten Jahrzehnte in der Computertechnik möglich gemacht, dass nun hunderte Mikroskopaufnahmen schnell segmentiert und analysiert werden können und sich die Analysedauer von Stunden auf wenige Minuten verkürzt. In halbautomatischen und automatischen Prozessen kommen Bildanalysepakete zum Einsatz. Hier muss der Anwender bestimm-

in algorithms which enable them to locate the particles with ease in each micrograph. Additionally, calculations concerning the individualistic particle characteristics such as size, diameter, circularity etc., can automatically be carried out [5,6]. The technological improvement and ease in alloy development have led to the production of complex alloys for special applications (high temperature, nuclear, space etc.) and it is imperative to distinguish the delicate microstructural features between the alloys for a more efficient usage in the intended application. In this regard, the human eye might not be capable to differentiate the intricacies between the phases and a computer-based program, which is objective and reliant on math, would be better suited.

te Eingaben vornehmen, bevor eine Analyse durchgeführt werden kann. In diesen Paketen enthaltene integrierte Algorithmen ermöglichen eine problemlose Lokalisierung der Partikel in den entsprechenden Aufnahmen. Zusätzlich können Berechnungen im Zusammenhang mit bestimmten Partikeleigenschaften wie Größe, Durchmesser, Zirkularität etc. automatisch ausgeführt werden [5, 6]. Der technologische Fortschritt und die nun einfachere Legierungsentwicklung haben komplexe Legierungen für spezifische Anwendungen hervorgebracht (Hochtemperatur, nuklear, Raumfahrt etc.). Dabei ist es im Sinne einer effizienteren Nutzung im vorgesehenen Anwendungsbereich unerlässlich, die subtilen Mikrostrukturmerkmale der einzelnen Legierungen unterscheiden zu können. Diesbezüglich ist das menschliche Auge möglicherweise nicht in der Lage, die feinen Unterschiede zwischen den Phasen zu erkennen, so dass ein objektives, mathematikbasiertes, computergestütztes Programm, hierfür besser geeignet wäre.

There are several commercial image processing programs such as Amira [7], A4i Aquinto©, Mipar©, AxioVision©, PixelFerber© etc., where automated image analysis can easily be carried out. Considering the competition, warranty and reliability are of utmost priority to these companies. Granted that the commercial programs have the added advantage of one click solutions, a dedicated customer support team, an interactive graphical user interface (GUI) and the ability to use it without an in-depth knowledge of the modules, the cost associated to licensing it limits the general metallographic community to employ it.

Mehrere kommerzielle Bildverarbeitungsprogramme, beispielsweise Amira [7], A4i Aquinto©, Mipar©, AxioVision©, PixelFerber© etc. bieten die Möglichkeit einer einfach durchführbaren automatischen Bildanalyse. Vor dem Hintergrund des Wettbewerbs haben Garantieleistung und Zuverlässigkeit für diese Unternehmen oberste Priorität. Bei kommerziellen Programmen, die den zusätzlichen Vorteil von Ein-Klick-Lösungen, ein spezialisiertes Team für Kundensupport, eine interaktive grafische Benutzeroberfläche (GUI) und die Möglichkeit einer Anwendung ohne fundierte Kenntnisse der Module bieten, führen die damit einhergehenden Lizenzgebühren dazu, dass nur eine begrenzte Anzahl von Metallographen auch von diesen Vorteilen profitieren kann.

Open source platforms on the other hand, are free and easily available wherein, the absence of a dedicated support team is supplemented through constant support and development by a strong community of developers. The transparency with which it

Open-Source-Plattformen hingegen sind kostenlos und leicht zugänglich. Die Tatsache, dass keine spezialisierten Support-Teams zur Verfügung stehen, wird durch die permanente Unterstützung und Weiterentwicklung im Rahmen einer starken Community aus Entwicklern

operates allows users and researchers from various domains to contribute to the development of the software. Moreover, the addition of plugins and other functions greatly extends its applicability in a wide variety of fields ranging from biology [8] to geology [9,10] to materials science [5]. Prominent examples for wide-spread open source tools include Irfanview [Supplementary Information (S.I.) 1] or GIMP [S.I. 2] for image processing, Gwyddion for analysis of atomic force microscope data [11], DREAM.3D for generating synthetic microstructures [12] etc. However, compared to a readily working commercial software, basic proficiency in the setup of the analysis pipeline may be required by the user to carry out microstructural analyses using an open source platform.

The main objective of the present manuscript is to showcase the applicability of an open source image processing package, FIJI (Fiji Is Just Image J), for image segmentation and quantitative stereology in materials science. It is worth to note that the current manuscript is in no way discrediting the commercially available image processing platforms, but rather providing information about the implementation of freely available open source software in carrying out microstructural analysis. This article aims to make the reader familiar with the functionality of the FIJI software, and provide a systematic guideline to carry out image segmentation and quantitative microstructural analyses.

2 Methodology

Although the domain of image processing is diverse, the present article will deal with two aspects i. e., 1) Microstructural Segmentation and 2) Quantitative Image Analysis. A brief overview of the steps involved right from basic sample preparation to image

teilweise kompensiert. Die Systemtransparenz ermöglicht Anwendern und Forschern verschiedener Bereiche, zur Entwicklung der Software beizutragen. Zudem sorgen ergänzende Plugins und weitere Funktionen dafür, dass sie in einer Vielzahl von Anwendungsbereichen, von der Biologie [8] über die Geologie [9, 10] bis hin zu den Materialwissenschaften [5], genutzt werden kann. Zu den bekannten Beispielen für weitverbreitete Open-Source-Tools gehören IrfanView [w. I. (weiterführende Informationen) 1] oder GIMP [w. I. 2] im Bereich der Bildverarbeitung, Gwyddion für die Analyse von Daten der Rasterkraftmikroskopie [11] und DREAM.3D für die Erzeugung synthetischer Mikrostrukturen [12] etc. Will man Gefügeanalysen mithilfe einer Open-Source-Plattform durchführen, werden vom Anwender im Gegensatz zu einsatzbereiten kommerziellen Software-Produkten allerdings möglicherweise Grundkenntnisse im Aufbau der Analysepipeline gefordert.

Hauptziel der vorliegenden Arbeit ist es, die Anwendbarkeit eines Open-Source-Bildverarbeitungspakets, FIJI (Fiji Is Just ImageJ) für die Bildsegmentierung und quantitative Stereologie in der Materialwissenschaft aufzuzeigen. An dieser Stelle sei anzumerken, dass diese Arbeit keinesfalls die im Handel erhältlichen Bildverarbeitungsplattformen diskreditieren, sondern vielmehr Informationen zu frei erhältlicher Open-Source-Software bei der Durchführung einer Gefügeanalyse liefern soll. Mithilfe dieses Beitrags soll der Leser mit der Funktionsweise der FIJI-Software vertraut gemacht und ein systematischer Leitfaden für die Durchführung von Bildsegmentierungen und quantitativen Gefügeanalysen angeboten werden.

2 Methodik

Der Bereich der Bildverarbeitung ist sehr vielfältig. Die vorliegende Arbeit aber beschränkt sich auf zwei Aspekte: die 1) Gefügesegmentierung und die 2) quantitative Bildanalyse. Bild 2 gibt, ausgehend von der grundlegenden Probenpräparation über die Bildsegmen-

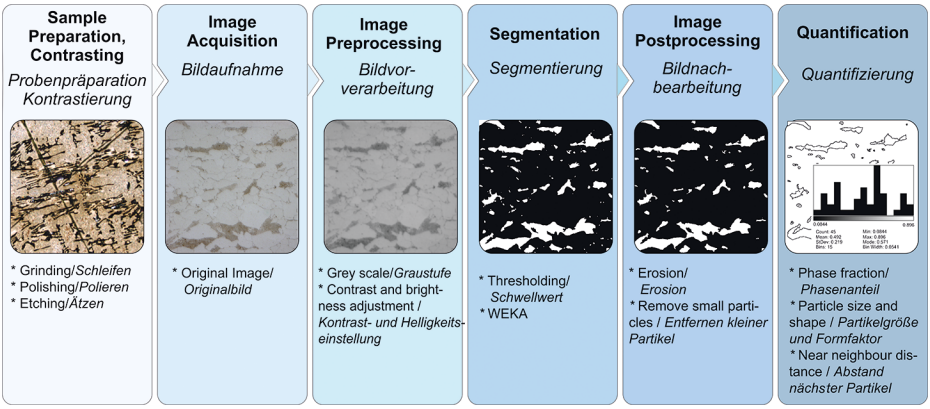

Fig. 2: *An overview of the steps involved from metallographic preparation to phase segmentation and quantification.*

Bild 2: *Übersicht über die einzelnen Schritte von der metallographischen Präparation über die Phasensegmentierung bis hin zur Quantifizierung.*

segmentation to the final phase quantification is presented in Fig. 2.

2.1 Metallographic Preparation

The first step towards extracting crucial microstructural information from the material is a proper metallographic preparation of the sample. This involves following the right protocol i. e., grinding → polishing → etching. Depending upon the material, the specifics vary, but it is imperative to find the optimal polishing parameters to obtain a scratch-free mirror finished surface [13]. Moreover, another important pre-requisite for subsequent image segmentation is the availability of a micrograph which has a good contrast (chemical or topographical), which can be achieved by etching the sample under optimal conditions to ensure no microstructural features are lost in the process [14]. The necessity to create a contrast on the metallic surface stems from the fact that under a microscope, a finely polished surface looks like a white cloud. Etchants are solutions that help in creating a contrast between the phases in the microstructure. They induce

tierung bis hin zur abschließenden Phasenquantifizierung, einen kurzen Überblick über die entsprechenden Schritte.

2.1 Metallographische Präparation

Der erste Schritt, um aus dem Gefüge wesentliche Informationen über den Werkstoff gewinnen zu können, ist eine ordnungsgemäße metallographische Präparation der Probe. Dabei gilt es, sich an das entsprechende Protokoll zuhalten, also Schleifen → Polieren → Ätzen. Die Spezifika sind werkstoffabhängig, doch ist es unerlässlich, optimale Polierparameter zu ermitteln, um eine kratzerfreie spiegelblanke Oberfläche zu erhalten [13]. Eine weitere wichtige Voraussetzung für die nachfolgende Bildsegmentierung ist außerdem eine Mikroskopaufnahme, die einen guten (chemischen oder topographischen) Kontrast bietet. Dieser kann durch Ätzen der Probe unter optimalen Bedingungen hervorgebracht werden, die gewährleisten, dass während des Vorgangs keine Gefügemerkmale verloren gehen [14]. Die Notwendigkeit der Kontrastierung der Metalloberfläche ist darauf zurückzuführen, dass eine fein polierte Oberfläche in einem Mikroskop einer weißen Wolke gleicht. Ätzmittel sind Lösungen, die bei der Bildung

site-specific chemical reactions greatly aiding in visual observations, which will provide valuable information regarding the grain size, distribution of the phases, segregation, foreign particles etc., through which the alloys' behavior may be determined [15, 16].

2.2 FIJI (Fiji Is Just ImageJ)

ImageJ is an open source, Java-based image processing program which was initially developed at the National Institutes of Health and the Laboratory for Optical and Computational Instrumentation (LOCI, University of Wisconsin) to analyze biological samples [S.I. 3] [17]. Over the years, modifications were made by users around the world with the addition of plugins and specific packages to suit the various needs of different communities and one such project was FIJI.

FIJI is an open source image processing package based on ImageJ [18]. It combines the interface present in ImageJ with the added functionalities through the presence of several bundled plugins, which the users can independently install. FIJI can be downloaded and installed for a specific operating system by visiting [S.I. 4] and following the instructions. Fig. 3 represents the GUI of FIJI after the successful installation. The GUI is concise, allowing the user to explore additional features by clicking on the respective tabs.

2.3 Microstructural Segmentation/ Image Segmentation

The process of dividing an image into different regions and assigning a label to each pixel (px) within an image is the essentiality of image segmentation [5]. The pixels lying

eines Kontrasts zwischen den Phasen im Gefüge unterstützen. Sie rufen stellenspezifische chemische Reaktionen hervor, die bei visuellen Betrachtungen sehr hilfreich sind und wertvolle Informationen hinsichtlich der Korngröße, der Verteilung der Phasen, der Seigerung, von Fremdkörpern etc. liefern, anhand derer sich das Legierungsverhalten bestimmen lässt [15, 16].

2.2 FIJI (Fiji Is Just ImageJ)

ImageJ ist ein Java-basiertes Open-Source-Bildverarbeitungsprogramm, das ursprünglich an den National Institutes of Health (Gesundheitsbehörde) und dem Laboratory for Optical und Computational Instrumentation, LOCI (etwa: Labor für optische Messtechnik und rechnergestützte Instrumentierung) der Universität Wisconsin, USA, für die Analyse biologischer Proben entwickelt wurde [w. I. 3] [17]. Im Laufe der Jahre wurden von Anwendern weltweit Änderungen an der Software in Form von ergänzenden Plug-ins und spezifischen Paketen vorgenommen, um unterschiedlichen Anforderungen verschiedener wissenschaftlicher Gemeinschaften und ihrer Projekte gerecht werden zu können. Eines dieser Projekte war FIJI.

FIJI ist ein auf ImageJ basierendes Open-Source-Bildverarbeitungpaket [18]. Es kombiniert die ImageJ-Schnittstelle mit zusätzlichen Funktionen in Form von mehreren gebündelten Plug-ins, die der Anwender unabhängig voneinander installieren kann. FIJI steht als Download unter [w. I. 4] bereit, wo den entsprechenden Anweisungen zu folgen ist, und kann für ein bestimmtes Betriebssystem installiert werden. Bild 3 zeigt die FIJI-GUI (GUI, grafische Benutzeroberfläche) nach erfolgreicher Installation. Sie ist präzise und Anwender können durch einen Klick auf entsprechende Registerkarten zusätzliche Funktionen nutzen.

2.3 Gefügesegmentierung/Bildsegmentierung

Im Grunde genommen ist unter Bildsegmentierung die Aufteilung eines Bildes in verschiedene Bereiche sowie die Zuordnung eines Labels zu jedem Pixel (px) in einem Bild

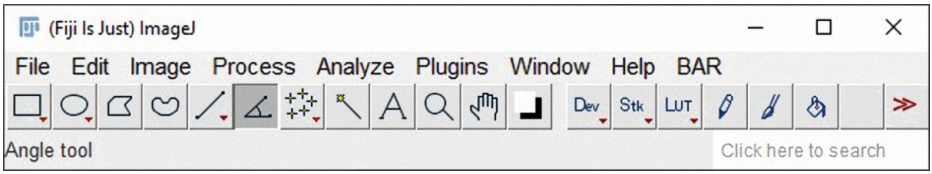

Fig. 3: *GUI of FIJI.*

Bild 3: *GUI von FIJI.*

within a region should have similar properties and this is achieved by assigning a 'label' to each pixel within an image. It is worth to note that the size of an individual px is always dependent on the resolution of the image. The two segmentation approaches which will be elucidated are thresholding and WEKA segmentation.

2.3.1 Thresholding (Threshold Segmentation)

Thresholding is the simplest way of segmenting a given micrograph. The division is based on the intensity value from 0 to 255 for 8-bit images (brighter objects have higher intensity and darker objects have lower intensity). Global thresholding works by choosing a value cutoff, such that every pixel less than that value is considered one class, while every pixel greater than that value is considered the other class.

Fig. 4 represents the threshold segmentation of an optical micrograph of a DP steel consisting of a ferritic matrix and a carbon-rich second phase. As the micrograph consists of two distinct phases, thresholding commences by assigning a 'value' and categorizing the phase based on whether it is above or below the assigned 'value'. The resulting image is referred to as a binary image, as represented in Fig. 4 (b)–(d). The corresponding steps to obtain the segmented image are as follows:

zu verstehen [5]. Die in einem Bereich liegenden Pixel sollten ähnliche Eigenschaften aufweisen. Das wird erreicht, indem jedem Pixel in einem Bild ein „Label" zugewiesen wird. Es sollte an dieser Stelle angemerkt werden, dass die Größe eines einzelnen px stets von der Bildauflösung abhängt. Die zwei Verfahren, die hier erläutert werden, sind die Schwellwertbildung und die WEKA-Segmentierung.

2.3.1 Schwellwertbildung (Schwellwertsegmentierung)

Die Schwellwertbildung ist die einfachste Möglichkeit, eine gegebene Mikroskopaufnahme zu segmentieren. Die Aufteilung basiert auf dem Intensitätswert von 0 bis 255 für 8-Bit-Bilder (Hellere Objekte weisen eine höhere Intensität, dunklere Objekte eine geringere Intensität auf). Bei der globalen Schwellwertbildung wird ein „Cut-off"-Wert (Grenzwert) gewählt, wobei jedes Pixel, dessen Wert unter dem entsprechenden Wert liegt, einer Klasse zugeordnet und jedes Pixel, dessen Wert darüber liegt, der anderen Klasse zugeordnet wird.

Bild 4 zeigt die Schwellwertsegmentierung an einer lichtmikroskopischen Aufnahme eines DP-Stahls, der sich aus einer ferritischen Matrix und einer kohlenstoffreichen zweiten Phase zusammensetzt. Da die Aufnahme zwei unterschiedliche Phasen enthält, beginnt die Schwellwertbildung mit dem Festlegen eines „Werts" und der Einordnung der Phase basierend darauf, ob diese über oder unter dem zugeordneten „Wert" liegt. So entstehende Bilder, wie sie in Bild 4 (b)–(d) zu sehen sind, werden als Binärbilder bezeichnet. Mit folgenden Schritten können solch segmentierte Bilder erzeugt werden:

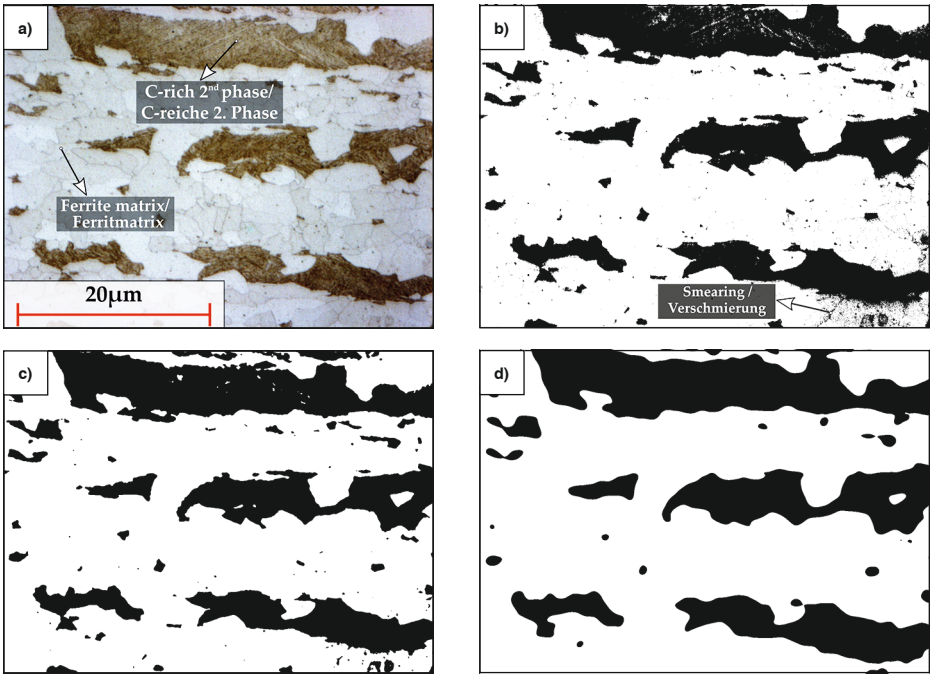

Figs. 4a to d: *Image segmentation of a micrograph consisting of carbon-rich second phase using simple thresholding with (a) original optical micrograph, (b) segmentation with no filter, and the occurrence of 'smearing' marked for reference, (c) segmentation with a 2px gaussian blur and (d) segmentation with a 10px gaussian blur.*

Bilder 4a bis d: *Bildsegmentierung einer Mikroskopaufnahme eines Gefüges mit einer kohlenstoffreichen zweiten Phase mittels einfacher Schwellwertbildung: (a) lichtmikroskopische Originalaufnahme, (b) Segmentierung ohne Filter (im Bild entsprechend gekennzeichnetes Auftreten von „Verschmierungen"), (c) Segmentierung mit einem Gaußschem Weichzeichner von 2px sowie (d) Segmentierung mit einem Gaußschem Weichzeichner von 10px.*

- Open the optical micrograph in FIJI (Fig. 4 (a)) (File → Open).
- Outline the area to be analyzed and duplicate it (Ctrl + Shift + D).
- Convert the image to 8-bit (Image → Type → 8-bit).
- Apply the threshold (Image → Adjust → Threshold → Apply) or alternatively, Ctrl + Shift + T.

- Öffnen der lichtmikroskopischen Aufnahme in FIJI (Bild 4 (a)) („File" (Datei) → „Open" (Öffnen))
- Umreißen und Duplizieren der zu analysierenden Fläche (Strg + Shift + D).
- Konvertieren des Bildes in ein 8-Bit-Bildformat („Image" (Bild) → „Type" (Typ) → „8-bit" (8-Bit))
- Anwenden des Schwellenwerts („Image" (Bild) → „Adjust" (Anpassen) → „Threshold" (Schwellenwert) → „Apply" (Anwenden)) oder alternativ Strg + Shift + T

Fig. 4 (b) represents the segmented image after applying the threshold. It is observed that at certain regions in the micrograph (bottom-right and inside the second phase), some 'smearing' has taken place. This is attributable to the non-uniformity in etching and/or illumination during image acquisition. It is worth to note that image segmentation is always an estimate as the boundary between the regions (edges) is ambiguous. To reduce the uncertainty, additional operations might be performed on the image such as filtering, background subtraction, contrast enhancement etc.

Filtering essentially refers to simple arithmetic operations which are performed on a small number of pixels that comprise the image and it is known to improve segmentation capability, as it reduces the 'noise' in the image. Some filtering methods include mean filtering, median filtering, gaussian filtering etc., which smoothen the image based on their respective functions [5, 19]. The influence of applying a gaussian filter before thresholding can be visualized in Fig. 4 (c) and Fig. 4 (d). Comparing them to Fig. 4 (b), the segmented images are relatively smoother with little to no 'smearing' present. The filtering functionality in FIJI can be applied by accessing the 'Process' menu as seen in the GUI in Fig. 3 (Process → Filters).

In addition to the filtering method, the chosen filtering radius also influences the result. Increasing the filter radius makes the image smoother (by removing more of the noise) but care must be taken because along with the noise, some information is also lost. This is observed by comparing Fig. 4 (c) and Fig. 4 (d). The filter radius of 10 px has resulted in a morphological variation of the second phase regions, in addition to the removal of smaller particles. Despite the

Bild 4 (b) zeigt das segmentierte Bild nach Anwendung des Schwellenwerts. Es kann beobachtet werden, dass es in bestimmten Bereichen der Mikroskopaufnahme (unten rechts und innerhalb der zweiten Phase) zu „Verschmierungen" gekommen ist. Das kann auf Ungleichmäßigkeiten beim Ätzen und/oder der Beleuchtung während der Bilderfassung zurückgeführt werden. Es sei darauf hingewiesen, dass es sich bei der Bildsegmentierung stets um eine Schätzung handelt, da Grenzen zwischen den Bereichen (Ränder) nicht eindeutig sind. Am Bild können zusätzliche Operationen durchgeführt werden, beispielsweise Filterprozesse, Hintergrundsubtraktion, Verstärkung des Kontrasts etc., um solche Uneindeutigkeiten zu reduzieren.

Der Begriff „Filtern" bezieht sich hier im Wesentlichen auf einfache arithmetische Operationen, die an einer kleinen Anzahl von Pixeln durchgeführt werden, die das Bild enthält. Bekannt ist, dass sich hierdurch die Segmentierungsfähigkeit verbessert, da hierbei das „Rauschen" im Bild reduziert wird. Einige dieser Filterverfahren sind das Mittelwert-Filtern, das Median-Filtern, das Gauß-Filtern etc., bei denen das Bild basierend auf den entsprechenden Funktionen geglättet wird [5, 19]. Aus Bild 4 (c) und Bild 4 (d) geht hervor, wie sich die Anwendung eines Gauß-Filters vor der Schwellwertbildung auswirkt. Im Vergleich mit Bild 4 (b) sind die segmentierten Bilder bei wenig oder keinen „Verschmierungen" verhältnismäßig glatter. Auf die Filterfunktion greift man in FIJI über das Menü „Process" (Prozess) zu. Siehe hierzu die GUI in Bild 3 („Process" (Prozess) → „Filters" (Filter)).

Nicht nur das Filterverfahren wirkt sich auf das Ergebnis aus, sondern auch der gewählte Filterradius. Durch Erhöhen des Filterradius wird das Bild glatter (indem mehr Rauschen entfernt wird). Allerdings ist hier Vorsicht geboten, denn zusammen mit dem Rauschen geht auch ein Teil der Informationen verloren. Das wird an einem Vergleich der Bilder 4 (c) und 4 (d) deutlich. Der Filterradius von 10 px führte, von einer Entfernung kleinerer Partikel abgesehen, auch zu einer morphologischen Variation der Bereiche der zweiten

seemingly different visual characteristics of the segmented images (Fig. 4 (b)–(d)), the amount of the second phase calculated is similar (~ 29 %). This can be attributed to the compensatory effect between the removal of smaller discrete regions (dots) and the dilation at the edges of the bigger regions.

Simple thresholding was successfully applied to distinguish the second phase region from the rest of the microstructure, as seen from Fig. 4. Nevertheless, this approach is not always advisable, especially when dealing with a multi-phase microstructure. The simple thresholding approach binarizes the image and therefore, to perform a multi-threshold segmentation and handle complex segmentation tasks, the trainable WEKA segmentation (which is more automatic and robust to segment more than 2 classes) may be an interesting solution within FIJI.

2.3.2 WEKA Segmentation (Waikato Environment for Knowledge Analysis)

The trainable WEKA segmentation [S.I. 5] is an inbuilt FIJI plugin that combines a collection of machine learning algorithms with a set of selected image features to produce pixel-based segmentations [20, 21]. It contains a collection of visualization tools and algorithms for data analysis and predictive modeling, together with a GUI for easy access to this functionality [22]. This approach was successfully implemented to segment micrographs consisting of a multi-phase microstructure [23, 24]. The initial process involves, 'training' the classifier with a set number of classes (different phases) and further continuing by adding more data to make the training robust and finally saving the classifier. The 'saved' classifier is then applied to another set of micrographs to obtain the respective segmented result.

Phase. Trotz der scheinbar unterschiedlichen optischen Merkmale der segmentierten Bilder (Bild 4 (b)–(d)) ähnelt sich der jeweils für die zweite Phase berechnete Mengenwert (~ 29 %). Das kann auf eine ausgleichende Wirkung zwischen dem Entfernen kleiner diskreter Bereiche (Punkte) und der Dilation an den Rändern der größeren Bereiche zurückgeführt werden.

Zur Abgrenzung des Bereichs der zweiten Phase vom Rest des Gefüges wurde erfolgreich eine einfache Schwellwertbildung angewendet. Siehe hierzu Bild 4. Dieser Ansatz ist, insbesondere bei der Arbeit mit einem mehrphasigen Gefüge, allerdings nicht immer empfehlenswert. Bei der einfachen Schwellwertbildung wird das Bild binarisiert. Daher könnte die trainierbare WEKA-Segmentierung (mehr Automatisierung und Robustheit bei einer Segmentierung mit mehr als zwei Klassen) in FIJI eine interessante Lösung darstellen, um eine Mehrschwellensegmentierung durchzuführen und komplexe Segmentierungsaufgaben zu lösen.

2.3.2 WEKA-Segmentierung (Waikato-Umgebung für die Wissensanalyse)

Die trainierbare WEKA-Segmentierung [w. l. 5] ist ein in FIJI integriertes Plug-in, das eine Sammlung von Algorithmen für maschinelles Lernen mit einem Satz ausgewählter Bildmerkmale kombiniert, um pixelbasierte Segmentierungen zu erzeugen [20, 21]. Sie umfasst neben einer GUI für einen einfachen Zugriff auf die Funktionen eine Sammlung von Visualisierungswerkzeugen und Algorithmen für die Datenanalyse und prädiktives Modellieren [22]. Dieses Verfahren wurde erfolgreich bei der Segmentierung von Mikroskopaufnahmen mit mehrphasigem Gefüge angewendet [23, 24]. In einem einleitenden Schritt wird der Klassifikator mit einer bestimmten Anzahl von Klassen (verschiedene Phasen) „trainiert". Im weiteren Verlauf werden weitere Daten ergänzt, um eine robuste Trainingsqualität zu erzielen. Schließlich wird der Klassifikator gespeichert. Der „gespeicherte" Klassifikator wird anschließend auf den anderen Satz von Mikroskopaufnahmen angewandt, um ein entsprechend segmentiertes Ergebnis zu erhalten.

The applicability of WEKA segmentation was exemplified by considering a multiphase micrograph as shown in Fig. 5 (a). The three distinct phases were labelled, and the objective was to segment them based on the gray scale values by applying a simple thresholding, as shown in Fig. 5 (b). This resulted in over detection of the carbide phase as some pixels inside the austenite region have the same gray value as the carbide, which is erroneous. Moreover, it was not possible to quantify the three distinct phases from the binarized image with two distinct gray values (like solving a system of two equations with three unknowns!).

To overcome the issue of pixel over detection, WEKA segmentation was carried out and the corresponding steps is as follows:

- Open the image, outline the intended area, and duplicate it (Ctrl + Shift + D).

Bild 5 (a) zeigt die Anwendung der WEKA-Segmentierung am Beispiel eines mehrphasigen Gefüges. Die drei unterschiedlichen Phasen wurden mit einem Label versehen, um sie basierend auf den Graustufenwerten durch Anwendung einer einfachen Schwellwertbildung zu segmentieren. Siehe hierzu Bild 5 (b). Dies führte zu einer Übererfassung der Carbidphase, da einige Pixel im Austenitbereich fälschlicherweise den gleichen Grauwert aufweisen wie das Carbid. Darüber hinaus war es auf Grundlage von zwei unterschiedlichen Grauwerten nicht möglich, die drei unterschiedlichen Phasen im binarisierten Bild zu quantifizieren (Das wäre wie das Lösen eines Systems aus zwei Gleichungen mit drei Unbekannten!).

Um dem Problem der Pixel-Überdetektion zu begegnen, wurde eine WEKA-Segmentierung durchgeführt. Die hierfür erforderlichen Schritte sind:

- Öffnen des Bildes, Umreißen und Duplizieren des Bereichs von Interesse (Strg + Shift + D)

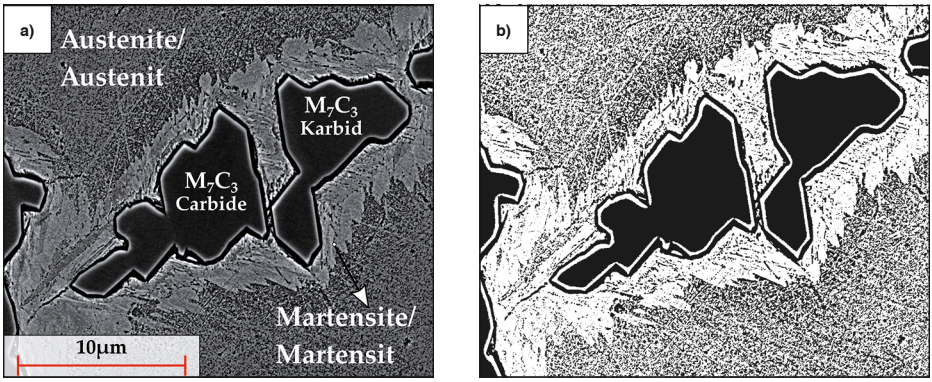

Figs. 5a and b: *(a) SEM micrograph of a high chromium cast iron alloy with the austenite, carbide and martensite phase labelled, (b) binarized image after simple thresholding segmentation.*

Bilder 5a und b: *(a) REM-Aufnahme einer hochchromhaltigen Gusseisenlegierung mit Kennzeichnung der Austenit-, Carbid- und Martensitphase, (b) binarisiertes Bild nach einfacher Schwellwertsegmentierung.*

- Open the trainable WEKA segmentation plugin (Plugins → Segmentation → Trainable WEKA segmentation) (Fig. 6 (a)).
- Create a new class and rename it by clicking on Settings.
- Start training the classifier by drawing lines and assigning them to the corresponding class (Fig. 6 (b)).
- Click on 'Train Classifier' and subsequently, 'Create Result' to obtain the micrograph with the distinct colors (Fig. 6 (c)).
- Convert the image to 8 bit and apply the threshold to obtain a histogram with three (in this case) distinct peaks (Fig. 6 (d)).
- Move the bar to obtain the value (indicating the percentage) of the corresponding phase.

The classifier can be saved ('Save Classifier') and continued to be trained and applied (Load Classifier → Apply Classifier → Train Classifier → Save Classifier) to other micrographs to make it more robust and reliable.

2.4 Quantitative Image Analysis

In addition to segmentation, quantitative stereology plays a crucial role in understanding the structure-property correlation. The evaluation of the particle size, volume fraction, shape etc., is beneficial for further development of the material [2]. Using FIJI, it is possible to analyze and extract quantitative microstructural information by clicking on the 'Analyze' tab, present in Fig. 3. The key to reliable particle analysis is a well contrasted micrograph, which defines the particle boundaries as lucidly as possible

- Öffnen des Plug-ins der trainierbaren WEKA-Segmentierung („Plugins" (Plug-ins) → „Segmentation" (Segmentierung) → „Trainable WEKA Segmentation" (trainierbare WEKA-Segmentierung)) (Bild 6 (a))
- Erstellen einer neuen Klasse und Umbenennen der Klasse durch einen Klick auf „Settings" (Einstellungen)
- Starten des Klassifikatortrainings durch Zeichnen von Linien und deren Zuordnung zur jeweiligen Klasse (Bild 6 (b))
- Klick auf „Train Classifier" (Klassifikator trainieren) und anschließend auf „Create Result" (Ergebnis erstellen), um die Mikroskopaufnahme mit den unterschiedlichen Farben zu erhalten (Bild 6 (c))
- Konvertieren des Bildes in ein 8-Bit-Format und Anwenden des Schwellenwerts, um ein Histogramm mit (in diesem Fall) drei unterschiedlichen Peaks zu erhalten (Bild 6 (d))
- Bewegen des Balkens, um den Wert (Es wird der Prozentwert angezeigt.) der entsprechenden Phase zu erhalten

Der Klassifikator kann gespeichert („Save Classifier"),weiter trainiert und auf andere Mikroskopaufnahmen angewendet werden, um ihn robuster und zuverlässiger zu machen („Load Classifier" (Klassifikator laden) → „Apply Classifier" (Klassifikator anwenden) → „Train Classifier" (Klassifikator trainieren) → „Save Classifier" (Klassifikator speichern)).

2.4 Quantitative Bildanalyse

Neben der Segmentierung spielt für das Verständnis der Korrelation Struktur/Eigenschaft auch die quantitative Stereologie eine wesentliche Rolle. Die Auswertung der Größe, des Volumenanteils, der Form etc. der Partikel ist für die Weiterentwicklung des Werkstoffs von Vorteil [2]. Durch einen Klick auf die Registerkarte „Analyze" (Analysieren) (siehe Bild 3) können mit FIJI quantitative Informationen über das Gefüge analysiert und extrahiert werden. Entscheidend für eine zuverlässige Partikelanalyse ist eine gut kontrastierte Mikroskop-

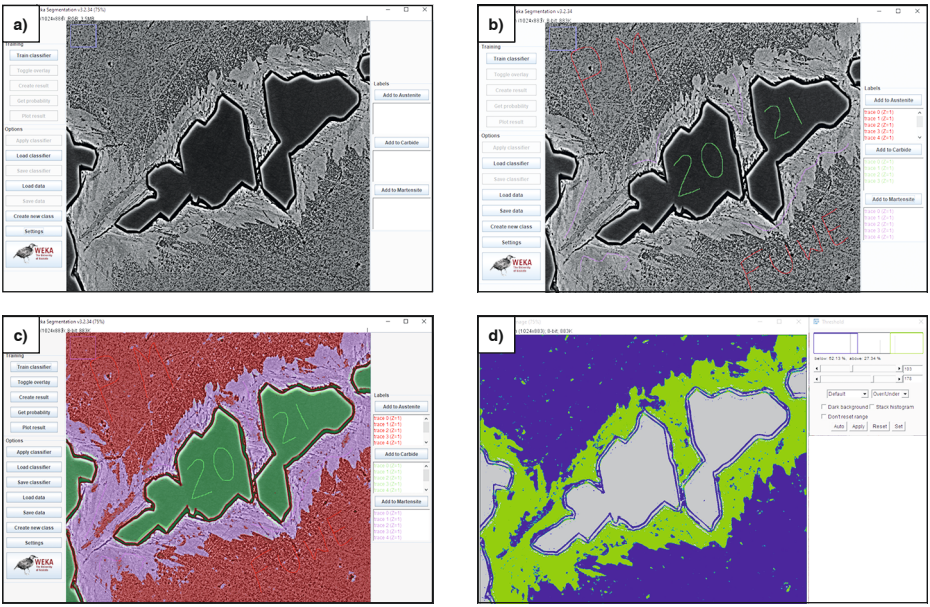

Figs. 6a to d: *Process flow for WEKA segmentation with (a) opening the micrograph in the WEKA segmentation plugin, (b) training the classifier by drawing lines and assigning it to the respective class, (c) result of the training and (d) the segmented image after performing thresholding with the window representing the percentage of each phase.*

Bilder 6a bis d: *Prozessablauf der WEKA-Segmentierung mit dem (a) Öffnen der Mikroskopaufnahme im Plug-in der WEKA-Segmentierung, dem (b) Trainieren der Klassifikatoren durch Zeichnen von Linien und deren Zuordnung zu einer entsprechenden Klasse, dem (c) Ergebnis des Trainings und dem (d) segmentierten Bild nach Anwendung des Schwellwertverfahrens (Das Fenster zeigt den prozentualen Anteil der einzelnen Phasen an).*

(so that the binarization will be easy). Therefore, to ensure good detectability and avoid erroneous results, it is imperative to have a clear distinction between the background and the edges of the particles.

To illustrate, a high chromium cast iron alloy, possessing a multiphase microstructure was considered [25]. The sample was subjected to heat treatment resulting in the precipitation of fine secondary carbides as depicted in Fig. 7 (a), which, is the focus of the current particle analysis. Fig. 7 pictorially represents the process flow to quantify

aufnahme, in der die Partikelgrenzen möglichst klar definiert sind (was die Binarisierung erleichtert). Daher ist eine klare Abgrenzung des Hintergrunds von den Rändern der Partikel unerlässlich, um eine gute Erkennbarkeit zu gewährleisten und fehlerhafte Ergebnisse zu vermeiden.

Um diesen Sachverhalt zu veranschaulichen, wurde eine hochchromhaltige Gusseisenlegierung mit einem mehrphasigen Gefüge betrachtet [25]. Die Probe wurde einer Wärmebehandlung unterzogen, was, wie in Bild 7 (a) zu erkennen, zur Ausscheidung feiner sekundärer Carbide, dem Schwerpunkt unserer Partikelanalyse, führte. Bild 7 zeigt den Prozess-

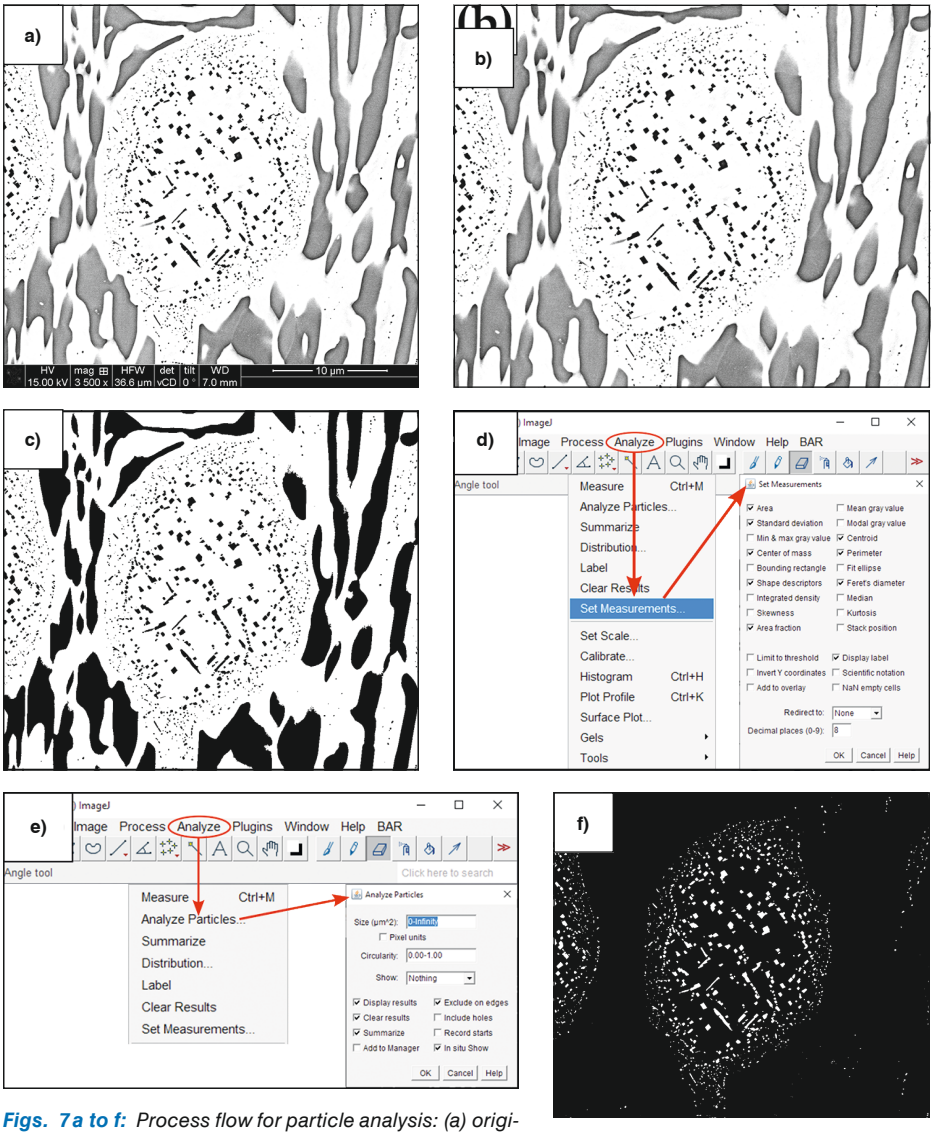

Figs. 7a to f: *Process flow for particle analysis: (a) original SEM micrograph, (b) cropping the scale bar after setting the scale, (c) segmented image, (d) setting the necessary morphological measurements, (e) 'Analyze Particles' command window with the possibility to set a size threshold and customize other options and (f) the final binarized image after the analysis.*

Bilder 7a bis f: *Prozessablauf der Partikelanalyse: (a) REM-Originalaufnahme, (b) Zuschneiden des Maßstabsbalkens nach der Skalierungseinstellung, (c) segmentiertes Bild, (d) Einstellung der erforderlichen morphologischen Messparameter, (e) Befehlsfenster „Analyze Particles" (Partikel analysieren) mit der Möglichkeit, einen Größenschwellenwert festzulegen und andere Optionen individuell einzustellen, und (f) das finale binarisierte Bild nach der Analyse.*

the microstructure and the following steps were followed to obtain Fig. 7 (f):

- Opening the desired micrograph (Ctrl + O) (Fig. 7 (a)).
- With the micron marker (scale bar) as a reference, setting the scale with the help of the line tool (Analyze → Set Scale).
- Outlining the intended area of the micrograph using the rectangle tool and cropping it (Ctrl + Shift + X) (Fig. 7 (b)).
- Generating a binary image for easier quantification (Thresholding, WEKA etc.) (Fig. 7 (c)).
- Setting the necessary parameters to be measured (Analyze → Set Measurements) (Fig. 7 (d)). Further information concerning the different morphological aspects of the particles is elucidated in [26, 27].
- Analyzing the particles (Analyze → Analyze Particles) (Fig. 7 (e)).

The final binarized image after the particle analysis is observed in Fig. 7 (f). Depending on the restrictions, thresholds can be implemented (with respect to min/max size etc.). Moreover, certain binary operations such as dilation, erosion, opening, closing, watershed can also be applied to remove outliers within the already binarized image. In addition to the binarized image, a 'Result' (with measurements for each particle) and 'Summary' (summary of all particles, i. e., showing the phase fraction) window will pop with all the data that was checked in 'Set Measurements' window. The user can then save the data, export it, and proceed with further analysis.

ablauf für die Quantifzierung des Gefüges in Bildern. Um Bild 7 (f) zu erhalten, wurden die nachfolgend aufgeführten Schritte ausgeführt:

- Öffnen der Mikroskopaufnahme von Interesse (Strg + O) (Bild 7 (a))
- Skalieren mithilfe des Linienwerkzeugs. Hierbei dient der Mikrometer-Marker (Maßstabsbalken) als Referenz („Analyze" (Analysieren) → „Set Scale" (Maßstab einstellen))
- Umreißen des entsprechenden Bereichs der Mikroskopaufnahme mithilfe des Rechteckwerkzeugs und Zuschneiden (Strg + Shift + X) (Bild 7 (b))
- Erzeugen eines Binärbildes für eine einfachere Quantifizierung (Schwellwertbildung, WEKA etc.) (Bild 7 (c))
- Einstellen der erforderlichen zu messenden Parameter („Analyze" (Analysieren) → „Set Measurements" (Messparameter einstellen) (Bild 7 (d)). Weiterführende Informationen zu den unterschiedlichen morphologischen Aspekten der Partikel finden Sie in [26, 27]
- Analysieren der Partikel („Analyze" (Analysieren) → „Analyze Particles" (Partikel analysieren)) (Bild 7 (e))

Bild 7 (f) zeigt das finale binarisierte Bild nach der Partikelanalyse. Je nach Einschränkungen können Schwellenwerte (bezüglich der minimalen bzw. maximalen Größe etc.) angewendet werden. Darüber hinaus können außerdem bestimmte binäre Operationen, beispielsweise Dilation, Erosion, Öffnen, Schließen und Watershed, angewendet werden, um Ausreißer im bereits binarisierten Bild zu entfernen. Zusätzlich zum binarisierten Bild werden auch ein „Result"-Fenster (Ergebnis mit den Messwerten für die einzelnen Partikel) sowie ein „Summary"-Fenster (Zusammenfassung aller Partikel mit Anzeige des Phasenanteils) angezeigt, die alle Daten enthalten, die im Fenster „Set Measurements" (Messparameter einstellen) ausgewählt wurden. Der Anwender kann diese Daten anschließend speichern, exportieren und mit weiteren Analysen fortfahren.

The same process flow was followed for the successful quantification of the carbides present in high chromium cast iron alloys in the as-cast and heat-treated condition. In addition to the carbide volume fraction, emphasis was placed on calculating the average carbide size (μm^2) and distribution, and it has been elucidated in [25, 28].

2.5 Plugins and Macros

ImageJ's functionality can be expanded using plugins as they offer several additional commands and can add support for new file formats. Plugins can be created/installed by using the 'Plugins' menu. When placed in the ImageJ plugins directory, they are automatically identified by ImageJ and become available. The user can visit [S.I. 6] to check out the different plugins and download them.

In addition to the stereological characteristics (size, shape, volume fraction etc.) of the precipitates, another important factor to be considered is their distribution within the microstructure. This can be quantified by finding out the average nearest neighbor distance (nnd). The nnd can play a vital role in microstructural evolution during recrystallization and coarsening and gives information about certain strengthening mechanisms such as Orowan strengthening [1]. The plugin developed by Yuxiong Mao, allows to calculate the near neighbor distances of the particles by considering the particle's centroid (Analyze → Set Measurements → Check 'Centroid'), and generates the result [29].

Moreover, plugins that specifically go deeper into the morphological aspects of the particles can be downloaded and added, such as:

Für die erfolgreiche Quantifizierung der in hochchromhaltigen Gusseisenlegierungen im Gusszustand sowie im wärmebehandelten Zustand vorhandenen Carbide wurde der gleiche Prozessablauf angewendet. Zusätzlich zum Volumenanteil des Carbids wurde ein spezielles Augenmerk auf die Berechnung der durchschnittlichen Carbidgröße (μm^2) und die Verteilung gelegt. Siehe hierzu [25, 28].

2.5 Plugins und Makros

Der ImageJ-Funktionsumfang kann mithilfe von Plug-ins erweitert werden, die mehrere zusätzliche Befehle bereitstellen und neue Dateiformate unterstützen können. Plug-ins können über das Menü „Plugins" erstellt bzw. installiert werden. Werden sie im ImageJ-Plug-in-Verzeichnis abgelegt, erkennt ImageJ sie automatisch und es kann auf sie zugegriffen werden. Anwender finden die unterschiedlichen Plug-ins hier: [w. I. 6]. Von dort können sie auch heruntergeladen werden.

Neben den stereologischen Merkmalen (Größe, Form, Volumenanteil etc.) der Ausscheidungen ist auch deren Verteilung im Gefüge ein wichtiger Faktor, der zu berücksichtigen ist. Die Verteilung kann durch eine Messung des durchschnittlichen Abstands zum nächsten Nachbarn (nearest neighbor distance, nnd) quantifiziert werden. Der Wert „nnd" kann bei der Mikrostrukturentwicklung während der Rekristallisation und der Vergröberung eine entscheidende Rolle spielen und Informationen über bestimmte Verfestigungsmechanismen, beispielsweise die Orowan-Verfestigung, liefern [1]. Das von Yuxiong Mao entwickelte Plug-in ermöglicht die Berechnung der Abstände der Partikel zum nächsten Nachbarn durch Berücksichtigung des Partikelschwerpunkts („Analyze" (Analysieren) → „Set Measurements" (Messparameter einstellen) → „Check Centroid" (Schwerpunkt prüfen)) und erzeugt das Ergebnis [29].

Darüber hinaus können Plug-ins heruntergeladen und hinzugefügt werden, die näher auf die morphologischen Aspekte der Partikel eingehen, beispielsweise:

- MorpholibJ [S.I. 7][30]
- BioVoxxel [S.I. 8][31]

Macros are programs that automate a series of ImageJ commands. Although prior knowledge with scripting and programming would be particularly beneficial in creating a macro, the user can also record the series of steps by using the inbuilt macro recorder. By clicking on Plugins → Macros → Record, the macro recorder window opens, and the user can start clicking on the desired options, following a predetermined sequence and the commands will simultaneously be recorded. This is primarily intended for processing a large batch of images which need the same treatment, thus saving a lot of time. To illustrate, a macro was created for the purpose of cropping the micrograph to remove the scale bar, adjusting the brightness and the contrast, converting it to 8 bit and then saving it. Fig. 8 represents the macro recorder after the sequential commands were recorded. The macro can then be saved, and further used for editing or adding new commands. The macro can be run using Plugins → Macros → Run macro.

- MorpholibJ [w. I. 7][30]
- BioVoxxel [w. I. 8][31]

Makros sind Programme, die eine Reihe von ImageJ-Befehlen automatisieren. Auch wenn Vorkenntnisse im Scripting und der Programmierung besonders vorteilhaft bei der Erstellung von Makros sind, kann der Anwender die entsprechenden Schritte auch mit dem integrierten Makrorekorder aufzeichnen. Mit einem Klick auf „Plugins“ (Plug-ins) → „Macros“ (Makros) → „Record“ (Aufzeichnen) öffnet sich das Makrorekorderfenster und der Anwender kann damit beginnen, die gewünschten Optionen in einer bestimmten Abfolge anzuklicken, wobei die Befehle gleichzeitig aufgezeichnet werden. Das dient vorwiegend der Verarbeitung eines großen Stapels von Bildern, die alle der gleichen Behandlung unterzogen werden müssen, wodurch viel Zeit gespart werden kann. Zur Veranschaulichung wurde ein Makro mit dem Ziel erstellt, die Mikroskopaufnahme zuzuschneiden, um den Maßstabsbalken zu entfernen, Helligkeit und Kontrast einzustellen, sie in ein 8-Bit-Format zu konvertieren und dann abzuspeichern. Bild 8 zeigt den Makrorekorder nach der Aufzeichnung der sequentiellen Befehle. Das Makro kann anschließend gespeichert und zum Bearbeiten oder Hinzufügen neuer Befehle weiterverwendet werden. Das Makro wird durch folgende Schritte ausgeführt: „Plugins“ (Plug-ins) → „Macros“ (Makros) → „Run Makro“ (Makro ausführen).

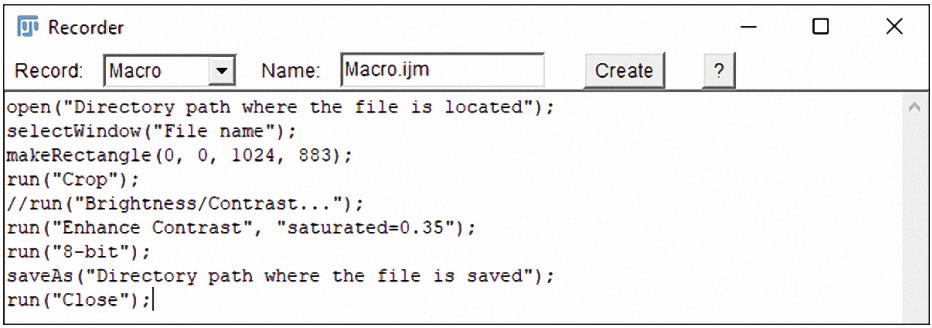

Fig. 8: *Macro recorder window with the recorded commands.*

Bild 8: *Fenster des Makrorekorders mit den aufgezeichneten Befehlen.*

Finally, more information concerning the various other functionalities and capabilities of FIJI (Fiji Is Just ImageJ) can be explored by checking the interactive user guide [32].

3 Conclusion and Outlook

This work demonstrated the successful applicability of the open source program, FIJI, in segmenting microstructural constituents and quantifying the microstructure for various micrographs ranging from a two phase to a multi-phase microstructure. One of the major pre-requisites before implementing image processing is the availability of a well-contrasted micrograph, which can be achieved by following proper metallographic protocols. Furthermore, by incorporating certain pre-processing commands, the ambiguity in segmentation can be lowered leading to a more reliable result. The necessary steps to be followed for phase segmentation and/or quantitative microstructural analysis were provided along with the respective illustrations to make the user more familiar with the software. Finally, more information in the form of references were mentioned throughout the manuscript so that the user is free to learn more about the growing capabilities of image processing and open source platforms.

Before using the results of microstructure quantification to build process-microstructure-property links, it is beneficial to first perform a microstructure classification. Considering dual-phase steel microstructures, the carbon-rich second phase objects can be of different microstructural types, i. e., pearlite, bainite or martensite. By quantifying microstructural characteristics of light optical micrographs (e. g., object size and shape) and scanning electron micrographs (morphological characteristics

Schließlich sind weitere Informationen in Bezug auf die verschiedenen anderen Funktionen und den Leistungsumfang von FIJI (Fiji Is Just ImageJ) im interaktiven Benutzerhandbuch abrufbar [32].

3 Schlussfolgerung und Ausblick

Die vorliegende Arbeit hat demonstriert, dass sich das Open-Source-Programm FIJI für eine erfolgreiche Segmentierung von Gefügebestandteilen und Quantifizierung von Gefügen (von Zweiphasengefügen bis hin zu mehrphasigen Gefügen) in unterschiedlichen Mikroskopaufnahmen eignet. Eine der wesentlichen Voraussetzungen für die Durchführung einer Bildverarbeitung ist die Verfügbarkeit einer gut kontrastierten Mikroskopaufnahme, was durch Einhalten eines hierfür geeigneten metallographischen Protokolls gewährleistet werden kann. Darüber hinaus können Uneindeutigkeiten bei der Segmentierung durch Integration bestimmter Vorverarbeitungsbefehle reduziert und so ein zuverlässigeres Ergebnis erzielt werden. Die für die Phasensegmentierung und/oder quantitative Gefügeanalyse erforderlichen Schritte wurden zusammen mit entsprechenden Abbildungen angegeben, um den Anwender mit der Software vertraut zu machen. Die Arbeit enthält Verweise auf weiterführende Informationen. Dem Anwender steht es also frei, mehr über die wachsenden Möglichkeiten der Bildverarbeitung und die zunehmende Leistungsfähigkeit von Open-Source-Plattformen zu erfahren.

Bevor anhand der Ergebnisse der Gefügequantifizierung Zusammenhänge zwischen Prozess, Gefüge und Eigenschaften hergestellt werden, ist es von Vorteil, zunächst eine Gefügeklassifikation durchzuführen. Bei der Betrachtung von Mikrostrukturen von Dualphasenstahl können die Objekte einer kohlenstoffreichen zweiten Phase verschiedenen Gefügearten angehören, beispielsweise Perlit, Bainit oder Martensit. Durch eine Quantifizierung der mikrostrukturellen Merkmale lichtmikroskopischer Auf-

of substructure, its density, and the image texture [33]), characteristic data for each microstructural constituent can be extracted. Consequently, microstructural classification can be accomplished by applying machine learning algorithms to these data, as shown in [34–36].

nahmen (z. B. Objektgröße und -Form) und rasterelektronenmikroskopischer Aufnahmen (morphologische Merkmale der Substruktur, deren Dichte und die Bildtextur [33]) können charakteristische Daten für die einzelnen Mikrostrukturbeastandteile extrahiert werden. Somit kann, wie in [34–36] ausgeführt, durch Anwendung von Algorithmen für maschinelles Lernen eine Klassifikation der Mikrostrukturen vorgenommen werden.

4 Acknowledgement

The authors wish to acknowledge the EFRE Funds of the European Commission and the State Chancellery of Saarland for support of activities within the ZuMat project. Additionally, U.P.N. is grateful to DAAD for the financial support.

4 Danksagung

Die Autoren bedanken sich beim EFRE-Fonds der Europäischen Kommission und der Staatskanzlei des Saarlandes für die Förderung der Aktivitäten im Rahmen des ZuMat-Projekts. Darüber hinaus bedankt sich U.P.N. beim DAAD für die finanzielle Unterstützung.

References / Literatur

[1] Abbaschian, R.; Abbaschian, L.; Reed-Hill, R.E.: Physical Metallurgy Principles. Stamford, Connecticut (USA): Cengage Learning, 2008

[2] Ohser, J.; Mücklich, F.: Statistical Analysis of Microstructures in Materials Science. 1st ed. Wiley, 2000

[3] Tasan, C.C.; Diehl, M.; Yan, D.; Bechtold, M.; Roters, F.; Schemmann, L. et al.: An Overview of Dual-Phase Steels: Advances in Microstructure-Oriented Processing and Micromechanically Guided Design. Vol. 45, Annual Review of Materials Research. Annual Reviews Inc., 391–431 (2015)
DOI: 10.1146/annurev-matsci-070214-021103

[4] Al-Abbasi, F.M.; Nemes, J.A.: Micromechanical modeling of dual phase steels. Int J Mech Sci. 45(9): 1449–65 (2003)
DOI: 10.1016/j.ijmecsci.2003.10.007

[5] Friel, J.J.: Practical guide to image analysis. ASM International, 2000

[6] Pyrz, W.D.; Buttrey, D.J.: Particle size determination using TEM: A discussion of image acquisition and analysis for the novice microscopist. Langmuir. 24(20): 11350–60 (2008)
DOI: 10.1021/la801367j

[7] Stalling, D.; Westerhoff, M.; Hege, H.C.: Amira: A highly interactive system for visual data analysis. In: Visualization Handbook. Elsevier Inc., 749–67 (2005)
DOI: 10.1016/B978-012387582-2/50040-X

[8] Carpenter, A.E.; Jones, T.R.; Lamprecht, M.R.; Clarke, C.; Kang, I.H.; Friman, O. et al.: CellProfiler: Image analysis software for identifying and quantifying cell phenotypes. Genome Biol. 7 (10): 1–11 (2006)
DOI: 10.1186/gb-2006-7-10-r100

[9] Barnaby, R.J.: Quantitative image analysis for geologic core description. J Sediment Res. 87(5): 460–85 (2017)
DOI: 10.2110/jsr.2017.25

[10] Lindqvist, J.; Åkesson, U.: Image analysis applied to engineering geology, a literature review. Bull Eng Geol Environ. 60(2): 117–22 (2001)
DOI: 10.1007/s100640100106

[11] Nečas, D.; Klapetek, P.: Gwyddion: An open-source software for SPM data analysis. Vol. 10, Central European Journal of Physics. Versita, 181–8 (2012)
DOI: 10.2478/s11534-011-0096-2

[12] Groeber, M.A.; Jackson, M.A.: DREAM.3D: A Digital Representation Environment for the Analysis of Microstructure in 3D. Integr Mater Manuf Innov. 3(1): 56–72 (2014)
DOI: 10.1186/2193-9772-3-5

[13] Vander Voort, G.F.: Metallography: Principles and Practice. 1999

[14] Petzow, G.: Metallographisches, Keramographisches, Plastographisches Ätzen – Eisen Stahl und Gusseisen. 6th ed. Gebrüder Borntraeger, 1994

[15] Baldwin, W.: Metallography and Microstructures. Metallogr Microstruct. 2018

[16] Vander Voort, G.F.: Color Metallography. In: ASM Handbook, Volume 9: Metallography and Microstructures. ASM International, 493–512 (2004)
DOI: 10.31399/asm.hb.v09.a0003752

[17] Schneider, C.A.; Rasband, W.S.; Eliceiri, K.W.: NIH Image to ImageJ: 25 years of image analysis. Vol. 9, Nature Methods. Nature Publishing Group, 671–5 (2012)
DOI: 10.1038/nmeth.2089

[18] Schindelin, J.; Arganda-Carreras, I.; Frise, E.; Kaynig, V.; Longair, M.; Pietzsch, S.: Fiji – an open-source platform for biological-image analysis.PDF. 2012
DOI: 10.1038/nmeth.2019

[19] Jähne, B.: Digital Image Processing, 5th revised and extended edition. Vol. 13, Measurement Science and Technology. 2002
DOI: 10.1088/0957-0233/13/9/711

[20] Chowdhury, A.; Kautz, E.; Yener, B.; Lewis, D.: Image driven machine learning methods for microstructure recognition. Comput Mater Sci. 123: 176–87 (2016)
DOI: 10.1016/j.commatsci.2016.05.034

[21] Müller, M.; Britz, D.; Mücklich, F.: Machine Learning for Microstructure Classification – How to Assign the Ground Truth in the Most Objective Way? ASM Adv Mater Process. 179(1): 16–21 (2021)

[22] Arganda-Carreras, I.; Kaynig, V.; Rueden, C.; Eliceiri, K.W.; Schindelin, J.; Cardona, A. et al.: Trainable Weka Segmentation: A machine learning tool for microscopy pixel classification. Bioinformatics. 33(15): 2424–6 (2017)
DOI: 10.1093/bioinformatics/btx180

[23] Müller, M.; Britz, D.; Mücklich, F.: Application of trainable segmentation to microstructural images using low-alloy steels as an example. Prakt Metallogr Metallogr. 57(5): 337–58 (2020)
DOI: 10.3139/147.110640

[24] Nayak, U.P.; Guitar, M.A.; Mücklich, F.: Evaluation of etching process parameter optimization in the objective specific microstructural characterization of as-cast and heat treated HCCI alloy. Prakt Metallogr. 57(10): 688–713 (2020)
DOI: 10.3139/147.110682

[25] Nayak, U.P.; Guitar, M.A.; Mücklich, F.: A comparative study on the influence of chromium on the phase fraction and elemental distribution in as-cast high chromium cast irons: Simulation vs. experimentation. Metals (Basel). 10(1): 30 (2020)
DOI: 10.3390/met10010030

[26] Igathinathane, C.; Pordesimo, L.O; Columbus, E.P.; Batchelor, W.D.; Methuku, S.R.: Shape identification and particles size distribution from basic shape parameters using ImageJ. Comput Electron Agric. 63(2): 168–82 (2008)
DOI: 10.1016/j.compag.2008.02.007

[27] Soille, P.: Morphological Image Analysis: Principles and Applications. Springer-Verlag Berlin Heidelberg GmbH. 2004
DOI: 10.1007/978-3-662-05088-0

[28] Guitar, M.A.; Nayak, U.P.; Britz, D.; Mücklich, F.: The Effect of Thermal Processing and Chemical Composition on Secondary Carbide Precipitation and Hardness in High-Chromium Cast Irons. Int J Met. 14(3): 755–65 (2020)
DOI: 10.1007/s40962-020-00407-4

[29] Mao, Y.: Nearest Neighbor Distances Calculator. https://icme.hpc.msstate.edu. 2016

[30] Legland, D.; Arganda-Carreras, I.; Andrey, P.: MorphoLibJ: Integrated library and plugins for mathematical morphology with ImageJ. Bioinformatics. 32(22): 3532–4 (2016)
DOI: 10.1093/bioinformatics/btw413

[31] Brocher, J.; Wagner, T.; BioVoxxel Toolbox – ImageJ. 2015

[32] Ferreira, T.; Rasband, W.: ImageJ User Guide User Guide ImageJ. Image J user Guid. 1.46r (2012)

[33] Webel, J.; Gola, J.; Britz, D.; Mücklich, F.: A new analysis approach based on Haralick texture features for the characterization of microstructure on the example of low-alloy steels. Mater Charact. 144: 584–96 (2018) DOI: 10.1016/j.matchar.2018.08.009
[34] Gola, J.; Britz, D.; Staudt, T.; Winter, M.; Schneider A.S.; Ludovici, M. et al.: Advanced microstructure classification by data mining methods. Comput Mater Sci. 148: 324–35 (2018) DOI: 10.1016/j.commatsci.2018.03.004
[35] Gola, J.; Webel, J.; Britz, D.; Guitar, A.; Staudt, T.; Winter, M. et al.: Objective microstructure classification by support vector machine (SVM) using a combination of morphological parameters and textural features for low carbon steels. Comput Mater Sci. 160: 186–96 (2019) DOI: 10.1016/j.commatsci.2019.01.006
[36] Müller, M.; Britz, D.; Ulrich, L.; Staudt, T.; Mücklich F.: Classification of bainitic structures using textural parameters and machine learning techniques. Metals (Basel). 10(5): 630 (2020) DOI: 10.3390/met10050630

Supplementary Information (S. I.) / Weiterführende Informationen (w. I.)

1. https://www.irfanview.com
2. https://www.gimp.org
3. https://imagej.net/Welcome
4. https://imagej.net/Fiji/Downloads
5. https://imagej.net/Trainable_Weka_Segmentation
6. https://imagej.nih.gov/ij/plugins/index.html
7. https://imagej.net/MorphoLibJ
8. https://www.biovoxxel.de/development/

Bibliography
DOI 10.1515/pm-2021-0039
Pract. Metallogr. 58 (2021) 8; page 484–506

ISSN 0032-678X · e-ISSN 2195-8599

Ullal Pranav Nayak

born in 1993, he completed his undergraduate studies at NITK Surathkal, India and MSc in Materials Science under the Erasmus Mundus FAME Program. Since 2018, he is a doctoral candidate at the Chair of Functional Materials with his research focusing on the microstructure tailoring in HCCI alloys through heat treatment design.

IV. The Effect of Thermal Processing and Chemical Composition on Secondary Carbide Precipitation and Hardness in High Chromium Cast Irons

María Agustina Guitar, **U. Pranav Nayak**, Dominik Britz, Frank Mücklich
Department of Materials Science and Engineering, Saarland University, 66123 Saarbrücken, Germany

Published in "***International Journal of Metalcasting***" (2020)

(IF (2023): 2.263)

Accessible online at: *https://doi.org/10.1007/s40962-020-00407-4*

Own Contribution: Conceptualization and methodology; sample preparation; simulation and experimental validation; data analysis; paper writing – section contribution; scientific discussion

THE EFFECT OF THERMAL PROCESSING AND CHEMICAL COMPOSITION ON SECONDARY CARBIDE PRECIPITATION AND HARDNESS IN HIGH-CHROMIUM CAST IRONS

M. Agustina Guitar, U. Pranav Nayak, Dominik Britz and Frank Mücklich
Department of Materials Science, Saarland University, Campus D3.3, 66123 Saarbrücken, Germany

Dominik Britz and Frank Mücklich
Material Engineering Center Saarland, Campus D3.3, 66123 Saarbrücken, Germany

https://doi.org/10.1007/s40962-020-00407-4

Abstract

The excellent abrasion resistance of high-chromium cast irons (HCCIs) is given by an optimal combination of hard eutectic and secondary carbides (SC) and a supporting matrix. The tailoring of the microstructure is performed by heat treatments (HTs), with the aim to adjust the final properties (such as hardness and abrasion resistance). In this work, the influence of chemical composition on the microstructure and hardness of HCCI_26%Cr is evaluated. An increase in the matrix hardness was detected after HTs resulting from combining precipitation of $M_{23}C_6$ SC during destabilization, and austenite/martensite transformation during quenching. Kinetic calculations of the destabilization process showed that M_7C_3 secondary carbides are the first to precipitate during heating, reaching a maximum at 850 °C. During subsequent heating up to 980 °C and holding at this temperature, they transformed completely to $M_{23}C_6$. According to the MatCalc simulations, further precipitation of $M_{23}C_6$ occurred during cooling, in the temperature range 980–750 °C. Both phenomena were related to experimental observations in samples quenched after 0-, 30-, 60- and 90-min destabilization, where $M_{23}C_6$ SC were detected together with very fine SC precipitated in areas close to eutectic carbides.

Keywords: *High chromium cast iron, Microstructure tailoring, Secondary carbide precipitation*

Introduction

High-chromium cast irons (HCCIs) are used for wear-resistant components in the mining and mineral processing industries, given their outstanding wear and erosion resistance.[1] HCCIs can be considered as composite materials, showing a structure composed of large eutectic M_7C_3 (M: Cr–Fe) carbides embedded in a softer ferrous matrix, which could be austenitic in the as-cast condition or martensitic after a subsequent thermal treatment.[2,3] The microstructure and mechanical properties of HCCI are a direct consequence of the eutectic carbide (EC) content, matrix microstructure and the presence of secondary carbides (SC) homogeneously distributed throughout the metallic matrix.[4] Particularly, the presence of secondary carbides has shown to improve the wear resistance behavior of the whole "composite."[5] Consequently, the properties of the material are dependent upon the volume fraction, size and distribution of the second phase,[6] and especially of the SC precipitated during thermal treatment. This controlled precipitation improves the mechanical properties of HCCI, mainly those related to friction reduction and abrasive wear resistance.[7–9]

The microstructure in HCCI can be modified through alloy design, processing route and heat treatments (HTs), which can include destabilization, sub-critical and quenching treatments, or a combination thereof.[10,11] An optimal destabilization process is highly dependent on the temperature (900–1150 °C) and holding time (5 min to 8 h), and thus, the used parameters together with the chemical

This paper is an invited submission to IJMC selected from presentations at the 2nd Carl Loper 2019 Cast Iron Symposium held September 30 to October 1, 2019, in Bilbao, Spain.
Published online: 03 February 2020

composition (especially the Cr/C ratio) will determine the type of SC.[9,12–15] The parameters used during destabilization also determine the amount of carbon that remains in solution in the austenitic matrix and therefore the amount of retained austenite, its final hardness and subsequent resistance.[14] Destabilization at higher temperatures leads to a reduction in the driving force for carbide precipitation, resulting in a lower Ms temperature, and therefore, a large amount of austenite will be retained within the martensitic matrix, with lower overall material hardness.[14] On the other hand, destabilizing at lower temperatures results in an extensive precipitation of SC and a low-hardness martensite, as a consequence of the low carbon content.[7,12,14–16]

A sub-critical treatment, or tempering, is usually employed to reduce the amount of retained austenite (RA) and increase the spalling resistance.[14,17] The final microstructure after tempering is highly dependent on the materials' chemical composition, temperature and time of the treatment and the prior thermal history.[8,14] Typically, temperatures range between 200 and 650 °C and times up to 12 h.[11,14] Excess of temperature or time results in softening and drastic reduction in abrasion resistance, whereas insufficient tempering results in incomplete elimination of austenite.[8] The sequence of the different steps in the heat treatment is also crucial in the resulting material. Applying a sub-critical treatment before or after a destabilization leads to a completely different final microstructure.[11]

As described, many parameters related to the HT play a fundamental role in the final microstructure of HCCI and thus in their mechanical response. By systematically varying and combining these parameters, a tailored microstructure might be obtained, which ensures the optimal balance between the tribological behavior and fracture toughness necessary for each particular case.

A multi-step HT was proposed by Guitar et al.,[9] where the sub-critical process is carried out directly following the destabilization of the austenite. Later, a second destabilization step was performed followed by a quenching in air. The implementation of this multi-step HT to HCCI_16%Cr showed an improvement of 69% in the wear resistance in comparison with the destabilized and quenched material.

The objective of the present work is, on the one hand, to implement the same multi-step HT previously applied in HCCI_16%Cr to a HCCI containing a higher amount of Cr (26%) in order to evaluate the influence of the chemical composition, especially the Cr content, in the final microstructure. On the other hand, this work intends to evaluate the influence of varying some parameters at different stages of the HT in the SC precipitation. Finally, the first attempts in the implementation of thermodynamic and kinetic calculations for microstructural design will be detailed and correlated to the experimentally obtained results. Specifically, the holding time during the destabilization will be modified, to evaluate its influence on the SC size and fraction.

Experimental

HCCI samples were manufactured in an arc furnace and cast in cubic sand molds. Chemical composition was determined by emission spectroscopy methods using a GNR Metal Lab 75/80 Optical Emission Spectroscope. The chemical composition of the studied HCCI is: C (2.53 wt%)–Si (0.37 wt%)–Mn (0.66 wt%)–Cr (26.6 wt%)–Ni (0.26 wt%)–S (0.04 wt%)–P (< 0.01 wt%)–Cu (0.03 wt%)–Fe (balance). The as-cast microstructure is composed of $(Fe,Cr)_7C_3$ eutectic carbides (EC) embedded in an austenitic matrix. In addition to the major phases, austenite and M_7C_3 EC, a thin layer of martensite is present at the periphery of the carbides. The martensite formation is associated with the local C and Cr depletion which takes place during the solidification of the EC in contact with the pro-eutectic austenite.

The multi-step HT described in Refs.[9,18] was applied to the HCCI_26%Cr in order to evaluate the applicability of a successful HT to a material with the different chemical composition and therefore evaluate the influence to the Cr content in the modified microstructure. The multi-step HT includes destabilization at 980 °C for 1.5 h, sub-critical diffusion (SCD) step at 650 °C for 12 h [followed by air cooling until room temperature (RT)] and a final destabilization (980 °C/1.5 h) and quenching (air quenched) step. In this work, samples in three different states are evaluated: (1) sample Q: destabilized (980 °C/1.5 h) + quenching; (2) sample SCD: destabilized (980 °C/1.5 h) + sub-critical diffusion (650 °C/12 h) and (3) sample SCD + Q: a combination of the two previous. Additionally, and in order to evaluate the influence of destabilization holding time on the SC fraction and size, another set of samples was destabilized at 980 °C for different times (0, 0.5, 1 h) and air cooled to RT.

The samples were ground with embedded SiC disks (up to grit 1200) and polished using diamond powder suspensions up to 1 μm mean diameter. The samples were etched with Vilella's reagent (1 g picric acid + 5 mL HCl + 95 mL C_2H_5OH) for microstructural characterization and with a variation of Murakami's reagent (4 g $K_3[Fe(CN)_6]$ + 8 g NaOH + 100 mL H_2O) for 15 s at RT for the calculation of carbide volume fraction (CVF) and size of the SC. In all cases, the samples were immersed in the etchant for the appropriate time, rinsed with water and ethanol and air dried.

SEM characterization was carried out with a FE-SEM Helios Nanolab 600 (FEI company) working with an acceleration voltage of 10 kV and a 1.4 nA beam current. For a proper contrast between phases, a high-sensitivity

solid-state backscattered electrons detector (vCD) was used. The size and volume fraction (VF) of the SC were determined using the image analysis software, ImageJ.[19] 10–12 micrographs were considered for each sample, and the average was calculated. Phase identification was performed using a PANalytical Empyrean X-ray diffractometer coupled with a Co source, an acceleration voltage of 40 kV and a 40 mA tube current. Secondary carbides identification was performed by transmission electron microscope (TEM) using a JEOL JEM-2010F equipment with a field emission gun operating at 80–200 kV. It is equipped with an imaging spherical aberration corrector (CEOS), an Oxford INCA Energy TEM 200 EDS system, a high-angle annular dark field detector, a Gatan annular dark field/bright field STEM detector, as well as a Gatan Tridiem image filter system. The TEM samples were prepared with focus ion beam (FIB—Helios Nanolab 600—FEI Company) as detailed in Reference 20.

For thermodynamic and kinetic calculations, the software MatCalc v.6.03 with the thermodynamic and diffusion databases "ME_Fe 1.2" and "ME_Fe 1.1," respectively, was used. The chemical composition of the matrix, measured using electron probe microanalysis (EPMA), was used as the input to the calculations: C (0.43 wt%)–Si (0.36 wt%)–Mn (0.66 wt%)–Cr (18.2 wt%)–Ni (0.20 wt%)–Fe (balance). Two precipitate domains, austenite and martensite, and two precipitate phases, M_7C_3 and $M_{23}C_6$, were initially created. The HT cycle included a continuous heating from RT to 980 °C at a rate of 0.5 °C/s, holding at various times (0 min, 30 min, 60 min and 90 min) and finally cooling to RT at a rate of 1 °C/s. The initial domain was set to austenite, whereas during the cooling stage, at 210 °C, the domain was changed to martensite as dilatometry studies indicated an austenite to martensite transformation around this temperature for a cooling rate of 1 °C/s.

Results and Discussion

Multi-step Heat Treatment

The microstructure of the HCCI_26%Cr samples was evaluated after the different stages of the multi-step HT, i.e., in the Q, SCD and SCD + Q states, as previously described. The SCD sample was subjected to a destabilization, followed directly by a sub-critical diffusion step and finally slow cooled until room temperature. The Q sample was destabilized and quenched in air, and the SCD + Q was subjected to the whole multi-step HT (i.e., destabilization, sub-critical diffusion and posterior quenching). Temperatures, heating/cooling rate and holding times used for the different HT steps, as described in "Experimental" section, are the same as previously applied for the HCCI_16%Cr.[9,21]

Comparing the results corresponding to HCCI_26%Cr with the previously obtained in HCCI_16%Cr,[9,21] some differences can be appreciated, principally related to the precipitated SC. For instance, in HCCI_16%Cr only rounded M_7C_3 carbides were observed after all the heat treatment steps, whereas for the HCCI_26%Cr, different types of carbides were identified depending on the thermal processing, as shown in Figure 1.

In the Q sample (Figure 1b), square-shaped $M_{23}C_6$ carbides (white arrows) can be observed together with some small carbides at areas in contact with the eutectic carbides (red arrows). The latter show a different contrast in the backscatter (BSE) mode images, which might indicate that they possess different chemical composition than the already identified $M_{23}C_6$ carbides. After quenching in air, the matrix transformed to martensite due to a reduction of C content in the austenitic matrix as shown in Figure 2a, which allows the martensite start temperature (Ms) to increase.

After the SCD step (Figure 1a), square-shaped carbides of $M_{23}C_6$ type (white arrows) precipitated during destabilization, together with some rod-like Fe_3C carbides precipitated during the SCD step (blue arrows) embedded in a ferritic matrix (Figure 2a), were observed. In the case of HCCI_16%Cr, no evidence of Fe_3C formation during the SCD step was found, with M_7C_3 being the only carbide type detected.

In the SCD + Q sample (Figure 1c), it is possible to observe the square-shaped carbides of the $M_{23}C_6$ type (white arrows) embedded in a martensitic matrix (Figure 2a). In contrast to sample Q, the $M_{23}C_6$ carbides are aligned forming a grid-like pattern (Figure 1c).

The $M_{23}C_6$ square-shaped carbides observed in all of the samples were precipitated during the destabilization process and were identified by TEM diffraction, as shown in Figure 2b. Rod-like carbides observed in SCD sample were not possible to be identified using TEM, due to their size and the insufficient resolution of the equipment used in this work. However, their morphology (Fig. 1a) is typically the pearlite microstructure. Furthermore, the $M_{23}C_6$ and Fe_3C secondary carbides were not possible to be unambiguously identified using XRD, since their phase fraction is too low compared to the matrix and eutectic carbides, and thus, their diffraction peaks are located within the background noise. Moreover, the peaks for the different carbide types overlap, making their identification arduous. For these reasons, combining different characterization techniques, such as SEM and XRD, is highly valuable for the identification of secondary carbides.

As previously described, HCCI_16%Cr showed the presence of only M_7C_3, independent of the HT applied.[9] Based on that, it is clear that the chemical composition of HCCI

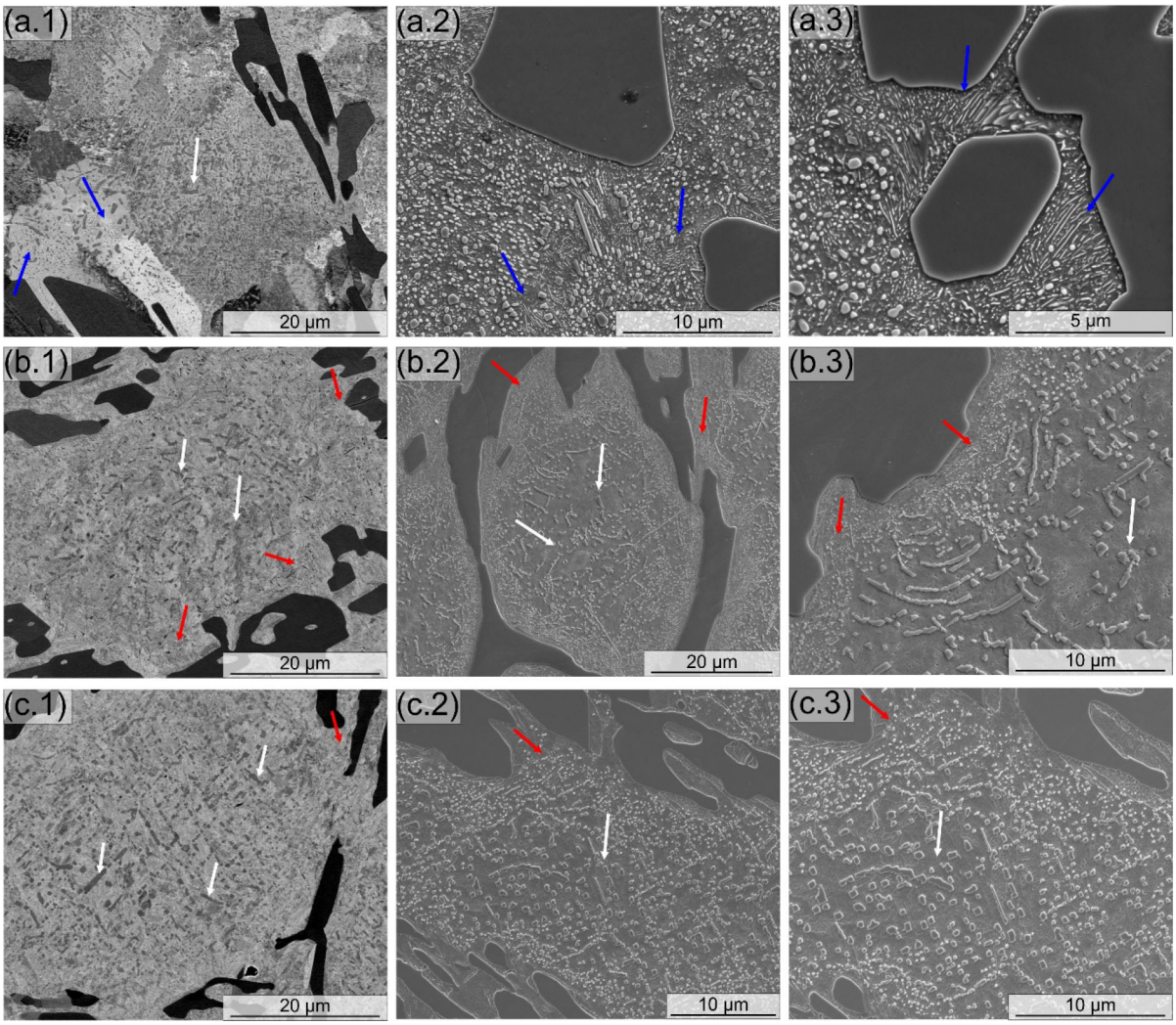

Figure 1. SEM images of the heat-treated samples: (a) SCD, (b) Q and (c) SCD + Q. Images a.1), b.1) and c.1) correspond to BSE mode.

strongly influenced the nature and type of the secondary carbides precipitated during the different stages of HT. Moreover, it is evident that it is not possible to directly transfer a successful heat treatment from one material composition to another, and the heat treatment must be designed for each case in particular.

Microstructural modification plays a fundamental role in the mechanical response of the material. The latter highly depends on the type, morphology and distribution of carbides, and on the nature of the supporting matrix. Even in cases where the microstructural constituents are of similar nature, the thermal history influences the final mechanical response, as was the case for HCCI_16%Cr in the Q and SCD + Q states.[9] Figure 3 shows the microhardness of the heat-treated HCCI_26%Cr measured in the region of matrix, i.e., the EC were not included in the indentation. A hardness increment is observed in the Q (757 HV0.1) and SCD + Q (862 HV0.1) samples compared to as-cast material (360 HV0.1), which is related to the carbide precipitation and the austenite/martensite transformation. Moreover, a decrease in hardness of about 10% in comparison with the as-cast is observed in the SCD sample, which is related to the ferritic matrix, which is much softer than austenite or martensite. Additionally, the Fe_3C carbides that precipitated during this stage offer less resistance than the $M_{23}C_6$ carbides observed in the Q and SCD + Q samples.

Although the SC precipitation of the M_7C_3 or $M_{23}C_6$ type is beneficial for improving the material hardness and its abrasion resistance,[14,22] the role of the matrix in the mechanical properties must be taken into account, since it acts as a mechanical support to the carbides.[9] An improvement in wear resistance was previously observed in HCCI_16%Cr after SCD + Q in comparison with Q treatment [9] for microhardness values of the same magnitude (770 ± 10 and 745 ± 26 HV0.5, respectively), which was not possible to be directly addressed to the material hardness or size of SC, whereas in the case of

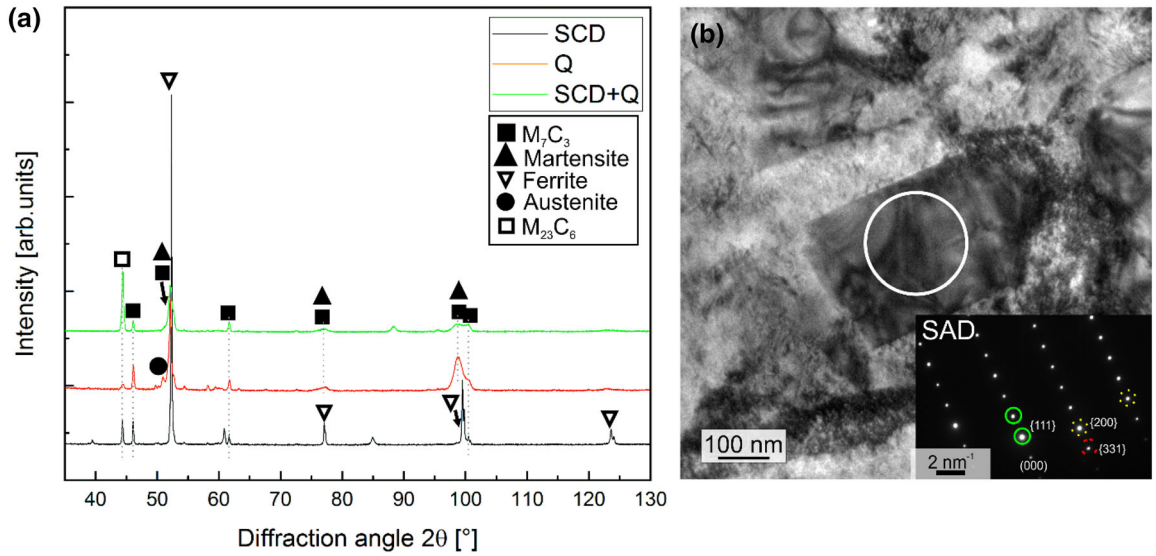

Figure 2. (a) XRD of the samples after different heat treatment steps. It shows that a martensitic matrix is obtained after Q and SCD + Q treatments, whereas ferritic matrix is present after SCD treatment; (b) TEM bright field image and selected area diffraction (SAD) of the square-shaped secondary carbides, identified as $M_{23}C_6$.

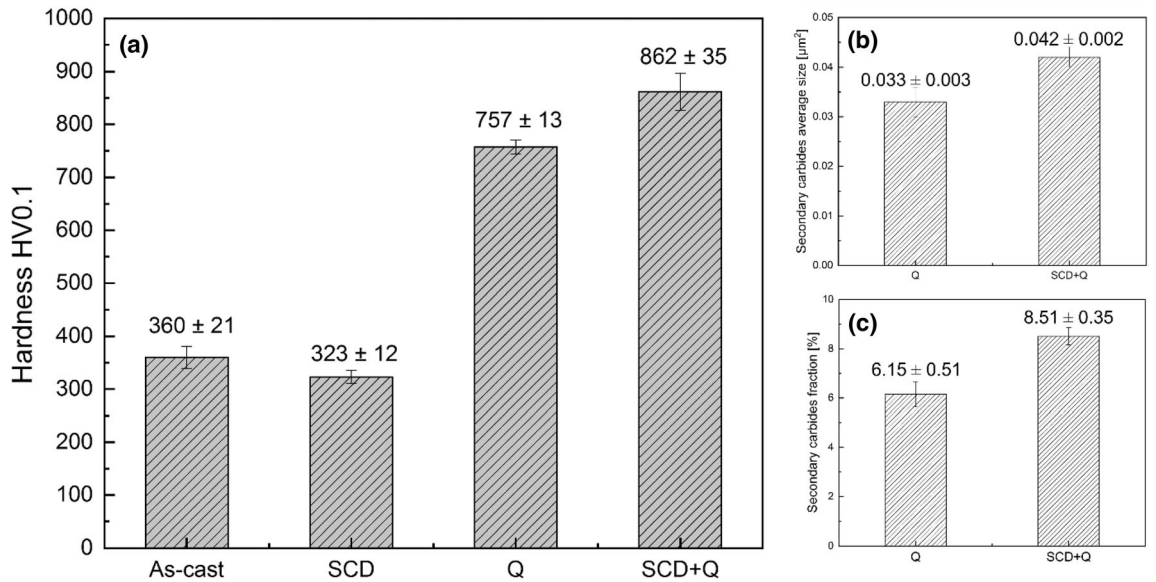

Figure 3. (a) Microhardness (HV0.1) of the as-cast and heat-treated samples; (b) average size of the secondary carbides corresponding to samples Q and SCD + Q; (c) volume fraction of the secondary carbides corresponding to the Q and SCD + Q samples.

HCCI_26%Cr, a difference in hardness is already noticeable between SCD + Q and Q samples, being higher for the SCD + Q one (Figures 3b, 3c). This difference might be related to the size of the SC, the martensitic matrix properties or a combination thereof.

For optimal abrasion resistance, SC of the M_3C type, as those found in the SCD sample, are not desired since they offer less resistance to deformation.[23] However, the precipitation of this type of carbides during intermediate steps might be beneficial for obtaining a tailored microstructure for proper abrasion response. As shown in Figure 1, the SCD + Q sample shows the SC forming a grid-like pattern, which cannot be observed in the Q sample. This can indicate that the SCD step might allow the redistribution of the alloy elements, with the addition that the M_3C carbides might act as precursors for the formation $M_{23}C_6$ during the subsequent HT steps through the diffusion of Cr,[24, 25] which might be the case for HCCI_26%Cr since after the complete thermal cycle (i.e., SCD + Q), only $M_{23}C_6$ carbides were detected.

Implementation of Kinetics Calculations for Microstructure Tailoring

Several research works concerning the effect of thermal treatment and chemical composition on the microstructure and properties of HCCI have been carried out,[3,8,9,14–16,26] with the efforts only focused on the formation, type and morphology of the secondary carbides precipitated after the heat treatments. Experimental tailoring of the microstructure is tedious and resource intensive, since there are countless number of parameters that can be modified and added to all possible combinations. For this reason, the first approaches in the implementation of kinetic calculations for the design of a proper HT for a microstructure tailoring are presented in this work. As a starting point, the destabilization process followed by a quenching step was simulated in MatCalc for the evaluation of carbide precipitation during this process. The starting of the SC precipitation and the effect of the holding time in the type and SC volume fraction at the destabilization temperature were evaluated.

Figure 4 shows the SC phase fraction during destabilization process at 980 °C for 0, 30 and 90 min calculated using MatCalc. Simulated results show two clearly separated processes. The first one, occurring during heating, indicates that the precipitation of SC starts with the formation of M_7C_3 carbides, which reaches a maximum at a temperature of around 850 °C. From this point onward, simulations show carbides of the $M_{23}C_6$ type, which seems to occur at the expense of the M_7C_3. When the temperature reaches 980 °C, almost all M_7C_3 SC have either dissolved or transformed to $M_{23}C_6$ and after that, during holding, only carbides of this type can be found. A small fraction of M_7C_3 carbides is still present in the sample quenched directly after heating, presumably due to insufficient time for M_7C_3 to $M_{23}C_6$ transformation. No further SC precipitation is observed during soaking (given by a constant phase fraction) until cooling, where the second interesting process is observed. At this point, and in the range of temperatures between 980 and 750 °C, further $M_{23}C_6$ SC precipitation takes place, given by the increase in the phase fraction of $M_{23}C_6$. The carbides precipitating in this range during simulations might correspond to those small carbides observed in SEM images at the areas in contact with the eutectic carbides (red arrow in Figure 1b), since they are much smaller than the $M_{23}C_6$ SC precipitated in the middle of the matrix, and thus, they probably precipitated later during the HT not having time to grow or coalesce.

Some studies have shown that carbides usually form by following a reaction sequence $M_3C \rightarrow M_7C_3 \rightarrow M_{23}C_6$.[24,25] In this case, the destabilization temperature is too high for the presence of M_3C, reason why it is not seen as the precursor for the M_7C_3 formation. Inoue-Masumoto[25] showed the in situ transformation of M_7C_3 to $M_{23}C_6$ when annealing a 18.6 wt% Cr–3.40 wt% W–3.63 wt% C steel tempered for 10 h at 700 °C. No apparent specific crystallographic relationship between the lattices of both carbides was observed, and thus, the $M_7C_3 \rightarrow M_{23}C_6$ transformation occurs through the diffusion of alloying elements from the matrix and the former carbides to the resultant carbides, or that of carbon from the former carbides to the matrix is thought to be rate controlling.

After the implementation of the kinetic calculations, experimental HT was performed for the corroboration of the theoretical results. For that, the holding time at the destabilization temperature was varied from 0 to 90 min, and later, the samples were air quenched. Figure 5 shows the microstructure for the different holding times, 0, 30, 60 and 90 min. In all cases, $M_{23}C_6$ SC were detected using the same methodology as previously described for samples in Figure 1, showing larger sizes at the central region of the matrix and very small carbides in the area in contact with the eutectic carbides. The latter might correspond, again, to SC precipitated during the cooling. Phase identification in Figure 6 shows the final microstructure being martensite with some fraction of retained austenite, which is expected to be larger in the samples destabilized for shorter times.

The size and fraction of secondary carbides were determined by I–A using the software ImageJ[19] and are displayed in Figure 7. It shows that the average particle size increases with the holding time, supporting the fact that during holding, the SC fraction remains unchanged and only SC growth is occurring, as suggested by the kinetic calculations (Figure 4). However, only a slight difference in size can be seen when destabilizing for 60 and 90 min. The same tendency is shown in the carbide volume fraction, suggesting a steady state in the precipitation and growth of SC after 60 min of destabilization. Fraction of SC calculated from IA for 60 and 90 min shows a good correlation with the fraction predicted by the simulations in Figure 4. However, for shorter holding time (0 and 30 min) the prediction seems not to correlate well with the experimental results. One of the reasons might be related to the presence of very small carbides not detected during the metallographic characterization, leading to the calculation of smaller carbide fraction.

Even though destabilization treatments are a common practice in the hardening of HCCI, there are still some discussions concerning the exact occurrence of SC precipitation. It was suggested that the SC precipitate within the first 15 min of the treatment as a result of re-ordering of the carbon within the austenitic matrix,[12] and holding for longer times would lead to coarsening of the carbides. The results shown here are not only in accordance with this assumption, but they also suggest that the precipitation starts even during heating. Moreover, it seems that the growth of SC reaches a steady state at some point, which is assumed to be after 60-min destabilization. Other authors suggested that nucleation also occurs during the cooling

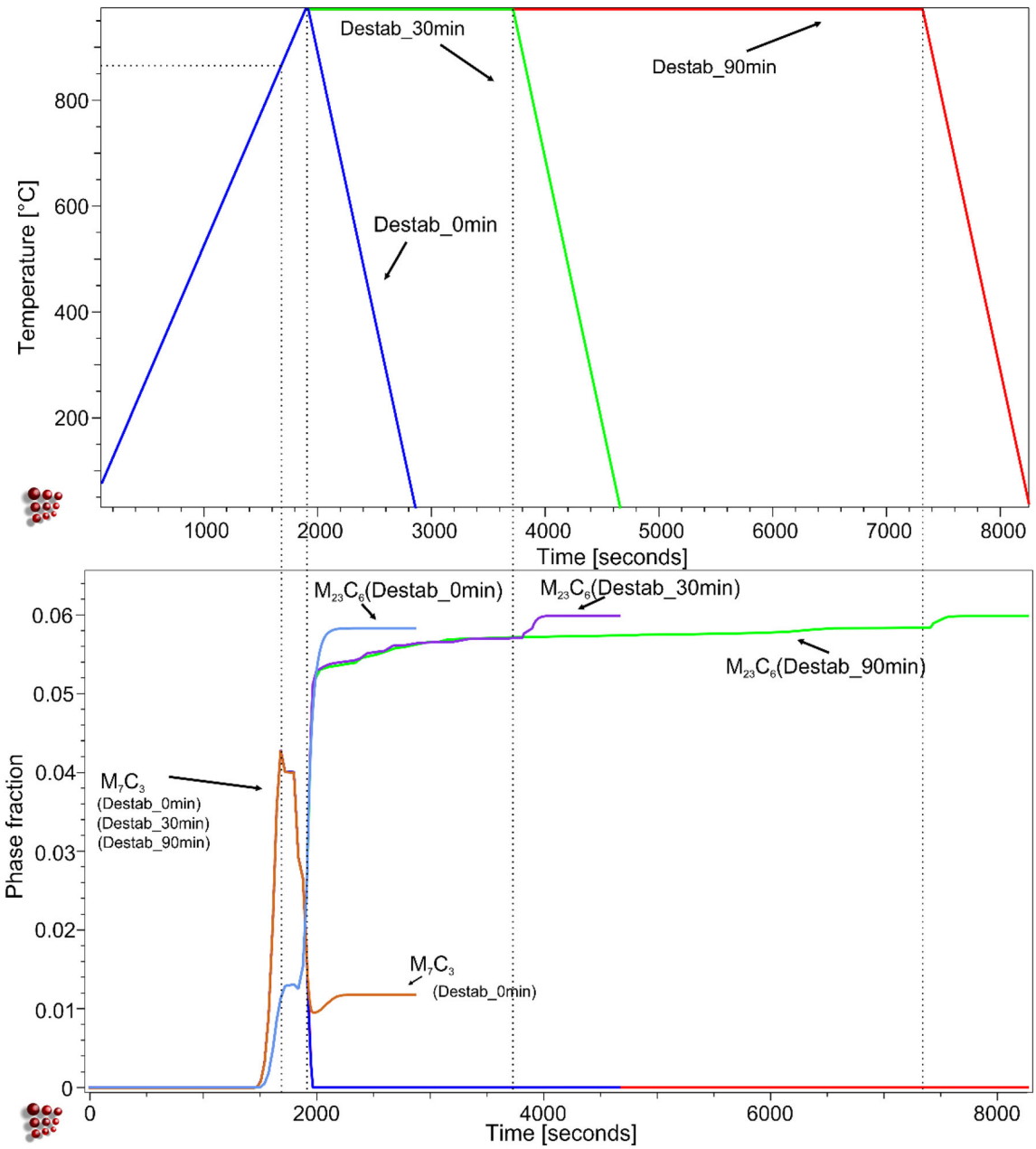

Figure 4. Destabilization process at 980 °C for different times (0, 30 and 90 min) calculated using MatCalc and the corresponding SC type and fraction. Thermal cycle for the destabilization process (on top) and the SC type and fraction during HT as a function of time (low).

process, after detecting much finer $M_{23}C_6$ SC after quenching to a cryogenic temperature.[27] This suggestion might also be upheld by the kinetic calculations and microstructural analysis, where the increase in SC volume fraction during cooling shown in Figure 4 is supported by the presence of very small SC in Figures 1b and 5.

After the destabilization for different times, microhardness measurements (Figure 8) were carried out in order to evaluate the influence of the holding time on the mechanical response. The lower microhardness value (Figure 8) for the sample Destab_0min is related to the lower SC size and volume fraction shown in Figure 7, whereas the sample Destab_90min showing the highest hardness value corresponds to the highest volume fraction and largest SC size. Additionally, the amount of retained austenite (RA) is also expected to vary with the holding time,[28] where the sample destabilized for 0 min should contain the largest amount of RA due to the still large amount of carbon within the matrix. Therefore, both the matrix, and volume fraction and size of SC play together for the final hardness value.[28]

The tendency is that the longer the holding times at the destabilization temperature, the higher the hardness[10]. It also can be related to the SC precipitation process. The

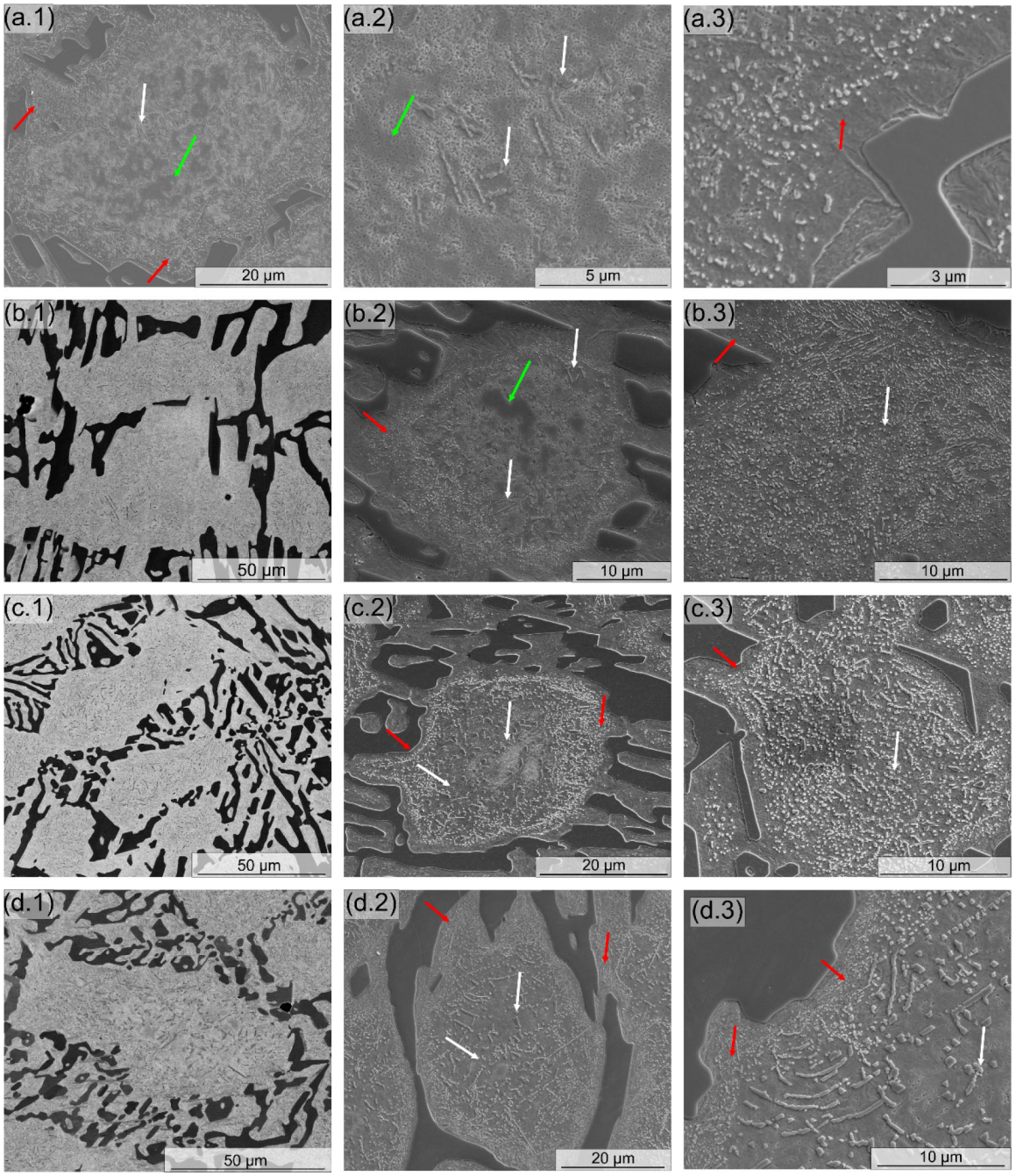

Figure 5. Samples destabilized at 980 °C for different times, (a) 0, (b) 30, (c) 60 and (d) 90 min. Images d.1–d.3 are the same as previously shown in Figure 1, which were included here for reference.

soaking time for reaching the maximum hardness is highly dependent on the destabilization temperature.[28] After that, the hardness starts to decrease as a consequence of coalescence and dissolution of SC, as explained by Bedolla–Jacuinde.[28] Figures 7 and 8 show almost no difference in the microhardness and SC volume fraction values for the samples destabilized for 60 and 90 min, which might indicate the reaching of a steady state in the hardening of the material. However, destabilization for longer times should be performed for assuring the soaking time for maximum hardness, which is not the objective of the present work. Besides the hardness, also the tribological response of the material might be altered by the soaking time, since it will control the carbon content in the martensite after quenching. This is the critical point which must be examined in detail, since the characteristic of the matrix supporting the carbides will determine the final response of the material.

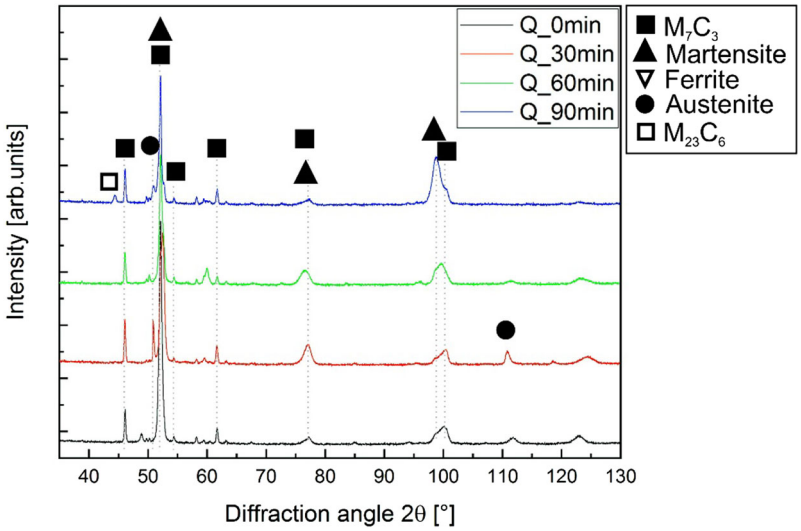

Figure 6. XRD of the samples destabilized for different times.

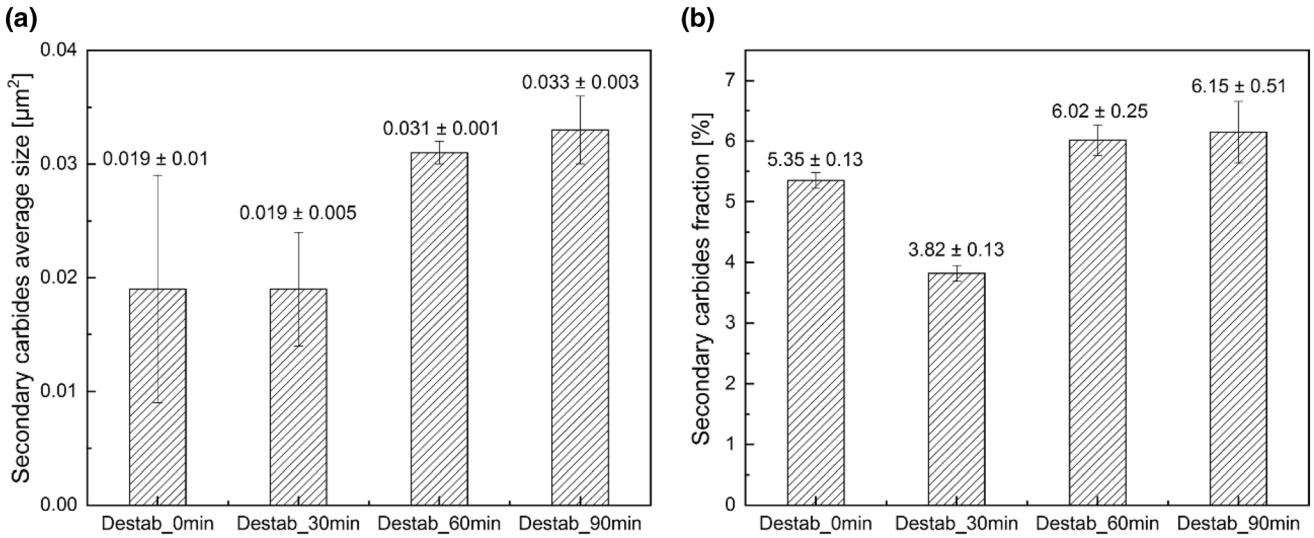

Figure 7. (a) Size and (b) volume fraction of secondary carbides after destabilization at 0, 30, 60 and 90 min.

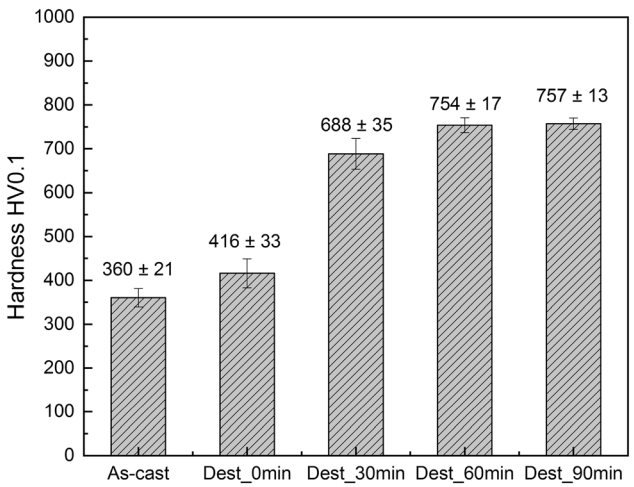

Figure 8. Microhardness (HV0.1) of the samples destabilized at 980 °C for 0, 30, 60 and 90 min.

Conclusions

In this work, we evaluated the influence of the chemical composition, especially the Cr content, in the microstructure after employing a multi-step HT that was successfully applied in HCCI_16%Cr. It was observed that the Cr content influences the nature of the SC precipitated during the different steps of the HT, changing from M_7C_3 to $M_{23}C_6$ when Cr increases. SCD treatment led to a microstructure composed by ferrite, M_3C and $M_{23}C_6$. Q and SCD + Q produced $M_{23}C_6$ SC embedded in a martensitic matrix, obtained after quenching.

Microhardness followed the same tendency than that observed in HCCI_16%Cr.[9] The sample with ferritic matrix showed the lowest hardness value. Variations in the values for Q and SCD + Q were observed, which might be

related to the size of the SC. However, the influence of the supporting matrix must not be dismissed, since the SCD might be beneficial for the alloy elements partitioning.

Samples destabilized for 60 and 90 min showed almost no difference in the microhardness and SC volume fraction values, which might indicate the reaching of a steady state in the hardening of the material. However, destabilization for longer times should be performed for assuring the soaking time for maximum hardness, which was not the objective of the present work.

Thermodynamic and kinetic calculations of the destabilization process showed that M_7C_3 are the first to precipitate during heating. After destabilization temperature is reached, they completely transform to $M_{23}C_6$, which grow throughout the holding time. Further precipitation of $M_{23}C_6$ occurred during cooling, in the temperature range 980–750 °C. The SC precipitated at this point are observed in the quenched samples in the area in contact with the EC.

Acknowledgements

Open Access funding provided by Projekt DEAL. The authors wish to acknowledge the EFRE Funds (C/4-EFRE-13/2009/Br) of the European Commission for supporting activities within the AME-Lab project and would also like to thank Dr. Martín Duarte Guigou from Universidad Católica del Uruguay and Tubacero S.A. for providing the material. P. Nayak wishes to thank the German Academic Exchange Service (DAAD) for their financial support.

REFERENCES

1. R.J. Llewellyn, S.K. Yick, K.F. Dolman, Wear **256**, 592–599 (2004)
2. S.D. Carpenter, D.E.O.S. Carpenter, J.T.H. Pearce, J. Alloys Compd. **494**, 245–251 (2010)
3. S.D. Carpenter, D. Carpenter, J.T.H. Pearce, Mater. Chem. Phys. **85**, 32–40 (2004)
4. ASM International, in *Heat Treating*, vol. 4 (ASM International, OH, 1997)
5. X.H. Tang, R. Chung, D.Y. Li, B. Hinckley, K. Dolman, Wear **267**, 116–121 (2009)
6. D.B. Miracle, Compos. Sci. Technol. **65**, 2526–2540 (2005)
7. G.L.F.F. Powell, J.V. Bee, J. Mater. Sci. **31**, 707–711 (1996)
8. K. Abdel-Aziz, M. El-Shennawy, A.A. Omar, Int. J. Appl. Eng. Res. **12**, 4675–4686 (2017)
9. M.A. Guitar, S. Suárez, O. Prat, M. Duarte Guigou, V. Gari, G. Pereira, F. Mücklich, J. Mater. Eng. Perform. **27**, 3877–3885 (2018)
10. V. Efremenko, K. Shimizu, Y. Chabak, Metall. Mater. Trans. A Phys. Metall. Mater. Sci. **44**, 5434–5446 (2013)
11. A.E. Karantzalis, A. Lekatou, H. Mavros, J. Mater. Eng. Perform. **18**, 174–181 (2009)
12. G.L.F. Powell, G. Laird, J. Mater. Sci. **27**, 29–35 (1992)
13. H. Gasan, F. Erturk, Metall. Mater. Trans. A Phys. Metall. Mater. Sci. **44**, 4993–5005 (2013)
14. C.P. Tabrett, I.R. Sare, M.R. Ghomashchi, Int. Mater. Rev. **41**, 59–82 (1996)
15. A. Wiengmoon, T. Chairuangsri, J.T.H. Pearce, ISIJ Int. **44**, 396–403 (2004)
16. E. Karantzalis, A. Lekatou, H. Mavros, Int. J. Cast Met. Res. **22**, 448–456 (2009)
17. A. Wiengmoon, J.T.H. Pearce, T. Chairuangsri, Mater. Chem. Phys. **125**, 739–748 (2011)
18. M.A. Guitar, A. Scheid, S. Suárez, D. Britz, M.D. Guigou, F. Mücklich, Mater. Charact. **144**, 621–630 (2018)
19. S. Johannes, E.F. Ignacio Arganda-Carreras, V. Kaynig, M. Longair, T. Pietzsch, S. Preibisch, C. Rueden, S. Saalfeld, B. Schmid, J.-Y. Tinevez, D.J. White, V. Hartenstein, K. Eliceiri, P. Tomancak, A. Cardona, Nat. Methods **9**, 676–682 (2012)
20. J. Ayache, L. Beaunier, J. Boumendil, G. Ehret, D. Laub, *Sample Preparation Handbook for Transmission Electron Microscopy*, vol. 136 (Springer, Berlin, 2007)
21. M.A. Guitar, A. Scheid, D. Britz, F. Mücklich, *Prakt. Metallogr.* **56**, 1–16 (2019)
22. C.P. Tabrett, I.R. Sare, Metall. Mater. Trans. A **26**, 357–370 (1995)
23. Ö.N. Doğan, J.A. Hawk, G. Laird, Metall. Mater. Trans. A Phys. Metall. Mater. Sci. **28**, 1315–1328 (1997)
24. B.A. Senior, Mater. Sci. Eng. A **103**, 263–271 (1988)
25. A. Inoue, T. Masumoto, Metall. Trans. A **11**, 739–747 (2007)
26. A.E. Karantzalis, A. Lekatou, E. Diavati, J. Mater. Eng. Perform. **18**, 1078–1085 (2009)

27. J. Wang, J. Xiong, H. Fan, H.-S. Yang, H.-H. Liu, B.-L. Shen, J. Mater. Process. Technol. **209**, 3236–3240 (2009)
28. A. Bedolla-Jacuinde, L. Arias, B. Hernández, J. Mater. Eng. Perform. **12**, 371–382 (2003)

V. Load Dependent Microstructural Evolution in an As-cast 26% Cr High Chromium Cast Iron during Unlubricated Sliding

U. Pranav Nayak[1], Sebastian Suárez[1], Valentin Pesnel[2], Frank Mücklich[1], María Agustina Guitar[1]

[1] Department of Materials Science and Engineering, Saarland University, 66123 Saarbrücken, Germany

[2] EEIGM, Université de Lorraine, 54000 Nancy, France

Published in "***Friction***" (2022) *(IF (2023): 4.924)*

Accessible online at: *https://doi.org/10.1007/s40544-021-0553-x*

Own Contribution: Conceptualization and methodology; sample preparation; experimentation; microstructural and tribological characterization; data analysis; scientific discussion; paper writing – original draft preparation

Friction
https://doi.org/10.1007/s40544-021-0553-x
ISSN 2223-7690
CN 10-1237/TH
RESEARCH ARTICLE

Load dependent microstructural evolution in an as-cast 26% Cr high chromium cast iron during unlubricated sliding

U. Pranav NAYAK[1, *], Sebastian SUÁREZ[1], Valentin PESNEL[3], Frank MÜCKLICH[1,2], María Agustina GUITAR[1]

[1] *Department of Materials Science, Saarland University, Saarbrücken 66123, Germany*

[2] *Materials Engineering Center Saarland, Saarbrücken 66123, Germany*

[3] *Ecole Européenne d'ingénieurs en Génie des Matériaux, Université de Lorraine, Nancy 54000, France*

Received: 12 April 2021 / Revised: 07 June 2021 / Accepted: 05 September 2021

Abstract: In the current study, an as-cast 26% Cr high chromium cast iron (HCCI) alloy was subjected to dry-sliding linear wear tests, under different loads. The loads were selected based on analytically computing the critical load (P_C) i.e., the load necessary to induce plastic deformation. The P_C was calculated to be 15 N and accordingly, a sub-critical load (5 N) and an over-critical load (20 N) were chosen. The influence of increasing the load during the wear test was investigated in terms of the matrix microstructural behaviour and its ability to support the surrounding carbides. The morphological aspects of the wear tracks, and the deformed matrix microstructure adjacent and underneath the track was analysed by confocal laser scanning microscope (CLSM) and scanning electron microscope (SEM), respectively. No evidence of plastic deformation of the matrix was observed below P_C. On the contrary, at loads equal to and higher than P_C, the austenitic matrix plastically deformed as evidenced by the presence of slip bands. Electron backscattered diffraction (EBSD) measurements in terms of grain reference orientation deviation, and micro-Vickers hardness of the austenitic matrix indicated a deformation depth of about 40 μm at the maximum applied load of 20 N. The active wear mechanisms during sliding were a combination of both adhesive and abrasive wear, although increasing the load shifted the dominant mechanism towards abrasion. This was primarily attributable to the increased propensity for carbide cracking and fracturing, combined with the inability of the hardened austenitic matrix surface and sub-surface to adequately support the broken carbide fragments. Moreover, the shift in the dominant wear mechanism was also reflected in the wear volume and subsequently, the wear rate.

Keywords: high chromium cast iron; unlubricated sliding; plastic deformation; wear resistance; carbide spallation; matrix hardness

1 Introduction

The ASTM A532 describes high chromium cast irons (HCCIs) as alloys containing 15–30 wt% Cr and 2.4–4 wt% C (with minor additions of Mn, Ni, Cu, and Mo), belonging to the Fe–Cr–C ternary system [1, 2]. They were created in the 1930's, with continuous improvements made over the years and are already being used in applications that demand excellent wear resistance and moderate toughness in coal and mineral industries [3]. Their applicability in ore crushers, ball mill liners, and pulverizing equipment is mainly due to the presence of hard, dispersed chromium-iron carbides, in the as-cast state. Moreover, combining the hard carbides with the relatively softer matrix surrounding it, and the overall associated cost, makes it an attractive choice to be used in these industries [4–7].

In HCCI alloys, increasing the Cr content will modify the type and nature of the eutectic carbides

* Corresponding author: U. Pranav NAYAK, E-mail: pranav.nayak@uni-saarland.de

(EC), from a continuous M_3C type to a discontinuous M_7C_3 type [8, 9]. Given the inherent brittleness associated with the carbide, continuous precipitates are not favoured for abrasion resistance and therefore, the discontinuous, and relatively tougher M_7C_3 carbides are advantageous [10]. The M_7C_3 hardness is about 1,200–1,600 HV depending on the chemical composition and the orientation, which, is much higher than austenitic or martensitic matrix structures encountered in hypoeutectic HCCI variants [11]. Additionally, the carbide volume fraction (CVF) and the orientation of the carbides influence the overall wear resistance [12, 13].

Several works focus on the influence of alloying and CVF on the final wear properties of the HCCI alloys, and studies are devoted to find the optimum CVF for a given chemical composition to obtain the maximum wear resistance [13–17]. Initially, the resistance to wear was thought to be mainly influenced by the hardness of the material, as empirically demonstrated by Archard [18]. It is now understood that a lot of factors contribute to the overall wear resistance, such as the carbide's type, morphology, volume fraction, and its interaction with the host matrix. Therefore, the overall wear resistance can be thought of a synergistic contribution between both the carbide and the matrix that surrounds it [19, 20].

Despite the crucial contribution of the hard M_7C_3 carbides in improving the overall wear resistance of the HCCI alloy, the degree of mechanical support provided by the matrix structure plays a pivotal role [21, 22]. This was evident in the study carried out by Doğan et al. [23], where the increase in the CVF did not necessarily increase the wear resistance in the examined HCCI alloys. Therefore, it can be said that the wear behaviour of a material is not an inherent property but is defined wholly by the system and in this regard, the carbides' hardness contributes partly to the wear resistance [24].

As far as the matrix structure is concerned, pearlitic and ferritic matrix is avoided as their presence will reduce both wear and fracture resistance [10, 25]. Austenite in general is thought to provide a better mechanical support for the carbides compared to pearlite/bainite due to its ability to absorb the crack propagation and strain harden progressively during service [26–28]. This was apparent in the work carried out by Doğan et al. [23], where it was observed that the HCCI with an austenitic matrix and CVF of 28% showed a decrease in the volume wear rate by almost 50% compared to the alloy with a pearlitic/bainitic matrix having a CVF of 45%.

It was shown in several studies that heat treatment modifications made to the as-cast HCCI alloy have improved the wear resistance [29–33]. On the other hand, there are studies which indicate that a harder martensitic matrix might not be the most optimal choice [23, 25]. Moreover, numerous studies indicate a tendency of increasing wear resistance with increasing CVF when an abrasive softer than the M_7C_3 carbide is used, although there is no consensus among the community when the hardness exceeds that of the carbide (SiO_2/Al_2O_3) [26, 34]. Thus, the wear behaviour is not only influenced by the microstructure of the HCCI alloy, but also by other factors such as the experimental environment, loading conditions, the relative movement of the contact surface, the abrasive type, and hardness [21]. This just elucidates the complexity and the variables associated with tribological testing.

Among a multitude of studies dealing with wear in cast irons, only a limited number of investigations dealt with sliding wear [21, 35, 36] and even fewer studies emphasised on the matrix modifications taking place during sliding [14, 24]. It is thought that in addition to the dislocation interactions, the formation of strain induced martensite (SIM) also contributes to the work hardening behaviour of austenite [37]. Although the transformation from austenite to martensite under abrasion is mentioned by Pokusová et al. [38], it is not described as such. The ability of the austenite matrix to plastically deform during service and its ability to form SIM gives scope for further improvement in creating a self-replacing wear resistance surface, increasing the longevity of the wear parts [10, 25].

In the current work, an attempt was made to investigate the microstructural evolution of an as-cast 26% Cr HCCI alloy under three different loading conditions during dry-sliding. The loads were selected after performing analytical calculations based on the materials' parameters using Hertzian contact theory. The wear tracks were subjected to confocal laser scanning microscopy (CLSM) and scanning electron

microscopy (SEM) to examine the morphological aspects of the tracks and ascertain the acting wear mechanisms. This was further complemented by performing electron backscattered diffraction (EBSD) measurements on the regions adjacent to, and underneath the wear tracks. Furthermore, quantification of wear, in terms of wear rate, and the coefficient of friction (COF) evolution with increasing loads, were assessed. In the current alloy, as the matrix is predominately austenitic, understanding its behaviour under the given tribological conditions will bolster the alloy's further development in applications involving sliding wear such as liner plates and vertical roller mill liners [5, 21].

2 Materials and methodology

The bulk chemical composition (in wt%) of the 26% Cr HCCI alloy was determined by optical emission spectroscopy (GNR Metal Lab 75/80; G.N.R. S.r.l., Agrate Conturbia, Novara, Italy) and is presented in Table 1. The specifics of the casting are mentioned in [39]. An abrasive disk was used to cut the cast samples measuring 20 mm × 20 mm × 10 mm and later, hot embedded using a conductive resin for microstructural characterization. Standard metallographic procedure was followed as detailed in Ref. [40], to obtain a scratch-free, mirror polished surface. The microstructure of the as-cast sample composed of M_7C_3 (~ 30%) (M: Cr, Fe) eutectic carbides (EC) dispersed in an austenitic matrix (γ) (~ 60%), and a thin layer of martensite (α') (~10%) sandwiched between the EC and γ, as depicted in Fig. 1(a). Further microstructural analyses, concerning the phase fraction and elemental composition has previously been carried out [39, 40]. The presence of

Table 1 Bulk chemical composition (wt%) of the HCCI alloy.

C	Cr	Mn	Ni	Mo	Si	Cu	P	S	Fe
2.53	26.60	0.66	0.26	0.24	0.37	0.03	<0.01	0.04	Bal.

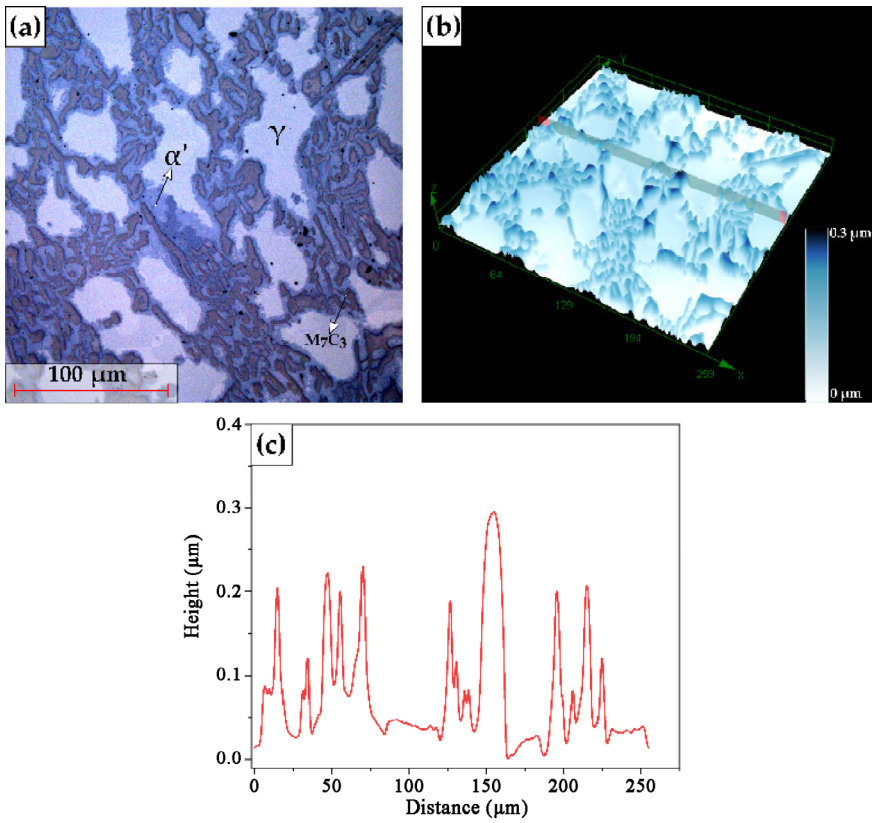

Fig. 1 (a) Representative CLSM micrograph of the as-cast HCCI sample in the unworn state, with the austenitic matrix (γ), M_7C_3 EC, and interfacial martensite (α') indicated; (b) 3D view of the topographical map along with the height range; and (c) height profile taken across the sample surface.

martensite between the γ–M_7C_3 interface is a common occurrence during the casting of HCCI alloys and is a well-documented phenomenon [9, 31, 41, 42].

Dry-sliding wear tests in a linear reciprocating motion were conducted using a ball-on-disc micro-tribometer (CSM Instruments), while the whole setup was placed in an environmental chamber to control the temperature and humidity. 3 mm alumina (Al_2O_3) balls (99.00%–99.99 % purity; Grade GD28) were used as the sliding counter-body. The roughness of the sample and balls was measured using a LEXT OLS 4100 Olympus CLSM (Olympus Corporation, Tokyo, Japan). The CLSM uses a laser with 405 nm wavelength and, a lateral and vertical resolution of 120 and 10 nm, respectively. Figure 1(b) depicts a 3D topographical map of Fig. 1(a), and Fig. 1(c) represents the height profile taken across the sample surface. It is worth to mention that height variation is a direct consequence of the difference in the removal rates between the matrix and carbide phase during metallographic preparation, owing to their dissimilar hardness. This is reflected in the sample roughness. The roughness, described by the root mean square (RMS) value, S_q, was 0.07 ± 0.01 μm for the sample, measured in an area of 650 μm × 650 μm. The ball roughness was 0.250 ± 0.05 μm. It should be noted that before commencement of the wear testing, the balls were rinsed in an ultrasonic bath separately with acetone and isopropanol for 10 minutes each.

The value of the critical load (P_C) i.e., the load at which the outset of plastic deformation takes place in the material, was determined applying the Hertzian contact theory, using Eqs. (1) and (2) [43, 44]. It should be noted that the values considered while carrying out these approximations are of the material that fails first. Since the matrix is the relatively softer phase compared to the M_7C_3 carbide, it will yield first. Hence, the P_C calculations were carried out by considering the properties of the alumina ball and the austenitic matrix.

$$P_c = \frac{4}{3}\left(\frac{R}{E'}\right)^2\left(\frac{C}{2}\pi \cdot S_y\right)^3 \quad (1)$$

$$\frac{1}{E'} = \frac{1-\nu_1^2}{E_1} + \frac{1-\nu_2^2}{E_2} \quad C = 1.295\exp(0.736\nu) \quad (2)$$

where P_C is the critical contact force at yielding (N), R is the radius of the alumina ball (m), E' is the equivalent elastic modulus (GPa), E_1 and E_2 represent the elastic modulus of the alumina ball and the austenitic matrix, respectively, ν_1 and ν_2 are the Poisson's ratio of the ball and the matrix, respectively, C is the yield strength coefficient and S_y is the yield strength of the matrix. The hardness (H) and Young's modulus (E) values of the austenitic matrix (in GPa) were obtained from nano-indentation measurements (Hysitron TI 900 TriboIndenter), using a Berkovich tip, with a tip depth of 200 nm used in displacement mode. A loading/unloading rate of 50 was maintained and the scan size was approximately 30 μm [39]. Each indentation time was 2 min, and the values were averaged over 25 readings. The S_y of the matrix was determined from the H using a variant of the Tabor relationship ($S_y = H/2.84$) [45]. The values of the parameters used in the Eqs. (1) and (2) are given in Table 2.

The P_C was found out to be ~ 15 N and accordingly, three loads (P), 5, 15, and 20 N, were chosen for the wear tests. Moreover, the specifics concerning the tribological testing parameters are given in Table 3. Three trials were performed for each load.

Table 2 Parameters used for the critical load calculations.

Parameter	Value
R (m)	1.50×10^{-3}
E_1 (Pa) [46]	3.65×10^{11}
E_2 (Pa)	2.38×10^{11}
ν_1 [47]	0.22
ν_2 [48]	0.28
E' (Pa)	1.54×10^{11}
H (Pa)	5.60×10^{9}
S_y (Pa)	1.97×10^{9}
C	1.5914

Table 3 Tribological testing parameters.

Parameter	Value
Temperature (°C)	25
Relative humidity (%)	45
Load (N)	5, 15, 20
Sliding velocity (m/s)	0.02
Stroke length (mm)	5.5
No. of cycles	2,000
Data acquisition frequency (Hz)	50

CLSM was used to analyse the evolution of the wear tracks with increasing load and the corresponding morphological aspects, whereas the fine microstructural details were observed using a FEI Helios Nanolab field emission scanning electron microscope (FE-SEM). The SEM was operated at an acceleration voltage of 5–15 kV and a beam current of 1.4 nA. Moreover, a high sensitivity backscattered electron detector (vCD) was used to obtain a better contrast between the phases. Energy-dispersive X-ray spectroscopy (EDS) was used to evaluate the chemical composition of the worn, and unaffected surfaces. Furthermore, to observe the deformed microstructure underneath the wear track and to prevent further modifications from the mechanical sectioning and polishing, the surface was electrolytically coated with Ni.

EBSD was used to investigate the local deformation and the strain distribution in the austenitic matrix, adjacent and beneath the wear track. The measurements were performed at an acceleration voltage of 20 kV and a beam current of 11 nA, using a field emission gun in the FE-SEM workstation equipped with an EDAX Hikari EBSD camera. Kernel average misorientation (KAM) measurements were carried out to extract orientation data within the deformed regions. Owing to the very small step size (30–50 nm), 2nd neighbour KAM with a 5° threshold was considered for the analysis. Additionally, grain reference orientation deviation (GROD) analysis was performed within the austenitic regions to obtain the orientational variation, with increasing cross-sectional depth. The EBSD data was analysed using the Orientation Imaging Microscopy (OIM™ v. 7) Data Analysis software by EDAX Inc.

Furthermore, the hardness of the austenitic matrix adjacent and underneath the wear track, was determined using the Vickers method. A Struers Dura Scan 50 microhardness tester (Struers Inc., Cleveland, OH, USA) with a load of 0.09807 N (HV 0.01) was used for this purpose. During the testing, the dwell time was 15 s and an average of 15–20 readings were considered. The load was chosen such that the surrounding entities are not participating in the evaluation of the matrix hardness and the indentation mark was clearly resolvable using the optical microscope.

Wear quantification was described in terms of wear rate, and it was proceeded by calculating the volume loss encountered in each track, using the LEXT software. The entire wear track, including the ends were considered in the calculations, and Eq. (3) was used to compute the wear rate. Similar variations of Eq. (3) were used in other studies to quantify wear, where mass loss and density had been considered [49–51]. In Eq. (3), V represents the wear volume (mm^3), l is the total sliding distance (5.5 × 2 × 2,000 mm), P is the applied load (N), and K represents the wear rate (mm^3/(N·mm)).

$$K = \frac{V}{l \times P} \tag{3}$$

3 Results and discussions

3.1 Microstructural characterization of the worn samples

Figures 2(a)–2(c) represent the CLSM micrographs of the sample surface with a 50% overlay of the height profile, for the increasing loads, after wear. The 'composite' CLSM micrograph was divided based on height (left-half) and intensity (right-half) to have a better visualization across the wear track. The height range (pertaining only to the height profile) and the sliding direction (SD) is also mentioned for reference. The variation in the height from the wear track edge towards the centre, with increasing load, can be clearly observed. The depth profile, taken across the wear track (as indicated by the horizontal red dashed line), is graphically represented in Fig. 2(d). Additionally, the wear width increased with increasing load, as shown in Fig. 2(e).

3.1.1 Sub-critical load (P = 5 N)

Figure 3 represents the SEM micrographs of the worn surface morphology after subjecting it to sliding at 5 N. Initially, as the Al_2O_3 ball traverses over the sample surface, some material transfer takes place owing to the high contact pressure established by the ball's asperities, causing adhesion [27, 52]. Furthermore, the reciprocating effect of sliding and the subsequent shearing action results in adhesive wear and the formation of wear debris as indicated in Fig. 3(a). A closer examination of the wear track in Fig. 3(b) reveals carbide micro-cracking, primarily perpendicular to the

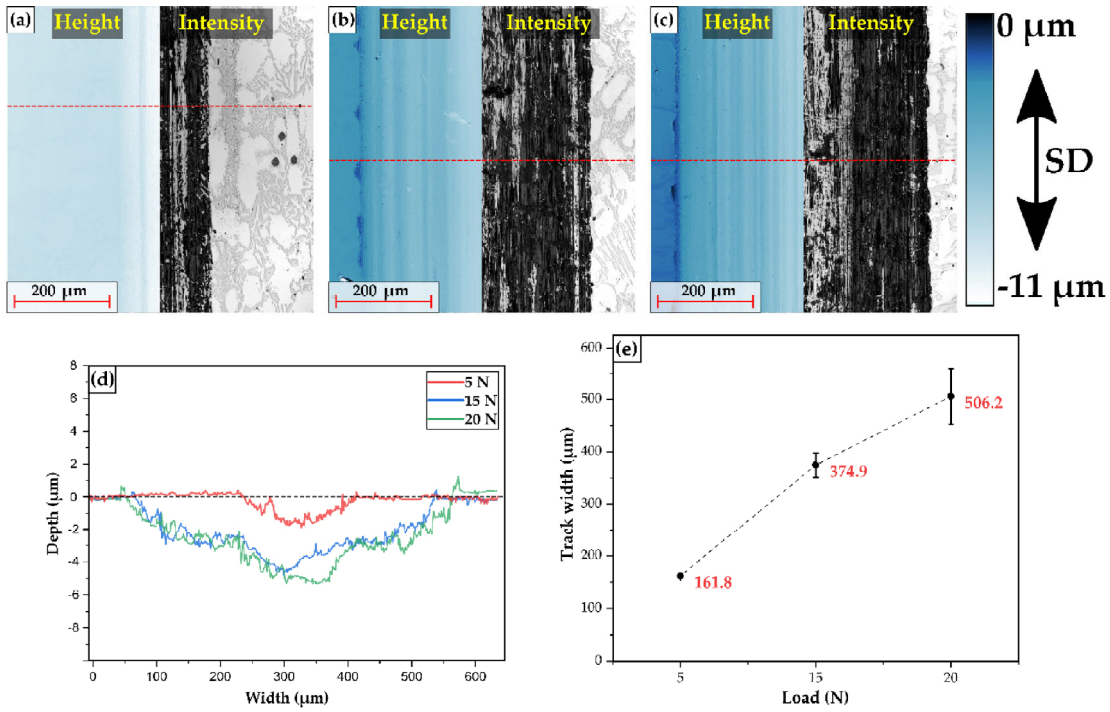

Fig. 2 CLSM micrographs of the wear tracks with a 50% overlay of the height profile for (a) 5 N, (b) 15 N, and (c) 20 N. The part of the CLSM micrograph based on height, and intensity is indicated within the micrograph for reference. The height range (pertaining only to the height profile) and the sliding direction (SD) is also mentioned. (d) Depth profile taken across the wear tracks for the different load as indicated by the horizontal red dashed line in the differently loaded micrographs. (e) Average wear track width for each load.

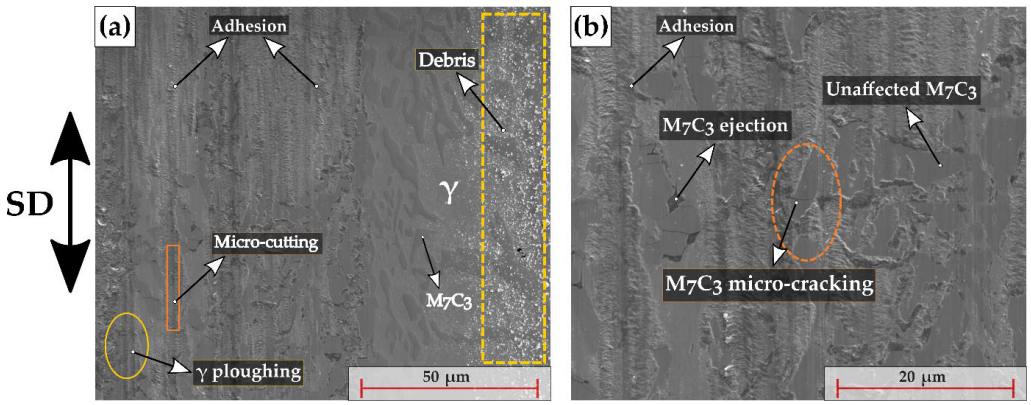

Fig. 3 (a) and (b) SEM micrographs in secondary electron (SE) mode of the wear track loaded at 5 N, with the various wear track aspects delineated within the micrograph. The austenitic matrix (γ) and the eutectic carbides (M_7C_3) are indicated in (a). The orange solid rectangle represents the micro-cutting phenomena whereas the orange dashed ellipse indicates the carbide micro-cracking. The wear debris generated is indicated by the yellow dashed rectangle whereas the yellow solid ellipse represents the ploughing of the austenitic matrix. The SD is also mentioned for reference.

sliding direction. Even though the load used currently is below P_C, given the higher hardness of the Al_2O_3 balls (~ HV 1,500) compared to the M_7C_3 carbides (~ HV 1,200), they are able to crack and fracture the carbides, in addition to affecting the matrix [10, 25]. The carbide cracking and fragmentation eventually leads to its ejection. The fractured carbides can then act as third-body entities, causing further grooving in the material, leading to the phenomenon of micro-cutting and micro-ploughing, characteristics of abrasive wear, as delineated in Fig. 3(a). It is also worth to note that the majority of M_7C_3 carbides were cracked, but not ejected from their position. This was attributable to the ductility of the austenitic matrix which provided

adequate mechanical support, preventing carbide spallation. Subsequently, it was concluded that the active wear mechanisms were adhesion with mild abrasion.

Although no evidence of plastic deformation of the austenitic matrix adjacent to the wear track was observed from the SEM micrographs, EBSD measurements indicated the sporadic presence of slip lines adjacent to the track, as seen in Fig. 4(a). Comparing the image quality (IQ) map (Fig. 4(a)) to the phase map (Fig. 4(b)), the slip lines were seen to be originating from the martensitic area adjacent to the wear track and not directly from the austenite. Hence, this can be thought more of a local deformation caused by the compressive nature of the hard martensite present in between the carbide and austenite, rather than a shear deformation induced by the ball. The material flow stemming from the wear testing, combined with the associated presence of martensite at the carbide–austenite interface could impart some compressive action leading to a slight local deformation, resulting in the occurrence of slip traces.

Figures 4(c) and 4(d) represent the IPF and KAM maps of the austenite matrix, respectively. KAM is basically the average misorientation between each pixel and the chosen neighbours. Increased misorientation indicates the accumulation of strain inside the material and it is used to study the sub-structures [53]. It is evident from both maps that no misorientation within the austenite matrix has occurred. Indeed, the misorientation at the periphery of the matrix is higher than the centre which can be attributable to the presence of the martensitic layer, engulfing and straining the matrix. However, it must also be noted that the uncertainty associated with filtering the artefacts at the edge boundaries can also play a role.

3.1.2 *Critical load (P = 15 N)*

The wear was conducted at the critical load, and the SEM micrographs depicting all the effects that resulted during the wear test are represented in Fig. 5. Similar to Fig. 3, characteristics of both adhesive and abrasive wear was seen on the wear tracks, as indicated in Fig. 5(a). Owing to the increased load, plastic deformation of the austenitic matrix adjacent to the wear track took place, as evidenced from the presence of slip traces, and predicted by the calculations. These slip traces are formed to accommodate the deformation endured by the austenitic matrix owing to the tangential forces exerted by the ball during the test [54]. Moreover, a second set of slip traces was revealed adjacent to the wear track, present closer to the martensite layer and can be visualised in Fig. 5(b). The second slip system activation could take place to accommodate the higher local deformation exerted by the shearing action of the ball and due to the increased local strain closer to the martensite layer. The carbide micro-cracking and ejection can be visualized in Fig. 5(c). It was observed that the proportion of the spalled carbides had increased compared to the wear testing under 5 N load, resulting in a shift in the active wear mechanism towards abrasive wear. Unlike the previous case, where the austenitic matrix was mainly undeformed, the increased load resulted in its plastic deformation rendering it unable to support the fractured carbides. This led to an increased occurrence of micro-cutting and micro-ploughing, as indicated by the orange solid rectangle and the yellow solid ellipse, respectively.

Furthermore, the difference in brightness between

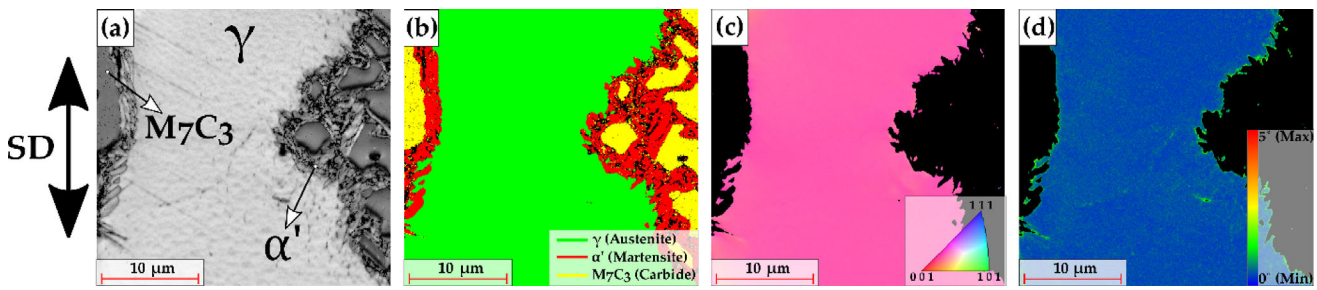

Fig. 4 EBSD measurements on the region adjacent to the 5 N track with (a) IQ map of the scanned region with the respective phases indicated, (b) phase map with the phases marked in different colours, (c) inverse pole figure (IPF) map of the austenite matrix, and (d) KAM map of the austenite matrix.

the deformed and the undeformed austenite, as observed in Fig. 5(d), stems from the orientational gradients during the plastic deformation. Additionally, the two different sets of slip traces are marked, as indicated in Fig. 5(e). The increased matrix hardening associated with the higher load combined with the increased propensity for carbide cracking, could prove detrimental to the overall wear behaviour of the alloy. This is evident in Fig. 5(a) where the carbides have been cracked and removed, resulting in the formation of debris, and as seen further, wear loss. Hence, it was concluded that the active wear mechanism had shifted from a primarily adhesive wear with mild abrasion, to an abrasion-dominated wear with signs of mild adhesion in the track.

Analogous to the 5 N wear track, EBSD analysis was performed on the 15 N track, with particular emphasis being placed on the austenite matrix adjacent to the wear track. The influence of using a higher load can be acknowledged. It seems that the slip lines terminate as they reach the martensite phase, as depicted in Fig. 6(a), which can be attributed to the difference in the crystal structure and higher hardness. The IPF map of the austenite matrix, in Fig. 6(c), indicates a variance in the crystal orientation especially at regions where the two sets of slip lines intersect. The same can be visualized from the KAM map, in Fig. 6(d), wherein a higher misorientation is present where the intersection of the slip lines takes place.

3.1.3 *Over-critical load (P = 20 N)*

Finally, wear testing at 20 N was carried out and the SEM micrographs of the wear track in BSE mode are shown in Fig. 7. It was observed from Figs. 7(a)

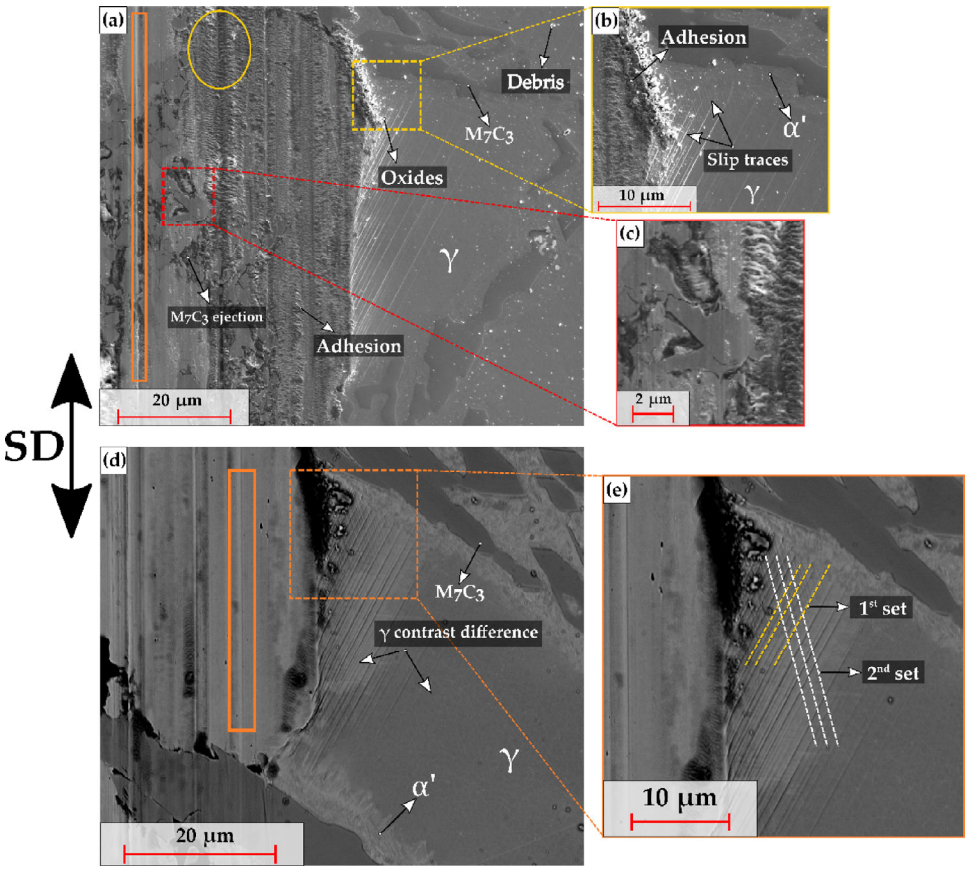

Fig. 5 (a) SEM micrograph in SE mode of the wear track loaded at 15 N, with the austenitic matrix (γ), M_7C_3 carbides, oxides, and the wear debris delineated within the micrograph. The presence of slip traces along with the martensite phase (α'), and the phenomenon of adhesion is indicated in (b) whereas, the partially cracked and removed carbide is observed in (c). The orange solid rectangle represents the micro-cutting phenomena, and the yellow solid ellipse represents the ploughing of the austenitic matrix. (d) SEM micrograph in the backscattered electron (BSE) mode where, the varying contrast between the deformed and undeformed austenite is observed and finally, the two sets of slip planes are indicated in (e).

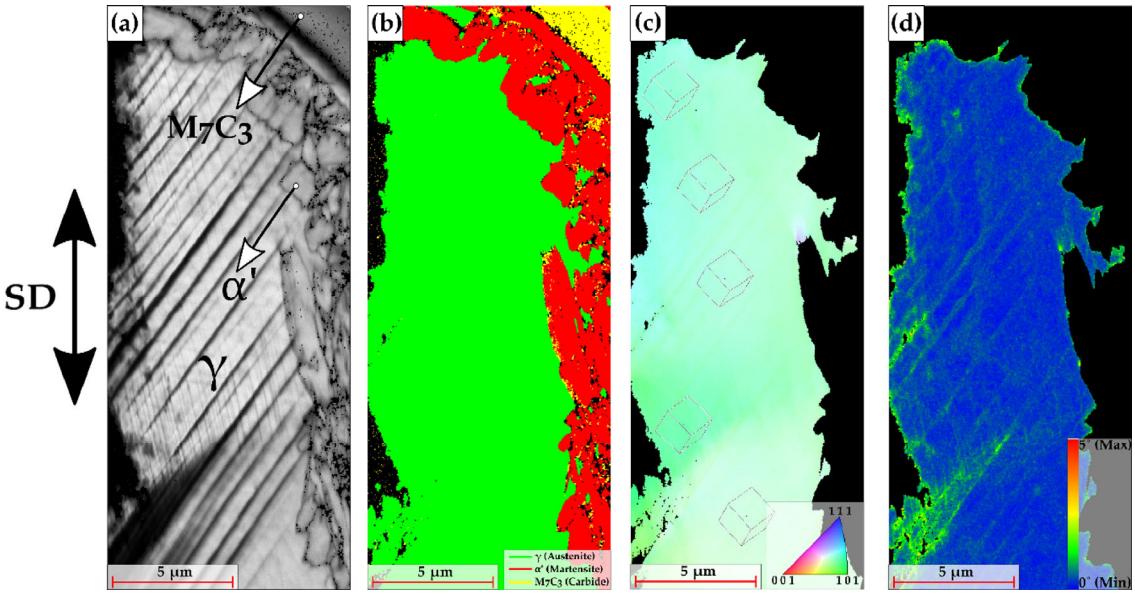

Fig. 6 EBSD measurements on the region adjacent to the 15 N track with (a) IQ map of the scanned region with the respective phases indicated, (b) phase map, with the phases marked in different colours, (c) IPF map of the austenite matrix, overlayed with the local lattice rotation, and (d) KAM map of the austenite matrix.

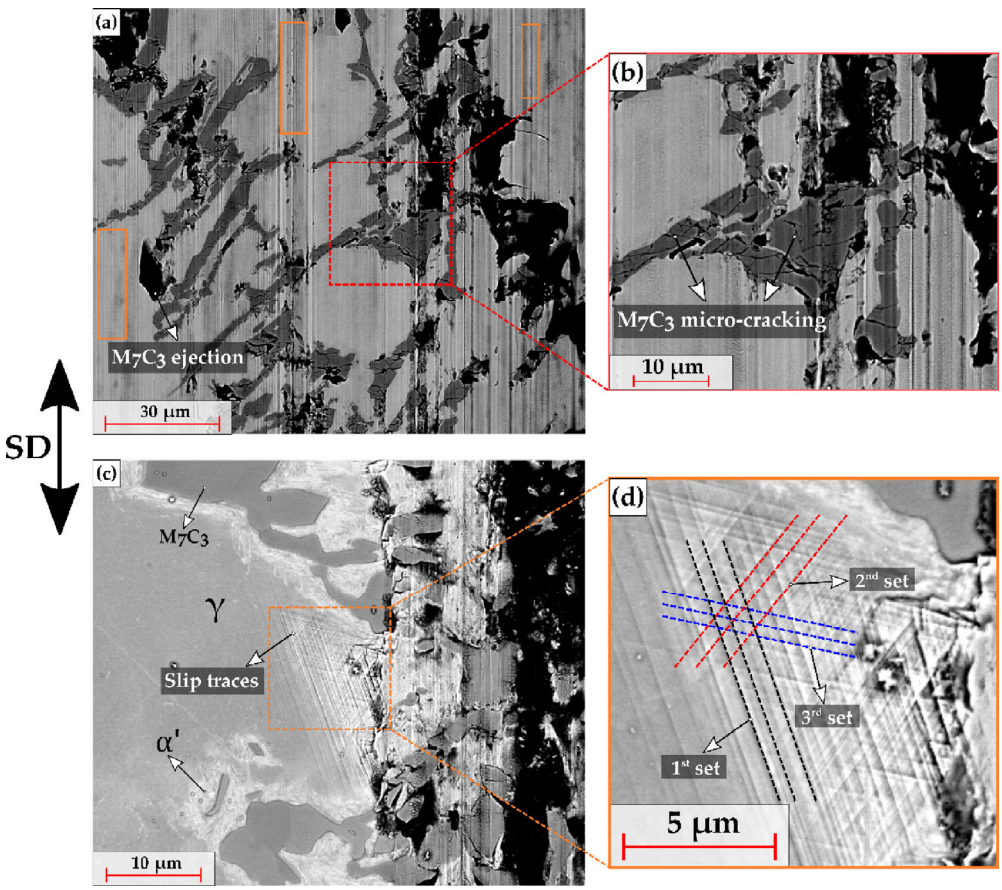

Fig. 7 (a) SEM micrograph in BSE mode of the wear track loaded at 20 N wherein the orange solid rectangle represents the micro-cutting phenomena. The partially cracked and removed carbide is observed in (b). (c) SEM micrograph in the BSE mode where the austenitic matrix (γ), M_7C_3 carbides, martensite phase (α'), and the slip traces are delineated and finally, the three different sets of slip planes are indicated in (d).

and 7(b) that the proportion of cracked and spalled carbides increased compared to the previous loads. Expectedly, in addition to the presence of slip traces, a third set of slip planes was activated, as observed in Fig. 7(c) and marked in Fig. 7(d). The increased load would increase the amount of plastic deformation undergone by the austenitic matrix and thereby, to accommodate the increased dislocation activity, a third set was activated. This third system might have a higher critically resolved shear stress (CRSS) and hence, a larger load was necessary to activate it [54, 55].

Figure 8(a) represents the SEM micrograph of the region adjacent to the wear track where the EBSD measurements were carried out. The IQ map in Fig. 8(b) clearly indicates the variance in the slip band directions, and its consequence is reflected in the IPF map depicted in Fig. 8(d). A variation in the crystal orientation is seen within the austenite, especially at regions where two or even three sets of slip traces intersect, as evident from the crystal lattice rotations in Fig. 8(d). Depending upon the direction of the slip bands with respect to the neighbouring region and the associated strain incompatibilities, a localized lattice rotation occurs within the region [56]. As a result of this, the local misorientation also varies, as observed in the austenite KAM map in Fig. 8(e). Moreover, the difference between the misorientation within the austenite region and the mean orientation was visualized by performing the GROD measurements, as represented in Fig. 8(f). A clear orientational difference between the austenitic region bordering the wear track and the rest of the austenite can be observed. This was further elucidated by calculating the point-to-point and point-to-origin misorientation profile chart across the austenite grain, as represented in Fig. 8(g). The line profile is marked in Fig. 8(f) as the horizontal white dashed line. Clearly, while crossing over the point at approximately 2 μm from the origin, a spike can be seen in the blue curve, which indicates the orientational difference. Furthermore, the point-to-origin curve indicates a maximum gradient of about 40° within the austenite region. The different regions within the austenite rotate independently depending on the number of slip systems activated and the direction of the slip bands, to accommodate the imposed plastic strain.

From the SEM micrographs, cracks and grooves were visible on all the worn surfaces. Comparing Fig. 2 with the respective magnified SEM micrographs for all loads, it was evident that the wear mechanism was a combination of both adhesive and abrasive wear. At loads below P_C, adhesion was the dominant wear mechanism with signs of mild abrasion, but at loads equal to and above P_C, a shift was observed with the dominant wear mechanism being abrasion. Given the inherent ductility of the austenitic matrix, micro-ploughing ensued whereas micro-cutting affected the harder, more brittle M_7C_3 EC, owing to its inability to plastically deform. The M_7C_3 carbides had cracked and fractured owing to the higher hardness of the abrasive, and the inability of the hardened austenitic matrix in adequately providing the necessary mechanical support resulted in its spallation. The spallation of carbides results in the formation of voids that can act as a reservoir to trap the particles generated during the wear process, potentially altering the wear behaviour during sliding [57, 58]. Moreover, the cracked carbide could act as a third body which can affect other carbides as well, leading to the formation of grooves in the leading edge of the carbide during abrasion [23, 59]. Therefore, the likelihood for micro-cutting increased with increasing load and it could be attributed to the higher propensity for carbide spallation combined with the increased rate at which the austenite plastically deforms. As the micro-cutting mechanism causes a greater loss in the material [10, 60], and given its proclivity with increasing load, it could be postulated that a higher volume loss can be expected.

Furthermore, the increased rate of the strain hardening of the austenitic matrix was reflected in the hardness values that were measured vicinal to the wear track, as indicated in Table 4. Compared to the hardness value of the undeformed austenitic matrix, an increase in the matrix hardness was observed at regions adjacent to the wear track and as the load increased, the average hardness value increased as well. This was attributable to the increase in the dislocation activity within the austenite leading to the activation of multiple slip systems and increased strain hardening, and subsequently, a higher hardness.

In addition to the oxide-based counter-body used in the current study, given the environmental conditions of testing (25 °C and 45% humidity), there

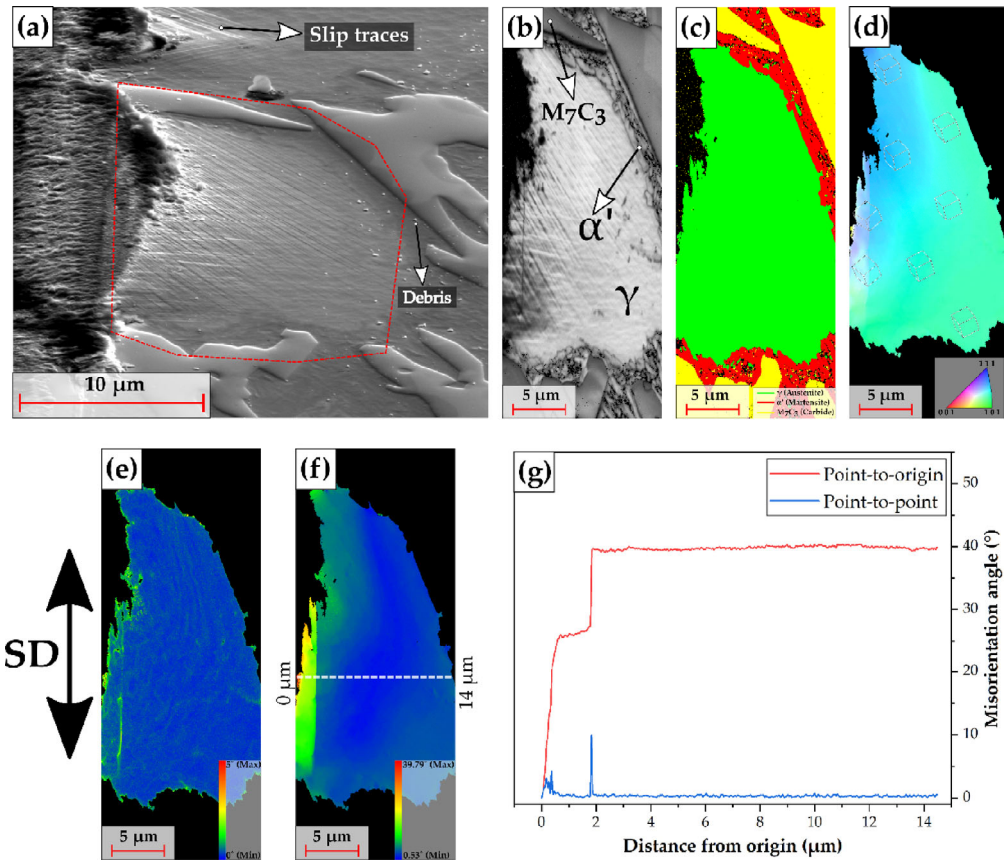

Fig. 8 (a) SEM SE micrograph of the region adjacent to the 20 N wear track where the slip traces and wear debris are marked for reference. The red dashed enclosure in (a) represents the area where the EBSD measurements were carried out, with (b) IQ map of the scanned region with the respective phases indicated, (c) phase map with the phases marked in different colours, (d) IPF map of the austenite matrix, overlayed with the local lattice rotation, (e) KAM map of the austenite matrix, and (f) GROD map of the austenite matrix. The variation of the misorientation angle across the austenite grain, following a path (0 → 14 μm) indicated by the dashed white line in (f), is graphically represented in (g).

Table 4 Matrix hardness adjacent to the wear tracks for the different loads.

Undeformed matrix hardness	Matrix hardness adjacent to wear track		
	5 N	15 N	20 N
336 ± 6	354 ± 7	375 ± 7	406 ± 19

is a high tendency for oxidation to occur [61]. This can be qualitatively appreciated in the EDS measurements. Figure 9(a) represents the SEM micrograph with a 50% overlay of the oxygen EDS concentration map for the wear track loaded at 20 N. It indicates the preferential accumulation of oxides at areas where the carbides were cracked and spalled. As the wear mechanism is abrasion-dominated, micro-cutting and ploughing contribute to surface deterioration resulting in the generation of numerous defects such as cracks and voids. This is a crucial factor to consider, as the rate of carbide removal essentially indicates the rate at which the oxides accumulate and eventually breakdown, altering the subsequent wear behaviour [37]. Additionally, Fig. 9(b) represents a closer view of the oxide accumulation at the location where the M_7C_3 carbide was ejected and from the elemental EDS concentration maps (Figs. 9(c)–9(e)), it can be deduced that oxide formed is iron-chromium oxide.

Another important aspect to take into consideration is the temperature rise at the contact interface (i.e., flash temperature) between the ball and the sample surface, as it could engender structural changes and/or phase transformations [59]. The flash temperature

was previously estimated by several researchers who demonstrated that under similar conditions, the rise in temperature was not significant [62–65]. Nevertheless, the peak flash temperature was calculated for the current study, based on the equations provided in Ref. [27] and it yielded a value of 17 K for the maximum load (20 N). This value can be considered very minimal for any thermally induced structural changes and/or phase transformations to occur [66].

Therefore, it can be conclusively stated that the thermal effects emanating during the dry sliding tests are negligible and the microstructural changes occurring around the wear track are predominately mechanically induced. It is also worth to note that as the diffusivity of oxygen is faster under mechanically driven conditions, oxidation is favoured [61, 67].

To observe the deformed microstructure directly beneath the wear track, transverse cuts were made across the track to obtain the desired cross-sections. Prior to cutting, the sample surface was protected by electrolytically coating it with Ni. The evaluation of the deformed microstructure and deformation depth, especially under the centre of the track would be beneficial for further analysis, as the maximum stress is experienced at the centre of the wear track width [57, 65].

Figure 10 represents the cross-section microstructure of the sample after subjecting it to sliding at the maximum load (20 N). It was observed that the EC closer to the worn surface had broken whereas the EC located further below are intact despite belonging to the same EC, as indicated in the orange dashed ellipse. Nevertheless, the presence of the uniformly coated Ni layer protected the carbides from ejection during the mechanical cross-sectioning and preparation.

The extent of deformation depth was visualized with the help of EBSD measurements. Figure 11(a) represents the SEM micrograph of the area underneath the wear track loaded at 20 N and Fig. 11(b) focuses on the area considered for the EBSD measurements. The scanned area was 10 μm × 120 μm. In addition to the IQ and the phase map, GROD analysis of the austenitic regions was carried out to obtain the variation in orientation within each grain with increasing cross-sectional depth, as represented in Fig. 11(e). Moreover, considering the undeformed austenite as the starting point, point-to-origin misorientation graph was plotted, as shown in Fig. 11(f).

The GROD maps in Fig. 11(e) clearly indicate the evolution of the microstructure directly beneath the wear surface. It starts with an increase in the misorientations within the grain and presence of slip bands as seen from the IQ maps. The austenite grain has clearly undergone plastic deformation owing to the stress exerted on it and moreover, it has extended across the carbide, towards the austenite grain located below. Comparing Fig. 10 with the IQ map in Fig. 11(c), it can be assessed that even though the eutectic carbides are broken, they are fairly supported by the highly dislocated austenitic matrix.

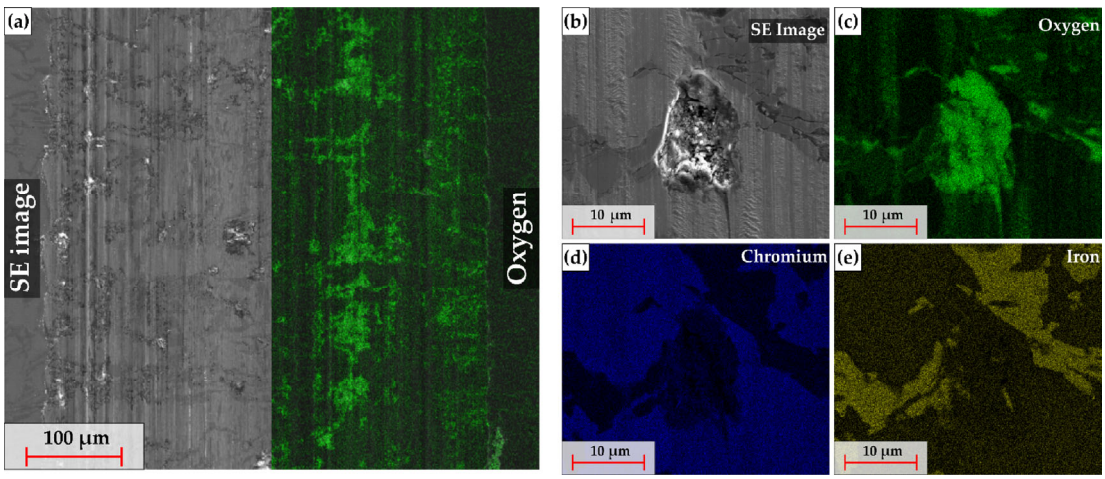

Fig. 9 (a) SEM micrograph in SE mode, with a 50% overlay of the oxygen EDS concentration map. The SEM SE micrograph of a magnified region in the wear track is represented in (b) whereas, the EDS concentration maps pertaining to oxygen, chromium, and iron, are indicated in (c), (d), and (e), respectively.

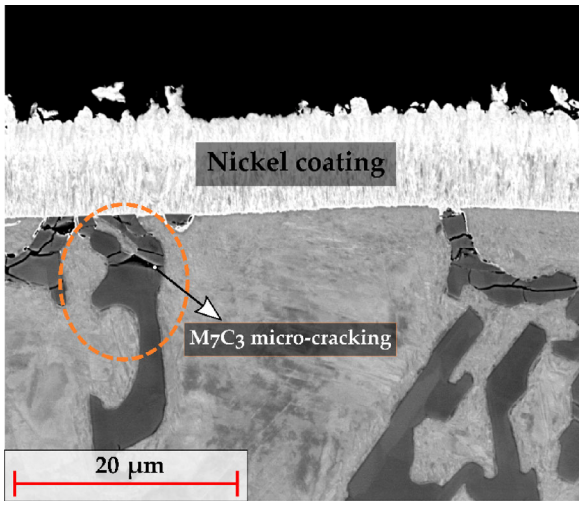

Fig. 10 Representative SEM micrograph in BSE mode of the cross section of the worn sample coated with Ni and loaded at 20 N. The orange dashed ellipse represents the carbide micro-cracking.

The point-to-origin misorientation plot indicates a maximum misorientation of about 13°, between the undeformed austenite and the austenite that was heavily deformed. As the strain experienced by the austenite decreases with increasing depth, from the above measurements, the deformation depth was estimated to be about 40 μm.

Additionally, the hardness of the austenitic matrix with increasing cross-sectional depth was measured using the Vickers method and is graphically represented in Fig. 12. An exponential decrease in hardness with increasing distance from the wear surface was seen. Likewise, it was observed that the matrix hardness rapidly approaches the mean undeformed matrix hardness after about 40 μm from the wear surface. This further signifies that the deformation depth is around 40 μm under the wear track loaded with 20 N.

In addition to the ability of the austenitic matrix to plastically deform owing to the dislocation interactions, its ability to transform to martensite (SIM) during service is also thought to contribute to the work hardening behaviour [37]. Nevertheless, the EBSD measurements on the wear track loaded maximally (20 N), did not show the presence of SIM at the deformed zone, adjacent (Fig. 8) or under the wear track (Fig. 11). This could be attributable to two reasons: (1) low strain rate in the present study and (2) the absence of shear band intersections, which act as potential nucleating sites for SIM formation [66, 68, 69]. In fact, the formation of shear bands in the microstructure usually stems from application of high strain rates which lead to local plastic instability. They are narrow regions of intense shear, resulting in inhomogeneous deformation, possessing orientations that are quite different from the parent matrix orientation [70]. Additionally, EBSD scanning over areas consisting of shear bands would lead to 'black

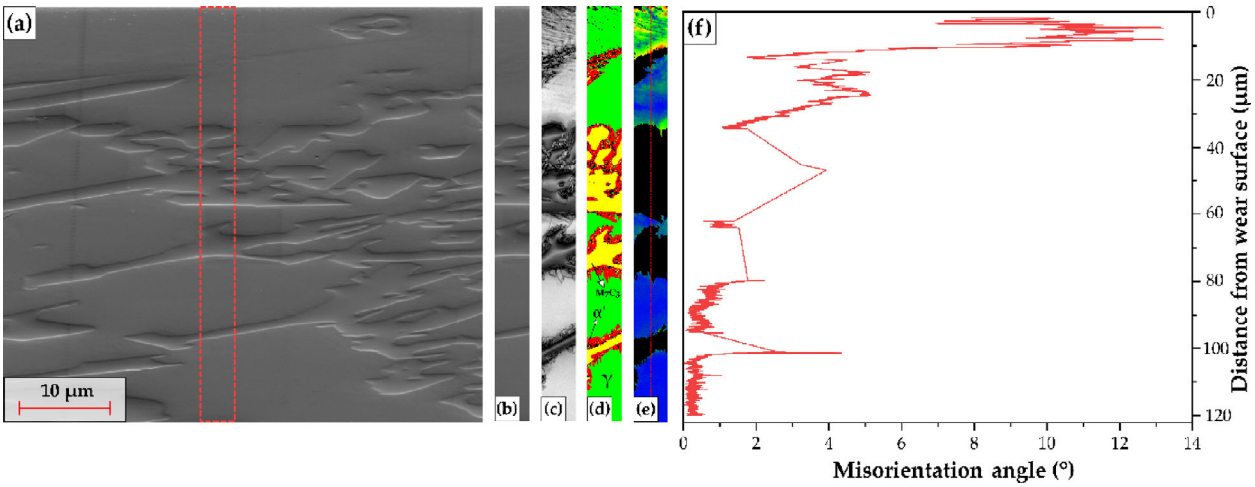

Fig. 11 (a) SEM micrograph in the SE mode of the area beneath the wear track loaded at 20 N, with the red dashed rectangle indicating the region (10 μm × 120 μm) considered for the EBSD measurements, as seen in (b). The IQ map of the scanned region is indicated in (c) whereas (d) represents the phase map, with the respective phases marked. The GROD maps of only the austenite regions are represented in (e). The red dashed vertical line within (e) indicates the line profile followed to obtain the misorientation angle as a function of the distance from the wear surface, as graphically represented in (f).

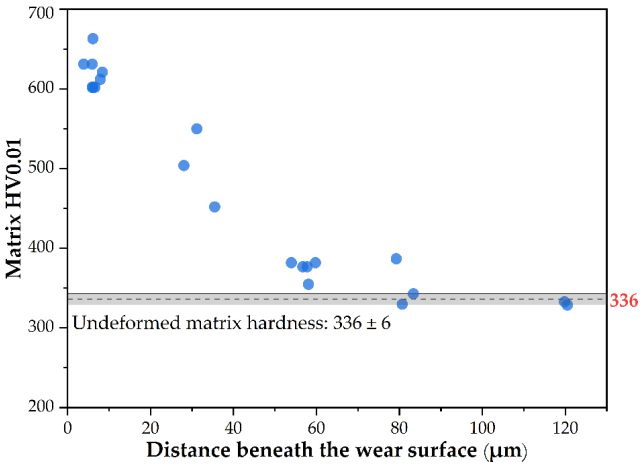

Fig. 12 Variation of matrix hardness with increasing distance from the surface of the wear track, loaded at 20 N.

spots' which is categorized as unable-to-index pixels [60].

In the current study, the formed 'lines' adjacent and underneath the wear track were inferred as slip traces based on the minimal orientation change between the slip band boundary and the austenitic matrix, as evidenced by EBSD. Moreover, it was possible to index the entire region that included the slip bands.

3.2 Wear rate and friction behaviour

The average wear volume (mm^3) calculated using the LEXT software and the wear rate, computed using Eq. (3), for each load is presented in Fig. 13. As expected, increasing the load led to an increase in the wear volume and consequently, the wear rate.

The increased load led to increased plastic deformation, dislocation activity, and the subsequent

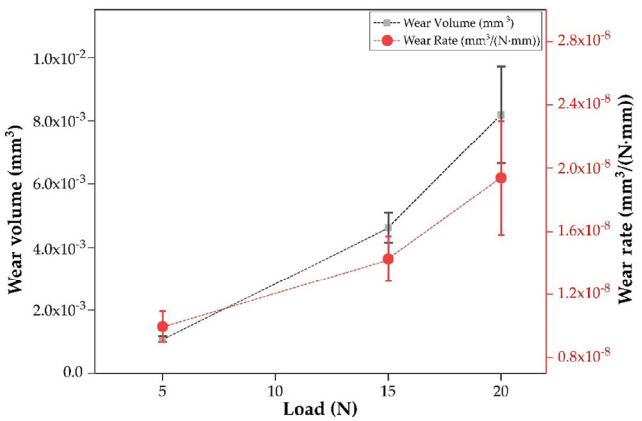

Fig. 13 Average wear volume and wear rate for each load.

activation of multiple slip systems resulting in a harder austenitic matrix, as evidenced from the hardness values adjacent to the wear track. Moreover, given that the hardness of the counter-body used is higher than the M_7C_3 EC, carbide micro-cracking ensued, leading to eventual ejection from the surface [25, 26]. This, in conjunction with the inability of the deformed, harder austenitic matrix to mechanically support the broken carbide fragments proved deleterious thereby, increasing the wear rate of the system. Furthermore, the oxidation taking place at the contact surface, preferentially accumulating at areas where the carbides have been removed, can also lead to increased wear activity, owing to its inherent brittleness.

The frictional behaviour of the samples under varying loads is expressed in terms of COF. The mean COF was plotted for each load and is represented in Fig. 14. In all cases, the curves initially rose quickly to reach a peak (running-in), before decreasing and reaching a steady state behaviour. The COF development within the first 100–200 cycles is similar for all cases, resembling a type b curve from those shown by Blau, which is a characteristic of non-lubricated dry metallic sliding systems [71]. This evolution is characterized by the removal of the initial asperities of both contact bodies, which results in higher local contact pressures and consequently, higher friction. The running-in behaviour could be further explained by the surface compositional changes caused due to the sliding action between the ball and the sample surface [52, 71]. Once conformality is achieved, the COF is settled at its steady state value. It is also interesting to note that the running-in and steady state behaviour is achieved earlier for the 5 N compared to the other loads and this can be due to the lower damage sustained by the ball thereby, establishing a stable contact faster. With increased load, the contact radius increases, and more dynamic processes transpire leading to a delay in reaching steady state. Nevertheless, the steady state COF is observed to be about 0.4 in all cases. In the case of the 20 N sample, stronger COF fluctuations are observed during the steady state. This might be related to the heterogeneity of the contact interface (Figs. 1(b) and 1(c)), consisting of a larger amount of the matrix and the carbides, which destabilize the COF development [72].

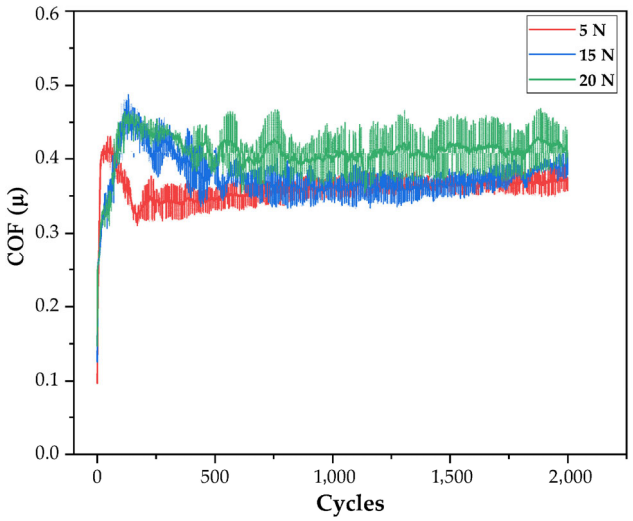

Fig. 14 Evolution of COF with increasing cycles for the differently loaded wear samples.

In both Figs. 13 and 14, the standard deviations pertaining to 20 N are more spread out. Given the increased propensity for carbide cracking, an oxide layer is formed (as suggested from Figs. 9(a) and 9(c)), which temporally increases in thickness until reaching a critical value. Upon reaching a critical thickness value, the shear stresses exerted during the wear is large enough to cause film rupture. This process continues, inducing a dynamic cycle of oxide layer formation and breakage [72]. The ensuing breakage also aids in the formation of wear debris which is visible in the SEM micrographs. Moreover, the geometrical orientation of the EC with respect to the sliding direction could also play a crucial role.

4 Conclusions

In the current study, dry-sliding linear reciprocating tribological tests were performed on a 26% Cr as-cast HCCI alloy with varying loads. The influence of increasing the load on the matrix microstructural evolution and the subsequent wear behaviour of the alloy was examined and the following conclusions were drawn.

1) The determination of P_C by analytical calculations were in accordance with the microstructural observations carried out using SEM. No evidence of plastic deformation of the austenitic matrix adjacent to the wear track was observed for 5 N, whereas the wear tracks loaded with 15 and 20 N showed the presence of slip traces (evidence of plastic deformation). Moreover, the number of activated slip systems increased with increasing load.

2) The deformation of the austenitic matrix beneath the wear track was successfully visualized using electron backscattered diffraction (EBSD). Grain reference orientation deviation (GROD) and image quality (IQ) maps indicated a decrease in the misorientation and deformation, respectively, with increasing depth.

3) At loads below P_C, adhesion was the dominant wear mechanism with signs of mild abrasion, but at loads equal to and above P_C, a shift was observed with the dominant wear mechanism being abrasion. The increased tendency for spalling combined with the strain hardening proclivity of the austenitic matrix led to poor mechanical stability being imparted.

4) The shift in the dominant wear mechanism was also reflected in the wear volume and the wear rate, which increased with increasing load.

5) The running-in and steady state behaviour is achieved earlier for samples tested with 5 N, compared to the other loads. This can be attributed to the stable contact established by the lower load, and the increased tendency for plastic deformation and associated effects at higher loads.

To sum up, Hertzian contact theory was used to determine the critical load based on the materials' properties and accordingly, the loads were defined. The calculated values were in good correspondence with the microstructural and/or morphological observations. Moreover, a clear shift in the dominant wear mechanism was identified owing to the behaviour of the austenitic matrix and the carbide during the wear process. Consequently, this methodology can be further extended to other alloys in the high chromium cast iron (HCCI) family to establish the load limits and to better understand the interaction between the different components in the system.

Acknowledgements

The present work is supported by funding from the Deutsche Forschungsgemeinschaft (DFG, project: GU 2102/2-1). The authors would like to thank Martin

Duarte from Tubacero S.A. for providing the materials, and Prof. Christian Motz for granting access to perform nanoindentation measurements. Additionally, U.P.N. is grateful to DAAD for the financial support.

References

[1] Tabrett C P, Sare I R, Ghomashchi M R. Microstructure-property relationships in high chromium white iron alloys. *Int Mater Rev* **41**(2): 59–82 (1996)

[2] ASTM International. Standard Specification for Abrasion Resistance Cast Irons: ASTM Standard A 532/A 532M-93a. West Conshohocken, PA, USA, 2003

[3] Xu H, Xu Y, He Y, et al. Two-stage warm cross rolling and its effect on the microstructure, texture and magnetic properties of an Fe-6.5 wt% Si non-oriented electrical steel. *J Mater Sci* **55**(26): 12525–12543 (2020)

[4] Maratray F. Choice of appropriate compositions for chromium-molybdenum white irons. *AFS Trans* **79**: 121–124 (1971)

[5] Llewellyn R J, Yick S K, Dolman K F. Scouring erosion resistance of metallic materials used in slurry pump service. *Wear* **256**(6): 592–599 (2004)

[6] Karantzalis E, Lekatou A, Mavros H. Microstructure and properties of high chromium cast irons: Effect of heat treatments and alloying additions. *Int J Cast Met Res* **22**(6): 448–456 (2009)

[7] Wiengmoon A, Pearce J T H, Chairuangsri T. Relationship between microstructure, hardness and corrosion resistance in 20 wt%Cr, 27 wt%Cr, and 36 wt%Cr high chromium cast irons. *Mater Chem Phys* **125**(3): 739–748 (2011)

[8] Rivlin V G. 14: Critical review of constitution of carbon–chromium–iron and carbon–iron–manganese systems. *Int Met Rev* **29**(1): 299–327 (1984)

[9] Maratray F, Usseglio-Nanot R. Factors affecting the structure of chromium and chromium-molybdenum white irons. *Climax Molybdenum SA*, 1971: 1–32

[10] Pearce J T H. Structure and wear performance of abrasion resistance chromium white cast irons. *Trans Am Foundrymen's Soc* **92**: 599–622 (1984)

[11] Wiengmoon A. Carbides in high chromium cast irons. *Naresuan Univ Eng J* **6**(1): 64–70 (2011)

[12] Doğan Ö N, Hawk J A. Effect of carbide orientation on abrasion of high Cr white cast iron. *Wear* **189**(1–2): 136–142 (1995)

[13] Fulcher J K, Kosel T H, Fiore N F. The effect of carbide volume fraction on the low stress abrasion resistance of high Cr–Mo white cast irons. *Wear* **84**(3): 313–25 (1983)

[14] Bedolla-Jacuinde A, Correa R, Mejía I, Quezada J G, Rainforth W M. The effect of titanium on the wear behaviour of a 16%Cr white cast iron under pure sliding. *Wear* **263**(1–6): 808–820 (2007)

[15] Bedolla-Jacuinde A, Guerra F V., Mejía I, Zuno-Silva J, Rainforth M. Abrasive wear of V–Nb–Ti alloyed high-chromium white irons. *Wear* **332–333**: 1006–1011 (2015)

[16] Correa R, Bedolla-Jacuinde A, Zuno-Silva J, Cardoso E, Mejía I. Effect of boron on the sliding wear of directionally solidified high-chromium white irons. *Wear* **267**(1–4): 495–504 (2009)

[17] Cortés-Carrillo E, Bedolla-Jacuinde A, Mejía I, Zepeda C M, Zuno-Silva J, Guerra-Lopez F V. Effects of tungsten on the microstructure and on the abrasive wear behavior of a high-chromium white iron. *Wear* **376–377**: 77–85 (2017)

[18] Archard J F. Contact and rubbing of flat surfaces. *J Appl Phys* **24**(8): 981–988 (1953)

[19] Zum Gahr K H, Doane D V. Optimizing fracture toughness and abrasion resistance in white cast irons. *Metall Trans A* **11**(4): 613–620 (1980)

[20] Asensio J, Pero-Sanz J A, Verdeja J I. Microstructure selection criteria for cast irons with more than 10 wt% chromium for wear applications. *Mater Charact* **49**(2): 83–93 (2002)

[21] Laird G, Gundlach R, Rohrig K. *Abrasion-resistant Cast Iron Handbook*. Schaumburg (USA): American Foundry Society, 2000.

[22] Avery H S. The measurement of wear resistance. *Wear* **4**(6): 427–449 (1961)

[23] Doğan Ö N, Hawk J A, Laird G. Solidification structure and abrasion resistance of high chromium white irons. *Metall Mater Trans A Phys Metall Mater Sci* **28**(6): 1315–1328 (1997)

[24] Turenne S, Lavallée F, Masounave J. Matrix microstructure effect on the abrasion wear resistance of high-chromium white cast iron. *J Mater Sci* **24**(8): 3021–3028 (1989)

[25] Gundlach R B, Parks J L. Influence of abrasive hardness on the wear resistance of high chromium irons. *Wear* **46**(1): 97–108 (1978)

[26] Zum Gahr K H, Eldis G T. Abrasive wear of white cast irons. *Wear* **64**(1): 175–194 (1980)
[27] Hutchings I M. *Tribology: Friction and Wear of Engineering Materials*. Oxford (UK): Butterworth-Heinemann, 1992.
[28] Porter D A, Easterling K E, Sherif M Y. *Phase Transformations in Metals and Alloys*. Boca Raton (USA): CRC Press, 2009.
[29] Tabrett C P, Sare I R. Effect of high temperature and sub-ambient treatments on the matrix structure and abrasion resistance of a high-chromium white iron. *Scr Mater* **38**(12): 1747–1753 (1998)
[30] Higuera-cobos O F, Dumitru F-D, Mesa-Grajales D H. Improvement of abrasive wear resistance of the high chromium cast iron ASTM A-532 through thermal treatment cycles. *Rev Fac Ing* **25**(41): 93–103 (2015)
[31] Guitar M A, Suárez S, Prat O, Duarte Guigou M, Gari V, Pereira G, et al. High chromium cast irons: Destabilized-subcritical secondary carbide precipitation and its effect on hardness and wear properties. *J Mater Eng Perform* **27**(8): 3877–3885 (2018)
[32] Inthidech S, Kosasu P, Yotee S, Matsubara Y. Effect of repeated tempering on abrasive wear behavior of hypoeutectic 16 mass% Cr cast iron with molybdenum. *Mater Trans* **54**(1): 28–35 (2013)
[33] Abdel-Aziz K, El-Shennawy M, Omar A A. Microstructural characteristics and mechanical properties of heat treated high-cr white cast iron alloys. *Int J Appl Eng Res* **12**(14): 4675–4686 (2017)
[34] Watson J D, Mutton P J, Sare I R. Abrasive wear of white cast irons. *Met forum* **3**(1): 74–88 (1980)
[35] Scandian C, Boher C, de Mello J D B, Rézaï-Aria F. Effect of molybdenum and chromium contents in sliding wear of high-chromium white cast iron: The relationship between microstructure and wear. *Wear* **267**(1–4): 401–408 (2009)
[36] Pintaude G, Bernardes F G, Santos M M, Sinatora A, Albertin E. Mild and severe wear of steels and cast irons in sliding abrasion. *Wear* **267**(1–4): 19–25 (2009)
[37] Bedolla-Jacuinde A, Rainforth W M. Electron microscopy analysis on the worn surface of a high-chromium white iron during dry sliding contact. *Mater Res Soc Symp Proc* **843**: 299–304 (2005)
[38] Pokusová M, Berta I, Šooš Ľ. Abrasion resistance of as-cast high-chromium cast iron. *Sci Proc* **22**(1): 74–79 (2014)
[39] Nayak U P, Guitar M A, Mücklich F. A comparative study on the influence of chromium on the phase fraction and elemental distribution in as-cast high chromium cast irons: Simulation vs. experimentation. *Metals (Basel)* **10**(1): 30 (2020)
[40] Nayak U P, Guitar M A, Mücklich F. Evaluation of etching process parameter optimization in the objective specific microstructural characterization of as-cast and heat treated HCCI alloy. *Prakt Metallogr* **57**(10): 688–713 (2020)
[41] Laird G, Powell G L F. Solidification and solid-state transformation mechanisms in Si alloyed high-chromium white cast irons. *Metall Trans A* **24**(4): 981–988 (1993)
[42] Carpenter S D, Carpenter D, Pearce J T H. XRD and electron microscope study of an as-cast 26.6% chromium white iron microstructure. *Mater Chem Phys* **85**(1): 32–40 (2004)
[43] Greenwood J A, Williamson J B P. Contact of nominally flat surfaces. *Proc R Soc London A* **295**(1442): 300–319 (1966)
[44] Jackson R L, Green I. A finite element study of elasto-plastic hemispherical contact against a rigid flat. *J Tribol* **127**(2): 343–354 (2005)
[45] Tabor D. *The Hardness of Metals*. Oxford (UK): Claredon Press, 1951.
[46] Kugel Pompel. Datenblatt Data sheet, https://www.kugelpompel.at/de/Prazisionskugeln/kugeln/aluminiumoxydkeramikkugel-3000-mm-g28, 2020.
[47] Auerkari P. Mechanical and physical properties of engineering alumina ceramics. Technical Research Centre of Finland, Espoo, Finland, 1996: 26.
[48] ASM International. ASM Handbook: Properties and Aelection: Irons, Steels, and High Performance Alloys. Novelty (USA): ASM International, 2001.
[49] Rabinowicz E, Dunn L A, Russell P G. A study of abrasive wear under three-body conditions. *Wear* **4**(5): 345–355 (1961)
[50] Atabaki M M, Jafari S, Abdollah-pour H. Abrasive wear behavior of high chromium cast iron and hadfield steel—A comparison. *J Iron Steel Res Int* **19**(4): 43–50 (2012)
[51] Penagos J J, Pereira J I, Machado P C, Albertin E, Sinatora A. Synergetic effect of niobium and molybdenum on abrasion resistance of high chromium cast irons. *Wear* **376–377**: 983–992 (2017)
[52] Hurricks P L. Some Metallurgical Factors Controlling the adhesive and abrasive wear resistance of steels: A review. *Wear* **26**: 285–301 (1973)
[53] Schwartz A J, Kumar M, Adams B L, Field D P. *Electron Backscatter Diffraction in Materials Science*. Boston (USA): Springer US, 2009.
[54] Reza Abbaschian, Abbaschian L, Reed-Hill R E. *Physical Metallurgy Principles*. Stamford (USA): Cengage Learning, 2008.
[55] Hull D, Bacon D J. *Introduction to Dislocations*. Oxford (UK): Elsevier Ltd., 2011.
[56] Di Gioacchino F, Quinta Da Fonseca J. An experimental study of the polycrystalline plasticity of austenitic stainless steel. *Int J Plast* **74**: 92–109 (2015)
[57] Menezes P L, Ingole S P, Nosonovsky M, Kailas S V., Lovell M R. *Tribology for Scientists and Engineers: From Basics to Advanced Concepts*. New York (USA): Springer-Verlag New York, 2013.
[58] Ghabchi A. Wear resistant carbide-based thermal sprayed coatings: Process, properties, mechanical degradation and wear. Ph.D. Thesis. New York (USA): Stony Brook University, 2011.
[59] Chen L, Persson J, Ståhl J E, Zhou J M. Nano-scratching resistance of high-chromium white cast iron and its correlation with wear of cBN tool in machining. *J Superhard Mater* **39**(5): 365–372 (2017)

[60] Kazemipour M, Shokrollahi H, Sharafi S. The influence of the matrix microstructure on abrasive wear resistance of heat-treated Fe–32Cr–4.5C wt% hardfacing alloy. *Tribol Lett* **39**(2): 181–192 (2010)
[61] Sullivan J L, Quinn T F J, Rowson D M. Developments in the oxidational theory of mild wear. *Tribol Int* **13**(4): 153–158 (1980)
[62] So H, Yu D S, Chuang C Y. Formation and wear mechanism of tribo-oxides and the regime of oxidational wear of steel. *Wear* **253**(9–10): 1004–1015 (2002)
[63] Ashby M F, Abulawi J, Kong H S. Temperature maps for frictional heating in dry sliding. *Tribol Trans* **34**(4): 577–582 (1991)
[64] Lingard S. Estimation of flash temperatures in dry sliding. *Proc Inst Mech Eng Part C J Mech Eng Sci* **198**(2): 91–97 (1984)
[65] Grützmacher P G, Rammacher S, Rathmann D, Motz C, Mücklich F, Suarez S. Interplay between microstructural evolution and tribo-chemistry during dry sliding of metals. *Friction* **7**(6): 637–650 (2019)
[66] Levitas V I, Idesman A V, Olson G B. Continuum modeling of strain-induced martensitic transformation at shear-band intersections. *Acta Mater* **47**(1): 219–233 (1998)
[67] Rigney D A. Transfer, mixing and associated chemical and mechanical processes during the sliding of ductile materials. *Wear* **245**(1–2): 1–9 (2000)
[68] Talonen J, Hänninen H. Formation of shear bands and strain-induced martensite during plastic deformation of metastable austenitic stainless steels. *Acta Mater* **55**(18): 6108–618 (2007)
[69] Mao B, Chu S, Wang S. Effect of grain size on the friction-induced martensitic transformation and tribological properties of 304 austenite stainless steel. *Metals (Basel)* **10**(9): 1–14 (2020)
[70] Gottstein G. *Physical Foundations of Materials Science*. Berlin (Germany): Springer Berlin Heidelberg, 2004.
[71] Blau P J. Interpretations of the friction and wear break-in behavior of metals in sliding contact. *Wear* **71**(1): 29–43 (1981)
[72] Blau P J. On the nature of running-in. *Tribol Int* **38**(11–12): 1007–1012 (2005)

U. Pranav NAYAK. He received his B.Tech. degree in metallurgical and materials engineering in 2014 from the National Institute of Technology Karnataka (NITK), Mangalore, India. He obtained his M.Sc. degree in materials science under the Erasmus Mundus FAME Program in 2016. Since 2018, he is a doctoral candidate at the Chair of Functional Materials (Saarland University) with his research focusing on the microstructure tailoring in high chromium cast iron (HCCI) alloys through heat treatment design.

María Agustina GUITAR. She received her electromechanical engineering degree in 2005 from the National Technical University in Argentina, her master degree in materials science in 2007 from the National University of San Martin in Argentina, and her Ph.D. degree in materials science and engineering in 2014 from Saarland University, Germany. She currently leads the Steel and Ferrous-based Materials Group at the Chair of Functional Materials (Saarland University). Her research focuses in tailoring the microstructure of high chromium cast irons for performance optimization.

VI. Development of a Protective Coating for Evaluating the Sub-surface Microstructure of a Worn Material

U. Pranav Nayak[1], Johannes Webel[1], Valentin Pesnel[2], Frank Mücklich[1], María Agustina Guitar[1]

[1] Department of Materials Science and Engineering, Saarland University, 66123 Saarbrücken, Germany

[2] EEIGM, Université de Lorraine, 54000 Nancy, France

Published in "***Tribology Letters***" (2021) *(IF (2023): 3.327)*

Accessible online at: *https://doi.org/10.1007/s11249-022-01683-3*

Own contribution: Conceptualization and methodology; sample preparation; experimentation; coatings characterization; scientific discussion; paper writing – original draft preparation

Tribology Letters (2021) 69:165
https://doi.org/10.1007/s11249-021-01541-8

TRIBOLOGY METHODS

Development of a Protective Coating for Evaluating the Sub-surface Microstructure of a Worn Material

U. Pranav Nayak[1] · Johannes Webel[1] · Valentin Pesnel[3] · Frank Mücklich[1,2] · María Agustina Guitar[1]

Received: 9 September 2021 / Accepted: 2 November 2021

Abstract
In the current study, electrolytic deposition using two different electrodes, copper (Cu) and nickel (Ni) was investigated with the aim of protecting the worn surface during mechanical sectioning and polishing, for a posterior examination of the sub-surface microstructure. The efficacies of the two coatings were visually assessed based on its adhesivity and the ability to protect the wear tracks of an as-cast 26% Cr high chromium cast iron (HCCI) alloy. It was observed that electrodeposition using Cu as the electrode was ineffective owing to a poor adhesivity of the coating on the HCCI surface. The coating had peeled off at several regions across the cross-section during the mechanical sectioning. On the other hand, Ni electroplating using Ni strike as the electrolyte was successfully able to protect the wear track, and the sub-surface characteristics of the wear track could be clearly visualized. A uniform coating thickness of about 8 µm was deposited after 30–40 min with the current density maintained between 1 and 5 A/dm^2. The presence of the Ni coating also acted as a protective barrier preventing the ejection of the broken carbide fragments underneath the wear track.

Keywords Surface protection · Electrolytic deposition · Nickel coating · Sub-surface microstructure/characterization · Unlubricated sliding · Particle ejection · High chromium cast iron

1 Introduction

Nearly a quarter of the world's energy produced is spent in overcoming issues related to tribology [1]. Moreover, the failures associated with friction and wear in the mining and mineral sector alone constitute for about 6% of the annual global energy consumption [2]. To mitigate the monetary and energy loss encountered during the operation, researchers are constantly seeking to understand the wear mechanisms and subsequently, improve the material in use [3, 4]. In addition to employing new materials apt for wear-related applications, existing materials can be microstructurally modified, or coated with a suitably wear resistant material such as high chromium cast iron (HCCI) to increase their longevity [5].

HCCIs are alloys containing a dispersion of hard M_7C_3 (M: Cr, Fe) type carbides in a supportive, modifiable matrix (austenite, martensite, ferrite), enabling it to be used in a wide variety of applications in the mining and mineral sector, such as ball mill liners, pulverizing equipment, feeders, etc. [6–9].The versatility in the alloy's applicability in wear and/or corrosion resistant applications stems from the flexibility to vary the amount of chromium during the alloy's solidification [10–12].

A thorough characterization of the worn surface is imperative for understanding the ensuing wear mechanisms aiding in the subsequent development of better wear resistant materials. In addition to the wear-induced microstructural modifications taking place at the sample surface, examining the microstructure underneath the wear track would be beneficial for further analysis [13, 14]. The interaction of the various phases during the wear adjacent and underneath the wear track can shed further light as the wear resistance is not an inherent property. In the specific case of HCCIs, the overall wear behaviour is a synergistic contribution between the hard carbide and the matrix that surrounds it [3, 11].

✉ U. Pranav Nayak
pranav.nayak@uni-saarland.de

[1] Department of Materials Science, Saarland University, Campus D 3.3, 66123 Saarbrücken, Germany

[2] Materials Engineering Center Saarland (MECS), Campus D3.3, 66123 Saarbrücken, Germany

[3] Ecole Européenne d'ingénieurs en Génie des Matériaux (EEIGM), Université de Lorraine, 54000 Nancy, France

Published online: 13 November 2021

As the maximum stress is experienced at the centre of the wear track [15, 16], it would be necessary to make a transverse cut across the entire track. Using a focused ion beam (FIB) to cut such a large section is both time and resource intensive [17]. In this regard, mechanically sectioning the sample would facilitate a complete observation of the sub-surface microstructure beneath the wear track. As the mechanical sectioning of the samples might induce certain undesired microstructural modifications, it is essential that the wear track and the underlying microstructure be suitably protected.

Electrodeposition, also known as electroplating, has long been carried out on various materials to impart certain characteristic properties [18, 19]. It involves passage of a direct current between the substrate and the metal electrode whilst they are immersed in a solution of the metal. It is one of the few surface-finishing techniques wherein the requirements of both functional and aesthetic applications can be satisfied [20, 21]. Moreover, owing to the high degree of controllability obtainable by varying the experimental parameters, it is gaining a lot of attention from the scientific community [22, 23]. Indeed, the deposit characteristics are highly dependent on various factors such as current density, deposition time and temperature, bath composition, pH, etc. [24, 25].

Amongst a multitude of potential electrodes, copper (Cu) and nickel (Ni) are widely used owing to their availability and versatility in the deposition process [2, 20, 22, 26]. To prevent inaccurate analysis and erroneous interpretation, electroless Ni coating was employed in coating the oxide layers generated during the wear of a TWIP steel [13]. Moreover, edge retention during the metallographic preparation of two porous implants was also possible by electroless Ni coating [27]. This sheds light on the versatility of the coating methodology. Furthermore, the importance of protecting the sub-surface during mechanical sectioning can be clearly visualized in [14] where a lack of surface protection resulted in the ejection of the carbide. Therefore, it is imperative to coat the worn surface to protect the deformed sub-surface generated during the tribological testing.

The main objective of the current work was to develop a simple, yet effective approach to coat the worn surface of an HCCI sample in order to investigate the deformed microstructure underneath the wear track. Subsequently, electrodeposition was carried out using Cu and Ni as the electrodes, and their efficacies were tested. Different parameters were varied throughout the course of obtaining an optimal coating on the wear track to protect it from the ensuing mechanical sectioning and damage. Optical microscopy (OM) and scanning electron microscopy (SEM) were employed to visually assess the uniformity and adhesivity of the coatings. Additionally, EDS was used to chemically map the cross-section containing both the coating and the sub-surface. Finally, electron backscattered diffraction (EBSD) measurements were carried out to observe the deformation behaviour of the HCCI alloy underneath the wear track.

2 Materials and Methodology

For this work, an as-cast 26% Cr HCCI alloy (~Cr: 26.6 wt%; C: 2.5 wt%; Fe: Bal.), measuring $12 \times 15 \times 10$ mm^3 was subjected to dry sliding linear reciprocating tribological tests. The tests were conducted using a ball-on-disc micro-tribometer (CSM Instruments), while the whole setup was placed in an environmental chamber to control the temperature and humidity. 3 mm alumina (Al_2O_3) balls (99.00–99.99% purity; Grade GD28) was used as the sliding counter-body. The bulk chemical composition and the microstructural characterization of the HCCI alloy are given in [28], whereas the specifics of the tribological tests are described in [29]. The microstructure of the as-cast sample composed of M_7C_3 (~30%) (M: Cr, Fe) eutectic carbides (EC) dispersed in an austenitic matrix (γ) (~60%), and a thin layer of martensite (α′) (~10%) sandwiched between the EC and γ.

Two electrolytic depositions with Cu and Ni as electrodes were tested. Initially, the electrodeposition with Cu was tested owing to the ease of availability and non-toxicity in handling the Cu electrolyte and later, with Ni. A generator was used to apply of voltage of up to 1.5 V whereas a multimeter was used to monitor the current during the process. Figure 1 represents the schematic of the Ni electrolytic coating setup. Prior to coating, the worn sample was de-embedded from the resin and then positioned about 1 cm away from the electrode making sure the surfaces are parallel to each other.

Different parameters were varied throughout the course of obtaining an optimal coating on the wear track to protect it from the ensuing mechanical sectioning and damage. Tables 1 and 2 represent the various coating parameter variations employed with Cu and Ni, respectively. During both the electrodeposition processes, a voltage of 1.5 V and a current density (J) between 1 and 5 A/dm^2 was maintained.

For the Ni electro-deposition, a Ni strike electrolyte (hydrochloric acid, nickel dichloride) from Schlötter GmbH was used. It is important to note that the Ni strike electrolyte is highly toxic and hence, proper protective gear and precautionary measures have to be considered.

The coated samples were then mechanically sectioned to obtain the transverse section which contains the sub-surface region underneath the wear track. An abrasive disk (Struers 50A20) rotating at 2500 rpm, with a feed rate of 0.03 mm/s was used to obtain the cross-section of the coated samples. The transverse section was embedded in a conductive resin (WEM REM, Cloeren Technology GmbH, Germany) and metallographically prepared following the instructions

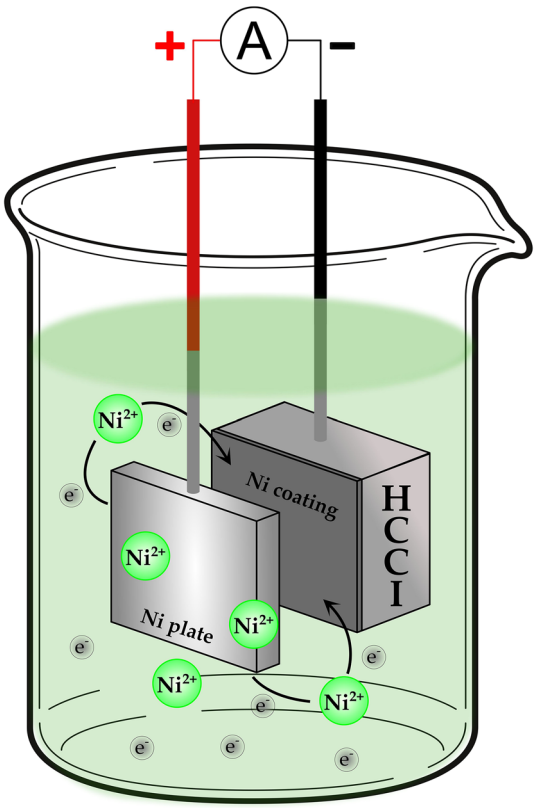

Fig. 1 Schematic of the nickel electrodeposition process

Table 1 Cu electrodeposition parameters

Coating	Electrolyte	Time (min)
Cu #1	120 mL H_2O, 24 g $CuSO_4{\cdot}5H_2O$	10
Cu #2	120 mL H_2O, 24 g $CuSO_4{\cdot}5H_2O$	20
Cu #3	3 min gold sputtering on worn surface + **Cu #1**	
Cu #4	240 g/L H_2SO_4, 110 g/L $CuSO_4{\cdot}5H_2O$, H_2O	5
Cu #5	240 g/L H_2SO_4, 110 g/L $CuSO_4{\cdot}5H_2O$, H_2O	10
Cu #6	3 min gold sputtering on worn surface + **Cu #4**	

Cu #1 and Cu #4 represents the specifics of the electrolyte used as can be seen in the first row and fourth row, are given in bold

Table 2 Ni electrodeposition parameters

Coating	Electrolyte	Time (min)
Ni #1	Nickel strike (HCl + NiCl2)	3
Ni #2		40
Ni #3		30

presented in [30] to obtain a scratch-free, mirror polished surface.

The quality of the coatings was assessed using a Leica CTR6000 optical microscope (Leica Camera AG, Wetzlar, Germany) coupled with a Jenoptik CCD camera (Jenoptik AG, Jena, Germany), and FEI Helios Nanolab 600 field emission scanning electron microscope (FE-SEM; ThermoFisher Inc., Waltham, MA, USA, formerly FEI Company, Hillsboro, OR, USA). The SEM was operated at an acceleration voltage of 5–15 kV and a beam current of 1.4 nA. Moreover, a high sensitivity backscattered electron detector (vCD) was used to obtain a better contrast between the phases. Finally, energy-dispersive X-ray spectroscopy (EDS) was used to chemically map the cross-section containing both the coating and the sub-surface.

The local deformation and the strain distribution within the austenitic matrix underneath the wear track was investigated by electron backscatter diffraction (EBSD). The measurements were performed at an acceleration voltage of 20 kV and a beam current of 11 nA, using a field emission gun in the FE-SEM workstation equipped with an EDAX Hikari EBSD camera (EDAX Corporation, Mahwah, NJ, USA). Additionally, misorientation profile analysis was performed within the austenitic region to obtain the orientational variation, with increasing cross-sectional depth. The EBSD data was analysed using the Orientation Imaging Microscopy (OIM™ v. 7) Data Analysis software by EDAX Corporation.

3 Results and Discussion

The passage of an electric current between two electrodes immersed in an electrolyte is the essentiality of electrodeposition. During the electrolytic process, metal atoms lose electrons at the anode (oxidation) and get deposited at the cathode (reduction). The electrolyte contains ions, which migrate towards the electrodes with the opposite charge (positively charged ions to the cathode and negatively charged ions to the anode). The ion mobility results in the generation of a current flow, owing to the transfer of electrons, thus completing the electrical circuit [24, 26, 31]. Equations 1 and 2 represent the general half-cell reactions that take place at the anode and the cathode, respectively, where M is the metal atom, M^{n+} is the metal ion, n is the valency, and e^- is the electron charge.

$$M \rightarrow M^{n+} + n\,e^- \quad (1)$$

$$M^{n+} + n\,e^- \rightarrow M \quad (2)$$

The properties and structures of the electrodeposits are closely related to the electrolyte composition and electroplating parameters [26, 32]. In the current study, only the type of electrode (Cu/Ni), electrolyte, and time was varied to reduce the degrees of freedom.

3.1 Copper Electrodeposition

Figure 2 represents the optical micrograph (OM) of the samples' sub-surface after Cu electrodeposition using recipe #4 (Table 1). The bright field (BF) (Fig. 2a) mode of the optical microscope was used in conjunction with the differential interference contrast (DIC) mode (Fig. 2b) to reveal the various characteristics of the sub-surface and the Cu coating. The different phases present in the HCCI sample is indicated in Fig. 2a, whereas the inherent topography present between the EC and the matrix was visualized using the DIC mode, indicated in Fig. 2b [33, 34]. From Fig. 2b, a lack of adhesion of the Cu coating with the HCCI substrate was observed. Consequently, the coating was peeled off at several regions across the cross-section during the mechanical sectioning. The dashed yellow ellipse in Fig. 2a is indicative of one such incidence. Despite a lack of adhesivity, the coating thickness was fairly uniform across the surface, and it was measured to be 6.5 ± 0.3 µm.

During the electrodeposition process, oxidation of Cu takes place at the anode resulting in the generation of copper ions (Cu^{2+}) and free electrons (e^-). The copper salt ($CuSO_4 \cdot 6H_2O$) present in the electrolyte dissociates into the respective copper and sulphate ions (SO_4^{2-}). When the potential is applied, the mobile copper ions combine with the free electrons to form metallic copper at the cathode (HCCI substrate). In addition to the generation of copper ions, the dissociation of water also generates hydrogen ions (H^+) ions. As the cationic activity of Cu^{2+} ions are higher than H^+ ions, its tendency to gain electrons is higher and hence, Cu is formed at the cathode [24, 25]. Similarly, the anionic activity of OH^- is higher than SO_4^{2-} and therefore, loses its electron more readily. Finally, the H^+ ion combines with the SO_4^{2-} ion to form H_2SO_4, a colourless liquid.

The lack of adhesion could be attributed to: (i) the sulphate bath's acidity combined with the high activity of Cu resulting in the formation of a non-adherent immersion deposit upon solution contact [24] and/or (ii) the presence of an inherent passive oxide film on the HCCI substrate and the inability of the sulphate-based electrolyte to destroy it. The passive oxide layer could hinder the formation of a mechanically stable copper/oxide interface. The HCCI family of alloys owe their superior wear and corrosion resistance to the presence of chromium, which contributes to the formation of hard chromium-based carbides within the microstructure, and an impervious oxide film on the surface [6, 7]. This allows them to be used in applications in the mining and mineral industries, where both dry and/or wet corrosive environments are encountered [8, 11, 35]. Additionally, it was reported in [36] that a chromium content of above 16 wt% will generate an oxide layer of the type $FeO \cdot Cr_2O_3$. In the current alloy, the bulk Cr composition is about 26 wt% which is distributed between the EC and the matrix. It is worth to note that the formation of the oxide film is dependent on the chromium content present in the matrix alone [7, 36]. In a previous study [28], the chromium content of the

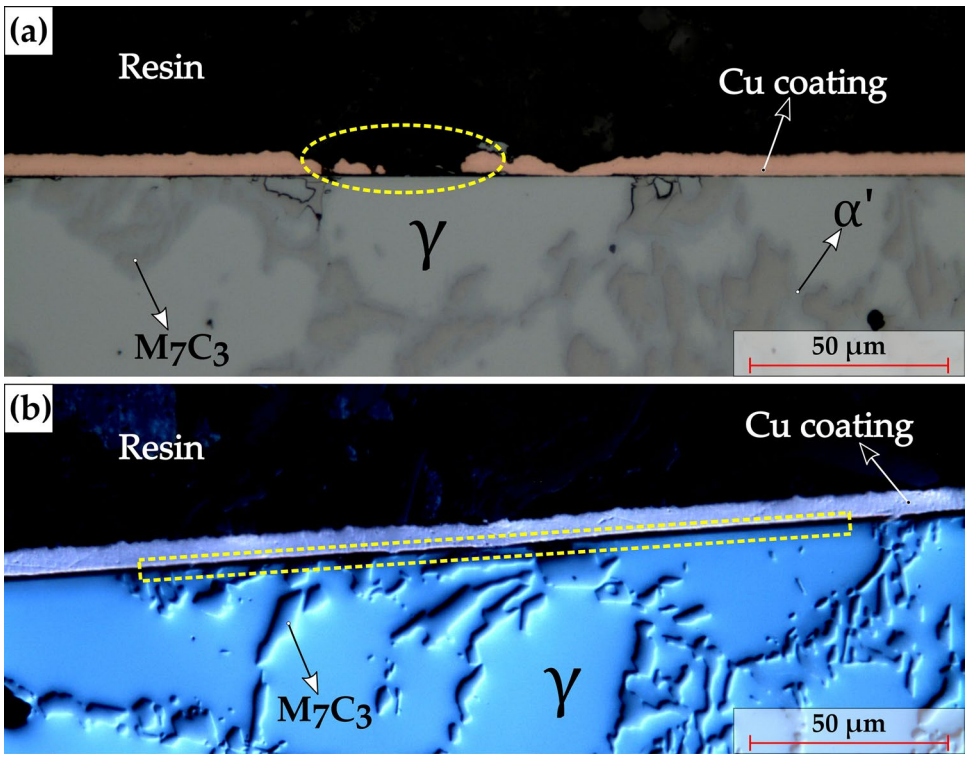

Fig. 2 OM of the cross-section of the sample surface after Cu #4 electrodeposition where: **a** BF micrograph indicating the various phases within the HCCI microstructure as well as the Cu coating. A non-uniformity in the coating is represented by the dashed yellow ellipse and **b** DIC micrograph wherein the dashed yellow rectangle indicates a lack of adhesion of the Cu coating with the HCCI substrate (Color figure online)

matrix was calculated using electron probe micro analysis (EPMA) and MatCalc simulations, and it was found to be around ~ 18 wt%. Hence, in the current alloy, an oxide film consisting of a complex mixture of iron and chromium can be expected. Although an iron-based oxide film could be removed by immersion into sulphuric acid, the chromium-based oxide is impervious to it [31].

It must be noted that in all the cases, the Cu coatings were extremely fragile and not adherent on the HCCI sample substrate. The lack of adhesion of direct Cu on steel substrates was also seen in other studies [37]. Cu #4 coatings were relatively better compared to the rest which could be attributed to the presence of sulphuric acid and the increased concentration of the $CuSO_4$ salt. The sulphuric acid ensures an increase in conductivity and a corresponding decrease in the anode and cathode polarization, preventing the precipitation of basic Cu salts [26]. Nevertheless, the inability of the coating to protect the wear surface as observed from Fig. 2, renders it ineffective. Table 3 sums up the remark for each case with the final observations.

Alternatively, it is reported that usage of an alkaline or a cyanide-based bath would aid in the initial deposition of a thin (< 2.5 µm) adherent layer on the surface of active metal (iron, in our case). Further increase in the deposit thickness can be facilitated using an acid sulphate bath [24, 38]. Nonetheless, considering the toxicity and the health hazards associated with cyanide and its handling, it was decided to proceed with Ni electrodeposition.

Table 3 Remarks on the coating characteristics for the Cu electrodeposited samples with varying parameters

Coating	Remark
Cu #1	No adhesion. Fragile coating
Cu #2	No adhesion. Fragile coating
Cu #3	No adhesion. Fragile coating
Cu #4	Sporadic adhesion. Better results than #1, #2 and #3
Cu #5	Sample corroded due to sudden voltage increase to 18 V
Cu #6	No adhesion

3.2 Nickel Electrodeposition

In the present study, a pure Ni plate was used as the anode and the electrolyte was a Ni strike solution. The Ni strike contains soluble nickel salts ($NiCl_2 \cdot 6H_2O$) along with other constituents (HCl + additives). The dissolution of the salts produces positively charged, divalent nickel ions (Ni^{2+}) and upon the application of an electric potential, the positive ions react with the free electrons (e^-) to convert to metallic Ni at the cathode surface (HCCI substrate), as schematically shown in Fig. 1.

3.2.1 Ni Electrodeposition: 3 min

Figure 3 represents the SEM backscattered electron (BSE) micrographs of the sub-surface after a 3-min Ni electrolytic deposition. The deformed austenitic matrix under the worn surface is clearly visible and the Ni coating is uniform across the surface with a measured thickness of 0.7 ± 0.1 µm. Despite the uniformity in the coating thickness, the adhesiveness is sporadic as visualized by comparing Fig. 3b and c. Moreover, the dashed red enclosures in

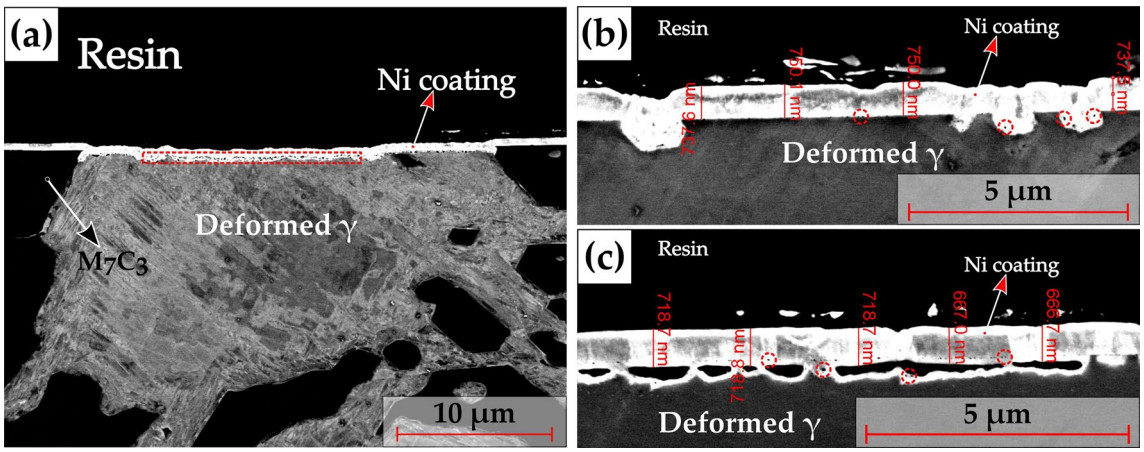

Fig. 3 Representative BSE micrograph of the sub-surface after a 3-min Ni electrodeposition with **a** low magnification image showing the Ni coating along with the characteristics of the sub-surface after the tribological test, **b**, **c** showing the sporadicity in the adhesion of the Ni coating. The coating is fairly uniform with a thickness of about 0.7 µm. The dashed red circles indicate the presence of a black pits which could be a consequence of hydrogen evolution during the electrolytic process (Color figure online)

Fig. 3 indicate the presence of black pits inside the coating which could be a consequence of hydrogen evolution at the cathode [25, 39, 40]. In the case of Ni electroplating, hydrogen co-deposition is practically unavoidable as Ni ions are thermodynamically more stable in aqueous solutions than hydrogen ions. Therefore, the reduction of hydrogen to hydrogen gas is thermodynamically more favourable and will occur simultaneously in conjunction with the reduction of Ni ions [41, 42]. As the present electrolyte used is acidic in nature, hydrogen ion reduction ($2H^+ + 2e^- \rightarrow H_2\uparrow$) preferentially occurs compared to the reduction of water molecules ($2H_2O + 2e^- \rightarrow H_2\uparrow + 2OH^-$) [23, 31]. Moreover, considering that the experiment was carried out in air, the aqueous solution will facilitate in the reduction of oxygen too ($O_2 + 4H^+ + 4e^- \rightarrow 2H_2O$). All of these reactions result in a decrease in the cathodic current efficiency (CCE). As the CCE is less than 100%, there is a tendency for the pH to increase temporally as the H^+ ions are discharged to liberate hydrogen gas (H_2).

The co-deposition of hydrogen in the metallic substrate occurs initially as H atoms and not as H_2 molecules. The reduced hydrogen ions can seep in through the broken passive oxide layer, facilitating hydrogen absorption and with time, they may congregate in vacancies or voids leading to hydrogen embrittlement [20]. The hydrogen bubbles evolved at the vicinity of the cathode cling to the freshly electrodeposited surface in an adsorbed state (H_{ads}), resulting in the development of gas pores in the deposit [39]. Consequently, they could act as an obstacle for subsequent deposition, resulting in the formation of black pits as seen in Fig. 3 [38]. Moreover, the presence of additives in the electrolyte could also contribute to the formation of gas pores due to their ability to modify the surface tension. The proton electronation and the hydrogen evolution at the cathode can be broken down as the following [31, 39–41]:

$$H^+ + e^- \rightarrow H_{ads} \tag{3}$$

$$H_{ads} + H^+ + e^- \rightarrow H_2 \tag{4}$$

$$2H_{ads} \rightarrow H_2\uparrow \tag{5}$$

Despite the presence of hydrogen and its impact during the Ni electrodeposition, the improved adhesivity of the Ni coating compared to its Cu counterpart could stem from the breakage of the passive oxide film by the chloride ions (Cl^-), which is elucidated further.

3.2.2 Ni Electrodeposition: 40 min

3.2.2.1 Unworn Surface Figure 4a represents the SEM BSE micrograph of the transverse section of the HCCI surface, away from the wear track after a 40-min Ni electrodeposition. The various phases present within the HCCI microstructure along with the Ni coating is marked for reference. Figure 4b represents a magnified image of the dashed orange enclosure indicated in Fig. 4a, where the EDS measurements were carried out. Three EDS select area scans, focusing on the Ni coating (Area 1), the austenitic matrix (Area 2), and the EC (Area 3), in addition to two EDS line scans (A and B) were performed as delineated in Fig. 4b. The resulting EDS spectra along with the semi-quantitative phase analysis for the three corresponding areas (1, 2, and 3) is represented in Fig. 4c–e. Finally, the results of the EDS line scans with A and B as the starting points is graphically represented in Fig. 4f and g, respectively.

Visual observations from Fig. 4a and b indicate that the Ni coating was uniform and adherent across the substrate, with a measured thickness of 8.0 µm ± 0.9 µm. Comparing Figs. 3 and 4b, the amount of pitting has significantly decreased and intuitively, the coating thickness has increased about ten-fold. Moreover, the sporadicity of adhesion as seen in Fig. 3 is not observed here, as enough time was given for the coating to adhere and grow.

The improved adhesivity can be attributed to the ability of the chloride ions (Cl^-) to breakdown the tenacious chromium oxide-based passive film (unlike the SO_4^{2-}), inherently present on the HCCI surface [36, 43–47]. This results in the exposure of a fresh, oxide-free surface towards the Ni reduction, enabling an adherent coating during the electrodeposition. As the electrolyte used in the current electrodeposition consists of a chloride-based nickel salt ($NiCl_2 \cdot 6H_2O$), the chloride ions present in the bath displaces the water molecules and forms various complexes increasing the bath's acidity, thereby damaging the complex chromium-iron oxide layer. The temporal increase in the bath's acidity (decrease in the pH) has a dual effect, of lowering the film breakdown potential (making it easier for film rupture) and increasing the substrate passivation potential (making it difficult for re-passivation) [19, 31]. Granted that re-passivation can take place, the presence of HCl prevents it [48]. Moreover, the removal of the passive layer may trigger a localized corrosion of the underlying metallic surface, but the presence of the M_7C_3 chromium carbides (EC) in combination with the chromium and molybdenum in the matrix can greatly inhibit this [7, 12, 49].

Depending on whether the select area scan falls inside the coating (Fig. 4c), matrix (Fig. 4d) or the carbide (Fig. 4e), the corresponding EDS spectra evidenced an abundance in nickel, iron and chromium, respectively. The EDS line scans in Fig. 4f and g depicts a decrease in the Ni intensity while crossing over from the coating to the substrate. Comparing the line scans, a sharper drop in Ni is seen when the carbide is present at the interface. Whenever a matrix or the carbide is encountered, a corresponding increase in iron or chromium is observed. Nevertheless, the integrity of the

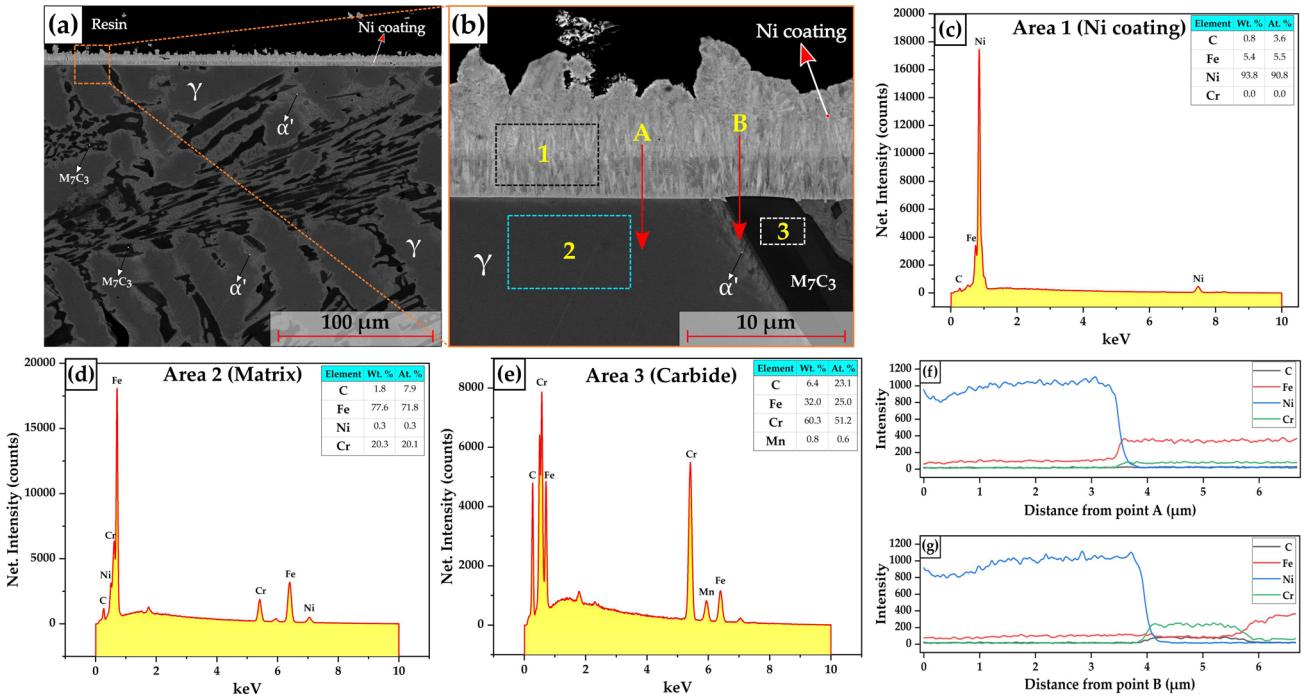

Fig. 4 **a** BSE micrograph of the sub-surface away from the wear track with the various HCCI phases and the Ni coating labelled for reference; **b** represents the magnified image of the dashed orange square marked in **a** where the EDS select area scans and line scans were performed; **c**–**e** represent the resulting EDS select scan spectrum with the semi-quantitative analysis of the phases indicated in the respective graphs and finally, **f**, **g** represent the results of the EDS line scan performed with A and B [marked in (**b**)] as the starting point (Color figure online)

coating seems to be uniform across the entire interface with no difference if it is in contact with the matrix or the carbide. Furthermore, the EDS line profile does not indicate any diffusion of Ni into the substrate suggesting that the sub-surface chemistry is unaltered by the presence of the Ni coating.

3.2.2.2 Worn Surface The SEM BSE micrograph of the transverse section encompassing both the worn and the unworn region is represented in Fig. 5a, with a visualization of the sub-surface characteristics. The dashed orange vertical line represents the wear track edge, and the various phases are marked for reference. Focusing on the left side of the wear track edge, the area immediately underneath the track was categorized as a tribologically transformed zone (TTZ), owing to the refinement that had taken place [16, 50]. The TTZ contains austenitic regions that were heavily deformed and is delineated with a dashed red enclosure in Fig. 5a. Figure 5b represents a magnified image emphasizing on the worn region and the TTZ. Although no significant refinement had taken place in the austenite region away from the wear track, it showed signs of plastic deformation. Additionally, the extent of plastic deformation diminished as we moved away from the wear track edge, finally reaching the undeformed austenite. Further characterization and elaboration concerning the deformation behaviour of the alloy under dry sliding can be found in [29]. Comparing the coating on either side of the wear track edge, no significant differences in the thickness and adhesivity of the coating is visible, indicating uniformity. The coating was able to cover the worn surface completely despite the presence of a topography and a higher roughness compared to the unworn region. The existence of a distinct deformed and undeformed austenite across the entire sub-surface indicates that the metallographic preparation of the transverse section did not induce any additional deformation. Consequently, it can be stated that the austenitic deformation is solely due to the tribological testing.

Figure 6a represents the SEM BSE micrograph of the sub-surface directly under the wear track with the various constituents delineated. A magnified image of the dashed yellow and orange enclosures marked in Fig. 6a, is presented in Fig. 6b and c, respectively. From Fig. 6b, small black pits (marked with the dashed red enclosure) were observed at the contact interface which could be attributed to the hydrogen adsorption (H_{ads}) during the electrodeposition process, as elucidated before. The location and morphology of the pits suggest they could be bridged pores, as nomenclated by Dini [38]. Even though the efficiency of the Ni deposition is

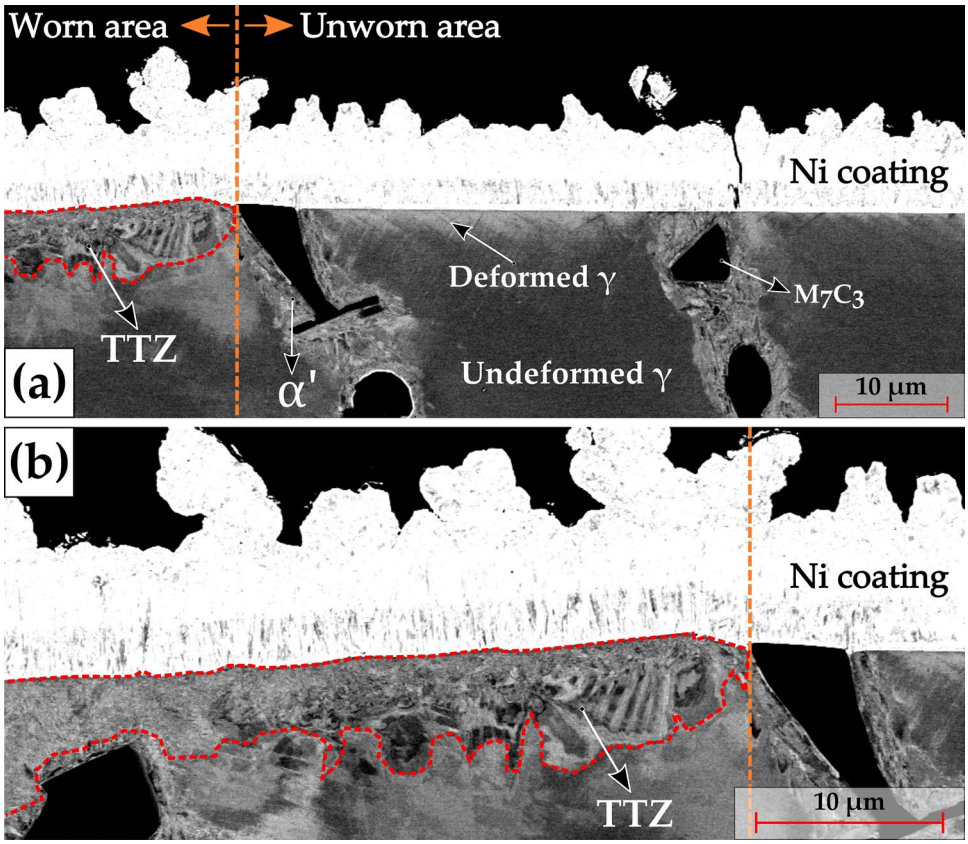

Fig. 5 **a** SEM BSE micrographs of the transverse section encompassing both the worn and the unworn regions. The dashed orange vertical line represents the wear track edge. The respective HCCI microstructural phases are marked for reference along with the Ni coating. The dashed red enclosure represents the tribologically transformed zone (TTZ); **b** Magnified BSE micrograph of the worn area as indicated in (**a**). The Ni coating is marked for reference and the dashed enclosure indicates the TTZ (Color figure online)

affected by H_{ads}, its presence did not hinder the formation of a compact metallic deposit [40], and the subsequent protection of the material´s sub-surface.

In addition to the plastic deformation undergone by the austenite during the tribological testing, the EC had also succumbed to micro-cracking, as indicated within the dashed orange ellipse Fig. 6c. This behaviour of the EC during the tribological testing can have an influence on the overall wear behaviour of the alloy [51, 52]. Interestingly, it is observed that the Ni coating had infiltrated these crevices and acted as an anchor to prevent the carbide's ejection during the mechanical sectioning, post-wear. This can be clearly visualized in Fig. 6c and also from the nickel EDS map in Fig. 6d. Additionally, the elemental distributions pertaining to chromium, iron and carbon are represented in Fig. 6e–g, respectively.

Increasing the deposition time facilitated a uniform adhesive Ni coating and ultimately allowed to characterize the material volume just below the worn and unworn surface. The coating had helped in preservation of the edge where the deformed structure was visible in the as-is condition. Chemical and structural analysis was carried out to assure no changes due to the Ni electrodeposition had occurred.

Figure 7a represents the SEM SE micrograph of the region underneath the wear track and the orange dashed enclosure is indicative of the area where the EBSD measurements were performed. It is worth to note that in the current study, dry sliding wear tests were carried out at a load of 20 N, which is higher than the critical load (P_C) of the HCCI alloy under study. More information concerning the critical load calculations is given in [29]. From the image quality (IQ) map in Fig. 7b, the plastic deformation of the austenitic region can be clearly visualized, and its consequence is reflected in the inverse pole figure (IPF) maps in Fig. 7c and d. Additionally, the variance in the slip directions is marked with the red-dashed lines in the IQ map for reference. The activation of slip traces is a manifestation to accommodate the deformation endured by the austenitic matrix during the tribological test [53–55].

Owing to the identical Bravais lattice structure of austenite and Ni, i.e., face centered cubic (FCC), it was not possible to distinguish them using the EBSD phase map. However, from the IQ (Fig. 7b) and EDS map (Fig. 6), a distinction between the two could be made. It was also observed that the Ni coating had not been subjected to deformation during the metallographic preparation of the specimen. Moreover, the identicality of the crystal structures of austenite and Ni could influence the coating's growth characteristics. As seen from the IPF map in Fig. 7c, the Ni coating grows in a columnar fashion, although further discussion on this aspect is out of scope

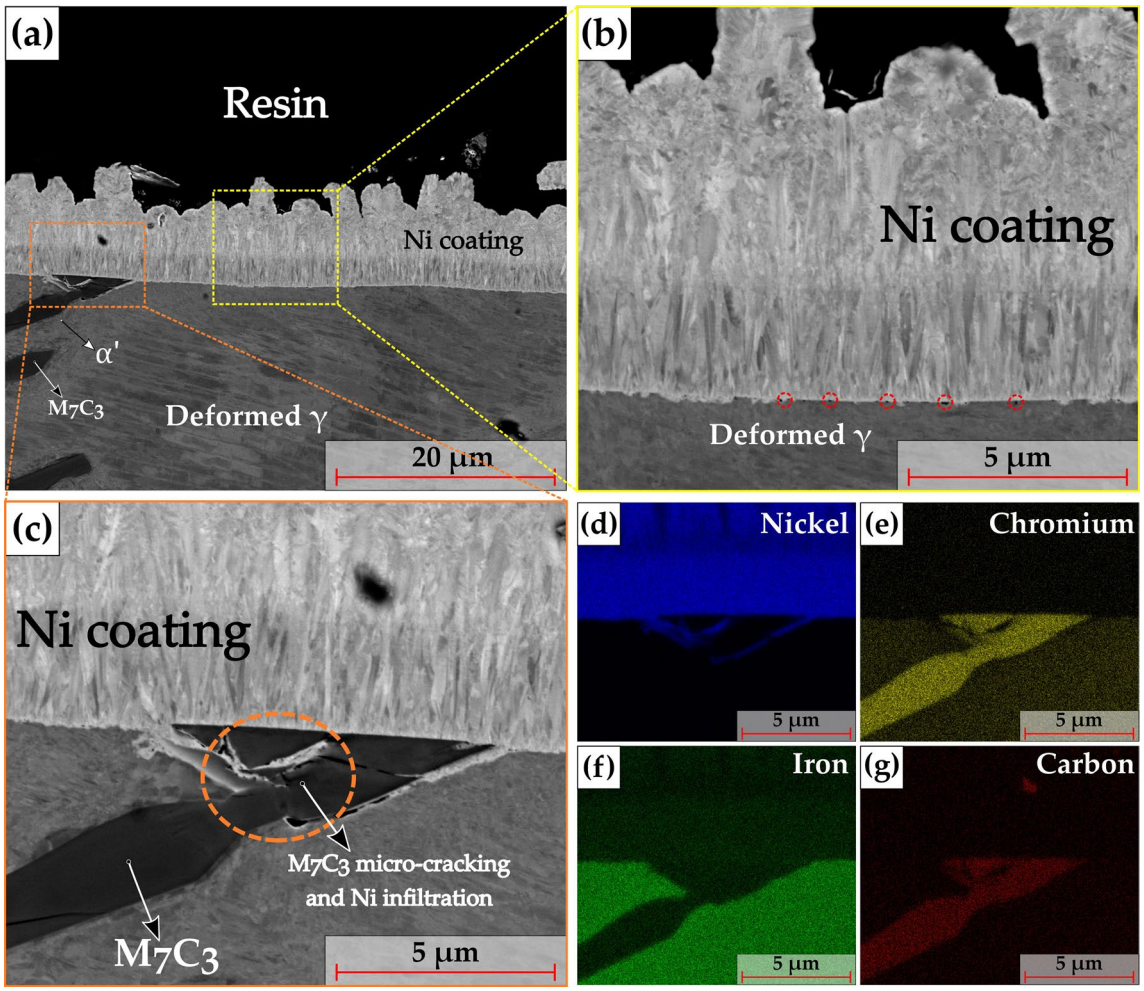

Fig. 6 **a** BSE micrograph of the sub-surface under the wear track with the various HCCI phases and Ni coating labelled for reference; **b**, **c** represent the magnified BSE micrographs of the dashed yellow and orange rectangle, respectively. The red circles in **b** indicate the formation of black pits (hydrogen pitting), an unwanted product during the electrolytic deposition. Carbide microcracking is visible in (**c**) along with the Ni infiltration in between the cracks. **d**–**g** represent the EDS concentration maps of Ni, Cr, Fe and C, respectively, of the micrograph presented in (**c**) (Color figure online)

for the present work. Nevertheless, the integrity of the coating across the entire substrate is intact.

Furthermore, the variation in the orientation across the austenite grain was elucidated by calculating the point-to-point and point-to-origin misorientation profile (MP) chart, as represented in Fig. 7e. The point O (as marked in Fig. 7d) was selected as the origin point, as it lies away from the immediate wear surface and the MP measurements were carried out proceeding closer towards the deformed austenite. The point-to-origin plot indicates a maximum gradient of about 12° between the undeformed and deformed austenite region.

Finally, to visualize the influence of Ni electrodeposition in protecting the wear track, a piece of transparent tape was applied to half of the worn sample, effectively inhibiting the Ni coating. The Ni electrodeposition was carried out for 30 min by keeping the rest of the parameter's constant. Figure 8a and b represent the SEM BSE micrographs of the two opposite surfaces underneath the wear track with, and without the Ni coating, respectively.

Clearly, the presence of a uniformly coated Ni layer has protected the worn surface and prevented the chipping of the brittle EC during the sectioning. The coating thickness was measured to be 7.9 ± 0.3 μm which was similar to the Ni electrodeposition at 40 min, indicating a saturation level. It was seen from Fig. 8a that the EC closer to the worn surface had cracked owing to the stress exerted on them and moreover, the Ni coating had infiltrated the cracks acting as an anchor to prevent their ejection. On the other hand, Fig. 8b shows that the fragmented carbides were ejected during the mechanical sectioning process (as

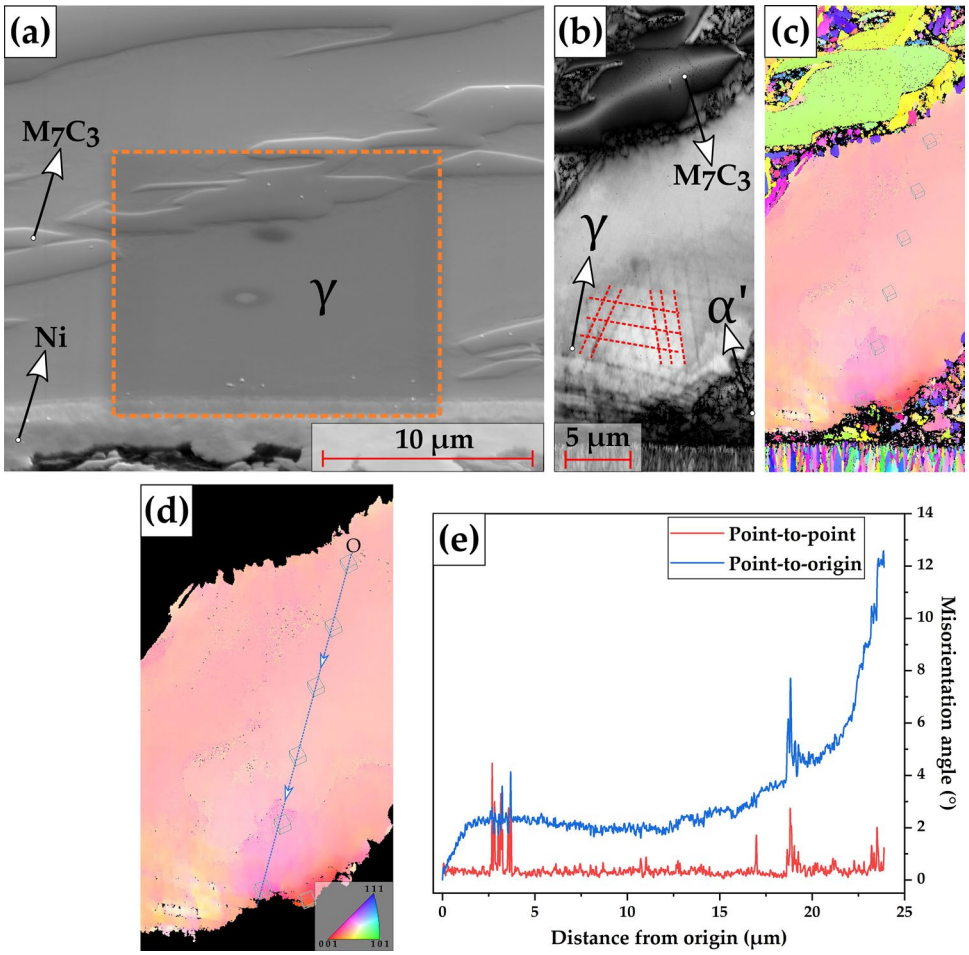

Fig. 7 **a** SEM SE micrograph of the region underneath the wear track, with the respective phases marked. The dashed orange rectangle in **a** represents the area where the EBSD measurements were carried out, with **b** IQ map of the scanned region, with the red-dashed lines indicating the various slip traces in the deformed austenitic matrix. **c**, **d** represent the IPF map overlayed with the local lattice rotation of the entire region and the single austenitic region, respectively. The variation of the misorientation angle across the austenite grain from the point O following a path indicated by the dashed blue line in (**d**), is graphically represented in (**e**) (Color figure online)

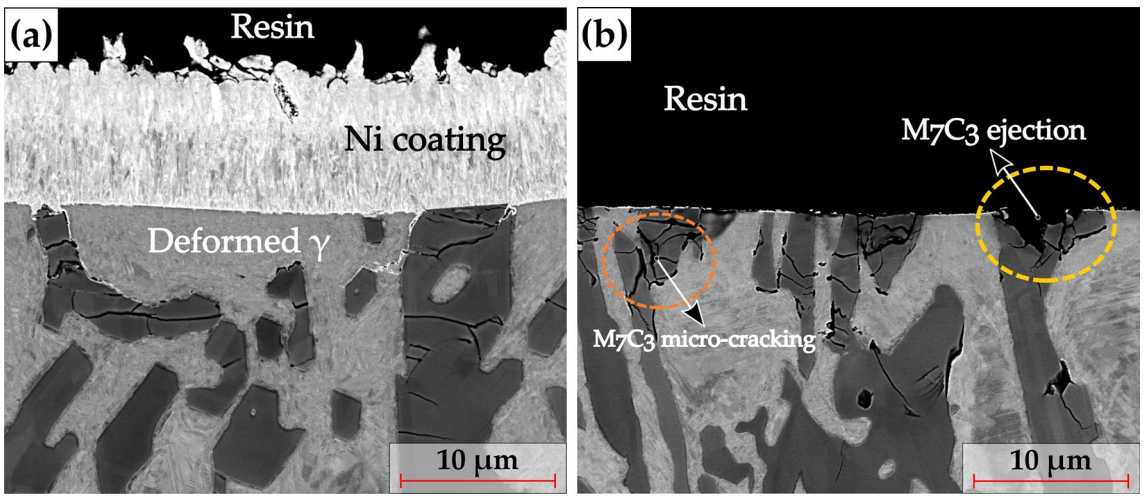

Fig. 8 Representative SEM BSE micrographs of the cross-section of the worn sample **a** with the electrolytic Ni deposition for 30 min, and **b** without Ni electrodeposition. The dashed orange ellipse and the dashed yellow ellipse in **b** indicates the fragmentation and ejection of the M_7C_3 carbide, respectively. It can be visualized from **a** that the presence of the Ni coating layer has protected the spalled carbides from being ejected (Color figure online)

indicated in the dashed yellow ellipse), thus emphasizing the benefits of Ni electrodeposition.

4 Conclusions

In the current work, electrolytic deposition was carried out on the worn surface of an as-cast HCCI alloy to prevent any unwanted microstructural modifications during the mechanical sectioning and polishing, in order to examine the microstructure of the sub-surface. The efficacies of electrodeposition using Cu and Ni as the electrode were assessed by changing various experimental parameters and the following conclusions were drawn:

1. Electrodeposition using Cu did not yield satisfactory results as the coatings were non-uniform and poorly adhered to the substrate and were hence deemed ineffective.
2. Ni electroplating using the Ni strike electrolyte produced a uniform and adherent coating with a thickness of about 8 µm after 30–40 min with the current density maintained between 1 and 5 A/dm^2 for the HCCI sample. Furthermore, this coating methodology was successfully applied to other ferrous alloys such as 316L stainless steel and a low-carbon steel with 5 wt% Ni. The Ni coating had helped in preserving the sample edge and the sub-surface characteristics underneath the wear track could be clearly visualized.
3. EDS maps clearly show the presence of a uniform Ni layer whereas the line scan across the interface shows no chemical alteration of the surface in the sub-micron range. No significant differences in the integrity of the coating were observed between a Ni-matrix and a Ni-carbide contact.
4. The Ni infiltration into the broken carbide fragments acted as an anchor preventing its ejection during the mechanical sectioning and polishing, as evident from Figs. 6 and 8.

Acknowledgements The authors are thankful to Martin Duarte from Tubacero S.A. for providing the material. The authors would like to thank the Saarland State Chancellery for financial support within the ZuMat Project funded by the European Regional Development Fund (ERDF). Additionally, U.P.N. is grateful to DAAD for the financial support and J.W. gratefully acknowledges the financial support by CBMM (Brazil).

Funding Open Access funding enabled and organized by Projekt DEAL. The present work is supported by funding from the Deutsche Forschungsgemeinschaft (DFG, Project: GU 2102/2-1).

Data Availability The data used in this study are available from the corresponding author at reasonable request.

Declarations

Conflict of interest The authors declare that they have no conflict of interest.

References

1. Holmberg, K., Erdemir, A.: Influence of tribology on global energy consumption, costs and emissions. Friction **5**, 263–284 (2017). https://doi.org/10.1007/s40544-017-0183-5
2. Holmberg, K., Kivikytö-Reponen, P., Härkisaari, P., Valtonen, K., Erdemir, A.: Global energy consumption due to friction and wear in the mining industry. Tribol. Int. **115**, 116–139 (2017). https://doi.org/10.1016/j.triboint.2017.05.010
3. Zum Gahr, K.H., Doane, D.V.: Optimizing fracture toughness and abrasion resistance in white cast irons. Metall. Trans. A. **11**, 613–620 (1980). https://doi.org/10.1007/BF02670698
4. Oliveira, C.G., Pinheiro, I.P.: Effect of niobium on the microstructure of high chromium white cast iron. In: MRS Advances, pp. 9–16. Springer, Berlin (2015)
5. Shchegolev, A.V., Ishkov, A.V., Ivanayskiy, V.V.: Comparative study of high-chromium cast iron coatings modified with WC-W2C/Co+B4C+Ni/Al complexes and Cr3C2/PG-US25 ceramet. In: Solid State Phenomena, pp. 818–826. Trans Tech Publications Ltd, Freienbach (2020)
6. Tabrett, C.P., Sare, I.R., Ghomashchi, M.R.: Microstructure-property relationships in high chromium white iron alloys. Int. Mater. Rev. **41**, 59–82 (1996). https://doi.org/10.1179/095066096790326075
7. Maratray, F.: Choice of appropriate compositions for chromium–molybdenum white irons. AFS Trans. **79**, 121–124 (1971)
8. Llewellyn, R.J., Yick, S.K., Dolman, K.F.: Scouring erosion resistance of metallic materials used in slurry pump service. Wear **256**, 592–599 (2004). https://doi.org/10.1016/j.wear.2003.10.002
9. Karantzalis, E., Lekatou, A., Mavros, H.: Microstructure and properties of high chromium cast irons: effect of heat treatments and alloying additions. Int. J. Cast Met. Res. **22**, 448–456 (2009). https://doi.org/10.1179/174313309X436637
10. Maratray, F., Usseglio-Nanot, R.: Factors affecting the structure of chromium and chromium-molybdenum white irons. Climax Molybdenum, Paris (1971)
11. Asensio, J., Pero-Sanz, J.A., Verdeja, J.I.: Microstructure selection criteria for cast irons with more than 10 wt.% chromium for wear applications. Mater. Charact. **49**, 83–93 (2002). https://doi.org/10.1016/S1044-5803(02)00260-7
12. Wiengmoon, A., Pearce, J.T.H., Chairuangsri, T.: Relationship between microstructure, hardness and corrosion resistance in 20 wt.%Cr, 27 wt.%Cr and 36 wt.%Cr high chromium cast irons. Mater. Chem. Phys. **125**, 739–748 (2011). https://doi.org/10.1016/j.matchemphys.2010.09.064

13. Mercado, V.H., Mejía, I., Bedolla-Jacuinde, A.: Effect of load and sliding rate on the wear behavior of Ti-containing TWIP steel. J. Mater. Eng. Perform. **26**, 2213–2225 (2017). https://doi.org/10.1007/s11665-017-2635-5
14. Todaka, T., Shimizu, K., Kusumoto, K., Purba, R.H., Gaqi, Y.: Effect of carbon content on three-body abrasive wear characteristics of 28Cr–3Ni cast alloys. ISIJ Int. **61**, 2274–2283 (2021). https://doi.org/10.2355/isijinternational.isijint-2021-099
15. Ruff, A.W.: Deformation studies at sliding wear tracks in iron. Wear **40**, 59–74 (1976). https://doi.org/10.1016/0043-1648(76)90018-1
16. Grützmacher, P.G., Rammacher, S., Rathmann, D., Motz, C., Mücklich, F., Suarez, S.: Interplay between microstructural evolution and tribo-chemistry during dry sliding of metals. Friction **7**, 637–650 (2019). https://doi.org/10.1007/s40544-019-0259-5
17. Volkert, C.A., Minor, A.M.: Focused ion beam microscopy and micromachining. MRS Bull. **32**, 389–399 (2007). https://doi.org/10.1557/MRS2007.62
18. Brenner, A.: Electrodeposition of Alloys: Principles and Practice. Academic Press, Cambridge (1963)
19. Shreir, L.L., Jarman, R.A., Burstein, G.T.: Corrosion Vol. 2: Corrosion Control. Butterworth-Heinemann, Oxford (1994)
20. Awang, M., Khalili, A.A., Pedapati, S.R.: A review: thin protective coating for wear protection in high-temperature application. Metals (Basel) **10**, 42 (2020). https://doi.org/10.3390/met10010042
21. Parangusan, H., Bhadra, J., Al-Thani, N.: A review of passivity breakdown on metal surfaces: influence of chloride- and sulfide-ion concentrations, temperature, and pH. Emergent Mater. (2021). https://doi.org/10.1007/s42247-021-00194-6
22. Oriňáková, R., Turoňová, A., Kladeková, D., Gálová, M., Smith, R.M.: Recent developments in the electrodeposition of nickel and some nickel-based alloys. J. Appl. Electrochem. **36**, 957–972 (2006)
23. Palumbo, G.: Smart coatings for corrosion protection by adopting microcapsules. Phys. Sci. Rev. **1**, 1–32 (2019). https://doi.org/10.1515/psr-2015-0006
24. ASM International: ASM Handbook Volume 5: Surface Engineering. ASM International, Novelty (2002)
25. Fontana, M.G.: Corrosion Engineering. McGraw-Hill, Singapore (1987)
26. Reid, J.: Copper electrodeposition: principles and recent progress. Jpn. J. Appl. Phys. **40**, 2650 (2001). https://doi.org/10.1143/JJAP.40.2650
27. Medlin, D.J., Lucas, G.M., Vander Voort, G.F.: Metallographic preparation of orthopedic medical devices. Med. Device Mater. II—Proc. Mater. Process. Med. Devices Conf. 2004. 75–80 (2005)
28. Nayak, U.P., Guitar, M.A., Mücklich, F.: A comparative study on the influence of chromium on the phase fraction and elemental distribution in as-cast high chromium cast irons: simulation vs. experimentation. Metals (Basel) **10**, 30 (2020). https://doi.org/10.3390/met10010030
29. Nayak, U.P., Suárez, S., Pesnel, V., Mücklich, F., Guitar, M.A.: Load dependent microstructural evolution in an As-cast 26% Cr high chromium cast iron during unlubricated sliding. Friction (2021). https://doi.org/10.1007/s40544-021-0553-x
30. Nayak, U.P., Guitar, M.A., Mücklich, F.: Evaluation of etching process parameter optimization in the objective specific microstructural characterization of as-cast and heat treated HCCI alloy. Prakt. Metallogr. **57**, 688–713 (2020). https://doi.org/10.3139/147.110682
31. Sato, N.: Basics of corrosion chemistry. In: Green Corrosion Chemistry and Engineering: Opportunities and Challenges, pp. 1–32. Wiley, Hoboken (2011)
32. Lin, C.S., Hsu, P.C., Chang, L., Chen, C.H.: Properties and microstructure of nickel electrodeposited from a sulfamate bath containing ammonium ions. J. Appl. Electrochem. **31**, 925–933 (2001). https://doi.org/10.1023/A:1017970417874
33. Vander Voort, G.F.: Metallography: Principles and Practice. ASM International, Novelty (1999)
34. Hann, S.K., Gates, J.D.: A transformation toughening white cast iron. J. Mater. Sci. **32**, 1249–1259 (1997). https://doi.org/10.1023/A:1018544204267
35. Dodd, J.: Recent developments in abrasion resistant high chromium-molybdenum irons, low-alloy manganese steels and alloyed nodular irons of importance in the extraction and utilization of energy resources. J. Mater. Energy Syst. **2**, 65–76 (1980). https://doi.org/10.1007/BF02833432
36. Zumelzu, E., Goyos, I., Cabezas, C., Opitz, O., Parada, A.: Wear and corrosion behaviour of high-chromium (14–30% Cr) cast iron alloys. J. Mater. Process. Technol. **128**, 250–255 (2002). https://doi.org/10.1016/S0924-0136(02)00458-2
37. Ivshin, Y.V., Shaikhutdinova, F.N., Sysoev, V.A.: Electrodeposition of copper on mild steel: peculiarities of the process. Surf. Eng. Appl. Electrochem. **54**, 452–458 (2018). https://doi.org/10.3103/S1068375518050046
38. Dini, J.W.: Electrodeposition: The Materials Science of Coatings and Substrates (Materials Science and Process Technology Series). William Andrew (1994)
39. Gabe, D.R.: The role of hydrogen in metal electrodeposition processes. J. Appl. Electrochem. **27**, 908–915 (1997). https://doi.org/10.1023/A:1018497401365
40. Gómez, E., Pollina, R., Vallés, E.: Nickel electrodeposition on different metallic substrates. J. Electroanal. Chem. **386**, 45–56 (1995). https://doi.org/10.1016/0022-0728(95)03817-Z
41. Schoeman, L., Sole, K.C.: Accurate measurement of polarization potentials during electrodeposition of nickel metal from sulphate electrolytes. J. S. Afr. Inst. Min. Metall. **117**, 622–628 (2017). https://doi.org/10.17159/2411-9717/2017/V117N7A3
42. Holm, M., O'Keefe, T.J.: Evaluation of nickel deposition by electrochemical impedance spectroscopy. J. Appl. Electrochem. **30**, 1125–1132 (2000). https://doi.org/10.1023/A:1004002303181
43. Böhni, H.: Breakdown of passivity and localized corrosion processes. Langmuir **3**, 924–930 (1987). https://doi.org/10.1021/la00078a010
44. Cheng, Y.F., Wilmott, M., Luo, J.L.: Role of chloride ions in pitting of carbon steel studied by the statistical analysis of electrochemical noise. Appl. Surf. Sci. **152**, 161–168 (1999). https://doi.org/10.1016/S0169-4332(99)00328-1
45. Zhang, B., Wang, J., Wu, B., Guo, X.W., Wang, Y.J., Chen, D., Zhang, Y.C., Du, K., Oguzie, E.E., Ma, X.L.: Unmasking chloride attack on the passive film of metals. Nat. Commun. **9**, 1–9 (2018). https://doi.org/10.1038/s41467-018-04942-x
46. Elfström, B.O.: The effect of chloride ions on passive layers on stainless steels. Mater. Sci. Eng. **42**, 173–180 (1980). https://doi.org/10.1016/0025-5416(80)90026-9
47. Horvath, J., Uhlig, H.H.: Critical potentials for pitting corrosion of Ni, Cr–Ni, Cr–Fe, and Related Stainless Steels. J. Electrochem. Soc. **115**, 791 (1968). https://doi.org/10.1149/1.2411433
48. Richardson, T., Cottis, B., Lindsay, R., Lyon, S., Scantlebury, D., Stott, H., Graham, M. (eds.): Shreir's Corrosion. Elsevier, Amsterdam (2010)
49. Giourntas, L., Brownlie, F., Hodgkiess, T., Galloway, A.M.: Influence of metallic matrix on erosion-corrosion behaviour of high chromium cast irons under slurry impingement conditions. Wear **477**, 203834 (2021). https://doi.org/10.1016/J.WEAR.2021.203834
50. Kapoor, A., Franklin, F.J.: Tribological layers and the wear of ductile materials. Wear **245**, 204–215 (2000). https://doi.org/10.1016/S0043-1648(00)00480-4

51. Ghabchi, A.: Wear Resistant Carbide-based Thermal Sprayed Coatings: Process, Properties, Mechanical Degradation and Wear. Stony Brook University, Stony Brook (2011)
52. Menezes, P.L., Ingole, S.P., Nosonovsky, M., Kailas, S.V., Lovell, M.R.: Tribology for Scientists and Engineers: From Basics to Advanced Concepts. Springer, New York (2013)
53. Miyamoto, G., Shibata, A., Maki, T., Furuhara, T.: Precise measurement of strain accommodation in austenite matrix surrounding martensite in ferrous alloys by electron backscatter diffraction analysis. Acta Mater. **57**, 1120–1131 (2009). https://doi.org/10.1016/j.actamat.2008.10.050
54. Abbaschian, R., Abbaschian, L., Reed-Hill, R.E.: Physical Metallurgy Principles. Cengage Learning, Stamford (2008)
55. Hull, D., Bacon, D.J.: Introduction to Dislocations. Elsevier Ltd, Oxford (2011)

VII. Time-dependant Microstructural Evolution and Tribological Behaviour of a 26 wt.% Cr White Cast Iron Subjected to a Destabilization Heat Treatment

U. Pranav Nayak, Frank Mücklich, María Agustina Guitar

Department of Materials Science and Engineering, Saarland University, 66123 Saarbrücken, Germany

Published in "***Metals and Materials International***" (2022)

(IF (2023): 3.451)

Accessible online at: *https://doi.org/10.1007/s12540-022-01276-8*

Own Contribution: Conceptualization and methodology; sample preparation; experimentation; microstructural and tribological characterization; data analysis; scientific discussion; paper writing – original draft preparation

Metals and Materials International
https://doi.org/10.1007/s12540-022-01276-8

Time-Dependant Microstructural Evolution and Tribological Behaviour of a 26 wt% Cr White Cast Iron Subjected to a Destabilization Heat Treatment

U. Pranav Nayak[1] · Frank Mücklich[1,2] · María Agustina Guitar[1]

Received: 17 March 2022 / Accepted: 10 July 2022

Abstract
By employing destabilization heat treatments (HT), it is possible to create microstructures possessing different fractions of carbides, martensite, and austenite, which lead to varying tribological responses in abrasion-resistant high-chromium white cast irons. In the current work, the destabilization temperature was kept constant at 980 °C, whereas the time was varied from 0 to 90 min. As a result, the microstructure of the 26 wt% Cr white cast iron had a mixture of $M_{23}C_6$ secondary carbides (SC), martensite, and a decrease in the amount of retained austenite (RA) with increasing destabilization holding time. The microstructures as well as their tribological characteristics were evaluated by combining confocal laser scanning microscopy, SEM, XRD, and EBSD, together with dry-sliding linear reciprocating wear tests. Results show that the volume fraction of SC were statistically comparable in samples destabilized for 0 and 90 min, although the average size was almost two-fold in the latter. This had direct implications on the wear properties where a decrease of up to 50% in the wear rate of destabilized samples compared to the non-treated material was observed. Furthermore, the sample with the lowest increase in the matrix hardness (~ 20% higher than non-treated), showed the highest wear resistance. This was attributed to a favourable distribution of the RA (~ 10%) and SC volume fraction (~ 5%), in combination with the harder martensitic matrix. Finally, the results obtained from this study shed light on the ability to alter the HT parameters to tune the microstructure depending upon the application prerequisite.

Keywords High chromium cast iron · Destabilization heat treatment · Retained austenite · Secondary carbides · Wear rate · Microstructural tailoring

1 Introduction

Almost 25% of the world's energy production is spent in overcoming tribology-related issues [1]. Additionally, the friction and wear-related failures in the mining and mineral sector alone constitute for about 6% of the global energy consumption [2]. To reduce the energy and economic loss faced during operation run-time, scientists are constantly on the look out to develop better wear-resistant materials by understanding the wear mechanisms [3–5]. The application's longevity can be extended by either employing new materials apt for wear-related applications or suitably modifying the existing material's microstructure.

High chromium white cast irons (HCWCIs) are alloys primarily belonging to the Fe–Cr–C ternary system, containing 15–30 wt% Cr and 2.4–4 wt% C (with additions of Ni, Cu, Mn and Mo), as described by the ASTM A532 [6, 7]. Their microstructure is characterized by the presence of Cr-rich M_7C_3 type carbides and a modifiable (ferrite, austenite, martensite) matrix. This combination of hard carbides (1200–1600 HV) dispersed in a versatile matrix enables it to be used in a wide variety of applications such as ore crushers, ball mill liners and pulverizing equipment, in the coal and mineral sector [7–10]. The versatility of the matrix stems from the ability to modify it by employing suitable heat treatments such as destabilization and/or sub-critical treatments [11, 12]. During destabilization, the precipitation of fine secondary carbides (SC) takes place, in addition to the transformation of the austenitic matrix to

✉ U. Pranav Nayak
pranav.nayak@uni-saarland.de

[1] Department of Materials Science, Saarland University, Campus D3.3, 66123 Saarbrücken, Germany

[2] Materials Engineering Center Saarland (MECS), Campus D3.3, 66123 Saarbrücken, Germany

Published online: 11 August 2022

martensite during cooling [7, 13]. Moreover, the characteristics of the SC are highly dependent on the destabilization specifics and the Cr/C ratio [14, 15].

Several works found in the literature evaluate the wear properties of HCWCI alloys as a result of varying the alloying elements [16–19] and heat treatment (HT) [11, 12, 20–23], where a strong correlation between the microstructural characteristics and wear resistance was observed. Although it was thought that a high hardness (i.e., maximum carbide precipitation and martensite formation) was the primary dictating factor for improving the wear resistance, it is now understood that a synergistic contribution between the carbide and matrix is key [4, 24]. This was evident in the studies carried out by Zum Gahr et. al. [25] and Doğan et. al. [26], wherein an increase in the hardness/carbide volume fraction (CVF) did not correspond to an increase in the wear resistance. Notwithstanding the contribution of the hard M_7C_3 carbides in improving the overall wear resistance of the HCWCI alloy, the degree of mechanical support provided by the matrix structure plays a crucial role [27, 28]. Furthermore, the stereological characteristics of the SC (size, type, volume fraction, etc.) may have an influence on the overall wear behaviour, as in the case of low-stress abrasion applications [29–31].

As far as the matrix structure is concerned, austenite in general is thought to provide good mechanical support to the carbides due to its ability to absorb the crack propagation and strain harden progressively during service [25, 32, 33]. Some studies indicate that the presence of retained austenite (RA) helps in improving the wear resistance by virtue of its inherent ductility [26, 32] and others suggest possessing a harder martensitic matrix might be the better option owing to the mechanical support it could provide [12, 22, 34–36]. Nevertheless, there is often conflicting information in the literature whether heat treatment modifications made to the as-cast hypoeutectic HCWCI alloy has improved the wear resistance or not. Additionally, numerous studies indicate a tendency of increasing wear resistance with increasing CVF when an abrasive softer than the M_7C_3 carbide is used, although there is no consensus among the community when the hardness of the abrasive (SiC/Al_2O_3) exceeds that of the carbide [3, 25], which elucidates the complexity associated with tribological testing [27]. Among a multitude of studies dealing with wear in cast irons, only a limited number of investigations dealt with sliding [19, 27, 37] and even fewer studies placed emphasis on the differential response of each individual microstructural constituent to the tribo-system after conducting dry-sliding wear tests [18, 38].

In the present work, an attempt was made to derive a mutual relationship between the volume fraction of RA, the stereological characteristics of SC precipitates and the matrix hardness of a 26 wt% Cr white cast iron, with the wear rate (WR), when destabilization holding time is increased. Subsequently, a destabilization HT was experimentally conducted wherein the samples were heated to 980 °C, held for various times ranging from 0 to 90 min, followed by air cooling. Microstructural characterization was performed on all the samples by confocal laser scanning microscopy (CLSM) and scanning electron microscopy (SEM). Additionally, the stereological characteristics of the SC precipitates were assessed in terms of volume fraction, size and near neighbour distance (nnd), and their respective distributions, by conducting image analysis on the SEM micrographs. To quantify the amount of RA present in heat-treated samples, X-ray diffraction measurements were combined with Rietveld analysis. The samples were later subjected to dry-sliding linear reciprocating wear tests to determine the wear volume loss and subsequently, the WR. Finally, SEM was used for the characterization of the wear tracks to correlate the improved wear resistance with the associated changes taking place during the destabilization treatment.

2 Experimental Methodology

2.1 Material and Heat Treatment

The bulk chemical composition (in wt%) of the HCWCI alloy used in the current work was determined by optical emission spectroscopy (GNR Metal Lab 75/80) and is presented in Table 1, whereas the specifics of the casting are mentioned in [39].

An abrasive disk was used to cut the cast samples measuring $20 \times 20 \times 10$ mm. Moreover, the smaller sample thickness ensures a quick thermal equilibration with the furnace and a uniform heating during the destabilization. Three samples were subjected to a destabilization heat treatment at 980 °C for 0 (Q_0), 30 (Q_30) and 90 (Q_90) minutes followed by air cooling and later, hot mounted in a conductive resin for metallographic preparation. The metallographic protocol as specified in [40] was followed to obtain a scratch-free, mirror polished surface. The schematic of the HT is represented in Fig. 1.

Table 1 Bulk chemical composition (wt%) of the HCWCI alloy used in this study

C	Cr	Mn	Ni	Mo	Si	Cu	P	S	Fe
2.53	26.60	0.66	0.26	0.24	0.37	0.03	< 0.01	0.04	Bal

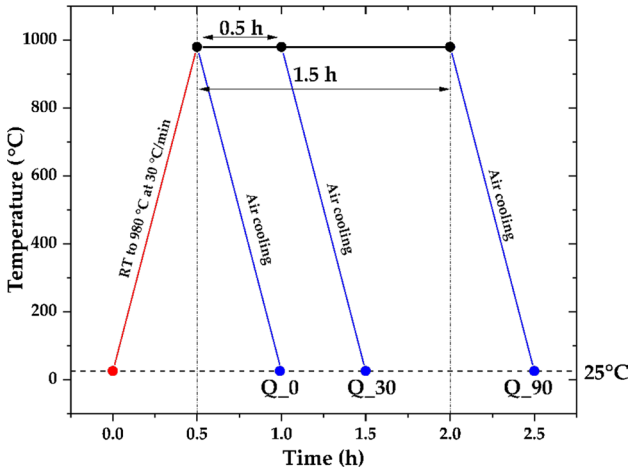

Fig. 1 Schematic of the destabilization heat treatment employed

2.2 Tribological Tests

Dry-sliding linear reciprocating wear tests were conducted on the as-cast (AC) and the HTed samples using a ball-on-disc micro-tribometer (CSM Instruments), while the whole setup was placed in an environmental chamber to control the temperature and humidity. 3 mm alumina (Al_2O_3) balls (99.00%–99.99% purity; Grade GD28) were used as the sliding counter-body. Table 2 represents the tribological testing parameters used during the test. Presently, a load of 20 N was used based on a previous work wherein the critical load was obtained using Hertzian contact theory based on the material that deforms first [41]. Moreover, at least three trials were performed for each sample.

2.3 Microstructural and Wear Track Characterization

Optical microscopy (OM) observations of the AC and HTed samples were carried out using a LEXT OLS 4100 Olympus CLSM. The CLSM uses a laser with 405 nm wavelength and, a lateral and vertical resolution of 120 and 10 nm, respectively. The fine microstructural details of the samples were obtained using a FEI Helios™ Nanolab 600 field emission SEM (FE-SEM) in conjunction with a Thermo-Fisher Helios™ G4 PFIB (Plasma Focused-Ion Beam) CXe DualBeam™ FIB/SEM. The SEM was operated at an acceleration voltage of 5–15 kV and a beam current of 1.4 nA. The AC microstructure is characterized by the presence of Cr-rich M_7C_3 type intergranular eutectic carbides (EC) (~ 30%) dispersed in an austenitic matrix (γ) (~ 60%), and a thin layer of martensite (α') (~ 10%) sandwiched between the EC and γ, as indicated in Fig. 2. The phases present in the microstructures are colour-arrow coded throughout the paper according to the following terminology:

Austenite (γ): Red arrow pointing downwards
Martensite (α'): Green arrow pointing upwards
M_7C_3 carbide (EC): Yellow arrow pointing right
$M_{23}C_6$ carbide (SC): Blue arrow pointing left

The back-scattered electron (BSE) micrographs obtained from the SEM were used in determining the stereological characteristics (volume fraction, size, nnd etc.) of the SC, using the open-source image analysis software, FIJI (Fiji Is Just ImageJ) [42]. Prior to obtaining the BSE SEM micrographs, the samples were etched with a modified Murakami's reagent (4 g $K_3[Fe(CN)_6]$ potassium ferricyanide + 8 g NaOH sodium hydroxide + 100 mL H_2O water) at RT for 15 s [40]. The micrographs were captured at a magnification of 2500× (~ 50 × 50 μm^2) and at least 5 micrographs were considered in each case. A threshold segmentation was applied to the BSE micrographs to obtain a binarized image comprising of the carbides and the matrix. This was followed by selectively eliminating the larger EC from the image and performing the particle analysis on the

Table 2 Tribological testing parameters

Parameters	Value
Temperature (°C)	25
Relative humidity (%)	45
Load (N)	20
Sliding velocity (ms^{-1})	0.02
Stroke length (mm)	5.5
No. of cycles	2000
Data acquisition frequency (Hz)	50

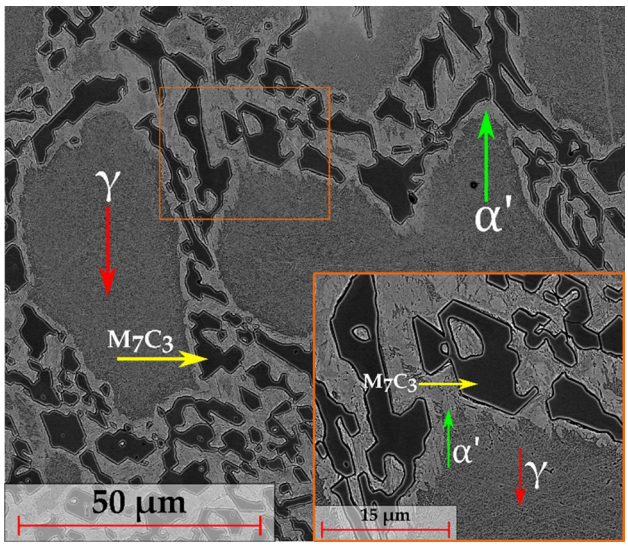

Fig. 2 Representative SEM micrograph of the AC sample after etching with Vilella's reagent. The various phases are marked for reference

SC. Considering the magnification and resolution of image acquisition, all pixelated particles having a diameter less than 100 nm were excluded from the analysis. Further details concerning the determination of the SC specifics is given in [43].

It was assumed that the carbide size and nnd's were log normally distributed as evidenced by the presence of skewness in the raw data. Moreover, an additional factor namely the coefficient of variation (COV) was introduced to measure the homogeneity of the SC distribution based on the log normal distribution data of the nnds [44, 45]. In Eq. (1), σ_{ln} is the standard deviation of the nnd data after a natural log transformation. It is worth to note that lower the COV value, more homogeneous the sample data.

$$\mathrm{COV} = \sqrt{e^{\sigma_{ln}^2} - 1} \tag{1}$$

X-ray diffraction measurements of the AC and the HTed samples were carried out at room temperature using a PANalytical Empyrean diffractometer system equipped with a novel Bragg Brentano^{HD} module (to obtain a monochromatized divergent incident beam) and an ultra-fast PIXcel^{3D} detector (used in linear scanning mode). An X-ray tube with cobalt (Kα = 0.1791 nm) as the anode material was utilized as the radiation source along with a θ−2θ scan geometry. The acceleration voltage and current applied during the measurements were 40 kV and 40 mA, respectively. The scans were made over a 2θ range of 40° to 130° with a step size of 0.013° and a counting time of 250 s, constituting a total scanning time of approximately 2 h. Moreover, the pulse height distribution settings were set to a range of 25.5% (3.53 keV)–80% (11.09 keV). The peak positions and phase identification was performed using the X'Pert High Score Plus software. Additionally, the volume fraction of the RA in the HTed samples was estimated by the Rietveld refinement approach [46], using the software Material Analysis Using Diffraction (MAUD) [47].

The matrix hardness was determined using the Vickers method using a Struers Dura Scan 50 microhardness tester with a load of 0.9807 N (HV0.1). During the testing, the dwell time was 15 s and the readings were averaged over 15–20 measurements. The load was chosen ensuring that the surrounding entities (EC and/or the interfacial α') are not participating in the evaluation of the matrix hardness and, the indentation mark was clearly resolvable using the optical microscope.

The morphological aspects of the wear tracks as well as the acting wear mechanisms were ascertained using CLSM and FE-SEM. A high-performance ion conversion and electron detector was employed during the SEM analysis to obtain a better phase contrast and emphasize on certain regions of interest within the wear track. Energy-dispersive X-ray spectroscopy (EDS) was used to chemically map the worn and the unworn surface.

The local deformation and the strain distribution at the vicinity of the wear track was investigated by electron backscattered diffraction (EBSD). The measurements were performed at an acceleration voltage of 20 kV and a beam current of 11nA, using the FE-SEM workstation equipped with an EDAX Hikari EBSD camera. The EBSD data was analysed using the Orientation Imaging Microscopy (OIM™ v. 7) Data Analysis software by EDAX Corporation. Kernel average misorientation (KAM) measurements were carried out to extract orientation data within the deformed regions. Owing to the very small step size (30–50 nm), 2nd neighbour KAM with a 5° threshold was considered for the analysis. Additionally, misorientation profile analysis was performed around the deformed region to obtain the orientational variation.

Wear quantification was described in terms of WR, and it was proceeded by calculating the volume loss encountered in each track using the proprietary LEXT software in the CLSM. The entire wear track, including the ends were considered in the calculations, and Eq. (2) was used to compute the WR, where V represents the wear volume (mm^3), l is the total sliding distance ($5.5 \times 2 \times 2000$ mm), P is the applied load (N), and WR represents the wear rate ($mm^3\ N^{-1}\ mm^{-1}$).

$$\mathrm{WR} = \frac{\mathrm{V}}{\mathrm{l} \times \mathrm{P}} \tag{2}$$

3 Results and Discussion

3.1 Microstructural Characterization of the Destabilized Samples

Figure 3 represents the micrographs obtained from CLSM and SEM, and the EBSD phase maps for the destabilized samples. The HTed microstructure is characterized by the presence of a primarily martensitic matrix (α'), finely precipitated SC ($M_{23}C_6$ type), the original (as-cast) EC (M_7C_3 type) and RA. The EC (in terms of volume fraction and size refinement) are relatively immune to the HT considering their thermal stability [7, 13, 48] and the destabilization temperature used in the present work. Hence, it is assumed that all the changes are taking place predominately in the matrix.

Comparing the CLSM micrographs (a.1, b.1 and c.1 in Fig. 3) of the HTed samples, a reduction in the RA content (white patches) was observed with increasing destabilization holding time. Moreover, the SEM micrographs (a.2, b.2 and c.2 in Fig. 3) give a visual perspective of the SC distribution throughout the material. In fact, the precipitation of SC and the reduction of RA is an interdependent process [11, 12].

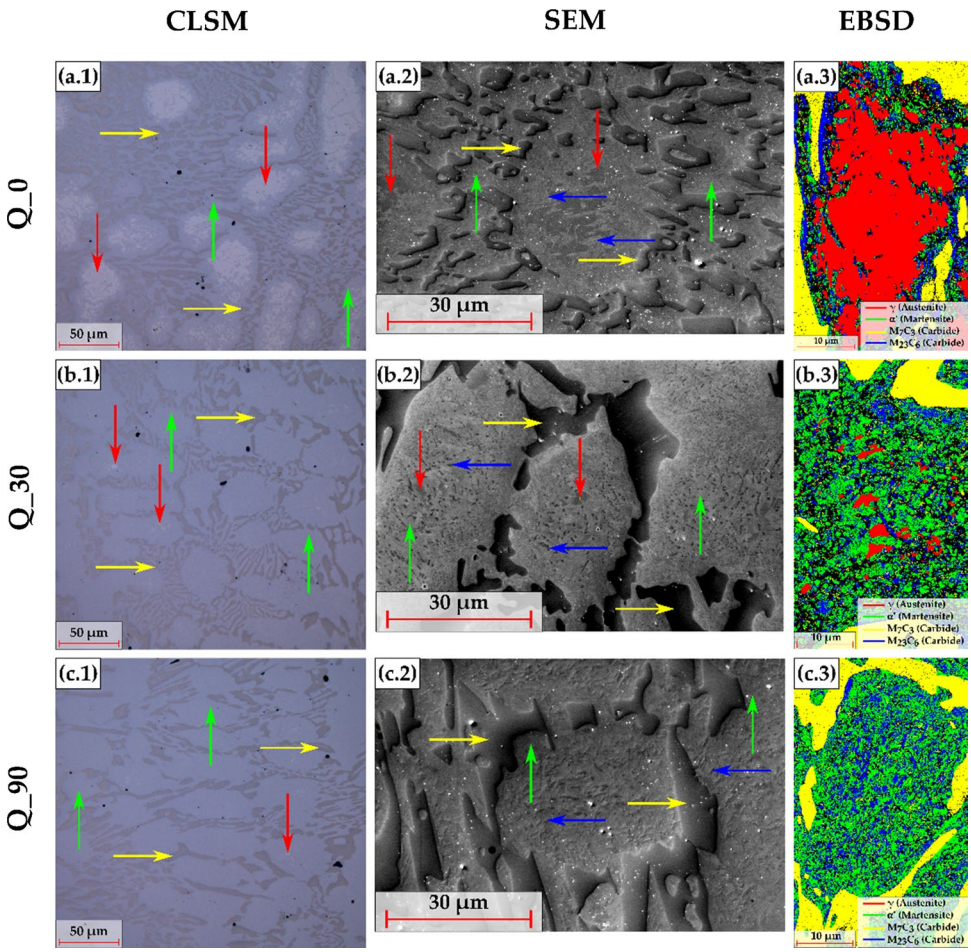

Fig. 3 Micrographs of the destabilized samples obtained using CLSM (1) and SEM (2), and the EBSD phase maps (3), for Q_0 **a**, Q_30 **b** and Q_90 **c**, respectively. The phases are accordingly colour and arrow-labelled for reference

During destabilization, the increased driving force for alloy redistribution results in the precipitation of $M_{23}C_6$ type SC [49]. In the Q_0 sample, they are primarily located at the periphery of the matrix, whereas in the case of Q_30 and Q_90, they are also located within the body of the matrix. This indicates that the precipitation initially occurred at the periphery and proceeded inwards into the body of the matrix. This sequence was also observed in other studies [13, 14, 50, 51].

Additionally, the variation in the size and shape of the SC indicate that they may have precipitated at different times during the destabilization heat treatment. In a recent work, simulations using MatCalc predicted that precipitation started during heating at approximately 800 °C and additional precipitation took place during the initial cooling phase (980–750 °C) [49]. Considering the sample size used in the present work and the fact that it was kept inside the furnace during the heating, and not inserted once the intended destabilized temperature was reached, precipitation had taken place during the heating. Consequently, the stability of the austenite is reduced owing to the depletion in carbon, leading to a partial transformation to martensite upon cooling.

Furthermore, the EBSD phase maps (a.3, b.3 and c.3 in Fig. 3) of the matrix region indicate both the reduction in the RA with increasing destabilization holding time, and the distribution variation in the SC precipitates. Although the CLSM and SEM micrographs can be considered representative, it is worth to note that the EBSD phase map was obtained from a very small region and should be treated with caution. Nevertheless, the correlative microscopy (CLSM—SEM—EBSD) approach was very useful in the assessment of the destabilized microstructure.

The X-ray diffractograms of the AC and HTed samples are presented in Fig. 4a wherein the various phases are indexed for reference. Moreover, the 2θ values ranging from 51° to 54° (as indicated by the dashed-black enclosure in Fig. 4a) were subjected to peak deconvolution and fitting, as represented from Fig. 4b–e. A clear shoulder is seen for the AC sample which was separated into two individual peaks of M_7C_3 and α' using a pseudo-Voigt function. Comparing the most intense peak of the HTed samples i.e., the (110) martensite peak, a shift in the peak position is observed. The (110) α' peak in Q_0 is slightly shifted at a higher 2θ angle compared to the Q_30 and Q_90 which is an indication of lower carbon in the martensite phase. The presence of

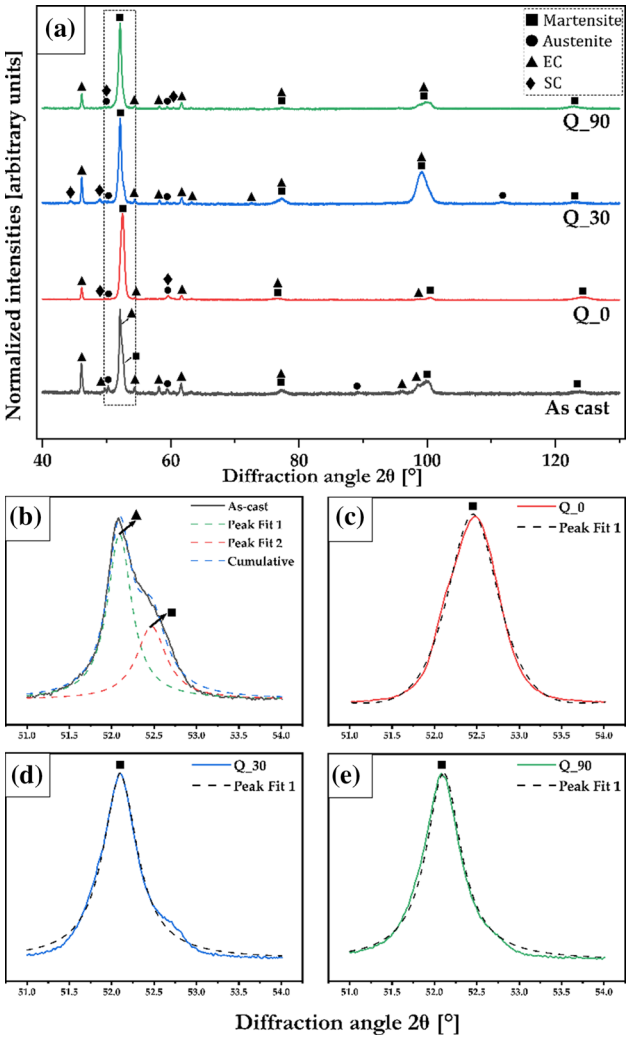

Fig. 4 **a** X-ray diffractograms of the AC and HTed samples. **b–e** represent a corresponding magnified view of the peaks and the associated peak deconvolution from 2θ values ranging from 51° to 54°, as indicated by the dashed black enclosure in **a**

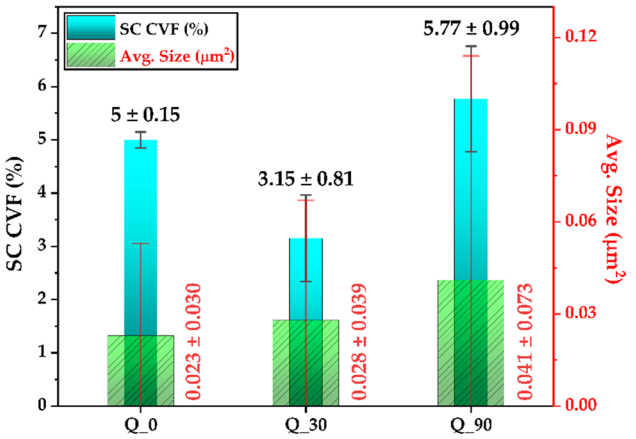

Fig. 5 The secondary carbide volume fraction (%) and the corresponding average size (μm^2) for the destabilized samples

a higher amount of carbon in the martensite lattice distorts it even more increasing the interplanar spacing. Considering the inverse relationship between the interplanar spacing and the Bragg's angle in the Bragg equation, this leads to a shift in the peak towards lower 2θ values which is observed in the X-ray diffractograms. Considering the similarity between the positions of the (110) α' peaks in Q_30 and Q_90, a larger lattice deformation compared to the Q_0 sample can be inferred, which should lead to a harder martensitic phase [52].

The calculated CVF (%) and average size (μm^2) of the SC are represented in Fig. 5. A decrease in the CVF is observed in the first 30 min and later, it increases from Q_30 to Q_90. The CVF values of Q_0 and Q_90 is statistically comparable, although the average size increased two-fold in the latter. Comparing Q_0 with the Q_30 sample, even though the CVF reduced (~40%), the average size remained within the tolerance interval ((Mean + S.D.)—(Mean—S.D.)). Additionally, the distribution of the SC in terms of size and nnd can also provide crucial information in understanding the precipitation specifics [7, 11, 51].

The log normal size distribution (in terms of particle count vs. area (μm^2)) for the three HTed samples is graphically represented in Fig. 6a. The average size for the corresponding samples is indicated in the inset table in Fig. 6a. The cumulative distribution curve is plotted in Fig. 6b which shows that for a given size, the percentage of particles falling within that size range decreases from Q_0 to Q_90. This is further exemplified by the distribution-rug plot in Fig. 6c, plotted on a log–log scale for better visualization, where it is indicated that the Q_90 sample possesses a higher number of particles with larger sizes, whereas the particle distribution between Q_0 and Q_30 is similar. Combining the information obtained from Fig. 6a concerning the reduction in particle count, with the rug plot in Fig. 6c, it is evident that the average size increases from Q_0 to Q_90.

As the precipitation takes place by nucleation and growth phenomena, they need to overcome a certain activation barrier to achieve a critical size to nucleate. Moreover, new phases tend to favour precipitating on heterogeneous surfaces such as defect clusters, sub-grain boundaries, etc., where it is thermodynamically more favourable [53, 54]. The fresh precipitation could be presumed to have taken place during two stages of the HT i.e., heating and cooling. During heating, the transformation of the interfacial martensite to austenite at the periphery results in the austenite possessing a large number of defects. This stems from the stresses generated owing to the differences in coefficient of thermal expansion between the hard M_7C_3 EC and the austenitic matrix. This generation of defect clusters at the periphery reduces the activation energy required to achieve the critical

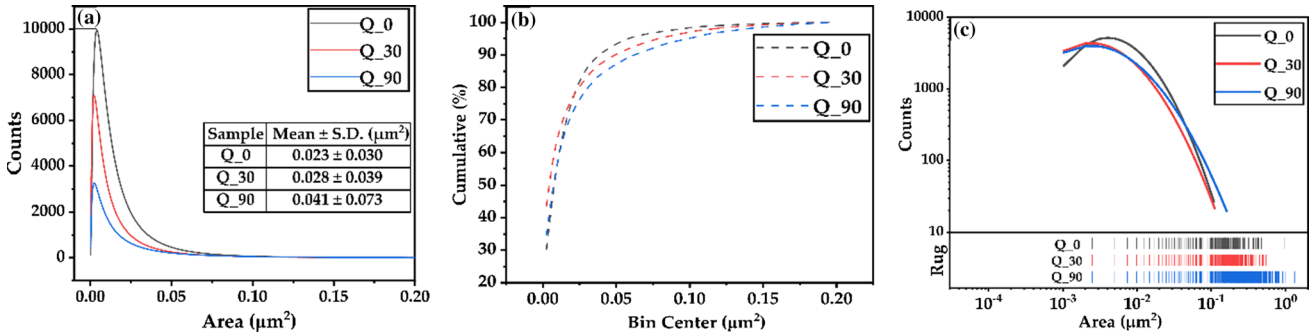

Fig. 6 **a** log normal size distribution of the SC for the HTed samples with the inset table representing the average size for each of the destabilized samples. The peak of the distribution curves signifies the corresponding modes. The cumulative distribution curve is plotted in **b** and, **c** distribution-rug plot plotted on a log–log scale, which is indicative of a histogram with zero-width bins and used to visualise distribution of the data

size, resulting in a large number of small-sized carbides nucleating at those regions [48, 50]. Subsequently, some of the freshly precipitated carbides can also partially redissolve into the matrix. This can be thought to take place in the first 30 min (Q_0 → Q_30) wherein the particle count and CVF is decreasing with the average size remaining statistically within range, as indicated in Figs. 5 and 6. Simultaneously, the continuous alloy redistribution taking place during the isothermal holding results in the growth and coalescence (Ostwald ripening) of SC in other regions of the matrix. This is expected to take place from Q_30 → Q_90, as evident from Fig. 6, where the average size and CVF is increasing, and the number of particles is decreasing. Nevertheless, the presence of small-sized carbides at the periphery of all the HTed samples is indicative of the fact that additional precipitation took place during the cooling stage, but no time was given to facilitate their growth [49, 55].

The nnd distribution was also log normally plotted and is represented in Fig. 7a. The inset table in Fig. 7a indicates the mean nnd value for the three HTed samples, being the lowest for the Q_0 amongst all the conditions. Although the mean nnd values of the HTed samples fall within the tolerance interval, analysing their distribution gives information on their homogeneity. Figure 7 (b) and Fig. 7c represent the nnd cumulative distribution curve and the nnd distribution-rug plot, respectively. The COV was determined for each of the HTed samples considering the standard deviation of the log normally distributed nnd values (σ_{ln}) and using Eq. (1). Sample Q_0 had a COV of about 40% whereas the Q_30 and Q_90 samples showed COV values of 49% and 47%, respectively. It also worth to mention that although the COV value of Q_0 is the lowest indicating that the dispersion of SC precipitates relatively more homogeneous, this should not be considered as the sole deciding factor. This approach fails to consider the fact that in the Q_0 sample, most of the precipitates are located around the periphery of the matrix and therefore, are considerably more closely spaced compared to the Q_30 and Q_90 samples. In the case of the Q_30 and Q_90 samples, the particles are also predominately present at the body of the matrix (Fig. 3). The slight increase in the COV value of Q_30/Q_90 could be explained by the dissolution of the carbides at the periphery and the presence of carbides in the matrix body, leading to a higher absolute average nnd value. This trend is also exemplified in the rug

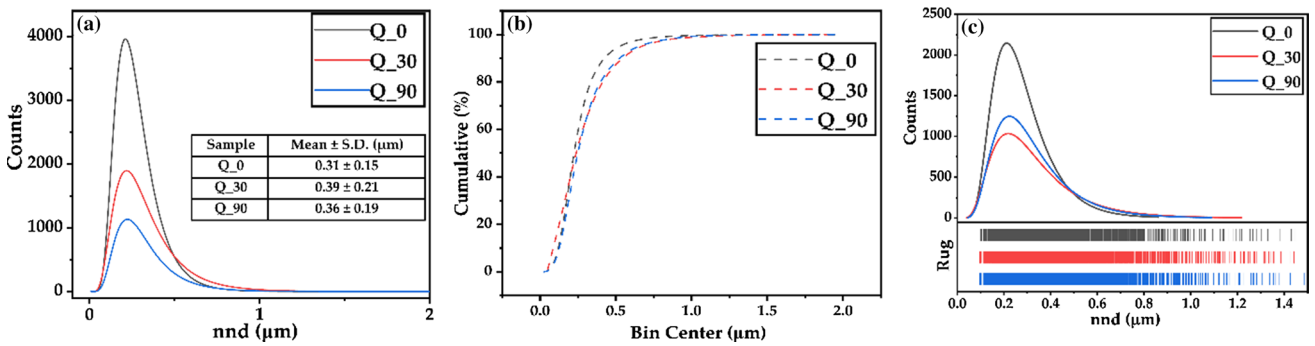

Fig. 7 **a** log normal near neighbour distance (nnd) distribution of the SC for the HTed samples with the inset table representing the average nnd for each of the destabilized samples. The cumulative distribution curve is plotted in **b** and, **c** distribution-rug plot plotted on a linear scale

plot in Fig. 7c) where the increased dispersion in the red vertical lines (Q_30) can be observed. The information obtained from the homogeneity calculations should also be combined with the size and nnd analysis to explain the changes taking place during the HT.

The estimation of the RA content in AC and HTed samples, along with the measured matrix hardness is given in Table 3. A clear trend is visible with respect to the RA content i.e., increasing the destabilization holding time results in the reduction of the RA, as also indicated by the correlative microscopy analysis of Fig. 3. Moreover, the implications of the SC distribution and the associated $\gamma \rightarrow \alpha$' matrix transformation on the hardness is evident. The presence of a large number of small-sized carbides located at the periphery of the matrix renders the central part of the matrix primarily austenitic, as observed from Fig. 3 (a.1) and Fig. 3 (a.3). As a result, the hardness of the Q_0 sample is increased marginally compared to the AC. With increasing holding time, the precipitation proceeds inwards into the matrix tending to grow and coalesce. This results in more of the austenite being transformed to martensite upon cooling and eventually a substantial increase in the matrix hardness, as evidenced from Table 3. Furthermore, it could be deduced from XRD that the martensite formed in the Q_30 and Q_90 samples is harder compared to the Q_0 owing to the shift in the (110) α' peak, contributing to the two-fold increase in the matrix hardness. The similitudes in the hardness of the Q_30 and Q_90 could be attributed to the like nature and distribution of the microstructural constituents.

Table 3 The values of the retained austenite estimated using MAUD and the corresponding matrix hardness (HV0.1). The RA value of the As-cast was determined metallographically*, whereas Rietveld analysis by MAUD** was used for the HTed samples

Sample	Retained austenite (MAUD) (%)	Matrix hardness (HV0.1)
As-cast*	58.1	347 ± 24
Q_0**	10.2	412 ± 31
Q_30**	7.1	759 ± 22
Q_90**	5.1	775 ± 33

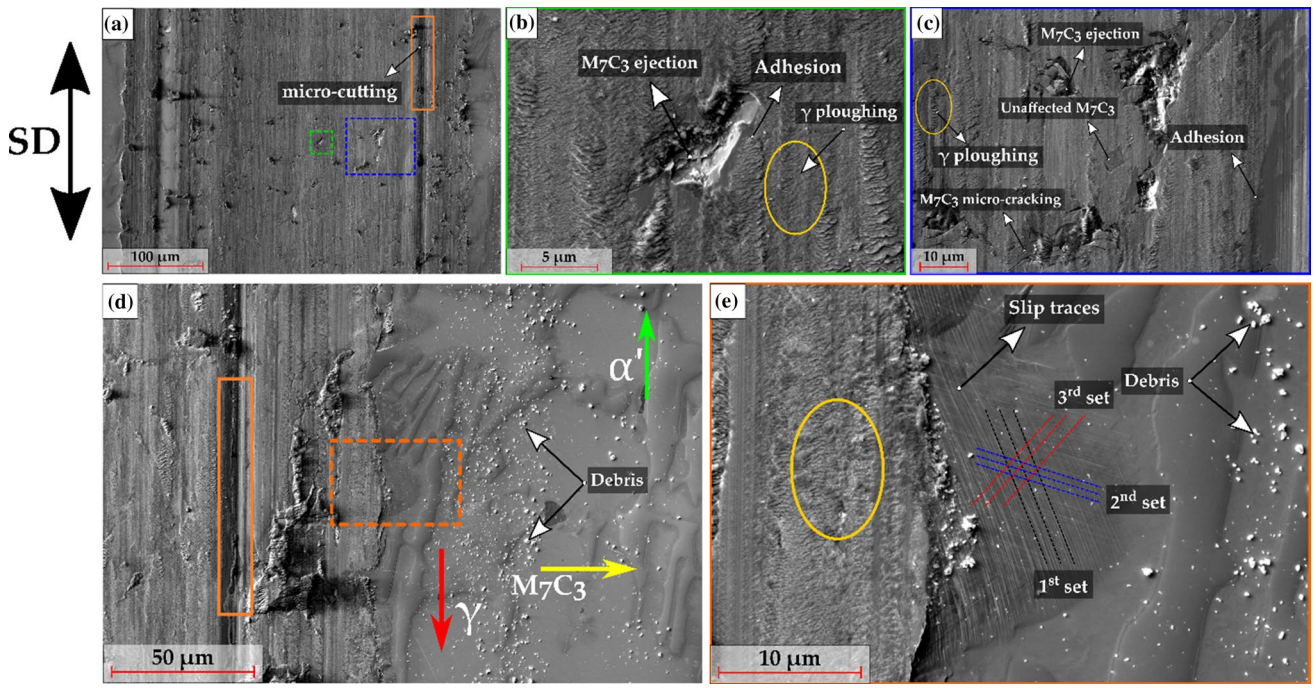

Fig. 8 **a**–**c** SEM secondary electron (SE) micrographs of the wear track for the AC sample with the various aspects of the wear track delineated and the corresponding magnified SE micrographs of the dashed-green and the dashed-blue areas. The γ, α' and M_7C_3 (EC) phases are marked in **d**, along with the wear debris. **e** SE micrograph of the dashed-orange enclosure marked in **d**. The slip traces, in addition to the three different sets of activated slip planes are indicated in **e**. The solid-orange enclosure and solid-yellow ellipse is indicative of the micro-cutting and austenite (γ) ploughing phenomena, respectively. The sliding direction (SD) is also mentioned for reference

3.2 Tribological Response of the AC and HTed Samples

3.2.1 As-Cast

Figure 8a–c represents the SEM SE micrograph encompassing the entire track width, together with the corresponding magnifications of the dashed-green and dashed-blue enclosures. From the micrographs, it was observed that the wear track had shown traits of adhesion especially at the matrix-carbide interface. Moreover, micro-cutting of the carbide and micro-ploughing of the austenite matrix (as evidenced by the presence of grooves bordered by lateral ridges), characteristic mechanisms of abrasive wear, was also observed. Figure 8d represents the SE SEM micrograph of the wear track with emphasis on the matrix region adjacent to the wear track and the corresponding magnified micrograph of the dashed-orange enclosure is depicted in Fig. 8e. Plastic deformation of the austenitic matrix can be observed, evidenced by the slip traces at the region adjoining the wear track, which are a manifestation to accommodate the deformation endured by the austenite. As a result of micro-cutting and micro-ploughing, cracking, and ejection of small fragments of EC ensue, as detailed in a previous work dealing with the analysis of the microstructural evolution of the AC 26 wt% Cr white cast iron under identical sliding conditions [41].

3.2.2 Destabilization for 0 min (Q_0)

The SEM SE micrographs of the Q_0 wear track is represented in Fig. 9. Two scenarios are depicted depending on whether the matrix adjacent to the wear track was martensite (Fig. 9a, b) or austenite (Fig. 9c, d). The presence of slip traces is a clear indication of the austenite deformation and is marked in Fig. 9c, d. On the contrary, no slip traces were observed when the martensite was adjacent to the wear track, owing to its inability to plastically deform considering the load used in the present study [41, 56]. The phenomenon of adhesion was observed, as in the AC condition, primarily at the matrix-carbide interface. The O EDS concentration map (Fig. 9e) indicates the preferential accumulation of oxides where the carbides have been cracked and/or ejected [41, 57].

Figure 10a represents the SEM SE micrograph of the area adjacent to the wear track edge where the EBSD measurements (dashed-blue enclosure) were carried out. The phase map in Fig. 10b clearly shows that the area adjacent to the wear track was primarily austenitic and the manifestation of slip bands is an indication of the austenite deformation, as marked by the dashed-orange enclosure in Fig. 10a. Comparing Fig. 10a, b, the slip lines terminate

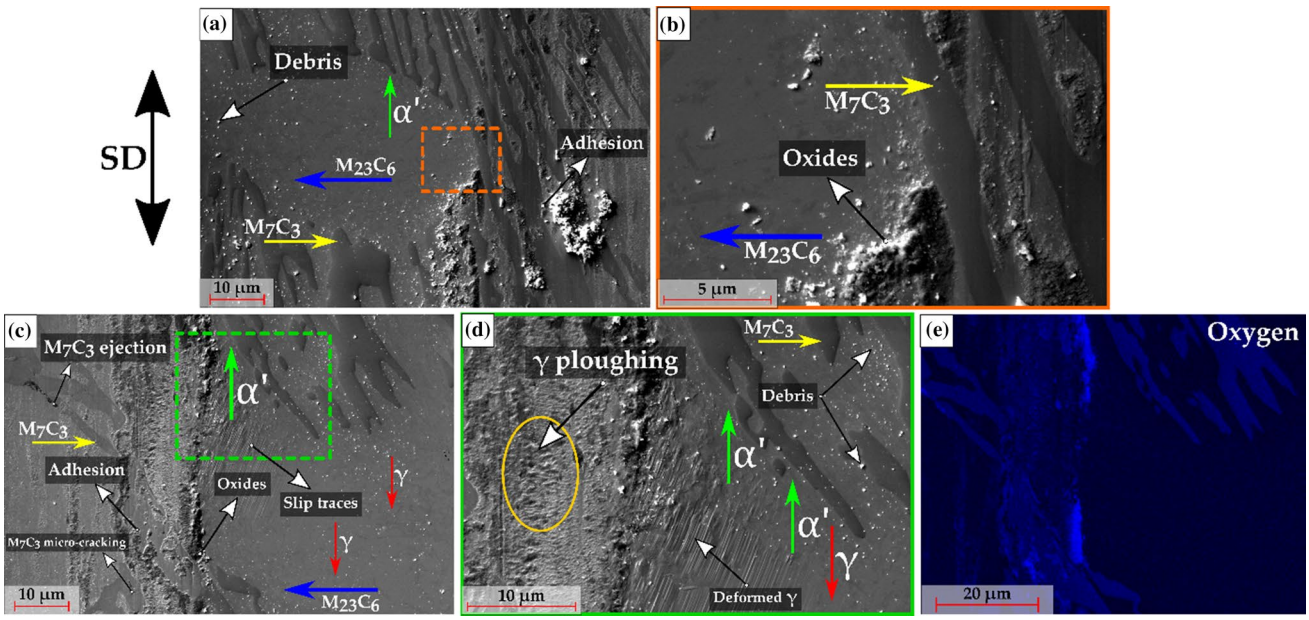

Fig. 9 **a** SEM SE micrograph of the wear track for the Q_0 sample when the matrix adjacent to the track is primarily martensitic. **b** magnified SE micrograph of the dashed-orange enclosure marked in **a**. **c** SEM SE micrograph of the wear track when the austenite phase is adjacent to the wear track, indicating the adhesion, carbide micro-cracking and ejection. **d** magnified SEM micrograph of the dashed-green enclosure in **c**. The wear debris, the deformed austenite and ploughing effect is marked in **d**. **e** O EDS concentration maps of the micrograph presented in **c**. The SD is also mentioned for reference

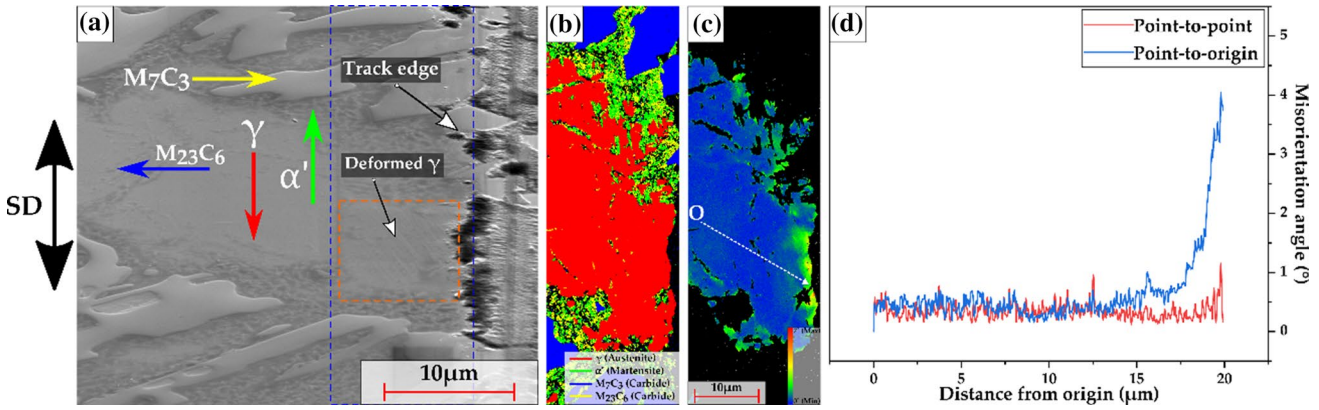

Fig. 10 **a** SEM SE micrograph of the wear track for the Q_0, with the various phases and the deformed γ delineated. **b** EBSD phase map of the dashed-blue enclosure in **a**, **c** KAM map of the austenite region. The variation of the misorientation angle (point-point and point-origin) across the austenite region starting from the point O following a path indicated by the dashed-white line in **c** is graphically represented in **d**. The SD is also marked for reference

upon encountering the martensite phase. This is attributable to the difference in crystal structure and a higher hardness. Figure 10c indicates the KAM map of the isolated austenite region. The orientational variation of the adjacent austenite region was exemplified by calculating the point-to-point and point-to-origin misorientation profile chart, as represented in Fig. 10d. A variation of about 4° was observed between the deformed and undeformed austenite region. This rotation of the austenite crystal lattice allows a quantitative evaluation of the local plastic deformation [58].

3.2.3 Destabilization for 30 min (Q_30)

Figure 11 represents the SEM SE micrograph of the Q_30 wear track with Fig. 11b indicating a magnified micrograph of the dashed-orange enclosure in Fig. 11a. Unlike the Q_0 sample where the region adjacent to the wear track could be either RA or martensite, the Q_30 sample had a predominately martensitic matrix, and no austenite was visible next to the wear track. Since the martensite is not able to undergo plastic deformation, no slip traces are visible next to the track. Moreover, as the hardness of the alumina counter body (~ 1500 HV) is higher than the

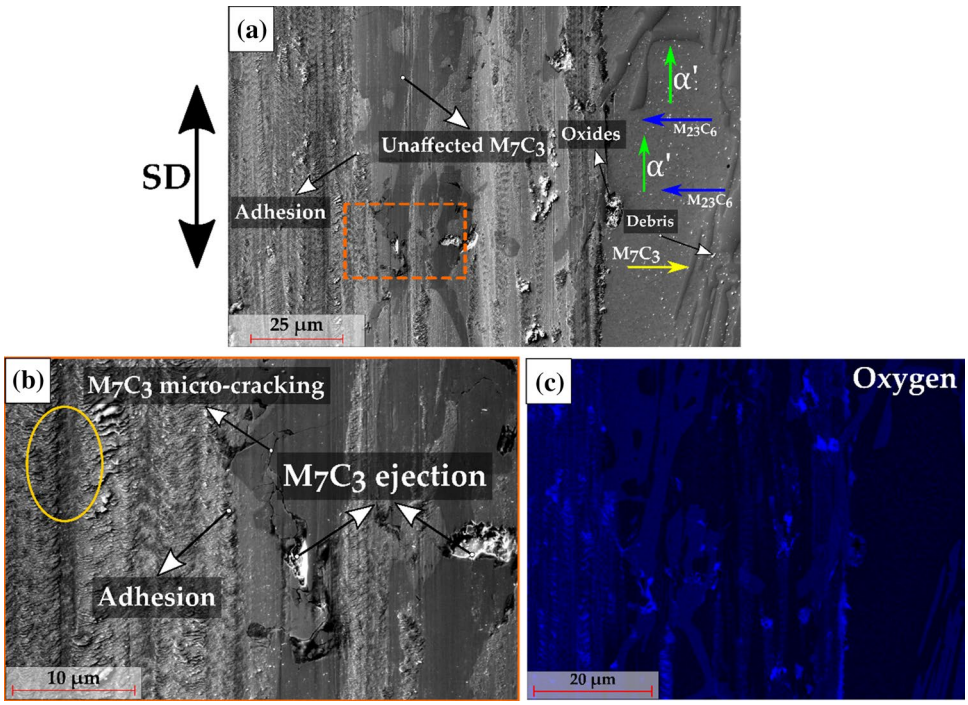

Fig. 11 **a** SEM SE micrograph of the wear track for the Q_30 sample, with the phases and various aspects of the wear track delineated. The wear debris, the oxides and the unaffected EC is marked in **a**. **b** magnified SE micrograph of the dashed-orange enclosure marked in **a**, wherein the phenomenon of adhesion along with the carbide micro-cracking and ejection is indicated. The O EDS concentration maps is indicated in **c** of the micrograph presented in **a**. The SD is also mentioned for reference

HCWCI material and/or the Cr-rich M_7C_3 carbide hardness (~ 1200 HV), the carbides are prone to micro-cracking [32, 33]. Additionally, the presence of the unaffected M_7C_3 carbide in Fig. 11a is an indication that not all carbides had undergone cracking. This could be attributed to the carbide's geometric orientation and the increased load-bearing capacity of the martensite [59–62]. Comparing the O EDS concentration maps of Q_0 (Fig. 9e) and Q_30 (Fig. 11c), it can be qualitatively appreciated that the latter possesses a greater area where oxides have accumulated throughout the wear track.

3.2.4 Destabilization for 90 min (Q_90)

The SEM SE micrographs of the Q_90 wear track and the O EDS map is represented in Fig. 12. No major differences were observed between the wear behaviour of Q_30 and the Q_90 sample. Similar to the Q_30 sample, the wear track had shown indications of adhesion, micro-cutting, and ploughing, as well as carbide spallation and ejection. From Fig. 12c, it was observed that the carbide cracking had taken place perpendicular to the sliding direction. This is a commonly observed phenomenon in HCWCIs in response to the tangential stresses acting during the sliding process, leading to brittle fracture [59, 60]. Moreover, the similarities in the values of the matrix hardness and RA are suggestive that the samples show a similar wear rate.

Although the microstructural constituents of the HTed samples are identical, the differences in their amounts and distribution had a consequence on the final tribological behaviour of the alloy. In the case of the samples possessing a higher amount of austenite (as-cast and Q_0), the wear mechanisms can be thought of a combination of mild adhesion and abrasion (as evident from the micro-cutting and ploughing) although, the influence of oxidation cannot be completely dismissed. Whereas, in the Q_30 and Q_90 samples, in addition to adhesion and abrasion, oxidation also plays a big role in the wear behaviour due to the detachment of secondary carbides from the matrix, as evident from the EDS concentration maps (Figs 11 and 12) and as seen further, the frictional behaviour.

3.2.5 Wear Rate and COF

The mutual dependence of the WR ($mm^3\ N^{-1}\ mm^{-1}$) on the rest of the microstructural characteristics for all samples is graphically represented in Fig. 13a, and two major observations were made. Firstly, all the destabilized samples had shown a lower WR compared to the AC sample and secondly, a harder matrix did not necessarily guarantee a better wear resistance. Interestingly, the Q_0 sample with the lowest hardness among all the HTed samples, showed the lowest WR (i.e., highest wear resistance). Compared to the AC sample, the Q_0 showed a reduction of about 50%, whereas in the Q_30 and Q_90 samples, a decrease of up

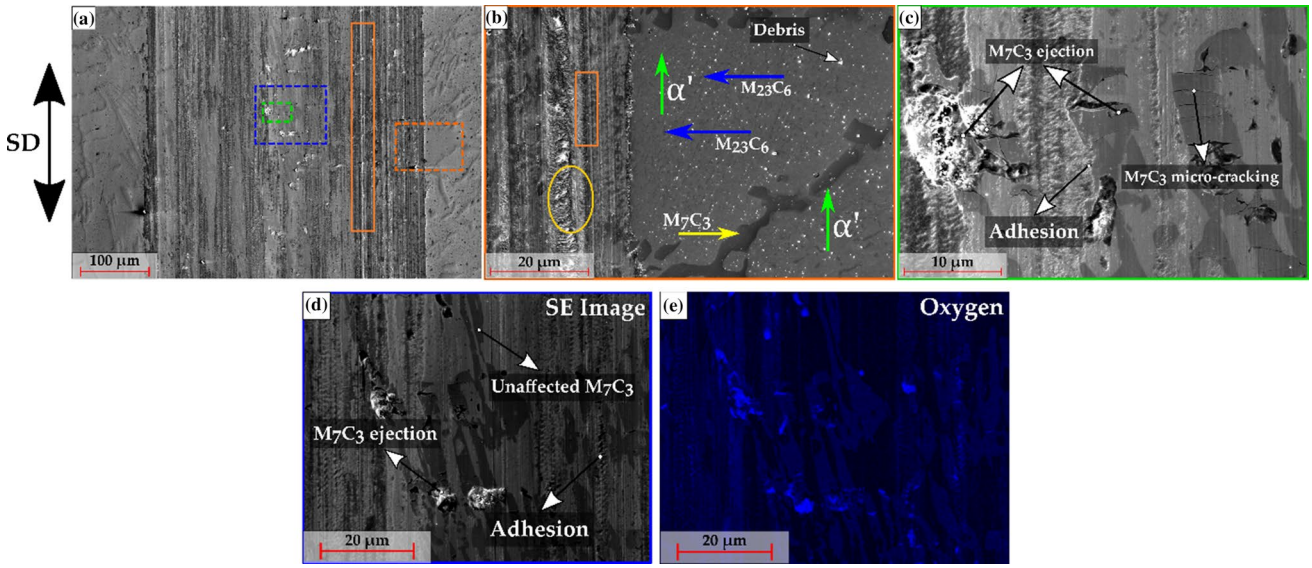

Fig. 12 **a** SEM SE micrograph of the wear track for the Q_90 sample, with the micro-cutting phenomenon delineated. The wear debris, the oxides and the unaffected EC is marked in **a**. **b** depicts the magnified SE micrograph of the dashed-orange enclosure marked in **a**, wherein the various phases, wear debris and the phenomenon of micro-cutting and ploughing is indicated. **c** magnified SE micrograph of the dashed-green enclosure in **a** where the phenomenon of adhesion along with the carbide micro-cracking and ejection is visible. **d** A magnified SE micrograph of the dashed-blue enclosure in **a**. The EDS concentration maps of O is indicated in **e** of the micrograph presented in **d**. The SD is also mentioned for reference

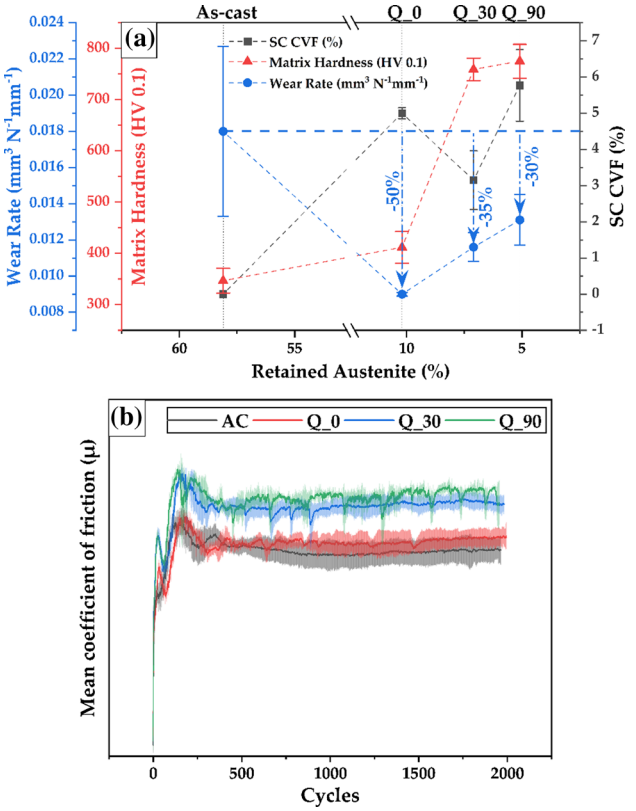

Fig. 13 **a** Graphical representation of the RA, WR, SC CVF (%) and matrix hardness (HV 0.1) values and **b** Mean coefficient of friction (COF) evolution for all the samples

to 35% was observed. Moreover, no major differences in the WR between the Q_30 and Q_90 samples were seen as hypothesized based on the microstructural characterization.

The frictional behaviour of the samples (expressed in terms of mean coefficient of friction (COF)) is represented graphically in Fig. 13b. In all cases, the curves reach a peak (running-in) before decreasing and reaching a steady state (SS). It is interesting to note that apart from the AC sample, all the HTed samples show a 'double running-in' behaviour. The initial peak is reached after about 75–100 cycles before showing a slight decrease after which it again ramps up to a higher peak value after about 250 cycles before settling at a SS value. The mean SS COF values of the AC and the Q_0 sample is comparable whereas the corresponding values of Q_30 and Q_90 are similar, indicating a distinction between the two groups. The main distinguishing feature is the presence of a relatively higher percentage of austenite in the AC and Q_0 sample compared to the latter two. In the Q_0 sample, the relatively higher amount of austenite could be thought to have provided additional mechanical support to the surrounding carbides by undergoing plastic deformation during the wear test. This was evident in Figs. 9 and 10 where the slip lines are visible emanating from the austenite region. In the Q_30 and Q_90 samples, the predominately martensitic matrix is unable to plastically deform compared to the austenitic matrix and thus incapable of providing the necessary support for its surrounding carbides leading to carbide micro-fracture and eventual ejection. The increased carbide ejection results in an increasing number of voids allowing the oxide to accumulate in those regions and further influence the wear behaviour [41]. This can be appreciated in the steady state behaviour of the Q_30 and Q_90 samples, wherein the continuous fluctuations indicate the formation and breakage of the oxide layer [63]. Although these fluctuations stop after about 1000 cycles for the Q_30 sample indicating conformality has reached, they continue for the Q_90 sample for the whole duration of the wear test.

As the matrix is worn out by the abrasive process, the support it offers to the carbides dwindles, resulting in an increased abrasive wear volume loss [64]. In the Q_90 sample, even though the CVF is comparable to that of the Q_0 sample, the decreased amount of RA and the increase in the average carbide size led to a higher probability of SC being ejected, leading to a change in wear mechanism towards oxidative wear and an increase in the WR. A decrease in the average carbide size for a constant carbide volume shortens the mean distance between the carbides, thereby minimizing the matrix exposure to contact damage [31].

Another factor for the lower WR of the HTed samples compared to the AC could be attributed to the cracking of the large EC. It was markedly higher in the AC sample compared to the HTed samples. Although the M_7C_3 type of EC has a higher inherent fracture toughness, the assumption that the EC are unaffected during the heat treatment implies the reduced prevalence of cracking is due to the changes taking place in the matrix during destabilization. This could be attributed to the presence of the hard martensite which improves the load-bearing capacity, thereby reducing the tendency for carbide micro-fracture [12, 29]. Additionally, the varying size distributions of the finely dispersed SC led to smaller SC particles participating in the intermixing of the tribologically transformed zone whereas the larger particles assisted in distributing the load. Although at higher destabilization holding times, the increasing average size of the SC made its ejection more probabilistic, especially with a martensitic matrix surrounding it. This led to the wear mechanism tilting in favour of oxidation, negatively impacting the WR. Nevertheless, the presence of a harder martensitic matrix and the distribution of SC throughout the HTed samples ensured an increased wear resistance compared to the AC sample.

4 Conclusions

In the current study, dry sliding linear-reciprocating wear tests were performed on a destabilized 26 wt% Cr white cast iron. The effect of increasing the destabilization holding time on the microstructural evolution and the subsequent tribological behaviour of the alloy was examined and the following conclusions were drawn.

- Microstructural observations revealed that destabilization resulted in the precipitation of fine SC and a temporal increase in the transformation of austenite to martensite, whereas the EC remained relatively immune to the HT.
- Stereological characterization of SC indicated a decrease in the CVF in the first 30 min and later, an increase from Q_30 to Q_90. The CVF values of Q_0 and Q_90 is statistically comparable, although the average size increased two-fold in the latter.
- The matrix hardness of the HTed samples increased up to 125% compared to the AC sample (owing to the presence of SC and a martensitic matrix) although, there was no significant rise between the Q_30 and Q_90 sample, indicating stagnation.
- All the HTed samples showed a reduction in the WR compared to the AC sample, with the Q_0 sample presenting the highest reduction (50%).
- The Q_0 sample showed the lowest WR, even though it did not present the highest matrix hardness among all the samples. This sheds light on the importance of an optimal distribution between the microstructural constituents after destabilization.
- Selection of the right heat treatment is highly dependent on the intended application. Samples Q_30 or Q_90 could be chosen if having a high hardness is a prerequisite as both the samples show a hardness of about twice that of the Q_0 sample. Hence, for applications where a high hardness is a requirement, it is recommended to destabilize for a longer period to ensure the amount of RA is reduced whereas for wear resistant applications, the presence of ~ 10% RA in addition to the precipitated SC (~ 5%) is advantageous.

Acknowledgements The present work is supported by funding from the Deutsche Forschungsgemeinschaft (DFG, project: GU 2102/2-1). The authors would like to thank the Saarland State Chancellery for financial support within the ZuMat Project funded by the European Regional Development Fund (ERDF). Moreover, the funding for the PFIB/SEM instrument by DFG is greatly acknowledged (INST 256/510-1 FUGG). The authors would also like to thank Martin Duarte from Tubacero S.A. for providing the materials and finally, U.P.N. is grateful to DAAD for the financial support.

Funding Open Access funding enabled and organized by Projekt DEAL.

Declarations

Conflict of interest The authors declare that they have no conflict of interest.

References

1. K. Holmberg, A. Erdemir, Friction **5**, 263 (2017). https://doi.org/10.1007/s40544-017-0183-5
2. K. Holmberg, P. Kivikytö-Reponen, P. Härkisaari, K. Valtonen, A. Erdemir, Tribol. Int. **115**, 116 (2017). https://doi.org/10.1016/j.triboint.2017.05.010
3. J.D. Watson, P.J. Mutton, I.R. Sare, Met. forum **3**, 74 (1980)
4. K.H. Zum Gahr, D.V. Doane, Metall. Trans. A **11**, 613 (1980). https://doi.org/10.1007/BF02670698
5. C.G. Oliveira, I.P. Pinheiro, MRS Online Proceedings Library **1816**, 65 (2016). https://doi.org/10.1557/opl.2016.65
6. ASTM A532/A532M-93a, Standard Specification for Abrasion Resistance Cast Irons (ASTM International, West Conshohocken, 2003)
7. C.P. Tabrett, I.R. Sare, M.R. Ghomashchi, Int. Mater. Rev. **41**, 59 (1996). https://doi.org/10.1179/095066096790326075
8. R.J. Llewellyn, S.K. Yick, K.F. Dolman, Wear **256**, 592 (2004). https://doi.org/10.1016/j.wear.2003.10.002
9. E. Karantzalis, A. Lekatou, H. Mavros, Int. J. Cast. Met. Res. **22**, 448 (2009). https://doi.org/10.1179/174313309X436637
10. F. Maratray, AFS Trans. **79**, 121 (1971)
11. A.E. Karantzalis, A. Lekatou, H. Mavros, J. Mater. Eng. Perform. **18**, 174 (2009). https://doi.org/10.1007/s11665-008-9285-6
12. M.A. Guitar, S. Suárez, O. Prat, M.D. Guigou, V. Gari, G. Pereira, F. Mücklich, J. Mater. Eng. Perform. **27**, 3877 (2018). https://doi.org/10.1007/s11665-018-3347-1
13. H. Gasan, F. Erturk, Metall. Mater. Trans. A **44**, 4993 (2013). https://doi.org/10.1007/s11661-013-1851-3
14. G.L.F. Powell, G. Laird, J. Mater. Sci. **27**, 29 (1992). https://doi.org/10.1007/BF02403640
15. A. Wiengmoon, T. Chairuangsri, J.T.H. Pearce, ISIJ Int. **44**, 396 (2004). https://doi.org/10.2355/isijinternational.44.396
16. R. Correa, A. Bedolla-Jacuinde, J. Zuno-Silva, E. Cardoso, I. Mejía, Wear **267**, 495 (2009). https://doi.org/10.1016/j.wear.2008.11.009
17. E. Cortés-Carrillo, A. Bedolla-Jacuinde, I. Mejía, C.M. Zepeda, J. Zuno-Silva, F.V. Guerra-Lopez, Wear **376–377**, 77 (2017). https://doi.org/10.1016/j.wear.2017.02.043
18. A. Bedolla-Jacuinde, R. Correa, I. Mejía, J.G. Quezada, W.M. Rainforth, Wear **263**, 808 (2007). https://doi.org/10.1016/j.wear.2006.12.011

19. C. Scandian, C. Boher, J.D.B. de Mello, F. Rézaï-Aria, Wear **267**, 401 (2009). https://doi.org/10.1016/j.wear.2008.12.095
20. H. Gasan, F. Erturk, Metall. Mater. Trans. A **44**, 4993 (2013). https://doi.org/10.1007/s11661-013-1851-3
21. K.A. Kibble, J.T.H. Pearce, Cast. Met. **6**, 9 (1993). https://doi.org/10.1080/09534962.1993.11819121
22. C.P. Tabrett, I.R. Sare, Scripta Mater. **38**, 1747 (1998). https://doi.org/10.1016/S1359-6462(98)00118-3
23. A. Wiengmoon, T. Chairuangsri, J.T.H. Pearce, Key Eng. Mater. **658**, 76 (2015). https://doi.org/10.4028/www.scientific.net/KEM.658.76
24. J. Asensio, J.A. Pero-Sanz, J.I. Verdeja, Mater. Charact. **49**, 83 (2002). https://doi.org/10.1016/S1044-5803(02)00260-7
25. K.-H. Zum Gahr, G.T. Eldis, Wear **64**, 175 (1980). https://doi.org/10.1016/0043-1648(80)90101-5
26. Ö.N. Doğan, J.A. Hawk, G. Laird, Metall. Mater. Trans. A **28**, 1315 (1997). https://doi.org/10.1007/s11661-997-0267-3
27. G. Laird, R. Gundlach, K. Rohrig, *Abrasion-Resistant Cast Iron Handbook* (American Foundry Society, Schaumburg, Illinois (USA), 2000)
28. H.S. Avery, Wear **4**, 427 (1961). https://doi.org/10.1016/0043-1648(61)90301-5
29. S. Inthidech, Y. Matsubara, Mater. Trans. **49**, 2322 (2008). https://doi.org/10.2320/matertrans.MRA2008079
30. J.K. Fulcher, T.H. Kosel, N.F. Fiore, Wear **84**, 313 (1983). https://doi.org/10.1016/0043-1648(83)90272-7
31. C. Rodenburg, W.M. Rainforth, Acta Mater. **55**, 2443 (2007). https://doi.org/10.1016/j.actamat.2006.11.039
32. R.B. Gundlach, J.L. Parks, Wear **46**, 97 (1978). https://doi.org/10.1016/0043-1648(78)90113-8
33. J.T.H. Pearce, Trans. Am. Foundrymen's Soc. **92**, 599 (1984)
34. O.F. Higuera-cobos, F.-D. Dumitru, D.H. Mesa-Grajales, Rev. Fac. Ing. **25**, 93 (2016). https://doi.org/10.19053/01211129.4141
35. S. Inthidech, P. Kosasu, S. Yotee, Y. Matsubara, Mater. Trans. **54**, 28 (2013). https://doi.org/10.2320/matertrans.M2012185
36. K. Abdel-Aziz, M. El-Shennawy, A.A. Omar, Int. J. Appl. Eng. Res. **12**, 4675 (2017)
37. G. Pintaude, F.G. Bernardes, M.M. Santos, A. Sinatora, E. Albertin, Wear **267**, 19 (2009). https://doi.org/10.1016/j.wear.2008.12.099
38. S. Turenne, F. Lavallée, J. Masounave, J. Mater. Sci. **24**, 3021 (1989). https://doi.org/10.1007/BF02385662
39. U.P. Nayak, M.A. Guitar, F. Mücklich, Metals **10**, 30 (2020). https://doi.org/10.3390/met10010030
40. U.P. Nayak, M.A. Guitar, F. Mücklich, Pract. Metallogr. **57**, 688 (2020). https://doi.org/10.3139/147.110682
41. U.P. Nayak, S. Suárez, V. Pesnel, F. Mücklich, M.A. Guitar, Friction **10**, 1258 (2022). https://doi.org/10.1007/s40544-021-0553-x
42. J. Schindelin, I. Arganda-Carreras, E. Frise, V. Kaynig, M. Longair, T. Pietzsch, S. Preibisch, C. Rueden, S. Saalfeld, B. Schmid, J.-Y. Tinevez, D.J. White, V. Hartenstein, K. Eliceiri, P. Tomancak, A. Cardona, Nat. Methods **9**, 676 (2012). https://doi.org/10.1038/nmeth.2019
43. U.P. Nayak, M. Müller, D. Britz, M.A. Guitar, F. Mücklich, Pract. Metallogr. **58**, 484 (2021). https://doi.org/10.1515/pm-2021-0039
44. E. Limpert, W.A. Stahel, M. Abbt, BioScience **51**, 341 (2001). https://doi.org/10.1641/0006-3568(2001)051[0341:LNDATS]2.0.CO;2
45. N. Yang, J. Boselli, I. Sinclair, J. Microsc. **201**, 189 (2001). https://doi.org/10.1046/j.1365-2818.2001.00766.x
46. H.M. Rietveld, J. Appl. Crystallogr. **2**, 65 (1969). https://doi.org/10.1107/s0021889869006558
47. L. Lutterotti, Nucl. Instrum. Methods Phys. Res. Sect. B **268**, 334 (2010). https://doi.org/10.1016/j.nimb.2009.09.053
48. A. Bedolla-Jacuinde, L. Arias, B. Hernández, J. Mater. Eng. Perform. **12**, 371 (2003). https://doi.org/10.1361/105994903770342881
49. M.A. Guitar, U.P. Nayak, D. Britz, F. Mücklich, Int. J. Metalcast. **14**, 755 (2020). https://doi.org/10.1007/s40962-020-00407-4
50. V.G. Efremenko, Y.G. Chabak, M.N. Brykov, J. Mater. Eng. Perform. **22**, 1378 (2013). https://doi.org/10.1007/s11665-012-0434-6
51. J. Ohser, F. Mücklich, *Statistical Analysis of Microstructures in Materials Science*, 1st edn. (Wiley, Hoboken, 2000)
52. B.D. Cullity, S.R. Stock, *Elements of X-Ray Diffraction*, 3rd edn. (Pearson Education, London, 2001)
53. D.A. Porter, K.E. Easterling, M.Y. Sherif, *Phase Transformations in Metals and Alloys*, 3rd edn. (CRC Press, Boca Raton, 2009)
54. X.Y. Liu, J. Chem. Phys. **112**, 9949 (2000). https://doi.org/10.1063/1.481644
55. J. Wang, C. Li, H. Liu, H. Yang, B. Shen, S. Gao, S. Huang, Mater. Charact. **56**, 73 (2006). https://doi.org/10.1016/j.matchar.2005.10.002
56. R. Abbaschian, L. Abbaschian, R.E. Reed-Hill, *Physical Metallurgy Principles*, 4th edn. (Cengage Learning, Stamford, 2009)
57. A. Bedolla-Jacuinde, W.M. Rainforth, MRS Online Proceedings Library **843**, 74 (2005). https://doi.org/10.1557/proc-843-t7.4
58. C. Schayes, J. Bouquerel, J.-B. Vogt, F. Palleschi, S. Zaefferer, Mater. Charact. **115**, 61 (2016). https://doi.org/10.1016/j.matchar.2016.03.020
59. J.J. Coronado, Wear **270**, 823 (2011). https://doi.org/10.1016/j.wear.2011.02.009
60. Ö.N. Doğan, J.A. Hawk, Wear **189**, 136 (1995). https://doi.org/10.1016/0043-1648(95)06682-9
61. M. Jokari-Sheshdeh, Y. Ali, S.C. Gallo, W. Lin, J.D. Gates, Wear **492–493**, 204208 (2022). https://doi.org/10.1016/j.wear.2021.204208
62. J.J. Penagos, F. Ono, E. Albertin, A. Sinatora, Wear **340–341**, 19 (2015). https://doi.org/10.1016/j.wear.2015.03.020
63. P.J. Blau, Tribol. Int. **38**, 1007 (2005). https://doi.org/10.1016/j.triboint.2005.07.020
64. Y. Sano, T. Hattori, M. Haga, ISIJ Int. **32**, 1194 (1992). https://doi.org/10.2355/ISIJINTERNATIONAL.32.1194

VIII. Wear Induced Sub-Surface Deformation Characteristics of a 26 wt.% Cr White Cast Iron Subjected to a Destabilization Heat Treatment

U. Pranav Nayak[1], Florian Schäfer[2], Frank Mücklich[1], María Agustina Guitar[1]

[1] Department of Materials Science and Engineering, Saarland University, 66123 Saarbrücken, Germany

[2] Department of Materials Science and Methods, Saarland University, 66123, Saarbrücken, Germany

Published in "***Tribology Letters***" (2023) *(IF (2023): 3.327)*

Accessible online at: *https://doi.org/10.1007/s11249-022-01683-3*

Own Contribution: Conceptualization and methodology; sample preparation; experimentation; wear track characterization; data analysis; scientific discussion; paper writing – original draft preparation

Tribology Letters (2023) 71:9
https://doi.org/10.1007/s11249-022-01683-3

ORIGINAL PAPER

Wear Induced Sub-surface Deformation Characteristics of a 26 Wt% Cr White Cast Iron Subjected to a Destabilization Heat Treatment

U. Pranav Nayak[1] · Florian Schäfer[3] · Frank Mücklich[1,2] · María Agustina Guitar[1]

Received: 19 September 2022 / Accepted: 28 November 2022

Abstract
In the present work, the sub-surface microstructure of a heat treated and worn 26 wt% Cr white cast iron was investigated to gain better insight into the tribological behaviour of the material. The samples were destabilized at 980 °C for 0 (Q_0), 30 (Q_30) and 90 (Q_90) minutes followed by air cooling, and later subjected to dry-sliding linear reciprocating wear tests. The microstructural characterization of the area under the wear track was carried out using a combination of SEM, EDS and EBSD. Additionally, nanoindentation (NI) measurements were used to corroborate the mechanical behaviour with the microstructural observations. EBSD and NI measurements indicated that the matrix area underneath the wear track in Q_0 had undergone significant plastic deformation resulting in a drastic increase in hardness, whereas no such phenomena was observed in the Q_90. This was attributable to the relatively high amount of retained austenite in the former and a predominately martensitic matrix in the latter. Moreover, the large M_7C_3 eutectic carbides were less cracked in the destabilized samples compared to the as-cast sample owing to the presence of martensite and dispersed secondary carbides, leading to an increased matrix load-bearing capacity. These factors led to the destabilized samples showing a lower wear rate compared to the as-cast sample, and the Q_0 showing the best wear resistance amongst all the samples.

Keywords High chromium cast iron · Destabilization heat treatment · Sub-surface microstructure · Nanoindentation · Retained austenite · Wear rate

1 Introduction

Considering the money and energy that is being spent on overcoming tribological related issues during the operation run time, it is imperative to develop better wear-resistant materials by understanding the underlying wear mechanisms [1–3]. The dispersion of hard carbides in a supportive, modifiable matrix makes high chromium cast iron (HCCI) alloys viable candidates for wear-resistant applications, particularly in the mining and mineral industry [4–7]. By employing suitable heat treatment (HT) procedures such as destabilization and/or sub-critical treatments, the matrix can be accordingly modified [8, 9]. Moreover, the type and nature of the secondary carbides (SC) which precipitate during the destabilization HT are highly dependent on the Cr/C ratio, in addition to the HT parameters [4, 10, 11].

The influence of heat treatment conditions on the wear properties of HCCI's has been evaluated by several studies, where a strong interdependence between the microstructural characteristics and wear resistance was observed [8, 9, 12–15]. Moreover, as the maximum stress is experienced at the centre of the wear track, making transverse cuts across the entirety of the track would be beneficial [16, 17]. This will help in gaining a better insight into the tribological behaviour of the material aiding in further development [18, 19]. Therefore, in addition to the wear-induced microstructural modifications on the sample's surface, examining the region under the wear track is crucial. Microstructural characterization was previously done to assess the deformation behaviour at the sub-surface level on copper and iron [16, 20, 21]. Furthermore, evaluating the sub-surface microstructure greatly benefited in understanding the tribological behaviour of certain HCCI alloys as well [22–24].

✉ U. Pranav Nayak
pranav.nayak@uni-saarland.de

[1] Department of Materials Science, Saarland University, Campus D3.3, 66123 Saarbrücken, Germany

[2] Materials Engineering Center Saarland (MECS), Campus D3.3, 66123 Saarbrücken, Germany

[3] Department of Materials Science and Methods, Saarland University, Campus D2.3, Saarbrücken, Germany

Published online: 04 December 2022

Penagos et al., [22] investigated the influence of structure refinement on the wear resistance of a hypoeutectic HCCI alloy that was casted in a single mould such that a fine to coarse M_7C_3 carbide gradient existed in the microstructure. Upon analysing the sub-surface, they observed that the microstructure consisting of coarse M_7C_3 carbides showed sub-critical cracking and no fracture, compared to its finer counterpart. This was reflected in the abrasion tests wherein the microstructure with refined carbides showed a lower abrasion resistance compared to the coarser carbides. In fact, the larger M_7C_3 carbides were acting as a barrier to the abrasive grit resulting in a higher wear resistance.

On the other hand, Matsuo et al., [23] studied the wear behaviour of three different spray formed HCCI alloys and compared them to their respective conventionally cast counterparts. The analysis of the sub-surface shed further light on the improved wear resistance of the spray-formed HCCI over the conventionally cast HCCI. They observed that the matrix and the carbide had deeper cracks underneath the wear track in the conventionally cast alloy compared to the spray-formed. This was attributed the spray-formed HCCI possessing a finer and more homogeneously distributed M_7C_3 carbides, and a well-balanced matrix consisting of austenite and martensite.

The above two investigations clearly depict the ambivalence between them, where one study claims having a finer carbide distribution is better for wear, whereas the other study mentions the opposite. This just elucidates the complexity between the microstructure and wear relationship, and the dependence on the conditions under which the tests were undertaken. Owing to the 'composite' like behaviour in HCCIs, the overall tribological behaviour is not an inherent property but a synergistic contribution between the hard carbides and the matrix that engulfs it [3, 25, 26]. In addition to the characteristics of the hard M_7C_3 carbides, the degree to which the matrix provides the necessary mechanical support is crucial [27, 28]. Furthermore, depending on the applicability, the stereological characteristics of the secondary carbides may also have an influence on the overall behaviour [29, 30].

Previously, a destabilization HT was experimentally conducted on as-cast (AC) 26 wt% Cr white cast iron samples wherein they were heated to 980 °C for various times ranging from 0 to 90 min, followed by air cooling. They were later subjected to dry-sliding linear reciprocating tribological tests in order to derive a mutual relationship between the wear rate and the varying microstructural characteristics. Subsequently, it was observed that: (1) all the HTed samples showed a lower wear rate compared to the AC, and (2) amongst the HTed samples, the sample with the lowest surface matrix hardness showed the best wear resistance. These changes were attributed to the varying fractions of the microstructural constituents and their respective distribution within the destabilized microstructure [31].

The main objective of the present work is to gain a better understanding of the tribological behaviour of the destabilized samples by investigating the area directly underneath the wear track. Microstructural characterization of the sub-surface was carried out using scanning electron microscopy (SEM) in conjunction with electron backscattered diffraction (EBSD). Finally, nanoindentation (NI) measurements were performed around the vicinity of the wear track with increasing cross-sectional depth to corroborate the deformation behaviour with the destabilized microstructure.

2 Experimental Methodology

An as-cast HCCI alloy (~Cr: 26.6 wt%; C: 2.5 wt%; Mn: 0.66 wt%; Mo: 0.24 wt%; Ni: 0.26 wt%; Si: 0.37 wt%; Fe: Bal.) measuring 20 × 20 × 10 mm was subjected to a destabilization HT at 980 °C (1253 K) for 0 (Q_0), 30 (Q_30) and 90 (Q_90) minutes, followed by air cooling. The increase in the destabilization holding time resulted in variable fractions of the micro-constituents i.e., retained austenite (RA), martensite and SC, in addition to the relatively unchanged M_7C_3 eutectic carbides (EC), as previously described in [31]. Dry-sliding linear reciprocating tribological tests were later performed on the HTed samples using 3 mm alumina (Al_2O_3) balls (99.00–99.99% purity; Grade GD28) as the sliding counter-body.

The surface and sub-surface underneath the wear track were protected with an electrolytically deposited Ni coating and then mechanically sectioned. Further specifics concerning the Ni electrodeposition process are elaborated in [32]. Subsequently, a scratch-free, mirror-polished surface of the transverse section was obtained by following the metallographic protocol as described in [33]. Microstructural characterization of the sub-surface was carried out with a Thermo-Fisher Helios™ G4 PFIB (Plasma Focused-Ion Beam) CXe DualBeam™ FIB/SEM which was operated at an accelerated voltage of 5–15 kV and a beam current of 1.6 nA. Additionally, energy-dispersive X-ray spectroscopy (EDS) was used to chemically map the cross section containing both the sub-surface and the Ni coating. The SEM micrographs were taken in backscattered mode for a better contrast between the different phases. The microstructural constituents are colour arrow coded throughout the paper according to the following terminology:

Austenite (γ): Red arrow pointing downwards.
Martensite (α'): Green arrow pointing upwards.
M_7C_3 carbide (EC): Yellow arrow pointing right.
$M_{23}C_6$ carbide (SC): Blue arrow pointing left.

EBSD was employed to investigate the strain distribution and local deformation around the regions underneath the wear track. The measurements were performed at an acceleration voltage of 20 kV and a beam current of 11 nA using the FEI Helios™ Nanolab 600 field emission SEM (FE-SEM) workstation equipped with an EDAX Hikari EBSD camera. Furthermore, the orientational variation of the matrix region with increasing cross-sectional depth was obtained by grain reference orientation deviation (GROD) maps and performing misorientation profile (MP) analysis. The GROD was performed by considering a 3rd degree neighbour owing to the very small step size (50 nm) used. The EBSD data was analysed using the Orientation Imaging Microscopy (OIM™ v. 7) Data Analysis software by EDAX Corporation.

NI measurements were carried out using a Hysitron TI900 TriboIndenter® Nanomechanical Testing System with nanoDMA upgrade with a Berkovich 142.3°, 3-sided pyramidal indenter. Open-loop intrinsic load-controlled tests were performed with a loading rate of 1 mN/s and a peak load of 3 mN. To account for a potential drift, the drift rate was measured at a pre-load of 2 µN for 20 s and the results were drift-corrected. During the test, drift was checked by additional hold segments of 2 s at 100 µN before and after applying the peak load. Datasets that suffer from drift were excluded from the subsequent evaluation. To account for creep, the peak load was held for 2 s. The values of the nanoindentation hardness (H) and the reduced indentation modulus (E) were obtained after analysing the NI curves employing the Oliver-Pharr method [34, 35]. To achieve a good spatial resolution and to reduce the influence of sub-surface in-depth microstructural and mechanical gradients, a small indentation depth of less than 100 nm was used. Therefore, special attention was laid on the probe calibration. The validity of the probe calibration was guaranteed by an almost constant reduced indentation modulus over the indentation depth, measured using nanoDMA, for all indents included in the subsequent evaluation. At least 100 indentations (10 by 10) were performed in a regularly spaced grid directly underneath the wear track, and also away from the wear track. Moreover, to avoid any overlapping effect, a distance of 3 µm was maintained between two indents regarding a maximum indent diameter below 1 µm.

3 Results and Discussion

In an own previous study, the influence of increasing the destabilization holding time on the microstructural evolution and tribological behaviour of the same sample was investigated [31]. In the AC sample, the microstructure primarily consisted of an austenitic matrix and dispersed M_7C_3 EC with the martensite sandwiched at the interface. The destabilization heat treatment resulted in the precipitation of fine $M_{23}C_6$ type SC within the matrix, whereas the EC remained relatively immune. Finally, the extent to which the austenite had transformed to martensite during cooling varied as a function of holding time. Table 1 briefly summarizes the quantification of the microstructural constituents such as RA, secondary carbide size and carbide volume fraction (CVF), and the surface matrix hardness.

It is observed from Table 1 that increasing the holding time during destabilization results in a reduction of the amount of RA and a corresponding increase in the matrix hardness. Moreover, it was seen that the volume fraction of SC was statistically comparable in the samples destabilized for 0 and 90 min, although the average size almost doubled in the latter. The mutual dependence of the wear rate (WR) ($mm^3\ N^{-1}\ mm^{-1}$) on the amount of retained austenite and the matrix hardness is graphically represented in Fig. 1. Additionally, representative BSE SEM micrographs of the AC, Q_0 and Q_90 samples are shown. In the Q_0 sample, the central part of the matrix is austenite (retained austenite) while little to no austenite is seen in the Q_90 sample's matrix. Although the microstructural constituents of the destabilized samples were identical, the differences in their amounts and distribution had a consequence on the final tribological properties of the alloy, as previously discussed in [31].

Figure 1 indicates that all the destabilized samples showed a lower WR compared to the AC sample, and a harder matrix did not necessarily guarantee a better wear resistance. Interestingly, the Q_0 sample displayed the lowest WR (i.e., highest wear resistance) despite showing the smallest increase in the matrix hardness compared to the AC. This was attributed to a favourable distribution of the RA (~ 10%) and SC volume fraction (~ 5%) in combination with a harder martensitic matrix.

In order to gain a better understanding of the tribological behaviour of the destabilized samples, it is imperative to characterize the sub-surface microstructure. Therefore, by observing the deformation characteristics of the surface directly underneath the wear track, more insight could be gained as to why the Q_0 sample showed the highest wear resistance.

Table 1 Quantification of retained austenite, SC characteristics and matrix hardness in the as-cast and destabilized samples [31]

Sample	RA (%)	SC CVF (%)	SC size (μm^2)	Matrix hardness (HV0.1)
As-cast	58.1	–	–	347 ± 24
Q_0	10.2	5 ± 0.15	0.023 ± 0.030	412 ± 31
Q_30	7.1	3.15 ± 0.81	0.028 ± 0.039	759 ± 22
Q_90	5.1	5.77 ± 0.99	0.041 ± 0.073	775 ± 33

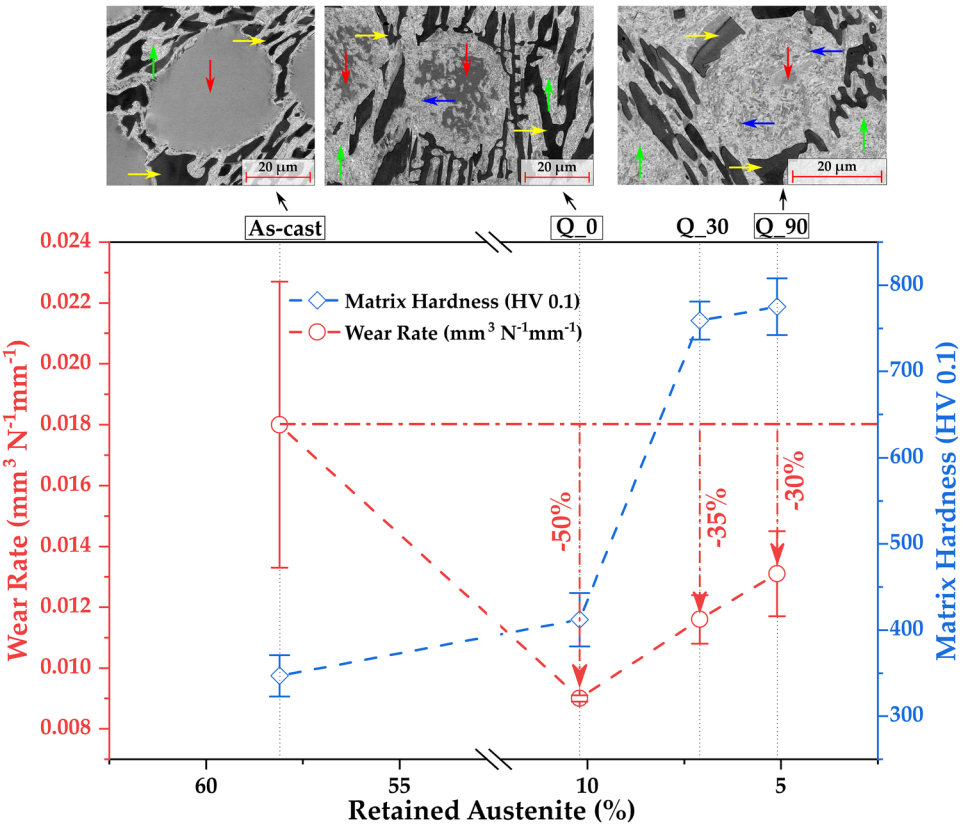

Fig. 1 The dependence of WR on the amount of RA and the matrix hardness in all samples. Representative BSE SEM micrographs of AC, Q_0 and Q_90 samples are also presented. The various microstructural constituents are colour-arrow coded for reference (Color figure online)

3.1 Microstructural Characterization of the Sub-surface

Figure 2 represents the BSE SEM micrographs of the transverse section of the AC, Q_30 and Q_90 samples. In all cases, the Ni coating was uniform and adherent across the entire surface and was successful in protecting the worn surface during the polishing and the subsequent mechanical sectioning. Figure 2a.1 and a.2 indicate the transverse section of the unworn and the worn surface in the AC sample, respectively. Figure 2a.3 is a magnified region of the dashed-blue enclosure in Fig. 2a.2. Comparing Fig. 2a.1 with a.2, it was seen that the EC underneath the wear track had undergone cracking, primarily perpendicular to the sliding direction. Moreover, the Ni coating was successful in preventing the cracked carbides from ejecting out by acting as an anchor between the cracks, as shown in Fig. 2a.3.

Figure 2b.2 represents the EDS concentration maps of Ni and Cr of the SEM micrograph presented in Fig. 2b.1. The EDS spectra for the whole region is presented in Fig. 2b.3 and the distribution of the SC can be visualized from the Cr map. Figure 2c.1 indicates the BSE SEM micrograph of the transverse section of the Q_90 sample containing the wear track with the inset representing a magnified image of the cracked EC. Similar to the AC, the carbide had cracked perpendicularly to the sliding direction, and it is worth to note that the crack had terminated at the edge of the carbide. This was attributable to the variation in the crystal structure and hardness between the EC and the matrix [36]. Moreover, the inset clearly shows that some transformation had taken place (indicated by the dashed-green enclosure) as visualized by the contrast difference. This was also observed in other studies [37–39] and could be attributed to the destabilization process. The EDS concentration map (Fig. 2c.2) clearly shows the distribution of Ni and Cr within the sample. The EDS line spectra in Fig. 2c.3 tracing the line marked in Fig. 2c.2 indicates the abundance of Cr and Fe as it traces the carbide or the matrix, respectively.

The inverted BSE SEM micrograph of the area underneath the wear track, where the EBSD measurements were carried out, is indicated in Fig. 3a.1. Figure 3a.2 and a.3 represents the phase map and the IPF map of the entire region. Figure 3a.4 represents the GROD map of only the austenitic region under the wear track. Furthermore, the orientational variation across the entire austenite grain was visualized by calculating the point-to-point and point-to-origin misorientation profile chart, as graphically represented in Fig. 3a.5. The point O (as marked in Fig. 3a.4) was selected as the origin point, as it lies away from the immediate wear surface, and the MP measurements were carried out proceeding closer towards the deformed austenite. The point-to-origin

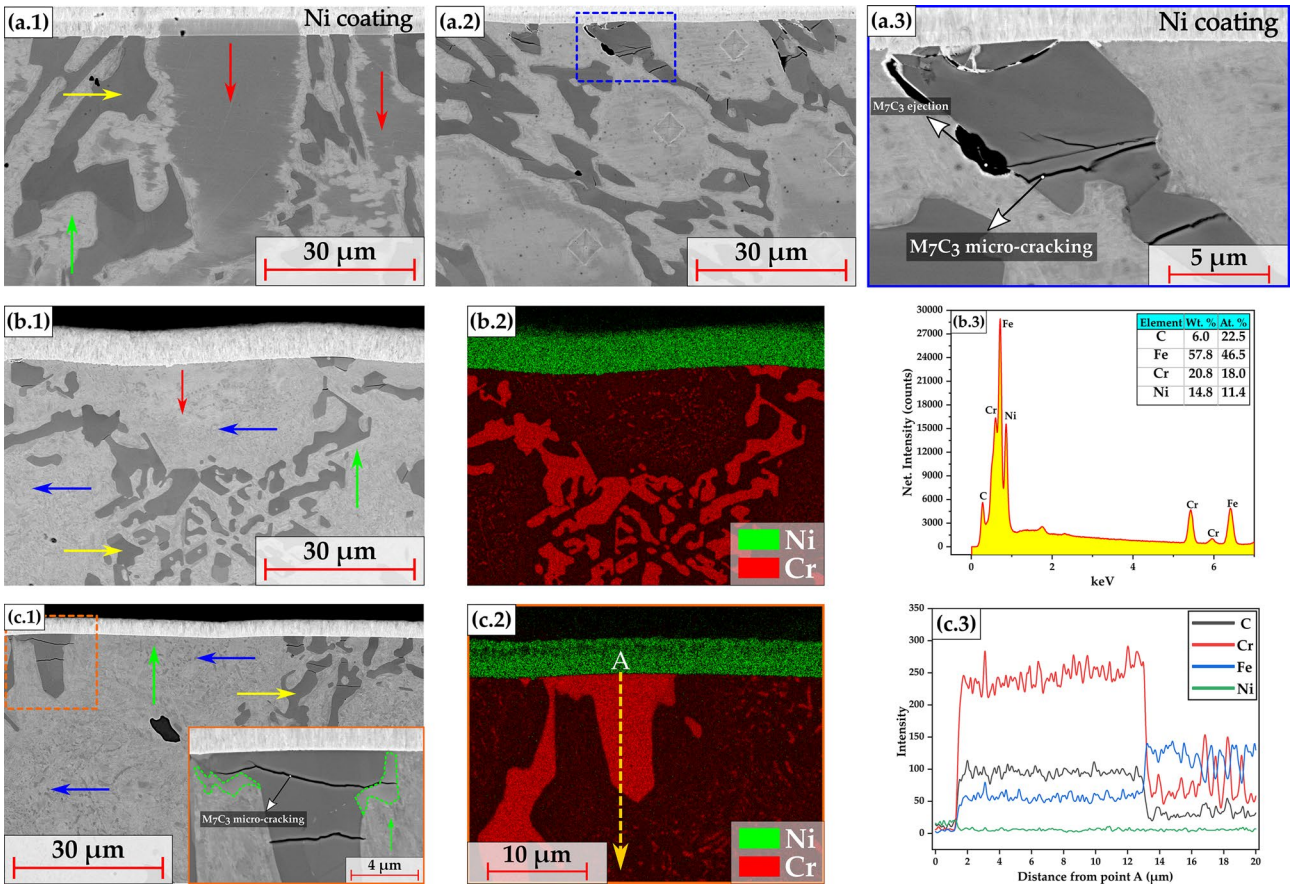

Fig. 2 Representative BSE SEM micrographs of the transverse section of the AC sample **a.1** away from the wear track, **a.2** underneath the wear track, **a.3** magnified view of the dashed-blue enclosure in **a.2** depicting the cracking of the EC carbide. **b.1** representative BSE SEM micrographs of the transverse section of the Q_30 sample underneath the wear track, **b.2** overlayed EDS concentration maps of Ni and Cr, **b.3** resulting EDS scan with the semi-quantitative analysis of the phases. **c.1** representative BSE SEM micrograph of the transverse section of the Q_90 sample underneath the wear track. The inset in **c.1** is a magnified view of the dashed-orange enclosure indicating the EC carbide micro-cracking, and the partial transformation, represented by the dashed-green enclosure. **c.2** overlayed EDS concentration maps of Ni and Cr and **c.3** EDS line scan result with A as the starting point [marked in **c.2**] (Color figure online)

plot indicates a maximum gradient of about 11° between the undeformed and deformed austenite region.

Similarly, EBSD measurements were also carried out in the unworn region across the wear track as represented in the dashed enclosure in Fig. 3b.1. The phase maps and IPF maps are presented in Fig. 3b.2 and b.3, respectively. The GROD map in Fig. 3b.4 clearly shows that the austenite under the coating did not experience any deformation. This is also indicative that the mechanical sectioning and polishing had no influence on the deformation of the cross section, and the deformed regions underneath the wear track were a consequence of the tribological test in itself.

Analogous to the Q_0 sample, similar EBSD measurements were carried out on the Q_90 sample. Figure 4a.1 and Fig. 4b.1 represents the SEM micrographs of the region directly underneath the wear track, and about 350 µm below the Ni coating, respectively. The dashed-yellow and dashed-red enclosures represent the areas where the EBSD measurements were carried out. Comparing the phase maps (Fig. 4a.2 and b.2), IPF (Fig. 4a.3 and b.3) and GROD maps (Fig. 4a.4 and b.4) amongst the two regions, no major differences were seen indicating that the region immediately underneath the wear track was not subjected to deformation as in the case of the Q_0 sample. This was attributed to the predominately martensitic matrix in the Q_90 sample which is harder compared to its austenite counterpart. The presence of relatively larger amount of austenite in the Q_0 sample results in its plastic deformation under the wear track leading to the gradient as observed in Fig. 3a.4.

Figure 5a is indicative of the inverted SEM micrograph on which the EBSD measurements were done, with Fig. 5b representing the phase map. The orientational variation within the M_7C_3 carbide was visualized by overlaying the IQ map with the GROD map as represented in Fig. 5c. The propagation and termination of the cracks can be clearly seen, and the area immediately underneath the wear track

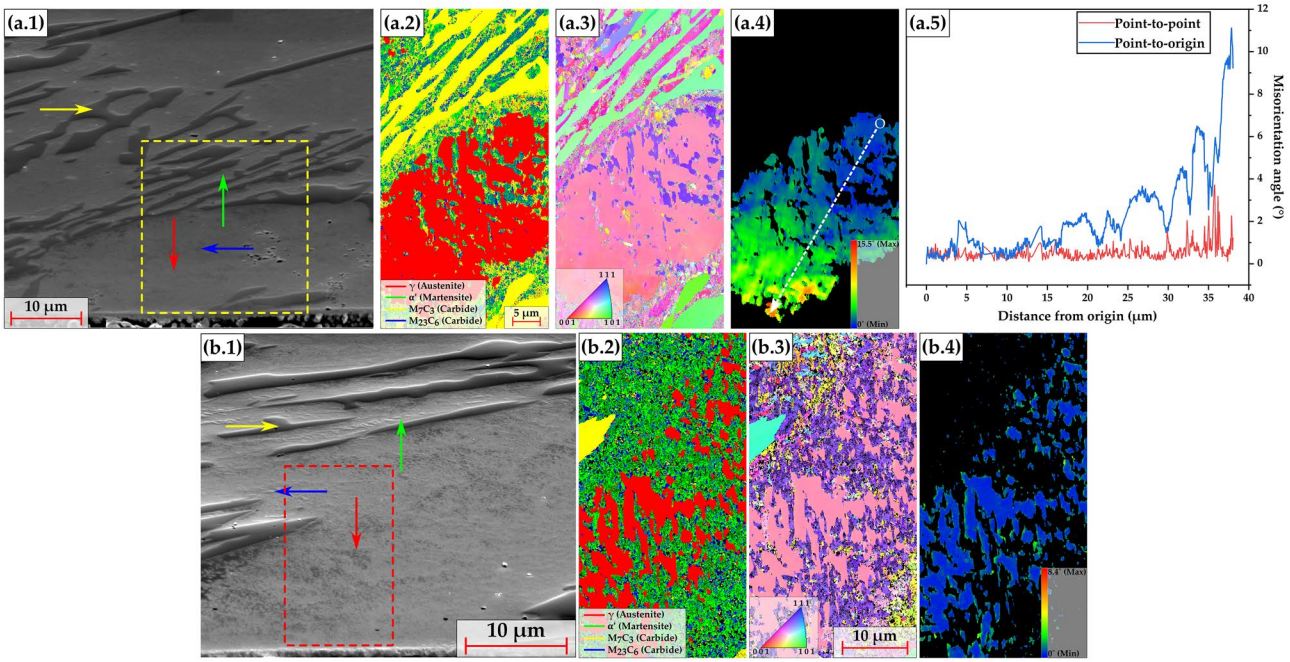

Fig. 3 Representative inverted SEM micrographs of the Q_0 sample **a.1** underneath the wear track and **b.1** away from the wear track. The dashed-yellow (in **a.1**) and the dashed-red enclosures (in **b.1**) indicate the region where the EBSD measurements were carried out. **a.2**, **a.3**, **a.4** represent the phase map, IPF, and GROD map for the austenite at the worn surface, respectively, whereas **b.2**, **b.3** and **b.4** represents the same for the unworn surface. **a.5** MP chart with O as the starting point and proceeding towards the worn region, as indicated in **a.4** (Color figure online)

and the dashed-white enclosed region had undergone deformation due to the compressive stress acting on the carbide. Indeed, the orientational tolerance of the carbide before it underwent cracking was very low as it is unable to plastically deform. Nevertheless, by implementing EBSD, these minute changes within the carbide can be visualized and a better understanding can be obtained.

3.2 Nanoindentation Measurements of the Sub-surface

Figures 6 and 7 represent the NI grid measurements that were performed on the transverse section containing the wear track in the Q_0 and Q_90 sample, respectively. The dashed enclosure in Fig. 6a represents the area where the NI mapping took place and Fig. 6b shows the hardness contour plot that was obtained after performing the necessary corrections (following the Oliver and Pharr method). From the contour plot, it can be visualized that the area immediately under the wear track was harder as opposed to 20 µm below. Moreover, the EC and the areas surrounding them were harder as observed from the contour plot. A heat map of the reduced elastic modulus is represented in Fig. 6c mimicking the trend shown from the contour plot. Comparing Fig. 6a to the EBSD Phase Map in Fig. 3a.2, correlations can be drawn that the area immediate underneath the wear track was a mixture of martensite plus the dispersed secondary carbides. Notwithstanding the plastic deformability of the austenite which reduced with increasing cross-sectional depth, the hardness contour plot reflects the different regions under the wear track. The solid white line enclosure basically represents the dispersed SC plus the martensite, whereas the dashed-white enclosure represents the hardness range < 7.5 GPa, where the austenite (both deformed and undeformed) falls in.

As far as the Q_90 sample is concerned, not a lot of variation in hardness is seen immediately below the track, as observed from Fig. 7b. Compared to Q_0, the mean value of the matrix hardness is higher (darker shade of blue) owing to the presence of a martensitic matrix, larger-sized SC, and a low content of retained austenite (~ 5%). The NI measurements corroborate the observations made from the EBSD measurements, i.e. the matrix area immediately beneath the wear track was not subjected to deformation. The notion that the matrix hardness within the Q_90 sample remains mainly invariant is further bolstered by observing the histogram of the NI measurements which were carried out immediately underneath and at ~ 350 µm below the wear track. In both cases, the two peaks in the graph represent the matrix and the eutectic carbides, with the mean value of the matrix centred at around 8 GPa. The load used in this study was below the threshold for

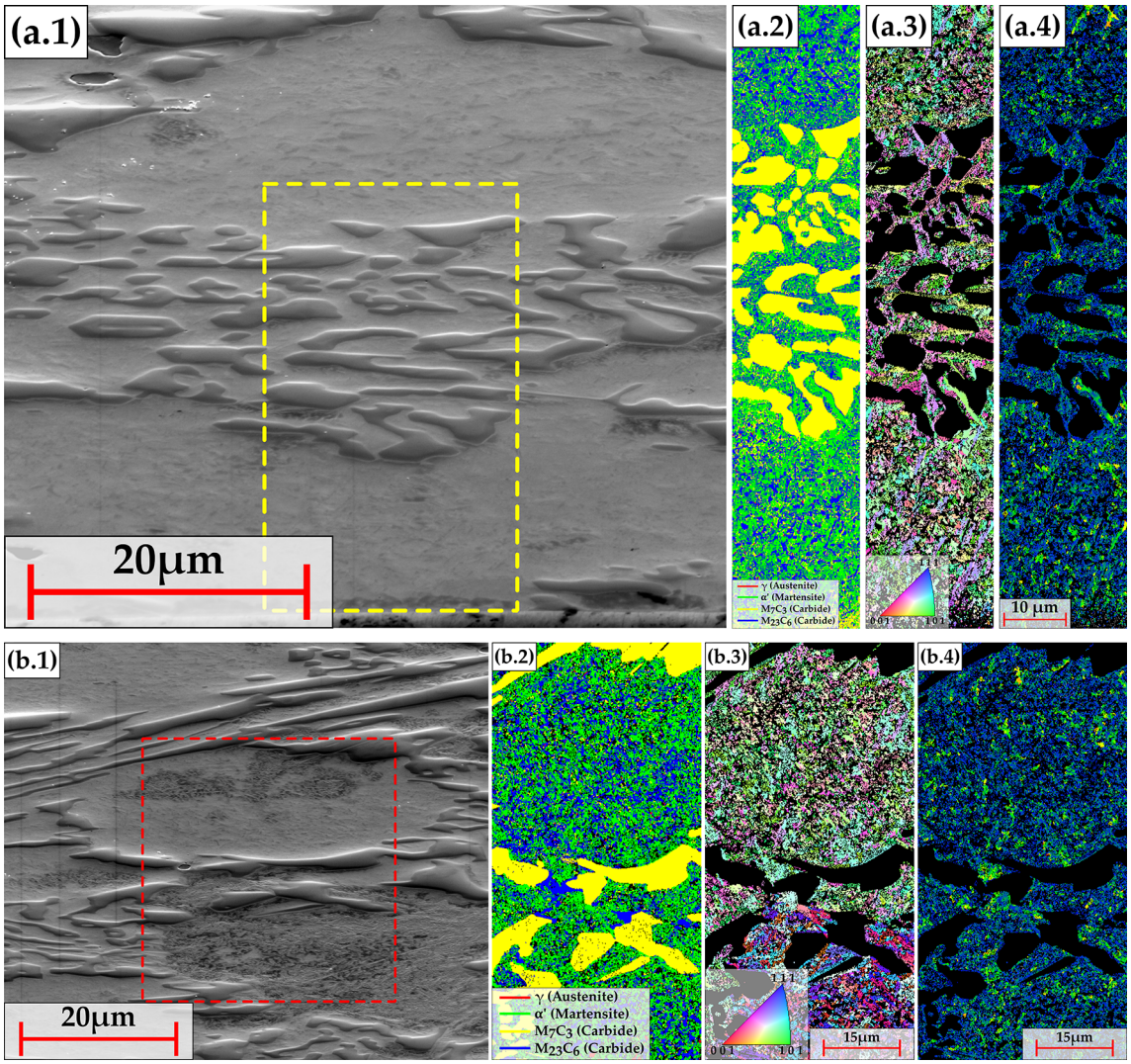

Fig. 4 Representative inverted SEM micrographs of the Q_90 sample **a.1** underneath the wear track and **b.1** 350 µm below the wear track. The dashed-yellow (in **a.1**) and the dashed-red enclosures (in **b.1**) indicate the region where the EBSD measurements were carried out. (**a.2**), (**a.3**) and (**a.4**) represent the phase map, IPF and GROD map at the worn surface, respectively, whereas (**b.2**), (**b.3**) and (**b.4**) represents the same for the unworn surface (Color figure online)

martensite to plastically deform. Nevertheless, comparing the hardness contour plots with the respective EBSD mappings, the changes in the matrix hardness within the Q_0 sample can be observed.

Finally, the variation of the matrix hardness with increasing cross-sectional depth for the destabilized samples is graphically represented in Fig. 8. Additionally, the average hardness value for austenite (γ) and martensite (α') for the AC sample is also indicated. Amongst the Q_0 and the Q_90 sample, major variation in the hardness can be seen going away from the wear track. In the Q_0 sample, the region immediately below the wear track showed the highest hardness amongst all the samples. This increase was not only attributed to the plastic deformation of the austenite alone, but also the presence of the martensite and the SC located primarily around the periphery of matrix. This combination resulted in a high hardness for the Q_0 sample below the wear surface. Additionally, the SC precipitation and the alloy distribution that takes place during the destabilization HT results in the final remaining austenite to be further enriched in carbon and other elements, increasing its inherent hardness. This was reflected in the NI measurements wherein the AC austenite had a hardness of about 4.7 GPa, whereas in the Q_0, it was 5.3 GPa. The Q_90 sample maintained its hardness throughout the measured depth (up to ~ 350 µm) indicating that no increase in hardness underneath the wear track was observed. Previously, a homogeneity factor termed the coefficient of variation (COV) was introduced to determine the uniformity in the SC dispersion in the destabilized samples wherein a lower COV value

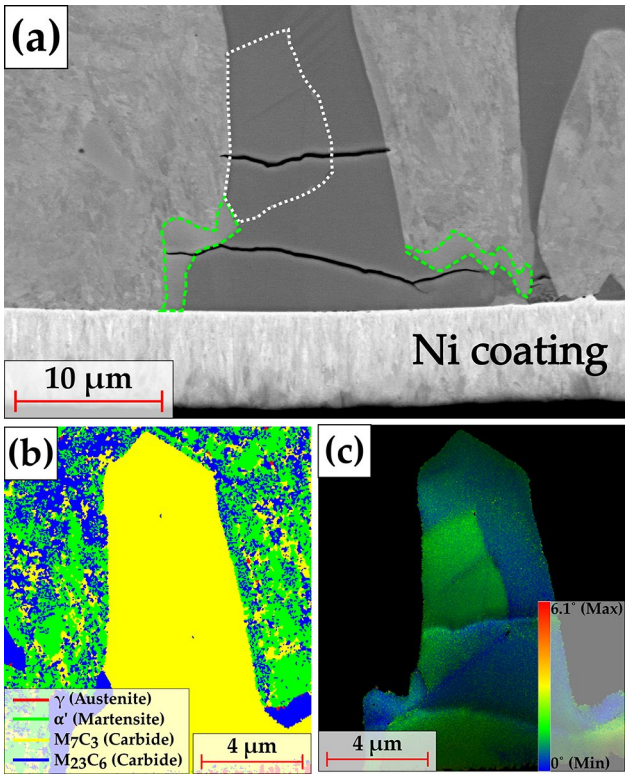

Fig. 5 **a** Representative inverted SEM micrograph of the Q_90 sample under the wear track indicating the cracked M_7C_3 EC. The dashed-green enclosures at the periphery indicate the partial transformation to $M_{23}C_6$. **b** EBSD phase map and **c** IQ + GROD map of the large EC (Color figure online)

implied a higher homogeneity. In the case of Q_0, the COV was around 40%, whereas in the Q_90 sample it was almost 50% [31]. The increased homogeneity in the Q_0 sample combined with its small-sized carbides, primarily dispersed around the periphery, led to the region below the wear track to show such an increase in the hardness.

Classical wear theories emphasize on the hardness as the defining property of a surface's wear resistance [3, 40]. The ratio of H/E is widely considered to be a valuable parameter in determining the elastic behaviour of a surface contact, as popularized by Oberle [41]. This parameter has also been used in other studies to gain an idea of the wear resistance based on the NI measurements [42–44]. It is worth to note that the higher the H/E ratio, the higher the wear resistance. Figure 9 represents the H/E histograms for all the samples (AC and destabilized) including their distribution curves and rug plots.

The two distinct peaks from the distribution curves for every sample represent the matrix and the carbide H/E values, analogous to the hardness histogram curve in Fig. 7d. From the graph, two definite separations can be made based on the mean matrix H/E ratio (the 1st peak of the curve) wherein the mean H/E value of the AC is slightly lower compared to the destabilized one. Therefore, one may hypothesize that the wear resistance of the AC is lower than the destabilized ones, which was true in our case. Nevertheless, it should be treated with caution as the graph does not consider the complexities and the varying parameters that the tribological test may include, i.e. the atmospheric conditions, the counter-body used etc., in addition to the dynamic microstructural changes that take place during the sliding wear such as phase transformations, plastic deformation of the austenite etc. [45]. Although the graph considers the variation in the hardness between the austenite and martensite (as evident from the AC and destabilized samples), amongst the destabilized samples, further factors come into play, such as the stereological characteristics of the secondary carbides. As mentioned earlier, despite having the same micro-constituents, their amounts and distribution play a major role in determining the final tribological properties. Even if no major conclusions can be drawn between the destabilized samples solely from this graph, by combining the information obtained from microstructural characterization with the NI measurements, the differences in the tribological behaviour can be explained.

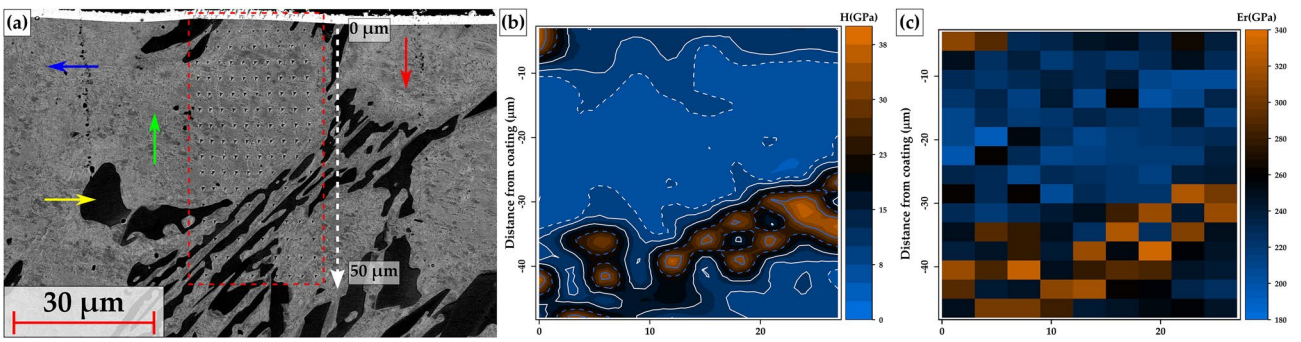

Fig. 6 **a** Representative BSE SEM micrograph of the transverse section of the Q_0 sample with the dashed-red enclosure indicating the region where the NI grid measurements were carried out, **b** hardness contour plot and **c** heat map of the reduced elastic modulus of the mapped region (Color figure online)

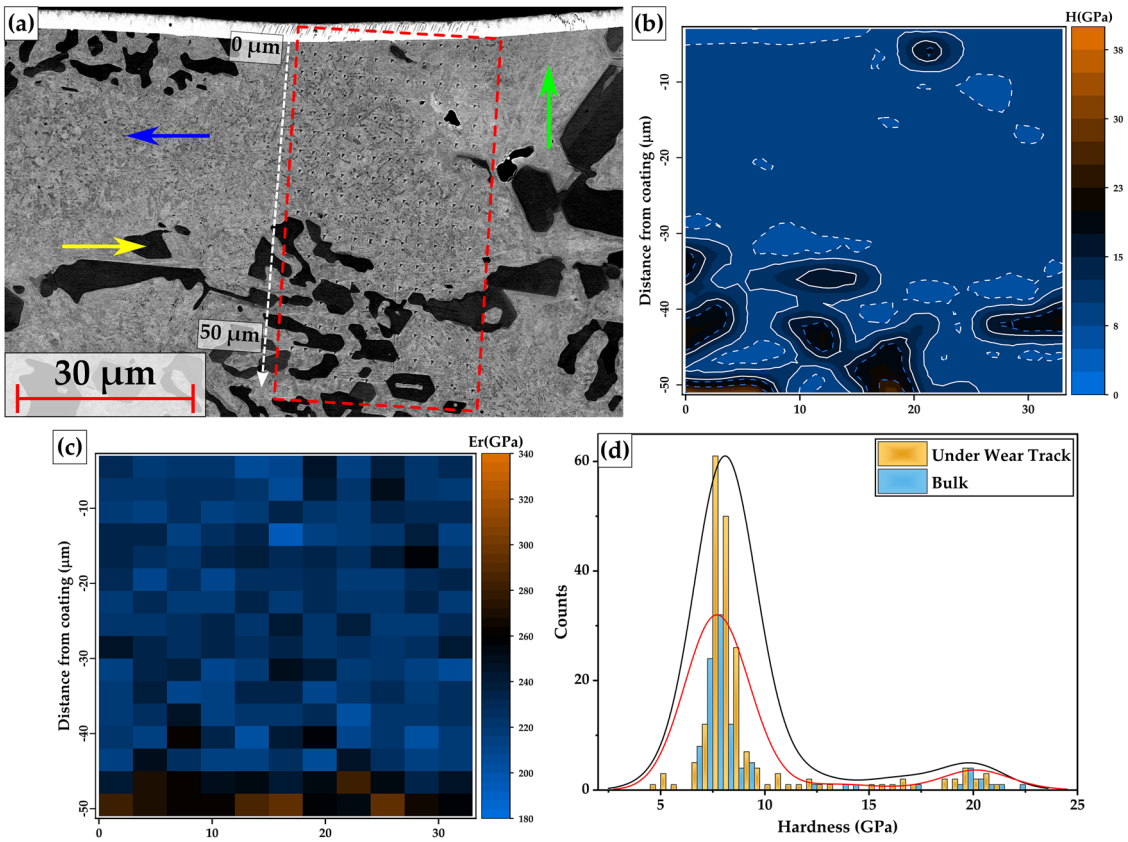

Fig. 7 **a** Representative BSE SEM micrograph of the transverse section of the Q_90 sample with the dashed-red enclosure indicating the region where the NI grid measurements were carried out, **b** hardness contour plot, **c** heat map of the reduced elastic modulus of the mapped region and **d** histogram of the hardness measurements with the respective distribution curves carried out in the region underneath and 350 µm below the wear track (Color figure online)

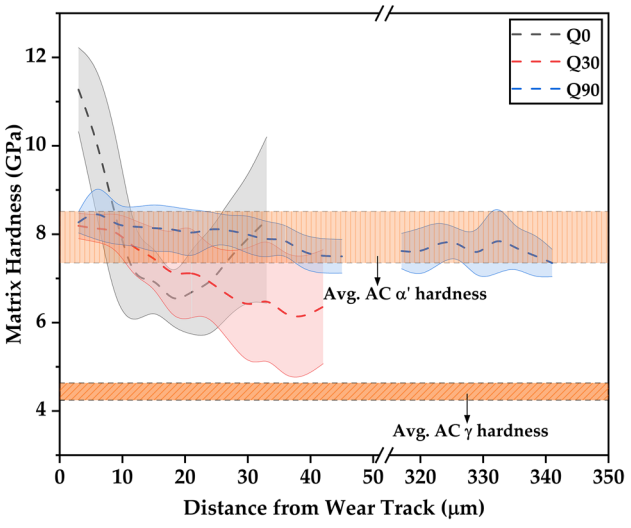

Fig. 8 Variation of matrix hardness with increasing cross-sectional depth in the destabilized samples. The average austenite and martensite hardness in the AC sample is also indicated

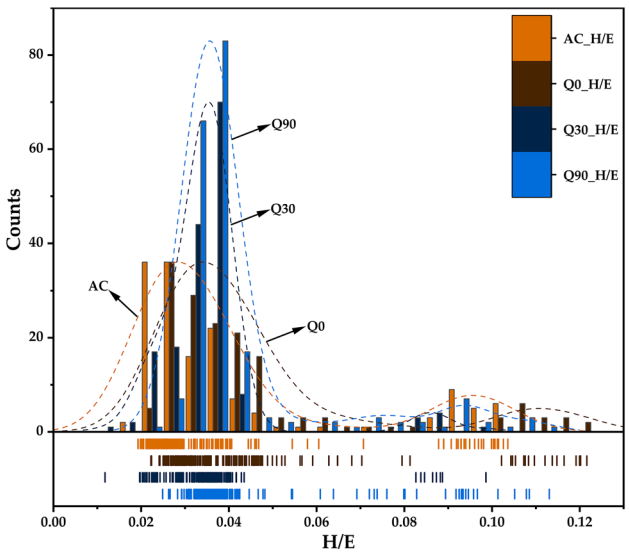

Fig. 9 Histogram of the measured H/E values for all the samples with the respective distribution curves and rug plots

Another observation was the increased prevalence in the cracking of the large EC in the AC sample compared to the destabilized samples. Although it was hypothesized in our previous work during the examination of the wear surface, investigating the sub-surface shed further light on this matter. In the destabilized samples, the presence of a predominately martensitic matrix and the dispersion of SC improves the load-bearing capacity in distributing the load so that the EC alone do not have to bear the brunt [22, 46, 47]. In the AC sample, only a small fraction of the microstructure is martensitic, which are primarily located at the interface between the EC and the austenite. As a result, the EC will succumb to cracking and eventual ejection during the tribological tests. The cracking of the large EC will further accelerate the wear rate and eventually lower the wear resistance.

4 Conclusions

In the present work, the sub-surface microstructure of a destabilized and worn 26 wt% Cr white cast iron was investigated to gain better insight into the tribological behaviour of the material, and the following conclusions were drawn.

- In the Q_0 sample, EBSD measurements indicated that the austenite region directly underneath the wear track had deformed and this was also corroborated with NI measurements.
- The presence of a predominately martensitic matrix combined with the dispersed SC in the Q_90 sample did not cause a substantial increase in the hardness under the wear track compared to the bulk.
- Despite the Q_0 having the lowest increase in matrix surface hardness amongst the HTed samples, it showed the highest sub-surface hardness. This was attributed to the presence of small-sized, homogeneously distributed SC around the periphery combined with the martensite, and the relatively higher amount of RA, which underwent plastic deformation.
- In all the destabilized samples, the presence of martensite and the dispersion of SC around the larger M_7C_3 EC led to an improvement in the load-bearing capacity, thereby reducing the tendency for EC micro-fracture, compared to the AC.

Acknowledgements The authors would like to thank the Saarland State Chancellery for financial support within the ZuMat Project funded by the European Regional Development Fund (ERDF). The authors would also like to thank Martin Duarte from Tubacero S.A. for providing the materials and finally, U.P.N. is grateful to DAAD for the financial support.

Author contributions UPN: Conceptualization and methodology, experimentation, formal analysis, data curation and writing - original draft preparation.FS: Nanoindentation measurements, formal analysis, writing - review and editing.FM: Project administration and funding acquisitionMAG: Conceptualization and methodology, writing - review and editing, funding acquisition.

Funding Open Access funding enabled and organized by Projekt DEAL. The authors have not disclosed any funding. The present work is supported by funding from the Deutsche Forschungsgemeinschaft (DFG, project: GU 2102/2-1). Moreover, the funding for the PFIB/SEM instrument by DFG is greatly acknowledged (INST 256/510-1 FUGG).

Declarations

Conflict of Interest The authors declare that they have no conflict of interest.

References

1. Holmberg, K., Kivikytö-Reponen, P., Härkisaari, P., Valtonen, K., Erdemir, A.: Global energy consumption due to friction and wear in the mining industry. Tribol. Int. **115**, 116–139 (2017). https://doi.org/10.1016/j.triboint.2017.05.010
2. Watson, J.D., Mutton, P.J., Sare, I.R.: Abrasive wear of white cast irons. Metals Forum. **3**, 74–88 (1980)
3. Zum Gahr, K.H., Doane, D.V.: Optimizing fracture toughness and abrasion resistance in white cast irons. Metall. Trans. A. **11**, 613–620 (1980). https://doi.org/10.1007/BF02670698
4. Tabrett, C.P., Sare, I.R., Ghomashchi, M.R.: Microstructure-property relationships in high chromium white iron alloys. Int. Mater. Rev. **41**, 59–82 (1996). https://doi.org/10.1179/095066096790326075
5. Karantzalis, E., Lekatou, A., Mavros, H.: Microstructure and properties of high chromium cast irons: effect of heat treatments and alloying additions. Int. J. Cast Met. Res. **22**, 448–456 (2009). https://doi.org/10.1179/174313309X436637
6. Maratray, F.: Choice of appropriate compositions for chromium-molybdenum white irons. AFS Trans. **79**, 121–124 (1971)
7. Nayak, U.P., Guitar, M.A., Mücklich, F.: A comparative study on the influence of chromium on the phase fraction and elemental distribution in as-cast high chromium cast irons: Simulation vs. experimentation. Metals (Basel). (2020). https://doi.org/10.3390/met10010030

8. Karantzalis, A.E., Lekatou, A., Mavros, H.: Microstructural modifications of as-cast high-chromium white iron by heat treatment. J. Mater. Eng. Perform. **18**, 174–181 (2009). https://doi.org/10.1007/s11665-008-9285-6
9. Guitar, M.A., Suárez, S., Prat, O., Duarte Guigou, M., Gari, V., Pereira, G., Mücklich, F.: High chromium cast irons: destabilized-subcritical secondary carbide precipitation and its effect on hardness and wear properties. J. Mater. Eng. Perform. (2018). https://doi.org/10.1007/s11665-018-3347-1
10. Wiengmoon, A., Chairuangsri, T., Pearce, J.T.H.: A microstructural study of destabilised 30wt%Cr-2.3wt%C high chromium cast iron. ISIJ Int. **44**, 396–403 (2004). https://doi.org/10.2355/isijinternational.44.396
11. Powell, G.L.F., Laird, G.: Structure, nucleation, growth and morphology of secondary carbides in high chromium and Cr-Ni white cast irons. J. Mater. Sci. **27**, 29–35 (1992). https://doi.org/10.1007/BF02403640
12. Guitar, M.A., Nayak, U.P., Britz, D., Mücklich, F.: The effect of thermal processing and chemical composition on secondary carbide precipitation and hardness in high-chromium cast irons. Int. J. Metalcast. **14**, 755–765 (2020). https://doi.org/10.1007/s40962-020-00407-4
13. Gasan, H., Erturk, F.: Effects of a destabilization heat treatment on the microstructure and abrasive wear behavior of high-chromium white cast iron investigated using different characterization techniques. Metall. Mater. Trans. A. **44**, 4993–5005 (2013). https://doi.org/10.1007/s11661-013-1851-3
14. Kibble, K.A., Pearce, J.T.H.: Influence of heat treatment on the microstructure and hardness of 19% high-chromium cast irons. Cast Met. **6**, 9–15 (1993). https://doi.org/10.1080/09534962.1993.11819121
15. Tabrett, C.P., Sare, I.R.: Effect of high temperature and sub-ambient treatments on the matrix structure and abrasion resistance of a high-chromium white iron. Scr. Mater. **38**, 1747–1753 (1998). https://doi.org/10.1016/S1359-6462(98)00118-3
16. Ruff, A.W.: Deformation studies at sliding wear tracks in iron. Wear **40**, 59–74 (1976). https://doi.org/10.1016/0043-1648(76)90018-1
17. Grützmacher, P.G., Rammacher, S., Rathmann, D., Motz, C., Mücklich, F., Suarez, S.: Interplay between microstructural evolution and tribo-chemistry during dry sliding of metals. Friction. **7**, 637–650 (2019). https://doi.org/10.1007/s40544-019-0259-5
18. Mercado, V.H., Mejía, I., Bedolla-Jacuinde, A.: Effect of load and sliding rate on the wear behavior of Ti-containing TWIP steel. J. Mater. Eng. Perform. **26**, 2213–2225 (2017). https://doi.org/10.1007/s11665-017-2635-5
19. Todaka, T., Shimizu, K., Kusumoto, K., Purba, R.H., Gaqi, Y.: Effect of carbon content on three-body abrasive wear characteristics of 28Cr-3Ni cast alloys. ISIJ Int. **61**, 2274–2283 (2021). https://doi.org/10.2355/isijinternational.isijint-2021-099
20. Dautzenberg, J.H., Zaat, J.H.: Quantitative determination of deformation by sliding wear. Wear **23**, 9–19 (1973). https://doi.org/10.1016/0043-1648(73)90036-7
21. Kirk, J.A., Swanson, T.D.: Subsurface effects during sliding wear. Wear **35**, 63–67 (1975). https://doi.org/10.1016/0043-1648(75)90142-8
22. Penagos, J.J., Ono, F., Albertin, E., Sinatora, A.: Structure refinement effect on two and three-body abrasion resistance of high chromium cast irons. Wear **340–341**, 19–24 (2015). https://doi.org/10.1016/j.wear.2015.03.020
23. Matsuo, T.T., Kiminami, C.S., Fo, W.J.B., Bolfarini, C.: Sliding wear of spray-formed high-chromium white cast iron alloys. Wear 445–452 (2005)
24. Sun, T., Song, R.B., Wang, X., Deng, P., Wu, C.J.: Abrasive wear behavior and mechanism of high chromium cast iron. J. Iron Steel Res. Int. **22**, 84–90 (2015). https://doi.org/10.1016/S1006-706X(15)60014-0
25. Asensio, J., Pero-Sanz, J.A., Verdeja, J.I.: Microstructure selection criteria for cast irons with more than 10 wt.% chromium for wear applications. Mater. Charact. **49**, 83–93 (2002). https://doi.org/10.1016/S1044-5803(02)00260-7
26. ASM International: ASM Handbook Volume 5: Surface Engineering. ASM International, Novelty, OH (2002)
27. Laird, G., Gundlach, R., Rohrig, K.: Abrasion-Resistant Cast Iron Handbook. American Foundry Society, Schaumburg, IL (USA) (2000)
28. Avery, H.S.: The measurement of wear resistance. Wear **4**, 427–449 (1961). https://doi.org/10.1016/0043-1648(61)90301-5
29. Fulcher, J.K., Kosel, T.H., Fiore, N.F.: The effect of carbide volume fraction on the low stress abrasion resistance of high Cr-Mo white cast irons. Wear **84**, 313–325 (1983). https://doi.org/10.1016/0043-1648(83)90272-7
30. Rodenburg, C., Rainforth, W.M.: A quantitative analysis of the influence of carbides size distributions on wear behaviour of high-speed steel in dry rolling/sliding contact. Acta Mater. **55**, 2443–2454 (2007). https://doi.org/10.1016/j.actamat.2006.11.039
31. Nayak, U.P., Mücklich, F., Guitar, M.A.: Time-dependant microstructural evolution and tribological behaviour of a 26 wt% Cr white cast iron subjected to a destabilization heat treatment. Met. Mater. Int. (2022). https://doi.org/10.1007/s12540-022-01276-8
32. Nayak, U.P., Webel, J., Pesnel, V., Mücklich, F., Guitar, M.A.: Development of a protective coating for evaluating the subsurface microstructure of a worn material. Tribol Lett. **69**, 1–13 (2021). https://doi.org/10.1007/s11249-021-01541-8
33. Nayak, U.P., Guitar, M.A., Mücklich, F.: Evaluation of etching process parameter optimization in the objective specific microstructural characterization of as-cast and heat treated HCCI alloy. Praktische Metallographie/Pract. Metall.. **57**, 688–713 (2020). https://doi.org/10.3139/147.110682
34. Oliver, W.C., Pharr, G.M.: An improved technique for determining hardness and elastic modulus using load and displacement sensing indentation experiments. J. Mater. Res. **7**, 1564–1583 (2011). https://doi.org/10.1557/JMR.1992.1564
35. Oliver, W.C., Pharr, G.M.: Measurement of hardness and elastic modulus by instrumented indentation: advances in understanding and refinements to methodology. J. Mater. Res. **19**, 3–20 (2004). https://doi.org/10.1557/JMR.2004.19.1.3
36. Nayak, U.P., Suárez, S., Pesnel, V., Mücklich, F., Guitar, M.A.: Load dependent microstructural evolution in an as-cast 26% Cr high chromium cast iron during unlubricated sliding. Friction. **10**, 1258–1275 (2022). https://doi.org/10.1007/s40544-021-0553-x
37. Inoue, A., Masumoto, T.: Carbide reactions (M3C→M7C3→M23C6→M6C) during tempering of rapidly solidified high carbon Cr-W and Cr-Mo steels. Metall. Trans. A **11**, 739–747 (1980). https://doi.org/10.1007/BF02661203
38. Vardavoulias, M., Papadimitriou, G., Pantelis, D.: Effect of M7C3→M23C6 transformation on fracture behaviour of cast ferritic stainless steels. Mater. Sci. Technol. **9**, 711–717 (1993). https://doi.org/10.1179/MST.1993.9.8.711
39. Wang, K., Li, D.: Formation of core (M7C3)-shell (M23C6) structured carbides in white cast irons: a thermo-kinetic analysis. Comput. Mater. Sci. **154**, 111–121 (2018). https://doi.org/10.1016/j.commatsci.2018.07.032
40. Archard, J.F.: Contact and rubbing of flat surfaces. J. Appl. Phys. **24**, 981–988 (1953). https://doi.org/10.1063/1.1721448
41. Oberle, T.L.: Wear of metals. JOM. **3**, 438–439 (1951). https://doi.org/10.1007/BF03397325

42. Roa, J.J., Fargas, G., Mateo, A., Jiménez-Piqué, E.: Dependence of nanoindentation hardness with crystallographic orientation of austenite grains in metastable stainless steels. Mater. Sci. Eng. A **645**, 188–195 (2015). https://doi.org/10.1016/j.msea.2015.07.096
43. Leyland, A., Matthews, A.: On the significance of the H/E ratio in wear control: a nanocomposite coating approach to optimised tribological behaviour. Wear **246**, 1–11 (2000). https://doi.org/10.1016/S0043-1648(00)00488-9
44. Tsui, T.Y., Pharr, G.M., Oliver, W.C., Bhatia, C.S., White, R.L., Anders, S., Anders, A., Brown, I.G.: Nanoindentation and nanoscratching of hard carbon coatings for magnetic disks. MRS Online Proc. Library. **383**, 447–452 (2011). https://doi.org/10.1557/PROC-383-447
45. Chen, L., Persson, J., Ståhl, J.E., Zhou, J.M.: Nano-scratching resistance of high-chromium white cast iron and its correlation with wear of cBN tool in machining. J. Superhard Mater. **39**, 365–372 (2017). https://doi.org/10.3103/S1063457617050094
46. Coronado, J.J.: Effect of load and carbide orientation on abrasive wear resistance of white cast iron. Wear **270**, 823–827 (2011). https://doi.org/10.1016/j.wear.2011.02.009
47. Jokari-Sheshdeh, M., Ali, Y., Gallo, S.C., Lin, W., Gates, J.D.: Comparing the abrasion performance of NiHard-4 and high-Cr-Mo white cast irons: The effects of chemical composition and microstructure. Wear **492–493**, 204208 (2022). https://doi.org/10.1016/j.wear.2021.204208

IX. *Analysis of the Carbide Precipitation and Microstructural Evolution in HCCI as a Function of the Heating Rate and Destabilization Temperature*

María Agustina Guitar[1] , **U. Pranav Nayak** [1,] *, Lucía Campo Schneider[1], Jörg Schmauch [3] , Frank Mücklich[1,2]

[1] Department of Materials Science, Saarland University, Campus D 3.3, 66123 Saarbrücken, Germany

[2] Materials Engineering Center Saarland (MECS), Campus D3.3, 66123, Saarbrücken, Germany

[3] Department of Experimental Physics, Saarland University, Campus D2.2, 66123 Saarbrücken, Germany

Submitted to ***"Scientific Reports"*** *(2023) (IF (2023): 4.997)*

Own Contribution: Conceptualization and methodology; sample preparation; experimentation; data analysis; paper writing – section contribution, review and editing; scientific discussion

Analysis of the carbide precipitation and microstructural evolution in HCCI as a function of the heating rate and destabilization temperature

M. Agustina Guitar[1*], U. Pranav Nayak[1], Lucía Campo Schneider[1], Jörg Schmauch [2], Frank Mücklich[1,]

1 Department of Materials Science, Saarland University, Campus D3.3, 66123 Saarbrucken, Germany

2 Department of Experimental Physics, Saarland University, Campus D2.2, 66123 Saarbrücken, Germany

Abstract

Microstructural modification of high chromium cast irons (HCCI) through the precipitation of secondary carbides (SC) during destabilization treatments is essential for improving their tribological response. However, there is not a clear consensus about the first stages of the SC precipitation and how both the heating rate (HR) and destabilization temperature can affect the nucleation and growth of SC.

The present work shows the microstructural evolution, with a special focus on the SC precipitation, in a HCCI (26 wt.% Cr) during heating up to 800, 900, and 980 °C. It was seen that the HR is the most dominant factor influencing the SC precipitation as well as the matrix transformation in the studied experimental conditions. Finally, this work reports for first time in a systematic manner, the precipitation of SC during heating of the HCCI, providing a further understanding on the early stages of the SC precipitation and the associated microstructural modifications.

Introduction

High chromium cast irons (HCCI) are abrasion-resistant materials usually employed in applications where a high wear resistance is required, such as mining and mineral processing industries [1,2]. Heat treatments (HT) are employed for microstructure modification after solidification, where secondary carbides (SC) precipitate during the austenite destabilization process [3,4].

Destabilization of the carbon supersaturated austenite is the most common HT for HCCI. This process allows carbon and chromium to come out of the austenitic matrix by precipitating Cr-rich SC. The carbon depletion from the austenite results in an increase of the martensite start temperature (Ms), allowing the HCCI to be hardened by both carbide precipitation, and martensite formation [4–9] during quenching. Usually, the destabilization (also called critical) process takes place at temperatures range between 800-1150 °C and holding times up to 8 hours for maximum hardening of the alloy [2,3,9–12]. The type of SC formed during destabilization depends on several factors, including the destabilization temperature, the alloy composition (especially Cr/C ratio), and the destabilization holding time. Precipitation of M_7C_3 is expected for alloys with Cr/C < 6.8 [1,3], whereas for alloys with higher Cr content (>25 wt.% Cr; Cr/C > 6.8), the precipitated carbides are of the $M_{23}C_6$ type [1,9,10]. However, despite the alloy composition for which M_7C_3 are predicted to be thermodynamically stable, Powell observed the preferential formation of $M_{23}C_6$ type SC in an alloy with Cr/C ratio of 5.7, owing to the better austenite/$M_{23}C_6$ lattice match [10]. It was also observed that M_7C_3 was present after 4 hours of destabilization at 1000°C, but it was uncertain whether the $M_{23}C_6/M_7C_3$ in-situ transformation was primarily due to the internal diffusion process.

Nevertheless, it is not possible to find a clear consensus concerning the initial stages of carbide precipitation. Most of the studies dealing with the kinetics of SC precipitation agreed that the precipitation occurs actually during the first 5-30 minutes of the holding period, depending on the employed temperature, as a result of re-ordering of the carbon within the austenitic matrix [10,11,13]. After that, only growth and coalescence of carbide can occur. Efremenko et al. observed the starting of the precipitation process after an incubation period of 10 seconds, independent of the alloy´s composition studied [13]. Furthermore, carbide precipitation during cooling was also mentioned in the review published by Tabrett, especially in the temperature range 800-900 °C [1]. This phenomena was also suggested by Wang [14] after detecting very fine

$M_{23}C_6$ SC after quenching to a cryogenic temperature. Additionally, in an own previous work [4], thermodynamic and kinetic simulations suggested that the SC precipitation starts already during the heating process at temperatures around 800 °C. During this stage, M7C3 carbides precipitate initially, and eventually give way to the precipitation of M23C6 carbides once the destabilization temperature of 980 °C is attained. However, from the simulations alone it is not possible to inquire whether the M_7C_3 carbides dissolve or transform, by a diffusion process, into $M_{23}C_6$. Additionally, the simulations also suggested that during the first stage of the cooling further precipitation can take place, as mentioned by Wang and Tabrett [1,14].

Based on the previous, it is seen that there are still some controversies about the exact occurrence of the SC precipitation. This is combined with a poor understanding and a lack of information about the SC formation during heating as well as the effect of heating rate on the precipitation process. For these reasons, the purpose of the present work is to study the microstructural evolution, especially of the SC, in a HCCI (26 wt.% Cr) during heating up to different temperatures. Additionally, the effect of the heating rate (HR) in the carbide precipitation as well as in the matrix transformation are also analysed and discussed here. Furthermore, the presence of M_7C_3 SC precipitating during heating (as suggested by the simulations performed by Guitar et al. [4]) will be evaluated by implementing transmission electron microscopy (TEM) and atom probe tomography (APT) analysis.

Materials and Methodology

For this work, 20 mm x 20 mm x 10 mm samples of a HCCI alloy containing 2.53 wt.% C, 26.6 wt.% Cr and other minor alloy elements [15] were heat treated up to three different temperatures (800, 900, and 980 °C) using two different HR, 1 and 10 °C/minute. The nomenclature corresponding to each of the samples is shown in Table 1. Once the target temperature was reached, the samples were taken from the oven and immediately water quenched to retain the microstructure. The as-cast material consisted of M_7C_3 eutectic carbides (EC), an austenitic matrix and a martensitic layer at the matrix/EC interface, as previously described [4,7,15].The treatment temperatures were selected based on previous MatCalc simulations [4] and the temperatures typically employed for the destabilization of HCCI [4,16], where the temperature range of 950-1000 °C corresponds to the highest precipitation rate [13].

Table 1: Nomenclature of the heated samples at the different HR, up to the three different temperatures

HR \ T	800 °C	900 °C	980 °C
1 °C/min	800_1	900_1	980_1
10 °C/min	800_10	900_10	980_10

Phase identification was performed by X-ray diffraction using a PANalytical Empyrean diffractometer system equipped with a Bragg Brentano-HD (BBHD) module and an ultra-fast PIXcel-3D detector. A symmetrical θ-2θ scan geometry and Cobalt (Co) (Kα = 0.1791 nm) radiation source were used. The applied acceleration voltage and current were 40 kV and 40 mA, respectively. The scan range was 40° to 130° with a step size of 0.013° and a counting time of 250s. Moreover, the pulse height distribution (PHD) settings were set to a range of 25.5% (3.53 keV) – 80% (11.09 keV). The X'Pert High Score Plus software and ICDD Database were used for peak indexing.

Post HT, the samples were ground and polished following the procedure described in [17,18] to obtain a scratch free, mirror polished surface. For general microstructure revelation, the samples heated up to 800 °C were etched with Villella´s reagent (1 g picric acid + 5mLHCl + 95mL C_2H_5OH) [8,17], whereas samples heated up to 900 and 980 °C were etched with Nital (98 mL ethanol + 2 mL nitric acid + 0.5 mL HCl) [17]. The microstructure was analysed using a FEI Helios Nanolab field emission scanning electron microscope (FE-SEM) working with an acceleration voltage of 5–15 kV and a beam current of 1.4 nA. Electron backscattered diffraction (EBSD) was used to investigate the distribution of the microstructural constituents, especially the retained austenite (RA). The measurements were performed at an acceleration voltage of 20 kV and a beam current of 11 nA. The EBSD data was analysed using the Orientation Imaging Microscopy (OIM^{TM} v. 7) Data Analysis software by EDAX Inc.

For the determination of the size and volume fraction of the SC, the samples were etched with a modified Murakami's reagent (4 g $K_3[Fe(CN)_6]$ + 8 g NaOH + 100 mL H_2O) at room temperature for 15 seconds and analysed with the FE-SEM using a high sensitivity backscattered electron detector (vCD) for a better contrast between the phases, as shown [17]. The carbide volume fraction (CVF) and the SC size were calculated after a post processing of the images using the image analysis (I-A) software, ImageJ (version 1.52p) [19]. The same area was evaluated in all the images and at least 5 micrographs were processed in each case [20]. Only particles composed for at least 2 pixels were included in the analysis, i.e., considering the magnification (2500x)

and resolution (4088 pixel x 3523 pixel) of the image, all pixelated particles having a diameter less than 30 nm were disregarded.

For the identification of the SC, TEM and APT samples were extracted from the regions next to the EC, where a higher density of SC was observed (Figure 1). For that, measurements with high-resolution transmission electron microscopy (HR-TEM) using a JEOL ARM 200 TEM/STEM equipped with a Cs corrector (CEOS GmbH), and atom probe tomography (APT) in a LEAP™ 3000 HR (CAMECA Instruments, Madison, Wi, USA) were performed. The APT measurements were carried out in voltage mode, pulse frequency 200 kHz, voltage pulse 20% of standing voltage and evaporation target of 1 event per 200 pulses. Different measurements at temperatures between 60-70 K were performed to evaluate the effect of changing the temperature in the measured carbide composition. Finally, the best result which was obtained at 60 K is presented here. Further information about the results at the different measurement temperatures can be found in the supplementary material. The TEM samples as well as the needle shaped specimens for APT were prepared with focus ion beam (FIB, FEI Helios Nanolab 600, FEI Company) as detailed in reference [21] and [22], respectively. A final polishing with 5 kV (TEM samples) and 2 kV (APT samples) was performed in order to decrease the Ga contamination.

The 3D reconstruction and the peak decomposition from atom probe data was performed using the software IVAS™ 3.6.14 (CAMECA Instruments, Madison, Wi, USA), applying a tip profile algorithm. For that, SEM images of the tip before APT measurement were used. The peak decomposition results were exported for further calculations to MATLAB R2020b. The mass spectrums images and the multiple hit analysis were performed using APT toolbox for MATLAB [23]. Furthermore, the carbides were indexed on Fast Fourier Transform (FFT) images from HR-TEM micrographs, which contains similar information to electron diffraction patterns when a single crystal is analysed. For SC identification the CrysTBox software [24] was used.

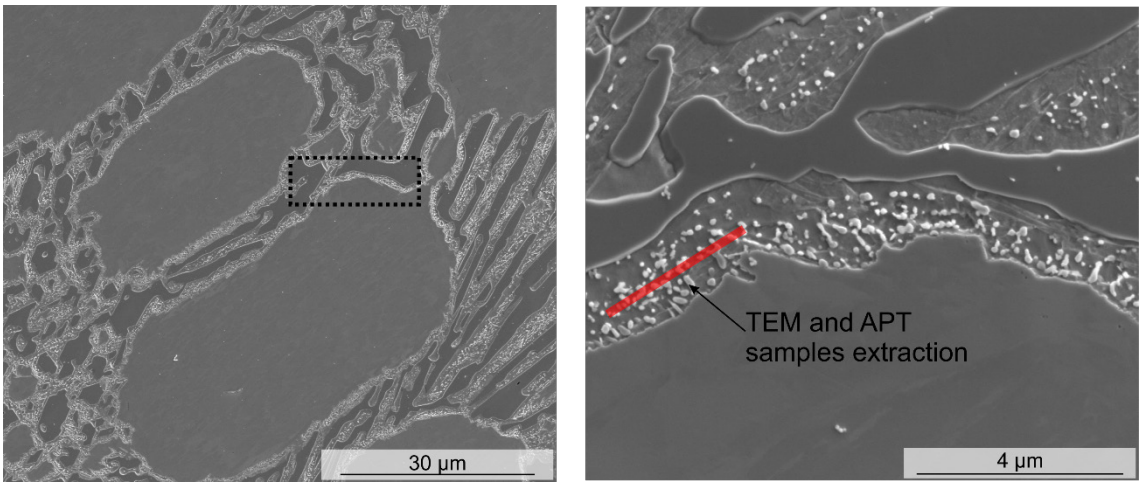

Figure 1: Representative extraction site for the TEM lamella and APT sample. For the analysis the 800_10 sample was used.

Results and discussion

The microstructure of the heat-treated samples after reaching the desired temperature and using two different HR is shown in Figure 2. The presence of SC can be observed even after heating up to a relatively low temperature (800 °C), which is an indication that precipitation occurs already during heating, starting at temperatures below 800 °C. In the literature, it is not possible to find a concurrence about the start of the carbide precipitation. Many authors report the presence of SC after a few minutes of holding at the destabilization temperature. Efremenko et al. [13] is one of the few suggesting that precipitation starts after soaking for only 10 seconds at 950 °C in HCCI with different compositions. Still, there is no mention or proof of precipitation during heating. Therefore, the results shown here represent the first experimental evidence of SC precipitating during heating, starting at temperatures below 800 °C. This is in agreement with the results previously shown in [4], where kinetic simulations predicted the precipitation of SC during this step of the HT.

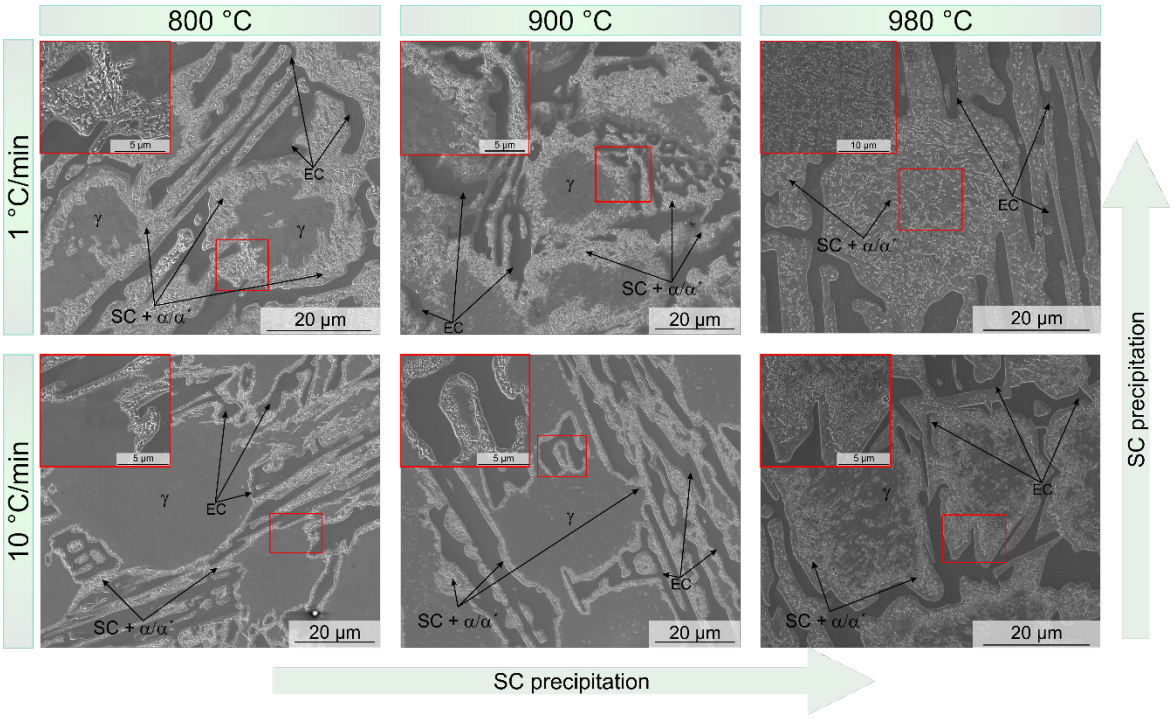

Figure 2: SEM images corresponding to the samples heated under the different conditions.

The SC start to precipitate at the regions next to the EC, evidenced by the relatively high density of small particles present there, where two clear trends can be seen in the microstructural evolution of the heated samples in Figure 2: i) SC precipitation increases with temperature, ii) SC precipitation increases with decreasing HR. Both the increase of the reached temperature

and the decreasing HR, led to SC precipitation towards the centre of the austenite grains (Figure 2). About twice the area is covered by SC in the 800 and 900 °C samples heated at 1°C/minute compared to those heated faster. Moreover, the re-distribution of alloy elements resulted in a partial transformation of austenite to martensite during cooling, even in regions free of detectable SC, as seen in EBSD maps (Figure 3) and BSE-SEM images (Figure 4). Karantzalis et al. reported that experiments carried out at 750 °C showed a partial transformation from austenite to ferrite and pearlitic-like structures whereas, the hardness increase reported after HT at 850 °C was related to the presence of martensite and SC [12]. Based on that, the microstructure of samples 800_1 and 800_10 may consist of both ferrite and martensite due to the temperature of 800°C utilized in the study, which is on the threshold between the "destabilization temperature" (referred to as the critical temperature) and "subcritical temperature" [12]. Since the martensite cannot be straightforwardly separated from the ferrite using the characterization techniques employed here, throughout the text martensite/ferrite phase will be utilized, when referring to the heat-treated conditions. Finally, Figure 3 (800_10) and Figure 4 a-b) show SC located at the vicinity of the EC however, the martensite/ferrite phase extends few microns along the matrix. Slower heating rates allow the homogenization of alloy elements distribution, leading to nucleation and growth of SC across a larger area of the matrix, where about 17% of the sample is not covered by SC in the 800_1 sample compared to about 35% of carbide-free area in the 800_10 sample.

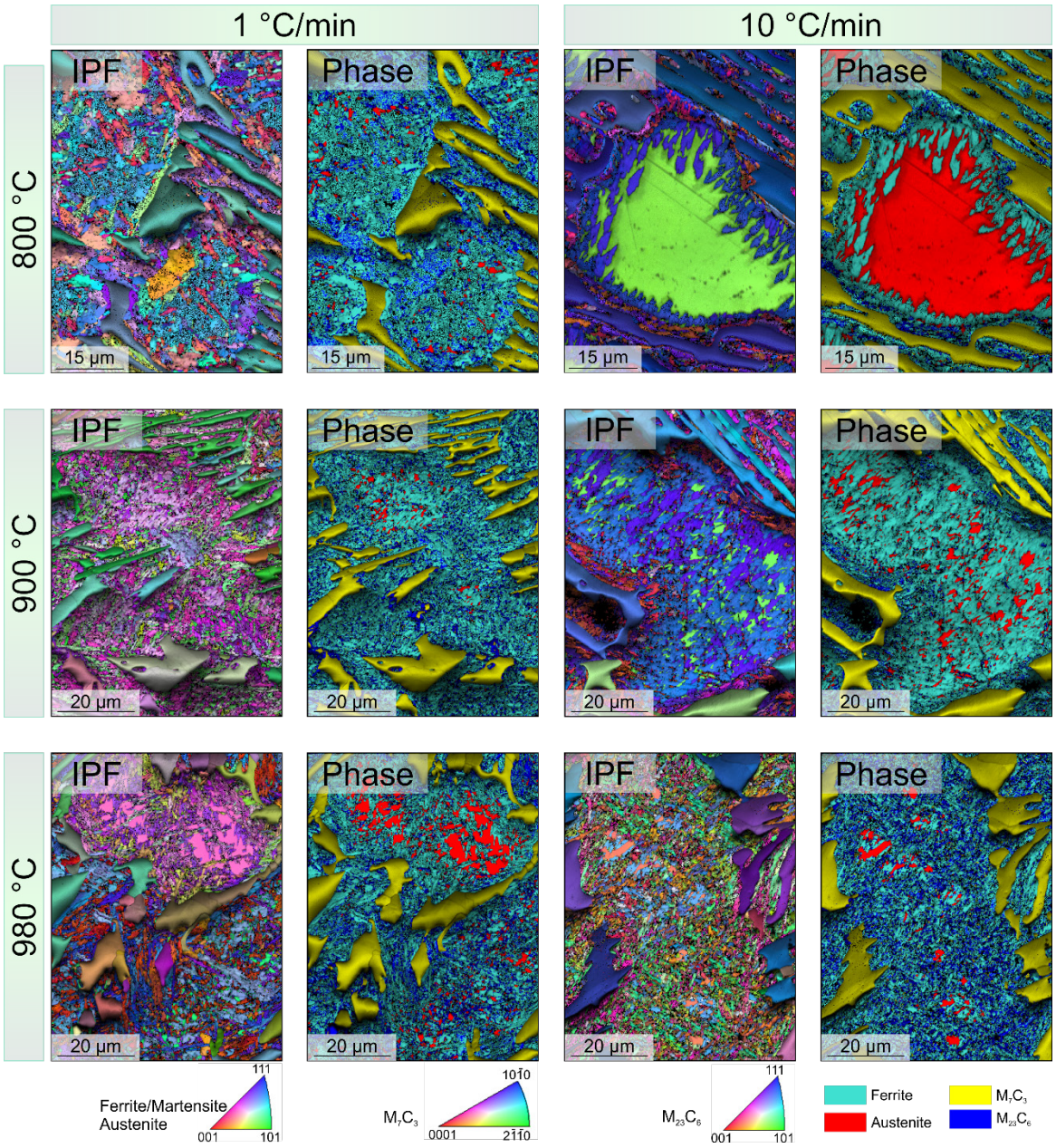

Figure 3: IPF+IQ and Phase+IQ maps corresponding to the samples heated at two heating rates up to the three analysed destabilization temperature. Larger transformed areas are observed in samples slow heated. Consider that EBSD maps might fail in the quantification of RA, due to low statistic and possible austenite to martensite transformation during preparation

The martensitic region at EC/austenite interface (as-cast condition) [15] possesses a large lattice distortion and non-equilibrium defects [25], resulting in a reduction of the activation energy required for nucleation of small-sized carbides [11,13]. As a consequence, the carbide precipitation is favoured at the vicinity of the EC (Figure 2, samples 800_10 and 900_10). Moreover, the carbon supersaturation of the martensitic phase combined with the faster diffusion coefficient also benefit the formation of SC on defect sites such as dislocations or lath boundaries

[26,27].Some authors suggested that the M_7C_3 EC might act as C reservoir, allowing the precipitation of SC by releasing C and increasing locally the amount of C [9,28]. The release of C leads to a partial transformation of the EC periphery from M_7C_3 to $M_{23}C_6$. The proposed mechanism seems not be the one acting for the beginning of precipitation in the samples studied here, since it was not possible to detect any M_7C_3 to $M_{23}C_6$ transformation at the periphery of the EC (Figure 2 and Figure 3).

Other authors [28] made reference to a precipitates free zone (PFZ) located at the primary carbides/austenite interface after long holding times (<16 hours). They suggested that the PFZ is the consequence of Cr solubility/concentration for SC precipitation not being reached at this region, concluding that PFZ will disappear without a Cr gradient. In the material studied in the present work, the martensitic region at the EC/austenite interface is the consequence of a Cr and C gradient. However, the only sample showing a PFZ is the one heated up to 980°C with the faster HR (Figure 4 d, e). Nonetheless, the differences in the treatment conditions and C content between Roussel´s work and the present work should be taken into consideration. However, it is of interest to evaluate the kinetic conditions leading to the precipitation of carbides, where the conditions, from the point of view of chemical gradients, are not the most optimum. On one hand, the martensitic region at the EC/austenite interface is supersaturated in C and contains a large number of defects, as discussed previously. With an increase of the temperature, the mobility of C in martensite increases rapidly [26]. On the other hand, due to a less availability of Cr in this region, the nucleation of low Cr carbides such as $(Cr,Fe)_7C_3$ might be possible, as suggested by previous kinetic simulations reported in [4].

An increase in the temperature from 800 to 900 °C (HR 10°C/min) led to additional SC precipitation along dendritic interfaces, as consequence of further alloy elements re-distribution. As seen in the sample 900_10 (Figure 4c), small precipitates have nucleated at dislocations or dendrite boundaries within the austenitic grain. The preferential SC precipitation at these sites is again related to a higher local density of defects [29]. Furthermore, for the same reached temperature and slower HR, the time provided for redistribution of alloy elements was enough for more massive carbide precipitation, evidenced by the larger area transformed during the process as shown in Figure 2 (samples 800_1 and 900_1). Finally, with an increase of temperature of only 80 °C, massive carbide precipitation can also be observed within the austenitic

region (Figure 2), for both conditions HR 1 °C/min and 10 °C/min. This corresponds to the observations in other works, where it was seen that the SC precipitation rate was the highest between 950 and 1000 °C [9,13].

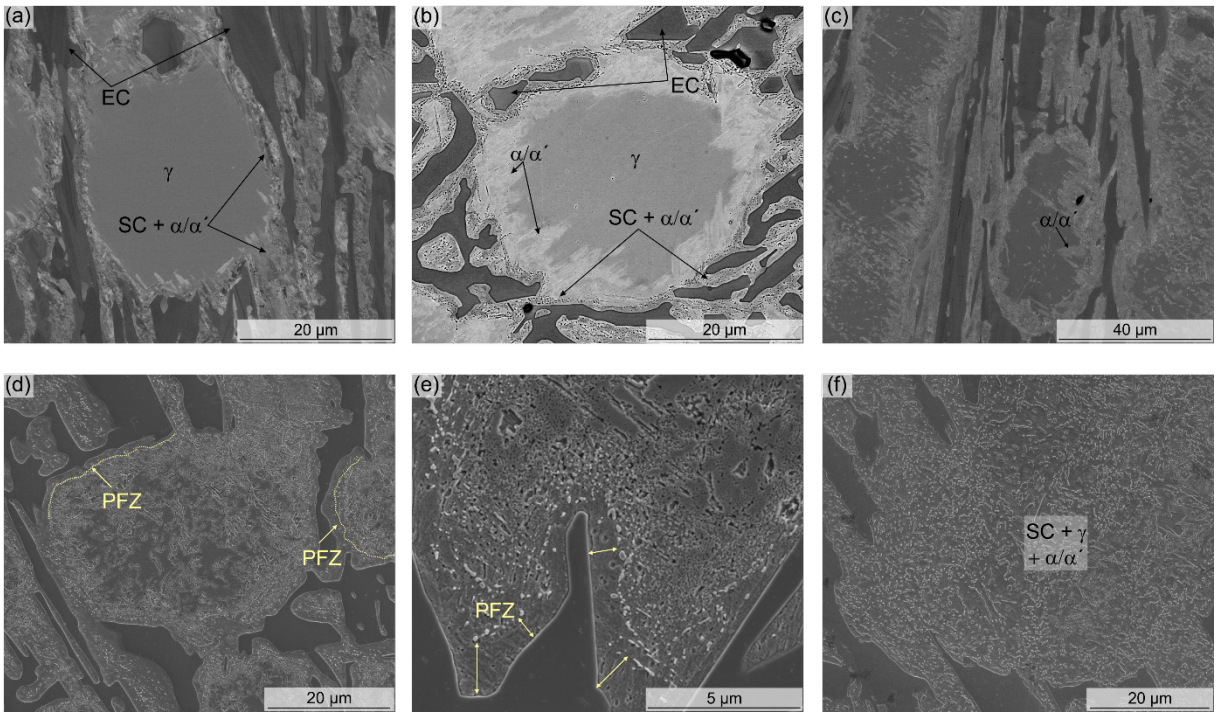

Figure 4: SEM images corresponding to the (a) 800_10 sample, polished with OPS; (b) 800_10 sample (Murakami etched) in vcD mode; (c) 900_10 sample, polished with OPS showing regions of martensite/ferrite free of visible carbides; d) and e) 980_10 sample showing precipitate free zone; and f) 980_1 sample showing the martensite/ferrite matrix covered by SC.

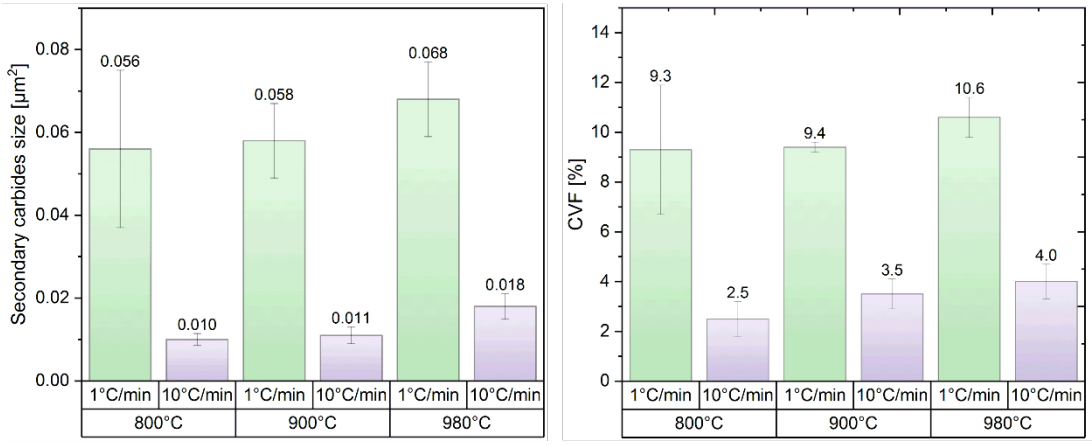

Figure 5: Size and volume fraction of the secondary carbides precipitated during heating, as a function of heating rate and reached temperature.

The calculated secondary carbide volume fraction (CVF) and the corresponding average size are represented in Figure 5. There, a strong effect of the HR can be seen in both the particle

size and secondary CVF. Although a slight tendency to larger size and CVF values can be distinguished with increasing temperature for a certain HR, they remain within the tolerance interval. An increment in the temperature from 800 to 980 °C led to an increase of about 30% in the particle size and about 14% in the CVF. On the other hand, for the fastest HR, the carbides doubled in size and CVF increased by 60% when reaching 800 and 980 °C, respectively. Moreover, a slow HR results in carbides size up to 5 times increase, whereas the CVF increased by about 3.5 times compared to the faster HR for the same reached temperature. From here, it is clear that the main factor affecting the SC size and CVF is the HR and to a lesser extent the reached temperature, as seen from Figure 5.

The reached temperature, as well as the HR, affect both the fraction and size of the SC, and the fraction of RA, since it is directly related to the C remaining for austenite stabilization. Austenite can be stabilized and retained using different routes. One is performing destabilization at high temperatures (above 1000 °C) [30,31], destabilizing for very short times (less than 5 minutes) [16], or performing the destabilization at low temperatures (under 900°C). The result, in terms of material´s response can be very different [32].

Figure 6 displays the diffractograms of the different heat-treated samples, showing the presence of M_7C_3 and $M_{23}C_6$ carbides, austenite, and martensite. Peaks of $M_{23}C_6$ carbides correspond to the SC precipitated during heating, which can be observed in the samples heated at 1 °C/minute and less intensely in the samples heated faster. Interesting is the case of the samples heated up to 800 and 900 °C at 10°C/minute, which apparently show same microstructural distribution and fraction of SC, show different fraction and distribution of RA (see Figure 3). In the latter case (900_10 sample), XRD shows an intense peak of RA, suggesting an additional process occurs during heating up to 900 °C related to alloy element redistribution, probably the formation of a few nm size carbide nuclei, small enough not to be detected by SEM. Even though it is expected that the samples heated up to 800 °C contain the largest fraction of RA, they show the less intense peak of austenite, which is probably related to a sampling effect of the large austenitic grains [33]. Even though EBSD maps in Figure 3 might not be representative enough, it shows a relatively good idea of RA distribution. In all cases, M_7C_3 peaks correspond to the EC, which do not show any visible modification, in terms of size and shape, during heat treatment such as refinement or fractioning. The potential presence of SC in form of M_7C_3 cannot be visualized by X-ray diffraction, due to the low fraction expected [4], which would not significantly alter the intensity of M_7C_3 peaks from the EC.

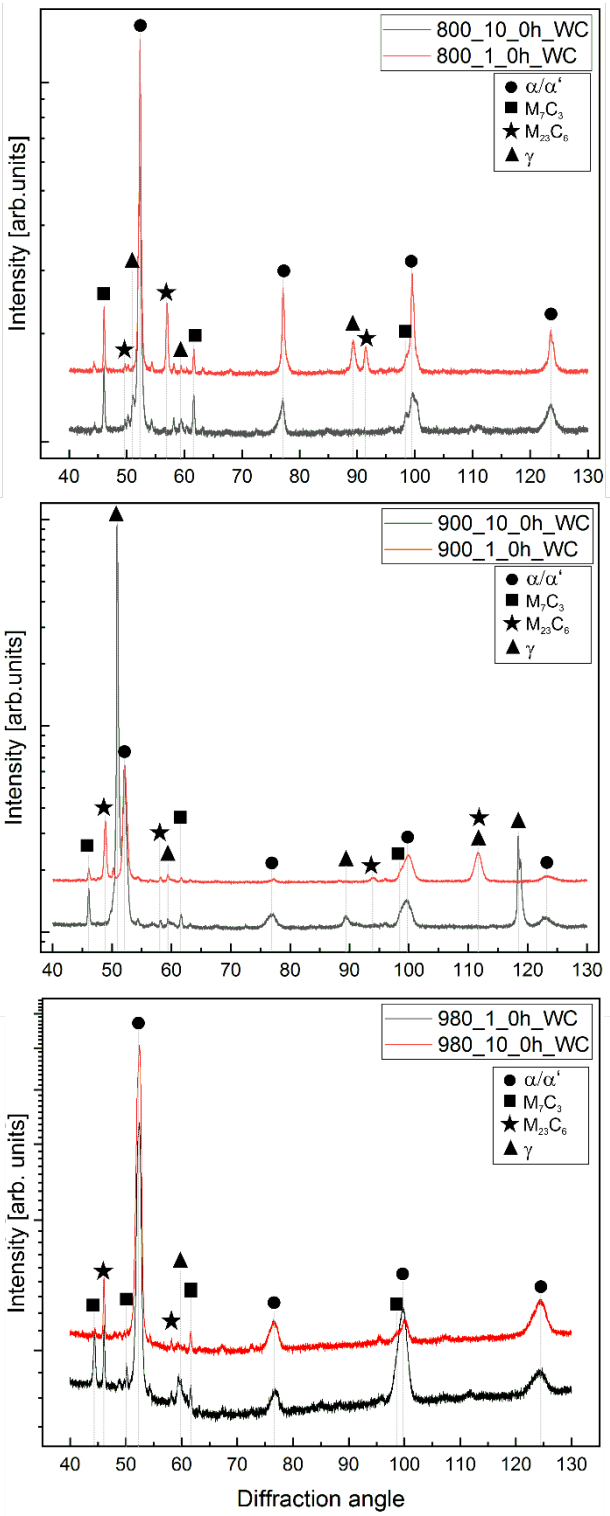

Figure 6: Diffractograms of the samples heat treated samples as a function of the heating rate for the different temperatures analysed. The intensity is shown in logarithmic scale for better comparison. Peaks corresponding to martensite and ferrite appear usually in almost same position and they cannot easily be separated, therefore the peaks were indexed as α/α'.

As mentioned previously, kinetic simulations and lower availability of Cr in the region next to the EC suggest the possibility of precipitation of $(Cr,Fe)_7C_3$ type SC. Due to their size and volume fraction, their detection with XRD is not viable. Therefore, TEM samples were extracted from the region next to the EC (Figure 1), where the beginning of SC precipitation was observed The particles with sizes of around 50-60 nm in diameter (Figure 7), were indexed by the CrysTBox [24] as M_7C_3.

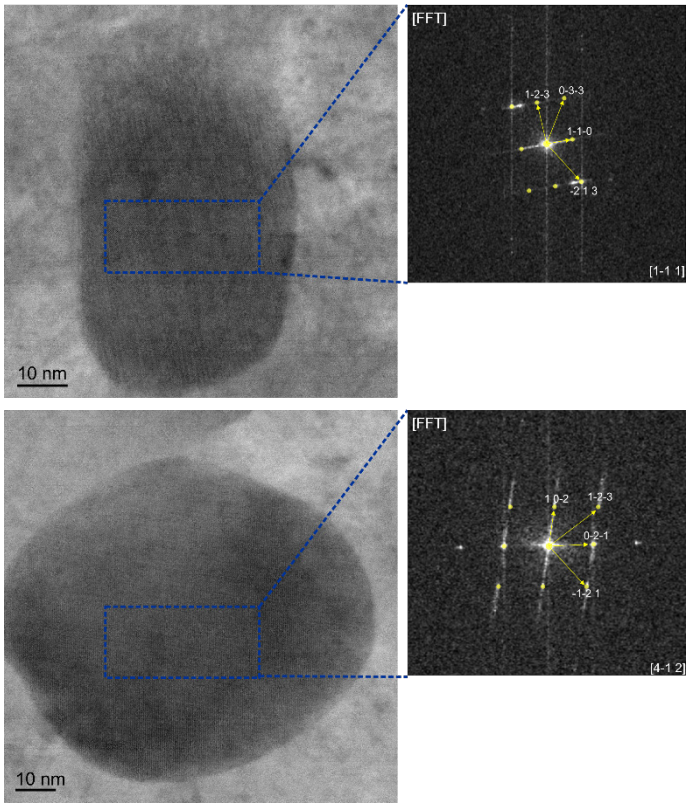

Figure 7: HR-TEM images of two different particles extracted from the 800_10_0h sample, which were identified as M_7C_3 carbides with help of the CrysTBox software [24]. The corresponding Fourier transformations are shown.

Moreover, APT samples extracted from a similar region as the TEM samples, were analysed for determination of the chemical composition of the particles, as shown in Figure 8. The reconstruction of a specimen containing part of a carbide can be seen in Figure 8b, where the Fe and Cr atoms are shown. A ROI including only the carbide volume (delimited by the 28 at.% iso-surface) was exported and analysed for determining the composition of the carbide. Regions close to the interface were avoided to minimize error generated by ion trajectory overlap that can occur due to the presence of phases with different evaporation field [34].

As a result of the peak decomposition analysis, a C content of 29 ± 1 at.% is obtained (Figure 8c) which is very close to the 30 at.% C expected for M_7C_3 carbide. It is important to remark

the challenges associated to the quantification of carbon-rich phases resulting from the over- [35–37] and underestimation [38–40] of carbon due to overlapping of molecular carbon preferential evaporation and pile up effect. However, the results reported by Takahashi et al. [37], and Marceau et al. [35], showed that for the working temperature range (70 K), the 24 Da is mainly C_2^+ (Figure 8a) and the peak decomposition algorithm provides a reliable result. A more detailed analysis of these effects and its impact in the carbon quantifications is provided in the supplementary material. Although the proxigram in Figure 8c) only shows the content of C, Cr, and Fe, all the elements labelled in Figure 8a) were included for the compositional analysis of the carbide. The individual element quantification can be seen in the supplementary material.

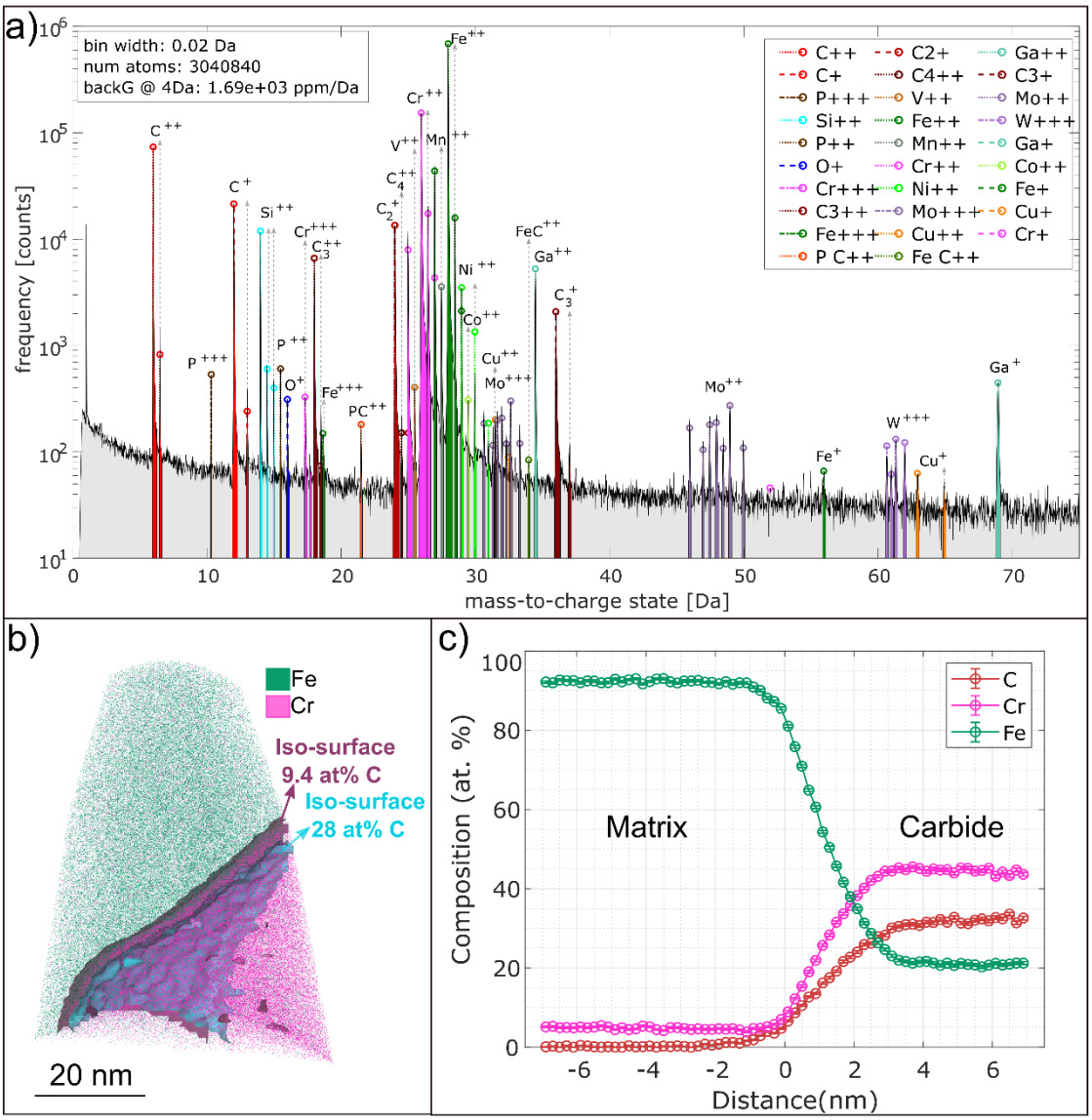

Figure 8: a) Mass spectrum of the specimen presented in b, measured at 60 K. The occurrence of different ions of single and molecular C is evidenced and the complexity of the spectrum due to overlapping of several peaks. The presence of Ga ions is

the result of the FIB preparation. b) Reconstruction of and specimen containing part of a carbide. For clarity Fe and Cr atom are shown. An iso-surface of C=9.3 at.% was created to calculate the variation of composition across the interface. The second iso-surface at 28 at.% was utilized to define a ROI where to perform the compositional analysis. c) Proxigram across the iso-surface at 9.3 at. % showing that after 2-3 nm the C content inside the carbide tends to 30 at.%. Please note that no peak decomposition is performed for the proxigram.

Results shown from HR-TEM and APT support the simulations performed in a previous work [4] that SC of the M_7C_3 nature start to precipitate during the heating of HCCI. It is also worth to note that the presence of $M_{23}C_6$ type SC was also detected during HR-TEM analysis, which was previously confirmed in samples of the same composition [4]. Powell [41] gave some indication of possible precipitation of M_7C_3 together with $M_{23}C_6$ carbides in HCCI 18% Cr when destabilizing for short times (0.25 h) at 1000 °C. It is known that M_7C_3 can be predecessor of $M_{23}C_6$, as well as $M_{23}C_6$ can be predecessor of M_7C_3, highly depending on the bulk local chemical composition [42]. Moreover, both type of carbides were seen after destabilizing for longer times, where also a partial transformation from $M_{23}C_6$ to M_7C_3 was observed [9,43,44]. In the current work, the presence of both M_7C_3 and $M_{23}C_6$ type of carbides were detected at the beginning of the destabilization process, i.e., during heating. However, from the results shown here, it is not completely clear whether the precipitates nucleating first as M_7C_3, with a $(Cr_{4.7}Fe_{2.3})C_3$ composition, transform later to $M_{23}C_6$ or they dissolve giving place for the precipitation and growth of $M_{23}C_6$.

Conclusions

The SC precipitation in HCCI during heating was evaluated as an influence of the HR and the reached destabilization temperature. The results presented here provide an understanding on the early stages of the SC precipitation and the associated microstructural modifications.

The microstructural modification of HCCI containing 26 wt.% Cr starts during heating with the precipitation of SC at temperatures around 800 °C. It is accompanied with a redistribution of alloy elements, which lead to the matrix transformation to α/α' and allows the retention of different fractions of RA. The morphology, fraction, and distribution of the phases within the material depends on both the HR and the reached temperature. These two parameters influence the size and VF of the carbides precipitated during heating. Despite a tendency towards an increased carbide size and CVF when the temperature is increased from 800 to 980 °C, it is clear that the HR has the strongest influence on the carbide volume fraction and particle size

reached after heating. A slow heating rate provides larger time at higher temperatures, allowing the nucleated particles to grow and coalesce during the heating period.

Finally, this work reports for first time, in a systematic manner, the precipitation of SC during heating of the HCCI, where the HR was the most dominant factor in the size and volume fraction of the SC present at different heating stages. Through crystallographic and chemical analysis, it was possible to support the theoretical aspects related to the precipitation of both type of carbides, M_7C_3 and $M_{23}C_6$ during the heating process, where M_7C_3 SC possess a $(Cr_{4.7}F_{2.3})C_3$ composition as shown by APT results.

Acknowledgements

The authors would like to thank Martin Duarte from Tubacero S.A. for providing the materials and to the Leibniz Institute for New Materials (INM) at Saarland University for providing access to the HR-TEM. U.P.N. is grateful to DAAD for the financial support.

Open Access funding enabled and organized by Projekt DEAL. The present work is supported by funding from the Deutsche Forschungsgemeinschaft (DFG, project: GU 2102/2-1).

Conflicts of interest: There is no conflict of interest

Availability of materials and data: The data and materials used in this study are available from the corresponding author at reasonable request.

Supplementary Information: This work contains supplementary information that is authorized by the authors and can be accessible for the readers.

Ethical approval: Not applicable

Bibliography

1. Tabrett, C. P., Sare, I. R. & Ghomashchi, M. R. Microstructure-property relationships in high chromium white iron alloys. *Int. Mater. Rev.* **41**, 59–82 (1996).

2. Karantzalis, A. E., Lekatou, A. & Diavati, E. Effect of destabilization heat treatments on the microstructure of high-chromium cast iron: A microscopy examination approach. *J. Mater. Eng. Perform.* **18**, 1078–1085 (2009).

3. Guitar, M. A. *et al.* High Chromium Cast Irons: Destabilized-Subcritical Secondary Carbide Precipitation and Its Effect on Hardness and Wear Properties. *J. Mater. Eng. Perform.* **27**, 3877–3885 (2018).

4. Guitar, M. A., Nayak, U. P., Britz, D. & Mücklich, F. The Effect of Thermal Processing and Chemical Composition on Secondary Carbide Precipitation and Hardness in High-Chromium Cast Irons. *Int. J. Met.* **14**, 755–765 (2020).

5. Gahr, K. H. Zum & Doane, D. V. Optimizing fracture toughness and abrasion resistance in white cast irons. *Metall. Trans. A* **11**, 613–620 (1980).

6. Filipovic, M., Kamberovic, Z., Korac, M. & Gavrilovski, M. Microstructure and mechanical properties of Fe–Cr–C–Nb white cast irons. *Mater. Des.* **47**, 41–48 (2013).

7. Guitar, M. A. *et al.* Quantification of the Phase Transformation Kinetics in High Chromium Cast Irons Using Dilatometry and Metallographic Techniques. *Metall. Mater. Trans. A Phys. Metall. Mater. Sci.* **51**, 3789–3801 (2020).

8. Guitar, M. A., Scheid, A., Britz, D. & Mücklich, F. Evaluation of the etching process for analysis of secondary carbides in HCCI by optical and confocal laser microscopy. *Prakt. Metallogr. Metallogr.* **56**, (2019).

9. Wiengmoon, A., Chairuangsri, T. & Pearce, J. T. H. A microstructural study of destabilised 30wt.%Cr-2.3wt.%C high chromium cast iron. *ISIJ Int.* **44**, 396–403 (2004).

10. Powell, G. L. F. & Laird, G. Structure, nucleation, growth and morphology of secondary carbides in high chromium and Cr-Ni white cast irons. *J. Mater. Sci.* **27**, 29–35 (1992).

11. Bedolla-Jacuinde, A., Arias, L. & Hernández, B. Kinetics of secondary carbides precipitation in a hiqh-chromium white iron. *J. Mater. Eng. Perform.* **12**, 371–382 (2003).

12. Karantzalis, A. E., Lekatou, A., Kapoglou, A., Mavros, H. & Dracopoulos, V. Phase transformations and microstructural observations during subcritical heat treatments of a high-chromium cast iron. *J. Mater. Eng. Perform.* **21**, 1030–1039 (2012).

13. Efremenko, V., Shimizu, K. & Chabak, Y. Effect of destabilizing heat treatment on solid-state phase transformation in high-chromium cast irons. *Metall. Mater. Trans. A* **44**, 5434–5446 (2013).

14. Wang, J. *et al.* Effects of high temperature and cryogenic treatment on the microstructure and abrasion

resistance of a high chromium cast iron. *J. Mater. Process. Technol.* **209**, 3236–3240 (2009).

15. Nayak, U. P., Guitar, M. A. & Mücklich, F. A comparative study on the influence of chromium on the phase fraction and elemental distribution in as-cast high chromium cast irons: Simulation vs. experimentation. *Metals (Basel).* **10**, (2020).

16. Nayak, U. P., Mücklich, F. & Guitar, M. A. Time - Dependant Microstructural Evolution and Tribological Behaviour of a 26 wt % Cr White Cast Iron Subjected to a Destabilization Heat Treatment. *Met. Mater. Int.* (2022). doi:10.1007/s12540-022-01276-8

17. Pranav Nayak, U., Guitar, M. A. & Mücklich, F. Evaluation of etching process parameter optimization in the objective specific microstructural characterization of as-cast and heat treated HCCI alloy. *Prakt. Metallogr. Metallogr.* **57**, 688–713 (2020).

18. Guitar, M. A. *et al.* Secondary carbides in high chromium cast irons: An alternative approach to their morphological and spatial distribution characterization. *Mater. Charact.* **144**, 621–630 (2018).

19. Schindelin Johannes *et al.* Fiji: an open-source platform for biological-image analysis. *Nat. Methods* **9**, 676–682 (2012).

20. Nayak, U. P., Müller, M., Britz, D., Guitar, M. A. & Mücklich, F. Image Processing using Open Source Tools and their Implementation in the Analysis of Complex Microstructures. *Pract. Metallogr.* **58**, 484–506 (2021).

21. Ayache, J., Beaunier, L., Boumendil, J., Ehret, G. & Laub, D. *Sample Preparation Handbook for Transmission Electron Microscopy*. *Journal of Experimental Psychology: General* **136**, (Springer, 2007).

22. Thompson, K. *et al.* In situ site-specific specimen preparation for atom probe tomography. *Ultramicroscopy* **107**, 131–9 (2007).

23. Felfer, P. APT toolbox for MATLAB. doi:https://github.com/peterfelfer/Atom-Probe-Toolbox

24. Klinger, M. More features, more tools, more CrysTBox. *J. Appl. Crystallogr.* **50**, 1226–1234 (2017).

25. Porter, D. A. & Easterling, K. E. *Phase Transformations in Metals and Alloys*. (CRC Press, Taylor and Francis Group, 1992).

26. Cermak, J. & Kral, L. Carbon diffusion in carbon-supersaturated ferrite and austenite. *J. Alloys Compd.* **586**, 129–135 (2014).

27. Gouné, M., Danoix, F., Allain, S. & Bouaziz, O. Unambiguous carbon partitioning from martensite to austenite in Fe-C-Ni alloys during quenching and partitioning. *Scr. Mater.* **68**, 1004–1007 (2013).

28. Roussel, M. *et al.* Influence of solidification induced composition gradients on carbide precipitation in FeNiCr heat resistant steels. *Materialia* **4**, 331–339 (2018).

29. Beckitt, F. R. & Clark, B. R. The shape and mechanism of formation of $M_{23}C_6$ carbide in austenite. *Acta*

Metall. **15**, (1967).

30. Abdel-Aziz, K., El-Shennawy, M. & Omar, A. A. Microstructural Characteristics and Mechanical Properties of Heat Treated High-Cr White Cast Iron Alloys. *Int. J. apllied Eng. Res.* **12**, 4675–4686 (2017).

31. Bedolla-Jacuinde, A., Arias, L. & Hernández, B. Kinetics of secondary carbides precipitation in a hiqh-chromium white iron. *J. Mater. Eng. Perform.* **12**, 371–382 (2003).

32. Gahr, K. H. Zum & Doane, D. V. Optimizing fracture toughness and abrasion resistance in white cast irons. *Metall. Trans. A* **11**, 613–620 (1980).

33. Buhrke, V. E., Jenkins, R. & Smith, D. K. *A practical guide for the preparation of specimens for x-ray fluorescence and x-ray diffraction analysis*. (Wiley-VCH Verlag GmbH, 1998).

34. Vurpillot, F., Bostel, A. & Blavette, D. Trajectory overlaps and local magnification in three-dimensional atom probe. *Appl. Phys. Lett.* **76**, 3127–3129 (2000).

35. Marceau, R. K. W., Choi, P. & Raabe, D. Understanding the detection of carbon in austenitic high-Mn steel using atom probe tomography. *Ultramicroscopy* **132**, 239–247 (2013).

36. Danoix, F., Julien, D., Sauvage, X. & Copreaux, J. Direct evidence of cementite dissolution in drawn pearlitic steels observed by tomographic atom probe. *Mater. Sci. Eng. A* **250**, 8–13 (1998).

37. Takahashi, J., Kawakami, K. & Kobayashi, Y. Quantitative analysis of carbon content in cementite in steel by atom probe tomography. *Ultramicroscopy* **111**, 1233–1238 (2011).

38. Thuvander, M. *et al.* Quantitative atom probe analysis of carbides. *Ultramicroscopy* **111**, 604–608 (2011).

39. Morsdorf, L., Emelina, E., Gault, B., Herbig, M. & Tasan, C. C. Carbon redistribution in quenched and tempered lath martensite. *Acta Mater.* **205**, 116521 (2021).

40. Sha, M., Chang, L., Smith, G. D. W., Cheng, L. & Mittemeijer, E. J. Some aspects of atom-probe analysis of Fe-C and Fe-N systems. *Surf. Sci.* **266**, 416–423 (1992).

41. Powell, G. L. F. F. & Bee, J. V. Secondary carbide precipitation in an 18 wt.%Cr-1 wt.% Mo white iron. *J. Mater. Sci.* **31**, 707–711 (1996).

42. Senior, B. A. A Critical Review of Precipitation Behaviour in lCr-Mo-V Rotor Steels tempering results in some coarsening and spner oidization of M , C [7], and a feathery lath-like a. *Mater. Sci. Eng. A* **103**, 263–271 (1988).

43. Wang, J. *et al.* The precipitation and transformation of secondary carbides in a high chromium cast iron. *Mater. Charact.* **56**, 73–78 (2006).

44. Karantzalis, E., Lekatou, A. & Mavros, H. Microstructure and properties of high chromium cast irons: effect of heat treatments and alloying additions. *Int. J. Cast Met. Res.* **22**, 448–456 (2009).

Analysis of the carbide precipitation and microstructural evolution in HCCI as a function of the heating rate and destabilization temperature

M. Agustina Guitar

U. Pranav Nayak

Lucía Campo Schneider

Jörg Schmauch

Frank Mücklich

Supplementary material

The composition of secondary carbides (SC) precipitated during the heating step was determined by Atom Probe Tomography (APT). The objective was to confirm the presence of M_7C_3 type SC at the initial stages of the precipitation. The analysis was performed on the sampled heated until 800ºC (HR 10 °C/min) and quenched, form regions close to EC, as shown in Figure 1 of the main text.

A total of 6 specimens were measured, from which 4 included parts of carbides. Here the analysis of 3 carbides are shown, measured in three different temperature conditions between 60 and 70 K. For the carbide compositional determination, a region of interest (ROI) including only the carbide volume was exported and analyzed. Regions close to the interface were avoided in order to minimize any error generated by ion trajectory overlap resulted from the presence of phases with different evaporation field [1].

Figure S1 shows the mass spectrum of one of the samples, measured at 70 K. There, it is seen that C is detected as C^{++}, C^{+}, C_3^{++}, C_2^{+}, C_4^{++}, C_3^{+}. The overlap between the different peaks is one of the issues affecting the carbon quantification. For example, the peak at 24 Da can be assigned to C_2^{+} or C_4^{++} (which would contribute to twice amount of C in that peak). As known from the literature, this peak is predominantly C_2^{+} and the contribution of C_4^{++} is calculated using a peak decomposition algorithm by the help of the peak at 25.5 Da which corresponds to C_4^{++} ($^{13}C^{12}C_3^{++}$) [2,3].

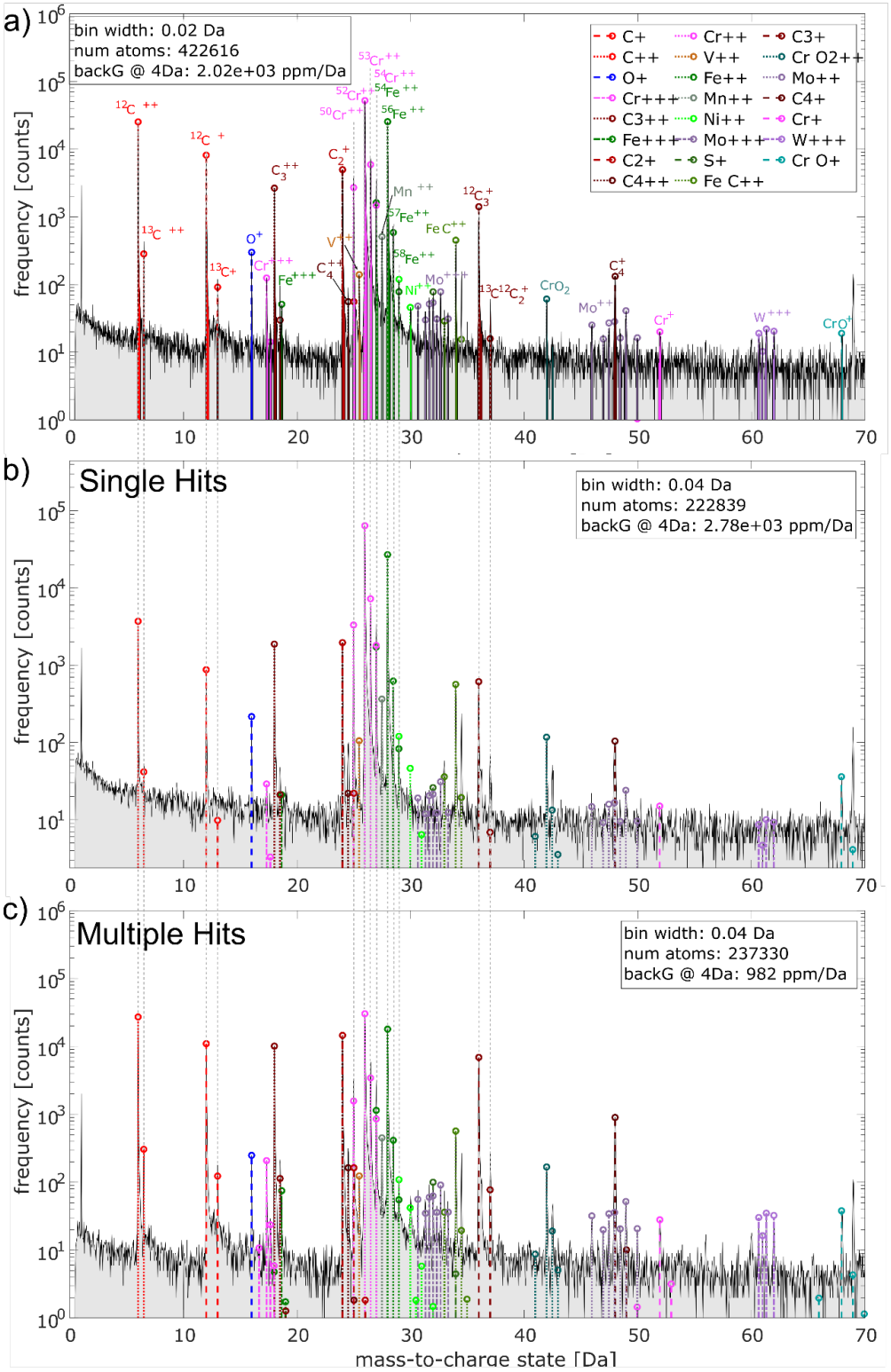

Figure S1: Mass spectrum of a carbide measured at 70ºK. a) Complete spectrum, b) Single hits, c) Multiple hits. C ions are relatively more frequent in multiple hits, but also the other elements have a high amount of multiple hit events. The ions that were analyzed for Miyamoto correction [4] are identified with grey lines and include the isotope ID.

Another possible source of error is the occurrence of preferential evaporation, since the ions with lower evaporation field (Fe and Cr respect to C) have more probability to evaporate between pulses and not be detected. This effect is more significant at high temperatures and lower pulse frequency [5]. However, in the present analysis, the composition obtained at different temperatures does not show a significant variation, indicating a low influence of the previous effect in the measurement conditions.

Finally, the carbon quantification can also be affected by the pile-up effect in the detector due to the occurrence of multiple hit events. Analysis of the multiple and single events (table S1 and Figure S1) showed that C is mostly detected in multiple hits, having thus more probability of not being detected due to pile up effect on the detector [3]. Also differences between measured and expected abundances of the most common isotopes are an indication of pile-up occurrence, since the higher the concentration, the higher the probability of pile-up [6]. As can be seen in the carbide mass spectrum for all events and for multiple hit events (Figure S1), the most important peaks in the spectrum are C++, C+, Cr++, Fe++ and C_3^+. When analyzing the ratio between the most abundant isotope and the total detection for those ions, it is observed that the measured ratio is always lower than the natural abundance (Figure S2), indicating a detection loss occurrence. Given that, a correction for Fe++ pile-up proposed by Miyamoto et.al 2012 [4] was applied, and extended for C++, C+, Cr++ and C3+.

Table S1. Multiple and single hit events occurrence for relevant ions. Just isotopes that do not overlap are included. Total ranged counts inside the carbide: 358 375. T:70 ºK.

Ion	Single Hits	Multiple Hits	Ratio Multiple/Single
$^{12}C++$	4278	30590	7.2
$^{13}C++$	86	565	6.6
$^{12}C+$	1306	14731	11.3
$^{13}C+$	48	259	5.4
$^{52}Cr++$	98232	56963	0.6
$^{53}Cr++$	10442	10488	1.0
$^{56}Fe++$	40016	29987	0.7
$^{57}Fe++$	1028	1008	1.0

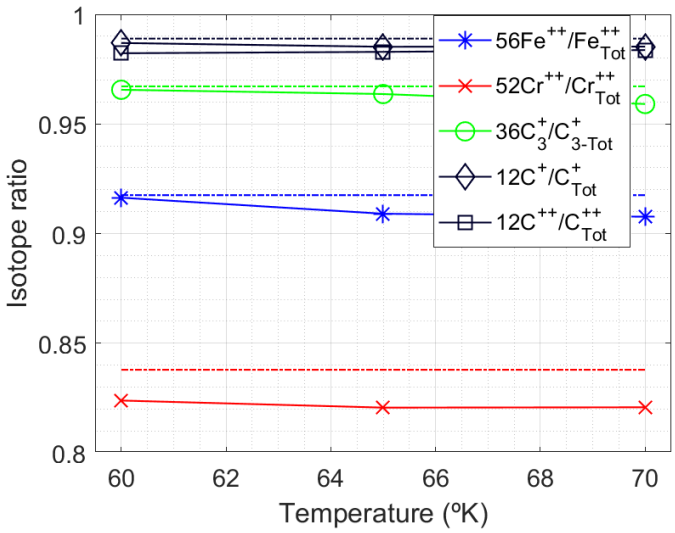

Figure S2: Isotope ratio for the most abundant ions measured inside the carbides. The solid line represent the measured ratio and the dashed line the natural abundance.

Miyamoto et.al 2012 [4] proposed that the detected events for the isotope i, n_{Zi} can be estimated as:

$n_{Zi} = N.p.X_{Zi} - \alpha.N.p.(X_{Zi})^2$ [equation 1]

With N= number of evaporated Z ions, p= detector efficiency, X_{Zi}=natural abundance of the isotope and α= parameter related to the possibility of multiple and close position evaporation. From that they derived the two following equations:

$\sum_i n_{Zi} = N.p.(1 - \alpha.\sum_i(X_{Zi})^2) = A$ [equation 2]

$\sum_i n_{Zi}.X_{Zi} = N.p.(\sum_i(X_{Zi})^2 - \alpha.\sum_i(X_{Zi})^3) = B$ [equation 3]

Since A and B can be determined from natural abundances and the experimental count of each isotope (after background subtraction), the parameter α as well $N.p$ can be calculated.

$N.p$ represents the number of ions, accounting all the isotopes, that would be detected if no detection loss for pile-up occurs. $\alpha.\sum_i(X_{Zi})^2$ corresponds to the detection loss.

Following this procedure, we corrected the total counts of C^{++}(i= 12, 13), C^+ (i=12, 13), C_3^+(i= 36, 37, 39), Cr^{++} (i= 50, 52, 53, 54) and Fe^{++} (i=54, 56, 57, 58) and we recalculated the carbide compositions. The natural abundances were extracted from IVAS™ 3.6.14 (CAMECA Instruments, Madison, Wi, USA).

The uncorrected and corrected C, Fe and Cr compositions as well as the % of detection loss are presented in figure S3. Moreover, the quantification of each individual element, measured at 3 different temperatures, is shown in the table below.

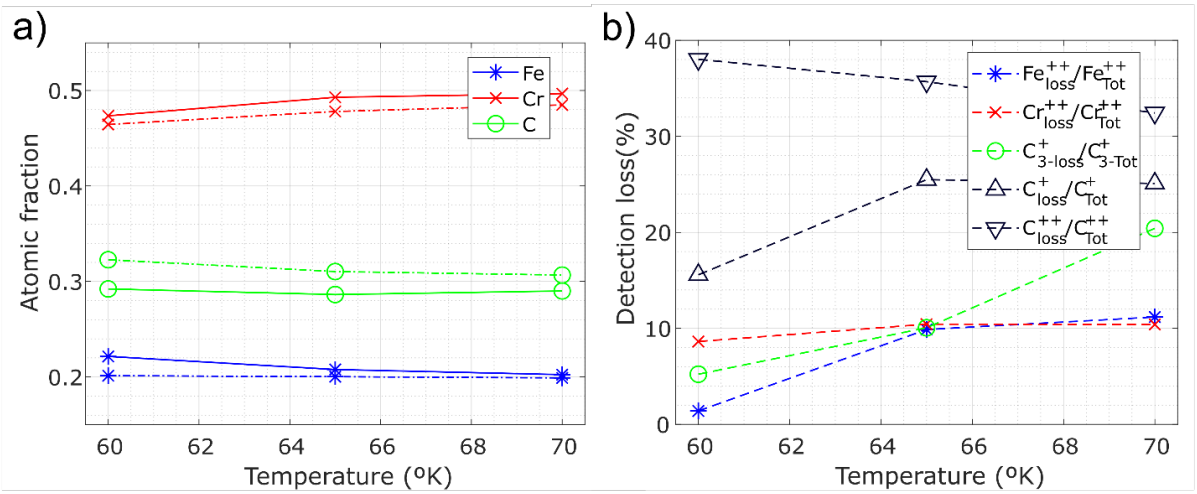

Figure S3: a) Fe, Cr and C content inside the carbides measured at different temperatures. The solid line correspond to the result obtained after peak decomposition while the doted line represent the composition after applying the correction suggested by Miyamoto et.al. 2012 [4]. b) % of ions non detected with respect to the total ions that would be detected if pile-up does not occur for the same ion [4]. As expected, the C ions that have a high occurrence of multiple events are relatively more affected by the pile-up phenomenon. Ion number in the analysis: 60ºK: 776.942, 65ºK: 1.107.086, 70ºK: 388.257.

Table S2: Chemical elements quantification measured at three different temperatures

	Composition (at%)					
T(ºK)	**60**		**65**		**70**	
	Decomposed	Corrected	Decomposed	Corrected	Decomposed	Corrected
C	29.2%	32.3%	28.6%	31.0%	29.0%	30.7%
Cr	47.4%	46.4%	49.3%	47.8%	49.7%	48.5%
Fe	22.2%	20.1%	20.8%	20.0%	20.2%	19.9%
Mn	0.601%	0.54%	0.57%	0.50%	0.37%	0.32%
Mo	0.372%	0.33%	0.39%	0.342%	0.342%	0.30%
Ni	0.004%	0.003%	0.008%	0.007%	0.050%	0.04%
S	0.011%	0.01%	0.001%	0.001%	0.017%	0.01%
Si	0.016%	0.014%	0.007%	0.006%	0.011%	0.01%
V	0.20%	0.18%	0.24%	0.21%	0.22%	0.19%
W	0.067%	0.060%	0.065%	0.056%	0.064%	0.056%

From those values it was determined that the final C content of the carbides is in average 31±1 at.%. From this analysis we can confirm that the carbides precipitating close to the EC corresponds to M_7C_3. We also observed that the most favorable measurement temperature is 70ºK, which gives a composition closer to the stoichiometric (30.7 at. %).

References

1. Vurpillot, F., Bostel, A. & Blavette, D. Trajectory overlaps and local magnification in three-dimensional atom probe. *Appl. Phys. Lett.* **76**, 3127–3129 (2000).

2. Takahashi, J., Kawakami, K. & Kobayashi, Y. Quantitative analysis of carbon content in cementite in steel by atom probe tomography. *Ultramicroscopy* **111**, 1233–1238 (2011).

3. Marceau, R. K. W., Choi, P. & Raabe, D. Understanding the detection of carbon in austenitic high-Mn steel using atom probe tomography. *Ultramicroscopy* **132**, 239–247 (2013).

4. Miyamoto, G., Shinbo, K. & Furuhara, T. Quantitative measurement of carbon content in Fe-C binary alloys by atom probe tomography. *Scr. Mater.* **67**, 999–1002 (2012).

5. Blavette, D., Déconihout, B., Chambreland, S. & Bostel, A. Three-dimensional imaging of chemical order with the tomographic atom- probe. *Ultramicroscopy* **70**, 115–124 (1998).

6. Takahashi, J., Kawakami, K. & Raabe, D. Comparison of the quantitative analysis performance between pulsed voltage atom probe and pulsed laser atom probe. *Ultramicroscopy* **175**, 105–110 (2017).

X. *Interplay between the Microstructure and Tribological Performance of a Destabilized 26 wt.% Cr HCCI: The Influence of Temperature and Heating Rate*

U. Pranav Nayak, Frank Mücklich, María Agustina Guitar

Department of Materials Science and Engineering, Saarland University, 66123 Saarbrücken, Germany

Accepted in ***"Tribology International"*** *(2023) (IF (2023): 5.62)*

Own Contribution: Sample preparation; experimental methodology; microstructural and tribological characterization; data analysis; paper writing – original draft preparation

Interplay between the microstructure and tribological performance of a destabilized 26 wt.% Cr HCCI: The influence of temperature and heating rate

U. Pranav Nayak [1,] *, Frank Mücklich[1,2] and María Agustina Guitar[1]

[1]Department of Materials Science, Saarland University. Campus D3.3, 66123, Saarbrücken, Germany

[2]Materials Engineering Centre Saarland (MECS), Campus D3.3, 66123, Saarbrücken, Germany

Correspondence: pranav.nayak@uni-saarland.de (U.P.N.); Tel.: +49-681-302-70517

Keywords: high chromium cast iron; destabilization heating rate; matrix transformation and secondary carbide precipitation; wear rate

Abstract

This study analysed the microstructural evolution and tribological performance of a 26 wt.% Cr HCCI alloy under varying heating rates (HR) and destabilization temperatures. Results showed that faster heating resulted in the formation of secondary carbides (SC) mainly at the periphery of the matrix, whereas slower heating led to carbides forming inside the matrix as well. The volume fraction and size of SC increased as HR decreased, with HR having a greater influence on their characteristics than temperature increase. All samples displayed abrasive and oxidative wear, with the lowest wear resistance at 800°C and the highest at 980°C. Interestingly, higher matrix hardness did not always correspond to increased wear resistance, highlighting the criticality of matrix support in improving tribological performance.

1. Introduction

Tribology-related problems, including friction and wear, consume a significant portion of global energy (~ 25%). In the mining and mineral sector alone, these issues account for 6% of energy usage [1,2]. Other industries can also experience significant economic losses as a result of this. For instance, increased friction and wear in engines and other components in the transportation industry can lead to reduced fuel efficiency, resulting in higher fuel costs and increased emissions. In addition to these direct costs, tribology-related issues can also lead to indirect costs such as decreased productivity, increased downtime, and degraded product quality [3]. To overcome these concerns, researchers and engineers are working to improve wear resistance by either developing new materials or modifying the microstructure of existing materials, to extend the lifespan of the application.

High chromium cast iron (HCCI) alloys, which are based on the Fe-Cr-C ternary system, are widely used in industrial applications where high abrasion resistance is a prerequisite [4,5]. They are considered to be the most abrasion-resistant of all ferrous alloys owing to the dispersion of hard M_7C_3 (M: Cr, Fe) eutectic carbides (EC) in a supportive and modifiable matrix [6]. By subjecting the alloy to suitable heat treatment (HT) processes such as destabilization or sub-critical treatments, diverse matrix microstructures (i.e., austenite, pearlite, martensite etc.,) can be produced leading to varying tribological performances [7–10]. The matrix structure in HCCI alloys plays an important role in promoting resistance to micro-cracking, deformation, and spalling [10,11]. Combining this with the hard Cr-rich carbides enables them to be used as wear-resistant parts for mining, cement, and power industries, as well as for slurry pumps, pipes, and valves for chemical and petrochemical industries [4,9,12,13].

During destabilization HT, the precipitation of secondary carbides (SC) occurs as well as the partial transformation of the austenitic matrix to martensite upon cooling [4,14]. The type and nature of the SC formed during the HT is highly dependent on the Cr/C ratio and the HT parameters, as they directly impact the amount of carbon that remains

in the solution, subsequently affecting the SC precipitation [15,16]. Performing destabilization at higher temperatures can reduce the driving force for carbide precipitation, which leads to a lower M_s temperature and greater retention of austenite in the martensitic matrix, resulting in a lower overall material hardness [4]. However, destabilization at lower temperatures can lead to a higher amount of carbide precipitation and a lower hardness martensite due to the low carbon content [4,16–18]. Retention of austenite in HCCI alloys can be achieved through various methods, such as destabilization at high temperatures above 1000°C [19,20], very short destabilization times (less than 5 minutes) [21], or destabilization at low temperatures below 900°C [22]. However, these different approaches can lead to varying material responses due to the intrinsic characteristics of each individual phase.

Generally speaking, increasing the carbon content will lead to an increase in the carbide volume fraction (CVF), which in turn will increase the bulk hardness and intuitively, the abrasion resistance [17,23,24]. However, CVF and hardness alone are not always sufficient for an increased wear resistance, as shown for various HCCI compositions [7,21,25]. In fact, it was found that wear resistance is not solely dependent on the CVF or hardness, but also on the overall microstructural characteristics [7,10,11,14,25,26]. This implies that the matrix structure plays a key role in determining the wear resistance of HCCI alloys, beyond the contribution of the hard M_7C_3 carbides.

Pearlitic and ferritic matrix structures are often considered to be undesirable as they tend to lower both wear and fracture resistance. Nevertheless, there is ongoing debate about the best matrix structure for HCCI alloys in terms of wear performance. Some researchers argue that an as-cast austenitic matrix is better [7,27–29], while others argue that heat-treated martensitic matrix is better [22,30–32]. Generally, it has been found that the martensitic microstructure performs better under low-stress abrasion, however, under high stress abrasion and with very hard abrasives, austenitic matrix is reported to perform better. This is because of the strain hardening capability, strain-

induced martensite, and higher ductility of the austenitic matrix [4]. Moreover, the wear behaviour of HCCI alloys is affected by more than just their microstructure. Other factors such as testing conditions, loading, movement of the contact surfaces, type and hardness of the abrasive material play a role, highlighting the complexity and variability involved in tribological testing [33].

It is reported that destabilization HT is typically carried out at temperatures ranging from 900 °C-1150 °C and holding times up to 8 hours [4,10,13,16]. However, in an own previous work, kinetic simulations suggested that SC precipitation had already begun when the temperature reached 800 °C for a relatively fast heating rate (HR) (15-30 °C/min.) [10], but its implications on the tribological behaviour of the alloy are not yet reported. Furthermore, when heating large industrial HCCI parts, thermal equilibrium may not be reached across the entirety of the sample especially if the HR is high. This is because the edges and sides of the sample may heat up faster than the centre, creating a gradient in the microstructure and leading to variations in properties.

In this regard, the primary objective was to investigate the impact of destabilization temperature and HR on the microstructural evolution and tribological performance of a 26 wt.% Cr HCCI alloy. Microstructures of heat-treated samples were evaluated using a combination of scanning electron microscopy (SEM) and electron backscattered diffraction (EBSD). The stereological characteristics of the precipitated SC were analysed in terms of volume fraction, size, and near neighbour distance (nnd) by carrying out image analysis on SEM micrographs. Wear volume loss and wear rate (WR) were determined through dry-sliding linear reciprocating wear tests, and the wear tracks were examined using confocal laser scanning microscopy (CLSM) and SEM to ascertain the underlying wear mechanisms. By gaining insight into the relationship between the microstructure and tribological behaviour for the different HT conditions, the applications' longevity can be prolonged, thereby reducing the energy and economic losses incurred during the run-time.

2. Experimental Methodology

2.1. Material and Heat Treatment

An as-cast HCCI alloy (~ Cr: 26.6 wt. %; C: 2.5 wt. %; Mn: 0.66 wt. %; Mo: 0.24 wt. %; Ni: 0.26 wt. %; Si: 0.37 wt. %; Fe: Bal.) measuring 20 x 20 x 10 mm was subjected to a destabilization HT at 800 °C, 900 °C and 980 °C for 0 minutes, followed by water quenching. Two different HRs were employed to reach the respective destabilization temperatures i.e., 1 °C/min. (800_1, 900_1, 980_1) and 10 °C/min. (800_10, 900_10, 980_10). Furthermore, the small sample thickness ensured a quick thermal equilibration with the furnace and uniformity in heating during the destabilization. The schematic of the HT is presented in Fig. *1*.

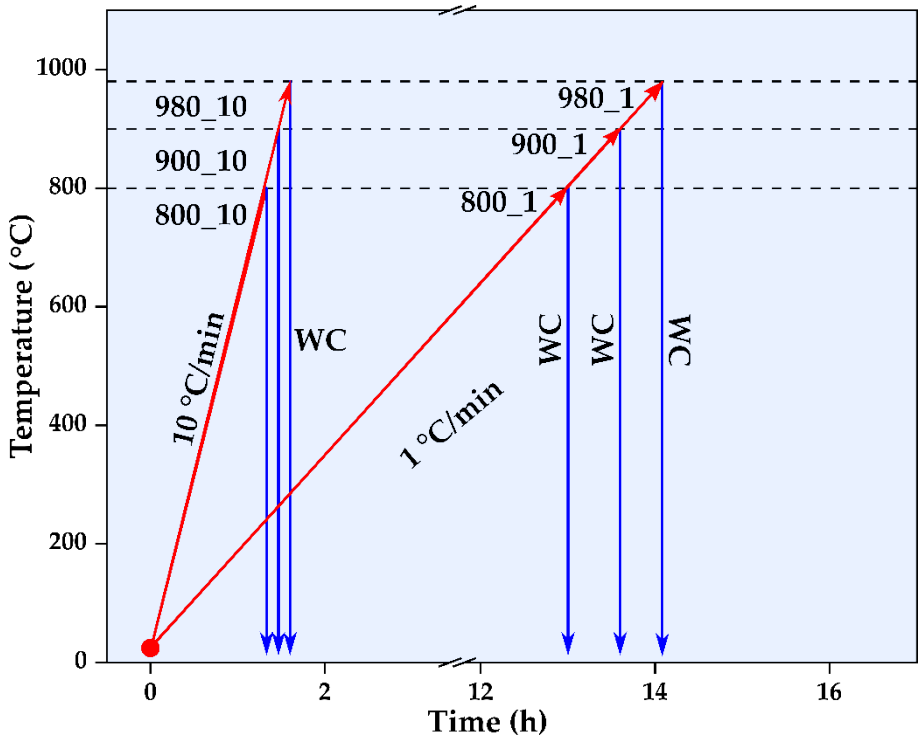

Fig. 1: Schematic of the destabilization heat treatment employed

2.2. Microstructural Characterization and Matrix Microhardness

The HTed samples were hot mounted in a conductive resin and metallographically prepared following the protocol described in [34], which basically involved grinding using SiC paper with a decreasing grit size (up to P1200), polishing using a diamond

suspension (up to 1 μm) and a final polishing round with a 0.04 μm colloidal silica suspension (OPS) to obtain a scratch-free, mirror polished surface. The polished samples were later etched with Vilella's reagent (100mL ethanol + 5mL HCl + 1g picric Acid), and Nital* (98mL ethanol + 2mL nitric acid + 0.5mL HCl) depending on the HTed sample.

Microstructural characterization of the polished surface was carried out with a FEI Helios™ Nanolab 600 field emission scanning electron microscope (FE-SEM) which was operated at an accelerated voltage of 5 – 15 kV and a beam current of 1.4 nA. The as-cast (AC) microstructure features a distribution of Cr-rich M_7C_3 eutectic carbides (EC) (~30%) throughout an austenitic matrix (γ) (~60%), with a thin layer of martensite (α') (~10%) situated between the two. Further microstructural analyses, concerning the phase fraction and elemental composition have been conducted previously [5,34]. The microstructural constituents are colour-arrow coded throughout the paper according to the following terminology:

Austenite (γ): Red arrow pointing downwards.

Ferrite (α) / Martensite (α'): Green arrow pointing upwards.

M_7C_3 Eutectic carbide (EC): Yellow arrow pointing right.

Secondary carbide (SC): Blue arrow pointing left.

The EBSD measurements were performed using the FEI Helios™ Nanolab 600 FE-SEM workstation equipped with an EDAX Hikari EBSD camera. An acceleration voltage of 20 kV, a beam current of 11 nA, 5 × 5 binning on a hexagonal grid and a step size of 100 nm were employed for all measurements. The EBSD data was analysed using the Orientation Imaging Microscopy (OIM™ v. 7) Data Analysis software by EDAX Corporation. The post processing of the obtained EBSD dataset commenced by applying the standard noise reduction algorithms (grain confidence index (CI) standardization and grain dilation), followed by removal of all points with a CI of less than 0.1. Kernel average misorientation (KAM) measurements were carried out to

extract orientation data within the matrix regions. Owing to the very small step size, 2nd neighbour KAM, corresponding to a distance of 200 nm, with a 5° threshold was considered for the analysis. This ensures the information obtained is scatter-free [35].

The back-scattered electron (BSE) micrographs obtained from the SEM were used in determining the stereological characteristics of the SC, using the open-source image analysis software, FIJI (Fiji Is Just ImageJ) [36]. The micrographs were captured at a magnification of 2500x, covering an area of approximately 50 × 50 μm^2. In each case, 6 micrographs were analysed. A threshold segmentation was used to separate the carbides (EC + SC) and the matrix in the BSE micrographs. This was followed by selectively eliminating the larger EC from the image and performing the particle analysis on the SC. To account for the resolution of the image (4088 × 3523 px^2), particles smaller than 30 nm in diameter were excluded from the analysis. Further details concerning the determination of the SC specifics is given in [37].

The matrix hardness was measured using the Vickers method, with a load of 0.9807N (HV0.1) applied via a Struers Dura Scan 50 microhardness tester. The indentation was held for 15s and the readings were taken an average of 15-20 times. The load was chosen to ensure that the matrix hardness measurement would not be affected by the surrounding entities (EC and/or the interfacial α') and the indentation marks were clearly visible under the microscope.

2.3. Tribological tests and Wear Track Characterization

Dry-sliding linear reciprocating wear tests were conducted on the HTed samples using a ball-on-disc micro-tribometer (CSM Instruments), while the whole setup was placed in an environmental chamber. 3 mm alumina (Al_2O_3) balls (99.00 – 99.99 % purity; Grade GD28) were used as the sliding counter-body. For each sample, at least three sets of tests were conducted, using the parameters listed in Table 1.

Table 1: Tribological testing parameters.

Parameters	Value
Temperature (°C)	25
Relative humidity (%)	45
Load (N)	20
Sliding velocity (ms^{-1})	0.02
Stroke length (mm)	5.5
No. of cycles	2000
Data acquisition frequency (Hz)	50

The morphological aspects of the wear tracks as well as the acting wear mechanisms were ascertained using a LEXT OLS 4100 Olympus CLSM and a Thermo-Fisher Helios™ G4 PFIB (Plasma Focused-Ion Beam) CXe DualBeam™ FIB/SEM. The CLSM uses a laser with 405 nm wavelength and, a lateral and vertical resolution of 120 and 10 nm, respectively. Furthermore, energy dispersive X-ray spectroscopy (EDS) was used to chemically map the worn and the unworn surface.

The wear quantification was measured in terms of wear rate (WR), it was calculated by determining the volume loss within each track using the proprietary LEXT software in the CLSM. The entire wear track, including the ends were considered in the calculations, and Equation (1) was used to compute the WR, where V represents the wear volume (mm^3), l is the total sliding distance (5.5 × 2 × 2000 mm), P is the applied load (N), and WR represents the wear rate ($mm^3\ N^{-1}\ mm^{-1}$).

$$WR = \frac{V}{l \times P} \quad (1)$$

3. Results and Discussion

3.1. Microstructural characterization

Fig. 2 represents the SEM micrographs of all the HTed samples. The microstructure of the HTed samples is characterized by finely precipitated SC, the original (as-cast) EC, retained austenite (RA), and a primarily martensitic matrix. Moreover, owing to the thermal stability of the EC [4,5,14] and the destabilization temperature/time used in the present work, it is assumed that all the changes are taking place in the matrix.

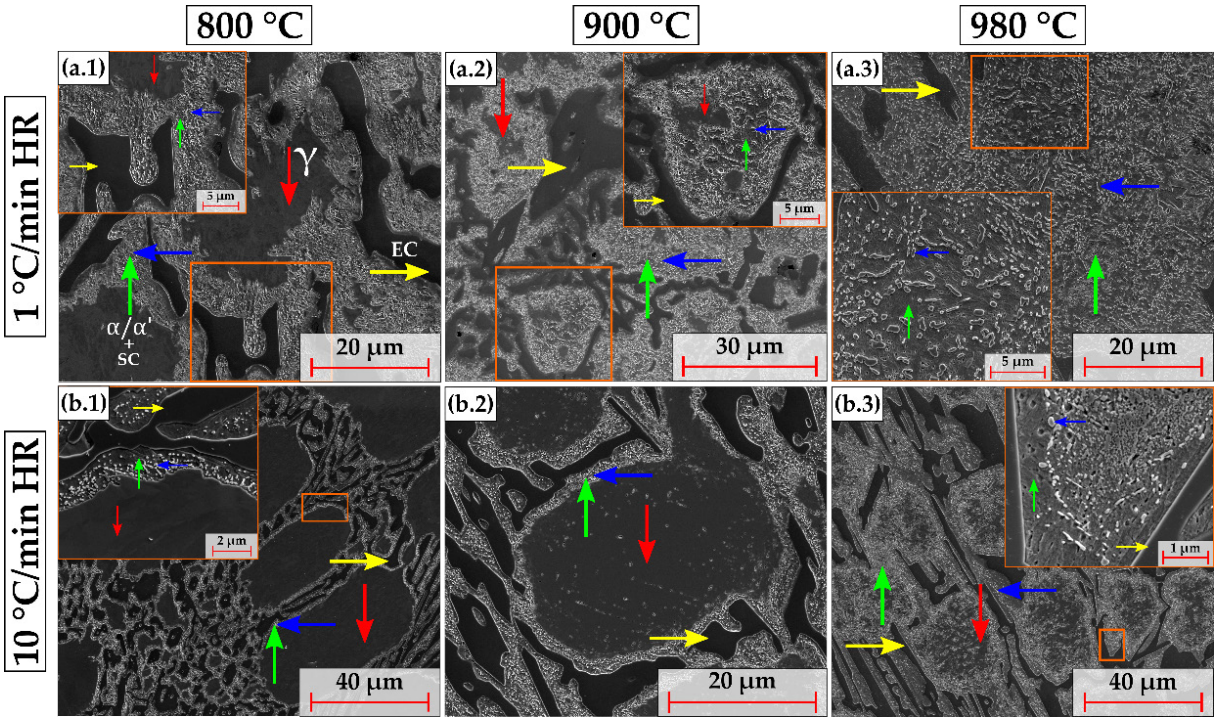

Fig. 2: Representative SEM micrographs of all the HTed samples. The various microstructural constituents are colour-arrow coded for reference.

As mentioned earlier, destabilization is typically carried out at temperatures ranging from 900 °C-1150 °C [10,14–16]. Nonetheless, the presence of SC even at 800 °C (Fig. 2 (a.1) and (b.1)) is indicative that precipitation takes place at temperatures lower than already reported, and is in agreement with our own previous work wherein MatCalc simulations predicted the precipitation to take place at this segment of the HT [18].

Examining the SEM micrographs provides a visual representation of the distribution of SC throughout the material. The samples heated at a faster rate showed the precipitation primarily at the matrix's periphery, whereas for the slower heated samples, it was also observed to have spread inward into the matrix. This sequence has also been reported in other studies [14,16,21,38]. The destabilization process leads to a redistribution of alloy elements, as the increased driving force causes precipitation of SC and a partial transformation of the matrix during cooling [10,13].

The tendency for precipitation to occur initially at the periphery is attributable to its thermodynamic favourability. As the precipitation takes place by nucleation and growth phenomena, they prefer precipitating on heterogeneous surfaces such as sub-grain boundaries, defect clusters, etc., [39,40]. The transformation of the interfacial martensite during heating results in the austenite possessing a large number of defects owing to the differences in the thermal expansion coefficients of the EC and austenite. This generates stresses, leading to a reduction in activation energy required to achieve the critical size for nucleation [19,38]. This results in a large number of small-sized carbides to precipitate at those regions as observed in Fig. 2 (b.1) and (b.2). The ongoing alloy redistribution during heating leads to the growth and coalescence of SC in other regions of the matrix.

Table 2: Quantification of the stereological characteristics of the SC in the HTed samples

Sample	Particle Count	SC CVF (%)	SC size (μm^2)	SC mean nnd (μm)	SC median nnd (μm)
Q800_1	23062	9.3 ± 2.6	0.056 ± 0.019	0.37 ± 0.18	0.34
Q900_1	22027	9.4 ± 1.2	0.058 ± 0.009	0.41 ± 0.17	0.38
Q980_1	21238	10.6 ± 0.9	0.068 ± 0.009	0.44 ± 0.19	0.41
Q800_10	33524	2.5 ± 0.7	0.010 ± 0.001	0.22 ± 0.14	0.19
Q900_10	45725	3.5 ± 0.6	0.011 ± 0.002	0.24 ± 0.13	0.21
Q980_10	30111	4.0 ± 0.7	0.018 ± 0.003	0.29 ± 0.17	0.25

Table 2 represents the SC CVF, size and nnd, quantified through image analysis. A clear distinction can be made between the samples that were heated using the different heating rates. The samples heated at a slower rate displayed a CVF and size increase of about 4 times and 5 times respectively, when compared to the samples heated at a faster rate. Amongst the samples that were heated at the same rate, the average SC CVF and size slightly increases with increasing temperature, although it is within the tolerance interval ((Mean + S.D.) – (Mean – S.D.)). Between the samples heated at 1 °C/min., a maximum variation of 15% in the CVF and 20% in the size is noticed. In comparison, the samples heated at a faster rate showed a 60% increase in the CVF and 80% increase in SC size between the 800_10 and 980_10 samples. For both HR, the sample treated at 980 °C had the highest average SC CVF and size.

The mean nnd for the faster heated samples is almost half that of the slower heated samples. However, it is important to note that these values are all within the tolerance interval, which means that comparing them does not provide much insight. To better understand the trend, it is recommended to look at the median nnd values, as over 20,000 particles were analysed in each case and the mean values are within the tolerance interval. Moreover, the median value is less liable to be distorted by outliers compared to the mean value [41]. Despite this, the trend is consistent across both mean and median nnd values, with an increase as temperature rises, and slower heated samples having almost double the nnd compared to faster heated samples.

It is clear from Table 2 that the SC stereological characteristics is more influenced by the HR than the temperature rise. In the slow heated samples, upon reaching the threshold temperature, a larger amount of time is provided for alloy redistribution to take place resulting in subsequent nucleation and growth of the SC precipitates. On the contrary, in the faster heated samples, the time dwelt above the threshold temperature is one-tenth compared to the slower heated samples, resulting in a lower value of CVF and a smaller size. Nevertheless, from the SEM micrographs, it was seen that massive precipitation had taken place within the body of the matrix when the

temperature was raised from 900 to 980°C even when the HR was 10 °C/min (Fig. 2 (b.3)). This corroborates with other works which had mentioned that the precipitation rate of SC is the highest between 950 °C and 1000 °C [15,38]. Furthermore, visualizing the distribution curves of SC size and nnd within the HTed samples can provide more insight [4,8,21].

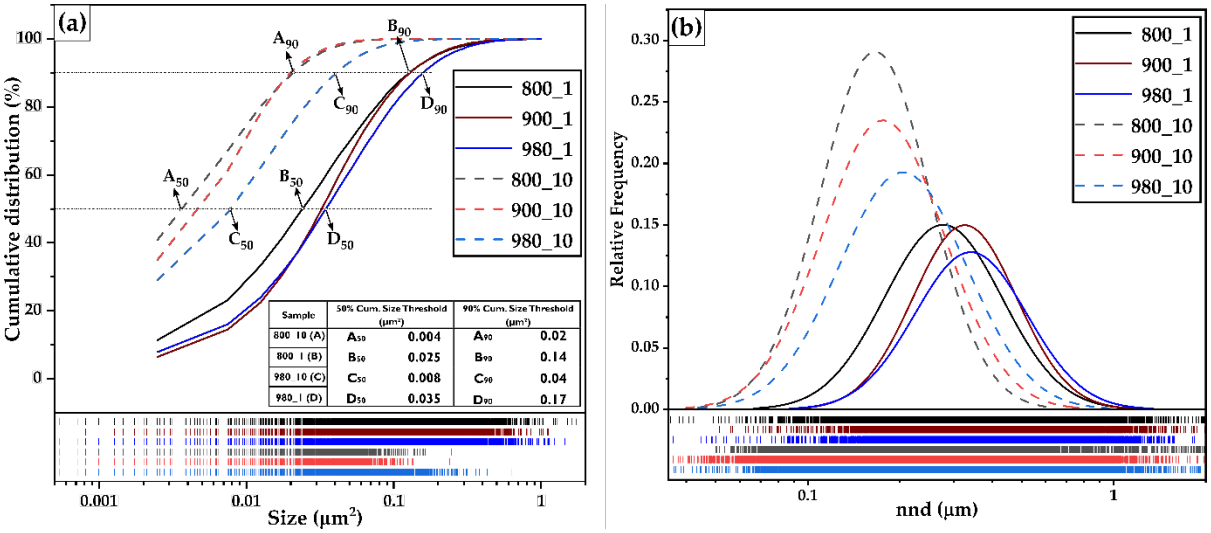

Fig. 3: (a) cumulative size distribution curve with the rug-plot plotted on a logarithmic scale. The inset table indicates the maximum size obtained for the applied size threshold; (b) nnd distribution with the rug-plot plotted on a logarithmic scale for all the samples. The peak of the nnd distribution curve represents the corresponding modes.

Fig. 3 (a) shows the cumulative size distribution curve plotted on a logarithmic scale, along with the respective rug-plots, which represents a histogram with zero-width bins and help visualize the distribution of data. The 50% and 90% size threshold are indicated by the dashed horizontal line and the inset table represents the maximum size obtained for the applied size threshold. When comparing the samples destabilized at 800 °C and 980 °C for both heating rates, it is apparent that there is a difference in size. For a given size threshold, the slower heated samples had a higher maximum size reached irrespective of the temperature, although the increase in the maximum size difference between the 1 °C/min. HR samples is far lower than the 10 °C/min. samples. The influence of increasing temperature on the size of the SC is greater on the faster heated samples compared to the samples heated at 1 °C/min. Observing the rug-plots

in the faster heated samples, the 800_10 and 900_10 samples show similarities whereas the presence of larger particles is observed in the 980_10 sample, further bolstering the notion that massive precipitation takes place once the temperature reaches above 950 °C. It is also interesting to note that the maximum size reached for a 50% threshold in the slower heated samples is similar to the 90% threshold in the faster heated samples (B_{50} vs. A_{90} and D_{50} vs. C_{90}), further emphasising the influence of the HR on the SC size.

The log normal nnd distribution (in terms of relative frequency vs. nnd (μm)) for the HTed samples is graphically represented in Fig. 3 (b). With increasing temperature, the peak of the curve (essentially indicating the mode) shifts towards higher values corroborating with the mean and the median nnd. The rug-plots reveal that the number of particles with a low nnd value is higher for the faster heated samples (10 °C/min. HR). From Table 2 and Fig. 3, it can be inferred that particle growth and coalescence had taken place in the slower heated samples based on the increasing value of CVF, size, nnd, and a decrease in the particle count.

3.2. Tribological response

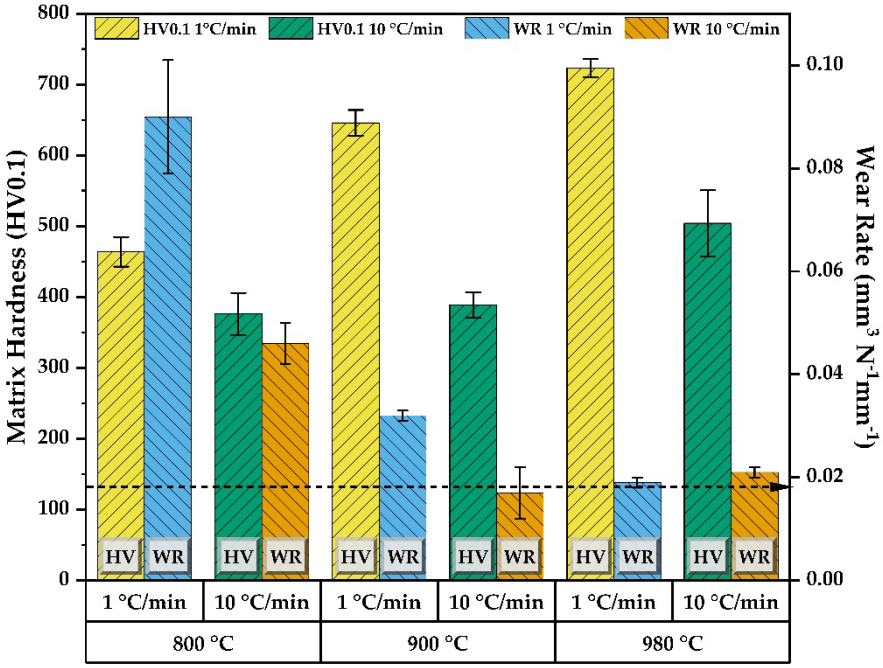

Fig. 4: Matrix hardness and wear rate of the different HTed samples. The horizontal dashed line represents the WR of the as-cast sample (0.018 $mm^3N^{-1}mm^{-1}$), taken from [42].

Fig. *4* represents the variation of the matrix hardness and the WR amongst all the HTed samples. The horizontal dashed line represents the WR of the as-cast sample (0.018 $mm^3N^{-1}mm^{-1}$), taken from [42]. As far as the matrix hardness is concerned, all the slower heated samples show a higher hardness compared to the faster heated counterparts, and the hardness rises with increasing temperature. This is attributable to the increased SC CVF and larger size in the slower heated samples. Moreover, the higher martensitic fraction in the samples destabilized at 980 °C further increases the hardness, with the 980_1 sample showing the highest matrix hardness. Although there is a clear trend between the samples with respect to the hardness, the same cannot be said for the WR. Typically, one would expect a lower WR (i.e., higher wear resistance) for harder samples. In contrast to the hardness, all the faster heated samples show a lower WR compared to the slower heated samples. Moreover, the samples treated at 980 °C show similar WR despite the matrix hardness of the 980_1 sample being ~ 45% higher than the 980_10. This clearly indicates that possessing a higher amount of CVF and a harder matrix doesn't necessarily guarantee a better wear resistance. In either case, the samples destabilized at 800 °C showed the highest WR whereas the samples destabilized at 980 °C showed the lowest WR. This is further exemplified upon examining the wear depth profile in Fig. *5* where the 800_1 sample showed a maximum depth of 20 μm which was 4 times as much as the 980_1 sample.

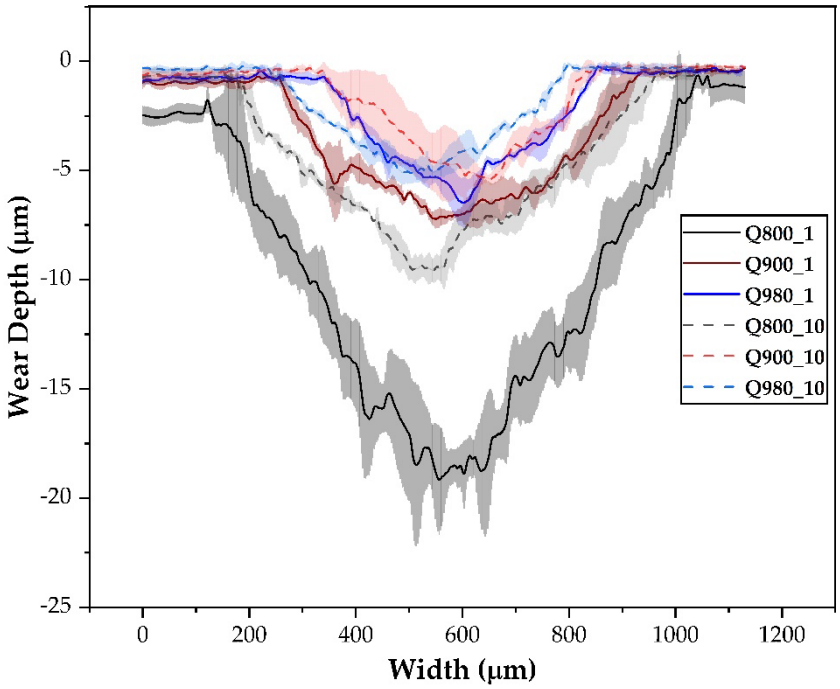

Fig. 5: Wear depth profile across the entire wear track for all the HTed samples.

Nevertheless, one may argue as to why the samples HTed at 800 °C show the highest WR (i.e., least wear resistance) despite having a relatively high amount of retained austenite in the matrix. In fact, despite the similarities in the matrix hardness and the SC stereological characteristics between the 800_10 and 900_10 samples, the WR is ~ 65% lower in the latter case. This places emphasis on the ability of the matrix to provide the support to the carbides during the wear test. It is important to note that the temperature of 800 °C can be considered as a limit in between the "destabilization" and "sub-critical" temperature. In the work carried out by [43], a partial transformation from austenite to ferrite/pearlite-like structures was observed at around 750 °C. The partial decomposition of austenite into ferrite at temperatures between 550 °C to 700 °C was also mentioned by [7]. Based on this, the presence of ferrite in the 800_1 and 800_10 samples cannot be completely dismissed. As it was not possible to specifically distinguish ferrite and martensite using metallography in the present work, EBSD was employed. Since ferrite and martensite have similar crystal structures, a distinction between the two is possible by observing the KAM map. A

lower KAM value indicates ferrite [35,44] and, in this work, a value of 0.25° was chosen as a threshold.

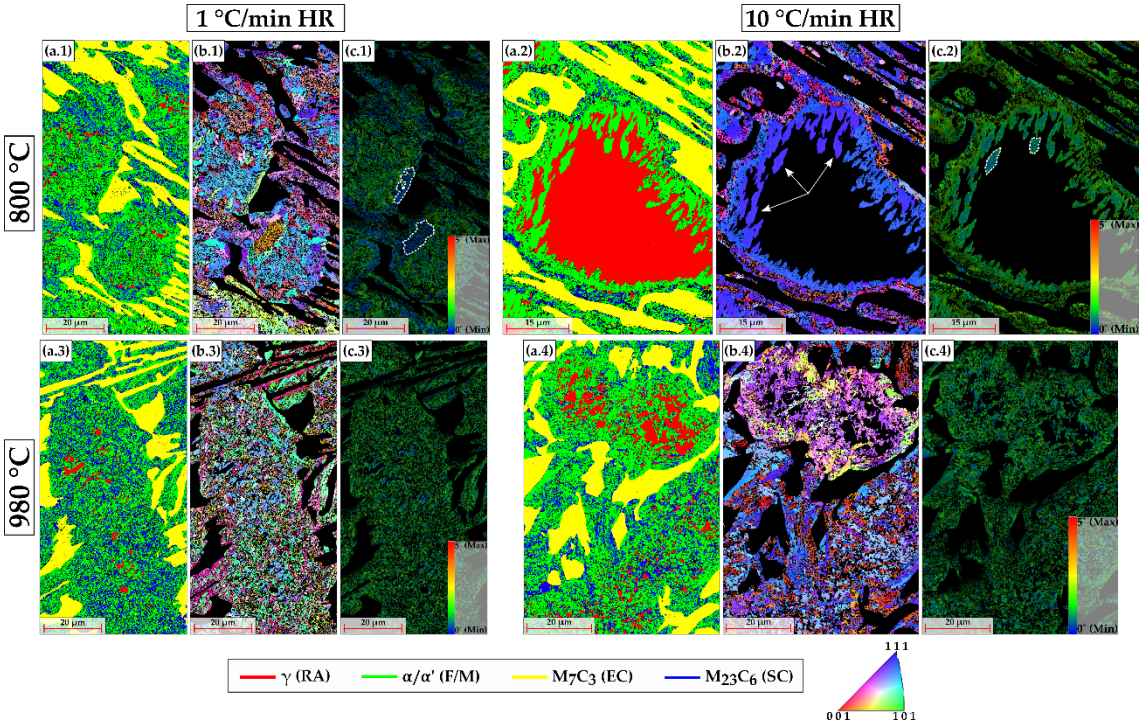

Fig. 6: (a) EBSD phase map, (b) IPF map of the α/α' matrix region and (c) KAM map of the α/α' matrix region for the various HTed samples/ for the 800_1 (x.1), 800_10 (x.2), 980_1 (x.3) and 980_10 (x.4) samples, respectively. The dashed-white enclosures in (c.1) and (c.2), and the white arrow in (b.2) represent the ferritic regions based on the low KAM value (<0.25), and a different crystallographic orientation compared to the neighbouring regions.

Fig. 6 represents the EBSD phase map (a), inverse pole figure map of the α/α' matrix region (b), and the kernel average misorientation (KAM) map of the α/α' matrix region (c), for the 800_1 (x.1), 800_10 (x.2), 980_1 (x.3) and 980_10 (x.4) samples, respectively. The EBSD phase map further corroborates the observations made in the SEM wherein the 800_10 samples have a larger amount of retained austenite within the matrix compared to the samples treated at 980 °C. It is noticed that the 800 °C samples have a higher number of regions with a different crystallographic orientation than its neighbouring regions. Additionally, by comparing the IPF maps with the corresponding KAM maps, it can be concluded that these specific grains have a lower KAM value and therefore, are associated with ferrite. The islands of ferrite present

throughout the matrix are deleterious to the wear resistance as they are unable to provide the necessary support to the surrounding carbides [27,30]. This is further exemplified by observing the KAM distribution in the aforementioned samples as shown in Fig. 7.

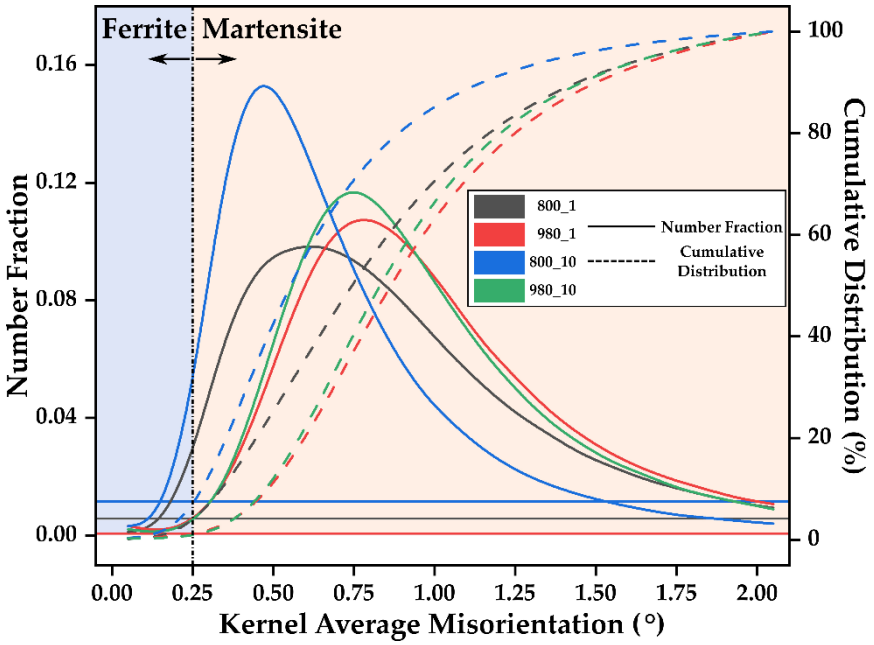

Fig. 7: Distribution of the KAM values of the samples destabilized at 800 °C and 980 °C. The solid line represents the distribution curve based on the number fraction, and the dashed line represents the cumulative distribution. A KAM value of 0.25° was used in this work to separate the ferrite from the martensite, which is indicated as the dotted vertical line.

From analysing the point at which the dotted vertical line (0.25 ° KAM threshold) intersects with the cumulative distribution curves, it is apparent that the 800°C-treated samples contain a greater proportion of ferrite regions than the samples treated at 980°C. In this study, a threshold value of 0.25° was used, but other studies have used threshold values ranging from 0.2° to 0.6° [35,45,46]. Using a higher threshold value will result in a higher quantification of ferrite regions in the samples, but the overall trend will remain the same. It is worth mentioning that the EBSD measurements are not necessarily representative and have to be treated with caution. Nevertheless,

combining this information with the microstructural evolution of the HTed samples, the qualitative trend can be appreciated.

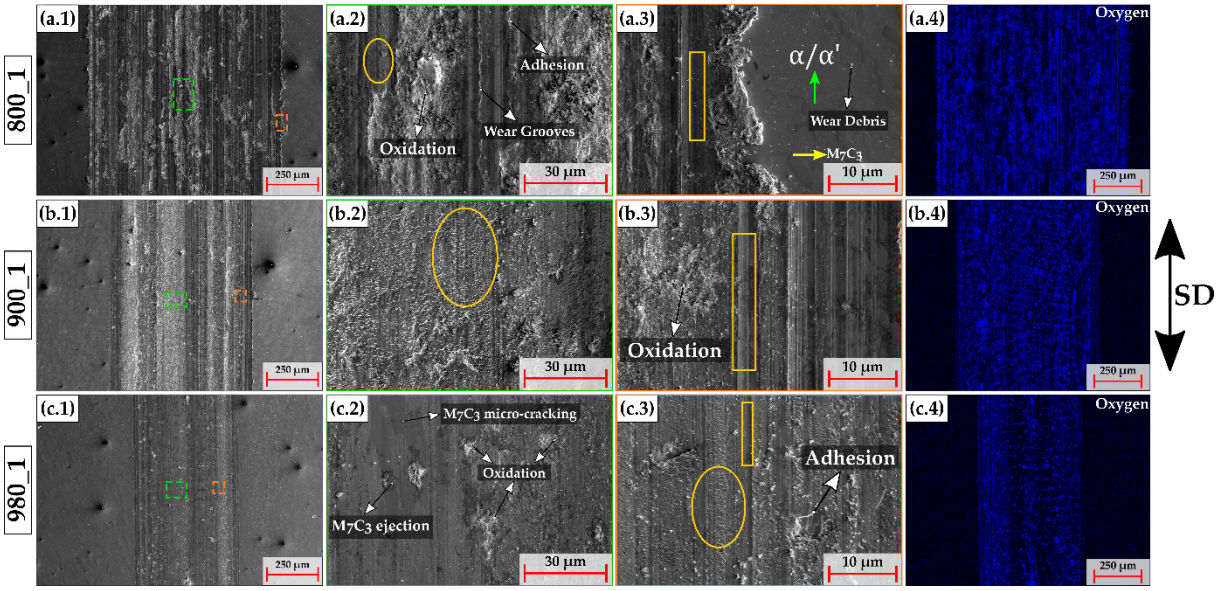

Fig. 8: Representative SEM micrographs of the wear tracks for the samples destabilized with a 1 °C/min. HR. (a.1), (b.1) and (c.1) indicate the micrograph of the entire width of the wear track for the 800_1, 900_1 and 980_1 sample, respectively. (a, b, c.2) and (a, b, c.3) represent a magnified view of the dashed-green and the dashed-orange enclosures in (a, b, c.1), respectively with the various aspects of the wear tracks delineated. The solid-yellow ellipse and solid-yellow enclosure represent the micro-ploughing and the micro-cutting phenomena, respectively. (a, b, c.4) Oxygen EDS concentration maps corresponding to the micrographs presented in (a, b, c.1), respectively. The sliding direction (SD) is also mentioned for reference.

The representative SEM micrographs of the wear tracks for the samples heated at a HR of 1 °C/min. and 10 °C/min., are shown in Fig. *8* and Fig. *9*, respectively. During the initial stages of the wear test, as the alumina ball traverses over the sample surface, adhesion takes place due to the high contact pressure established by the ball's asperities [47,48]. This leads to material transfer, especially at the carbide-matrix interface, as indicated in Fig. *8* (a.2), although this phenomenon was observed in all tracks. Upon closer examination of the wear track, micro-cutting and micro-ploughing, characteristic micro-mechanisms of abrasive wear were also observed. The solid-

yellow rectangular enclosure indicates micro-cutting, and micro-ploughing is delineated using a solid-yellow ellipse in the micrographs.

In addition to traits of abrasive wear, carbide micro-cracking was also observed throughout the wear track. This is attributable to the increased hardness of the alumina ball (~ HV 1500) compared to the EC (~ HV 1200) or the matrix material. Owing to the tangential stresses acting during the sliding process, the cracking had taken place primarily perpendicular to the sliding direction, which, is a commonly observed phenomena in these alloys [21,49]. The micro-cracking of the carbides results in its detachment from the matrix leading to the formation of voids in the track. This is a crucial factor to consider, as the rate of carbide removal essentially indicates the rate at which the loose wear particles accumulate, altering the subsequent wear behaviour [50]. Moreover, the cracked carbide could act as a third body which can affect other carbides as well, leading to the formation of grooves in the leading edge of the carbide during abrasion [25,51], as highlighted in Fig. *8* (a.2).

Due to the abrasive micro-mechanisms that are acting during wear, voids and grooves are also generated leading to surface deterioration. Furthermore, considering the environmental conditions under which the tribological testing was carried out, and the oxide-based counter-body used in the current study, there is a high tendency for oxidation to occur [52]. The O EDS concentration map in Fig. *8* and Fig. *9* indicate the preferential accumulation of oxides where the carbides have been cracked and/or ejected. However, it is worth to note that not all carbides had undergone cracking, as exemplified in Fig. *9* (b.2). This is attributed to the variation in the carbide's geometric orientation with respect to the sliding counter-body [49,53] and the increased load-bearing capacity of the martensitic matrix surrounding it [54]. From Fig. *9* (a.1), it is observed that carbide ejection predominately took place on one side of the wear track. Moreover, comparing it with Fig. *9* (b.3), the oxide accumulation at those specific ejected regions is observed.

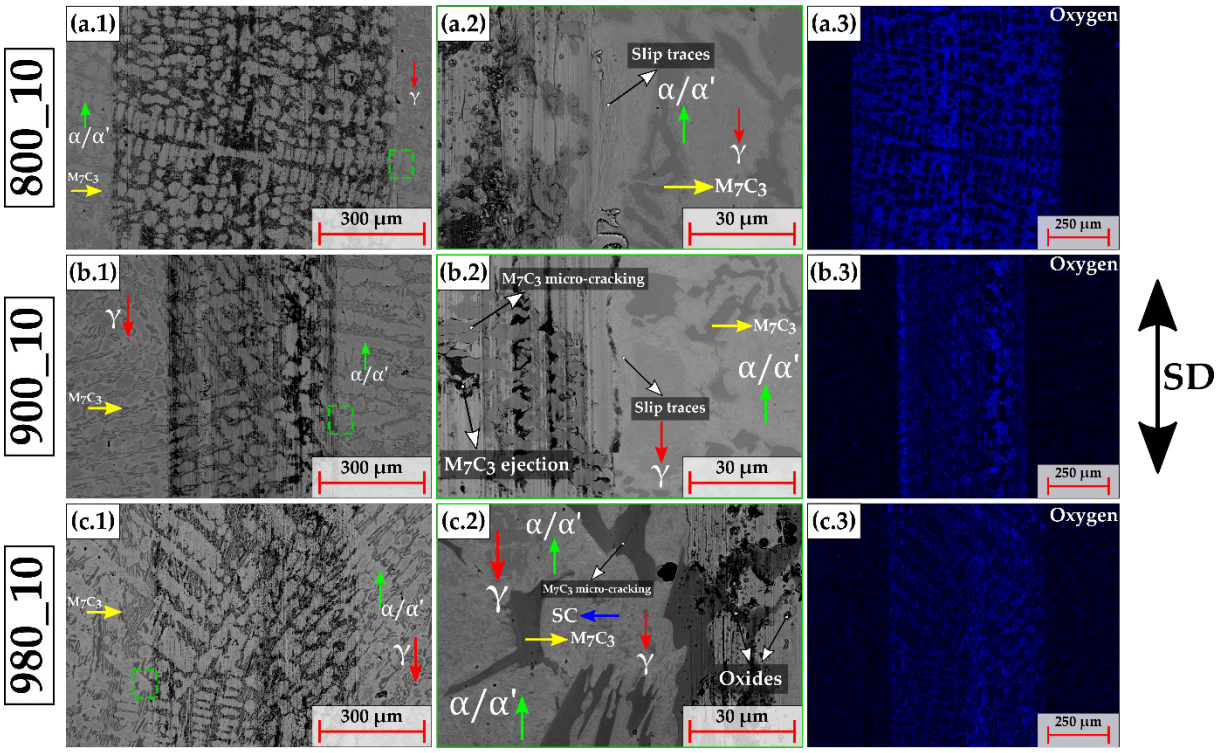

Fig. 9: Representative SEM micrographs of the wear tracks for the samples destabilized with a 10 °C/min. HR. (a.1), (b.1) and (c.1) indicate the micrograph of the entire width of the wear track for the 800_10, 900_10 and 980_10 sample, respectively. (a, b, c.2) represents a magnified view of the dashed-green enclosure at the edge of the wear track in (a, b, c.1), respectively. The microstructural constituents and various aspects of the wear track and are indicated. (a, b, c.3) Oxygen EDS concentration maps corresponding to the micrographs presented in (a, b, c.1), respectively. The sliding direction (SD) is also mentioned for reference.

In addition to the stereological characteristics of the carbides, the nature of the matrix encompassing these carbides have a prominent influence on the wear resistance of the alloy. This aspect is highlighted by comparing the wear tracks between the various HTed samples. The track width of the samples treated at 800 °C is considerably wider compared to the other two temperatures, irrespective of the HR. Moreover, comparing the samples treated at 800 °C, the WR of the 800_10 sample is 50% lower than the 800_1 sample, despite having a similar wear width. This is owing to the relatively high amount of RA in the former, which can plastically deform during the wear test and provide better support to the carbides. The plastic deformation which is manifested as slip traces is observed in Fig. 9 (a.2), and this is consistent with previous work under

the same applied load [21,42]. Additionally, the smaller size of the SC combined with the lower CVF in the 800_10 sample makes its ejection less probabilistic. In the slower heated samples, the increased CVF and size of the SC leads to a larger void upon detachment from the matrix. This allows more oxides and wear particles to accumulate, deteriorating the wear resistance.

Comparing the 800_1 and 980_1 sample, despite having similar SC stereological characteristics, the WR of the latter is 80% lower than the former. This is clearly due to the presence of ferrite regions in the 800_1 sample, which show poor resistance to wear [27,30]. As the matrix is worn out by the abrasive process, the support it offers to the carbides reduces, resulting in an increased wear volume loss [55]. Notwithstanding the matrix being a mixture of austenite and ferrite/martensite, the inability of the ferrite to plastically deform like the austenite or provide load bearing capacity like the martensite, allows the alumina ball to penetrate deeper into the matrix removing more material in the process. This is also reflected in the wear depth in Fig. *5*. Additionally, comparing Fig. *8* (a.1) with Fig. *8* (c.1), it is observed that larger chunks of material is removed in the former, which is eventually oxidized.

As mentioned earlier, the samples treated at 980 °C showed the best wear resistance (i.e., lowest WR). This is attributable to a synergistic contribution of different factors. Firstly, the matrix microstructure of the 980 °C samples is primarily composed of martensite, and some retained austenite, with the ferrite phase being absent. Moreover, the increased carbon solubility at this temperature further enriches the austenite phase with carbon during heating, leading to a harder martensite phase upon cooling [18,21]. This harder martensite phase combined with the dispersed SC improves the load bearing capacity thereby relieving the burden on the larger EC. This ensures that the EC ejection is reduced and the WR is minimized [54]. In the 980_10 sample, several smaller-sized carbides distributed throughout the matrix with a lower nnd ensured that the matrix is protected during the wear test. As far as the wear mechanisms are concerned, it could be inferred that in addition to micro-cutting and

micro-ploughing, oxidation plays a big role in the tribological behaviour owing to the detachment of the carbides from the matrix, as evidenced from the EDS concentration maps and as observed further, the frictional behaviour.

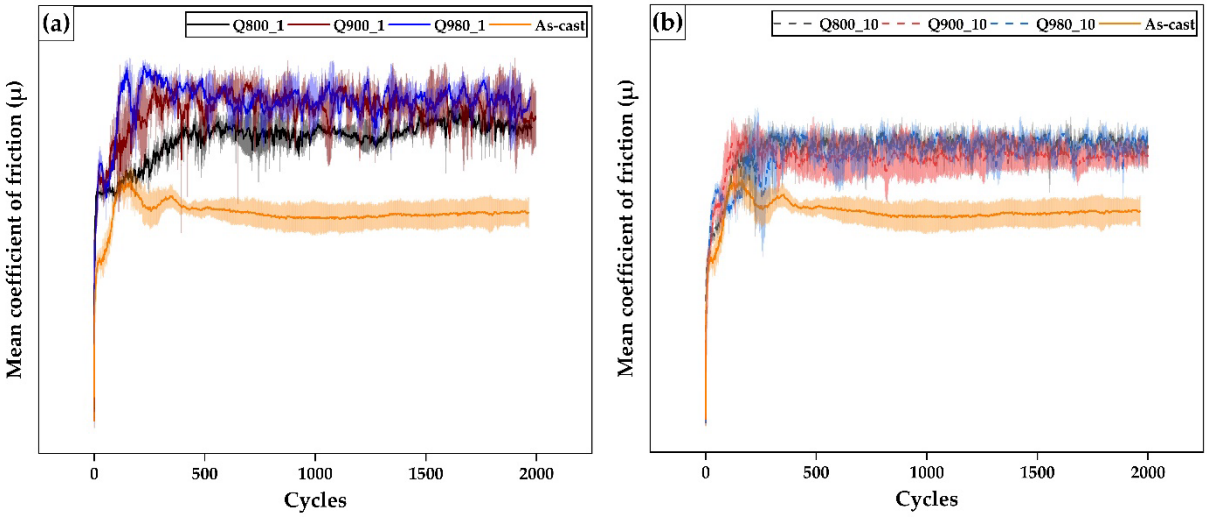

Fig. 10: Mean coefficient of friction (COF) evolution of the HTed samples destabilized at (a) 1 °C/min. HR and (b) 10 °C/min. HR.

The frictional behaviour of the samples destabilized at 1 °C/min. and 10 °C/min. HR (expressed in terms of mean coefficient of friction (COF)) is represented graphically in Fig. *10* (a) and Fig. *10* (b), respectively. In addition to the HTed samples, the COF behaviour of the as-cast sample (taken from [42]) is also indicated. All the HTed samples showed a higher COF compared to the as-cast sample. Additionally, comparing the two sets of samples destabilized at different heating rates, the faster heated samples show similar COF behaviour and have more overlap compared to the slower heated samples. The COF development in the as-cast sample is a characteristic of nonlubricated dry metallic sliding systems and resembles a type-b curve as shown by Blau [56]. The curve reaches a peak (running-in) before decreasing and eventually reaching a steady state (SS). Unlike the as-cast COF curve, all the HTed curves show a 'double running-in' behaviour, similar to the type-d curve as mentioned by Blau [56]. The interruption of the COF development in HTed samples might be associated with

the heterogeneity of the contact interface consisting of larger-sized carbides and the matrix around it [57]. When the two surfaces meet and continuously shear against each other, the initial roughness between the two produces a momentary rise in friction until conformality is reached and smoothening takes place, reducing the friction. This is clearly seen in the behaviour of the as-cast sample, where after about 300 cycles, the system reaches a steady state throughout the duration of test.

In the as-cast sample, the austenitic matrix can undergo plastic deformation during the wear test, thus providing additional mechanical support to the surrounding carbides (only EC) [42]. However, in the HTed samples, the predominately martensitic matrix is unable to plastically deform and therefore, incapable of providing the necessary support leading to carbide micro-fracture and eventual ejection. The ejection of the carbides results in the formation of voids allowing the oxides to accumulate in those regions, as evidenced by the EDS micrographs. This is seen in the COF behaviour of the HTed samples at > 300 cycles where continuous fluctuations indicate the formation and breakage of the oxide layer, owing to the shear stresses exerted during the wear test [55]. Furthermore, this behaviour is prominent in the slower heated samples, where the ejection of the larger-sized carbides creates a much bigger void compared to the faster heated samples. This is reflected in the amplitude of the undulations after the second running-in stage (> 300 cycles), where stronger COF fluctuations are observed. Moreover, the undulations continue throughout the entirety of the test indicating a continuous removal and formation of oxides. Eventually, this breakage results in the formation of wear debris as observed in the SEM micrographs.

4. Conclusions

In the current study, the influence of HR and the destabilization temperature on the microstructural evolution and the subsequent tribological performance of a 26 wt.% Cr HCCI was evaluated. SEM micrographs indicated that precipitation had primarily taken place at the periphery of the matrix and proceeded inward towards the centre.

The central part of the matrix was primarily austenitic in the 800_10 and 900_10 samples, whereas an 80 °C increase led to massive carbide precipitation throughout the matrix. The SC CVF and size in the slower heated samples were about 4 times and 5 times, respectively, compared to the faster heated samples, even though they showed similar values amongst each other. This indicated that the HR had a greater influence on the SC characteristics than the temperature.

The higher matrix hardness in the slower heated samples was linked to the increased SC CVF and size, although this did not result in an increased wear resistance. In fact, in all cases, the faster heated samples showed a lower WR (i.e., higher wear resistance) compared to its slower heated counterparts, despite the hardness being ~ 50% lower. In both cases, the samples treated at 800 °C and 980 °C showed the highest and lowest WR, respectively. EBSD measurements revealed the presence of ferrite islands throughout the matrix in the 800 °C samples whose presence is detrimental to the wear resistance. On the other hand, the optimal distribution of the microstructural constituents in the 980 °C ensured that it showed the best wear resistance. The 980 °C treated samples showed a similar WR despite the hardness of the 980_1 being ~ 45% higher, emphasising the importance of the matrix support in improving the tribological performance.

Optimal microstructural distribution can be achieved by carefully selecting destabilization parameters. However, it's important to keep in mind that the costs of destabilization should be outweighed by the benefits. While slower heating can result in higher hardness and larger SC volume and size, these benefits should be evaluated against the intended use of the material. As far as tribological applications are concerned, it is recommended to destabilize at a higher temperature with a faster heating rate, which, also corroborates with own previous work.

Acknowledgement

The present work is supported by funding from the Deutsche Forschungsgemeinschaft (DFG, project: GU 2102/2-1). Moreover, the funding for the PFIB/SEM instrument by DFG is greatly acknowledged (INST 256/510-1 FUGG). The authors would also like to thank Martin Duarte from Tubacero S.A. for providing the materials and finally, U.P.N. is grateful to DAAD for the financial support.

Author contributions

U.P.N: Conceptualization and Methodology; Sample preparation and characterization; Data curation; Formal Analysis; Investigation; Writing – Original draft.

F.M: Scientific discussion; Resources.

M.A.G: Conceptualization and Methodology; Writing – review and editing; Supervision; Project administration.

Conflict of Interest

The authors declare that they have no conflict of interest.

Data and code availability

The data used in this study are available from the corresponding author at reasonable request.

Supplementary information

Not Applicable

Ethical approval

Not Applicable

References

[1] Holmberg K, Erdemir A. Influence of tribology on global energy consumption, costs and emissions. Friction 2017;5:263–84. https://doi.org/10.1007/s40544-017-0183-5.

[2] Holmberg K, Kivikytö-Reponen P, Härkisaari P, Valtonen K, Erdemir A. Global energy consumption due to friction and wear in the mining industry. Tribol Int 2017;115:116–39. https://doi.org/10.1016/j.triboint.2017.05.010.

[3] Hutchings IM. Abrasion in wear and manufacturing processes. Proceedings of the Institution of Mechanical Engineers, Part J: Journal of Engineering Tribology 2002;216:55–62. https://doi.org/10.1243/1350650021543898.

[4] Tabrett CP, Sare IR, Ghomashchi MR. Microstructure-property relationships in high chromium white iron alloys. International Materials Reviews 1996;41:59–82. https://doi.org/10.1179/095066096790326075.

[5] Nayak UP, Guitar MA, Mücklich F. A comparative study on the influence of chromium on the phase fraction and elemental distribution in as-cast high chromium cast irons: Simulation vs. experimentation. Metals (Basel) 2020;10. https://doi.org/10.3390/met10010030.

[6] Sare IR, Arnold BK. The Effect of Heat Treatment on the Gouging Abrasion Resistance of Alloy White Cast Irons 1995;26:1785–93.

[7] zum Gahr KH, Eldis GT. Abrasive wear of white cast irons. Wear 1980;64:175–94. https://doi.org/10.1016/0043-1648(80)90101-5.

[8] Karantzalis E, Lekatou A, Mavros H. Microstructure and properties of high chromium cast irons: effect of heat treatments and alloying additions. International Journal of Cast Metals Research 2009;22:448–56. https://doi.org/10.1179/174313309X436637.

[9] Llewellyn RJ, Yick SK, Dolman KF. Scouring erosion resistance of metallic materials used in slurry pump service. Wear 2004;256:592–9. https://doi.org/10.1016/j.wear.2003.10.002.

[10] Guitar MA, Suárez S, Prat O, Duarte Guigou M, Gari V, Pereira G, et al. High Chromium Cast Irons: Destabilized-Subcritical Secondary Carbide Precipitation and Its Effect on Hardness and Wear Properties. J Mater Eng Perform 2018. https://doi.org/10.1007/s11665-018-3347-1.

[11] Tabrett CP, Sare IR. The effect of heat treatment on the abrasion resistance of alloy white irons. Wear 1997;203–204:206–19. https://doi.org/10.1016/S0043-1648(96)07390-5.

[12] Maratray F. Choice of appropriate compositions for chromium-molybdenum white irons. AFS Trans 1971;79:121–4.

[13] Karantzalis AE, Lekatou A, Mavros H. Microstructural Modifications of As-Cast High-Chromium White Iron by Heat Treatment. J Mater Eng Perform 2009;18:174–81. https://doi.org/10.1007/s11665-008-9285-6.

[14] Gasan H, Erturk F. Effects of a Destabilization Heat Treatment on the Microstructure and Abrasive Wear Behavior of High-Chromium White Cast Iron Investigated Using Different Characterization Techniques. Metallurgical and Materials Transactions A 2013;44:4993–5005. https://doi.org/10.1007/s11661-013-1851-3.

[15] Wiengmoon A, Chairuangsri T, Pearce JTH. A Microstructural Study of Destabilised 30wt%Cr-2.3wt%C High Chromium Cast Iron. ISIJ International 2004;44:396–403. https://doi.org/10.2355/isijinternational.44.396.

[16] Powell GLF, Laird G. Structure, nucleation, growth and morphology of secondary carbides in high chromium and Cr-Ni white cast irons. J Mater Sci 1992;27:29–35. https://doi.org/10.1007/BF02403640.

[17] Wiengmoon A, Pearce JTH, Chairuangsri T. Relationship between microstructure, hardness and corrosion resistance in 20 wt.%Cr, 27 wt.%Cr and 36 wt.%Cr high chromium cast irons. Mater Chem Phys 2011;125:739–48. https://doi.org/10.1016/j.matchemphys.2010.09.064.

[18] Guitar MA, Nayak UP, Britz D, Mücklich F. The Effect of Thermal Processing and Chemical Composition on Secondary Carbide Precipitation and Hardness in High-Chromium Cast Irons. International Journal of Metalcasting 2020;14:755–65. https://doi.org/10.1007/s40962-020-00407-4.

[19] Bedolla-Jacuinde A, Arias L, Hernández B. Kinetics of secondary carbides precipitation in a hiqh-chromium white iron. J Mater Eng Perform 2003;12:371–82. https://doi.org/10.1361/105994903770342881.

[20] Abdel-Aziz Kh, El-Shennawy M, Omar AA. Microstructural Characteristics and Mechanical Properties of Heat Treated High-Cr White Cast Iron Alloys. International Journal of Apllied Engineering Research 2017;12:4675–86.

[21] Nayak UP, Mücklich F, Guitar MA. Time-Dependant Microstructural Evolution and Tribological Behaviour of a 26 wt% Cr White Cast Iron Subjected to a Destabilization Heat Treatment. Metals and Materials International 2022. https://doi.org/10.1007/s12540-022-01276-8.

[22] zum Gahr KH, Doane D v. Optimizing fracture toughness and abrasion resistance in white cast irons. Metallurgical Transactions A 1980;11:613–20. https://doi.org/10.1007/BF02670698.

[23] Tang XH, Chung R, Li DY, Hinckley B, Dolman K. Variations in microstructure of high chromium cast irons and resultant changes in resistance to wear, corrosion and corrosive wear. Wear 2009;267:116–21. https://doi.org/10.1016/j.wear.2008.11.025.

[24] Mandal SS, Ghosh KS, Mondal DK. Correlation between microstructure, hardness, wear and electrochemical behaviour in 8.0%, 16.0% and 20.0% (by wt) chromium white irons. Mater Chem Phys 2017;193. https://doi.org/10.1016/j.matchemphys.2017.02.041.

[25] Doğan ÖN, Hawk JA, Laird G. Solidification structure and abrasion resistance of high chromium white irons. Metall Mater Trans A Phys Metall Mater Sci 1997;28:1315–28. https://doi.org/10.1007/s11661-997-0267-3.

[26] Kibble KA, Pearce JTH. Influence of Heat Treatment on the Microstructure and Hardness of 19% High-chromium Cast Irons. Cast Metals 1993;6:9–15. https://doi.org/10.1080/09534962.1993.11819121.

[27] Gundlach RB, Parks JL. Influence of abrasive hardness on the wear resistance of high chromium irons. Wear 1978;46:97–108. https://doi.org/10.1016/0043-1648(78)90113-8.

[28] Watson JD, Mutton PJ, Sare IR. Abrasive Wear of White Cast Irons. Metals Forum 1980;3:74–88.

[29] Turenne S, Lavallée F, Masounave J. Matrix microstructure effect on the abrasion wear resistance of high-chromium white cast iron. J Mater Sci 1989;24:3021–8. https://doi.org/10.1007/BF02385662.

[30] Pearce JTH. Structure and Wear Performance of Abrasion Resistance Chromium White Cast Irons. Transactions of the American Foundrymen's Society 1984;92:599–622.

[31] Albertin E, Sinatora A. Effect of carbide fraction and matrix microstructure on the wear of cast iron balls tested in a laboratory ball mill. Wear 2001;250:492–501. https://doi.org/10.1016/S0043-1648(01)00664-0.

[32] Higuera-cobos OF, Dumitru F-D, Mesa-Grajales DH. Improvement of abrasive wear resistance of the high chromium cast iron ASTM A-532 through thermal treatment cycles. Revista Facultad de Ingeniería 2015;25:93–103.

[33] Laird G, Gundlach R, Rohrig K. Abrasion-Resistant Cast Iron Handbook. Schaumburg, Illinois (USA): American Foundry Society; 2000.

[34] Nayak UP, Guitar MA, Mücklich F. Evaluation of etching process parameter optimization in the objective specific microstructural characterization of as-cast and heat treated HCCI alloy. Practical Metallography 2020;57:688–713. https://doi.org/10.3139/147.110682.

[35] Calcagnotto M, Ponge D, Demir E, Raabe D. Orientation gradients and geometrically necessary dislocations in ultrafine grained dual-phase steels studied by 2D and 3D EBSD. Materials Science and Engineering A 2010;527:2738–46. https://doi.org/10.1016/j.msea.2010.01.004.

[36] Schindelin J, Arganda-Carreras I, Frise E, Kaynig V, Longair M, Pietzsch T, et al. Fiji: An open-source platform for biological-image analysis. Nat Methods 2012;9:676–82. https://doi.org/10.1038/nmeth.2019.

[37] Nayak UP, Müller M, Britz D, Guitar MA, Mücklich F. Image Processing using Open Source Tools and their Implementation in the Analysis of Complex Microstructures. Practical Metallography 2021;58:484–506. https://doi.org/10.1515/pm-2021-0039.

[38] Efremenko VG, Chabak YG, Brykov MN. Kinetic parameters of secondary carbide precipitation in High-Cr white iron alloyed by Mn-Ni-Mo-V Complex. J Mater Eng Perform 2013;22:1378–85. https://doi.org/10.1007/s11665-012-0434-6.

[39] Porter DA, Easterling KE, Sherif MY. Phase transformations in metals and alloys, third edition. 2009.

[40] Liu XY. Heterogeneous nucleation or homogeneous nucleation? J Chem Phys 2000;112:9949. https://doi.org/10.1063/1.481644.

[41] Kwak SK, Kim JH. Statistical data preparation: management of missing values and outliers. Korean J Anesthesiol 2017;70:407–11. https://doi.org/10.4097/KJAE.2017.70.4.407.

[42] Nayak UP, Suárez S, Pesnel V, Mücklich F, Guitar MA. Load dependent microstructural evolution in an as-cast 26% Cr high chromium cast iron during unlubricated sliding. Friction 2022;10:1258–75. https://doi.org/10.1007/s40544-021-0553-x.

[43] Karantzalis AE, Lekatou A, Kapoglou A, Mavros H, Dracopoulos V. Phase transformations and microstructural observations during subcritical heat treatments of a high-chromium cast iron. J Mater Eng Perform 2012;21:1030–9. https://doi.org/10.1007/s11665-011-9995-z.

[44] Wright SI, Nowell MM, Field DP. A review of strain analysis using electron backscatter diffraction. Microscopy and Microanalysis 2011;17:316–29. https://doi.org/10.1017/S1431927611000055.

[45] Martinez Ostormujof T, Purushottam Raj Purohit RRP, Breumier S, Gey N, Salib M, Germain L. Deep Learning for automated phase segmentation in EBSD maps. A case study in Dual Phase steel microstructures. Mater Charact 2022;184:111638. https://doi.org/10.1016/J.MATCHAR.2021.111638.

[46] Pinard PT, Schwedt A, Ramazani A, Prahl U, Richter S. Characterization of dual-phase steel microstructure by combined submicrometer EBSD and EPMA carbon measurements. Microscopy and Microanalysis, vol. 19, 2013, p. 996–1006. https://doi.org/10.1017/S1431927613001554.

[47] Hutchings IM. Tribology: Friction and Wear of Engineering Materials. Oxford (UK): Butterworth-Heinemann; 1992. https://doi.org/10.1016/0261-3069(92)90241-9.

[48] Hurricks PL. Some Metallurgical Factors Controlling the adhesive and abrasive wear resistance of steels: A Review 1973;26:285–301.

[49] Coronado JJ. Effect of load and carbide orientation on abrasive wear resistance of white cast iron. Wear 2011;270:823–7. https://doi.org/10.1016/j.wear.2011.02.009.

[50] Bedolla-Jacuinde A, Rainforth WM. Electron microscopy analysis on the worn surface of a high-chromium white iron during dry sliding contact. Materials Research Society Symposium Proceedings 2005;843:299–304. https://doi.org/10.1557/proc-843-t7.4.

[51] Chen L, Persson J, Ståhl JE, Zhou JM. Nano-Scratching resistance of high-chromium white cast iron and its correlation with wear of cBN tool in machining. Journal of Superhard Materials 2017;39:365–72. https://doi.org/10.3103/S1063457617050094.

[52] Sullivan JL, Quinn TFJ, Rowson DM. Developments in the oxidational theory of mild wear. Tribol Int 1980;13:153–8. https://doi.org/10.1016/0301-679X(80)90031-6.

[53] Doğan ÖN, Hawk JA. Effect of carbide orientation on abrasion of high Cr white cast iron. Wear 1995;189:136–42. https://doi.org/10.1016/0043-1648(95)06682-9.

[54] Nayak UP, Schäfer F, Mücklich F, Guitar MA. Wear Induced Sub-surface Deformation Characteristics of a 26 Wt% Cr White Cast Iron Subjected to a Destabilization Heat Treatment. Tribol Lett 2023;71. https://doi.org/10.1007/s11249-022-01683-3.

[55] Sano Y, Hattori T, Haga M. Characteristics of High-carbon High Speed Steel Rolls for Hot Strip Mill. ISIJ International 1992;32:1194–201. https://doi.org/10.2355/ISIJINTERNATIONAL.32.1194.

[56] Blau PJ. Interpretations of the friction and wear break-in behavior of metals in sliding contact. Wear 1981;71:29–43. https://doi.org/10.1016/0043-1648(81)90137-X.

[57] Blau PJ. On the nature of running-in. Tribol Int 2005;38:1007–12. https://doi.org/10.1016/j.triboint.2005.07.020.

6. CONCLUSIONS

This work presented a comprehensive investigation into the microstructural evolution of a 26 wt.% Cr HCCI alloy. The study involved subjecting the alloy to varying HT processes, with the selection of HT parameters based on computational simulations. The microstructural characterization was performed using multiple techniques at various length scales, allowing for a thorough understanding of the alloy's behaviour. The investigation of the tribological performance of the HCCI alloy included wear track characterization, which provided insights into the behaviour of the different microstructural constituents during tribological testing. This aided in identifying the dominant wear mechanisms and their influence on the wear rate of the alloy. The following summarizes the major conclusions that have been obtained, tailored to the specific objectives of the respective works.

The usage of MatCalc as a simulation tool has provided a reliable and accurate alternative to experimental procedures in the design of heat treatments. This is demonstrated by the accordance between the predictions made by MatCalc and the experimentally obtained results regarding the phase fraction and elemental composition of the HCCI alloy in the as-cast state. Furthermore, the kinetic simulations on the destabilization phase of the multi-step HT process predicted the precipitation of SC at temperatures around 800 °C. The results showed that M_7C_3 carbides precipitate initially, followed by the $M_{23}C_6$ carbides when the temperature of 980 °C was reached. The microstructural characterization and analysis of the material heated to 800 °C confirmed the nucleation of M_7C_3 type SC with a chemical composition of $(Cr_{4.7}Fe_{2.3})C_3$.

The comprehensive 'objective specific' metallographic and etching protocol developed allowed for the microstructural characterization of the AC and HTed samples, and the identification of the individual microstructural constituents. Additionally, a sequential methodology was devised, which enabled accurate

microstructural segmentation and quantification, with a particular focus on the stereological characteristics of the carbides. Furthermore, the coating methodology using electroplating successfully protected the alloy's worn surface from mechanical sectioning during the examination of the sub-surface microstructural characteristics of the wear track. This coating methodology was also successfully applied to other ferrous alloys, such as 316L stainless steel and low-carbon steel with 5 wt.% Ni.

To prevent arbitrary load selection during tribological tests, the critical load (P_c) was first determined using Hertzian contact theory based on the materials' properties. The loads were then chosen accordingly to evaluate the damage under different contact situations. The determination of P_c by analytical calculations was in accordance with the microstructural observations carried out using SEM. The austenitic matrix did not experience plastic deformation at sub-critical loads whereas the presence of slip traces was observed at and above the critical load. Finally, the methodology of determining the critical load using materials' properties can be extended to other alloys in the HCCI family to establish load limits and better understand the interaction between different components.

The implementation of HT resulted in microstructural variations depending on the chemical composition, as evidenced by the change in the SC type from M_7C_3 to $M_{23}C_6$ when the Cr content in the alloy increased from 16 wt.% to 26 wt.%. The destabilized microstructure comprised primarily of a martensitic matrix (α'), finely precipitated SC ($M_{23}C_6$ type), original (as-cast) EC (M_7C_3 type), and RA. A temporal decrease in RA was observed during the isothermal destabilization at 980 °C for up to 90 minutes. The distribution of SC precipitation within the matrix was affected primarily by the HR, with precipitation predominantly located at the matrix periphery for high HR, while it proceeded inwards into the matrix for slower HR. Furthermore, stereological analysis of the carbides revealed that the impact of HR on SC size and CVF was greater than that of an increase in temperature.

Despite the microstructural constituents of the HTed samples being identical, the differences in their amounts and distribution had significant consequences on the final tribological behaviour of the alloy. More specifically, the wear mechanisms varied depending on whether the matrix was predominantly austenite or martensite. The presence of a predominantly martensitic matrix and dispersed SC in the HTed samples resulted in an improved load-bearing capacity, preventing the ejection of large EC during wear tests, and leading to a decrease in WR of up to 50% compared to the as-cast. Interestingly, among the HTed samples, the one with the lowest increase in surface matrix hardness (980_0) displayed the best wear resistance (100% increase). Finally, these results highlighted the importance of optimal distribution of microstructural constituents after destabilization and the vital role of the matrix support.

As far as tribological applications are concerned, it is recommended to destabilize at higher temperatures by using a faster heating rate. However, for applications that require high hardness, it is suggested to destabilize for a longer duration to reduce the amount of RA. Overall, this work provides valuable insights into the HT processing and tribological performance of the HCCI alloy, with significant implications for its use in various industrial applications. In light of the findings presented in this thesis, there are several important directions for future research that warrant further exploration.

7. OUTLOOK

In the present work, it was observed that oxidation played a significant role in the tribological behaviour of the HCCI alloys, partly due to the usage of an oxide-based counter-body (Al_2O_3). To observe if there is any variation in the dominant wear mechanism and to enhance our comprehension of the alloys' performance under varying conditions, long-term tests (up to 100,000 cycles) using a non-oxide counter-body (Si_3N_4) should be performed in the future.

The composite-like behaviour exhibited by HCCIs allows for the establishment of a relationship between their microstructure and abrasive wear behaviour through the use of mathematical/numerical models, much like how simulation tools are utilized in HT implementation. The different models found in the literature describing the abrasion response of metal matrix composites can be used as a starting point to model the abrasion response of HCCI with varying volume fraction and size of SC. The microstructural data obtained from the present work's characterization can be used as an input to formulate a mathematical model to model abrasive wear in HCCIs.

The simulations conducted in this study were primarily focused on comprehending the carbide precipitation kinetics during the destabilization phase of heat treatment. However, by incorporating the knowledge gained from carbide stereology in the present research and including a tempering (SCD) step into the simulations, additional insights into the precipitation behaviour during HT can be obtained. This will further bolster the implementation of computational tools in simulating complex heat treatments.

In addition to being used in wear-related applications, HCCI alloys are also used in applications that require moderate toughness and impact resistance. Although it is agreed upon that the presence of RA is beneficial, the amount of RA is still under debate, with a wide range ranging from 20 to 50%. The present work showed

that the sample destabilized at 980 °C for 0 minutes and air cooled showed the best wear resistance amongst all samples, with a 100% increase in the wear resistance compared to the as-cast sample. The presence of an optimal distribution of the microstructural constituents, such as 10% RA, 5% SC CVF, and the support from the surrounding matrix enabled this. Nevertheless, through impact testing and analysis of fracture surfaces, the impact resistance of HTed samples can be further comprehended in terms of how the types and distribution of carbides impact their performance, whether positively or negatively. Accordingly, a controlled microstructure ensuring an optimal balance between the tribological behaviour and fracture toughness could be obtained.

OTHER RELATED PUBLICATIONS

- María Agustina Guitar, Anna Scheid, **U. Pranav Nayak**, Leandro Nakamura, Dirk Ponge, Dominik Britz, Frank Mücklich (2020), "Quantification of the phase transformation kinetics in high chromium cast irons using dilatometry and metallographic techniques", Metallurgical and Materials Transactions A, 51, 3789–3801. (https://doi.org/10.1007/s11661-020-05808-y)

REFERENCES

1. Wang, Q.J., Chung, Y.-W.: Encyclopedia of Tribology. Springer US, Boston, MA (2013)

2. Elango, B., Bornmann, L., Kannan, G.: Detecting the historical roots of tribology research: a bibliometric analysis. Scientometrics. 107, 305–313 (2016). https://doi.org/10.1007/s11192-016-1877-6

3. Jost, H.Peter.: Lubrication (tribology), education and research a report on the present position and industry's needs. H.M. Stationery Off., London (1966)

4. Dowson, D.: History of tribology. (1979). https://doi.org/10.2474/trol.6.ii

5. Tzanakis, I., Hadfield, M., Thomas, B., Noya, S.M., Henshaw, I., Austen, S.: Future perspectives on sustainable tribology. Renewable and Sustainable Energy Reviews. 16, 4126–4140 (2012). https://doi.org/10.1016/j.rser.2012.02.064

6. Hähner, G., Spencer, N.: Rubbing and Scrubbing. Phys Today. 51, 22–27 (1998). https://doi.org/10.1063/1.882435

7. Mang, T.: Encyclopedia of Lubricants and Lubrication. Springer Berlin Heidelberg, Berlin, Heidelberg (2014)

8. Bhushan, B.: Modern Tribology Handbook. CRC Press (2000)

9. Menezes, P.L., Ingole, S.P., Nosonovsky, M., Kailas, S. v., Lovell, M.R.: Tribology for scientists and engineers: From basics to advanced concepts. Springer-Verlag New York, New York (USA) (2013)

10. Jost, H.P.: Tribology — Origin and future. Wear. 136, 1–17 (1990). https://doi.org/10.1016/0043-1648(90)90068-L

11. Holmberg, K., Erdemir, A.: Influence of tribology on global energy consumption, costs and emissions. Friction. 5, 263–284 (2017). https://doi.org/10.1007/s40544-017-0183-5

12. Holmberg, K., Kivikytö-Reponen, P., Härkisaari, P., Valtonen, K., Erdemir, A.: Global energy consumption due to friction and wear in the mining industry. Tribol Int. 115, 116–139 (2017). https://doi.org/10.1016/j.triboint.2017.05.010

13. Hutchings, I.M.: Abrasion in wear and manufacturing processes. Proceedings of the Institution of Mechanical Engineers, Part J: Journal of Engineering Tribology. 216, 55–62 (2002). https://doi.org/10.1243/1350650021543898

14. Zum Gahr, K.-H.: Microstructure and Wear of Materials. Elsevier Science Publishers B.V., Amsterdam (1987)

15. Sare, I.R., Constantine, A.G.: Development of methodologies for the evaluation of wear-resistant materials for the mineral industry. Wear. 203–204, 671–678 (1997). https://doi.org/10.1016/S0043-1648(96)07398-X

16. Durman, R.W.: Progress in abrasion-resistant materials for use in comminution processes. Int J Miner Process. 22, 381–399 (1988). https://doi.org/10.1016/0301-7516(88)90074-9

17. Zhai, W., Bai, L., Zhou, R., Fan, X., Kang, G., Liu, Y., Zhou, K.: Recent Progress on Wear-Resistant Materials: Designs, Properties, and Applications. Advanced Science. 8, 2003739 (2021). https://doi.org/10.1002/ADVS.202003739

18. Laird, G., Gundlach, R., & Rohrig, K.: Abrasion Resistant Cast Iron Handbook. American Foundry Society, Schaumburg, Illinois (2000)

19. ASM International: ASM Handbook Volume 15 - Casting. ASM International, Ohio (2008)

20. Xu, H., Xu, Y., He, Y., Cheng, S., Jiao, H., Yue, S., Li, J.: Two-stage warm cross rolling and its effect on the microstructure, texture and magnetic properties of an Fe-6.5 wt% Si non-oriented electrical steel. J Mater Sci. 55, 12525–12543 (2020). https://doi.org/10.1007/s10853-020-04861-7

21. Charre, M.D.: Microstructure of Steels and Cast Irons. Springer; 2004 edition (2004)

22. Jackson, R.S.: Austenite liquidus surface and constitutional diagram for the iron-chromium-carbon metastable system. Journal of the Iron and Steel Institute. 208, 163–167 (1970)

23. Rivlin, V.G.: Critical review of constitution of carbon — chromium — iron and carbon — iron — manganese systems. International Metals Reviews. 29, 299–328 (1984). https://doi.org/10.1179/imtr.1984.29.1.299

24. ASTM International: Standard Specification for Abrasion Resistance Cast Irons: ASTM Standard A 532/A 532M - 93a. , West Conshohocken, PA, USA (2003)

25. Tabrett, C.P., Sare, I.R., Ghomashchi, M.R.: Microstructure-property relationships in high chromium white iron alloys. International Materials Reviews. 41, 59–82 (1996). https://doi.org/10.1179/095066096790326075

26. Dodd, J.: Recent developments in abrasion resistant high chromium-molybdenum irons, low-alloy manganese steels and alloyed nodular irons of importance in the extraction and utilization of energy resources. Journal of Materials for Energy Systems. 2, 65–76 (1980). https://doi.org/10.1007/BF02833432

27. Maratray, F.: Choice of appropriate compositions for chromium-molybdenum white irons. AFS Trans. 79, 121–124 (1971)

28. Maratray, F., Usseglio-Nanot, R.: Factors affecting the structure of chromium and chromium-molybdenum white irons. Climax Molybdenum S.A. Paris, Paris (1971)

29. Wiengmoon, A.: Carbides in high chromium cast irons. Naresuan University Engineering Journal. 6, 64–70 (2011). https://doi.org/10.14456/nuej.2011.6

30. Doğan, Ö.N., Hawk, J.A.: Effect of carbide orientation on abrasion of high Cr white cast iron. Wear. 189, 136–142 (1995). https://doi.org/10.1016/0043-1648(95)06682-9

31. Guitar, M.A., Suárez, S., Prat, O., Duarte Guigou, M., Gari, V., Pereira, G., Mücklich, F.: High Chromium Cast Irons: Destabilized-Subcritical Secondary Carbide Precipitation and Its Effect on Hardness and Wear Properties. J Mater Eng Perform. 27, 3877–3885 (2018). https://doi.org/10.1007/s11665-018-3347-1

32. Hinckley, B., Dolman, K.F., Wuhrer, R., Ray, A., Yeung, W.: SEM and EBSD investigations of high-chromium cast irons. Microscopy and Microanalysis. 14, 550–551 (2008). https://doi.org/10.1017/S1431927608084067

33. Karantzalis, A.E., Lekatou, A., Mavros, H.: Microstructural Modifications of As-Cast High-Chromium White Iron by Heat Treatment. J Mater Eng Perform. 18, 174–181 (2009). https://doi.org/10.1007/s11665-008-9285-6

34. Llewellyn, R.J., Yick, S.K., Dolman, K.F.: Scouring erosion resistance of metallic materials used in slurry pump service. Wear. 256, 592–599 (2004). https://doi.org/10.1016/j.wear.2003.10.002

35. Karantzalis, E., Lekatou, A., Mavros, H.: Microstructure and properties of high chromium cast irons: effect of heat treatments and alloying additions. International Journal of Cast Metals Research. 22, 448–456 (2009). https://doi.org/10.1179/174313309X436637

36. Wiengmoon, A., Pearce, J.T.H., Chairuangsri, T.: Relationship between microstructure, hardness and corrosion resistance in 20 wt.%Cr, 27 wt.%Cr and 36 wt.%Cr high chromium cast irons. Mater Chem Phys. 125, 739–748 (2011). https://doi.org/10.1016/j.matchemphys.2010.09.064

37. Matsubara, Y., Ogi, K., Matsuda, K.: Eutectic Solidification of High-Chromium Cast Iron--Eutectic Structures and Their Quantitative Analysis. In: Transactions of the American Foundrymen's Society. pp. 183–196 (1982)

38. Pearce, J.T.H.: Structure and Wear Performance of Abrasion Resistance Chromium White Cast Irons. Transactions of the American Foundrymen's Society. 92, 599–622 (1984)

39. Carpenter, S.D., Carpenter, D., Pearce, J.T.H.: XRD and electron microscope study of an as-cast 26.6% chromium white iron microstructure. Mater Chem Phys. 85, 32–40 (2004). https://doi.org/10.1016/j.matchemphys.2003.11.037

40. Abbaschian, R., Abbaschian, L., Reed-Hill, R.E.: Physical Metallurgy Principles. Cengage Learning, Stamford, Connecticut (USA) (2008)

41. Ohser, J., Mücklich, F.: Statistical Analysis of Microstructures in Materials Science. Wiley (2000)

42. Tabrett, C.P., Sare, I.R.: Effect of high temperature and sub-ambient treatments on the matrix structure and abrasion resistance of a high-chromium white iron. Scr Mater. 38, 1747–1753 (1998). https://doi.org/10.1016/S1359-6462(98)00118-3

43. Karantzalis, A.E., Lekatou, A., Diavati, E.: Effect of destabilization heat treatments on the microstructure of high-chromium cast iron: A microscopy examination approach. J Mater Eng Perform. 18, 1078–1085 (2009). https://doi.org/10.1007/s11665-009-9353-6

44. Gasan, H., Erturk, F.: Effects of a destabilization heat treatment on the microstructure and abrasive wear behavior of high-chromium white cast

iron investigated using different characterization techniques. Metall Mater Trans A Phys Metall Mater Sci. 44, 4993–5005 (2013). https://doi.org/10.1007/s11661-013-1851-3

45. Sare, I.R., Arnold, B.K.: The Effect of Heat Treatment on the Gouging Abrasion Resistance of Alloy White Cast Irons. 26, 1785–1793 (1995). https://doi.org/10.1007/BF02664672

46. Gelfi, M., Pola, A., Girelli, L., Zacco, A., Masotti, M., la Vecchia, G.M.: Effect of heat treatment on microstructure and erosion resistance of white cast irons for slurry pumping applications. Wear. 428–429, 438–448 (2019). https://doi.org/10.1016/j.wear.2019.03.011

47. Bedolla-Jacuinde, A., Correa, R., Mejía, I., Quezada, J.G., Rainforth, W.M.: The effect of titanium on the wear behaviour of a 16%Cr white cast iron under pure sliding. Wear. 263, 808–820 (2007). https://doi.org/10.1016/j.wear.2006.12.011

48. Correa, R., Bedolla-Jacuinde, A., Zuno-Silva, J., Cardoso, E., Mejía, I.: Effect of boron on the sliding wear of directionally solidified high-chromium white irons. Wear. 267, 495–504 (2009). https://doi.org/10.1016/j.wear.2008.11.009

49. Scandian, C., Boher, C., de Mello, J.D.B., Rézaï-Aria, F.: Effect of molybdenum and chromium contents in sliding wear of high-chromium white cast iron: The relationship between microstructure and wear. Wear. 267, 401–408 (2009). https://doi.org/10.1016/j.wear.2008.12.095

50. Cortés-Carrillo, E., Bedolla-Jacuinde, A., Mejía, I., Zepeda, C.M., Zuno-Silva, J., Guerra-Lopez, F. V.: Effects of tungsten on the microstructure and on the abrasive wear behavior of a high-chromium white iron. Wear. 376–377, 77–85 (2017). https://doi.org/10.1016/j.wear.2017.02.043

51. Kibble, K.A., Pearce, J.T.H.: Influence of Heat Treatment on the Microstructure and Hardness of 19% High-chromium Cast Irons. Cast Metals. 6, 9–15 (1993). https://doi.org/10.1080/09534962.1993.11819121

52. Wiengmoon, A., Chairuangsri, T., Pearce, J.T.H.: Effects of destabilisation heat treatment on microstructure, hardness and corrosion behaviour of 18wt.%Cr and 25wt.%Cr cast irons. Key Eng Mater. 658, 76–80 (2015). https://doi.org/10.4028/www.scientific.net/KEM.658.76

53. Powell, G.L.F., Laird, G.: Structure, nucleation, growth and morphology of secondary carbides in high chromium and Cr-Ni white cast irons. J Mater Sci. 27, 29–35 (1992). https://doi.org/10.1007/BF02403640

54. Zum Gahr, K.H., Eldis, G.T.: Abrasive wear of white cast irons. Wear. 64, 175–194 (1980). https://doi.org/10.1016/0043-1648(80)90101-5

55. Wiengmoon, A., Chairuangsri, T., Pearce, J.T.H.: A Microstructural Study of Destabilised 30wt%Cr-2.3wt%C High Chromium Cast Iron. ISIJ International. 44, 396–403 (2004). https://doi.org/10.2355/isijinternational.44.396

56. Turenne, S., Lavallée, F., Masounave, J.: Matrix microstructure effect on the abrasion wear resistance of high-chromium white cast iron. J Mater Sci. 24, 3021–3028 (1989). https://doi.org/10.1007/BF02385662

57. Albertin, E., Sinatora, A.: Effect of carbide fraction and matrix microstructure on the wear of cast iron balls tested in a laboratory ball mill. Wear. 250, 492–501 (2001). https://doi.org/10.1016/S0043-1648(01)00664-0

58. Zum Gahr, K.H., Doane, D. V.: Optimizing fracture toughness and abrasion resistance in white cast irons. Metallurgical Transactions A. 11, 613–620 (1980). https://doi.org/10.1007/BF02670698

59. Asensio, J., Pero-Sanz, J.A., Verdeja, J.I.: Microstructure selection criteria for cast irons with more than 10 wt.% chromium for wear applications. Mater Charact. 49, 83–93 (2002). https://doi.org/10.1016/S1044-5803(02)00260-7

60. Tabrett, C.P., Sare, I.R.: The effect of heat treatment on the abrasion resistance of alloy white irons. Wear. 203–204, 206–219 (1997). https://doi.org/10.1016/S0043-1648(96)07390-5

61. Guitar, M.A., Suárez, S., Prat, O., Duarte Guigou, M., Gari, V., Pereira, G., Mücklich, F.: High Chromium Cast Irons: Destabilized-Subcritical Secondary Carbide Precipitation and Its Effect on Hardness and Wear Properties. J Mater Eng Perform. (2018). https://doi.org/10.1007/s11665-018-3347-1

62. Gundlach, R.B., Parks, J.L.: Influence of abrasive hardness on the wear resistance of high chromium irons. Wear. 46, 97–108 (1978). https://doi.org/10.1016/0043-1648(78)90113-8

63. Çetinkaya, C.: An investigation of the wear behaviours of white cast irons under different compositions. Mater Des. 27, 437–445 (2006). https://doi.org/10.1016/j.matdes.2004.11.021

64. Matsubara, Y., Sasaguri, N., Shimizu, K., Kon Yu, S.: Solidification and abrasion wear of white cast irons alloyed with 20% carbide forming elements. Wear. 250–251, 502–510 (2001). https://doi.org/10.1016/S0043-1648(01)00599-3

65. Watson, J.D., Mutton, P.J., Sare, I.R.: Abrasive Wear of White Cast Irons. Metals forum. 3, 74–88 (1980)

66. Higuera-cobos, O.F., Dumitru, F.-D., Mesa-Grajales, D.H.: Improvement of abrasive wear resistance of the high chromium cast iron ASTM A-532 through thermal treatment cycles. Revista Facultad de Ingeniería. 25, 93–103 (2015). https://doi.org/10.19053/01211129.4141

67. Laird, G., Gundlach, R., Rohrig, K.: Abrasion-Resistant Cast Iron Handbook. American Foundry Society, Schaumburg, Illinois (USA) (2000)

68. Bedolla-Jacuinde, A., Arias, L., Hernández, B.: Kinetics of secondary carbides precipitation in a hiqh-chromium white iron. J Mater Eng Perform. 12, 371–382 (2003). https://doi.org/10.1361/105994903770342881

69. Efremenko, V.G., Chabak, Y.G., Brykov, M.N.: Kinetic parameters of secondary carbide precipitation in High-Cr white iron alloyed by Mn-Ni-Mo-V Complex. J Mater Eng Perform. 22, 1378–1385 (2013). https://doi.org/10.1007/s11665-012-0434-6

70. Guitar, M.A., Scheid, A., Nayak, U.P., Nakamura, L., Ponge, D., Britz, D., Mücklich, F.: Quantification of the Phase Transformation Kinetics in High Chromium Cast Irons Using Dilatometry and Metallographic Techniques. Metall Mater Trans A Phys Metall Mater Sci. 51, 3789–3801 (2020). https://doi.org/10.1007/s11661-020-05808-y

71. Porter, D.A., Easterling, K.E., Sherif, M.Y.: Phase transformations in metals and alloys. CRC Press, Boca Raton, Florida (USA) (2009)

72. Powell, G.L.F., Lloyd, P.G.: A deep etching technique for the examination of the carbide of high chromium cast iron in a scanning electron microscope. Metallography. 14, 271–274 (1981). https://doi.org/10.1016/0026-0800(81)90032-X

73. Collins, W.K., Watson, J.C.: Metallographic etching for carbide volume fraction of high-chromium white cast irons. Mater Charact. 24, 379–386 (1990). https://doi.org/10.1016/1044-5803(90)90044-K

74. Vander Voort, G.F.: Metallography: Principles and Practice. (1999)

75. Guitar, M.A., Scheid, A., Suárez, S., Britz, D., Guigou, M.D., Mücklich, F.: Secondary carbides in high chromium cast irons: An alternative approach to

their morphological and spatial distribution characterization. Mater Charact. 144, 621–630 (2018). https://doi.org/10.1016/j.matchar.2018.08.020

76. Ruangchai, K., Tongsri, R., Pearce, J.T.H., Chairuangsri, T., Nusen, S., Kurata, H., Haruta, M., Kiyomura, T., Yamaguchi, A., Wiengmoon, A.: Electron microscopy of carbides in annealed 28 wt% Cr - 1 wt% (Mo/W) cast irons. Mater Charact. 198, (2023). https://doi.org/10.1016/j.matchar.2023.112723

77. Davis, J.R.: Metals Handbook. Metals Handbook. 2571 (1998). https://doi.org/10.1017/CBO9781107415324.004

78. Callister, W.D.J.: Fundamentals of Materials Science and Engineering. (2001)

79. ASM International: Properties and Selection: Irons, Steels, and High-Performance Alloys. ASM International (1990)

80. Hume-Rothery, W.: The Structures of Alloys of Iron. Pergamon (1966)

81. Angus, H.T.: Cast Iron: Physical and Engineering Properties. (1978)

82. Yescas-Gonzalez, M.A., Bhadeshia, H.K.D.H.: Cast irons, https://www.phase-trans.msm.cam.ac.uk/2001/adi/cast.iron.html

83. Caesar, A.G.: Iron-carbon phase diagram under atmospheric pressure, https://commons.wikimedia.org/wiki/File:Iron_carbon_phase_diagram.svg#metadata, (2019)

84. Singh, R.: Applied Welding Engineering. Butterworth-Heinemann (2020)

85. International Organization for Standardization: Abrasion-resistant cast irons-Classification (ISO 21988:2006). , Geneva (2006)

86. Abd El-Aziz, Kh., Zohdy, Kh., Saber, D., Sallam, H.E.M.: Wear and Corrosion Behavior of High-Cr White Cast Iron Alloys in Different Corrosive Media. J Bio Tribocorros. 1, 25 (2015). https://doi.org/10.1007/s40735-015-0026-8

87. Chung, R.J.: Comprehensive study of the abrasive wear and slurry erosion behavior of an expanded system of high chromium cast iron and microstructural modification for enhanced wear resistance, (2014)

88. Becket, F.M.: U.S Patent No. 1,245,552, (1917)

89. Powell, G.L.F.: Morphology of Eutectic M3C and M7C3 in White Iron Castings. Metals Forum. 3, (1980)

90. Kaya, S., Yılan, F., Urtekin, L.: Influences of Cr on the microstructural, wear and mechanical performance of high-chromium white cast iron grinding balls. Journal of Materials and Manufacturing. 1, 23–30 (2022). https://doi.org/10.5281/zenodo.7107351

91. Maratray, F., Poulalion, A.: Austenite Retention in High-Chromium White Irons. In: Transactions of the American Foundrymen's Society. pp. 795–804 (1982)

92. Tang, X.H., Chung, R., Pang, C.J., Li, D.Y., Hinckley, B., Dolman, K.: Microstructure of high (45wt.%) chromium cast irons and their resistances to wear and corrosion. Wear. 271, 1426–1431 (2011). https://doi.org/10.1016/j.wear.2010.11.047

93. Zumelzu, E., Goyos, I., Cabezas, C., Opitz, O., Parada, A.: Wear and corrosion behaviour of high-chromium (14-30% Cr) cast iron alloys. J Mater Process Technol. 128, 250–255 (2002). https://doi.org/10.1016/S0924-0136(02)00458-2

94. Durman, R.W.: The application of alloyed white cast irons in crushing, grinding, and material handling processes. British Foundryman. 69, 141–149 (1976)

95. Tabrett, C.P.: Microstructure-Property Relationships in High Chromium White Irons, (1997)

96. Laird, G., Powell, G.L.F.: Solidification and solid-state transformation mechanisms in Si alloyed high-chromium white cast irons. Metallurgical Transactions A. 24, 981–988 (1993). https://doi.org/10.1007/BF02656520

97. Dodd, J.E., Parks, J.L.: Factors affecting the production and performance of thick section high chromium-molybdenum alloy iron castings. Presented at the (1980)

98. Maratray, F., Usseglio-Nanot, R.: Transformation characteristics of chromium and Chromium-Molybdenum White Irons, (1970)

99. Far, A.R.H., Anijdan, S.H.M., Abbasi, S.M.: The effect of increasing Cu and Ni on a significant enhancement of mechanical properties of high strength low alloy, low carbon steels of HSLA-100 type. Materials Science and Engineering: A. 746, 384–393 (2019). https://doi.org/10.1016/j.msea.2019.01.025

100. Thorpe, W.R., Chicco, B.: The Fe-rich corner of the metastable C-Cr-Fe liquidus surface. Metallurgical Transactions A. 16, 1541–1549 (1985). https://doi.org/10.1007/BF02663011

101. Raghavan V: C-Cr-Fe-N (Carbon-Chromium-Iron-Nitrogen). Journal of Phase Equilibria. 13, 119–129 (1992). https://doi.org/10.1007/BF02667472

102. Chipman, J.: Thermodynamics and phase diagram of the Fe-C system. Metallurgical and Materials Transactions B. 3, 55–64 (1972). https://doi.org/10.1007/BF02680585

103. Rhines, F.N.: Phase Diagrams in Metallurgy: Their Development and Application. McGraw-Hill Book Company, Inc., NY (1956)

104. Elliott, R.: Cast Iron Technology. (1988)

105. Doğan, Ö.N., Hawk, J.A., Tylczak, J.H.: Wear of cast chromium steels with TiC reinforcement. Wear. 250, 462–469 (2001). https://doi.org/10.1016/S0043-1648(01)00635-4

106. Guitar, M.A., Nayak, U.P., Britz, D., Mücklich, F.: The Effect of Thermal Processing and Chemical Composition on Secondary Carbide Precipitation and Hardness in High-Chromium Cast Irons. International Journal of Metalcasting. 14, 755–765 (2020). https://doi.org/10.1007/s40962-020-00407-4

107. Pourasiabi, H., Gates, J.D.: Effects of niobium macro-additions to high chromium white cast iron on microstructure, hardness and abrasive wear behaviour. Mater Des. 212, (2021). https://doi.org/10.1016/j.matdes.2021.110261

108. Tabrett, C.P., Sare, I.R.: Fracture toughness of high-chromium white irons: Influence of cast structure. J Mater Sci. 35, 2069–2077 (2000). https://doi.org/10.1023/A:1004755511214

109. Liu, Q.: Microstructure Evaluation and Wear-Resistant Properties of Ti-alloyed Hypereutectic High Chromium Cast Iron, (2013)

110. Chung, R.J., Tang, X., Li, D.Y., Hinckley, B., Dolman, K.: Effects of titanium addition on microstructure and wear resistance of hypereutectic high chromium cast iron Fe-25wt.%Cr-4wt.%C. Wear. 267, 356–361 (2009). https://doi.org/10.1016/j.wear.2008.12.061

111. Bedolla-Jacuinde, A., Correa, R., Quezada, J.G., Maldonado, C.: Effect of titanium on the as-cast microstructure of a 16%chromium white iron. Materials Science and Engineering A. 398, 297–308 (2005). https://doi.org/10.1016/j.msea.2005.03.072

112. Bedolla-Jacuinde, A., Aguilar, S.L., Hernández, B.: Eutectic modification in a low-chromium white cast iron by a mixture of titanium, rare earths, and

bismuth: I. Effect on microstructure. J Mater Eng Perform. 14, 149–157 (2005). https://doi.org/10.1361/10599490523300

113. Zhi, X., Liu, J., Xing, J., Ma, S.: Effect of cerium modification on microstructure and properties of hypereutectic high chromium cast iron. Materials Science and Engineering A. 603, 98–103 (2014). https://doi.org/10.1016/j.msea.2014.02.080

114. Zhi, X., Xing, J., Fu, H., Xiao, B.: Effect of niobium on the as-cast microstructure of hypereutectic high chromium cast iron. Mater Lett. 62, 857–860 (2008). https://doi.org/10.1016/j.matlet.2007.06.084

115. Wu, X., Xing, J., Fu, H., Zhi, X.: Effect of titanium on the morphology of primary M7C3carbides in hypereutectic high chromium white iron. Materials Science and Engineering A. 457, 180–185 (2007). https://doi.org/10.1016/j.msea.2006.12.006

116. Chotěborský, R., Hrabě, P.: Effect of destabilization treatment on microstructure, hardness and abrasive wear of high chromium hardfacing. Research in Agricultural Engineering. 59, 128–135 (2013). https://doi.org/10.17221/6/2013-rae

117. Wang, Q., Li, X.: Effects of Nb, V, and W on microstructure and abrasion resistance of Fe-Cr-C hardfacing alloys. Welding Journal (Miami, Fla). 89, (2010)

118. Fan, C., Chen, M.C., Chang, C.M., Wu, W.: Microstructure change caused by (Cr,Fe)23C6 carbides in high chromium Fe-Cr-C hardfacing alloys. Surf Coat Technol. 201, 908–912 (2006). https://doi.org/10.1016/j.surfcoat.2006.01.010

119. Zhi, X., Xing, J., Gao, Y., Fu, H., Peng, J., Xiao, B.: Effect of heat treatment on microstructure and mechanical properties of a Ti-bearing hypereutectic high chromium white cast iron. Materials Science and Engineering A. 487, 171–179 (2008). https://doi.org/10.1016/j.msea.2007.10.009

120. Qi, X., Jia, Z., Yang, Q., Yang, Y.: Effects of vanadium additive on structure property and tribological performance of high chromium cast iron hardfacing metal. Surf Coat Technol. 205, 5510–5514 (2011). https://doi.org/10.1016/j.surfcoat.2011.06.027

121. Chen, Z., Fu, H., Wang, F., Yuan, N., Lin, J.: Effect of Si on Microstructure and Wear Resistance of Hypereutectic High-Chromium Cast Iron. J Mater Eng Perform. (2022). https://doi.org/10.1007/s11665-022-07475-z

122. Li, P., Yang, Y., Shen, D., Gong, M., Tian, C., Tong, W.: Mechanical behavior and microstructure of hypereutectic high chromium cast iron: The combined effects of tungsten, manganese and molybdenum additions. Journal of Materials Research and Technology. 9, 5735–5748 (2020). https://doi.org/10.1016/j.jmrt.2020.03.098

123. Jain, A.S., Mustafa, M.I., Sazili, M.I.I.M., Chang, H., Zhang, M.X.: Effects of destabilization and tempering on microstructure and mechanical properties of a hypereutectic high-chromium cast iron. J Mater Sci. 57, 15581–15597 (2022). https://doi.org/10.1007/s10853-022-07583-0

124. Liu, F., Jiang, Y., Xiao, H., Tan, J.: Study on fragmentation and dissolution behavior of carbide in a hot-rolled hypereutectic high chromium cast iron. J Alloys Compd. 618, 380–385 (2015). https://doi.org/10.1016/j.jallcom.2014.07.131

125. Tang, X.H., Chung, R., Li, D.Y., Hinckley, B., Dolman, K.: Variations in microstructure of high chromium cast irons and resultant changes in resistance to wear, corrosion and corrosive wear. Wear. 267, 116–121 (2009). https://doi.org/10.1016/j.wear.2008.11.025

126. Zhang, M.X., Kelly, P.M., Gates, J.D.: The effect of heat treatment on the toughness, hardness and microstructure of low carbon white cast irons. J Mater Sci. 36, 3865–3875 (2001). https://doi.org/10.1023/A:1017949600733

127. Hanlon, D.N., Rainforth, W.M., Sellars, C.M.: The rolling/sliding wear response of conventionally processed and spray formed high chromium content cast iron at ambient and elevated temperature. Wear. 225–229, 587–599 (1999). https://doi.org/10.1016/S0043-1648(99)00053-8

128. Hanlon, D.N., Rainforth, W.M., Sellars, C.M.: The effect of spray forming on the microstructure and properties of a high chromium white cast iron. J Mater Sci. 34, 2291–2301 (1999). https://doi.org/10.1023/A:1004573524282

129. Radulovic, M., Fiset, M., Peev, K., Tomovic, M.: The influence of vanadium on fracture toughness and abrasion resistance in high chromium white cast irons. J Mater Sci. 29, 5085–5094 (1994). https://doi.org/10.1007/BF01151101

130. Kopyciński, D., Guzik, E., Siekaniec, D., Szczęsny, A.: The effect of addition of titanium on the structure and properties of high chromium cast iron. Archives of Foundry Engineering. 15, 35–38 (2015). https://doi.org/10.1515/afe-2015-0055

131. Ikeda, M., Umeda, T., Tong, C.P., Suzuki, T., Niwa, N., Kato, O.: Effect of Molybdenum Addition on Solidification Structure, Mechanical Properties and Wear Resistivity of High Chromium Cast Irons. ISIJ International. 32, 1157–1162 (1992). https://doi.org/10.2355/ISIJINTERNATIONAL.32.1157

132. Imurai, S., Thanachayanont, C., Pearce, J.T.H., Tsuda, K., Chairuangsri, T.: Effects of Mo on microstructure of as-cast 28 wt.% Cr-2.6 wt.% C-(0-10) wt.% Mo irons. Mater Charact. 90, 99–112 (2014). https://doi.org/10.1016/j.matchar.2014.01.014

133. Imurai, S., Thanachayanont, C., Pearce, J.T.H., Tsuda, K., Chairuangsri, T.: Effects of W on microstructure of as-cast 28 wt.%Cr-2.6 wt.%C-(0-10)wt.%W irons. Mater Charact. 99, 52–60 (2015). https://doi.org/10.1016/j.matchar.2014.11.012

134. Lv, Y., Sun, Y., Zhao, J., Yu, G., Shen, J., Hu, S.: Effect of tungsten on microstructure and properties of high chromium cast iron. Mater Des. 39, 303–308 (2012). https://doi.org/10.1016/j.matdes.2012.02.048

135. Mousavi Anijdan, S.H., Bahrami, A., Varahram, N., Davami, P.: Effects of tungsten on erosion-corrosion behavior of high chromium white cast iron. Materials Science and Engineering A. 454–455, 623–628 (2007). https://doi.org/10.1016/j.msea.2006.11.128

136. He-Xing, C., Zhe-Chuan, C., Jin-Cai, L., Huai-Tao, L.: Effect of niobium on wear resistance of 15%Cr white cast iron. Wear. 166, 197–201 (1993). https://doi.org/10.1016/0043-1648(93)90262-K

137. Pourasiabi, H., Gates, J.D.: Effects of matrix chromium-to-carbon ratio on high-stress abrasive wear behavior of high chromium white cast irons dual-reinforced by niobium carbides. Tribol Int. 167, 107350 (2022). https://doi.org/10.1016/j.triboint.2021.107350

138. Junsamoot, R., Inthidech, S., Sriprateep, K.: Effect of Vanadium on Subcritical Heat Treatment Behavior of Hypoeutectic 16 wt % Cr Cast Iron containing 2 wt % Mo. Journal of Metals, Materials and Minerals. 21, 13–18 (2011)

139. Inthidech, S., Matsubara, Y.: Effect of Alloying Elements on Variation of Micro-Hardness during Heat Treatment of Hypoeutectic High Chromium Cast Iron. Mater Trans. 49, 2322–2330 (2008). https://doi.org/10.2320/matertrans.MRA2008079

140. Fusheng, H., Chaochang, W.: Modifying high Cr–Mn cast iron with boron and rare earth–Si alloy. Materials Science and Technology. 5, 918–924 (1989). https://doi.org/10.1179/mst.1989.5.9.918

141. Purba, R.H., Shimizu, K., Kusumoto, K., Gaqi, Y.: Comparison of Three-Body Abrasion Behaviors of High-Cr-Mo- and High-Cr-Based Multicomponent

White Cast Irons. J Mater Eng Perform. (2022). https://doi.org/10.1007/s11665-022-07360-9

142. Purba, R.H., Shimizu, K., Kusumoto, K., Gaqi, Y., Huq, M.J.: Tribological Characteristics of High-Chromium Based Multi-Component White Cast Irons. Crystals (Basel). 12, (2022). https://doi.org/10.3390/cryst12101488

143. Bedolla-Jacuinde, A.: Microstructure of vanadium-, niobium- and titanium-alloyed high-chromium white cast irons. International Journal of Cast Metals Research. 13, 343–361 (2001). https://doi.org/10.1080/13640461.2001.11819416

144. Bedolla-Jacuinde, A., Guerra, F. V., Mejía, I., Zuno-Silva, J., Rainforth, M.: Abrasive wear of V-Nb-Ti alloyed high-chromium white irons. Wear. 332–333, 1006–1011 (2015). https://doi.org/10.1016/j.wear.2015.01.049

145. Carpenter, S.D., Carpenter, D., Pearce, J.T.H.: XRD and electron microscope study of a heat treated 26.6% chromium white iron microstructure. Mater Chem Phys. 101, 49–55 (2007). https://doi.org/10.1016/j.matchemphys.2006.02.013

146. Kopyciński, D., Guzik, E., Siekaniec, D., Szczęsny, A.: Analysis of the High Chromium Cast Iron Microstructure after the Heat Treatment. Archives of Foundry Engineering. 14, 43–46 (2014). https://doi.org/10.2478/afe-2014-0059

147. Abdel-Aziz, Kh., El-Shennawy, M., Omar, A.A.: Microstructural Characteristics and Mechanical Properties of Heat Treated High-Cr White Cast Iron Alloys. International Journal of Applied Engineering Research. 12, 4675–4686 (2017)

148. Guo, Z., Xiao, F., Lu, S., Li, H., Liao, B.: Effects of Heat-Treatment on the Microstructure and Wear Resistance of a High-Chromium Cast Iron for Rolls. Advances in Materials Science and Engineering. 2016, 1–7 (2016). https://doi.org/10.1155/2016/9807685

149. Lai, J.P., Pan, Q.L., Wang, Z.B., Cui, H.R., Wang, X.D., Gao, Z.Z.: Effects of Destabilization Temperature on the Microstructure and Mechanical Properties of High Chromium Cast Iron. J Mater Eng Perform. 26, 4667–4675 (2017). https://doi.org/10.1007/s11665-017-2943-9

150. Wang, J., Li, C., Liu, H., Yang, H., Shen, B., Gao, S., Huang, S.: The precipitation and transformation of secondary carbides in a high chromium cast iron. Mater Charact. 56, 73–78 (2006). https://doi.org/10.1016/j.matchar.2005.10.002

151. Gorelik, S.S., Letyuk, L.M., Seleznev, A. v., Chomova, N.G.: Effect of heat treatment on the properties of high-chromium cast iron. Metal Science and Heat Treatment. 13, 69–71 (1971). https://doi.org/10.1007/BF00663805

152. Gahr, K.H. Zum, Doane, D. V.: Optimizing fracture toughness and abrasion resistance in white cast irons. Metallurgical Transactions A. 11, 613–620 (1980). https://doi.org/10.1007/BF02670698

153. Filipovic, M., Kamberovic, Z., Korac, M., Gavrilovski, M.: Microstructure and mechanical properties of Fe–Cr–C–Nb white cast irons. Mater Des. 47, 41–48 (2013). https://doi.org/10.1016/j.matdes.2012.12.034

154. Guitar, M.A., Scheid, A., Britz, D., Mücklich, F.: Evaluation of the etching process for analysis of secondary carbides in HCCI by optical and confocal laser microscopy. Praktische Metallographie/Practical Metallography. 56, (2019). https://doi.org/10.3139/147.110570

155. Guitar, M.A., Scheid, A., Britz, D., Mücklich, F.: Evaluation of the etching process for analysis of secondary carbides in HCCI by optical and confocal laser microscopy. Praktische Metallographie/Practical Metallography. 56, 246–261 (2019). https://doi.org/10.3139/147.110570

156. Wang, J., Xiong, J., Fan, H., Yang, H.-S., Liu, H.-H., Shen, B.-L.: Effects of high temperature and cryogenic treatment on the microstructure and abrasion

resistance of a high chromium cast iron. J Mater Process Technol. 209, 3236–3240 (2009). https://doi.org/10.1016/j.jmatprotec.2008.07.035

157. Hann, S.K., Gates, J.D.: A transformation toughening white cast iron. J Mater Sci. 32, 1249–1259 (1997). https://doi.org/10.1023/A:1018544204267

158. Zhao, Z., Cao, Y., Wan, X., Li, J., Li, G.: Effect of Cooling Rate on Carbide Characteristics of the High Vanadium High-speed Steel. ISIJ International. 62, ISIJINT-2021-244 (2022). https://doi.org/10.2355/isijinternational.ISIJINT-2021-244

159. Benz, R., Elliott, J.F., Chipman, J.: THERMODYNAMICS OF THE CARBIDES IN THE SYSTEM Fe-Cr-C. Metall Trans. 5, 2235–2240 (1974). https://doi.org/10.1007/BF02643938

160. Miyahara, H., Bravo, S.V., Yamamoto, K., Ogi, K.: Solute Concentration and Carbides Formation for Steel Milling Rolls. ISIJ International. 49, 1075–1079 (2009). https://doi.org/10.2355/isijinternational.49.1075

161. Chen, X., Li, Y.: Effect of heat treatment on microstructure and mechanical properties of high boron white cast iron. Materials Science and Engineering A. 528, 770–775 (2010). https://doi.org/10.1016/j.msea.2010.09.092

162. Powell, G.L.F., Bee, J. v.: Secondary carbide precipitation in an 18 wt %Cr-1 wt % Mo white iron. J Mater Sci. 31, 707–711 (1996). https://doi.org/10.1007/BF00367889

163. ASM International: ASM Handbook Volume 4 - Heat Treatment. ASM International, Ohio (1991)

164. Karantzalis, A.E., Lekatou, A., Kapoglou, A., Mavros, H., Dracopoulos, V.: Phase transformations and microstructural observations during subcritical heat treatments of a high-chromium cast iron. J Mater Eng Perform. 21, 1030–1039 (2012). https://doi.org/10.1007/s11665-011-9995-z

165. Bale, C.W., Bélisle, E., Chartrand, P., Decterov, S.A., Eriksson, G., Gheribi, A.E., Hack, K., Jung, I.-H., Kang, Y.-B., Melançon, J., Pelton, A.D., Petersen, S., Robelin, C., Sangster, J., Spencer, P., van Ende, M.-A.: FactSage thermochemical software and databases, 2010–2016. Calphad. 54, 35–53 (2016). https://doi.org/10.1016/j.calphad.2016.05.002

166. Kozeschnik, E., Buchmayr, B.: Matcalc - a simulation tool for multicomponent thermodynamics, diffusion and phase transformations. In: Mathematical Modelling of Weld Phenomena. pp. 349–361. . (2001)

167. Chen, S.-L., Daniel, S., Zhang, F., Chang, Y.A., Yan, X.-Y., Xie, F.-Y., Schmid-Fetzer, R., Oates, W.A.: The PANDAT software package and its applications. Calphad. 26, 175–188 (2002). https://doi.org/10.1016/S0364-5916(02)00034-2

168. Andersson, J.O., Helander, T., Höglund, L., Shi, P., Sundman, B.: Thermo-Calc & DICTRA, computational tools for materials science. CALPHAD. 26, 273–312 (2002). https://doi.org/10.1016/S0364-5916(02)00037-8

169. ASM International: Volume 3 - Alloy Phase Diagrams. (2018)

170. Kroupa, A.: Modelling of phase diagrams and thermodynamic properties using Calphad method - Development of thermodynamic databases. Comput Mater Sci. 66, 3–13 (2013). https://doi.org/10.1016/j.commatsci.2012.02.003

171. Li, D., Liu, L., Zhang, Y., Ye, C., Ren, X., Yang, Y., Yang, Q.: Phase diagram calculation of high chromium cast irons and influence of its chemical composition. Mater Des. 30, 340–345 (2009). https://doi.org/10.1016/j.matdes.2008.04.061

172. Albertin, E., Beneduce, F., Matsumoto, M., Teixeira, I.: Optimizing heat treatment and wear resistance of high chromium cast irons using computational thermodynamics. Wear. 271, 1813–1818 (2011). https://doi.org/10.1016/j.wear.2011.01.079

173. Akyildiz, Ö., Candemir, D., Yildirim, H.: Simulation of Phase Equilibria in High Chromium White Cast Irons. Uludağ University Journal of The Faculty of Engineering. 23, 179–190 (2018). https://doi.org/10.17482/uumfd.333701

174. Archard, J.F.: Contact and rubbing of flat surfaces. J Appl Phys. 24, 981–988 (1953). https://doi.org/10.1063/1.1721448

175. Avery, H.S.: The measurement of wear resistance. Wear. 4, 427–449 (1961). https://doi.org/10.1016/0043-1648(61)90301-5

176. Doğan, Ö.N., Hawk, J.A., Laird, G.: Solidification structure and abrasion resistance of high chromium white irons. Metall Mater Trans A Phys Metall Mater Sci. 28, 1315–1328 (1997). https://doi.org/10.1007/s11661-997-0267-3

177. Fulcher, J.K., Kosel, T.H., Fiore, N.F.: The effect of carbide volume fraction on the low stress abrasion resistance of high Cr-Mo white cast irons. Wear. 84, 313–325 (1983). https://doi.org/10.1016/0043-1648(83)90272-7

178. Rodenburg, C., Rainforth, W.M.: A quantitative analysis of the influence of carbides size distributions on wear behaviour of high-speed steel in dry rolling/sliding contact. Acta Mater. 55, 2443–2454 (2007). https://doi.org/10.1016/j.actamat.2006.11.039

179. Mercado, V.H., Mejía, I., Bedolla-Jacuinde, A.: Effect of Load and Sliding Rate on the Wear Behavior of Ti-Containing TWIP Steel. J Mater Eng Perform. 26, 2213–2225 (2017). https://doi.org/10.1007/s11665-017-2635-5

180. Todaka, T., Shimizu, K., Kusumoto, K., Purba, R.H., Gaqi, Y.: Effect of Carbon Content on Three-body Abrasive Wear Characteristics of 28Cr-3Ni Cast Alloys. ISIJ International. 61, 2274–2283 (2021). https://doi.org/10.2355/isijinternational.isijint-2021-099

181. Ruff, A.W.: Deformation studies at sliding wear tracks in iron. Wear. 40, 59–74 (1976). https://doi.org/10.1016/0043-1648(76)90018-1

182. Grützmacher, P.G., Rammacher, S., Rathmann, D., Motz, C., Mücklich, F., Suarez, S.: Interplay between microstructural evolution and tribo-chemistry during dry sliding of metals. Friction. 7, 637–650 (2019). https://doi.org/10.1007/s40544-019-0259-5

183. Dautzenberg, J.H., Zaat, J.H.: Quantitative determination of deformation by sliding wear. Wear. 23, 9–19 (1973). https://doi.org/10.1016/0043-1648(73)90036-7

184. Kirk, J.A., Swanson, T.D.: Subsurface effects during sliding wear. Wear. 35, 63–67 (1975). https://doi.org/10.1016/0043-1648(75)90142-8

185. Penagos, J.J., Ono, F., Albertin, E., Sinatora, A.: Structure refinement effect on two and three-body abrasion resistance of high chromium cast irons. Wear. 340–341, 19–24 (2015). https://doi.org/10.1016/j.wear.2015.03.020

186. Matsuo, T.T., Kiminami, C.S., Fo, W.J.B., Bolfarini, C.: Sliding wear of spray-formed high-chromium white cast iron alloys. Wear. 259, 445–452 (2005). https://doi.org/10.1016/j.wear.2005.01.021

187. Sun, T., Song, R. bo, Wang, X., Deng, P., Wu, C. jing: Abrasive wear behavior and mechanism of high chromium cast iron. Journal of Iron and Steel Research International. 22, 84–90 (2015). https://doi.org/10.1016/S1006-706X(15)60014-0

188. Nayak, U.P., Guitar, M.A., Mücklich, F.: Evaluation of etching process parameter optimization in the objective specific microstructural characterization of as-cast and heat treated HCCI alloy. Practical Metallography. 57, 688–713 (2020). https://doi.org/10.3139/147.110682

189. Schindelin, J., Arganda-Carreras, I., Frise, E., Kaynig, V., Longair, M., Pietzsch, T., Preibisch, S., Rueden, C., Saalfeld, S., Schmid, B., Tinevez, J.Y., White, D.J., Hartenstein, V., Eliceiri, K., Tomancak, P., Cardona, A.: Fiji: An

open-source platform for biological-image analysis. Nat Methods. 9, 676–682 (2012). https://doi.org/10.1038/nmeth.2019

190. Nayak, U.P., Müller, M., Britz, D., Guitar, M.A., Mücklich, F.: Image Processing using Open Source Tools and their Implementation in the Analysis of Complex Microstructures. Practical Metallography. 58, 484–506 (2021). https://doi.org/10.1515/pm-2021-0039

191. Rietveld, H.M.: A profile refinement method for nuclear and magnetic structures. J Appl Crystallogr. 2, 65–71 (1969). https://doi.org/10.1107/s0021889869006558

192. Lutterotti, L.: Total pattern fitting for the combined size-strain-stress-texture determination in thin film diffraction. Nucl Instrum Methods Phys Res B. 268, 334–340 (2010). https://doi.org/10.1016/j.nimb.2009.09.053

193. Nayak, U.P., Mücklich, F., Guitar, M.A.: Time-Dependant Microstructural Evolution and Tribological Behaviour of a 26 wt% Cr White Cast Iron Subjected to a Destabilization Heat Treatment. Metals and Materials International. (2022). https://doi.org/10.1007/s12540-022-01276-8

194. Klinger, M.: More features, more tools, more CrysTBox. J Appl Crystallogr. 50, 1226–1234 (2017). https://doi.org/10.1107/S1600576717006793

195. Ayache, J., Beaunier, L., Boumendil, J., Ehret, G., Laub, D.: Sample Preparation Handbook for Transmission Electron Microscopy. Springer New York (2010)

196. Thompson, K., Lawrence, D., Larson, D.J., Olson, J.D., Kelly, T.F., Gorman, B.: In situ site-specific specimen preparation for atom probe tomography. Ultramicroscopy. 107, 131–139 (2007). https://doi.org/10.1016/J.ULTRAMIC.2006.06.008

197. Nayak, U.P., Guitar, M.A., Mücklich, F.: A comparative study on the influence of chromium on the phase fraction and elemental distribution in

as-cast high chromium cast irons: Simulation vs. experimentation. Metals (Basel). 10, (2020). https://doi.org/10.3390/met10010030

198. Nayak, U.P., Schäfer, F., Mücklich, F., Guitar, M.A.: Wear Induced Sub-surface Deformation Characteristics of a 26 Wt% Cr White Cast Iron Subjected to a Destabilization Heat Treatment. Tribol Lett. 71, (2023). https://doi.org/10.1007/s11249-022-01683-3

199. Oliver, W.C., Pharr, G.M.: An improved technique for determining hardness and elastic modulus using load and displacement sensing indentation experiments. Journal of Materials Research 1992 7:6. 7, 1564–1583 (2011). https://doi.org/10.1557/JMR.1992.1564

200. Oliver, W.C., Pharr, G.M.: Measurement of hardness and elastic modulus by instrumented indentation: Advances in understanding and refinements to methodology. Journal of Materials Research 2004 19:1. 19, 3–20 (2004). https://doi.org/10.1557/JMR.2004.19.1.3

201. Nayak, U.P., Suárez, S., Pesnel, V., Mücklich, F., Guitar, M.A.: Load dependent microstructural evolution in an as-cast 26% Cr high chromium cast iron during unlubricated sliding. Friction. 10, 1258–1275 (2022). https://doi.org/10.1007/s40544-021-0553-x

202. Nayak, U.P., Webel, J., Pesnel, V., Mücklich, F., Guitar, M.A.: Development of a Protective Coating for Evaluating the Sub-surface Microstructure of a Worn Material. Tribol Lett. 69, 1–13 (2021). https://doi.org/10.1007/s11249-021-01541-8

203. Fischer-Cripps, A.C.: The IBIS handbook of nanoindentation. Fischer-Cripps Laboratories, Forestville, NSW, Australia (2009)

204. Greenwood, J.A., Williamson, J.B.P.: Contact of nominally flat surfaces. Proceedings of the Royal Society of London. A. 295, 300–319 (1966). https://doi.org/10.1098/rspa.1966.0242

205. Jackson, R.L., Green, I.: A finite element study of elasto-plastic hemispherical contact against a rigid flat. J Tribol. 127, 343–354 (2005). https://doi.org/10.1115/1.1866166

206. Tabor, D.: The Hardness of Metals. Claredon Press, Oxford (UK) (1951)

207. Kugel Pompel: Datenblatt | Data sheet, https://www.kugelpompel.at/upload/2312763_Datenblatt Aluminiumoxidkugel V1.01.pdf

208. Auerkari, P.: Mechanical and physical properties of engineering alumina ceramics. Technical Research Centre of Finland, Espoo (1996)

209. Chen, L., Persson, J., Ståhl, J.E., Zhou, J.M.: Nano-Scratching resistance of high-chromium white cast iron and its correlation with wear of cBN tool in machining. Journal of Superhard Materials. 39, 365–372 (2017). https://doi.org/10.3103/S1063457617050094

210. Hutchings, I.M.: Tribology: Friction and Wear of Engineering Materials. Butterworth-Heinemann, Oxford (UK) (1992)

211. Greenwood, J.A., Tripp, J.H.: The elastic contact of rough spheres. J Appl Mech. 34, 153–159 (1967). https://doi.org/10.1115/1.3607616

212. Fischer-Cripps, A.C.: Introduction to Contact Mechanics. Springer US, New York (USA) (2006)

213. Marín, E.: Characteristic dimensions for heat transfer. Lat. Am. J. Phys. Educ. 4, 56–60 (2010)

214. Manasijević, D., Radović, Ž., Štrbac, N., Balanović, L., Stamenković, U., Gorgievski, M., Minić, D., Premović, M., Grgurić, T.H., Tadić, N.: Study of microstructure and thermal properties of as-cast high carbon and high chromium tool steel. Metallurgical and Materials Engineering. 25, 1–10 (2019). https://doi.org/10.30544/392

215. Pearce, J.T.H.: The use of transmission electron microscopy to study the effects of abrasive wear on the matrix structure of a high chromium cast iron. Wear. 89, 333–344 (1983). https://doi.org/10.1016/0043-1648(83)90154-0

LIST OF FIGURES

APPENDIX A

Analysing the nanoindentation curve using the Oliver-Pharr method

Nanoindentation is a technique that involves applying loads in the sub-millinewton range (<1 mN) to obtain indent sizes in the sub-micron range. It is conventionally performed using instrumented indentation wherein both loading and unloading responses are recorded in the form of a load-displacement (P-h) curve. The three-sided Berkovich indenter, which has an apex angle of 142°, is the most frequently used geometry for nanoindentation testing. Elastic modulus and hardness are two crucial physical properties of materials, and the P-h curve can be analysed to calculate them without the need for direct measurement of the contact area (A_c). However, the curve needs to be corrected for contact depth determination, instrument compliance and indenter tip shape (area function) before analysis. A schematic P-h curve during a typical loading-unloading nanoindentation test is represented in *Figure 13*.

Oliver and Pharr proposed a standard method for analysing nanoindentation data in 1992, which is based on the Hertz theory for elastic contact. The method involves using the slope of the tangent to the unloading data at maximum load, to calculate the tip-sample contact size at the onset of unloading.

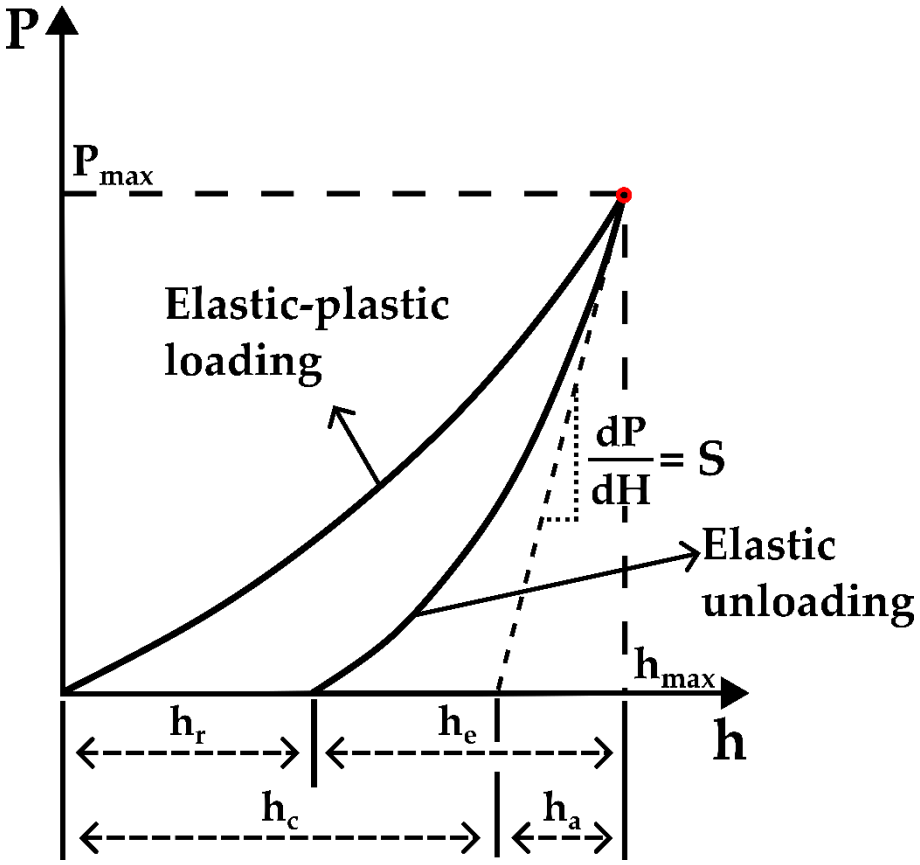

Figure 13: Schematic load-displacement (P-h) curve during nanoindentation testing. Redrawn from [203].

In the nanoindentation situation, the indenter exerts a pressure distribution over the tip–sample contact region and based on the results of Hertzian theory, we obtain the following results.

$$a = \left(\frac{3PR}{4E_r}\right)^{1/3} \qquad \text{A. 1}$$

$$h = \frac{a^2}{R} = \left(\frac{9P^2}{16RE_r^2}\right)^{1/3} \qquad \text{A. 2}$$

In Equations A. 1 and A. 2, a is the contact radius, P is the applied load, R is the effective radius, E_r is the reduced indentation modulus of the tip-sample contact and h is the relative displacement of the tip into the sample surface. If R_1, E_1 and ν_1, and R_2, E_2 and ν_2 represent the radius of curvature, elastic modulus and

Poisson's ratio of the tip and sample, respectively, then R and E_r can be expressed as Equation A. 3.

$$\frac{1}{R} = \frac{1}{R_1} + \frac{1}{R_2} \; ; \; \frac{1}{E_r} = \frac{1 - \nu_1^2}{E_1} + \frac{1 - \nu_2^2}{E_2} \qquad \text{A. 3}$$

A new Berkovich diamond indenter should have a tip radius, R_1 ~ 50 nm, and for a flat sample surface, $R_2 \to \infty$. Moreover, considering the standard values of E_1 (1140 GPa) and ν_1 (0.07) for diamond, if E_r is known, then the elastic modulus of the sample can be obtained.

The contact stiffness, S between two elastic spheres is defined as $S = dP/dh$, and from Equations A. 1 and A. 2, we get:

$$E_r = \frac{\sqrt{\pi}}{2} \frac{S}{\sqrt{A_c}} \qquad \text{A. 4}$$

Where $A_c = \pi a^2$ is the projected area of the tip-sample contact circle (assuming a spherical indenter). The tip-shape function for an ideal Berkovich tip is $A_c = 24.5 {h_c}^2$. Equation A. 4 suggests that if S and A_c are measured, E_r can be estimated. Moreover, from the knowledge of A_c we can estimate the hardness as expressed in Equation A. 5.

$$H = \frac{P_{max}}{A_c} \qquad \text{A. 5}$$

APPENDIX B

Theoretical description of the EBSD parameters

The utilization of misorientation profile (MP) analysis in EBSD aids in determining the orientational difference between two regions. Point-to-point MP analysis examines the variation in orientation between two adjacent points, while point-to-origin profile assesses the variation relative to a common point.

Kernel average misorientation (KAM) analysis is used to determine the average misorientation by evaluating the orientational difference between a central point of a grain and its nearby points within a defined kernel. In other words, it calculates the misorientation between a reference point and its nearest neighbours. Its value is highly dependent on the number of adjacent neighbours selected for the calculation i.e., 1st, 2nd, 3rd neighbour, and so on.

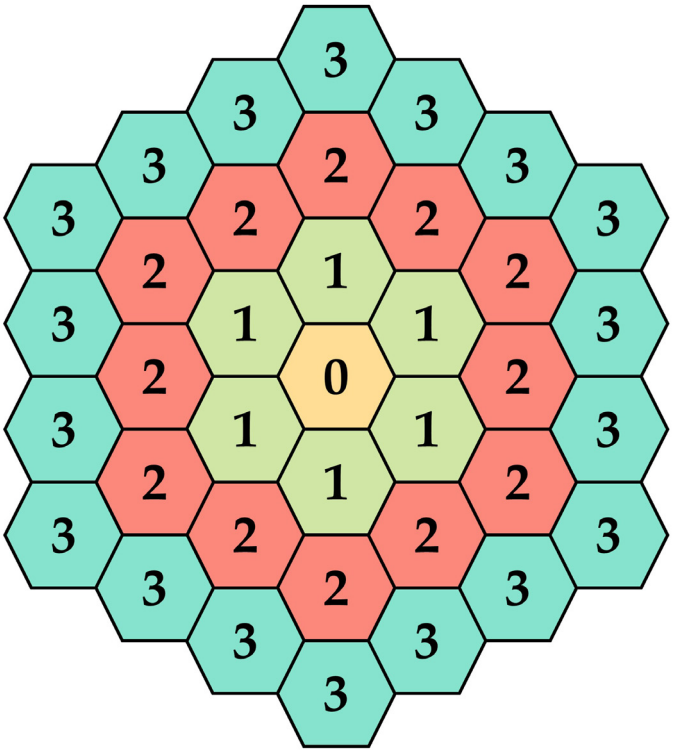

Figure 14: Schematic of the pixels arranged in a hexagonal grid of a grain. 0 represents the centre of the kernel with 1, 2 and 3 indicating the 1st, 2nd and 3rd neighbour, respectively.

If we define the orientation at the pixel position (a, b) as $o_{a,b}$, and N (a, b) as the set of all neighbouring pixels, the kernel average misorientation ($KAM_{a,b}$) at pixel position (a, b) can be expressed as Equation B. 1.

$$KAM_{a,b} = \frac{1}{|N(a,b)|} \sum_{(c,d)\in N(a,b)} \theta(o_{a,b}, o_{c,d}) \qquad \text{B. 1}$$

where $|N(a,b)|$ is the number of all the neighbouring pixels and $\theta(o_{a,b}, o_{c,d})$ is the misorientation angle between the orientation $o_{a,b}$ and the neighbouring orientation $o_{c,d}$. In Figure 14, point 0 represents the centre of the kernel with the 1st, 2nd and 3rd neighbours indicated as 1, 2 and 3, respectively.

Grain reference orientation deviation (GROD) is the misorientation between a user-defined reference value and each pixel within the grain. The reference value can either be the average orientation of the grain or the orientation of the grain with the lowest KAM value.

APPENDIX C

Determination of critical load (P_c) using Hertzian contact theory

Paper *V* adopted a methodology that involved the use of Hertzian contact theory to compute the critical load (P_c), as opposed to randomly selecting a load. The value of the critical load i.e., the load at which the outset of plastic deformation takes place in the material, was determined using Equations C. 1 and C. 2 [204, 205]. It is important to mention that the approximations made consider the properties of the material that fails first. In this case, since the M_7C_3 carbide is harder than the matrix, the latter will yield first. As a result, the P_c calculations were based on the properties of the austenitic matrix and the alumina ball.

$$P_c = \frac{4}{3}\left(\frac{R}{E'}\right)^2 \left(\frac{C}{2}\pi \cdot S_y\right)^3 \quad \text{C. 1}$$

$$\frac{1}{E'} = \frac{1-\nu_1^2}{E_1} + \frac{1-\nu_2^2}{E_2} \;\; ; \;\; C = 1.295\, exp\,(0.736\nu) \quad \text{C. 2}$$

In Equations C. 1 and C. 2, P_c is the critical contact force at yielding (N), R is the radius of the alumina ball (m), E' is the equivalent elastic modulus (GPa), E_1 and E_2 represent the elastic modulus of the alumina ball and the austenitic matrix, respectively, ν_1 and ν_2 are the Poisson's ratio of the ball and the matrix, respectively, C is the yield strength coefficient and S_y is the yield strength of the matrix. The yield strength of the matrix was determined from the hardness value (H) using a correction to the Tabor relationship ($S_y = H/2.84$) [206]. The values of the parameters used in the Equations C. 1 and C. 2 are given in *Table 4*.

Table 4: Parameters used for the critical load calculations.

Parameter	Value
R (m)	1.50×10^{-3}
E_1 (Pa) [207]	3.65×10^{11}
E_2 (Pa)	2.38×10^{11}
ν_1 [208]	0.22
ν_2 [79]	0.28
E′ (Pa)	1.54×10^{11}
H (Pa)	5.60×10^{9}
S_y (Pa)	1.97×10^{9}
C	1.5914

The P_C was found out to be ~ 15 N and accordingly, three loads (P), 5 N, 15 N and 20 N, were chosen for the wear tests.

APPENDIX D

Flash temperature calculations

Considering the absence of external lubrication in the study conducted in Paper ***V***, the supposed rise in temperature at the contact interface may engender some structural and/or phase transformations [209]. During the wear test, as the Al_2O_3 ball moves over the sample surface, heat is continuously generated and dissipated over the contact area. The rate of heat generated per unit area, q, can be calculated by considering a simplified model proposed by Hutchings et. al [210].

$$q = \frac{\mu P v}{\pi a^2} \qquad \text{D. 1}$$

In Equation D. 1, μ is the coefficient of friction, P is the applied load, v is the velocity and a is the contact radius. The contact radius was determined using Equation D. 2 by assuming a Hertzian contact between the spherical ball and the sample surface, both of which can be considered as nominally flat surfaces [211, 212]. The values of the contact radius for the applied loads are given in Table 5.

$$a = \sqrt[3]{0.75 \times \frac{P \times R}{E'}} \qquad \text{D. 2}$$

Table 5: Value of the contact radius (a) for varying loads (P).

Load, P (N)	Contact radius, a (μm)
20	52.6
15	47.9
5	33.2

Assuming a stationary heat source, the rise in temperature at the contact can be simplistically related to the heat generated at the surface, q, the contact radius, a, and the thermal conductivity, σ, as expressed in Equation D. 3 [210]. In the current study, as the ball traverses over the surface, it can be considered as a moving heat

source and the incremental rise in temperature at the surface, ΔT_f^S (owing to the heat conduction), can be expressed using Equation D. 4.

$$\Delta T_f = \frac{q.a}{\sigma} \quad \text{D. 3}$$

$$\Delta T_f^S = \frac{2.\mu.P.v}{\pi a[2\sigma_1 + \sigma_2\sqrt{4+\pi J}]} \quad \text{D. 4}$$

In Equation D. 4, $\sigma_1$and σ_2 represent the thermal conductivities of the Al_2O_3 ball and the austenitic matrix, respectively. *J* is a dimensionless quantity known as the Péclet number, signifying the depth of heat diffusion into the surface which can be expressed using Equation D. 5. It should be noted that *J* values close to 1 indicate that the frictional heating is concentrated at the surface [210]. κ_2 represents the thermal diffusivity of the sample in Equation D. 5.

$$J = \frac{v.a}{2\kappa_2} \quad \text{D. 5}$$

Finally, the distance travelled by the diffused heat inside the sample for a given time, *t*, i.e., the characteristic distance, *x* is calculated using Equation D. 6 [213]. The values of the parameters used to determine the flash temperature and associated variables are presented in Table 6.

$$x = \sqrt{4.\kappa_2.t} \quad \text{D. 6}$$

Table 6: Value of the parameters used to determine the peak flash temperature.

Parameter	Value
Coefficient of friction	0.4
Thermal conductivity of Al_2O_3, σ_1 (W/m. K) [207]	31
Thermal conductivity of the sample, σ_2 (W/m. K) [214]	25
Density of the sample (kg/m^3)	7341
Specific heat capacity of the sample, C_P (J/kg. K) [214]	520
Thermal diffusivity of the sample, κ_2 (m^2/s)	6.5491×10^{-6}
Péclet number, J	0.08

The peak flash temperature at the surface of the sample, ΔT_f^S was calculated for each load and it was observed that the flash temperature decreased with decreasing load, which, is intuitive. The maximum load used in this study (20 N) produced an interfacial temperature rise of about 17 K, which can be considered too low for any thermally induced structural changes and/or phase transformations to occur [215]. Moreover, the time needed for the heat to diffuse to a depth equal to the contact radius (52.6 μm) was estimated to be about 0.1 ms and combining this with the low value of the Péclet number, it can be deduced that the heat has a lot of time to dissipate, and no heat accumulation takes place at the surface. Therefore, it can be conclusively stated that thermal effects emanating during the dry-sliding tests are negligible and the microstructural changes occurring around the wear track are mainly mechanically induced.